University of Kent

School of Biosciences
Division of Natural Sciences

Development of Biophysical and Chemical Methods for Investigations into the Polymorphic Nature of Amyloid Fibril Structures

Thesis submitted in partial fulfilment of the requirements for
the degree of Doctor of Philosophy in Biochemistry

by

Liisa Lutter

October 2021
Number of pages: 358

ABSTRACT

Protein misfolding and self-assembly into the amyloid state is associated with a range of neurodegenerative diseases. These diseases affect an increasing number of patients every year and have significant detrimental human and economic impacts. Despite sharing the cross-β core architecture, amyloid fibrils exhibit polymorphism, which is likely to underpin the relationship between structure, function, and dysfunction. In this work, the nature of amyloid fibril structural polymorphism is investigated using chemical conjugation and biophysical methods. Amyloid-DNA conjugates were made, with the aim of altering amyloid suprastructure and thus modulate the transmission of amyloid between cells, as well as develop modular nanomaterials. A modified variant of the Sup35 prion protein was used as a model system to which complementary DNA strands or a nucleobase analogue were conjugated via thiol-maleimide reactions. Atomic force microscopy, a nanoscale imaging technique, was used to characterise the modified Sup35 fibrils. Furthermore, AFM image analysis methodologies were advanced through the development of image deconvolution and 3D reconstruction algorithms. This approach led to both *in silico* correction of an imaging artefact and an approximate doubling of local resolution. The AFM analysis approach was further improved by integrating data from cryo-EM with AFM 3D envelopes, in a developed comparative morphometrics approach. This was demonstrated on dGAE tau amyloid and cryo-EM density maps of tau fibrils from various tauopathies, as well as heparin-induced *in vitro* formed fibrils, showing that *in vitro* self-assembled dGAE is a physiologically relevant model system as it is similar to PHF fibrils from Alzheimer's disease patient brain tissue. Finally, a systematic meta-analysis of structural features across all amyloid fibril atomic models in the PDB and EMDB was carried out to investigate the structural basis of the different biological effects of amyloid. The work in thesis contributes to improving our fundamental understanding of amyloid structure-function relationships.

ACKNOWLEDGEMENTS

I would like to thank many people without whom this work would both not have been possible and as enjoyable as it has been. Firstly, I am very grateful for Dr Wei-Feng Xue, Dr Christopher Serpell and Prof Mick Tuite for giving me the opportunity to work on this project and for providing the flexibility to explore various exciting research directions that have emerged from out work together. I have greatly appreciated their kind advice and guidance during the PhD process.

I am grateful to the members of the Xue group for inspiring scientific discussions and the fun social events we have had, which have been especially memorable because of the restrictions more recently imposed by the pandemic. I would also like to thank members of the Kent Fungal Group for their friendly presence in the labs and offices. I am especially thankful to Prof Louise Serpell and her research group for the productive collaborative work that I have had the opportunity to participate in. I would also like to thank Louise for her helpful feedback on my work and for providing professional guidance.

I appreciate the work done by Hannah Crawford and Emerald Taylor on synthesising the linkers required for the amyloid conjugation part of this project and for kindly inviting me to the chemistry lab and demonstrating how the linkers were synthesised. I am also grateful to Hannah and Emerald, and to the rest of the Serpell group, for making me feel welcome in the chemistry lab and for fun the lab Christmas dinners. I also appreciate the expertise that Kevin Howland in the Biomolecular Science Facility and Ian Brown in the Imaging Facility provided during the project.

Finally, I would like to thank friends and family, whose encouragement has been invaluable during my PhD journey.

LIST OF PUBLICATIONS

Publications included in thesis

I. Lutter, L., Serpell, C. J., Tuite, M. F., & Xue, W.-F. (2019). The molecular lifecycle of amyloid – Mechanism of assembly, mesoscopic organisation, polymorphism, suprastructures, and biological consequences. Biochimica et Biophysica Acta (BBA) - Proteins and Proteomics, 1867(11), 140257. https://doi.org/10.1016/j.bbapap.2019.07.010

L.L. drafted and edited the manuscript.

II. Lutter, L., Aubrey, L. D., & Xue, W.-F. (2021). On the structural diversity and individuality of polymorphic amyloid protein assemblies. Journal of Molecular Biology, 167124. https://doi.org/10.1016/j.jmb.2021.167124

L.L. developed the analytical software tools, analysed the data, drafted and edited the manuscript.

III. Lutter, L., Serpell, C. J., Tuite, M. F., Serpell, L. C., & Xue, W.-F. (2020). Three-dimensional reconstruction of individual helical nano-filament structures from atomic force microscopy topographs. Biomolecular Concepts, 11(1), 102–115. https://doi.org/10.1515/bmc-2020-0009

L.L. designed the research, developed the analytical software tools, analysed the data, drafted and edited the manuscript.

IV. Lutter, L., Al-Hilaly, Y. K., Serpell, C. J., Tuite, M. F., Wischik, C. M., Serpell, L. C., & Xue, W.-F. (2021). Structural identification of individual helical amyloid filaments by integration of cryo-electron microscopy-derived maps in comparative morphometric atomic force microscopy image analysis. BioRxiv, 2021.10.19.464873. https://doi.org/10.1101/2021.10.19.464873 (preprint)

L.L. designed the research, developed the analytical software tools, analysed the data, drafted and edited the manuscript.

V. Lutter, L., Serpell, C. J., Tuite, M. F., Serpell, L. C., & Xue, W.-F. Multivariate analysis of amyloid fibril structural diversity. (manuscript draft)

L.L. designed the research, developed the analytical software tools, analysed the data, drafted and edited the manuscript.

Published papers are reprinted in the Appendix with permission from the publishers.

Publications not included in thesis

I. Al-Hilaly, Y. K., Foster, B. E., Biasetti, L., Lutter, L., Pollack, S. J., Rickard, J. E., Storey, J. M. D., Harrington, C. R., Xue, W.-F., Wischik, C. M., & Serpell, L. C. (2020). Tau (297-391) forms filaments that structurally mimic the core of paired helical filaments in Alzheimer's disease brain. FEBS Letters, 594(5), 944–950. https://doi.org/10.1002/1873-3468.13675

L.L. collected and analysed the AFM data, and reviewed the manuscript.

II. Aubrey, L. D.*, Blakeman, B. J. F.*, Lutter, L., Serpell, C. J., Tuite, M. F., Serpell, L. C., & Xue, W.-F. (2020). Quantification of amyloid fibril polymorphism by nano-morphometry reveals the individuality of filament assembly. Communications Chemistry, 3(1), 1–10. https://doi.org/10.1038/s42004-020-00372-3

* Authors contributed equally
L.L. wrote the analytical software tools and edited the manuscript.

LIST OF ABBREVIATIONS AND ACRONYMS

°C	degrees Celsius
3D	three-dimensional
Å	ångström
a. u.	arbitrary units
A_{280}	absorbance of a sample measured at 280 nm
AD	Alzheimer's disease
AFM	atomic force microscopy
AI	artificial intelligence
AL	amyloid light chain
$A\beta_{40}$	amyloid β peptide fragment, amino acid residues 1-40
$A\beta_{42}$	amyloid β protein fragment, amino acid residues 1-42
CASP	Critical Assessment of protein Structure Prediction
CASP14	14^{th} Community Wide Experiment on the Critical Assessment of Techniques for Protein Structure Prediction
CBD	corticobasal degeneration
cryo-EM	cryo-electron microscopy
CTE	chronic traumatic encephalopathy
Da	Dalton
dGAE	truncated form of tau protein comprising amino acid residues 297-391
DNA	deoxyribonucleic acid
DTT	dithiothreitol
E. coli	*Escherichia coli*
EM	electron microscopy
EMDB	Electron Microscopy Data Bank
GdnHCl	guanidine hydrochloride
IAPP	islet amyloid polypeptide
IPTG	isopropylthio-β-galactoside
kDa	kilodalton
LB	lysogeny broth
LCD	low-complexity domain
LCDs	low-complexity domain containing amyloid proteins

M	molar concentration
m/z	mass to charge ratio
mAu	milli-absorbance unit
microED	microcrystal electron diffraction
MWM	molecular weight marker
Ni-NTA	nickel-nitrilotriacetic acid
nm	nanometre
OD_{600}	optical density of a sample measured at a wavelength of 600 nm
PDB	Protein Data Bank
PHF	paired helical filament
PTMs	post-translational modifications
RCSB	Research Collaboratory for Structural Bioinformatics
RMSD	root-mean-square deviation
rpm	revolutions per minute
RT	room temperature
SASA	solvent-accessible surface area
SDS-PAGE	sodium dodecyl-sulphate polyacrylamide gel electrophoresis
SEC	size-exclusion chromatography
ssNMR	solid-state nuclear magnetic resonance
Sup35	eukaryotic peptide chain release factor GTP-binding subunit; also known as eRF3
Sup35NM-LCys	NM domains (residues 1-253) of Sup35 with an added N-terminal hexa-histidine tag, a C-terminal linker, and a cysteine residue
T	thymine
TCEP	tris(2-carboxyethyl)phosphine
TEM	transmission electron microscopy
TEMED	tetramethylethylenediamine
ThT	thioflavin T
WT	wild type

TABLE OF CONTENTS

Chapter 1: Introduction to amyloid assembly and structural polymorphism

1. 1 Summary

This introduction is based on papers I and II in the List of Publications included in the thesis (Lutter et al., 2019; Lutter, Aubrey, et al., 2021). The papers are included in published form in Appendices I and II, respectively. A summary is hereafter also provided for each of the thesis chapters.

In the first part of the introduction, entitled *The molecular lifecycle of amyloid – Mechanism of assembly, mesoscopic organisation, polymorphism, suprastructures, and biological consequences*, a general introduction into the molecular processes underlying amyloid self-assembly is provided. The kinetic mechanisms that are part of the amyloid lifecycle are first detailed and the techniques which are used to study amyloid kinetics both *in vitro* and *in vivo* are discussed. The polymorphic nature of amyloid self-assemblies is then addressed, with specific focus on suprastructural arrangements at the mesoscopic scale. The ways in which suprastructural properties may contribute to the biological consequences of amyloid are specifically examined. Finally, experimental studies on mechanisms of toxicity and prion-like transmission are reviewed, and current challenges in formulating the relationship between amyloid structure and function are considered.

In the second part of the introduction, entitled *On the structural diversity and individuality of polymorphic amyloid protein assemblies*, the polymorphism of amyloid fibrils is focused on through analysis of structural information provided by atomic force microscopy, cryo-electron microscopy and solid state nuclear magnetic resonance spectroscopy data. The hierarchical nature of the types of amyloid fibril polymorphism is visualised and the data set of all amyloid fibril structural information from the PDB and the EMDB up to March 2021 is systematically organised. Furthermore, the individuality of each fibril in heterogenous populations of amyloid fibrils is discussed, highlighting the application of atomic force microscopy as a technique which allows polymorphic fibril populations to be analysed on an individual fibril level. The effect of structural polymorphism on fibril physicochemical properties and the resulting biological consequences are discussed. Finally, the challenges of amyloid structure prediction in light of the recent success of AlphaFold2 are evaluated.

Finally, aims of the research carried out here and presented in the following chapters will be discussed.

1.2 The molecular lifecycle of amyloid – Mechanism of assembly, mesoscopic organisation, polymorphism

1.2.1 Abstract

The formation of a diverse range of amyloid structures from normally soluble proteins and peptides is a hallmark of devastating human disorders as well as biological functions. The current molecular understanding of the amyloid lifecycle reveals four processes central to their growth and propagation: primary nucleation, elongation, secondary nucleation and division. However, these processes result in a wide range of cross-β packing and filament arrangements, including diverse assemblies formed from identical monomeric precursors with the same amino acid sequences. Here, we review current structural and mechanistic understanding of amyloid self-assembly, and discuss how mesoscopic, i.e. micrometre to nanometre, organisation of amyloid give rise to suprastructural features that may be the key link between the polymorphic amyloid structures and the biological response they elicit. A greater understanding of the mechanisms governing suprastructure formation will guide future strategies to combat amyloid associated disorders and to use and control the amyloid quaternary structure in synthetic biology and materials applications.

1.2.2 Introduction

Amyloid forming proteins are at the centre of various protein misfolding disorders, as well as having normal physiological functions in a wide variety of organisms from bacteria to mammals. The main characteristic of amyloid forming proteins is their propensity to form ordered fibrils with a core made of tightly packed β-sheets perpendicular to the fibril axis. The organisation of soluble peptides or proteins into insoluble amyloid fibrils has been identified in many human pathologies (Soto, 2003), including amyloid β (Aβ) and tau involved in Alzheimer's disease (AD), α-synuclein (α-syn) in Parkinson's disease, and huntingtin in Huntington's disease (Chiti & Dobson, 2017; Eisenberg & Jucker, 2012). Other amyloid-associated disorders include type II diabetes and several types of systemic amyloidoses (Gertz et al., 2015; Merlini et al., 2018; Mukherjee et al., 2015). However, not all amyloid structures are disease associated. In fact, a range of non-disease associated amyloid structures participate in an array of normal physiological processes without any apparent harmful effects to their hosts (Chiti & Dobson, 2006; Fowler et al., 2007). Thus, it is difficult to establish direct causal relationships between amyloid protein precursors, the large range of structures they form, and the diseases they are associated with due to a lack of evidence linking structural and mechanistic understanding of neurodegenerative disease aetiology.

The building blocks of amyloid fibrils are soluble monomeric proteins or peptides. Their primary sequences typically include amyloidogenic motifs containing amino acids with high propensity to assembly into amyloid fibrils, influenced by both the physiochemical properties of these amino acids, as well as their order in the sequence. These motifs tend to be hydrophobic, more rigid and have a tendency to form β secondary structures (Burdukiewicz et

al., 2017). Despite differences in the primary sequence between amyloid-forming proteins, the monomeric precursors form fibrils with a characteristic cross-β structure in all amyloid (Jahn et al., 2010; Serpell et al., 1999). The cross-β architecture that defines the amyloid core is composed of β-strands packed perpendicularly to the fibril axis, and can be readily observed by X-ray fibre diffraction usually showing a characteristic 4.7 Å reflection on the meridian of the diffraction pattern that corresponds to the spacing between β-strands and indicates that they are stacked perpendicular to the fibril axis. The β-sheets can be arranged in parallel or antiparallel arrangements, forming a stable cross-β configuration that resists degradation by proteases, detergents and heat. Pairs of β-sheets usually intermesh with close side chain complementarity in a variety of possible steric zipper arrangements (Sawaya et al., 2007). The ~10 Å equatorial reflection corresponds to the spacing between β-sheets and indicates that there are usually two or more sheets in amyloid filaments (Serpell et al., 1999). The supramolecular fibril structure is supported by intermolecular hydrogen bonds parallel to the fibril axis, making amyloid fibrils strong fibrous materials (Smith, Knowles, Dobson, MacPhee, et al., 2006). Amyloid fibrils typically have diameters of approximately 5-20 nm and can be up to several micrometres long (B. Li et al., 2018; Meinhardt et al., 2009; Swuec et al., 2019).

The structure of amyloid fibrils has been studied to high detail using atomic force microscopy (AFM), solid state NMR spectroscopy (ssNMR) and cryo-electron microscopy (cryo-EM), which provide information on β-strand content within a monomer, arrangements of β-sheets, specific interactions between residues and the conformation of non-β-strand segments. In particular, the advent of high resolution cryo-EM and ssNMR methods has led to the elucidation of a range of amyloid species at near-atomic resolution, including several formed from the same monomeric precursors (**Fig. 1.1**). In this case, differences in fibril forming

conditions, such as pH, temperature and salt concentration affect the morphology of fibrils formed. In fact, identical monomers under the same conditions can often form a mix of highly polymorphic suprastructures, and the heterogeneity exhibited by amyloid samples complicates structural and functional studies while their mechanistic origins and biological consequences are not understood.

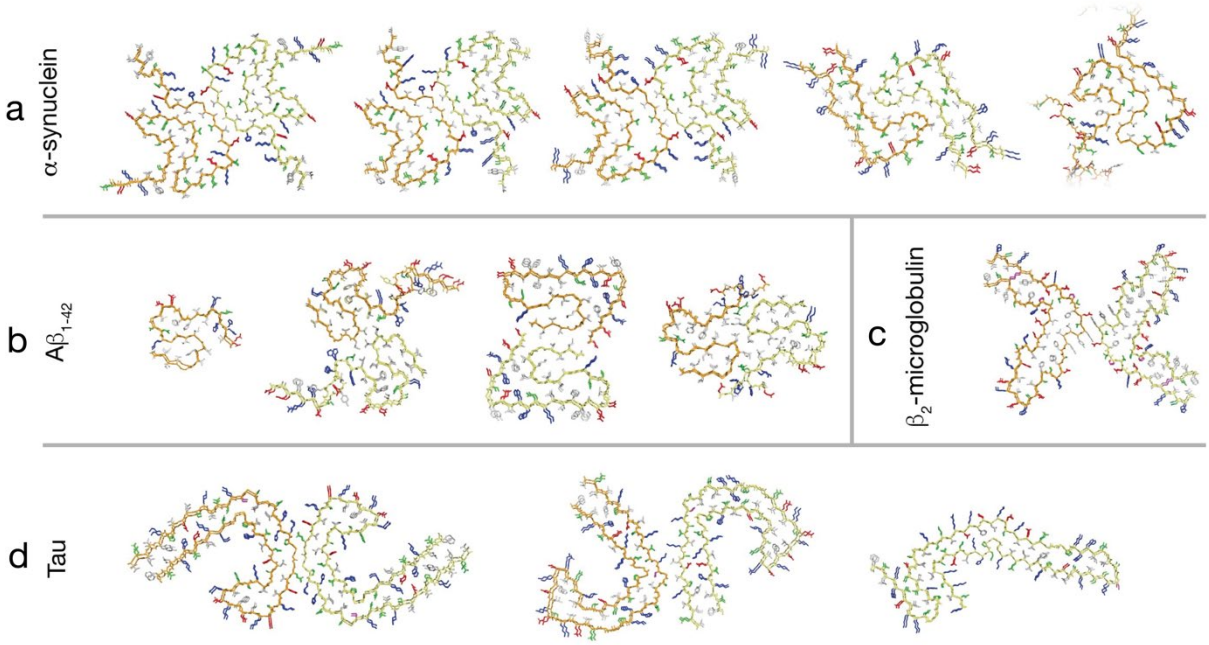

Figure 1.1 Recent structural models of amyloid fibrils determined using ssNMR and cryo-EM. These structures illustrate the similarities in cross-β core structure despite distinct primary sequences, as well as the different polymorphic structures that identical monomeric precursors can assemble into. PDB structures are shown with a yellow or orange backbone, blue basic side chain residues, red acidic side chain residues, grey hydrophobic side chain residues and green polar side chain residues. The models are oriented so that the fibrils are viewed from their ends and two layers along the fibril axis are shown for each fibril model for clarity. Structures are visualised in Pymol. **(a)** α-synuclein fibril structural models with PDB accession codes (from left to right): 6A6B (Y. Li et al., 2018), 6H6B (Guerrero-Ferreira et al., 2018), 6CU7 (B. Li et al., 2018), 6CU8 (B. Li et al., 2018), and 2N0A (Tuttle et al., 2016). **(b)** $A\beta_{42}$ fibril structural models with PDB accession codes (from left to right): 2MXU (Xiao et al., 2015), 2NAO (Wälti et al., 2016), and 5OQV (Gremer et al., 2017). **(c)** A structural model of

β_2-microglobulin fibril with the PDB ID 5KK3 (Colvin et al., 2016). **(d)** Tau fibril structural models with PDB accession codes (from left to right): 6GK3 (Iadanza, Silvers, et al., 2018), 5O3L (Fitzpatrick et al., 2017), 5O3T (Fitzpatrick et al., 2017), and 6GX5 (Falcon, Zhang, Murzin, et al., 2018).

The aggregation pathway by which soluble monomers form oligomeric intermediates and eventually fibrils is thought to be similar for all amyloid, despite differences in primary sequences and pathological presentation. The aggregation process starts with protein misfolding events in which native state monomers adopt amyloidogenic states and aggregate into nuclei that grow into oligomeric intermediates of increasing size distributions. Monomers are then added to the oligomeric intermediates, forming larger, more flexible, often elongated oligomers, frequently called protofibrils. These intermediate species are then lengthened into ordered assemblies of cross-β filaments that can elongate further with the addition of monomers at their ends. At the same time, two or more filaments can associate to form fibrils. Amyloid fibrils can further cluster into a variety of suprastructures, which include extracellular plaques, as in the case of Aβ, or intracellular inclusions, as in the case of huntingtin and tau.

Despite the shared core cross-β architecture, the detailed structures and surface features of oligomeric intermediates, fibrils and suprastructures depend on the specific precursor protein, and they elicit varied biological effects (Jackson & Hewitt, 2017). For example, polymorphs of *in vitro* formed $A\beta_{40}$ can have different levels of toxicity on neuronal cell cultures (Petkova et al., 2005). Amyloid fibrils are then able to undergo division, for example by fragmentation through mechanical stress, catalysis by specific cellular components such as chaperones (Winkler et al., 2012), or due to biochemical changes in the cellular environment, into shorter fibril particles that act as seeds. The seeds are further elongated by monomers, which are continuously produced by their host organism. Thus, rather than a linear process, amyloid

assembly represents a molecular lifecycle in which a 'cloud' of species and suprastructures in a heterogeneous mixture are continuously being produced, and the species populations in this cycle will evolve as a function of time in response to changes in the conditions.

This review will discuss the molecular lifecycle of amyloid assembly in terms of the current understandings of the key molecular processes involved. It remains poorly understood how some amyloid aggregates are tolerated or even beneficial while others, despite having similar core structures are associated with debilitating neurodegenerative diseases. Moreover, identical monomer sequences can also form fibrils with different morphological and phenotypic consequences, adding complexity to finding the structural determinants behind amyloid aggregation, toxicity, and biological response. The wide degree of heterogeneity and structural polymorphism of amyloid fibrils will be discussed in this review to demonstrate that all species in the amyloid lifecycle are an integral part of the lifecycle and form a population that may contribute to the pathogenic potential of amyloid as a whole. Finally, this review will also address in what manner the suprastructural arrangement of amyloid assemblies may represent a fundamental link between amyloid structures and their functional variations in biological systems. This will be discussed in terms of how suprastructures may affect fibril division and propagation of the amyloid state in the amyloid lifecycle, as well as how they affect the infectious and cytotoxic potentials of amyloid.

1.2.2.1 The amyloid lifecycle and its defining molecular processes

The molecular details of amyloid fibril formation are debated, but the self-assembly reaction fundamentally consists of four key processes: nucleation, elongation, division (Beal et al., 2020) and secondary nucleation (Törnquist et al., 2018) (**Fig. 1.2**). However, the current

description of amyloid aggregation and the resulting fibril assembly pathway is influenced by *in vitro* kinetic studies where the reactions are limited by the amount of monomers present. This process is better represented as a lifecycle, considering that *in vivo*, monomer production, misfolding, nucleation, elongation, division and secondary nucleation all occur continuously and simultaneously, and it is their relative rates that change over time as defined by the microscopic rate constants associated with each step. It should also be noted that all of the steps along the amyloid lifecycle are dynamic and reversible, although some reverse reactions are associated with high kinetic barriers.

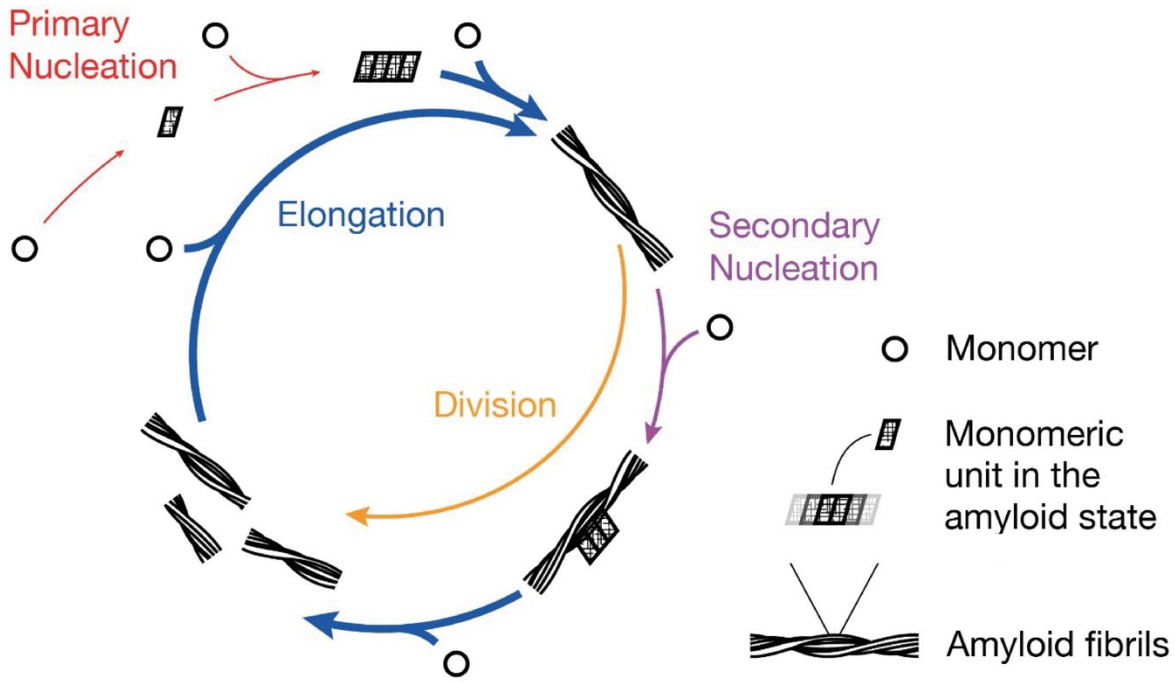

Figure 1.2 Schematic illustration of the amyloid lifecycle. Soluble monomeric proteins (circles) are continuously generated and can adopt the amyloid state with a cross-β conformation (parallelograms). Coloured arrows represent the four main processes in amyloid assembly: primary nucleation (red), which may occur as homogeneous nucleation in solution or heterogeneous nucleation at interfaces; secondary nucleation (purple), which may occur as heterogeneous nucleation on fibril surfaces; elongation, which is growth at fibril ends (blue); and fibril division, for example through spontaneous or catalysed fibril fragmentation (yellow). See Table 1.1 for glossary of terms associated with the amyloid lifecycle. The arrows represent dynamic and reversible steps along the lifecycle.

Table 1.1 Glossary of commonly used terms relevant to the amyloid lifecycle shown in Fig 1.1.

Term	Description
Elongation	Growth of fibrils in a direction parallel to the fibril axis by templated monomer addition at fibril ends.
Fibril ends	Active sites where elongation by templated monomer addition occur.
Fibril fragmentation	Breakage or division of fibrils, which can be mediated by mechanical agitation, thermal stress, chemical perturbation or chaperone catalysis.
Fibrils	Long filaments formed typically by two or more intertwined proto-filaments, sometimes loosely referred to as "mature" fibrils.
Nuclei	Smallest oligomeric aggregate on which further growth by attachment of a new monomers is faster than detachment of an existing monomer in the aggregate.
Oligomers	There is no universal definition but commonly sub-100-mer aggregates featuring a heterogeneous and transient nature, and small enough to be disperse and not sedimented by centrifugation.
Primary nucleation	*De novo* formation of the amyloid state through nucleated assembly of soluble monomers either in solution (primary homogeneous nucleation), or at surfaces or interfaces (primary heterogeneous nucleation).
Proto-filaments	Single elongated amyloid filament with a cross-β core structure.
Proto-fibrils	Curve-linear or worm-like fibrils that are less ordered and elongated compared to fibrils, thought to be structurally comparable to some oligomers.
Secondary nucleation	Special case of heterogeneous nucleation in which nucleation events occur on the surface of already existing fibrils.
Secondary processes	Secondary nucleation and fibril fragmentation, which result in the acceleration and exponential growth of amyloid, as opposed to primary processes of primary nucleation and elongation.
Seeds	Aggregates that are capable of accelerating amyloid assembly reactions, for example post-nucleation amyloid species capable of growth by elongation, or species capable of promoting secondary nucleation.

In the initial stages of the amyloid lifecycle, partial unfolding and/or conformational changes are required to convert amyloidogenic proteins in their native states to misfolded states capable of further conversion into the amyloid state. The monomeric or small oligomeric amyloid precursors initially exist in a dynamic equilibrium of conformations with varying degrees of structural order and can aggregate to form small amyloid oligomers. These intermediate oligomers can be structurally similar to fibrils in their conformation and β-sheet content as shown by binding of conformation-specific antibodies and analysis of secondary structure content. They can also be highly disordered, or indeed anywhere in-between (Breydo & Uversky, 2015). Thus, at some point along these initial aggregation events, monomers or small oligomers adopt a conformation with a high β-content. This process can be accelerated by specific mutations and environmental factors. This initial aggregation process of primary nucleation can be seen as a phase transition of the amyloidogenic protein from an aqueous solution phase to the 'solid phase' represented by amyloid fibrils. Primary nucleation can proceed as homogenous nucleation occurring in solution, or heterogeneous nucleation occurring on surfaces or interfaces. As biological environments are rich in surfaces, it is possible that many spontaneous primary amyloid nucleation events occur as heterogeneous nucleation *in vivo*. Thus, surfaces may have profound effects on aggregation kinetics depending on their composition and properties (Habchi et al., 2018). Nucleation events generally occur after a "critical concentration" of monomers in solution has been reached and exceeded (Blancas-Mejía et al., 2017; Novo et al., 2018); these solutions are called supersaturated solutions (Kashchiev & Auer, 2010). The smallest oligomeric aggregate on which further growth is more likely to occur than reduction in size is called the nucleus, although the generic nature of amyloid nuclei remains unresolved.

Once formed, amyloid nuclei can grow by templated elongation, in which free monomers are converted to the amyloid state and added to growing filament ends. Although elongation is a reversible reaction, dissociation of monomers is usually negligible due to the highly stable fibril structure contributing to a slower relative detachment rate compared to the attachment rate during elongation. Nucleation and elongation are concentration-dependent processes (W.-F. Xue et al., 2008), and their relative contributions to amyloid formation varies between different amyloid proteins and solution conditions (Blancas-Mejía et al., 2017; Buell et al., 2014; S. I. A. Cohen et al., 2013). Post-nucleation species capable of templating elongation growth are called seeds. Seeds can grow into protofilaments, which are elongated structures with monomeric units in the amyloid state. Protofilaments can subsequently twist around each other forming fibrils. Thus, fibril ends act as the growth active sites of amyloid fibrils. A fibril typically may consist of 2-6 protofilaments, and can be further elongated and adopt a more ordered fibril arrangement. Some fibrils are quite flexible and can circularise and grow into loops (Hatters et al., 2003). Adding to the ambiguity of amyloid formation terminology, there is no objective definition for "mature" fibrils. This term is typically used to refer to long and straight fibrils observed in an end-stage *in vitro* assembly reaction, but there is no formal length, width or twist definition for these.

In the *in vivo* amyloid lifecycle, the large and possibly biologically inert fibrillary aggregates will be part of a heterogeneous population of aggregates of a range of sizes and states, including small intermediate oligomeric species, often referred to simply as 'oligomers'. There is currently no universal definition of what constitutes an amyloid oligomer, but common features include a 'soluble' (i.e. not true soluble in a physiochemical sense but small enough to be disperse and not sedimented by centrifugation), heterogeneous and transient nature. Such small oligomeric amyloid aggregates vary in subunit composition and morphology, for example,

disordered, spherical and annular structures having been identified *in vitro* (S. W. Chen et al., 2015; Kotler et al., 2015; Parthasarathy et al., 2015). Major oligomer types include fibrillar oligomers, which structurally and immunochemically closely resemble short fibril particles, and prefibrillar oligomers, which are intermediate species having a distinct but not well characterised structure (Breydo et al., 2016). There is also a type of oligomer that is formed off-pathway from fibril formation that may be highly cytotoxic *in vitro* (M.-C. Lee et al., 2018). Additional complexity arises from the fact that oligomer populations are inherently highly polymorphic. Oligomeric structures have been determined under different conditions using diverse techniques, and it is not always clear whether, or in what form, they exist *in vivo*. This raises the question of what the toxic physiochemical or structural properties of amyloid species might be. In addition to the formation of amyloid species, which represents a phase transition of protein precursors in aqueous solution to an insoluble solid phase, amorphous aggregates with no ordered cross-β core may instead result from transition to a liquid phase, forming liquid droplets through liquid-liquid phase separation (LLPS). It has been hypothesized that the LLPS process is utilised by cells to compartmentalise proteins and biochemical reactions and consequently has physiological roles in cell signalling and regulation of gene expression (Chong & Forman-Kay, 2016). Such liquid phase separated structures include P granules, nucleoli and stress granules, and are typically made up of aggregates of nucleic acids and protein. Intrinsically disordered proteins are also often found in cellular liquid droplets as their exposed hydrophobic areas and structural freedom may facilitate aggregation. Similarly, amyloid liquid-liquid demixing could be promoted by molecular chaperones (Ambadipudi et al., 2017). Demixing allows high local concentrations of specific proteins, and as the droplets stabilise and mature over time, they may provide a driving force to further phase transition to a solid phase, characterised by amyloid fibril formation.

Lateral sides of protofilaments or fibrils are able to catalyse the formation of new amyloid nuclei and oligomeric species capable of growth by monomer addition in a process known as secondary nucleation (S. I. A. Cohen et al., 2013; Jeong et al., 2013). Secondary nucleation is a special case of heterogeneous nucleation where the catalysing surface is specifically that of preformed amyloid instead of any surface. New nuclei formed through this secondary process then detach and can be further elongated. Indeed, it has been suggested that once a critical concentration of fibrils has been reached, fibril-catalysed secondary nucleation becomes the major source of toxic oligomeric species (S. I. A. Cohen et al., 2013). Despite secondary nucleation events occurring on pre-existing fibrils, amyloid fibrils are not considered to grow into branched suprastructures as each protofilament in a fibril remains unbranched.

Finally, amyloid fibrils are capable of dividing into smaller fibril particles. The division of amyloid fibrils propagates the amyloid state and the conformation associated with the parent fibril assemblies (Beal et al., 2020). Amyloid division can occur due to fibril fragmentation caused by thermal energy or mechanical forces, or be catalysed enzymatically by chaperone proteins (Gao et al., 2015). Division increases the number of fibrils particles and, therefore, reactive fibril ends that can lead to further growth by elongation. For prions, which are amyloid that are transmissible between hosts, division of amyloid fibrils is required for infectivity and propagation of the prion phenotype (Tanaka et al., 2006), which suggests a similar mechanism could occur in prion-like amyloids correlated with neurodegenerative disease. As a single prion or amyloid forming sequence can assemble into a wide range of fibril polymorphs, the differences in their ability to divide may result in the selection of specific prion strains under specific corresponding conditions. These properties will affect phenotype strength of the prions and will depend on the structural stability of the amyloid fibrils. Thus, fibril stability changes may alter its propensity for division which, in turn, affects amyloid toxicity and prion

infectivity (W.-F. Xue, Hellewell, et al., 2009). The biological implications of these structural differences could reveal a key element of the amyloid structure-function relationship.

1.2.3 Mapping the kinetics mechanisms of amyloid assembly

The complex nature of amyloid aggregation kinetics due to non-linear growth processes in the amyloid lifecycle, combined with their high sensitivity to environmental and experimental factors, has challenged the development of kinetic assays and derivation of rate laws. While the outline of the amyloid lifecycle as discussed above is generally well understood and documented based on *in vitro* assembly experiments, the specific structures of the species involved, especially those of transient and heterogenous oligomeric populations, and the rates of their formation and exchange remain unclear (Breydo & Uversky, 2015; Gallardo, Ranson, et al., 2020).

1.2.3.1 Amyloid assembly in vitro

Currently, the kinetics of amyloid self-assembly is frequently assayed *in vitro* utilising the tinctorial property of amyloid following development of high-throughput microplate-based kinetic assays (W.-F. Xue et al., 2008) using the dye thioflavin T (ThT). ThT shows enhanced fluorescence emission upon binding to in-register side-chains within the β-sheets of amyloid fibrils, and a kinetic assay with ThT as amyloid reporter is widely used as it is simple and relatively sensitive to fibril formation compared to turbidity and light scattering approaches (Pedersen & Heegaard, 2013; C. Xue et al., 2017), with a fluorescence detection limit in the low μM concentrations (0.3 μM; (Younan & Viles, 2015)). ThT assays have allowed in-depth studies of amyloid formation kinetics and derivation of rate laws that have elucidated the

molecular mechanisms of amyloid assembly and aid in determining the mode of action of fibril formation inhibitors (Michaels et al., 2018). Also, ThT fluorescence intensity may reflect fibril morphology, regardless of the β-sheet content due to different accessibility to binding sites (Sidhu et al., 2018).

Although ThT is a useful tool for quantifying the relative amounts of fibrillar cross-β content over time, it does have some limitations and shortcomings. For example, ThT cannot be used for specific identification of amyloid fibrils, as it is not sufficiently specific to amyloid aggregates and can for example, bind to DNA (Biancardi et al., 2017), nor can it be used to distinguish between amyloid fibrils and prefibrillar species (Younan & Viles, 2015). Additionally, screening the effect of small molecule inhibitors on fibril formation using ThT is prone to false positives as the candidate inhibitors may interfere with the binding of the dye, rather than the fibrillation process (Jameson et al., 2012). The study of amyloid aggregation should always be complemented with various other biophysical techniques, including circular dichroism (CD) and Fourier transfer infrared spectroscopy (FTIR) for secondary structure characterisation, and AFM and EM for fibril imaging. Several derivatives of ThT have been developed for *in vivo* detection of amyloid fibrils in the organs and tissues of live patients (Cheng et al., 2015; Sulatskaya et al., 2019). Amyloid probes also include luminescent conjugated oligothiophenes, which are fluorescent amyloid ligands that can report on the fibrillar conformation, facilitating the *in vitro* and *ex vivo* analysis of polymorphism (Nilsson et al., 2007; Wegenast-Braun et al., 2012). The continued development of novel reporters for use in animal models and in future clinical applications will contribute to a better understanding of the formation and spread of amyloid aggregates under *in vivo* conditions.

The main distinctive characteristic of amyloid aggregation, as measured *in vitro* using ThT, which gives a fluorescent signal increase upon binding amyloid fibrils, is a sigmoidal growth curve (**Fig. 1.3**). The lag phase represents early reaction times where primary nucleation events that lead to nuclei and small intermediate oligomer formation dominates. Nucleation is initially thermodynamically unfavourable and kinetically rate limiting as the nucleation process is associated with a free-energy barrier, with pre-nucleation species in the reaction coordinate favouring dissociation compared to further growth by monomer association (Buell et al., 2012; Kashchiev et al., 2013; W.-F. Xue et al., 2008). The lag phase can be eliminated by introducing preformed fibrillar amyloid seeds, enabling the conversion and addition of monomers directly to fibril ends in the amyloid state, thereby bypassing the rate-limiting nucleation process. At the end of the lag phase, while most of the protein is still monomeric, there is a transient population of intermediate oligomeric species, some of which are referred to as protofibrils because they are sufficiently and observably elongated species (Arosio et al., 2015). Small transient oligomers grow and fully convert into protofilaments with amyloid cross-β core that are then elongated by further addition of monomers to fibril ends. As fibrils form during lag phase, secondary processes such as secondary nucleation and fibril fragmentation become the major mechanism of amyloid formation, peaking during the exponential growth phase (S. I. A. Cohen et al., 2013; W.-F. Xue et al., 2008). Fibril mass increases as protofilaments are elongated and twist around each other. Finally, growth plateaus as most monomers in solution have been added to fibril ends. The population in such a sample remains in dynamic exchange (**Fig. 1.2**). For example, monomers and oligomers may continuously break off and reattach to fibril ends (Carulla et al., 2005). Importantly, these key steps are part of the lifecycle of all amyloid fibril formation, but their rate constants and thermodynamic driving forces vary for different monomers (Buell et al., 2012).

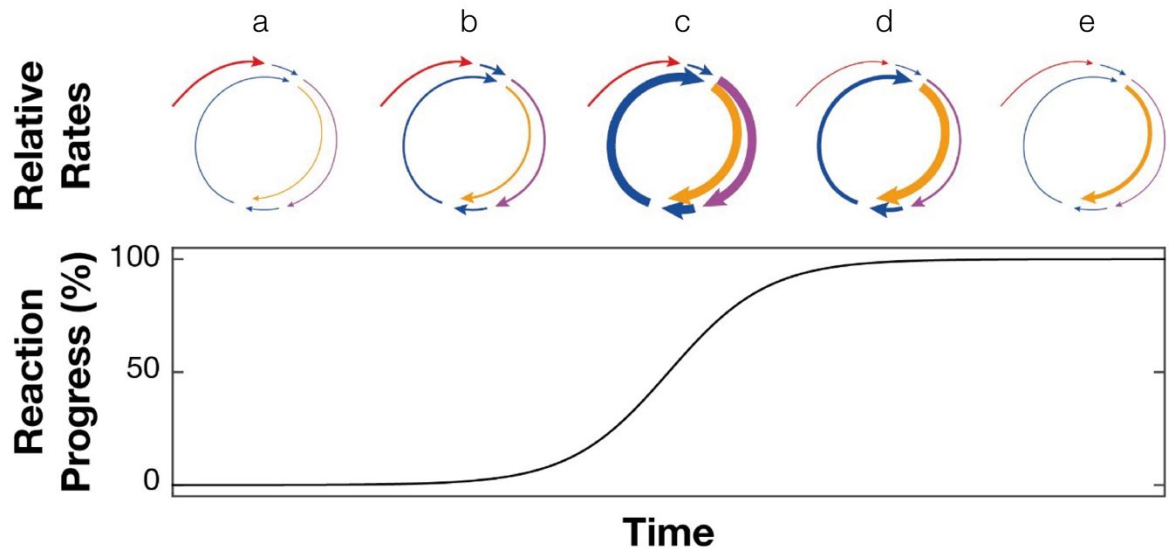

Figure 1.3 Schematic illustration of the amyloid aggregation growth curve as measured in vitro with kinetic ThT assay. Coloured arrows represent the four main processes in amyloid assembly (**Fig. 1.1**). Primary nucleation (red) is the driver of de novo amyloid aggregation in the initial stages of the reaction **(a-b)**, although primary nucleation will continue to take place, at much lower rates, in the later stages as free monomer concentration drop. The rate of elongation growth at fibril ends (blue) peaks during the exponential growth phase **(c)** of the fibrils. Elongation continues to occur once a plateau has been reached **(d-e)** as the fibrils are in dynamic equilibrium with residual monomers and/or small oligomers, as well as other species along the fibril formation pathway. Secondary nucleation (purple), which requires both the presence of monomers and fibrils, dominates nuclei formation as soon as first fibrils have formed in the lag phase. Fibril division through fragmentation (yellow) occurs continuously after the formation of first fibrils and continues to have a significant role in the capacity to increase fibril load. The relative magnitudes of the rates of these main processes (exemplified by the thickness of the arrows) also vary by the type of amyloid monomer, their concentration and environmental conditions.

1.2.3.2 Amyloid assembly in vivo

While the fundamental kinetic principles governing the self-assembly of amyloid are the same *in vitro* as *in vivo*, the kinetics of the amyloid lifecycle under *in vivo* conditions would be expected to be significantly different from the well-characterised *in vitro* conditions. One of

the main differences is the unlimited and continuous production of monomers *in vivo*. Other key differences include the added complexities associated with genetic variations of amyloid monomer or its precursor and other risk factors, components of the cellular and extracellular environment that affect amyloid aggregation kinetics, spatiotemporal variations in monomer production affecting local monomer concentrations, and amyloid clearance mechanisms. Using fluorescence lifetime imaging (FLIM), the kinetics of Aβ aggregation, as well as its cellular uptake and trafficking, have been studied in live neuronal cells (Esbjörner et al., 2014). The aggregation of Aβ in human APP-expressing mice was analysed using a fluorescent amyloid dye and a cranial window through which images were collected using two-photon imaging over a period of two years (Burgold et al., 2014). The plaque volume change was found to have a sigmoidal shape, with many small plaques forming initially, when the concentration of free Aβ is high, and growing in volume until they plateau when Aβ production becomes rate-limiting. However, while transgenic murine models of AD are useful research tools for familial AD, they fail to represent the most abundant type of AD in humans, which is sporadic. Amyloid positron emission tomography (PET), a method for visualizing amyloid deposition in the brain using radiopharmaceuticals that bind fibrillar amyloid, has also been used to collect and assemble Aβ load data from cognitively impaired patients to create a long-term disease model that showed a sigmoidal curve of increasing amyloid load in the brain over the course of more than 30 years (Jack et al., 2013). Overall, few studies have been done on the *in vivo* aggregation kinetics of amyloid in animal models or humans in any molecular detail.

The rates governing the amyloid lifecycle and its kinetics are specific to protein sequence and environmental conditions. For example, aggregation propensity is affected by charge and exposed hydrophobic surfaces of the monomer. The lag phase can also be shortened by an increased fragmentation propensity. Although a key feature of many amyloid-forming proteins

is being intrinsically disordered as monomers, or having significant stretch of unstructured regions due to extensive exposed hydrophobic areas, others can be folded, globular, and with low aggregation-propensity in their native states (Fändrich et al., 2001). Such proteins, including β_2 microglobulin associated with systemic dialysis related amyloidosis, require local unfolding to initiate aggregation (Eichner & Radford, 2011). In these cases, physiological thermal fluctuations may be sufficient for native conformation destabilisation (Chiti & Dobson, 2009) and hence enough for initiating assembly. Conditions such as temperature, pH, protein-denaturing agents, presence of other proteins, metal ions, surfaces and their composition and properties can have an impact on the aggregation of amyloid proteins (Faller et al., 2013; Galvagnion et al., 2015; Habchi et al., 2018; Moores et al., 2011; Morel et al., 2010). Even many physiologically non-amyloidogenic proteins can be made to adopt the characteristic cross-β structure under specific environmental conditions (Chiti et al., 1999; Goldschmidt et al., 2010). Deviations from the typical kinetic characteristics of amyloid aggregation have been identified under varying environmental conditions, which has implications for the biomedical use of amyloid-prone proteins, and for developing drugs targeting amyloid assembly. For example, the human glucagon-like peptide 1, analogues of which are used for treatment of type II diabetes, exhibits kinetics consistent with the standard nucleation-polymerisation mechanism at pH 8.2, but at pH 7.5 the kinetics showed a highly unusual profile, with the lag phase becoming longer with increasing monomer concentration (Zapadka et al., 2016). This was attributed to the formation of off-pathway oligomers, with unknown physiological effects. One plausible explanation is that metastable oligomers and protofibrils could be off-pathway competitors and inhibitors of fibril formation, instead of on-pathway precursors (Hasecke et al., 2018).

1.2.4 Amyloid assembly polymorphism

Amyloid fibrils, by definition, share a cross-β core arrangement. Their assembly, either from precursors of different or identical sequences, nevertheless result in fibrils with a varying degree of structural differences (**Fig. 1.1, Fig. 1.4**). Polymorphism of molecular crystals has been characterised in the context of small molecules and pharmaceuticals, for which the varying physiochemical properties including the stability and bioavailability of a substance with an identical molecular structure and dissimilar suprastructure has been documented (Bernstein, 2007; E. H. Lee, 2014). Analogously, the fibrillar amyloid state can be viewed as a pseudo one dimensional "crystal-like" form in which different polymorphs may also have varying biological properties. Variance in fibril structure, i.e. the polymorphic nature of amyloid fibrils, has been characterised for fibrils formed from synthetic or recombinant monomeric amyloid precursors, as well as those formed *in vivo* in tissue or by seeding with fibrils from brain tissue of patients with various neurodegenerative diseases (Annamalai et al., 2016; Close et al., 2018; Falcon, Zhang, Murzin, et al., 2018). Amyloid assembly polymorphism, resulting from assembly of precursors of identical sequence, can be broadly divided into two classes: core polymorphism with differences in the arrangement of monomeric units in the cross-β core, or filament polymorphism with differences in the lateral arrangement of protofilaments in a fibril and the specific contacts they form (**Fig. 1.4**). In core polymorphism, the core structure can vary in β-sheet content, conformation of non-β-strand segments, steric zipper packing and specific contacts between residues. Core polymorphism can be further categorised into segment polymorphism where different segments of a polypeptide may form different cross-β cores, and packing polymorphism where the same segment of a polypeptide chain is involved in the cross-β core. For example, inter-sheet contacts can be stabilised by steric zippers, as well as hydrophobic contacts and salt bridges.

Eight potential classes of steric zipper packing arrangements were described by Eisenberg and colleagues (Sawaya et al., 2007) forming the basis for core and assembly polymorphisms. These steric zipper arrangements vary by whether β-strands that make up β-sheets are parallel or antiparallel, whether adjacent β-sheets that form the steric zipper pack the same or different surfaces together, or whether the β-sheets themselves are oriented parallel or antiparallel relative to each other. In terms of filament polymorphism, the current confirmed examples include cryo-EM reconstructions of purified paired helical and straight tau filaments, which show indistinguishable cross-β and β-helical structures, surrounded by a fuzzy coat of disordered domains, but distinctive inter-protofilament arrangements (Fitzpatrick et al., 2017) and β_2-microglobulin, for which several morphologies were identified using cryo-EM, although all shared the same core structure, as shown by NMR (Iadanza, Silvers, et al., 2018).

Amyloid populations regularly contain heterogeneous mixtures of fibril polymorphs. Often, several subpopulations of amyloid fibril polymorphs can form under identical conditions, for example paired helical and straight fibrils of tau or striated ribbon and twisted fibrils of Aβ (Fitzpatrick et al., 2017; Tycko, 2015). In studies in which a single fibril structure is reconstructed, the sample may have contained a broad range of morphologies, as in the case of the recent β_2-microglobulin structure (Iadanza, Silvers, et al., 2018). These individual fibril polymorphs can sometimes be distinguished by their width, as they may vary in the number of protofilaments (**Fig. 1.4**), or other morphological differences such as twist periodicity and persistence length in terms of curvature. Additionally, fibril polymorphs may vary in stability and dynamic behaviour which may, for example, affect their fragmentation rate and consequently cytotoxicity (W.-F. Xue et al., 2010). Fibrils differing in twist and length can also result in differences in their cytotoxic potential (Petkova et al., 2005; W.-F. Xue, Hellewell, et al., 2009).

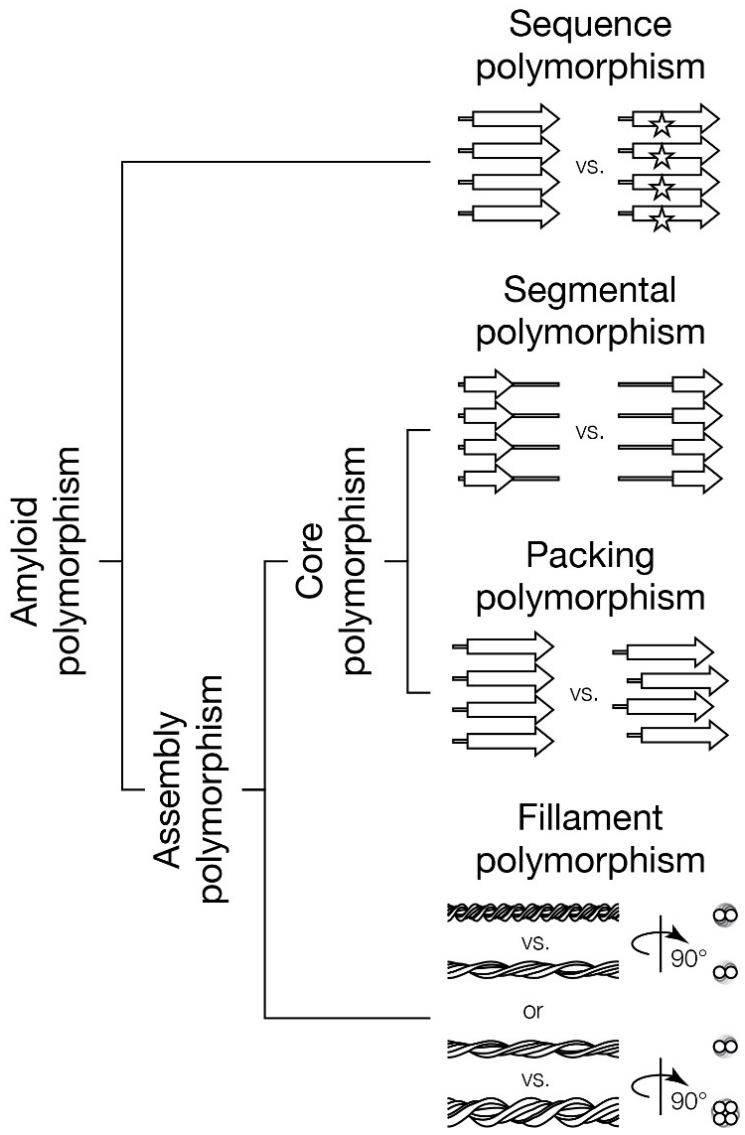

Figure 1.4 Hierarchical classification of amyloid polymorphism types with schematic illustrations exemplifying each type. Amyloid polymorphs can be classified into sequence polymorphs and assembly polymorphs. Assembly polymorphs can be further divided into core polymorphs and filament polymorphs, and core polymorphs can be divided in turn into segmental polymorphs and packing polymorphs. The different types of polymorphism are organised from top to bottom to indicate the hierarchical effects of polymorphism types. For example, sequence polymorphs where one polymorph contains a single amino acid residue change (top schematic, stars depict an amino acid sequence variation) would also affect which segment of the chain forms the amyloid core (segmental polymorphism), how the amyloid core is packed (packing polymorphism) and how the protofilaments are arranged (filament polymorphism). On the other hand, polymorphism based on the varied number and

arrangement of the protofilaments (bottom schematic depicting filament polymorphism) may occur without changes in the sequence, the core segment or the packing of the core (all placed above filament polymorphism in the schematic).

From fibril structures determined from patient brain tissue, it emerges that there may be disease-specific association with certain amyloid fibril polymorphs. For instance, tau fibrils from an Alzheimer's patient and a Pick's disease patient have remarkably different core arrangements (Falcon, Zhang, Murzin, et al., 2018; Fitzpatrick et al., 2017). Additionally, structural polymorphs of Aβ are thought to correlate with variations in AD pathological phenotypes (Qiang et al., 2017). For example, recent ssNMR analysis of Aβ fibrils seeded from AD patient brain tissue showed a link between clinical AD subtypes and specific features of fibril polymorphism. $A\beta_{40}$ aggregates were shown to have a single major morphology in patients with typical prolonged-duration AD and posterior cortical atrophy variant (PCA-AD) and a higher proportion of alternative structures in the rapidly progressive form of AD. By contrast, $A\beta_{42}$ aggregates were found as several polymorphs across both categories (Qiang et al., 2017). In another study, $A\beta_{40}$ fibrils seeded from brain tissue of two AD patients with different clinical histories were relatively homogenous for the individual patients, although analysis of the predominant fibril structures by ssNMR between the two patients indicated significant differences in their cores (J.-X. Lu et al., 2013).

Due to amyloid and prions have structural and mechanistic similarities, and the morphological heterogeneity of amyloid populations potentially linked with disease progression, the idea of whether structural amyloid polymorphs propagate phenotypically as strains has been tested. For prions, the prion strains give rise to specific pathologies and disease phenotypes, which are maintained when the strains are introduced *de novo* into a genetically identical host where they continue to be stably propagated. Some studies have also suggested the spread of tau and α-

synuclein as distinct strains (Kara et al., 2018). Thus, identifying the structure of distinct fibril polymorphs, the suprastructures they form, and characterising the environmental factors that drive structural changes, as well as their biological effects, could be the key link to elucidating the dramatic variations in amyloid disease pathological presentation and provide a structural rationalisation of the strain phenomenon. The structural differences between amyloid polymorphs could also be mediated by changing the propensity to the various fibril associated pathology mechanisms, including interactions with membranes, ability to sequester proteins essential for the cell, differences in metal binding and creation of reactive oxygen species, or some as yet unknown mechanism of fibril toxicity. Thus, in terms of disease association, environmental changes may modulate amyloid structure and exert pressure to select for specific polymorphs, and the selected polymorphs in turn reinforce the disease-associated environmental changes.

1.2.4.1 Amyloid suprastructures

As amyloid fibrils are highly polymorphic, the heterogeneous populations of amyloid species that result from the amyloid lifecycle also show a variety of different mesoscopic arrangements on the micrometre to nanometre scale, forming a variety of possible suprastructures (**Fig. 1.5**). Amyloid fibrils vary in width, with some self-associating into thick bundles by protofilament interactions, whereas other fibrils may consist of a single protofilament only (Khurana et al., 2003). The length distribution of the fibrils in a population can similarly vary, depending on the mechanical properties of the fibrils, such as stiffness, and their fragmentation rate (Beal et al., 2020). Each fibril population formed from the same amyloid sequence may contain varying proportions of fibril polymorphs, ranging from a uniform ensemble to almost continuous

variation in twist (J.-X. Lu et al., 2013; Meinhardt et al., 2009). While some fibrils self-associate into packed clusters or networks, others do not form such structures and remain separated, sometimes in a parallel alignment with directional order (Kollmer et al., 2016; Vigolo et al., 2017). Although various suprastructures have been identified, little is known about their relative biological impact. At liquid interfaces amyloid fibrils can exist in a liquid crystalline nematic phase in which the fibrils are aligned parallel to each other (Jordens et al., 2013). *In vitro* studies of entangled amyloid networks have also identified gel-like behaviour at the mesoscopic scale. Interestingly, elastic properties appear as early as during nucleation events in the lag phase (Manno et al., 2010). Electron tomography studies of Aβ suprastructures have revealed three main types of aggregates: amorphous meshwork, fibril bundle and amyloid star, all within the same overall deposit (Han et al., 2017). Interestingly in each case, the fibrils themselves were morphologically indistinguishable. Additionally amyloid fibrils have been observed to form spherulites which show a typical Maltese cross pattern when observed under polarised light in both *in vitro* and *ex vivo* (Jin et al., 2003; Krebs et al., 2004). Furthermore, between fibril networks, extracellular vesicles of various sizes are found (Han et al., 2017) and lipid membrane components have been identified also within and around dense Aβ plaques in human brains of AD patients (Liao et al., 2013).

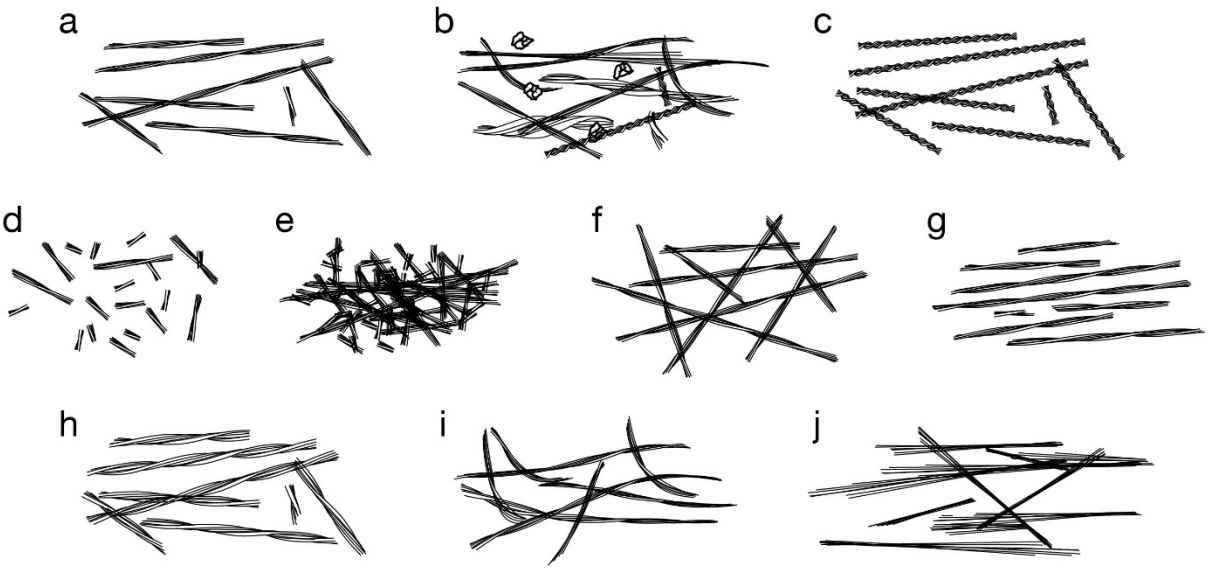

Figure 1.5 Schematic illustration of possible variations in the suprastructural properties of amyloid at mesoscopic (micrometre to nanometre) length scales: a) long-straight fibrils of varying length; b) highly heterogeneous population with filaments and bundles decorated with small oligomeric species; c) fibrils of tight twist properties; d) highly fragmented fibril population with abundance of small particles; e) fibril cluster; f) fibril network; g) aligned fibrils; h) thick and bundled fibrils; i) flexible or curve-linear fibrils with low persistence length; j) crystalline-like fibril bundles.

Morphological differences observed in plaque deposits reflect the suprastructural assembly preferences and features of amyloid aggregates, and seeded fibrils from AD patient brains have been correlated to differences in clinical subtypes (Qiang et al., 2017). Thus, it is possible that the different suprastructures that differ in their mesoscopic arrangements also have different toxic or infectivity profiles. The suprastructural arrangements of fibrils can also be affected by the dominance of individual fibril polymorphs as they can have different surface properties which affect their interactions. Thus, aggregates with different suprastructural features will also have different surface properties and propensities to sequester other metastable essential constituents of the cellular proteome. Characterising the various suprastructural parameters such as length and width distribution, twist, stiffness, clustering and heterogeneity of amyloid

assemblies and correlating these with biological activity could lead to essential insights into the amyloid structure-function relationship.

1.2.5 Regulation of functional and pathological amyloid structure and assembly

Defining an amyloid suprastructure-toxicity relationship would help us elucidate why some amyloid formations are highly toxic whereas others are inert. Given the presence of amyloid aggregates in numerous neurodegenerative diseases, it is perhaps surprising that an increasing number of amyloid structures have been found to participate in an array of normal physiological processes without any observable harmful effects to their hosts (Fowler et al., 2007). In humans these include melanin biosynthesis, regulation of long-term potentiation (LTP) and peptide hormone storage (Berson et al., 2003; Drisaldi et al., 2015; Maji et al., 2009). Functional amyloid assemblies have also been discovered in numerous other organisms, including bacteria, fungi and metazoa. For instance, in some bacteria, fibrillar matrix of extracellular amyloid proteins such as curli and Fap are required for surface adhesion and colony formation (Deshmukh et al., 2018; Rouse et al., 2018; Taylor & Matthews, 2015; Zeng et al., 2015). In insects and fish, the eggshell is primarily made up of chorion proteins with a characteristic amyloid fibril structure (Fowler et al., 2007). The line between functional and pathogenic amyloids is also increasingly blurred, as subtle changes in processing or regulation may cause an amyloid with normal physiological roles to become pathogenic. For example, Aβ is produced from the amyloid precursor protein (APP) in neural and other cells throughout the human lifetime (Masters et al., 2015). The precursor can be cleaved by α- and γ-secretases leading to production of non-amyloidogenic fragments or by β- and γ-secretases, which produces several isoforms of Aβ correlated with AD. However, there is evidence that

monomeric Aβ and other peptides resulting from precursor cleavage might have important roles in cellular signalling pathways, regulating synaptic activity and might even be essential for survival of neurons (Plant et al., 2003). Moreover, fibrillar forms of Aβ have been suggested to have protective effects against fungal and bacterial infections in mouse, nematode and cell culture models of Alzheimer's disease, thus suggesting that they might have a role in innate immunity (Kumar et al., 2016). Recently, human neural cell culture models have also been used to investigate the role of a herpes simplex 1 virus infection on amyloid aggregation and it was reported that Aβ oligomers bind virus surface glycoproteins and mediate resistance to the virus (Eimer et al., 2018). This finding suggests that even small oligomeric amyloid species may have functional roles.

Amyloidogenic proteins lack sequence homology and can have diverse structural and catalytic functions in their normal non-amyloid states. The ability to self-assemble into an amyloid state could be a generic structural feature of polypeptide chains (Dobson, 1999). Therefore, understanding the mechanistic and structural differences between functional and pathogenically-associated amyloid, which share the same cross-β core structure by definition, is a key requirement for treating amyloid-associated diseases as any potential treatment must be able to recognise essential functional features of amyloid and differentiate these from the pathogenically-associated features. A key aspect of functional amyloid may lie in their controlled and localised assembly initiation and termination in response to environmental cues, which is sometimes achieved with post-translational modifications. For example, the CPEB3 protein activates the transcription of mRNAs that promote long-term potentiation (LTP), but only when ubiquitylated and deSUMOylated, which promotes its assembly into the functional fibrillar form (Drisaldi et al., 2015; Stephan et al., 2015). SUMOylation of CPEB3 makes it soluble and inactive, although in other amyloid proteins it can promote aggregation and toxicity

(Rott et al., 2017). Additionally, many peptide hormones that are stored within endocrine granules require both the compartmentalised acidic pH environment and the presence of glycosaminoglycans (GAGs) for fibril formation. GAGs accelerate fibril formation by abolishing the lag-phase and some can interfere with potentially harmful fibril-membrane interactions (Sebastiao et al., 2019; Sheynis et al., 2013).

Another regulatory mechanism of controlling amyloid assembly involves chaperones. Recently chaperones DNAJB6 and Hsp70 were identified as part of a natural control mechanism to prevent the aggregation of α-synuclein, found as toxic aggregates in Parkinson's Disease patients (Aprile et al., 2017). α-syn is expressed at high levels in healthy individuals in various tissues of the body and, in the monomeric state, has important synaptic functions related to neurotransmitter release and synaptic plasticity, although the exact mechanisms are not known (Burré, 2015). Chaperone proteins such as Hsp70, Hsp40, and others are also involved degradation and refolding of amyloid aggregates. The chaperone Hsp104 is essential for propagation of [*PSI*$^{+}$] prion phenotype in yeast that is associated with the functional amyloid state of Sup35; Hsp104 promotes division and propagation of Sup35 amyloid by catalysing fibril fragmentation *in vivo* (Sweeny & Shorter, 2016; Torrente & Shorter, 2013).

On the basis that amyloid associated with pathology may have roles in normal physiological processes, it has been suggested that it is a dysfunctional protein degradation machinery that leads to disruption in proteostasis and build-up of toxic amyloid aggregates (Jackson & Hewitt, 2016). Some functional amyloid systems, for example pre-melanosomal protein, aggregate into fibrils much more rapidly than non-functional amyloid, thus preventing accumulation of intermediate oligomeric species with potential for harmful effects (Fowler et al., 2005).

All the above-mentioned mechanisms may have evolved to ensure the normal roles of functional and/or to prevent the pathogenic features of amyloid assemblies, which have important implications in numerous physiological processes involving amyloid or amyloid precursors with no deleterious effects. Safety mechanisms that control and regulate amyloid localisation, compartmentalisation, processing and degradation, as well as their assembly kinetics and interactions with other cellular structures, may present some of the differences between functional and disease associated amyloid.

1.2.6 Structural and molecular origins of amyloid toxicity

Although the hallmark of neurodegenerative disease is deposits of amyloid fibrils, the neuropathological and clinical symptoms vary significantly. Therefore, the identity of the toxic species, and the molecular origin of the cytotoxic potential associated with amyloid is widely debated (Marshall et al., 2014; Verma et al., 2015). For example, AD is characterised by progressive loss of synapses, neuronal death and atrophy of the affected areas, resulting in decline of memory and cognitive functions, whereas the main pathophysiological characteristic of Parkinson's disease is degeneration of dopaminergic neurons in the substantia nigra resulting in loss of motor function leading to rigidity and tremors. Other neurodegenerative and prion diseases also involve progressive neuronal death in various areas of the brain and result in different symptoms. Severe cases of amyloid deposition has also been found in the brains of human subjects with no cognitive decline or symptoms of dementia upon post-mortem assessment of neuropathology (SantaCruz et al., 2011). Thus, several underlying toxicity mechanisms involving a range of amyloid species have been suggested for these symptoms,

including disruption of cell membranes, dysregulation of calcium homeostasis, mitochondrial dysfunction and oxidative stress.

1.2.6.1 Toxicity potential of small oligomeric amyloid species

Amyloid toxicity is currently thought to result from pathological effects associated with small amyloid oligomers as they are ubiquitous in the brains of neurodegenerative amyloid disease patients and their cytotoxicity has been well characterised *in vitro*. According to this hypothesis, large deposits such as amyloid plaques and inclusion bodies are thought to be relatively inert. Indeed, small oligomeric species from post-mortem human brains can disrupt long-term potentiation, synaptic plasticity and memory when injected into a mouse hippocampus (Shankar et al., 2008). This view is supported by evidence of neurodegeneration and cognitive defects preceding plaque formation *in vivo* (Billings et al., 2005; Koistinaho et al., 2001). In the case of mutant huntingtin, the formation of inclusion bodies was also found to reduce the risk of cell death from toxic mutant huntingtin aggregates (Arrasate et al., 2004). Furthermore, the formation of prefibrillar oligomers is accelerated by mutations in α-syn causing a familial, early-onset form of Parkinson's (Conway et al., 2000). However, the precise molecular nature of the small oligomeric species that confers toxicity remains to be established and a large number of species of varied structures and suprastructures have been observed. For example, according to the 'ion channel hypothesis', oligomeric species with a ring-like structure insert into cell membranes and act as aberrant ion channels, disrupting the homeostasis of ions and leading to cell death (Quist et al., 2005). Such oligomers have been suggested to form membrane-associated annular structures *in vitro* through interactions with specific lipids in the membrane, and possibly form a β-barrel pore (Di Scala et al., 2016; Patel et al., 2015; Serra-Batiste et al., 2016). However, specific structural features may be required for ion channel formation, as it has been suggested that oligomers of $A\beta_{42}$ but not $A\beta_{40}$ are

capable of channel formation in membranes (Bode et al., 2017). Disruption of calcium homeostasis has been observed in proximity of amyloid plaques, which may act as a reservoir of cytotoxic species (Kuchibhotla et al., 2008). Loss of calcium compartmentalisation leads to distortion of neuritic morphology and as calcium is essential for neural integration of signals, dysregulation of its homeostasis disrupts local neural networks (Kuchibhotla et al., 2008). Amyloid oligomer cytotoxicity has also been linked to the size and conformation of the oligomers, with smaller and more exposed hydrophobic surfaces with structural flexibility displaying the most toxic potential (Campioni et al., 2010; Mannini et al., 2014). Thus, the dynamic and hydrophobic nature of prefibrillar oligomers may provide a rationale to their propensity to aggregate and display cytotoxic properties though their interaction with membrane bilayers.

The elucidation of the role of small oligomeric species in amyloid diseases is complicated not only due to their varied structures and heterogeneity, but also due to their transient nature. Thus, in terms of species formed during the amyloid lifecycle *in vivo*, due to experimental limitations it is only possible to study stable species secreted by *in vitro* cell cultures or those extracted from post-mortem patients' brains. Furthermore, the population and the concentration of amyloid species in the brain is unknown. Attempts to quantify the concentration of Aβ in the brain has focused mostly on mouse models, with some studies on human brain tissue and cerebrospinal fluid (Lesné et al., 2013; Simonsen et al., 2007; Waters, 2010). However, results are inconclusive as there is currently no method for quantifying whole amyloid populations ranging from prefibrillar oligomeric species to fibrillar species *in vivo* without exposing them to non-native conditions that could affect their aggregation states, leading to unreliable estimates. Additionally, very little is known about how the local environment in the *in vivo* human brain affects amyloid structure and toxicity, especially as the

amyloid population are likely to be highly heterogeneous and distinct oligomeric species can vary in toxicity.

1.2.6.2 Toxicity potential of fibrillar amyloid species

In addition to the cytotoxic effects displayed by prefibrillar oligomeric species, amyloid fibrils also have direct cytotoxic properties via disruptive effects on the phospholipid bilayer during fibril growth (Engel et al., 2008). Localised neuronal damage, characterised by progressive neuronal dystrophy and microglial activation, has been correlated with plaque formation and shown to worsen over the clinical course of the disease (Meyer-Luehmann et al., 2008; Serrano-Pozo et al., 2016). Several indirect mechanisms of fibril toxicity have been proposed, including secondary nucleation events where fibrils catalyse the formation of small oligomeric species through surface interactions, thereby contributing to the neurotoxic effects of amyloid (S. I. A. Cohen et al., 2013). Additionally, fibrils may act as a reservoir for toxic species, which may be released to generate a local pool of toxic species as a halo around fibrillar deposits (Koffie et al., 2009). Besides these indirect mechanisms, fibrils can also contribute directly to cell damage under conditions in which non-fibrillar aggregates are not detectable by spectroscopy or antibody-binding, thus suggesting a role as a direct contributor of cytotoxicity.

Fibril fragmentation is key to amyloid cytotoxicity by increasing the number of termini through division of fibrils, which provides increased reactive growth competent surface, and also creates smaller fibrillar amyloid species that decrease cell viability and increase disruptive effects on membrane bilayers. The increase in the toxic potential cannot be solely attributed to the increased number of fibril ends, suggesting other yet unknown surface-dependent mechanisms (W.-F. Xue, Hellewell, et al., 2009). Furthermore, short fibril particles are also readily internalised by endocytosis, causing disruption within the cell by inhibiting the

degradation of proteins within lysosomes and altering trafficking of lysosomal membrane proteins (Jakhria et al., 2014). Disruptive interactions of fibrils with membranes have been visualised in 3D using electron tomography, surrounded by lipid inclusions of varying sizes (Milanesi et al., 2012). Extraction and clustering of lipids around amyloid aggregates and their potential links to toxicity have also been previously characterised (Reynolds et al., 2011). Fibril-membrane interactions also promote the shedding of oligomers from fibril ends that then diffuse rapidly through the brain and impair cognitive function in mice (Martins et al., 2008). These oligomers formed through reverse assembly reactions were found to have a highly heterogeneous size distribution, but similar biochemical and physical properties to those formed by nucleation and forward assembly reactions (Martins et al., 2008). Another potentially physiologically harmful effect of amyloid could arise from fibril interactions with metal ions (Viles, 2012), as several co-localise with amyloid plaques in AD patient brains (Miller et al., 2006). $A\beta_{42}$ fibril interactions with copper (Cu^{2+}) enable retention of redox activity and generation of reactive oxygen species *in vitro* (Mayes et al., 2014). The presence of metal ions also affects fibril aggregation morphology, which may have additional consequences on biological and pathogenic properties (Matheou et al., 2015; Mayes et al., 2014; Viles, 2012).

1.2.6.3 Modulating factors of amyloid cytotoxicity

In the complex, crowded environment of cells and nervous tissue, the cellular milieu plays an important role in affecting how the amyloid lifecycle progresses, and how amyloid species and populations form and interact with other cellular structures. Surfaces, such as those presented by membranes, can promote protein misfolding and aggregation, thus potentially speeding up nucleation events in the amyloid lifecycle, promoting the *de novo* formation of amyloid species (Stefani, 2007). This effect depends on the lipid composition of the membrane. Differing

membrane composition could potentially explain the variable vulnerability of various cell types to toxic amyloid species. Phosphatidylserine and other acidic phospholipids could provide a local low-pH environment that promotes fibril formation (H. Zhao et al., 2004). Interestingly, functional amyloid assemblies are often compartmentalised into membrane-bound organelles without causing damage. A specific membrane composition could explain why this key toxicity target is not harmed by functional amyloid aggregates. Furthermore, hydrophobic surfaces and the air-water interface are also capable of inducing heterogeneous nucleation and formation of small amyloid oligomers, as well as leading to the formation of fibrils with a distinct morphology compared to fibrils formed by homologous nucleation away from surfaces (Chi et al., 2010; Jean et al., 2012).

The lack of clear correlation between amyloid fibril aggregates with clinical symptoms in neurodegenerative diseases promoted the view that small oligomeric pre-fibrillar species are the main toxic species. While some oligomeric species display significant cytotoxic potential, not all oligomeric species share this potential. In the same manner, some amyloid fibril structures possess cytotoxic potential while others appear to be inert. Difficulties in studying the mechanisms and structures associated with amyloid toxicity under physiologically relevant conditions also add to the fact that the composition of the amyloid populations that are associated with disease as a whole, and their combined modes of action, have not been resolved. It is possible that the incoherence between the amyloid species and the neurodegenerative disease symptoms and progression they are associated with could be better explained not by individual amyloid structures but the sum of their presence in a population as a whole. The variation in the composition of the heterogeneous amyloid population resulting from the amyloid lifecycle may drive different characteristics and clinical symptoms associated with amyloid.

1.2.7 The infectious potential of amyloid: prions and prion-like amyloid

Prions are infectious amyloid particles with the self-propagating amyloid cross-β state. Mammalian prions are correlated with a number of currently untreatable neurodegenerative diseases termed transmissible spongiform encephalopathies (TSEs) which include kuru, Creutzfeldt-Jakob disease, bovine spongiform encephalopathy, and scrapie in sheep. These diseases can arise spontaneously, be inherited, or acquired through an infection by prion particles. TSEs are caused by an amyloidogenic form of the mammalian prion protein (PrP) and can be transmitted between individuals and sometimes even across species (Prusiner, 1998; Tanaka et al., 2005). However, not all prion replication is disease-associated and in fungi in particular they can have neutral or beneficial effects. For example in yeast, prions confer phenotypic plasticity through evolutionary selective advantages (Shorter & Lindquist, 2005). For example, the *Saccharomyces cerevisiae* protein Sup35 is a subunit of the eukaryotic translation release factor, required for termination of mRNA translation. The amyloid form of Sup35 is associated with the [*PSI*$^{+}$] prion phenotype (Wickner, 1994). Similarly, [*URE3*] is the prion phenotype associated with the *S. cerevisiae* Ure2 protein (Wickner, 1994). Both of these prion proteins can form several strain variants with different characteristics and have been studied extensively to elucidate the molecular mechanisms and structural determinants of amyloid proteins (Tanaka et al., 2006).

Prions have been be considered a subclass of amyloid that can be transmitted between cells and organisms (Kushnirov et al., 2007). However, there is now increasing evidence to suggest that some pathogenic amyloid proteins can also be transmissible from cell-to-cell. For example,

cross-cell transmission has been demonstrated for Aβ (Nussbaum et al., 2012), α-syn (Tarutani et al., 2018), huntingtin (Jeon et al., 2016) and tau (Clavaguera et al., 2017), blurring the distinction between 'prions' and 'amyloid'. As the likelihood of transmissibility of these pathogenic amyloid proteins between individuals, an essential aspects of prion behaviour, is probably low, they are consequently typically classified as 'prion-like' amyloid. Nevertheless, these proteins may be infectious to an extent, as shown for tau where injection of tau-containing brain extract of human origin can induce tau inclusions in transgenic mice expressing wild type human tau (Clavaguera et al., 2013). Recently, further evidence was found to support iatrogenic transmission of Aβ by identifying $A\beta_{40}$ and $A\beta_{42}$, along with tau, in archived vials of human cadaveric pituitary-derived growth hormone (Purro et al., 2018), which was used to treat patients until 1985 when some were diagnosed with Creutzfeldt-Jacob-Disease (CJD) (Laron, 2018). This raises concerns over accidental transmission of prion and prion-like amyloid during medical procedures and through potentially amyloid-contaminated surgical equipment.

How some amyloid can show a type of prion-like behaviour is not known, but fibril fragmentation seems to play a key role in facilitating infectivity (Marchante et al., 2017), as in the case of prion particles, division and propagation through fibril fragmentation could also be a key determinant for infectivity and amyloid phenotype strength (Tanaka et al., 2006). Fibril fragmentation could facilitate vesicular cell-to-cell transport, due to the smaller size of fragmented particles, as cell-to-cell spreading is thought to be mediated by intracellular amyloid particles weakening the lysosomal protein degradation pathway, leading to exocytosis of oligomeric species capable of propagating the amyloid state that are then taken up by recipient cells (Danzer et al., 2012). Thus, the stability of amyloid particles towards fibril fragmentation, which may be modulated by their suprastructure, could represent a link between amyloid structure and their infective potential as prions.

1.2.8 Challenges in establishing amyloid structure-function relationships

Many important aspects of amyloid toxicity, propagation, and their role in neurodegenerative diseases remain elusive. A significant gap in knowledge relates to the specific mechanisms of amyloid pathogenicity in terms of the structural properties associated with the toxic and infective potential displayed by amyloid structures. To effectively develop therapeutics that specifically target toxic or infective properties or species, it is first necessary to understand the mechanisms of toxicity, transmission and propagation in detail. However, for amyloid-associated diseases it is not yet clear whether amyloid aggregates are a cause or a consequence of the disease, and by which mechanisms they could exert toxic effects to the cells. Consequently, no safe and effective anti-amyloid treatments have yet been developed despite efforts by academia and pharmaceutical companies alike. Although aggregates of amyloid fibrils are an important hallmark for diagnosis of amyloid disease, their role in pathology is debated. It is thought that earlier species in the amyloid lifecycle, specifically the small intermediate, oligomeric, pre-fibrillary species, are responsible for some of the cytotoxic and neurodegenerative effects in amyloid associated pathologies (Bucciantini et al., 2002). However, there is also evidence of fibrils with a shorter length distribution having cytotoxic effects (W.-F. Xue, Hellewell, et al., 2009). Additionally, they could have important roles in amyloid propagation and other indirect mechanisms of toxicity, as well as being involved in the infective activities associated with prions and prion-like amyloid. The problem is exacerbated by the lack of high-resolution structural information of intermediate species on or off the fibril formation pathway as they have remained largely elusive due to conformational heterogeneity and transient nature.

Often, populations containing a heterogeneous mixture of amyloid polymorphs or amyloid species from different precursor sequences can be present in the brain of an affected individual, which might be part of the complex and varied nature of neurodegenerative diseases (Annamalai et al., 2016; Jiménez et al., 2001). As discussed above, a plethora of amyloid fibril polymorphs may form and grow under the same conditions, but each individual polymorph may have different effects on cells. However, it is often necessary to achieve a homogenous sample of fibrils of a single morphology by progressive seeding or stabilising fibrils of a specific polymorph for structural characterisation and when assaying biological effects of amyloid fibrils. A nearly homogenous population can be achieved by repeated seeding because fibrils with different morphologies have different rates of self-assembly (Tycko, 2015). However, the species distribution as a whole may have an impact on the pathological properties associated with amyloid. For example, in a population, some species may contribute directly to the accelerated propagation of the amyloid state in the amyloid lifecycle and only indirectly in the accumulation of toxic species, while other species may act as cytotoxic entities directly. Whole population effects could also rest in the varied concentrations of different species in the population as the toxic potential of the whole amyloid population will be a sum of the toxic potential displayed by individual species in the population, weighted by their concentrations. Just like for any toxic substances, the classic principle "*sola dosis facit venenum*" (the dose makes the poison) will also apply to amyloid species. Furthermore, the infectious and toxic potential of amyloid will be modulated by their suprastructural states, such as clustering and filament lateral assembly, at a mesoscopic scale. This information can be obtained using - for example - atomic force spectroscopy (AFM) and transmission electron microscopy (TEM) and will be highly complementary to higher resolution structural information on individual filament types obtainable by ssNMR and cryo-EM.

Various anti-amyloid therapeutics targeting different processes in the amyloid lifecycle have reached clinical trials although other than the recent controversial approval of aducanumab by the US Food and Drug Administration in June 2021 (Tagliavini et al., 2021), the developed therapeutics have not been widely successful (Mehta et al., 2017). Part of the problem lies with the fact that the holistic role of amyloid lifecycle in disease mechanisms has not been fully elucidated. Potential mechanisms to target amyloid formation include kinetic stabilisation of native and inert states, inhibitors of enzymes that process amyloid precursors, sequestering small toxic oligomeric species with antibodies, inhibition of amyloid-membrane interactions, prevention of elongation through blocking fibril ends, and potentially increasing elongation rates to force smaller, more toxic, states to form part of longer fibrils with less cytotoxic potential. For example, a molecular chaperone BRICHOS can effectively bind to the surface of Aβ fibrils, thus preventing secondary nucleation (G. Chen et al., 2017; Willander et al., 2012). Engineered and enhanced disaggregases, including Hsp104, are capable of clearing amyloid inclusions and could also potentially lead to development of therapeutics that upregulate amyloid aggregate clearance (Jackrel et al., 2014). Immunotherapies targeting Aβ oligomers or fibrils have been thus far been unsuccessful, although results are yet to emerge for their ability to prevent disease in asymptomatic people with a genetic predisposition (Y. Wang et al., 2017). This highlights the fact that developing drugs for amyloid disease treatments is not as straightforward as designing an inhibitor for monomer production. A deeper holistic and systems understanding of the effects of pathogenic amyloid in the biological context is required for effective development of therapeutics.

The potential for exploiting functional amyloid as natural bio-nanomaterials has inspired the development and rational design of artificial nanomaterials which use their unique materials

properties for a variety of prospective applications in biotechnology and biomedicine. The self-assembly mechanism produces highly stable fibrils with a tensile strength comparable to that of steel (Smith et al., 2006). These properties make them highly lucrative for novel biomaterial development. Additionally, amyloidogenic proteins are amenable to significant sequence and chemical modifications to alter their physio-chemical properties as the fibrils are able to maintain their structure under a wide range of conditions. Potential applications of synthetic amyloids include mechanisms of drug delivery as a reservoir for controlled release of drugs, and tissue repair as a molecular scaffold promoting cell adhesion, migration and differentiation. Another possible use of amyloid fibrils includes forming biosensors by entrapping proteins or other sensory molecules, depending on the desired application, or the formation of nanowires by forming long hollow tubes (Mankar et al., 2011). Amyloid-carbon hybrid membranes have also been developed for inexpensive water purification, efficiently removing heavy metal ions and radioactive waste (Bolisetty & Mezzenga, 2016). Thus, if bespoke amyloid can be designed and negatively selected against molecular features that are associated with toxic properties, amyloid fibrils will make excellent nanomaterials for biotechnology and biomedical purposes.

1.2.9 Closing remarks

Despite increasing research efforts, the specific role of amyloid structures in neurodegenerative disease remains elusive. There is still a lack of clear understanding of the identity of the toxic amyloid species, their mechanism of action and their infectious potential in relation to their structural properties. Indeed, high-resolution structural models of amyloid fibrils have now been resolved using emergent ssNMR and cryo-EM methodologies, and these advances confirm that despite sharing the same cross-β core characteristics, amyloidogenic proteins form

fibrils with differences in the arrangements of the steric zipper core packing, β-sheet content, and the number and packing arrangement of protofilaments. The formation of different polymorphs and the heterogeneity of the amyloid populations can be affected by environmental conditions, and fibrils and small oligomeric species with different morphologies can form under the same conditions, including *in vivo* and in disease-affected patients. There is also now increasing evidence to show that fibrils are not inert end-stage structures, but are an integral member of the amyloid lifecycle. Through division, replication and propagation processes such as enzyme-catalysed fibril fragmentation, several potential pathways of toxicity can have key roles in the amyloid lifecycle and their pathological effects. Simultaneously, there is a large degree of variability in the biological roles of amyloid, ranging from those essential for physiological functions to those associated with debilitating neurodegenerative diseases.

Variability in fibril polymorphs and their suprastructures on the mesoscopic scale could rationalise the variations in functional and pathogenic consequences of amyloid. Thus, conflicting evidence regarding varied cytotoxicity of amyloid fibrils could be resolved by fibrils having different levels of stability, structural rigidity, surface properties, and suprastructural formations that affect cytotoxicity, aggregation, interactions with chaperones, propensity to shed oligomers or sequester essential cellular proteins. This could also rationalise why amyloid deposits in the brain do not always correlate well with clinical symptoms of neurodegenerative disease or how some amyloids can have important physiological roles without any harmful effects. Additionally, patients with the same neurodegenerative disease form different predominant types of polymorphs of the same amyloid protein that could influence disease progression and clinical symptoms. Thus, a key challenge is to establish a correlation between amyloid structure, specific mechanisms of toxicity, and variability in clinical symptoms. Fully understanding mechanisms of the amyloid lifecycle and the behaviour

of heterogeneous and polymorphous amyloid populations and their suprastructural properties in the mesoscopic scale is essential to ensure the efficacy of future therapeutics targeting amyloid as well as biotechnological applications of amyloids.

1.3 On the structural diversity and individuality of polymorphic amyloid protein assemblies

1.3.1 Abstract

The prediction of highly ordered three-dimensional structures of amyloid protein fibrils from the amino acid sequences of their monomeric self-assembly precursors constitutes a challenging and unresolved aspect of the classical protein folding problem. Because of the polymorphic nature of amyloid assembly whereby polypeptide chains of identical amino acid sequences under identical conditions are capable of self-assembly into a spectrum of different fibril structures, the prediction of amyloid structures from an amino acid sequence requires a detailed and holistic understanding of its assembly free energy landscape. The full extent of the structure space accessible to the cross-β molecular architecture of amyloid must also be resolved. Here, we review the current understanding of the diversity and the individuality of amyloid structures, and how the polymorphic landscape of amyloid links to biology and disease phenotypes. We present a comprehensive review of structural models of amyloid fibrils derived by cryo-EM, ssNMR and AFM to date, and discuss the challenges ahead for resolving the structural basis and the biological consequences of polymorphic amyloid assemblies.

1.3.2 Research Highlights

- Amyloid structures are highly polymorphic in that the folding/misfolding-assembly of a single polypeptide sequence into the amyloid state may result in many different fibril structures.
- Prediction of amyloid structures from a primary amino acid sequence is a ‘one sequence to many structures’ problem due to polymorphism, and this challenge is far from being resolved.
- Structural data of amyloid in the PDB and the EMDB released to date (up to March 2021) show considerable presence of polymorphism, and are summarised in this review.
- Cryo-EM and ssNMR have revealed extensive diversity of amyloid structures that all share the defining cross-β fibril core architecture of amyloid.
- AFM has revealed the individuality displayed by each fibril structure in heterogeneous amyloid populations.

1.3.3 Introduction

Amyloid structures represent a class of filamentous protein self-assemblies that are defined by their characteristic core structures containing β-strands arranged perpendicularly to the fibril axis (Eisenberg & Jucker, 2012; Riek, 2017). Compared to the folding reaction of globular proteins, amyloid formation stands out because it possesses unique properties. Firstly, the coupled folding-assembly reaction of monomeric peptide chains into the amyloid state occurs as a result of intermolecular interactions between a large but variable number of monomers. Secondly, the resulting protein conformations of amyloid fibrils are capable of self-propagation. This property allows the information encoded in the individual 3D structures of amyloid and prions, which represent a class of infectious amyloid that can spread between individual organisms (Scheckel & Aguzzi, 2018), to be transmitted to monomers not yet in the amyloid state. Thirdly, although the end-products of a single type of amyloid assembly reaction are fibrils sharing the defining cross-β core architecture, there may be a wide degree of variation between their specific structures, even when the assembly reactions start with identical monomeric polypeptide chains under identical conditions. This property, called structural polymorphism, is biologically important because it affects the physicochemical properties of the fibrils, which subsequently may reflect the variation in the biological response to amyloid *in vivo*. For example, specific amyloid polymorphs formed from the same tau protein are found in different tauopathies (Shi et al., 2021), and within each disease-specific amyloid population there can exist several types of polymorphic fibrils (Falcon et al., 2019; Fitzpatrick et al., 2017; Zhang et al., 2020). However, structural polymorphism complicates any attempt of predicting a protein's 3D shape from its amino acid sequence, because in the case of amyloid, one single amino acid sequence may fold/misfold and assemble into a spectrum of different 3D structures.

Experimental techniques that have been applied to study the polymorphous amyloid structures include cryo-electron microscopy, solid-state nuclear magnetic resonance spectroscopy, and atomic force microscopy (**Table 1.2**). Methodological advances in cryo-EM has, in recent years, led to the elucidation of numerous structural models of amyloid fibrils (Fitzpatrick & Saibil, 2019). These cryo-EM derived models are made with 3D Coulomb potential maps, reconstructed nowadays routinely to sub-4 Å resolutions, using 2D projection images of fibrillar samples collected on modern cryo-EM microscopes. For ssNMR, spectroscopic data of nuclear resonance frequencies are collected on fibril samples formed from isotopically labelled protein monomers. The interpretation of the resulting chemical shifts and atomic distance constraints are used to reconstruct an ensemble of possible conformations of each single structural model (Tycko, 2011). AFM allows the morphologies of individual fibrils to be directly visualised on 2D topology images to a low-nanometre resolution, from which 3D envelope models of each individually observed fibril can then be reconstructed (Lutter et al., 2020). Combining AFM with infrared spectroscopy (AFM-IR) (Ruggeri et al., 2015) or Raman spectroscopy (AFM-Raman) (Krasnoslobodtsev et al., 2016), allows the secondary structure content of individual fibrils or aggregates to also be assessed. The 3D structural models obtained by these techniques, and the subsequently observed structural polymorphism, are discussed in this review.

Table 1.2 Summary of experimental techniques for 3D structural characterisation of polymorphic amyloid fibrils. Data type and structural information obtainable from the three methods highlighted in this review, i.e., cryo-electron microscopy (cryo-EM), solid-state nuclear magnetic resonance spectroscopy (ssNMR), and atomic force microscopy (AFM), are described.

	Cryo-EM	**ssNMR**	**AFM**
Data type	Projection images/transmission electron micrographs	Resonance frequencies/chemical shifts of atomic nuclei	Surface topography (height) images
Structural information	3D coulomb potential maps	Atomic distances, bond angles, and local chemical environment information	3D molecular surface envelopes
Features	Can provide high-resolution (<4Å) averaged structural maps	Generates an ensemble of possible molecular models at sub-Ångström resolution	Can provide individual particle information at low-nanometre resolution, and allows collection of nano-mechanical or chemical information

Recently, advances in the prediction of protein structures from their primary sequences by AlphaFold 2, a deep learning-based method which uses attention mechanisms and was developed by Google's DeepMind AI research group, showed that its structural predictions can now nearly match experimental results (Jumper et al., 2020). This was demonstrated by participation in the 14th Community Wide Experiment on the Critical Assessment of Techniques for Protein Structure Prediction (CASP14), a biennial community experiment in which international research teams participate to evaluate the accuracy of their protein structure prediction methods (e.g. (Kryshtafovych et al., 2019; Moult et al., 2018)). Despite this important advance, AlphaFold 2 has not yet been applied to multimeric protein structure prediction (Jumper et al., 2020), even though accurate prediction of multi-protein complex structures such as amyloid fibrils could revolutionise aspects of key applications, including drug design. This highlights the magnitude of unresolved challenges in structural prediction of

large protein assemblies, and the need to establish a fundamental understanding between amino acid sequence, amyloid structure, function, and pathogenicity. Thus, predicting the 3D structures of polymorphic amyloid fibrils from primary amino acid sequences is exceptionally challenging, but also offers important opportunities for contributing to our fundamental understanding of coupled protein folding and assembly free energy landscapes, as well as for potentially important applications in the development of anti-amyloid drugs for neurodegenerative diseases. This challenge can only begin to be addressed through the characterisation of the extent of amyloid polymorphism as well as the individual 3D structures of polymorphs formed. Here, we review recent advances in our understanding of amyloid polymorphism through recent structural data that reveal the diversity of amyloid fibril structures that can be formed, and the individuality of filament structures that exists within heterogeneous amyloid populations. We discuss the resulting physicochemical and biological consequences of amyloid polymorphism, the challenges of amyloid structure prediction, and opportunities where such contributions could provide new fundamental insights or applications.

1.3.4 The paradox of amyloid polymorphism: from one amino-acid sequence to many three-dimensional structures

Recent studies of the 3D structures of amyloid fibrils have revealed extensive presence of structural polymorphism in high-resolution detail. Different, but ordered and stable amyloid structures have been shown to assemble from polypeptide chains of the same primary amino acid sequence. This contradicts the uniqueness condition of Anfinsen's dogma stating that a uniquely dominating energy minimum in the free energy landscape of a polypeptide chain is required for it to fold into a unique native 3D structure (Anfinsen, 1973). Instead, it appears

that the free energy landscape for amyloid protein folding/misfolding and assembly consists of many local minima of similar levels of free energy, and the extent of such local minima groups are affected by factors that include the primary amino acid sequence of the monomeric building blocks of the fibrils (Aubrey et al., 2020). This structural polymorphism creates a considerable challenge for 3D structure prediction from primary sequence as one sequence can result in many different stably observable structures. Importantly, the structural polymorphs observed to date do not only result from different contacts between residues in the fibril cores that then lead to different overall folds, but instead involves a number of possible variations which interplay in a hierarchical manner (D. Li & Liu, 2021; Lutter et al., 2019) (**Fig. 1.6**). Firstly, different amyloid structures may result from 'top-level' modifications in the primary amino acid sequence such as point-mutations, truncations/deletions and/or post-translational modifications (**Fig. 1.6a**). However, these 'top-level' modifications involve changes in the covalent bonding pattern and can be classified as sequence polymorphism rather than structural polymorphism, and thus do not wholly reflect the complexities of amyloid sequence-structure relationships. Secondly, further complexities arise from the conformational arrangements of protofilaments, which are filamentous building blocks that make up the fibril structures. In the protofilament core, the extent and the packing of β-sheet- and random coil-forming regions, as well as disordered regions, often vary even for monomeric polypeptide chains of identical sequences. Co-factors in the fibril core may also be necessary for stabilising specific folds, further contributing to structural polymorphism. There are also known instances where protofilaments are formed by multiple different polypeptide sequences, thus resulting in heteroamyloid fibrils (**Fig. 1.6b**). Thirdly, although conformational differences in the protofilament core formed from a single amyloid protein or peptide sequence can display remarkable structural diversity, it is also common for amyloid fibrils to assemble and form structures involving multiple protofilaments (**Fig. 1.6c**). In this case, each monomeric layer of

the fibril consists of multiple copies of the same peptide chain, which can be arranged in a number of different ways. Notably, the protofilament building blocks of amyloid fibrils can have identical or different folds, and their lateral arrangement can vary. Finally, structural polymorphism can also arise from variations in the fibrils' mesoscopic (nm to µm length-scale) arrangements like twist handedness, twist pitch, the position of the fibril screw-axis, and fibril length. These long-range properties contribute to the molecular individuality of amyloid fibrils, which may subsequently also impact the biological response the fibrils elicit.

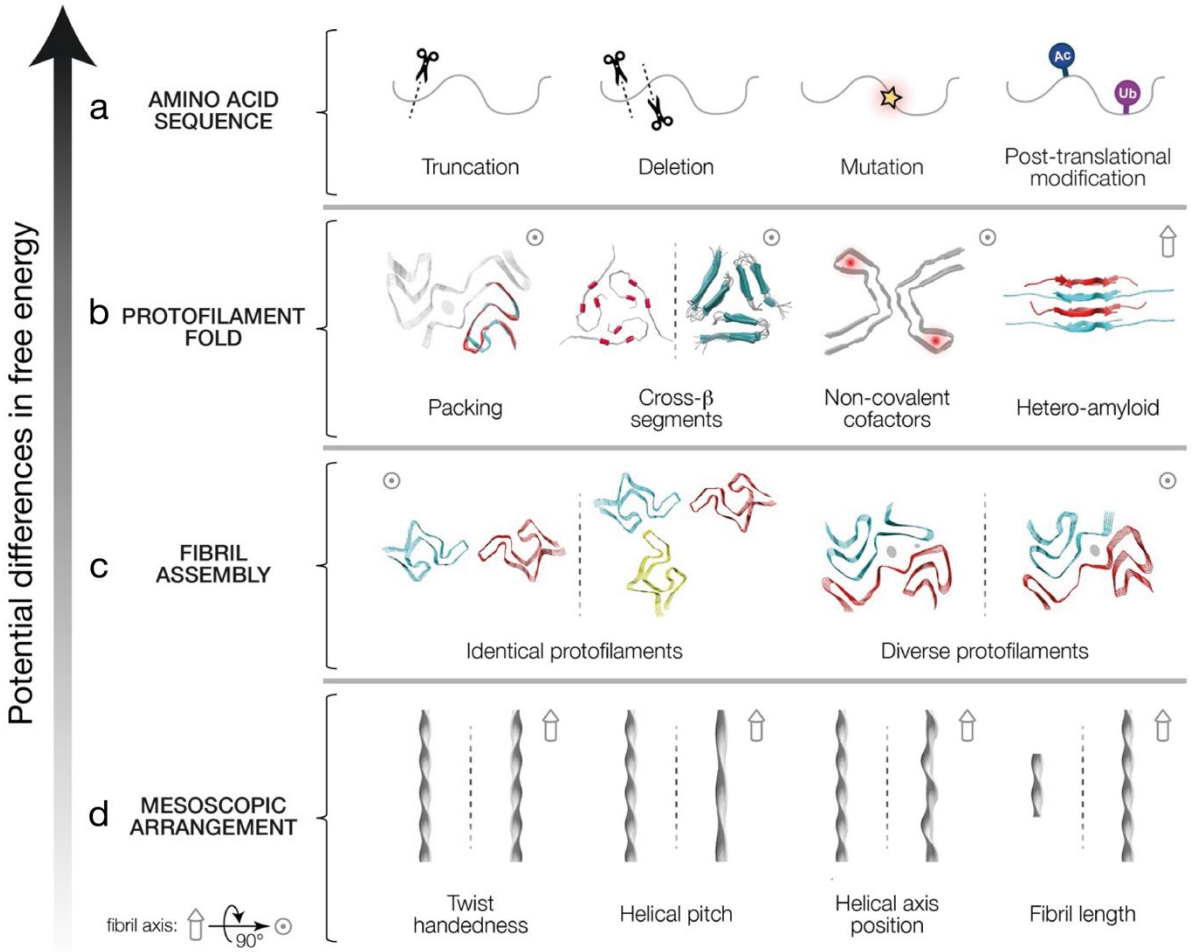

Figure 1.6 Hierarchical structural polymorphism of amyloid fibrils. (a) Modifications of the primary amino acid sequence, including truncations, deletions, mutations, and post-translational modifications, represent the first layer of complexity that leads to the diversity of amyloid structures. **(b)** Polypeptide chains with identical amino acid sequences may exhibit

further differences in the adopted protofilament fold upon assembly, including differences in the β-sheet forming regions (segmental polymorphism; demonstrated by $A\beta_{40}$ PDB IDs 2M4J and 2LMQ on the left and right, respectively), the arrangement of the core fold (packing polymorphism; demonstrated by overlay of α-synuclein PDB IDs 6XYP and 6XYQ) and the presence of noncovalent co-factors (tau PDB ID 6NWP). Interestingly, heteroamyloid can result from alternate stacking of monomers with different sequences to form a fibril (RIPK1/3 PDB ID 5V7Z). **(c)** Assembly of identical or different protofilaments by lateral associations can result in further diversity of amyloid structures. Assembly polymorphism with identical folds is illustrated by α-synuclein PDB IDs 6L1T (left) and 6L1U (right) and for fibrils with diverse folds the accession codes are 6XYO (left) and 6XYP (right), also showing α-synuclein fibrils. **(d)** Polymorphism can also arise in the mesoscopic length scale from differences in twist handedness, helical pitch, the position of the helical axis and the number of monomers in the fibril, which determines the length. Molecular models were generated using UCSF Chimera (Pettersen et al., 2004).

Due to polymorphic folding and assembly landscapes, the prediction of amyloid structures from their constituent monomeric amino acid sequences is challenging. The hierarchical nature of structural polymorphism, which has been experimentally observed to give rise to many diverse structures from identical protein sequences, may lead to a continuous cloud of polymorphs within a population of amyloid fibrils, with individual fibrils populating the structure space defined by local energy minima with differing probabilities. Thus, the possibility of diverse and individualistic amyloid structures resulting from the folding/misfolding-assembly of identical polypeptide chains presents a conundrum in terms of whether the cloud of structures formed also translates into equally diverse biological or phenotypical responses, and whether it is possible to predict amyloid structures and subsequent function with some degree of certainty. It is currently not possible to assess how well structural prediction tools would predict amyloid structures as none have yet been included as CASP targets. However, structural prediction of multimeric CASP targets is a greater challenge compared to monomeric targets due to the necessity of predicting how multiple monomeric

subunits interface with each other (Guzenko et al., 2019). Therefore, prediction of amyloid fibril structures, which have multiple interfacing monomeric subunits and, in addition, exhibit a wide degree of polymorphism (see **Fig. 1.6**), will require significant additional advances to current methods. Current prediction tools specifically designed for amyloid sequences are focused on predicting the amyloid forming propensity of sequence regions, with some offering additional predictions of intrinsic disorder and secondary structure (e.g. (Fernandez-Escamilla et al., 2004; Maurer-Stroh et al., 2010; Walsh et al., 2014)). Nevertheless, predicting the amyloidogenic regions and aggregation propensity has been challenging even for short peptides (Roland et al., 2013; Santos et al., 2020).

1.3.5 The structural diversity of filamentous amyloid assemblies

Amyloid fibrils are defined by a characteristic cross-β structure formed by β-strands with 4.7 Å spacing, stabilised by a hydrogen bonding network parallel to the fibril axis, and tight side-chain packing between two β-sheets with 10 Å spacing. This cross-β architecture can be experimentally readily observed in X-ray fibre diffraction patterns (Jahn et al., 2010). Importantly, the 3D structures of a growing number of amyloid fibrils have been experimentally resolved in the last five years, revealing extensive presence of structural polymorphism (see **Table 1.3** and **Fig. 1.7** for a summary of structural data in the EMDB and the PDB released up until March 2021).

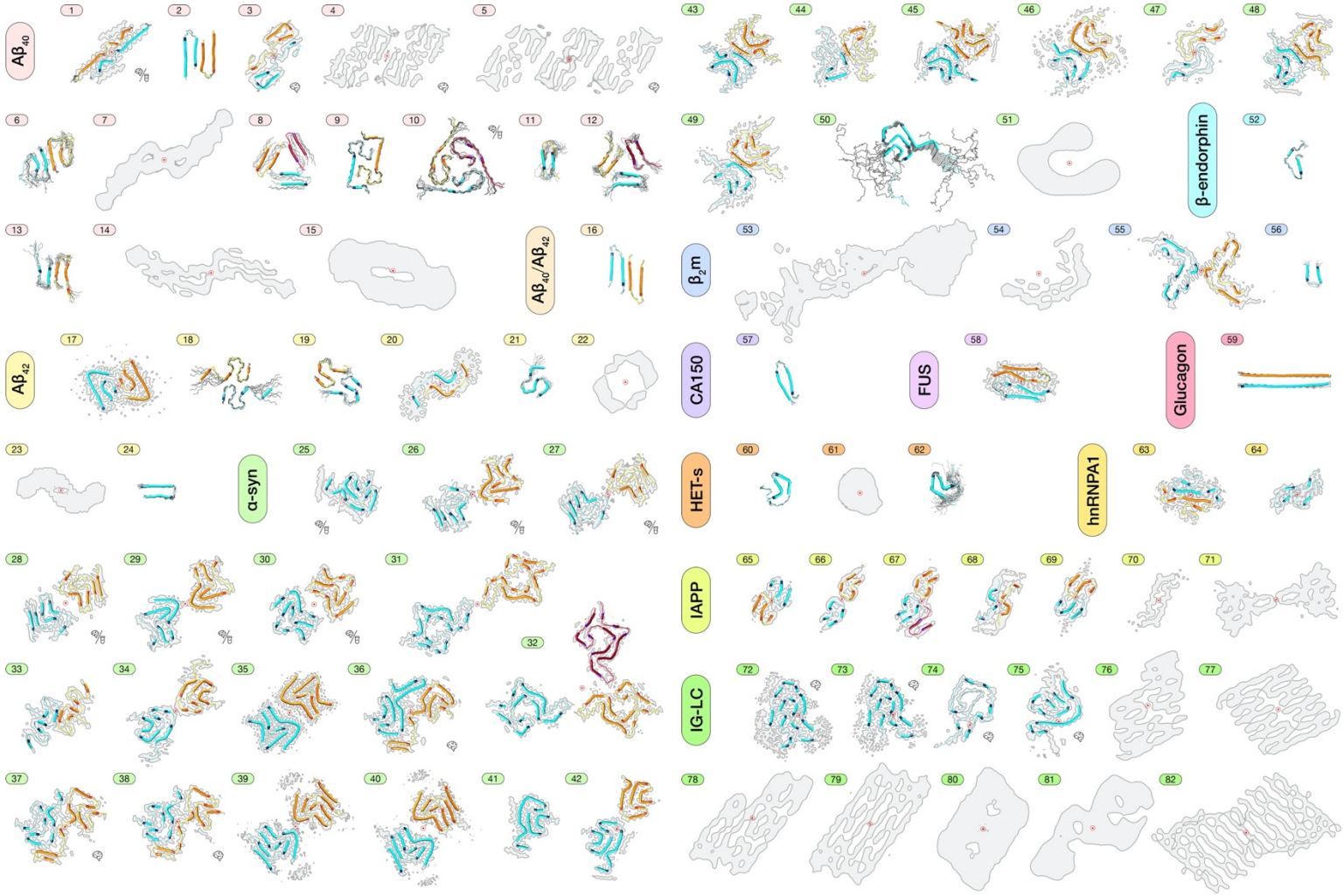

Figure 1.7 Diversity of cross-β structures demonstrated by a graphical summary of structural data of amyloid fibrils acquired by cryo-EM or ssNMR.

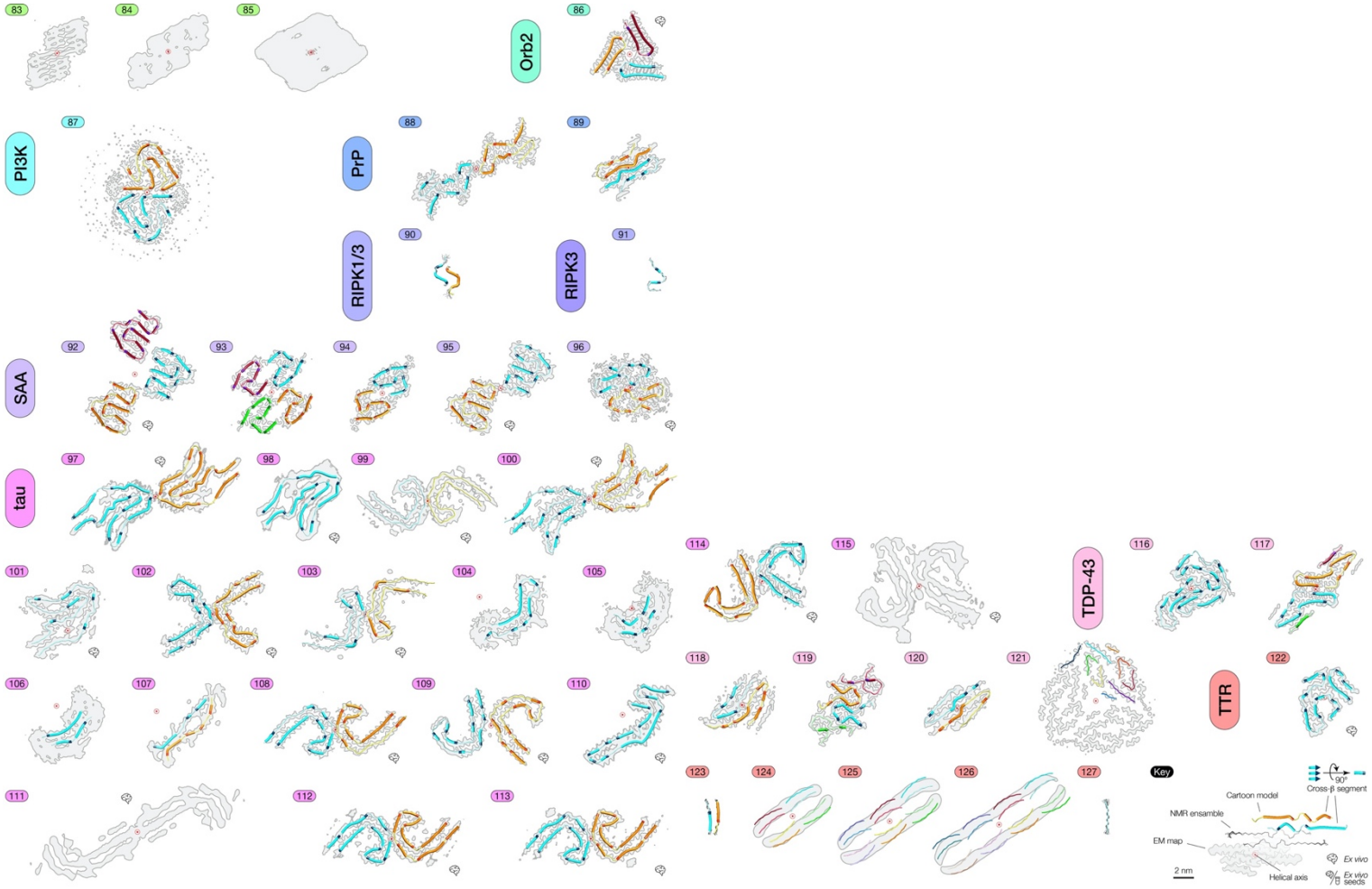

Figure 1.7 (continued) Average cross-section of cryo-EM density maps, ssNMR ensembles, and structural models of amyloid fibrils containing constituent polypeptide segments longer than 10 amino acids deposited in the EMDB and PDB databases up until March 2021 are shown in an orientation with the fibril axis perpendicular to the page plane. The entries are grouped by protein name and then by the release date of the data

entry, with the newest data entry shown first. The numbers shown correspond to the entry numbers listed in Table 1.3. Structural models are displayed by a coloured ribbon representation in cases where PDB entries are available. Each polypeptide chain in the cross-section view is coloured differently, with the cross-β segments, where such segments are determined and labelled in the PDB entry, shown as a wider chains in a darker shade and their C-terminal residues shown in an even darker shade. A single layer of each fibril model along the helical axis is shown only, for clarity. For ssNMR ensembles, the first model is shown in the coloured ribbon representation and other models are shown in grey wire representation. Cryo-EM maps are shown as grey average cross-sections with a darker grey outline representing the iso-line that defines the density boundary. The cross-sections were drawn by first untwisting the map to a single slice along the length of the fibril using published twist and rise values, and isolines were subsequently generated using the recommended isovalue provided by the authors in the EMDB entry. A key is provided in the bottom right corner of the figure, showing the cartoon labels for entries of *ex vivo* samples or of *ex vivo* seeded samples used throughout. All models and representations are scaled equally, with the scale bar representing the length of 20 Å. Molecular models were generated using UCSF Chimera (Pettersen et al., 2004).

Table 1.3 Three-dimensional structural data entries of amyloid fibrils acquired by cryo-EM or ssNMR. Entries that are released in the EMDB and PDB databases running up to March 2021 are shown.

	Amyloid name *	Sample origin §	Experimental method	PDB ID ‡	EMDB ID †	Release date	Reference
1	$A\beta_{40}$	AD brain, seeded	ssNMR & cryo-EM	6w0o	21501	13/01/2021	(U. Ghosh et al., 2021)
2	$A\beta_{40}$		ssNMR	6ti5		22/07/2020	(Cerofolini et al., 2020)
3	$A\beta_{40}$	AD brain	cryo-EM	6shs	10204	06/11/2019	(Kollmer et al., 2019)
4	$A\beta_{40}$	AD brain	cryo-EM		4864	06/11/2019	
5	$A\beta_{40}$	AD brain	cryo-EM		4866	06/11/2019	
6	$A\beta_{40}$		ssNMR	6oc9		05/06/2019	(Z.-W. Hu et al., 2019)
7	$A\beta_{40}$		cryo-EM		6326, 6327, 6328	29/04/2015	(Rohou & Grigorieff, 2014)
8	$A\beta_{40}$		ssNMR	2mpz		22/04/2015	(Sgourakis et al., 2015)
9	$A\beta_{40}$		ssNMR	2mvx		26/11/2014	(Schütz et al., 2015)
10	$A\beta_{40}$	AD brain, seeded	ssNMR	2m4j		25/09/2013	(J.-X. Lu et al., 2013)
11	$A\beta_{40}$		ssNMR	2lnq		08/02/2012	(Qiang et al., 2012)
12	$A\beta_{40}$		ssNMR	2lmq, 2lmp		28/12/2011	(Paravastu et al., 2008)
13	$A\beta_{40}$		ssNMR	2lmo, 2lmn		28/12/2011	
14	$A\beta_{40}$		cryo-EM		5008, 5132	08/10/2009	(Sachse et al., 2008, 2010)
15	$A\beta_{40}$		cryo-EM		1650	24/09/2009	(M. Schmidt et al., 2009)
16	$A\beta_{40}/A\beta_{42}$		ssNMR	6ti6, 6ti7		22/07/2020	(Cerofolini et al., 2020)
17	$A\beta_{42}$		cryo-EM	5oqv	3851	13/09/2017	(Gremer et al., 2017)
18	$A\beta_{42}$		ssNMR	2nao		27/07/2016	(Wälti et al., 2016)
19	$A\beta_{42}$		ssNMR	5kk3		13/07/2016	(Colvin et al., 2016)
20	$A\beta_{42}$		cryo-EM	5aef	3132	26/08/2015	(M. Schmidt et al., 2015)
21	$A\beta_{42}$		ssNMR	2mxu		06/05/2015	(Xiao et al., 2015)
22	$A\beta_{42}$		cryo-EM		5052	07/07/2010	(R. Zhang et al., 2009)
23	$A\beta_{42}$		cryo-EM		1649	24/09/2009	(M. Schmidt et al., 2009)
24	$A\beta_{42}$		ssNMR	2beg		22/11/2005	(Lührs et al., 2005)
25	α-syn	MSA brain, seeded	cryo-EM	7nck	12269	24/02/2021	(Lövestam et al., 2021)
26	α-syn	MSA brain, seeded	cryo-EM	7ncj	12268	24/02/2021	
27	α-syn	MSA brain, seeded	cryo-EM	7nci	12267	24/02/2021	
28	α-syn	MSA brain, seeded	cryo-EM	7nch	12266	24/02/2021	

29	α-syn	MSA brain, seeded	cryo-EM	7ncg	12265	24/02/2021	
30	α-syn	MSA brain, seeded	cryo-EM	7nca	12264	24/02/2021	
31	α-syn		cryo-EM	6l1t	0801	12/08/2020	(K. Zhao, Lim, et al., 2020)
32	α-syn		cryo-EM	6l1u	0803	12/08/2020	
33	α-syn		cryo-EM	6l4s	0833	29/04/2020	(K. Zhao, Li, et al., 2020)
34	α-syn		cryo-EM	6lrq	0958	08/04/2020	(Sun, Hou, et al., 2020)
35	α-syn		cryo-EM	6ufr	20759	19/02/2020	(Boyer et al., 2020)
36	α-syn	MSA brain	cryo-EM	6xyo	10650	12/02/2020	(Schweighauser et al., 2020)
37	α-syn	MSA brain	cryo-EM	6xyp	10651	12/02/2020	
38	α-syn	MSA brain	cryo-EM	6xyq	10652	12/02/2020	
39	α-syn		cryo-EM	6sst	10305	18/12/2019	(Guerrero-Ferreira et al., 2019)
40	α-syn		cryo-EM	6ssx	10307	18/12/2019	
41	α-syn		cryo-EM	6peo	20328	27/11/2019	(Boyer et al., 2019)
42	α-syn		cryo-EM	6pes	20331	27/11/2019	
43	α-syn		cryo-EM	6osj	20183	25/09/2019	(Ni et al., 2019)
44	α-syn		cryo-EM	6osm	20186	25/09/2019	
45	α-syn		cryo-EM	6osl	20185	25/09/2019	
46	α-syn		cryo-EM	6cu7	7618	12/09/2018	(B. Li et al., 2018)
47	α-syn		cryo-EM	6cu8	7619	12/09/2018	
48	α-syn		cryo-EM	6h6b	0148	08/08/2018	(Guerrero-Ferreira et al., 2018)
49	α-syn		cryo-EM	6a6b	0988	11/07/2018	(Y. Li et al., 2018)
50	α-syn		ssNMR	2n0a		23/03/2016	(Tuttle et al., 2016)
51	α-syn		cryo-EM		6482	16/12/2015	(Dearborn et al., 2016)
52	β-endorphin		ssNMR	6tub		28/10/2020	(Seuring et al., 2020)
53	β2m		cryo-EM		0019	19/06/2019	(Iadanza, Silvers, et al., 2018)
54	β2m		cryo-EM		0021	29/05/2019	
55	β2m		cryo-EM	6gk3	0014	14/11/2018	
56	β2m		ssNMR	2e8d		13/02/2007	(Iwata et al., 2006)
57	CA150		ssNMR	2nnt		14/11/2006	(Ferguson et al., 2006)
58	FUS		ssNMR & cryo-EM	6xfm	21169	07/10/2020	(M. Lee et al., 2020)
59	Glucagon		ssNMR	6nzn		05/06/2019	(Gelenter et al., 2019)
60	HET-s		ssNMR	2mus, 2lbu		01/02/2017	(Herrmann et al., 2015; Schütz et al., 2011)
61	HET-s		cryo-EM		2946	15/04/2015	(Mizuno et al., 2011)
62	HET-s		ssNMR	2kj3, 2rnm		02/06/2010	(Van Melckebeke et

							al., 2010; Wasmer et al., 2008)
63	hnRNPA1		cryo-EM	7bx7	30235	18/11/2020	(Sun, Zhao, et al., 2020)
64	hnRNPA2		cryo-EM	6wqk	21871	26/08/2020	(J. Lu et al., 2020)
65	IAPP		cryo-EM	6zrf	11380	30/09/2020	(Gallardo, Iadanza, et al., 2020)
66	IAPP		cryo-EM	6zrq	11382	30/09/2020	
67	IAPP		cryo-EM	6zrr	11383	30/09/2020	
68	IAPP		cryo-EM	6vw2	21410	10/06/2020	(Cao et al., 2020)
69	IAPP		cryo-EM	6y1a	10669	04/03/2020	(Röder et al., 2020)
70	IAPP		cryo-EM		10670	04/03/2020	
71	IAPP		cryo-EM		10671	04/03/2020	
72	IG LC	AL cardiac tissue	cryo-EM	6z1o	11031	24/02/2021	(Radamaker et al., 2021)
73	IG LC	AL cardiac tissue	cryo-EM	6z1i	11030	24/02/2021	
74	IG LC	AL cardiac tissue	cryo-EM	6ic3	4452	03/04/2019	(Radamaker et al., 2019)
75	IG LC	AL cardiac tissue	cryo-EM	6hud	0274	27/03/2019	(Swuec et al., 2019)
76	IG LC		cryo-EM		3986	28/02/2018	(Close et al., 2018)
77	IG LC		cryo-EM		3987	28/02/2018	
78	IG LC		cryo-EM		3988	28/02/2018	
79	IG LC		cryo-EM		3989	28/02/2018	
80	IG LC		cryo-EM		3990	28/02/2018	
81	IG LC		cryo-EM		3991	28/02/2018	
82	IG LC		cryo-EM		3992	28/02/2018	
83	IG LC		cryo-EM		3993	28/02/2018	
84	IG LC		cryo-EM		3994	28/02/2018	
85	IG LC		cryo-EM		3128	18/05/2016	(A. Schmidt et al., 2016)
86	Orb2	*D. melanogaster* brain	cryo-EM	6vps	21316	18/03/2020	(Hervas et al., 2020)
87	PI3K		cryo-EM	6r4r	4727	28/08/2019	(Röder et al., 2019)
88	PrP		cryo-EM	6lni	0931	10/06/2020	(L.-Q. Wang et al., 2020)
89	PrP		cryo-EM	6uur	20900	15/04/2020	(Glynn et al., 2020)
90	RIPK1/RIPK3		ssNMR	5v7z		28/03/2018	(Mompeán et al., 2018)
91	RIPK3		ssNMR	6jpd		28/10/2020	(Wu et al., 2021)
92	SAA	Murine liver	cryo-EM	6zch	11164	17/02/2021	(Bansal et al., 2021)
93	SAA		cryo-EM	6zcg	11163	17/02/2021	
94	SAA		cryo-EM	6zcf	11162	17/02/2021	
95	SAA	Murine spleen	cryo-EM	6dso	8910	13/03/2019	(Liberta et al., 2019)
96	SAA	Amyloidotic kidney	cryo-EM	6mst	9232	13/03/2019	

97	tau	CBD brain	cryo-EM	6vh7	21200	04/03/2020	(Arakhamia et al., 2020)
98	tau	CBD brain	cryo-EM	6vha	21201	04/03/2020	
99	tau	AD brain	cryo-EM	6vhl	21207	04/03/2020	
100	tau	CBD brain	cryo-EM	6tjx	10514	05/02/2020	(W. Zhang et al., 2020)
101	tau	CBD brain	cryo-EM	6tjo	10512	05/02/2020	
102	tau	CTE brain	cryo-EM	6nwp	0527	27/03/2019	(Falcon et al., 2019)
103	tau	CTE brain	cryo-EM	6nwq	0528	27/03/2019	
104	tau		cryo-EM	6qjh	4563	20/02/2019	(W. Zhang et al., 2019)
105	tau		cryo-EM	6qjm	4564	20/02/2019	
106	tau		cryo-EM	6qjp	4565	20/02/2019	
107	tau		cryo-EM	6qjq	4566	20/02/2019	
108	tau	AD brain	cryo-EM	6hre	0259	10/10/2018	(Falcon, Zhang, Schweighauser, et al., 2018)
109	tau	AD brain	cryo-EM	6hrf	0260	10/10/2018	
110	tau	Pick's disease brain	cryo-EM	6gx5	0077	12/09/2018	(Falcon, Zhang, Murzin, et al., 2018)
111	tau	Pick's disease brain	cryo-EM		0078	12/09/2018	
112	tau	AD brain	cryo-EM	5o3l	3741	26/07/2017	(Fitzpatrick et al., 2017)
113	tau	AD brain	cryo-EM	5o3o	3742	26/07/2017	
114	tau	AD brain	cryo-EM	5o3t	3743	26/07/2017	
115	tau	AD brain	cryo-EM		3744	26/07/2017	
116	TDP-43		cryo-EM	7kwz	23059	24/02/2021	(Q. Li et al., 2021)
117	TDP-43		cryo-EM	6n3a	9349	26/06/2019	(Cao et al., 2019)
118	TDP-43		cryo-EM	6n3b	9350	26/06/2019	
119	TDP-43		cryo-EM	6n3c	0334	26/06/2019	
120	TDP-43		cryo-EM	6n37	9339	26/06/2019	
121	TDP-43		cryo-EM	5w7v	8781	14/03/2018	(Guenther et al., 2018)
122	TTR	ATTR heart	cryo-EM	6sdz	10150	13/11/2019	(M. Schmidt et al., 2019)
123	TTR		ssNMR	2m5n		17/07/2013	(Fitzpatrick et al., 2013)
124	TTR		cryo-EM	2m5k	5590	03/04/2013	
125	TTR		cryo-EM	2m5m	2323	27/03/2013	
126	TTR		cryo-EM	3zpk	2324	27/03/2013	
127	TTR		ssNMR	1rvs		20/01/2004	(Jaroniec et al., 2004)

*. Database entries are ordered alphabetically by their protein name. Entries of amyloid formed from the same protein are ordered by release date from the newest to the oldest. Where several models have been published based on reanalysis of the same original data, the entries are grouped and all accession codes are included in the same row.

§. The origin of the tissue from which *ex vivo* fibrils were extracted is noted. Where the species is not specified, the tissue is of human origin, with the following abbreviations for disease diagnoses: AD – Alzheimer's Disease, MSA – multiple system atrophy, CBD – corticobasal degeneration, CTE – chronic traumatic encephalopathy, ATTR – transthyretin amyloidosis

†. The Protein Data Bank (PDB) ID code associated with the structural model.
‡. The Electron Microscopy Data Bank (EMDB) accession codes associated with the EM density map.

The elucidation of amyloid 3D structures in atomic detail was pioneered by X-ray diffraction experiments of amyloid peptide microcrystals, allowing the variation in the β-sheet arrangements to be experimentally characterised and the features that stabilise the cross-β fold to be studied (Sawaya et al., 2007). This revealed, for example, the tight inter-digitating side chains that make up the dry interface between β-sheets, termed steric zippers, and the hydrogen-bonding ladders formed by stacking of specific side-chains along the length of the long fibril axis. Eight different possible classes of steric zippers have been described, with differences arising from the parallel or antiparallel direction of the β-sheets, and the relative orientations of the two connecting β-sheets (Sawaya et al., 2007). More recently, microcrystal electron diffraction (microED) has been employed to elucidate the structures of amyloid peptide crystals, with the advantage that even nano-sized crystals too small for conventional X-ray crystallography experiments can be amenable for analysis (Rodriguez et al., 2015). Formation of crystals for structural studies is, however, limited by the length of the amyloid forming peptide. Therefore, amyloid structures formed from larger polypeptide fragments or full-length proteins have been mainly resolved using solid state nuclear magnetic resonance spectroscopy and cryo-electron microscopy. Although ssNMR has been used to generate structural models of amyloid fibrils for nearly two decades, it was the 'resolution revolution' of cryo-EM that led to the increased rate in the number of data entries of amyloid fibrils deposited to the EMDB and PDB databases in recent years. The average resolution of cryo-EM maps has also markedly improved in the last five years (**Fig. 1.8**). Advances in cryo-EM hardware and increased accessibility to equipment have driven the collection of evermore number of high-quality datasets of amyloid fibril samples, whereas improved software for helical reconstruction and refinement have facilitated 3D reconstruction with resolutions that

regularly allow *de novo* building of molecular models (Scheres, 2020). These recent advances have made possible the wide-ranging characterisation of amyloid fibril structures and the types of polymorphic features they exhibit in detail, revealing the diversity in the conformation of the fibril cores, the possible presence of post-translational modifications (PTMs) and co-factors, the span of cross-β forming regions, and the extent of ordered and dynamic regions within amyloid fibrils. Here, structural models of amyloid fibrils determined by cryo-EM and ssNMR available in the EMDB and PDB databases up to March 2021 are listed in Table 1.3 and correspondingly visualised in Fig. 1.7 to both illustrate the diversity of cross-β structures as well as provide an organised resource that facilitates comparison.

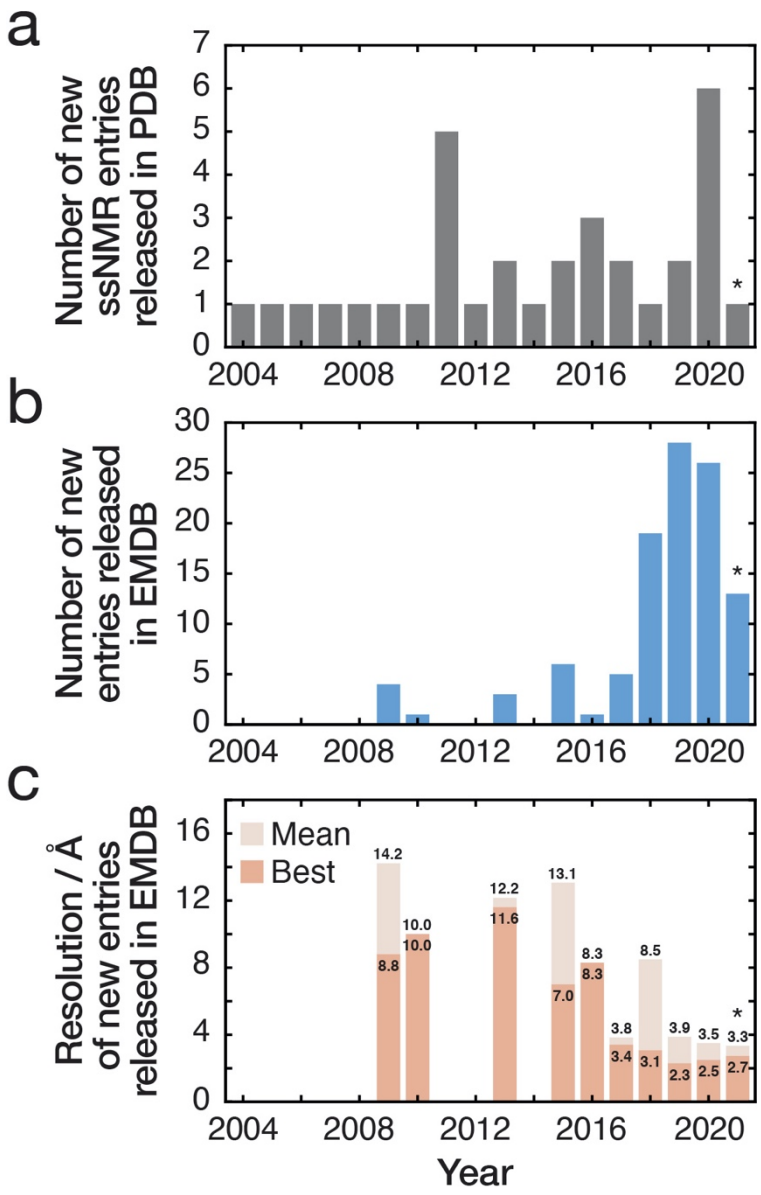

Figure 1.8 The number of structural data entries of amyloid fibrils deposited to the EMDB and PDB databases is rapidly growing, and the resolution of cryo-EM data is improving. (a) Number of new amyloid structural models determined by ssNMR deposited to the PDB released each year since 2004. **(b)** Number of new amyloid cryo-EM data deposited to the EMDB released each year since 2009. **(c)** Mean and best resolutions of cryo-EM data of amyloid fibrils each year. The star symbols (*) indicate that only entries released up until March are included for 2021.

The evermore detailed information on amyloid fibril core structures has revealed a large degree of polymorphism, which can be classified in a hierarchical manner as illustrated in Fig. 1.6.

Especially interesting are polymorphic structures formed from protein chains with an identical sequence, which exhibit fibril polymorphism in protofilament folds, filament assemblies, and mesoscopic properties, as these features indicate sensitivity of the assembly process to environmental conditions in determining the extent of polymorphism and the individuality of the formed fibril structures. For example, amyloid fibrils formed from $A\beta_{40}$ and $A\beta_{42}$ result in considerably different structures with different protofilament folds and assemblies (see **Fig. 1.7**, entries 1 to 24, and **Table 1.3** for accession codes), likely due to the different conditions in which the fibrils were formed. Structures of the same protein with different disease-associated mutations and post-translational modifications have also been shown to form structures with different morphologies. For example, structural data are available for α-synuclein with three different mutations related to early-onset Parkinson's disease, E46K, A53T, and H50Q (see **Fig. 1.7** and **Table 1.3**, entries 33, 34, 35, 41 and 42). Comparing the structures and their properties, such as stability and seeding propensity, to those of wild-type fibrils may indicate how polymorphism varies between familial and sporadic cases. Recently a combined cryo-EM and mass spectrometry approach has also revealed specific PTMs on tau fibrils from *ex vivo* patient brain tissue (see **Fig. 1.7** and **Table 1,3**, entries 97-99) (Arakhamia et al., 2020). Identification of disease-relevant modifications is crucial for understanding how PTMs may modulate fibril polymorphism and its biological effects. Importantly, the current structural data have shown differences between fibril structures extracted from *ex vivo* tissues and those assembled *in vitro* from recombinant protein monomers (e.g. see **Fig. 1.7** and **Table 1.3** entries 92-95) (Bansal et al., 2021). This is indicative of the importance and the challenge of studying amyloid polymorphism in disease contexts in order to understand possible disease-relevant sequence modifications and local *in vivo* environmental factors. Additionally, it was recently shown that seeded formation of amyloid using fresh monomer incubated with *ex vivo* fibril seeds does not necessarily replicate the structure of the seed in the case of α-synuclein

from multiple system atrophy patient brain tissue (Lövestam et al., 2021). It is currently not known if seeding may not propagate fibril structures due to a non-matched PTM pattern of the monomer compared to that of the seeds, if co-factors that may be present in the fibril core are missing in the seeded reactions, or if the assembly conditions during seeding are too different to those during the formation of the seeds in general. It is also unclear how this may vary for different amyloid systems that exhibit different kinetic rates for templated elongation and secondary nucleation (Meisl et al., 2014). Nevertheless, these results demonstrate that structures of fibrils formed from seeded growth using *ex vivo* fibril seeds should not necessarily be assumed to be identical to those of the patient derived seeds without further evidence (Koloteva-Levine et al., 2021; Peduzzo et al., 2020), due to the complexities arising from the polymorphism-prone nature of amyloid. In summary, detailed structural characterisation of amyloid fibrils, enabled by methodological advances in cryo-EM and ssNMR, has demonstrated a remarkable tendency for many amyloid forming polypeptide sequences to each form a diverse range of polymorphic cross-β amyloid structures.

1.3.6 The individuality of amyloid structures

The potential of amyloid fibrils to display a diverse range of cross-β structures (**Fig. 1.7**) due to polymorphism resulting from the vast number and combinations of possible arrangements of the polypeptide chains within each fibril (**Fig. 1.6**) means that the structures of amyloid fibrils should also be considered with respect to individual fibrils. Each individual fibril in a heterogeneous amyloid population may be distinguishable from every other fibril in the same population in terms of its precise structure, stability, and biological properties, even when the primary sequence of the monomeric polypeptide chains making up the fibrils is the same. This

is because many of the possible structural variations which underpin the observed amyloid polymorphism are based on differences in the pattern of the energetically weak non-covalent interactions (**Fig. 1.6b-d**), especially those peripheral to the cross-β protofilament core (**Fig. 1.6c-d**). Experimental observations by both negative-stain electron microscopy and atomic force microscopy have shown that amyloid fibril populations can be highly heterogeneous (Adamcik & Mezzenga, 2012; Fändrich et al., 2009; Goldsbury et al., 2005; Jiménez et al., 2002; Kad et al., 2003). Advances in AFM imaging over the last two decades have contributed with the discovery that the differences between structural polymorphs of amyloid, such as the number of protofilaments, twist patterns, and the thickness of fibrils, which are all influenced by the structure of the amyloid core, can indeed vary from fibril to fibril within a population (Adamcik et al., 2010; Aubrey et al., 2020; Goldsbury et al., 2005; Kad et al., 2003).

Modern AFM imaging methods can detect and characterise the structures of individual amyloid fibrils within complex and heterogeneous samples. While the imaging resolution achievable by AFM in one of the three spatial dimensions, i.e., the z- or height-axis, can now routinely reach sub-ångströms under ambient conditions, the overall 3D-resolution of AFM has not yet reached that currently achievable by cryo-EM and remains in the low-nanometre range. However, due to its underlying high signal-to-noise physics, the structures of individual particles of amyloid can be characterised to ~nm resolution without the extensive cross-particle averaging that cryo-EM methodologies rely on. Recently, we have developed a method to reconstruct the 3D surface envelopes of individual helical amyloid fibrils using the 3D information encoded in AFM height topology images (Lutter et al., 2020) (**Fig. 1.9**). This advance, combined with a systematic morphometric analysis and classification of individually reconstructed 3D fibril models, enables the detection and structural characterisation of individual, potentially rare, amyloid fibril species, and structural variations within individual

fibrils. The heterogeneity of a polymorphic amyloid population can also be quantitatively assessed using AFM data by analysing the variations in fibril width, cross-sectional area and shape, twist periodicity and twist handedness of individual fibrils within the population. We demonstrated the potential of this approach to map the assembly landscapes of amyloid by analysis of amyloid fibrils formed from three different peptide sequences (**Fig. 1.9** left column and **Fig. 1.10**). The assembly landscape of these peptides show amino acid sequence dependent continuums of structural polymorphs from each assembly population. This discovery was revealed through the analysis of hundreds of individual fibrils in the population, with the fibril structures subsequently hierarchically classified into polymorphic classes (Aubrey et al., 2020). In this study, each individual fibril observed on AFM images was used to generate a 3D model (e.g., left column in **Fig. 1.9c**), with no two fibril models being exactly the same. It is possible that the morphological differences observed between closely related but not identical fibrils are due to small variations in the helical twist and/or the packing of protofilaments with otherwise identical core conformations, but the differences can also reflect structural variations of the protofilament core. As illustrated in **Fig. 1.6**. Thus, the data demonstrates the potential of amyloid fibrils to display strong structural individuality within the heterogeneous amyloid populations.

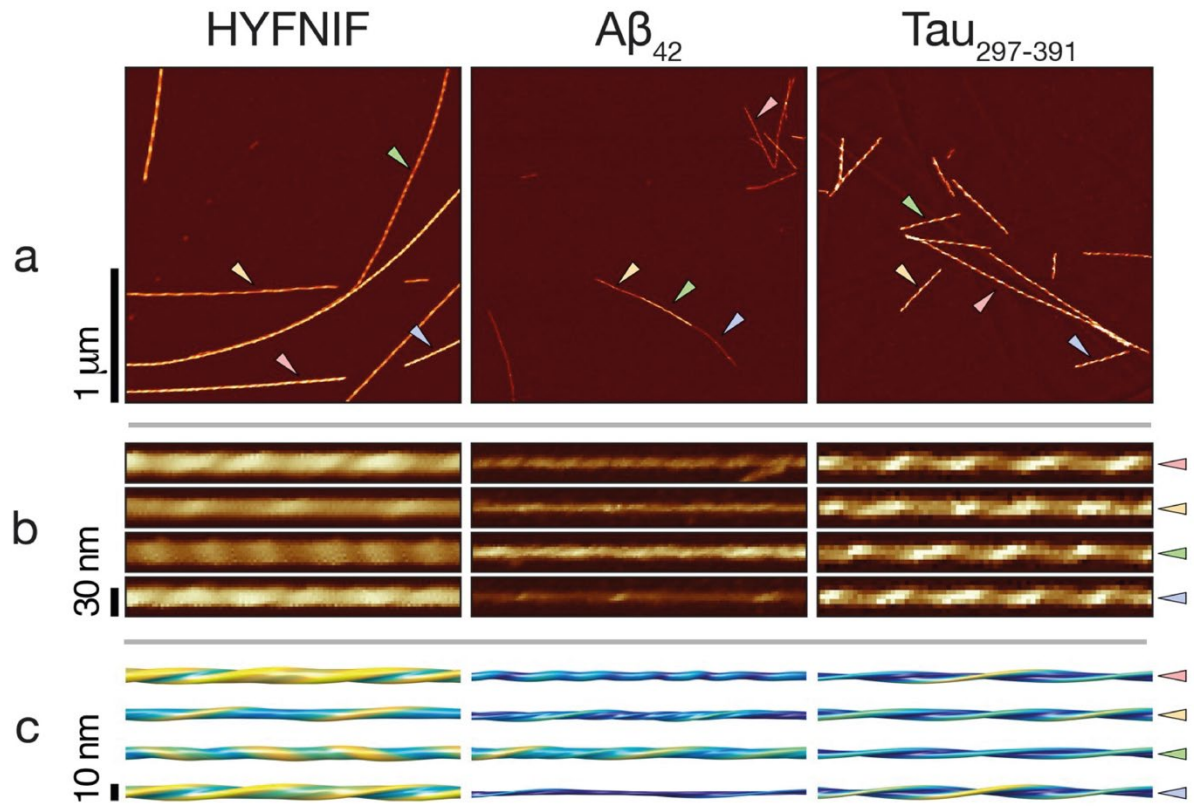

Figure 1.9 Structural details individual to each amyloid fibril are revealed by AFM. Gentle force-distance curve-based AFM imaging and 3D-reconstruction of fibril surface envelopes revealed the individuality of amyloid fibrils in amyloid populations, with no two fibrils being exactly the same. **(a)** AFM height topology images of amyloid fibrils formed from a hexa-peptide of the primary sequence HYFNIF (Aubrey et al., 2020), $A\beta_{42}$, and a $tau_{297\text{-}391}$ fragment (also called dGAE) (Al-Hilaly et al., 2020). The images are shown with the same length and colour scale, with the scale bar to the left indicating the length of 1µm in all three images. **(b)** Images of digitally straightened fibrils seen in the images in (a), with the coloured triangle markers indicating their position in a). A 350 nm segment of each fibril is shown. **(c)** The 3D surface envelope models individually reconstructed for each fibril in b) are shown with surface colours ranging from blue to yellow to indicate the distance to the fibril axis from thin to wide. A 200 nm segment of each 3D model is shown. These AFM images and individual fibril models suggest that the extent of structural polymorphism is not the same for different amyloid forming sequences, with fibrils formed from $tau_{297\text{-}391}$ showing the least extent of polymorphism amongst the three examples. Polymorphic structural variation within a fibril is also seen on the image of $A\beta_{42}$ fibrils.

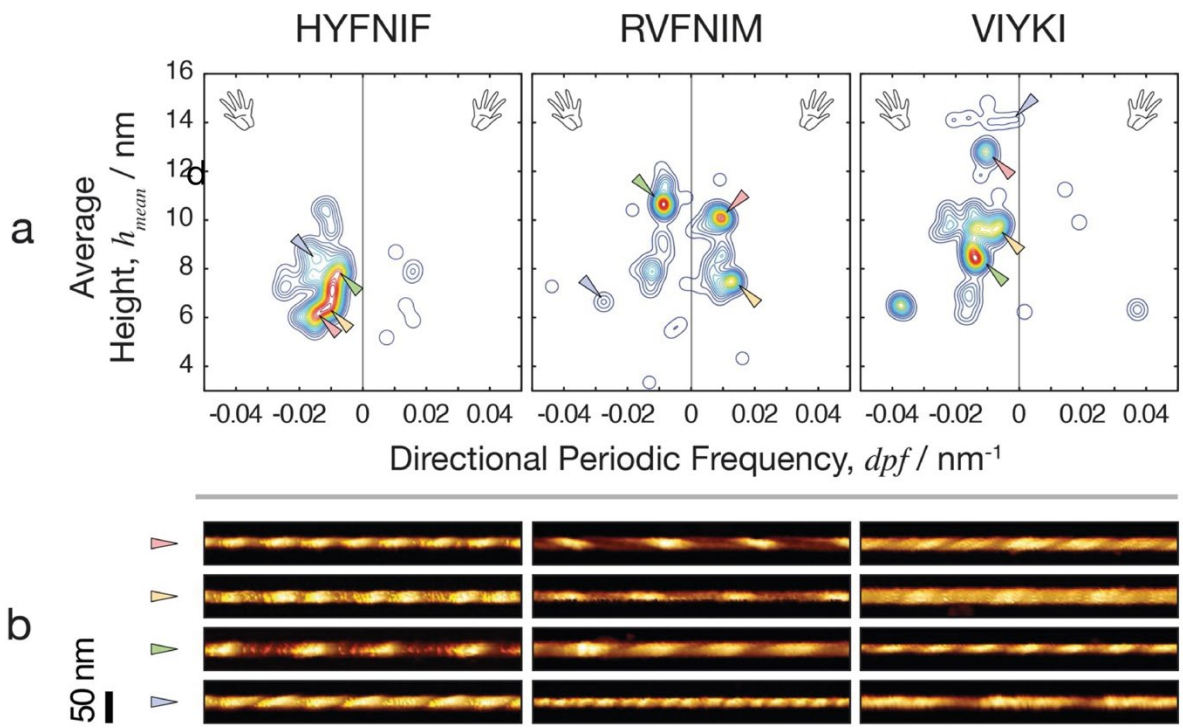

Figure 1.10 Structural analysis of individual fibrils using AFM allows mapping of the polymorphic amyloid assembly landscape. (a) The polymorphic amyloid assembly landscapes of three short amyloid forming peptide sequences are represented as smoothed 2D histograms and visualised as contour maps (Aubrey et al., 2020). The colouring represents the density of the morphometric parameters, which include the average height and the number of repeating units per nm (directional periodic frequency, dpf) of the individual fibrils observed on AFM height images. Negative and positive dpf values correspond to fibrils with left-handed twist and right-handed twist, respectively. **(b)** Example images of digitally straightened fibrils formed from the three peptide sequences in (a), with the coloured triangle markers indicating their position in the maps in (a). A 500 nm segment of each fibril is shown.

To date, AFM imaging has been used to characterise individual β-lactoglobulin amyloid fibrils by measuring their height profile and twist pattern (Adamcik et al., 2010), as well as to analyse and compare the morphologies of fibrils formed from wild-type α-synuclein and its disease-relevant variants (Ruggeri et al., 2020). AFM has also been used to structurally characterise individual $A\beta_{40}$ filaments, which revealed structurally polymorphic fibrils after long incubation times (Goldsbury et al., 2005). In addition, AFM methods have helped to reveal that when

samples containing different structural polymorphs, identified by ssNMR, were used to seed new fibril samples, the elongation rate within the new samples was specific to the structural polymorph of the seed (Qiang et al., 2013), highlighting the relationship between fibril structures and physicochemical properties such as kinetics. Furthermore, developments in high-speed AFM have revealed the dynamics of individual $A\beta_{42}$ fibril structures, including that elongation occurs preferentially at one end of the fibrils (Watanabe-Nakayama et al., 2016). This is a result that may contain clues to the organisation of protofilaments within individual fibrils. AFM can also provide complementary structural information in combination with other methods. An example of this includes the use of both AFM and cryo-EM to quantify the structural variation in samples of diabetes-related IAPP fibrils, from which structures of the fibril cores were also determined (Gallardo, Iadanza, et al., 2020), or the use of ssNMR, cryo-EM and AFM to determine the core structure of transthyretin fibrils (Fitzpatrick et al., 2013). Another example includes the use of AFM in combination with fluorescence microscopy, in which evidence of structural variation within individual fibrils was observed by AFM when mouse and hamster variant prion protein fibrils were used to seed each other, resulting in individual fibrils with a conformational change (Makarava et al., 2009). Structural variations within individual fibrils have recently also been observed in *ex vivo* samples of immunoglobulin light chain fibrils from patients with systemic AL amyloidosis and in Aβ fibrils from patients with Alzheimer's disease (AD), both demonstrated using cryo-EM (Kollmer et al., 2019; Radamaker et al., 2021). Using AFM, we have observed strong individuality and structural variations within $A\beta_{42}$ fibrils formed *in vitro* (**Fig. 1.9**, middle column), demonstrating the extensive polymorphism exhibited by Aβ sequences. Interestingly, AFM images of amyloid fibrils formed from $tau_{297-391}$ (also termed dGAE), with a morphology that mimics the core of paired helical filaments extracted from Alzheimer's patient tissue (Al-Hilaly et al., 2020), show little structural variations between individual fibrils within its fibril

population (**Fig. 1.9,** Tau$_{297-391}$ column), suggesting that the extent of structural polymorphism and fibril individuality is not the same for different amyloid forming sequences.

1.3.7 Physicochemical consequences of amyloid polymorphism

Structural variations within and between individual fibrils in typically heterogeneous amyloid populations can exist on multiple length scales (**Fig. 1.6**). These structural variations that define amyloid polymorphism can range from atomic scale differences in the order of ångströms, arising from packing variations of the polypeptide chains, to nanometre-scale variations in fibril width, or even reach the scale of hundreds of nanometres in variations of twist periodicity and handedness of amyloid fibrils (Aubrey et al., 2020). At these different length scales, as a consequence of the diversity and individuality of polymorphic amyloid structures, the physicochemical properties of individual fibrils, such as the overall accessible surface area (Fändrich et al., 2009), surface hydrophobicity and charge (Pansieri et al., 2018), growth and disassembly kinetics and thermodynamics (Qiang et al., 2013), and mechanical properties that include persistence length and the second moment of inertia (T. P. Knowles et al., 2007), can also vary within a population. Therefore, in contrast to globular proteins which typically have a single native fold, the structural variation between individual fibrils within a population may impact the functional properties of the amyloid population *in vivo*, mediated by variation in their specific physicochemical properties. For example, different amyloid structures have different cross-sectional dimensions and shapes. Thicker fibrils with rounded cross-sections are likely to have a higher second moment of inertia than thin fibrils with elliptical cross-sections, making them more resistant to breakage. Fibrils with higher fragmentation rates are more likely to generate a larger number of small active amyloid particles and subsequently may

be more effective in propagating their amyloid state (Beal et al., 2020), compared to fibrils that are more stable and less susceptible to breakage. This is demonstrated through the size-dependent transfection efficiency relationship of Sup35NM amyloid particles that confer the [*PSI*$^{+}$] phenotype when transfected into yeast cells (Marchante et al., 2017). In studies of transmissible amyloid known as prions, specific strains are found to selectively propagate from cell to cell (Atarashi et al., 2006; Bateman & Wickner, 2013; Bruce et al., 1991; Hannaoui et al., 2013), suggesting a possible relationship between the strain phenomenon, the structural polymorphism of amyloid fibrils, and the individual fibrils' stability towards fragmentation. Thus, the differences in the stability of individual fibrils, as a consequence of structural polymorphism, may lead to variations in the fitness of individual fibrils in an amyloid population, and subsequent 'selection' of specific amyloid conformation due to a polymorphic bias under certain conditions as well as adaptive 'evolution' processes of the dominant amyloid conformation due to changes in the environment. The structural constraints provided by the cross-β architecture coupled with a strong structural individuality in some amyloid populations, and the ability of some amyloid to efficiently propagate the information encoded in their conformational state, may suggest that some amyloid could behave in a manner similar to that of viral quasispecies. In addition to fibril fragmentation, secondary nucleation is another property that is affected by the fibril structural arrangement and could mediate the biological effects of amyloid. Fibrils with a higher surface-area-to-volume ratio might provide better access to active fibril surfaces that can catalyse secondary nucleation, compared to larger amyloid structures with proportionally less available surface area. Secondary nucleation is a process in which new amyloid are formed through catalysis by existing amyloid fibril surfaces. The importance of secondary nucleation, in particular with respect to the biological impact of $A\beta_{42}$ amyloid fibrils, has become increasingly evident. For example, by combining kinetic analysis of $A\beta_{42}$ aggregation with impaired secondary nucleation using the molecular

chaperone Brichos (Cohen et al., 2015) and antibodies that bind to the fibril surface (Michaels et al., 2020), it has been shown that secondary nucleation events may be the source of cytotoxic oligomeric species during $A\beta_{42}$ aggregation. It is further possible, that secondary nucleation on the surface of amyloid fibrils is site-specific, potentially occurring at sites of defects or at locations where structural breaks occur. Individual fibril polymorphs with higher propensity to contain defects, have structural breaks, or those that simply have a larger accessible surface area might then provide more efficient surfaces for secondary nucleation, and, therefore, be responsible for a greater cytotoxic potential within the amyloid population.

The polymorphic features of individual amyloid fibrils can both influence and be influenced by interactions with other biological structures. For example, the formation of α-synuclein amyloid fibrils *in vitro* is modulated by the air water interface (Campioni et al., 2014). Since α-synuclein fibrils are found *in vivo* in patients with various diseases, where the air-water interface is likely to be absent, it suggests that other biological interfaces may provide sites for the heterogeneous nucleation of α-synuclein assembly. This type of surface-catalysed aggregation of amyloidogenic proteins involves adsorption of amyloid forming proteins onto surfaces, followed by a step that includes a conformational change, whether that be from a random coil to the core fold of the resultant amyloid fibril or to an oligomeric intermediate state (Grigolato & Arosio, 2021). Importantly, the precise amyloid structures that form, amongst the diverse possible structures that can be formed, may be dependent on the physicochemical characteristics of the catalysing surface. High local concentrations of self-assembling proteins adsorbed onto a surface can increase the rate of heterogeneous primary nucleation in a manner which is dependent on the mobility of the proteins once adsorbed onto the surface. Cell membranes and, in particular, their lipid bilayer components are amongst the most well-studied biological structures known to interact with amyloidogenic proteins in such

a manner (Bode et al., 2017; Butterfield & Lashuel, 2010; Milanesi et al., 2012; Monsellier et al., 2016; Sciacca et al., 2018). Fibril formation reactions can be catalysed by lipid bilayers (Lindberg et al., 2017; Vahdat Shariat Panahi et al., 2019), but can also be damaging to lipid bilayers (Bode et al., 2017; Engel et al., 2008; Sparr et al., 2004). In fact, it may be possible to connect the aggregation kinetics to the toxicity of the aggregation reaction through their interaction with membranes (Flagmeier et al., 2020). In order for lipid bilayers to catalyse primary nucleation, the monomeric subunits must first adsorb to the bilayer surface. In some cases, lipid bilayers induce a conformational change in the monomeric subunits of an amyloidogenic protein. For example, α-synuclein undergoes a change in conformation, dependent on the fluidity of the lipid bilayer (Rovere et al., 2018). Additionally IAPP undergoes conformational changes upon insertion into a lipid bilayer, eventually forming amyloid fibrils in a lipid-mediated manner (Sasahara et al., 2012), and when mixed with large unilamellar vesicles it has been observed that the secondary nucleation of $A\beta_{42}$ can be accelerated through lipid bilayer interactions (Lindberg et al., 2017). Conformational changes upon binding to a surface imply that structural features of a resultant amyloid fibril can be dependent on the local physicochemical environment, and the precise structures of the fibrils, therefore, will vary and contribute to the individuality of each fibril in the population. Further biological structures which can impact fibril formation include additional cell membrane constituents such as gangliosides (Kakio et al., 2002), extracellular structures such as heparin (Goedert et al., 1996), as well as other heterologous amyloid fibrils through cross-seeding events. If cross-seeding events proceed through surface-catalysed reactions (Koloteva-Levine et al., 2021), the resulting new amyloid structures could result in considerable fibril diversity and individuality, as heterogeneous nucleation events may also introduce heterogeneity in the resulting amyloid population, depending on the physicochemical conditions of local interfaces.

Thus, surface interactions may enhance the potential for amyloid forming polypeptide sequences to display structural polymorphism.

1.3.8 Biological and pathological consequences of amyloid polymorphism

Amyloid fibrils display remarkable diversity in both the structures they form, as well as the biological contexts they are found in. Some amyloid structures are found to be disease-associated, while others may be essential for physiological functions. The wide range of *in vivo* biological functions or pathological consequences of amyloid may reflect the polymorphic diversity of amyloid fibril structures, mediated by the differing physicochemical properties of individual amyloid fibrils, as discussed above. However, specific molecular links between structural features, particular cellular pathways or processes, and biological consequences are not currently well-understood. One of such possible mediating properties could be the thermodynamic stability of the fibril core, determined by structural features like core hydrophobicity and steric zipper interactions, with lower stability leading to reversible assemblies (J. Lu et al., 2020; Ulamec & Radford, 2020). Furthermore, amyloid with assembly-dependent functional roles may show less polymorphism compared to disease-associated amyloid (Hervas et al., 2020; J. Lu et al., 2020; Murray et al., 2017), which could indicate that the specific core fold of amyloid fibrils may convey corresponding specific biological properties that facilitate functional roles. In contrast, a wide range of polymorphs of disease-associated amyloid structures have been observed, with diverse patterns of polymorphic extent that include patient-specific polymorphism, clinical-subtype specific polymorphism for the same disease, and disease-specific polymorphism (**Fig. 1.11**). Structural data obtained to date suggest that different amyloid systems behave differently in this respect, although more

structural data of *ex vivo* amyloid assemblies is needed to resolve how the polymorphic landscape varies in different disease-states, spatial localisations within organs, or individual patients. Further structural characterisation of physiologically functional amyloid structures and comparison of these structures with those of disease-associated amyloid is also necessary to fundamentally understand the amyloid structure-function links.

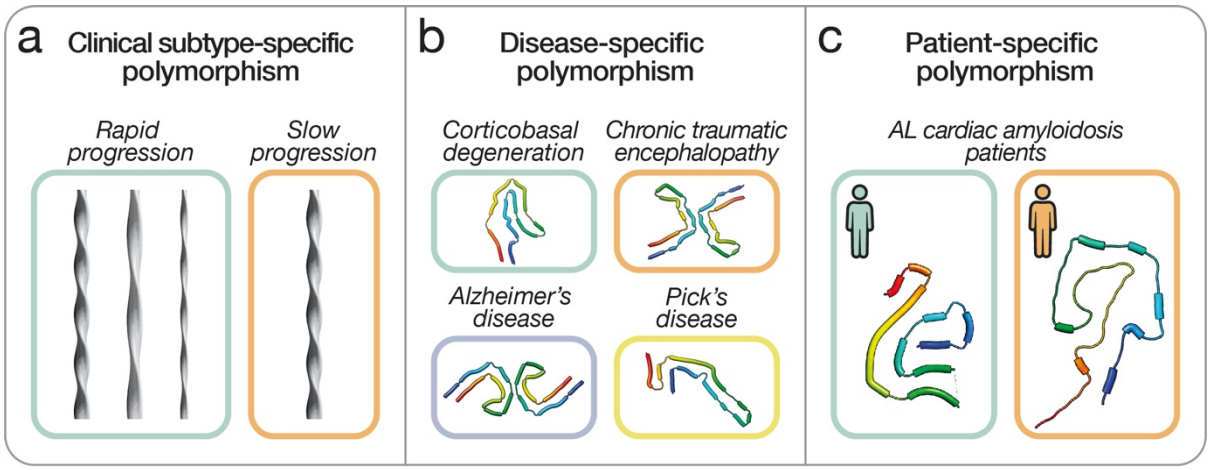

Figure 1.11 Amyloid polymorphism shows diverse patterns in disease-states. (a) Illustrations of the varying extent of structural polymorphism and the diverse types of polymorphic structures that may be present in clinical disease subtypes, for example shown for rapid and slow progressive Alzheimer's disease (M. L. Cohen et al., 2015; Qiang et al., 2017). **(b)** Disease-specific polymorphism has been demonstrated for amyloid structures formed from tau protein in various tauopathies. A single representative cartoon model is shown of amyloid fibril cross-sections from samples originating from the brain tissue of patients with four different neurodegenerative diseases, with the thicker sections denoting the cross-β segments, where such segments are determined and labelled in the PDB entry. PDB accession codes for the models shown are 6VHA, 6NWP, 5O3L and 6GX5 (Arakhamia et al., 2020; Falcon et al., 2019; Falcon, Zhang, Murzin, et al., 2018; Fitzpatrick et al., 2017), for chronic corticobasal degeneration, traumatic encephalopathy, Alzheimer's disease, and Pick's disease, respectively. **(c)** Individual patients with the same diagnosis may have distinct structures of the same protein, for example in the case of AL amyloidosis. Cartoon models of the cross-sections of *ex vivo* amyloid fibrils extracted from the cardiac tissue of two patients with AL amyloidosis are shown, with PDB accession codes 6HUD and 6IC3 (Radamaker et al., 2019; Swuec et al.,

2019), respectively. Molecular models were generated using UCSF Chimera (Pettersen et al., 2004).

Different neurodegenerative diseases show distinct patterns of spatial origins of amyloid aggregation as well as progression by prion-like spreading, which is mediated by neuronal connectivity and individual cell-type vulnerability (Brettschneider et al., 2015). For example, tau lesions originate in different regions of the brain in patients with Alzheimer's disease and chronic traumatic encephalopathy (CTE), despite being composed of the same protein isoforms (Katsumoto et al., 2019). The structural diversity of the amyloid aggregates involved can be affected by the local *in vivo* environment which could, in turn, elicit different biological effects based on the precise physicochemical properties of the individual fibrils formed. These complex relationships may result in biological feedback loops that subsequently contribute to the molecular and phenotypical differences between amyloid-associated diseases, even when the primary sequence of the original protein involved is identical. For example, in recent years, *ex vivo* amyloid fibrils of the tau protein have been well-characterised, and their structures have been resolved to high-resolution detail from the brain tissue of patients with various different diseases, including Alzheimer's disease, Pick's disease, corticobasal degeneration (CBD) and chronic traumatic encephalopathy (Falcon, Zhang, Murzin, et al., 2018; Falcon et al., 2019; Fitzpatrick et al., 2017; W. Zhang et al., 2020). Although tau isoforms forming the amyloid fibrils differ between some diseases, and thus have slightly different primary sequences, the structures of fibrils from Alzheimer's and CTE disease tissues, which both contain the 3R and 4R isoforms, are nevertheless different (**Fig. 1.11b**). Notably there is also polymorphism present within the fibril population of each disease-specific sample, e.g., paired helical filaments (see **Fig. 1.7** and **Table 1.3** entries 99, 108, 112 and 113) and straight filaments (see **Fig. 1.7** and **Table 1.3** entries 109, 114 and 115) in Alzheimer's disease brain tissue (Falcon, Zhang, Schweighauser, et al., 2018; Fitzpatrick et al., 2017). Other rare but potentially also

biologically important polymorphs of amyloid in the same disease-associated amyloid populations may also be present (Kollmer et al., 2019), but their 3D structures are currently inaccessible to characterisation by cryo-EM because they are present in low numbers, and therefore cannot satisfy the extensive particle-averaging required by cryo-EM methodologies.

In addition to disease-specific amyloid polymorphism, considerable structural variation may exist for Aβ amyloid from patients with different Alzheimer's disease clinical subtypes. Fibril samples formed through seeding with *ex vivo* fibrils extracted from the brain cortex of patients with Alzheimer's disease have been investigated by ssNMR (Qiang et al., 2017). While the structures of fibrils formed from seeding do not necessarily reflect that of the seeds (Lövestam et al., 2021), it has been found that seed samples originating from patients with prolonged-duration AD resulted in fibrils of a single predominant $A\beta_{40}$ polymorph, whereas samples originating from patients with rapidly progressive AD resulted in a wider degree of structural diversity, suggesting that the seeds' structures were different. Aβ amyloid fibrils from patient brain tissue with slowly and rapidly progressing AD have also been shown to have different biochemical characteristics, including different stability upon chemical and thermal denaturation, and higher levels of oligomeric $A\beta_{42}$ in the rapidly progressive form (M. L. Cohen et al., 2015), further evidencing the possible presence of complex, clinical subtype-dependent amyloid polymorphism.

Cryo-EM structures from four patients with Alzheimer's disease have demonstrated common paired helical and straight filament structures of tau amyloid (Falcon, Zhang, Schweighauser, et al., 2018), demonstrating that for some amyloid assemblies, the structures are specific to the disease, and not to the individual patients or disease subtypes. In addition, images of immunogold labelled tau amyloid fibril samples from 19 AD patients, as well as from different

brain regions of the same patients, also show similar patterns. Subsequently, disease-specific fibril structures have been reported for various tauopathies, giving rise to a structure-based classification approach for these neurodegenerative diseases (Shi et al., 2021). However, it is not yet known whether structures prevalent during earlier stages, which may drive disease progression, are also identical to those extracted from the tissues of individuals with end-stage AD and determined by cryo-EM.

Light chain (AL) amyloidosis is an example of patient-specific amyloid polymorphism. In AL amyloidosis, expansion of a B cell clone leads to overproduction of a free monoclonal immunoglobulin light chain protein, aggregation of which results in amyloid fibrils that accumulate in organs, such as the heart or the kidneys, leading to tissue damage. The specific sequence of the accumulating immunoglobulin light chain protein in each patient can affect the propensity of amyloid formation and thus, potentially also the disease aetiology through impact on the thermodynamic stability of the specific polypeptide sequence (Nokwe et al., 2016), the tissues where amyloid deposits, and the clinical outcome (Abraham et al., 2003). However, it has been recently shown that extrinsic factors, especially susceptibility to proteolytic cleavage and presence of proteases that fragment the immunoglobulin light chain proteins under physiological conditions, could instead be a strong determinant of amyloid formation *in vivo* (Sternke-Hoffmann et al., 2021). Amyloid structures have been resolved from the explanted cardiac tissue of three patients, demonstrating patient-specific structural differences in detail (Radamaker et al., 2019, 2021; Swuec et al., 2019). Contrary to the previous examples of tau and Aβ amyloid, the primary sequence of the monoclonal immunoglobulin light chain protein varies between patients as it depends on the selection of the germline gene and somatic mutations (Blancas-Mejia et al., 2018). Thus, patient-specific amyloid polymorphism stems from the 'top-level' patient-specific variations in the primary polypeptide sequence (**Fig. 1.6**

top row). It is, however, not yet known whether patient-specific amyloid polymorphism can arise for amyloid structures formed from the same monomeric polypeptide sequence. There remain many unanswered questions on the *in vivo* role of amyloid in disease-states, both related to how the environmental factors affect fibril growth and their structures, as well as how amyloid formation and structures affect the surrounding cells and tissue environments, including any cell-type specific vulnerabilities. Further insights into the relationship between fibril polymorphism and their biological consequences can be achieved from continued efforts in resolving *ex vivo* fibril structures from tissues of patients with different diagnoses or disease progression, from different regions of the brain or diseased tissues, and from multiple individual patients with the same diagnosis. Likewise, *in vitro* approaches in which the polymorphic landscape is modified in a controlled manner by systematically varying sequence or environmental factors to form specific structures will provide molecular and mechanistic evidence of pathological pathways. Both approaches will equally require the structural characterisation of amyloid fibrils to molecular and individual detail.

Challenges in predicting the polymorphic landscape of amyloid assembly

For globular proteins, AlphaFold 2 did exceptionally well in predicting 3D structures from primary amino-acid sequences (Jumper et al., 2020) in comparison to other structure prediction algorithms (Kryshtafovych et al., 2021). The achievements of 3D structure prediction through deep learning methods, e.g., the trained neural network architecture of AlphaFold 2, to date on monomeric proteins in CASP14, is a result of both extensive computational resources for model training and inference of new structures, as well as the availability of approximately 170,000 publicly available protein structure entries in the RCSB Protein Data Bank, and many

more protein sequences used for multiple sequence alignments, which inform structure prediction. Future developments to AlphaFold 2 will potentially include prediction of protein complexes. Although amyloid structures were not included as targets in CASP14, further developments in structure prediction of large protein complexes, including amyloid, could lead to fundamental understandings of how some of the biggest biological protein structures form. Considerable developments to the current prediction methods will, however, need to be incorporated to allow the prediction of many structures from a single primary sequence due to the extensive polymorphism displayed by amyloid fibrils, which form diverse structures even under identical environmental conditions and from identical amino acid sequences. This type of challenge can only be met if a sufficiently holistic understanding of the assembly landscape, in terms of both structures and energetics, is reached. However, with only around a hundred amyloid fibril structures currently available in the PDB for full-length or fragments of amyloidogenic proteins (**Table 1.3**, **Fig. 1.7** not including cases where the same data has been reanalysed), the limited training data available for structural prediction tool development, especially ones that rely on 'big-data' approaches, pose a severe limitation to such a holistic undertaking. A further 108 PDB structures are available for amyloid fibrils formed from microcrystals of amyloid forming peptide sequences ranging from 4 to 11 amino acids in length, determined by X-ray and electron diffraction techniques, which could be useful for the prediction of local structural arrangements of the various steric-zipper motifs. Nevertheless, to predict the structures of large, multi-polypeptide chain, and highly polymorphic protein assemblies like amyloid, significant effort must first be spent on matching the quantity of high-quality structural data, such as currently seen for globular proteins.

Another key challenge for amyloid structure prediction is the high potential sensitivity of the amyloid conformation to a multitude of environmental factors, such as pH, ionic strength and

interactions with other biomolecules and surfaces. As the precise local *in vivo* environments experienced by the various amyloid forming systems are unknown for disease-associated and functional amyloid, the characterisation of *ex vivo* amyloid fibrils needs to be carried out as indirect reporters on the relevant *in vivo* environments. These *in vivo* conditions are likely to differ from conditions used *in vitro,* since *ex vivo* amyloid structures have been found to differ compared to *in vitro* formed amyloid originating from monomers of the same amino acid sequence (Bansal et al., 2021; Fitzpatrick et al., 2017; W. Zhang et al., 2019). Direct structural characterisation for *ex vivo* amyloid without the need for further seeded amplification is currently only possible using cryo-EM. There are further challenges for resolving *ex vivo* amyloid structures, including limited access to patient-derived tissues, experimental challenges with extracting fibrils from these tissues, and the ability to only study the most prevalent fibril species despite the diversity of species present. As a result, currently, structural data of only fewer than thirty of such unseeded *ex vivo* amyloid have been deposited to the EMDB and the PDB. Although an increasing number of *ex vivo* amyloid fibrils are being studied every year, it remains a labour-intensive and costly endeavour. Thus, for predicting the 3D structures of amyloid under physiologically relevant environmental conditions, it may be necessary to first resolve how the assembly landscape is precisely modulated by environmental conditions through combined *ex vivo* and *in vitro* approaches, and then train a neural network using 3D structures formed under widely varying conditions.

The prediction of 3D protein structures gives rise to applications such as the ability to infer function associated with the predicted structure, as well as structure-based drug design. These applications rely on specific folds and motifs being predicted from amino acid sequences. For amyloid, there are likely to be unique challenges compared to other, well-studied classes of proteins such as enzymes, where a specific catalytic pocket could, for example, indicate a

specific functional role. As more structural data of amyloid from different biological contexts, both disease-associated and functional, become available, it may be possible to predict whether an amyloid forming sequence may be associated with the formation of assemblies with toxic or infective potential. More structural data will facilitate this type of analysis and may potentially reveal the mediating physicochemical factors involved in the link between amyloid structure, function, and pathogenicity. Only once this relationship has been firmly established based on both structural data and biological context, could a predicted 3D structure be used to explore the potential biological consequences and aid structure-based therapeutic interventions. A significant amyloid-specific opportunity for structure prediction lies in cases where structures are disease subtype- or patient-specific. For example, in AL amyloidosis, each patient has a slightly different immunoglobulin light chain amino acid sequence that can be noninvasively determined from urine (Solomon et al., 1998). If the fibril structures could then be predicted from the primary amino-acid sequence, it could be helpful in determining a specific clinical subtype or indicate specific pathways of pathology. Furthermore, structure-based inhibitors of amyloid aggregation have been demonstrated for some proteins such as Aβ in cell-culture models (Griner et al., 2019). If a structure-based approach would be demonstrated to be clinically effective, for example, for AL amyloidosis patients, prediction of structure from sequence could determine patient-specific epitopes that could be targeted in a personalised medicine approach.

1.3.9 Conclusions

Amyloid assembly presents unique challenges to protein 3D structure elucidation, prediction, and understanding of the relationship between structure and biological consequences. Unresolved challenges arise from the highly polymorphic nature of amyloid assembly, the

subsequent individuality of each fibril formed within the heterogeneous amyloid populations, and the resulting differences in the fibrils' physicochemical properties arising even from monomers with identical amino acid sequences. This structural diversity is reflected in amyloid-associated biological roles which range from functionality to pathogenic effects in neurodegenerative diseases and systemic amyloidoses, with a potentially wide variation in disease subtypes and clinical outcomes. Successful amyloid structure prediction from the primary amino acid sequence of its monomeric polypeptide components will need to contain robust predictions of whether an amino acid sequence is likely to form the cross-β amyloid fold in the first place, followed by precise structural predictions that holistically takes into account the assembly landscape and its sensitivity to the environmental conditions it experiences. Finally, the path towards solving the 'one sequence to many structures' problem amyloid assemblies represent, and the successful prediction of the full range of diverse amyloid structures, will inevitably push our fundamental understanding of the coupled protein folding-assembly processes commonly found in biology.

1.4 RESEARCH AIMS

The primary aim of this research project is to characterise and modulate the polymorphism of amyloid self-assemblies in order to investigate the relationship of amyloid structure, function, and dysfunction. Firstly, chemical conjugation techniques are used with the aim of modulating amyloid self-assembly and inhibiting the spread of amyloid between cells. Specifically, the Sup35 yeast prion protein is used as a model system in order to investigate whether conjugation of amyloid to complementary DNA strands could alter the resulting suprastructure, reduce fragmentation propensity, and thus also restrict cell-to-cell transmission of the prion phenotype. In addition, DNA origami-based methods will enable the development of amyloid-DNA conjugates as modular nanomaterials, which could further be functionalised, thus taking advantage of the unique materials properties of both DNA and amyloid. The effect of the modified Sup35 on amyloid self-assembly kinetics resulting morphology will be characterised by a fluorescent ThT dye assay and atomic force microscopy, respectively.

AFM data analysis has been largely limited to qualitative descriptions of sample morphology due to a lack of advanced computational analysis tools. This work further aims to improve the algorithms and workflows available for AFM topographic data, with specific focus on the analysis of amyloid fibril polymorphism. Additionally, AFM data on amyloid fibrils is highly complementary to data collected with other structural biology tools, such as cryo-EM or ssNMR, as it is capable of resolving the nanoscale morphology of individual fibrils. However, a lack of computational tools for integrating or comparing AFM data with data collected with these different techniques had hindered the use of AFM data in conjunction with molecular models generated with cryo-EM and ssNMR methods. Thus, computational tools to integrate AFM data of polymorphic amyloid fibrils with other structural biology data will be explored

in order to enhance the analysis of polymorphic amyloid populations. Finally, a systematic meta-analysis approach to further our fundamental understanding of the amyloid structure, function, and dysfunction relationship will be explored using data deposited to publicly available data banks.

Chapter 2: Amyloid-DNA conjugates as inhibitors of amyloid spread and functional nanomaterials

2.1 Summary

Chapter 2 is based on experimental work in which the Sup35 yeast prion protein is used as a model system for the modulation of amyloid self-assembly via conjugation to DNA. A modified variant of the protein is used, consisting of the NM-domains of the Sup35 protein, with an added C-terminal linker and cysteine residue (Sup35NM-LCys). The modified protein is conjugated to a chemical linker via thiol-maleimide reactions between the thiol side chain of cysteine and a maleimide group of the linker. Two different amyloid-DNA conjugation strategies are explored. The first strategy consists of separately conjugating two complementary single-stranded DNA (ssDNA) molecules with covalently bound maleimide-functionalised chemical linkers to the modified Sup35NM protein monomer. When mixed, the two strands will result in reversible, temperature-sensitive cross-linking between the amyloid monomers. In the second strategy, a nucleobase analogue is conjugated to the Sup35NM-LCys protein via the maleimide linker. The resulting construct is then capable of forming hydrogen bonds with thymine, which can be added in as ssDNA of defined length, thus forming seeds. In both strategies the amyloid-DNA conjugates are added to the WT Sup35NM protein in small proportions to modulate self-assembly.

The Sup35NM-LCys protein was recombinantly expressed in *E. coli* and purified by affinity and size-exclusion chromatography. The purified protein was analysed by SDS-PAGE and mass spectrometry, which confirmed the identity of the purified protein. The kinetics and morphology of Sup35NM-LCys and WT variants mixed in various ratios were characterised to assess their cross-elongation by following fibril formation with the small fluorescent dye ThT and imaging of the resulting samples by AFM. Both ThT curves and AFM images showed that the two proteins interact, as the mixed self-assemblies exhibited morphologies different from the individually assembled LCys and WT variants. However, further experiments are needed to establish whether the two variants are capable of cross-templating fibril elongation. Finally, the conjugation of ssDNA and nucleobase analogue linkers was carried out. Experimental analysis of SDS-PAGE and mass spectrometry results indicated that the correct conjugation products had formed for both ssDNA and nucleobase analogue linkers, respectively. In future research these amyloid-DNA conjugates may be added to WT Sup35NM to regulate the self-assembly process *in vitro* and *in vivo* in yeast cells.

2.2 Introduction to amyloid-DNA conjugates

Amyloidogenic proteins are involved in both progression of a range of neurodegenerative diseases, as well as essential biological functions (Dobson, 2017). The emerging polymorphic nature of amyloid and the diversity of the fibrils in amyloid populations could be a significant factor in in the wide degree of variation in the biological effects of amyloid (Lutter, Aubrey, et al., 2021), although a direct causal relationship is yet to be established. Thus, understanding and controlling the formation and structural state of amyloid is important, as it could contribute to developing effective therapeutic interventions for reducing pathological effects, as well as employing the distinct materials properties of amyloid for applications as functional bionanomaterials (Mankar et al., 2011).

Efforts to change amyloid aggregation behaviour to achieve a therapeutic benefit for the increasing numbers of patients suffering from neurodegenerative diseases have been underway for decades with varying strategies employed with limited success (Makin, 2018). This has led to the controversial approval of aducanumab in June 2021 (Mullard, 2021), after demonstrating that the monoclonal antibody significantly reduced amyloid plaques in patient brain, although improvements to cognitive function were not clear (Biogen, 2021). Despite all amyloid broadly following a nucleated polymerisation mechanism (Törnquist et al., 2018), there are variations in the structural properties of the monomers, for example whether they are folded or intrinsically disordered, which may propagate to differences in rate constants of the microscopic processes involved in self-assembly and lead to further changes to the fibril population diversity, as well as their surface and mechanical properties (Fändrich et al., 2018). As a result, different modulating strategies are likely to be required for different amyloid proteins. For example, the only other approved protein-targeting amyloid modulator tafamidis

stabilises a natively-folded tetrameric form of transthyretin, aggregation of which otherwise results in amyloidosis characterised by accumulation of amyloid plaques in organs including the heart (Bulawa et al., 2012).

The lack of amyloid modulating drugs capable of significantly preventing or reversing the decline of cognitive and motor functions, hallmarks of the associated neurodegenerative diseases (Dugger & Dickson, 2017), is thought to occur in large part as a result of the difficulty in translating the drugs from use in model systems to use in humans, and not from lack of basic research on identifying modulating compounds. A range of molecules with specific binding to amyloid structures have been identified and extensively studied, including amyloid-specific antibodies with differing kinetic effects (Linse et al., 2020), peptides-inhibitors capable of interfering with the self-assembly pathway (Armiento et al., 2020; Griner et al., 2019), as well as small molecules with varying proposed mechanisms of action (Young et al., 2017). For example, the fibril disaggregating effect of epigallocatechin gallate (EGCG), a small molecule natural product found in green tea, has been shown to reduce amyloid load and lead to cognitive benefits in an Alzheimer's disease mouse model (Rezai-Zadeh et al., 2008) and a cryo-EM study has revealed binding of EGCG to a cleft between two protofilaments, potentially disrupting their binding interface (Seidler et al., 2020).

Although many of these studies show positive results for disaggregating amyloid and reducing toxicity in model organisms, these results have not yet translated to clinical success for the treatment of amyloid-associated diseases (Mehta et al., 2017). The causes of this are not clear and there may be many possible explanations, including difficulty in getting the drugs across the blood-brain barrier, to a specific region in the brain or other organ, administering the drug too late in disease progression, not using high-enough doses, etc. However, in some cases it is

also possible that the disaggregation of amyloid itself could lead to the production of small oligomers and/or fibrillar seeds with cytotoxic potential. This is highlighted both by the requirement of Hsp104 chaperone for prion propagation in yeast through the generation of seeds (Chernoff et al., 1995), as well as the recent elucidation of the mechanisms employed by the Hsp70 chaperone machinery which operates both by extraction of monomers and fibril fragmentation, and could result in residual small aggregates (Wentink et al., 2020). Small oligomeric species have been hypothesised to be the primary driving force for neurodegeneration (Cline et al., 2018), whereas small fibrillar seeds participate in prion-like spreading of amyloid between cells (W.-F. Xue et al., 2010). Therefore, promoting amyloid aggregation into larger fibrillar networks and plaques, which may be comparatively inert, may be a potential alternative strategy for therapeutic interventions. For example, introducing fibrillisation-promoting peptides or small molecule chemicals has been shown to reduce prion-like spread and cytotoxicity of disease-associated amyloid in cell-culture models. (Jia et al., 2020; Yang et al., 2020) These modulators result in an increase in the size distribution rather than a decrease, as in the cases of the EGCG and antibodies discussed above. Furthermore, build-up of amyloid plaque may sequester smaller and more toxic oligomeric species, thus reducing the overall toxicity profile of the population. As it has been shown that the prion-like spread of amyloid between cells is modulated by size of the particles, (Marchante et al., 2017) increasing the population size distribution could thus result in a reduction in spread of the amyloid state between cells.

Here, a chemical conjugation approach of an amyloidogenic monomer to two different complementary single-stranded DNA molecules is devised, with the aim of promoting fibril aggregation into large networks through cross-elongation with endogenously expressed, non-modified monomer, when added into biological systems. The biological effects of the

intervention could then be assessed to determine whether a cross-linking approach could provide a beneficial mechanism of action against cytotoxic and prion-like spreading effects through sequestering of toxic oligomers and reducing fragmentation, or whether promoting an increased amyloid aggregate size distribution could further increase deleterious effects, for example through mechanical stress on membranes, sequestering lipids and other essential cellular components through non-specific surface interactions, or some alternative mechanism.

In addition to the pathogenic effects of amyloid proteins in neurodegenerative diseases, some amyloid also carry out functional roles within a range of organisms from bacteria to humans, facilitated by their unique materials properties (T. P. J. Knowles & Buehler, 2011). For example, it has been proposed that amyloid have a biological role in innate immunity via an antimicrobial effect, as some amyloid β (Aβ) species can bind to bacterial cells and prevent host-pathogen interactions (Kumar et al., 2016). The biological functions of amyloid aggregates, including surface adhesion and storage of peptide hormones, have inspired the use of amyloid as nanomaterials (Mankar et al., 2011). The adhesive properties of amyloid fibril surfaces make them suitable for synthetic biology approaches, including for the development of scaffolding for tissue engineering (Das et al., 2018), as well as further functionalisation of the surfaces to achieve desired physicochemical properties (Biverstål et al., 2020). Applications also include amyloid-carbon membranes for removal of heavy metal contaminants from water, which improve on previous methods as the amyloid-ion interactions are non-specific and thus able to remove a mix of contaminants with higher efficiency (Peydayesh & Mezzenga, 2021). Amyloid proteins have various properties that are desirable for materials development, most notably their self-assembly, stiffness similar to that of silk, and strength similar to that of steel (Smith, Knowles, Dobson, MacPhee, et al., 2006), as well as high thermal and chemical stability compared to proteins in natively folded states (Meersman & Dobson, 2006).

Furthermore, the physico-chemical properties can be altered by changing the aggregating amyloid sequence or assembly conditions, allowing tailoring of amyloid materials' properties for a specific application.

Aside from its fundamental biological role as the genetic material of living organisms, DNA also has properties which make it useful for nanomaterials purposes, including its simple amplification by polymerase chain reaction (PCR), and high-specificity reversible sequence-specific molecular recognition through base pairing. These properties have led DNA to be used as a versatile building block for various nanomaterials for several decades, starting with relatively simple cubes (J. Chen & Seeman, 1991) and leading to recently developed nanostructures with increased complexity through the use of new tools and strategies (Chidchob & Sleiman, 2018). Examples of these complex DNA nanostructures include DNA bricks, which allow scaffold-free assembly of DNA into LEGO-like 3D structures (Y. Chen et al., 2020), as well as DNA-based mimics of trans-membrane proteins (J. Li et al., 2021). One of the most significant advances in DNA nanotechnology is DNA origami, which allows the folding of DNA into well-defined and programmable structures of virtually any nanosized 2D or 3D shape (Dey et al., 2021; Rothemund, 2006). Even dynamic nanodevices have been created (Y. Hu et al., 2020), illustrating the versatile applications of DNA as a nanomaterial.

The conjugation of these two nanomaterials, amyloid and DNA, is explored here. Previously DNA has been conjugated to a short amyloidogenic peptide and used to form amyloid-DNA nanotubes via a DNA origami platform resulting in DNA-sheathed amyloid fibrils which can be arranged into organised patterns (Udomprasert et al., 2014). Here, in a second amyloid-DNA conjugation strategy, an amyloidogenic monomer is conjugated to a nucleobase analogue that can form hydrogen bonds with thymine. A single-stranded thymine DNA molecule with a

defined size can then be added to the amyloid-DNA conjugate to form seeds. Addition of unmodified monomer to the preformed seeds will result in the design modular amyloid-DNA nanomaterials.

2.3 Amyloid-DNA conjugation strategies

The *Saccharomyces cerevisiae* yeast prion Sup35 is here used as a model system to modulate amyloid self-assembly via DNA conjugates. In its native biological context, the C-terminal of Sup35 acts a translation terminator, whereas the N-terminal domain is required for amyloid aggregation, which leads to increased readthrough of stop codons and an associated [PSI^+] prion phenotype. The N- and C-terminal domains are separated by the M-domain which acts as a flexible linker (Tuite, 2000). The biological mechanisms and effects of [PSI^+] are not well understood, and the phenotype can be both detrimental to the host (McGlinchey et al., 2011), as well as provide growth advantages under some environmental conditions (Garcia & Jarosz, 2014). In addition to the self-propagation of the Sup35 amyloid within a cell, the prion phenotype is transmitted to progeny, as well as to other cells during yeast mating, through cytoplasmic transfer (Liebman & Derkatch, 1999). Thus, the use of Sup35 facilitates the characterisation of the effect of the amyloid-DNA conjugates on both *in vitro* amyloid self-assembly, and on the spread of the prion state in cellular systems.

The protein monomer used here comprises only the NM domains of Sup35 to facilitate recombinant protein production and purification, as the elongation termination function of the C-terminal is not required for amyloid formation. Sup35NM is capable of *in vitro* self-assembly, as well as inducing the [PSI^+] phenotype in yeast (Sant'Anna et al., 2016) and is

even capable of cell-to-cell transmission when expressed in multicellular organisms (Nussbaum-Krammer et al., 2013). The Sup35NM protein construct is here further modified to include a flexible linker and a terminal cysteine residue in the C-terminal (Sup35NM-LCys), which allows thiol-maleimide reactions with added maleimide-functionalised chemical linkers to occur. The added nine amino-acid residue flexible linker before the C-terminal cysteine of the protein is designed to ensure that the LCys variant is capable of templated cross-elongation with the WT Sup35NM, enabling it to be added in small amounts to control the self-assembly behaviour *in vitro* and potentially also *in vivo* in yeast cells.

In the first amyloid-DNA conjugation strategy (**Fig 2.1**), the Sup35NM-LCys protein undergoes coupling to a maleimide-functionalised small chemical linker, to which a short ssDNA polymer has been covalently added. The conjugation is carried out separately with linkers covalently bound to two different, complementary ssDNA strands termed DNA1 and DNA2. The formed Sup35NM-LCys-DNA1/2 can then both be added to the unmodified WT Sup35NM in a small proportion to modulate its aggregation behaviour. The DNA-conjugated Sup35NM-LCys monomers are expected to be incorporated into the fibrils formed by WT Sup35NM and the complementary DNA strands are expected to form cross-links, thus promoting aggregation of the formed amyloid into clusters, resulting in an increased size-distribution. DNA cross-linking is reversible and temperature-sensitive, with the possibility of changing the melting temperature of the two complementary DNA strands by changing the complementary sequences. This reversibility could be tested by thermal shift assays to identify effects on amyloid aggregation. The cross-linking could also change the spread of the Sup35NM prion state by reducing the effect of fragmentation and the release of small seeds, which could be tested by transfecting yeast cells expressing endogenous Sup35 with small

seeds of cross-linked Sup35NM-LCys-DNA1/2 fibrils and measuring the effect on the [PSI$^+$] prion state propagation.

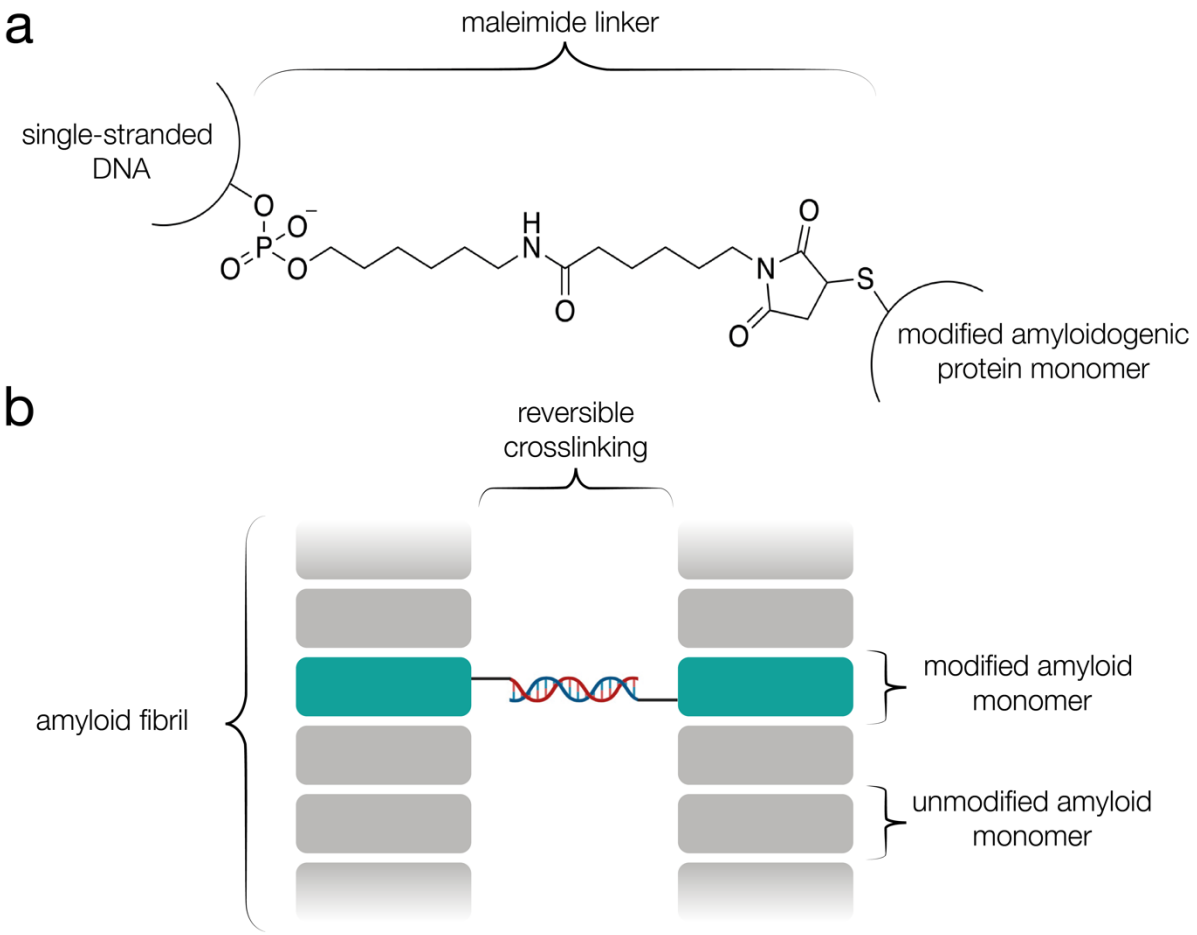

Figure 2.1 Conjugation of an amyloidogenic monomer to two complementary single-stranded DNA molecules. **(a)** Structure of the ssDNA-maleimide linker. **(b)** Cartoon representation of the amyloid aggregation modulation strategy.

A second strategy employed here is designed to conjugate the Sup35NM-LCys protein monomer to a nucleobase analogue via a maleimide linker, in order to form seeds of a defined size (**Fig. 2.2**). Amyloid-DNA conjugation is again carried out via thiol-maleimide reactions between the thiol group of the Sup35NM-LCys C-terminal cysteine side chain, and the maleimide-functionalised small molecule linker, to which a nucleobase analogue has been covalently attached. Hydrogen bonding between the nucleobase analogue and the thymine

nucleobase of an added poly(T) ssDNA will then result in the formation of seeds with a width defined by the length of the ssDNA strand, capable of promoting self-assembly of amyloid fibrils through elongation upon adding unmodified WT Sup35NM monomer. The resulting amyloid fibrils could potentially also be capped by a small peptide capable of inhibiting elongation, to achieve a length distribution defined by the added WT protein monomer concentration and elongation time. Furthermore, the resulting amyloid-DNA self-assemblies with defined width and length could be further used in a modular way to assemble nanomaterials of various 2D or 3D structures by adding flanking DNA sequences to the poly(T) strands, which can then hybridise and form DNA scaffolds of a desired shape and size.

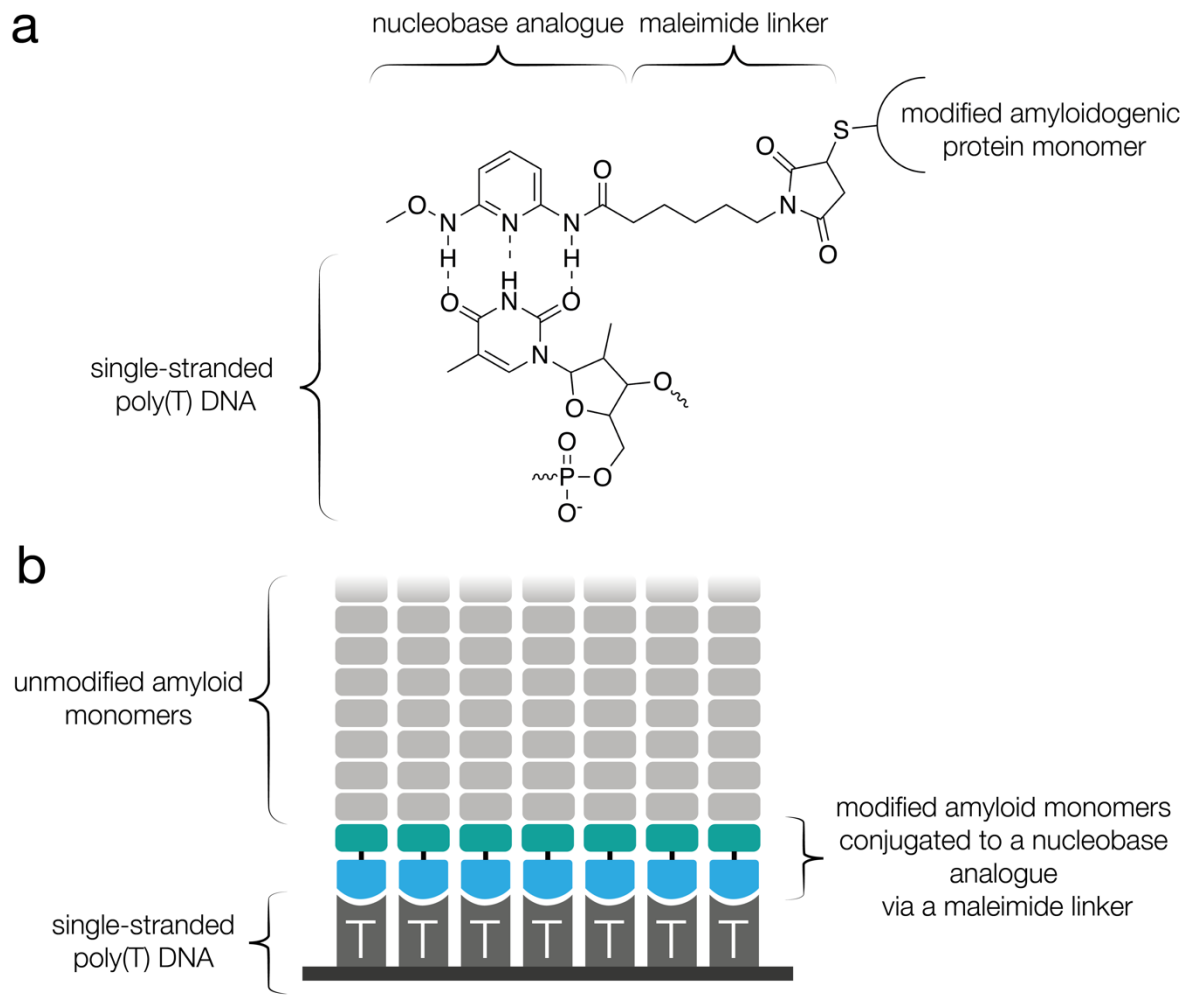

Figure 2.2 Conjugation of an amyloidogenic monomer to a nucleobase analogue and hydrogen bonding to single-stranded poly(T) DNA. **(a)** Structure of the nucleobase analogue-maleimide linker. **(b)** Cartoon representation of the amyloid aggregation modulation strategy.

2.4 Results

2.4.1 Expression and purification of Sup35NM-LCys

The Sup35NM-LCys protein used here as a model system for the modulation of amyloid self-assembly by DNA conjugates was expressed and purified from *E. coli* containing an expression plasmid. The expressed protein is found in inclusion bodies, so lysis of the harvested cells was carried out under denaturing conditions using guanidine hydrochloride (GdnHCl). In addition, this prevents the self-assembly of the protein monomer into an amyloid state during purification. Briefly, the purification was carried out by sonication of the cells, centrifugation of the cell suspension to remove debris, and an affinity chromatography step of the supernatant using Ni-NTA resin. The eluted fractions were then further purified in a size exclusion chromatography (SEC) step. As the Sup35NM-LCys protein contains a terminal cysteine residue, the protein is expected to exist in solution both as a monomer and dimer. Thus, DTT was initially added before the SEC step in order to reduce the disulphide bonds and purify the protein in a monomeric state. However, it was found that the major of the protein was already in a monomeric state (**Fig. 2.3b**) and avoiding reducing agents during purification resulted in a better separation of peaks in the SEC profile (**Fig. 2.3a**). A band corresponding to the approximate molecular weight of the Sup35NM-LCys protein (calculated as 31.3 kDa) was seen in fractions from peak 3 with SEC carried out in nonreduced conditions, and a band which upon addition of DTT reduces to the same size, thus corresponding to the dimeric form of the protein, was seen in fractions from peak 2. The molecular weight of the monomeric protein

band on SDS-PAGE results (~37 kDa) appeared higher than the calculated molecular weight of the protein, which has been observed in prior work with this construct. Thus, to confirm the identity of the protein, pooled fractions from peak 3 were analysed by mass spectrometry. A peak corresponding to the exact mass of the Sup35NM-LCys protein was seen on the mass spectrometry spectrum **(Fig 2.3c)**. A peak of ~300 Da larger mass was also seen, which may correspond to a contaminant protein not removed during the protein purification process.

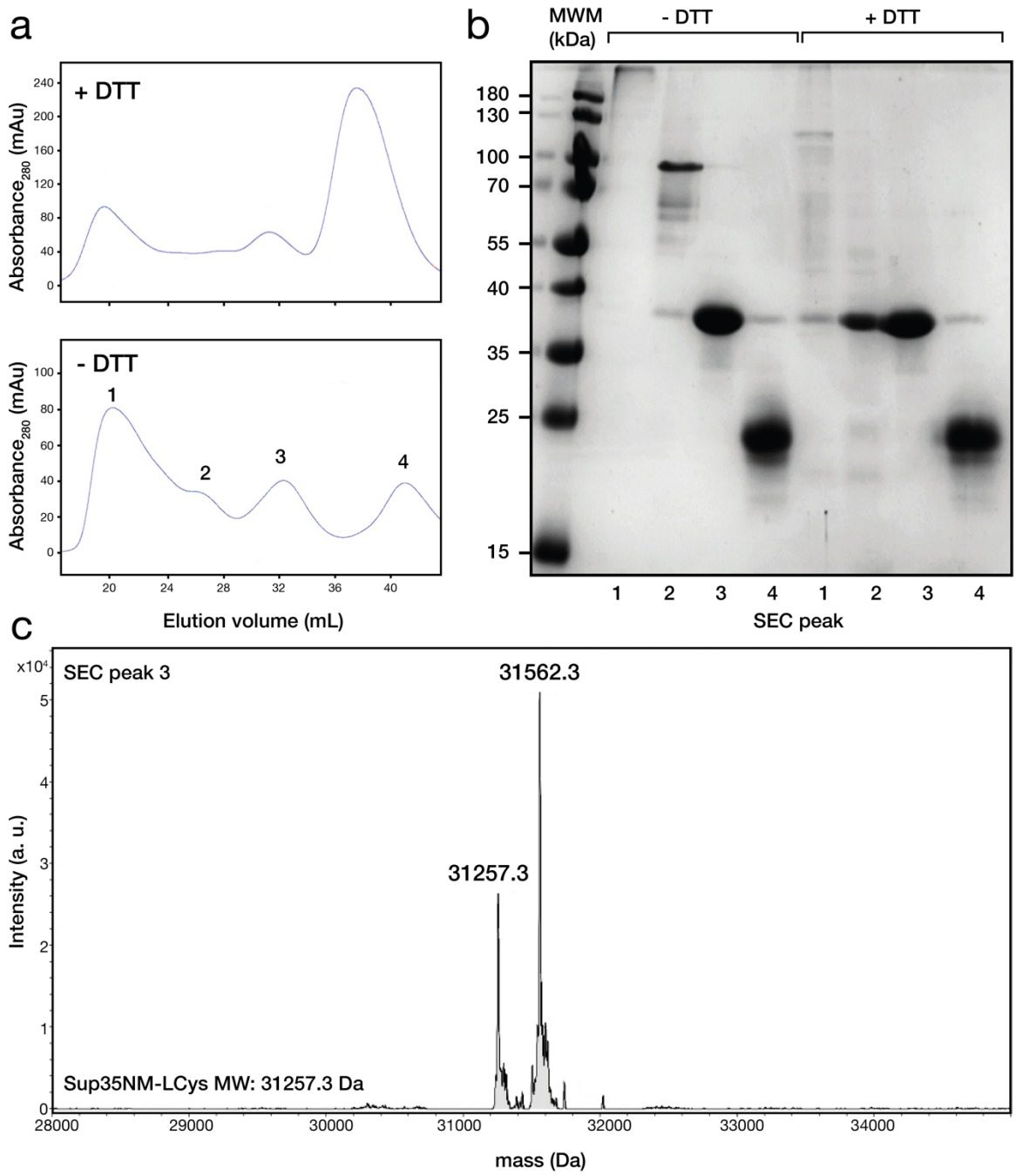

Figure 2.3 Purification of expressed Sup35NM-LCys. **(a)** Size exclusion chromatography profiles of Ni-NTA column eluate with (top) and without (bottom) added DTT. **(b)** 8 % SDS-PAGE of the peaks shown in the bottom SEC profile from (a) in reduced and unreduced conditions. **(c)** Mass spectrometry results of peak 3.

2.4.2 Co-assembly of WT and LCys Sup35NM

The design of amyloid-DNA conjugates here relies on the addition of the modified Sup35NM-LCys to the WT variant in order to regulate the self-assembly process. Therefore, the kinetics and the morphology of both WT and LCys Sup35NM, and their mixtures of varying proportions, were analysed. Sup35NM readily self-assembles into amyloid fibrils upon the removal of denaturing agents, here 6 M GdnHCl in which the protein monomers were stored after purification. To initiate fibril formation, buffer exchange from the denaturing guanidine buffer into a 20 mM phosphate buffer at pH 7.4 was carried out. The WT and LCys proteins were then mixed in various proportions, pipetted into a 96-well plate, and incubated at 37 °C in a microplate reader over several days. Fibril formation was followed with the fluorescent dye thioflavin T (ThT), which exhibits increased fluorescence upon binding amyloid (**Fig. 2.4a**), and by AFM imaging of the samples formed under identical conditions without the addition of ThT (**Fig. 2.4b**).

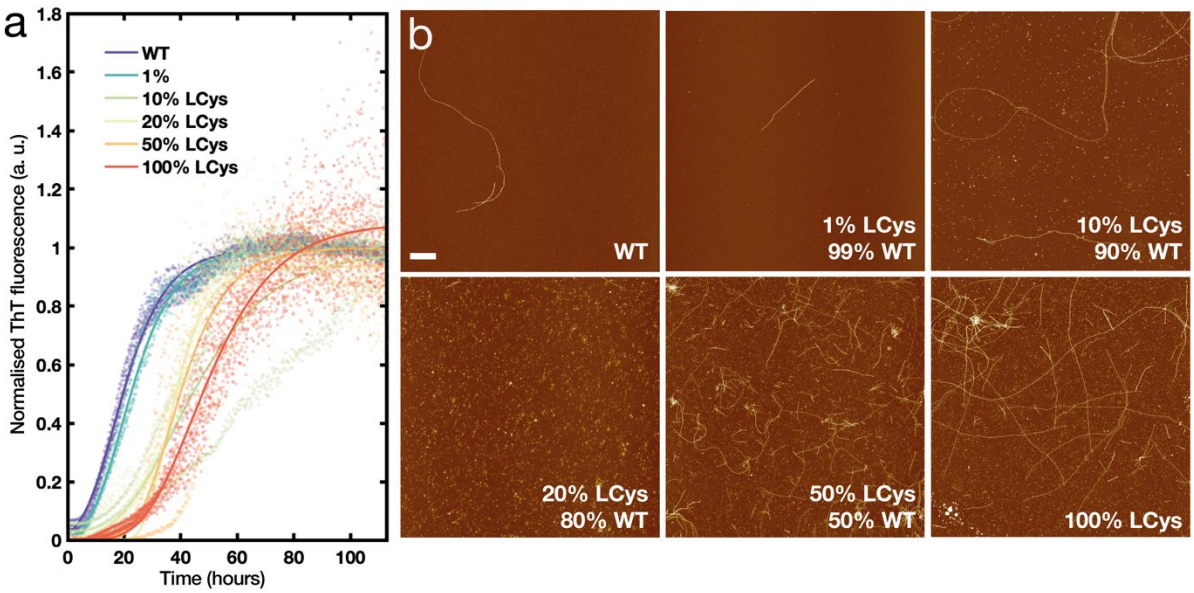

Figure 2.4 Kinetic and morphological analysis of Sup35NM WT and LCys co-aggregation. **(a)** Thioflavin T assay of aggregation kinetics with varying ratios of WT and LCys Sup35NM. Monomer concentration was 5 μM for both proteins. **(b)** Representative AFM images of the aggregation reactions without the addition of ThT. Scale bar represents 1 μm.

All ThT fluorescence curves exhibited the characteristic sigmoidal shape of amyloid fibril growth curves, although higher proportions of LCys to WT Sup35NM resulting in increased aggregation lag times. Additionally, an increase in both noise and variance between repeats was seen with an increasing proportion of LCys, which also corresponded to an increase in small fibrillar, oligomeric and amorphous aggregate species in the AFM images of sample morphologies. AFM imaging also showed that both WT and LCys Sup35NM formed fibrils, and the morphologies of the populations appeared distinct. Interestingly, the 20:80 LCys to WT ratio resulted in a mostly homogenous sample of small aggregate species. ThT and AFM results indicate that the LCys and WT proteins interact and affect both the kinetics of amyloid aggregation and the morphology of formed fibrils.

2.4.3 Conjugation of Sup35NM-LCys to complementary DNA strands

The conjugation of the Sup35NM-LCys protein monomer to the two complementary linkers, linker-DNA1 and linker-DNA2, was carried out separately, and the reaction proceeded through a thiol-maleimide coupling between the thiol group of the Sup35NM-LCys terminal cysteine residue and the maleimide group of the linker. Various denaturing reaction conditions were tested, and the reaction mixtures were analysed by both SDS-PAGE and mass spectrometry. The reducing agent TCEP was added to the protein sample prior to all conjugation trials in large molar excess to reduce any protein dimers formed via disulphide bonds between two Sup35NM-LCys C-terminal cysteines. Initially, the purified Sup35NM-LCys protein in Elution G buffer was mixed with linker-DNA1 and linked-DNA-2, in a molar equivalent ratio of ~15:1 and left to react at room temperature overnight. SDS-PAGE analysis showed a band shift of approximately the expected size (6.5 kDa) from the monomeric Sup35NM-LCys towards higher molecular weight, whereas the maleimide-conjugated control did not show a band shift on the gel (**Fig. 2.5a**), indicating that the reaction had been successful. It should be

noted that the total amount of protein loaded on the SDS-PAGE gels varied, leading to differences in total band intensities between gels and lanes, as a result of removing the guanidine buffer after the conjugation reaction, in order to avoid precipitation of SDS and distortion of the gel.

Interestingly, the sequence of the DNA strand added to the linker had an effect on conjugation efficiency, with DNA2 resulting in a higher yield of DNA-protein conjugate of approximately 15 % more conjugate formed, compared to DNA1, as measured by intensity of the SDS-PAGE bands from the digitalised image shown in Fig. 2.5a. In addition to SDS-PAGE, mass spectrometry was also used to analyse the conjugation reaction mixture. However, the mass spectrometry data were too noisy to identify whether molecules with the size corresponding to that of the Sup35NM-LCys-linker-DNA1/2 conjugates were present.

Changes to buffer conditions were then explored in order to improve the conjugation efficiency. The guanidine concentration was first lowered, to test whether interactions between guanidine and DNA may lead to a lower conjugation efficiency. However, decreasing the guanidine concentration of the conjugation reaction to 3 M did not have an effect on efficiency (**Fig. 2.5b**). Raising the pH of the denaturing buffer from 7 to 8 was then tried. Although maleimide-thiol reactions are specific in the pH range of 6.5 to 7.5, above pH 7.5 the specificity is lost as the maleimide competitively reacts with both thiols and primary amines in the N-terminal, as well as lysine side chains (Hermanson, 2013). However, raising the pH from 7 to 8 was tested to see if conjugation efficiency can be achieved at the expense of specificity. However, a similarly low conjugation efficiency to all previous trials was observed by SDS-PAGE when carrying out the reaction 6 M guanidine buffer at pH 8 (**Fig. 2.5c**) and no

conjugation was observed when the reaction was carried out in 8 M urea buffer at pH 8 (**Fig. 2.5d**).

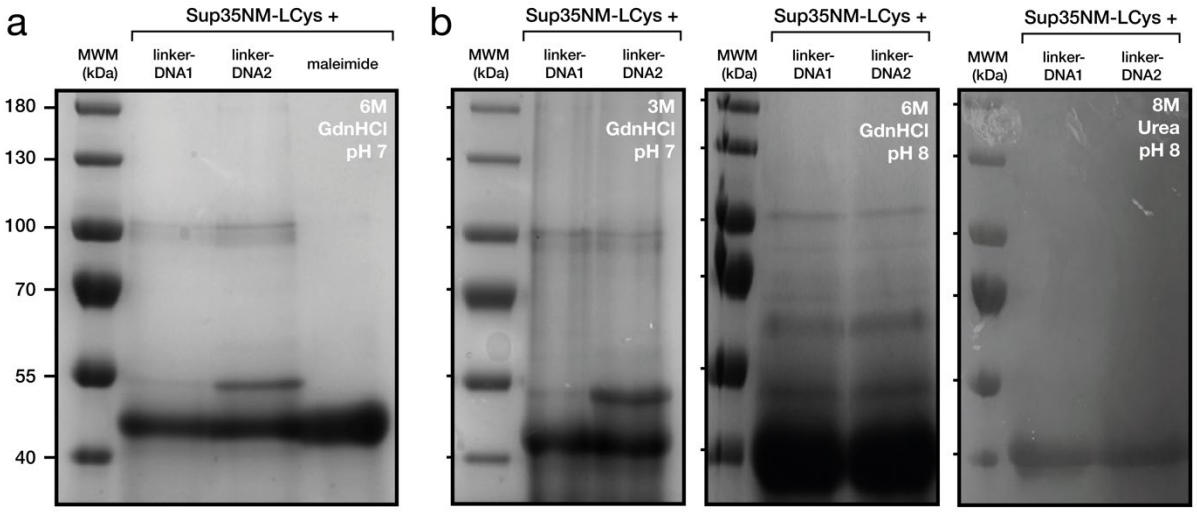

Figure 2.5 SDS-PAGE results of conjugating linker-DNA to the Sup35NM-LCys amyloidogenic monomer. **(a)** A band shift of the approximately expected size (~6.5 kDa) can be seen upon addition of linker-DNA and not when adding maleimide. The reaction was carried out in 6 M GdnHCl at pH 7. **(b)** A band shift of approximately expected size can also be seen in 3 M GdnHCl buffer at pH 7. **(c)** Conjugation carried out at 6 M GdnHCl pH 8. **(d)** Conjugation carried out at 8 M urea pH 8.

2.4.4 Conjugation of Sup35NM-LCys to a nucleobase analogue

The Sup35NM-LCys monomer was conjugated to a nucleobase analogue with a covalently attached maleimide-functionalised linker via a thiol-maleimide reaction between the thiol group on the Sup35NM-LCys C-terminal cysteine and the maleimide in the linker. The reaction was carried out in denaturing buffer containing 6 M GdnHCl at pH 7 (Elution G buffer). Various molar equivalent ratios were tested, ranging from 2-20 molar equivalents of linker-nucleobase analogue to 1 molar equivalent of protein. The reactions were carried out overnight at room temperature (RT) or 37 °C. Unlike the conjugation of the complementary DNA strands to Sup35NM-LCys demonstrated above, the conjugation of the nucleobase analogue cannot be

analysed by SDS-PAGE, as the size of the linker is 344 Da, which is too small to be detected by SDS-PAGE due to its limited resolution. Thus, the conjugation reaction mixtures were analysed by mass spectrometry (**Fig. 2.6**).

Mass spectrometry data showed the appearance of a peak approximately around the position of the expected peak for the protein-linker conjugate of an expected molecular weight of ~31.6 kDa. The peak in the approximate region of the conjugation product appeared to increase in intensity at high molar equivalent ratios of linker to protein for both RT and 37 °C reactions, indicating that protein and linker may be reacting and forming the conjugation product with a higher yield. The reaction was also more efficient at 37 °C compared to RT, as the peak in the expected region of the protein-linker conjugate was more intense at each successively higher ratio of linker to protein. However, the mass spectrometry results were noisy and inconclusive as peaks showed a wide distribution, and an unexpected peak ~200 Da larger than the expected protein-linker conjugate was present in all samples and also appeared to increase in intensity with higher linker:protein molar equivalent ratios. The wide distribution of the peak to the left of the red line and arrow on Fig. 2.6, which likely contains the unconjugated protein, indicates that the protein may be partially degraded or that the sample may contain impurities that were not removed during the chromatography steps.

As a result of the inconclusive mass spectrometry results, the experiment was repeated with a different batch of purified protein and using the most efficient conditions identified from Fig. 2.6, i.e. 20:1 molar equivalent ratio of linker to protein at 37 °C. A mass spectrometry analysis of the repeat conjugation experiment now showed a peak within 0.4 Da of the expected molecular weight of the protein-nucleobase analogue conjugate (**Fig. 2.7**). Although the similarity in size is enough to give confidence that the reaction had been successful, the mass

spectrometry data are still ambiguous, as there are two peaks to the left of the conjugation product, whereas only a single peak would be expected for the unreacted protein. Additionally, peaks were broad and showed various local maxima of unknown compositions.

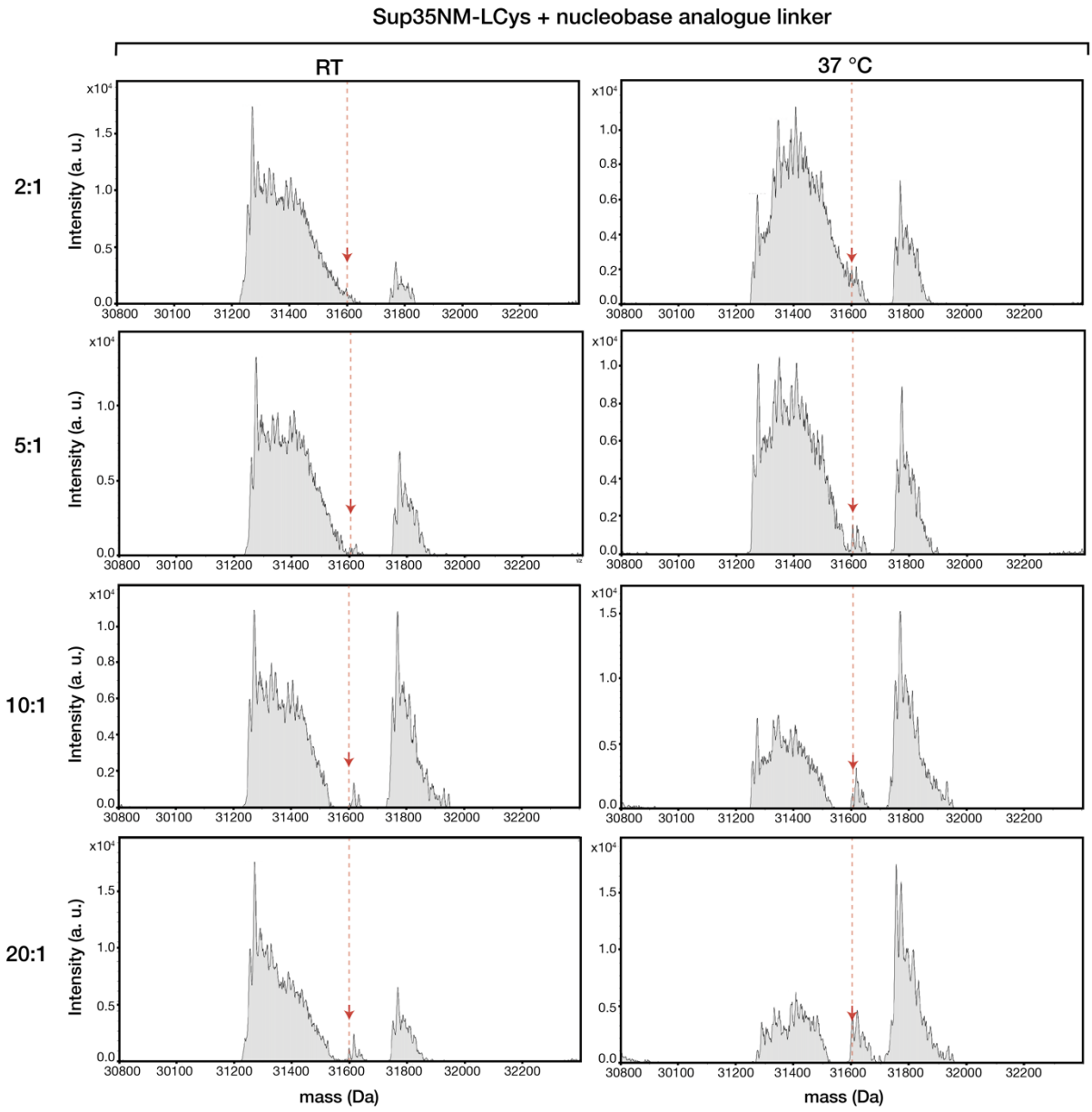

Figure 2.6 Mass spectrometry analysis of the reaction mixture after conjugation of a nucleobase analogue to Sup35NM-LCys amyloidogenic monomer with varying molar equivalent ratios of linker:protein at room temperature (RT) and at 37 °C. Red line and arrow indicate the position of the expected peak for the protein-linker conjugate at 31601.3 Da.

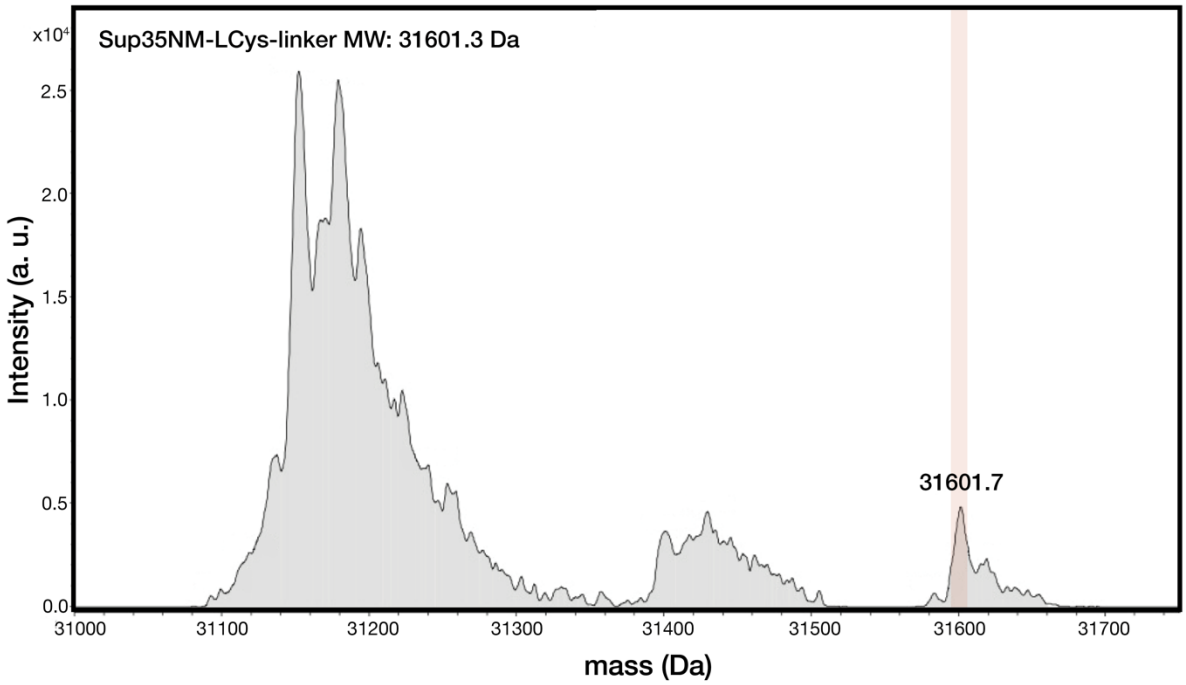

Figure 2.7 Mass spectrometry results showing a repeat experiment of the conjugation of Sup35NM-LCys to the nucleobase analogue linker at 37 °C at 20:1 molar equivalent ratio of linker:protein.

2.5 Discussion

Modulation of amyloid self-assembly is a key strategy for both the identification of potential therapeutic interventions to prevent the cytotoxicity and prion-like spread of pathogenic amyloid, as well as to facilitate the use of amyloid as nanomaterials. One potential mechanism for the modulation of amyloid aggregation is conjugation of amyloid to DNA, a versatile biological polymer with properties that can be modified by changes to the nucleic acid sequence.

Amyloid-DNA conjugates were here formed, in order to induce cross-linking of the Sup35NM prion protein and increase the size distribution of the fibril population. SDS-PAGE results indicated that the thiol-maleimide based conjugation reactions between two different,

complementary DNA strands with covalently attached linkers, and the Sup35NM-LCys protein monomer had been successful. Improving conjugation efficiency would be necessary in future work, followed by purification of the formed conjugation products and recycling of the unreacted protein and linker-DNA. A systematic screen to identify optimal reaction conditions, such as denaturing agent concentration, pH, reaction time, and ratio of protein-to-linker, could be useful for the improvement of conjugation efficiency. Once the amyloid-DNA conjugates with complementary strands can be purified from the reaction mixtures, studies on their effect on aggregation in physiological conditions could be carried out both *in vitro* by addition of WT Sup35NM and monitoring of amyloid aggregation by ThT and morphological analysis of the resulting samples by AFM and TEM. The conjugate could be further introduced into yeast cells through transfection of yeast with short pre-formed fibril fragments of Sup35NM-LCys-linker-DNA1/2, as previously demonstrated for various different amyloid (Marchante et al., 2017), in order to assess the spread of the endogenously expressed Sup35 protein and the $[PSI]^+$ prion state between cells.

In the second strategy employed here, Sup35NM-LCys monomers were conjugated to a nucleobase analogue, with the aim of forming seeds of defined size and shape through base pairing between the nucleobase analogue and the complementary nucleobase thymine. Mass spectrometry analysis of the conjugation reaction mixtures indicated that the correct product is likely to have formed, although contaminants and side-products were also present in high concentrations. The reaction proceeded more efficiently at higher linker:protein ratios, with 20:1 being the highest tested ratio. The reaction was also more efficient at 37 °C compared to room temperature conditions.

Characterisation of the amyloid aggregation kinetics and resulting sample morphologies between LCys and WT variants of Sup35NM was carried out by ThT assays and AFM imaging, respectively, in order to determine whether the two proteins are capable of cross-elongation, as designed by the addition of the C-terminal flexible linker to Sup35NM-LCys protein. Although both ThT and AFM data indicated that the proteins interacted with each other, resulting in differences in aggregation kinetics and morphologies when mixed in various ratios, compared to LCys or WT assemblies alone, it was not possible to determine from these data whether cross-elongation occurred. This could be determined in future experiments, for example, by confocal imaging of the co-aggregated sample of WT and LCys-linker-DNA amyloid by the addition of a fluorescent probe that recognises the cross-β backbone. A DNA strand complementary to that conjugated to the Sup35NM-LCys protein with an additional covalently attached fluorescent probe of a different colour could then be added to see whether the fluorescence emissions overlap, indicating co-fibrillation. Alternatively, an unconjugated long stretch of ssDNA with a complementary end to DNA1 could be added as a probe to fibrils formed through the addition of Sup35NM-LCys-linker-DNA1 to WT Sup35NM. The resulting sample could then be imaged by AFM to identify whether the long DNA probe co-localises with fibrils.

In summary, it was here shown that the designed amyloid-DNA conjugates can be formed from the Sup35NM-LCys protein and the maleimide-functionalised small chemical linkers with attached DNA. In future work, the formation of amyloid-DNA conjugates demonstrated here could be improved through optimisation of the various steps involved, such as improving the concentration and purity of the recombinantly expressed protein through modifications to the expression construct or purification protocols, as well as improvements to the conjugation reaction efficiency by systematic testing of various reaction conditions. The purification and

further characterisation of the formed conjugation products would then allow testing of their effect on amyloid self-assembly in both *in vitro* and *in vivo* conditions.

2.6 Materials and Methods

2.6.1 Expression of Sup35NM-LCys

The yeast prion protein Sup35NM with an added N-terminal His_6-tag and C-terminal flexible linker with terminal cysteine residue (LCys) had previously been transformed into BL21(DE3) *E. coli* strain in an ampicillin-selective plasmid, grown in LB media, and stored as a glycerol stock at -80 °C. The sequence of the Sup35NM-LCys protein is shown in Fig. 2.8 below, with the modified residues highlighted in colour and the calculated molecular weight of the protein is 31.3 kDa. Here, Sup35NM-LCys was expressed by streaking of an LB-ampicillin plate with a small amount of the glycerol stock culture. The plate was incubated overnight at 37 °C. Individual colonies from the LB-ampicillin plate were then used to inoculate four flasks with 100 mL of LB-ampicillin media and the cultures were incubated overnight at 37 °C while shaking at 180 rpm. The overnight cultures were spun down in Falcon tubes at 4000 rpm for 10 min and the supernatant was discarded. The cell pellets were then resuspended in 2 mL of fresh LB medium and used to inoculate four baffled flasks with 1 L of LB-ampicillin medium. The cells were again incubated at 37 °C with 180 rpm shaking, until reaching an OD_{600} of ~0.6, approximately 1 hour, determined by periodically measuring the absorbance. Expression of Sup35NM-LCys was then induced by addition of 1 mL of 1M IPTG to each culture, to a final concentration of 1 mM, followed by incubation of the cultures for 4 hours in the 37 °C shaking incubator. The cell pellets were then harvested by centrifugation at 4000 rpm for 10 min at 4 °C. The supernatant was discarded, and the cell pellets were stored at -80 °C until purification, typically overnight.

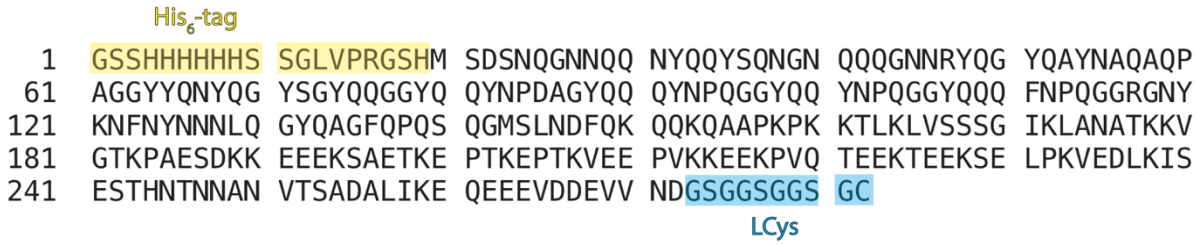

Figure 2.8 Sequence of the Sup35NM-LCys protein. N-terminal modifications are highlighted in yellow and C-terminal modifications in blue. Number of the first residue in each row is noted in the leftmost column.

2.6.2 Purification of Sup35NM-LCys

Sup35NM-LCys was purified from the frozen harvested *E. coli* cell pellets by consecutive affinity-chromatography and size exclusion chromatography steps. All buffers used are noted in Table 2.1. Firstly, the frozen cell pellets were resuspended in 30 mL of MLBG buffer and sonicated 6 times in 30 second intervals with ~2 min between intervals. Initially, DTT was added after sonication, to a final concentration of 5 mM but it was later found that subsequent purification steps were more efficient if reducing agents were added after purification. The cell lysates were then spun down at 13000 rpm for 30 min at 4 °C. Then, the Ni-NTA resin was prepared in two Falcon tubes by washing 5 mL of Chelating Sepharose Fast Flow resin (GE Healthcare) in each tube sequentially with milli-Q water, 0.2 M $NiCl_2$, MLB buffer, and MLBG buffer. Between each step the resin was spun down by centrifugation at 4000 rpm for 5 min and the supernatant was discarded. The centrifuged cell lysate supernatant was added to the prepared Ni-NTA resin and left on a tube roller at room temperature for 1 hour. The Ni-NTA resin was spun down at 4000 rpm for 5 min and the supernatant was discarded. The resin was washed with MLBG buffer twice and then loaded onto a column (Poly-Prep Chromatography Columns, BioRad), 7 mL of MLBGE buffer was used to elute the Sup35NM-LCys protein from the column, and the eluate was collected in 1 mL fractions. The absorbance of light at 280 nm (A_{280}) of each fraction was measured and the three fractions with the highest

absorbance values were pooled and further purified by size exclusion chromatography (SEC) on an ÄktaPrime Plus system using a HiLoad 16/600 Superdex 200 pg column (GE Healthcare). The column was equilibrated with both the Equilibration and Elution buffers prior to the injection of 1-3 mL of the pooled protein. The sample was run at a flow rate of 0.3 mL/min and 1 mL fractions were collected. The A_{280} of the eluting sample was continuously measured, allowing the fractions containing protein to be detected and collected. Two to three fractions from the appropriate peaks were then pooled, frozen in liquid nitrogen, and stored at -80 °C.

Table 2.1 Buffers used for the purification of Sup35NM-LCys.

Affinity chromatography			**Size exclusion chromatography**	
MLB (equilibration)	MLBG (denaturation)	MLBGE (elution)	Equilibration buffer	Elution G buffer
20 mM Tris-HCl (pH 8)	20 mM Tris-HCl (pH 8)	20 mM Tris-HCl (pH 8)	20 mM Tris-HCl (pH 8)	20 mM Tris-HCl (pH 8)
1 M NaCl	1 M NaCl	1 M NaCl	0.5 M NaCl	0.5 M NaCl
20mM imidazole	20 mM imidazole	0.5 M imidazole		6 M GdnHCl
	6 M GdnHCl	6 M GdnHCl		

2.6.3 SDS-PAGE analysis of purified Sup35NM-LCys

Samples containing guanidine hydrochloride (GdnHCl) were prepared for SDS-PAGE by changing the denaturing buffer to an 8 M urea buffer beforehand, as SDS can cause GdnHCl to precipitate and the lanes in the gel to become deformed. For this, the buffer containing GdnHCl was first removed through ethanol precipitation. Cold ethanol was added to the sample in a 9:1 ratio. The sample was mixed well and left at -20 °C for 1 hour. The sample was then

spun down at 13000 rpm for 10 min and the supernatant was discarded. The resulting white powder was washed with cold ethanol and mixed through brief vortexing before spinning down the sample again at 13000 rpm for 10 min. The supernatant was discarded, and the pelleted powder dried by a gentle stream of nitrogen air. The sample was then resuspended in 8 M urea, followed by addition of SDS-bromophenol blue loading dye. By resuspending the sample in a lower volume of buffer than the volume of the starting material, the sample was simultaneously concentrated as needed. A standard 8 % SDS-PAGE gel was then run. The gel was stained by InstantBlue Protein Stain (Expedeon Protein Solutions) and imaged for analysis.

2.6.4 Mass spectrometry of Sup35NM-LCys protein and conjugates

Mass spectrometry analysis was carried out by Kevin Howland in the Biomolecular Science Facility, University of Kent. Briefly, the electrospray mass spectrum was recorded on a Bruker micrOTOF-Q II mass spectrometer. An aliquot of the sample, corresponding to approximately 20 picomoles of protein, was desalted on-line by reverse-phase HPLC on a Phenomenex Jupiter C4 column (5 µm, 300Å, 2.0 mm × 50 mm) running on an Agilent 1100 HPLC system at a flow rate of 0.2 mL/min using a short water, acetonitrile, 0.05 % trifluoroacetic acid gradient. The eluent was monitored at 280 nm and then directed into the electrospray source, operating in positive ion mode, at 4.5 kV and mass spectra recorded from 500-3000 m/z. Data were analysed and deconvoluted to give uncharged protein masses with Bruker's Compass Data Analysis software.

2.6.5 Sup35NM-LCys and Sup35NM self-assembly

WT Sup35NM was provided by Jack Barber of the Xue lab, University of Kent. Both WT and LCys Sup35NM were prepared for self-assembly by buffer exchange from the Elution G buffer in which they were stored into sterile-filtered fibril formation buffer (20 mM phosphate, 50

mM NaCl, 0.1 % NaN_3, pH 7.4). Buffer exchange was carried out in a PD10 column (GE Healthcare) according to the manufacturer's instructions. The column eluate was collected in 0.5 mL fractions and the A_{280} of each fraction was measured. The fractions with the highest absorbance values were pooled and the final protein concentration was calculated. Both proteins were then diluted to the same concentration and pipetted in varying ratios to wells of a black 96-well plate with a transparent bottom (BRANDplate, Brand GMBH, 781608), with a final volume of 100 µL per well. The plates were sealed using transparent film (X-Clear Advanced Polyolefin StarSeal, Star Lab, E2796-9795) and incubated in a microplate reader (FLUOstar Omega, BMG Labtech). Samples were mixed by double orbital shaking at 700 rpm for 1 second.

2.6.6 Thioflavin T assay and data analysis

The samples were prepared for polymerisation as described above. ThT stock solution was added to 100 µL of protein solution in selected wells, with a final ThT concentration of 10 µL, whereas wells with sample for AFM imaging were incubated without ThT. ThT fluorescence was measured every 30 min by excitation at 440 nm and monitoring the emission of the sample at 480 nm. The collected data were analysed in Matlab by fitting of a sigmoidal curve to each time-course dataset to normalise it to the plateau phase via a nonlinear least-squares fitting approach. A sigmoidal curve was then also fitted to all the replicate data points of a single condition. The data points and fitted curve were then visualised in Matlab.

2.6.7 Atomic force microscopy sample preparation and imaging

Protein samples were prepared for AFM imaging at a monomer equivalent concentration of 5 µM, as described above, and 20 µL of the self-assembled protein sample was deposited on each freshly cleaved mica (Agar Scientific) attached to a steel disc (Agar Scientific) by double-sided

tape. The samples were left to deposit for 10 min in a covered Petri dish. The samples were then washed with 1 mL of sterile-filtered milli-Q water and dried using a stream of nitrogen gas. The samples were imaged using a Bruker Multimode 8 scanning probe microscope with a Nanoscope V controller operating in PeakForce Tapping mode using Bruker ScanAsyst-Air probes (nominal spring constant of 0.4 N/m and nominal tip radius of 2 nm). Images were collected at 10 × 10 μm size at a resolution of 2048 × 2048 pixels with a scan rate of 0.488 Hz. The images were flattened using Bruker Nanoscope Analysis software to remove the tilt and bow imaging effects.

2.6.8 Conjugation of Sup35NM-LCys to a linker-DNA

The DNA-maleimide linkers (**Table 2.2**) were synthesised by Hannah Crawford and Emerald Taylor of the Serpell group in the School of Physical Sciences, University of Kent. After synthesis the linker-DNA constructs were analysed by NMR and mass spectroscopy to verify that the correct product had been synthesised and purified. Prior to conjugation, solvent was removed from the linker-DNA samples using a rotary evaporator and the mass of the final product was weighed. The protein was then prepared for conjugation by thawing of an aliquot of the sample stored at -80 °C. TCEP at pH 7 was added to the protein in a ~500:1 molar equivalent ratio of TCEP:Sup35NM-LCys to reduce any disulphide bonds before addition of linker-DNA. The appropriate volume of Sup35NM-LCys was then added to the Eppendorf tubes with dried linker-DNA to achieve a desired molar equivalent ratio of linker to protein, typically in the range of 10:1 to 15:1. Linker-DNA with different sequences, i.e. linker-DNA1 and linker-DNA2 were conjugated to the Sup35NM-LCys protein in separate tubes. As a control, maleimide (Sigma-Aldrich) was added to a separate protein sample in large molar excess (>20000 times). The conjugation mixtures were left to react on a tube roller at room temperature before analysis by SDS-PAGE. Reaction time was varied from 1 to 72 hours.

Conjugated samples analysed by mass spectrometry were temporarily stored at 4 °C for ~2 weeks.

Table 2.2 DNA-maleimide linker sequences and molecular weights (MW).

	DNA Sequence	Linker-DNA MW (Da)
Linker-DNA 1	TT TTT CTG TAT GGT CAA CTG	6476
Linker-DNA 2	TT TTT CAG TTG ACC ATA CAG	6454

2.6.9 Conjugation of Sup35NM-LCys to a complementary nucleobase analogue

The DNA-maleimide linkers were synthesised by Hannah Crawford of the Serpell group in the School of Physical Sciences, University of Kent. After synthesis the linker-DNA constructs were analysed by NMR and mass spectroscopy. The conjugation was carried out by mixing the protein and linker in varying molar equivalent ratios in Protein LoBind Tubes (Eppendorf) at both room temperature and at 37 °C. TCEP at pH 7 was added to the protein in a ~500:1 molar equivalent ratio of TCEP to Sup35NM-LCys to reduce any disulphide bonds before addition of linker-nucleobase analogue. Protein concentration between conjugation trials varied from 7.5-10 μM but was kept constant between individual conditions of a single trial. Conjugation was carried out overnight on a tube roller (at RT) or quiescently (in a 37 °C incubator). Conjugated samples analysed by mass spectrometry were temporarily stored at 4 °C for ~2 weeks.

Chapter 3: Three-dimensional reconstruction of individual helical nano-filament structures from atomic force microscopy topographs.

3.1 Summary

This chapter is based on paper III in the List of Publications included in the thesis (Lutter et al., 2020). Atomic force microscopy is a type of scanning probe microscopy, which is used to record and analyse surface topographs of a wide range of samples from biomolecules to inorganic materials. Individual AFM scans have a high signal-to-noise ratio and a resolution typically in the low nanometre range, making AFM an excellent single molecule technique. AFM has also been widely used to characterise the morphology, suprastructural arrangement, and physical properties of amyloid fibrils. However, the resolution of AFM images is limited due to the underlying physical process of image collection, which involves probing the sample surface with a finitely sized, sharp tip. The interactions of the probe and the sample result in convolution, or widening, of surface features on AFM, and consequently the application of AFM to the analysis of sample surfaces is limited by the convolution effect.

Here, an AFM topograph deconvolution algorithm is demonstrated on polymorphic amyloid fibril samples formed from a hexapeptide with the amino acid sequence HYFNIF. The algorithm recovers the tip-sample contact points based on the modelling of the tip geometry and through iterative rounds of refinement, leading to both a correction of the imaging artefact and an approximate doubling of local resolution on concave surfaces. The deconvolution algorithm is here demonstrated to be applicable to any topograph, facilitating higher resolution and more accurate AFM data analysis. Furthermore, deconvolution also facilitates the reconstruction of samples with helical symmetry as 3D envelopes. A moving window approach is used to reconstruct the tip-inaccessible areas of the fibrils, thus preserving local intra-fibrillar variations. The single molecule 3D envelope reconstruction approach is demonstrated here on helically symmetrical hexapeptide amyloid fibrils, showing that the high signal-to-noise ratio of AFM data, combined with the deconvolution and reconstruction algorithms, allows the reconstructed fibrils to preserve structural details of polymorphism. The developed approach presents opportunities for further developments, including mapping of the population polymorphism of amyloid fibrils on a single molecule level, which can then be applied to determine the effects of primary amino acid sequence and other factors on the polymorphic landscape of amyloid assemblies (paper II in the List of Publications that were not included in the thesis; (Aubrey et al., 2020)).

3.2 ABSTRACT

Atomic force microscopy is a powerful tool that can produce detailed topographical images of individual nano-structures with a high signal-to-noise ratio without the need for ensemble averaging. However, the application of AFM in structural biology has been hampered by the tip-sample convolution effect, which distorts images of nano-structures, particularly those that are of similar dimensions to the cantilever probe tips used in AFM. Here we show that the tip-sample convolution results in a feature-dependent and non-uniform distribution of image resolution on AFM topographs. We show how this effect can be utilised in structural studies of nano-sized upward convex objects such as spherical or filamentous molecular assemblies deposited on a flat surface, because it causes 'magnification' of such objects in AFM topographs. Subsequently, this enhancement effect is harnessed through contact-point based deconvolution of AFM topographs. Here, the application of this approach is demonstrated through the 3D reconstruction of the surface envelope of individual helical amyloid filaments without the need of cross-particle averaging using the contact-deconvoluted AFM topographs. Resolving the structural variations of individual macromolecular assemblies within inherently heterogeneous populations is paramount for mechanistic understanding of many biological phenomena such as amyloid toxicity and prion strains. The approach presented here will also facilitate the use of AFM for high-resolution structural studies and integrative structural biology analysis of single molecular assemblies.

3.3 INTRODUCTION

Atomic force microscopy is a scanning probe microscopy method that enables the collection of three-dimensional topographic image data, and has been widely applied to characterisation of biological and non-biological macromolecules. AFM encompasses a range of techniques for structural studies of biological molecules, including the study of inter- and intramolecular interactions (Pfreundschuh et al., 2015), molecular dynamics (Parsons et al., 2019), molecular remodelling under force (Y. Chen et al., 2015) and imaging of molecules in air (Ares et al., 2016) or in liquid (Moreno-Herrero et al., 2004; Nowakowski et al., 2001). AFM operating in non-contact mode is capable of reaching atomic resolution on samples of small molecules (Gross et al., 2009), whereas AFM imaging of biomolecules routinely reaches nanometre resolutions in single high signal-to-noise images, and is able to characterise biological populations at a true single molecule level. This technique has been applied to a range of different bio-molecules, including membrane proteins (Haruyama et al., 2019), viral capsids (Ramalho et al., 2016) and filamentous biomolecules, such as amyloid fibrils (Adamcik et al., 2010), nucleic acids (Bose et al., 2018; A. Pyne et al., 2014), and various filaments involved in the cytoskeleton (Narita et al., 2016).

Amyloid fibrils represent a class of filamentous supramolecular assemblies frequently studied using AFM imaging. Although the amino acid sequences of the many amyloid forming proteins are typically unrelated, the fibrils they form share a well-defined common core structural architecture, namely the cross-β arrangement made up of β-strands that stack perpendicular to the fibril axis stabilised by intermolecular hydrogen bonds between β-strands that runs parallel to the fibril axis (Jahn et al., 2010; Serpell et al., 1999). Despite that all amyloid fibrils share these core structural features, variations in filament packing arrangements, including fibrils

assembled from the same precursors, result in a multitude of different fibril structures called polymorphs, which may be related to the varying types of biological response they elicit. Due to the unresolved nature of the amyloid assembly structure-function relationship, fibrillar amyloid specimen are widely studied using AFM imaging to resolve the mechanistic roles of amyloid assembly and polymorphism (Aubrey et al., 2020).

AFM imaging of a sample, e.g. amyloid fibrils deposited on a surface, with typical intermittent contact imaging mode such as the tapping mode is achieved by scanning a sample on a flat surface using a sharp tip attached to a cantilever. As the cantilever oscillates up and down, the tip and sample are moved relative to each other along the horizontal x and y axes in a raster pattern. When the tip interacts with the sample, vertical displacement of the cantilever relative to sample determines the surface height on the z-axis, measured at discrete pixel locations in the xy-plane. The lateral (x- and y-dimension) sampling is determined by the user in terms of the number of pixels collected per image and the pixel size, which tends to have edge length in the order of Ångströms to nanometres. The output of AFM scans is a 3-dimensional topography map, usually represented by a 2-dimensional coloured image where pixel values contain information on sample surface height, typically represented by the intensity of colour. Resolution in the vertical and lateral dimensions of AFM topographs are distinct. Topographs have a high vertical signal-to-noise ratio, limited by noise in the order of sub-Ångströms, due to electrical noise in the detector and thermal noise causing fluctuations in the cantilever (Butt & Jaschke, 1995; O'Connor et al., 1996), whereas lateral resolution is defined by the pixel size and the tip dimensions. Both vertical and lateral resolution can be affected by distortions or artefacts caused by drift, ambient noise or deformation of the sample or tip through their interactions. However, a significant limitation to the application of AFM to structural characterisation of biomolecules has been the tip-sample convolution effect, which causes

lateral broadening, or dilation, of upwards convex structural features on AFM topographs. Convolution arises from the finite size and geometry of the AFM probe tip and is especially pronounced when sample features are of similar size to the tip radius, usually between 1-10 nm, as is the case for many biological macromolecules. The tip convolution effect has been studied in detail since the development of the AFM technique in the 1980s (Binnig et al., 1986). In order to minimise the convolution effect, both experimental and computational approaches have been developed. For example, various tip modifications have been used in order to minimise the effect of tip-sample convolution some of which have led to atomic resolution topographs (Gross et al., 2009). However, this application is limited to small flat molecules and is not currently suitable for imaging biological macromolecules. The advantage of a computational approach to deconvolution is that an algorithm can be applied to a topograph of any specimen, after data collection. Many deconvolution methods have been reported to date. However common to these methods, they rely on the same concept based on the 'erosion' algorithm with various mathematical approaches (Canet-Ferrer et al., 2014; Keller & Franke, 1993; Villarrubia, 1997). Although erosion corrects for the dilation of the sample width, it leads to a significant loss of lateral structural information present in the AFM topology images because it does not recognise or recover the structural information that is present at subpixel locations, as we will show below.

Here, we show that the AFM tip-sample convolution effect result in a feature-dependent and non-uniform distribution of image resolution on AFM topographs, and is in fact an advantage in terms of image resolution, as it causes the 'magnification' of the sample surface. Upon correction, we reveal that subpixel resolution information of the sample surface can be recovered using a contact-point based deconvolution algorithm, thus revealing the enhanced lateral resolution encoded in the AFM topographs while minimising the dilation image

distortion. Furthermore, while AFM imaging provides only information on the top of 3-dimensional molecular surfaces of the sample structures, we show that helically symmetrical structures can be reconstructed as 3D surface envelopes from AFM topographs. This approach is demonstrated on imaging analysis of twisted amyloid fibrils formed from short peptide sequences which have been previously characterised using X-ray fibre diffraction (Morris et al., 2013). The deconvolution and 3D modelling approach facilitates the structural analysis of individual twisted filamentous assemblies at an individual particle level. It is therefore capable of resolving the structural variations of individual macromolecular assemblies within inherently heterogeneous populations such as amyloid fibrils, which is key for mechanistic understanding of many biological phenomenon such as amyloid toxicity and prion strains.

3.4 RESULTS

3.4.1 Structural information is lost through erosion deconvolution of AFM topographs

The tip-sample convolution artefact arises from the finite shape and geometry of the cantilever tip. When the tip interacts with the sample, the surface height at the bottom of the tip is recorded, whereas the true surface of the sample may lie at a different location, probed at the tip-sample contact points (**Fig. 3.1a**). This leads to convolution, or dilation in the case of upward convex surface features on AFM topographs. Image deconvolution by the erosion method corrects for the dilation of the sample by translating a model of the tip to the coordinates at which surface heights were recorded on the image and finding the tip's deepest penetration of the convoluted surface to reconstruct a deconvoluted image while conserving pixel coordinates and sampling in the xy-plane (**Fig. 3.1b-c**) (Keller, 1991; Villarrubia, 1997). Thus, erosion resolves apparent clashes between the tip and convoluted sample surface image by lowering sample surface heights according to the known surface values of the tip translates.

AFM tip geometry can be typically approximated as conical with varying apical radii, and side angles that can be modelled from the values provided by the manufacturer. Erosion deconvolution is efficient in minimising the dilating effect of convolution. However, it causes a significant loss of structural information (demonstrated on a twisted amyloid fibril in **Fig. 3.1c**), because it replaces the existing vertical surface height values with the surface of deepest tip penetration without finer resampling of surface heights at tip-sample contact points, which contain structural information in the images. These contact points lie off the pixel grid at subpixel locations and contain structural information on the true sample surface. As shown on the twisted amyloid fibril example (**Fig. 3.1**), deconvolution by erosion causes loss of information on the fibril helical periodicity and molecular surface features.

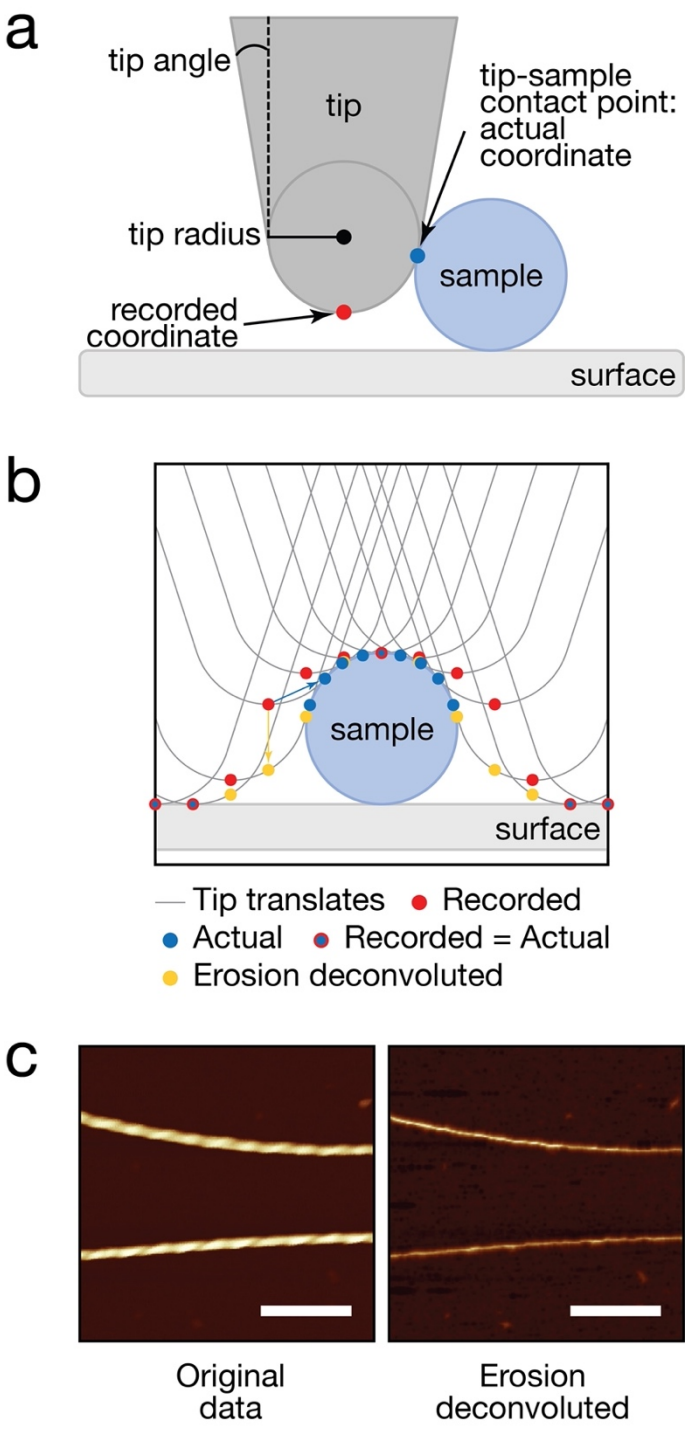

Figure 3.1 AFM image deconvolution by the erosion algorithm corrects for dilation but causes significant loss of structural information of the sample surface. **(a)** Schematic cross-sectional illustration of AFM tip-sample interactions that lead to lateral convolution and dilation of sample features. This imaging artefact is especially pronounced for sample objects on the same size range as the tip radius. **(b)** Schematic cross-sectional diagram of tip-sample deconvolution by erosion. The sample cross-section is illustrated as a blue circle. Red dots show original coordinates of the data, orange dots show erosion deconvoluted height coordinates at each pixel

location and blue dots show the coordinates at tip-sample contact points for each pixel location. **(c)** Example of deconvolution by the erosion algorithm demonstrated on an example image of a twisted amyloid fibril. Left is an AFM topology image showing twisted amyloid fibrils. Right image shows the erosion-deconvoluted image of the same data, demonstrating substantial loss of structural information due to the erosion algorithm. A symmetric conical tip with a side angle of 18° (estimated from the tip geometry information provided by the manufacturer) and tip radius of 11.2 nm (estimated using the image features as described in the Results) was used as a model of the tip. The scale bars represent 200 nm.

3.4.2 Tip-sample convolution results in enhanced lateral sampling

Although the tip-sample convolution effect causes upward convex surface features to appear dilated on topographs, this effect can in fact be use to advantage as it causes the 'magnification' of structural features present at tip-sample contact points located at subpixel coordinates, and results in higher lateral resolution topographic information to be captured than what is recorded at pixel grid coordinates. This information can be recovered by a deconvolution method in which the tip, with a known geometry, radius and angle, is modelled on the recorded surface scan at translations that correspond to original lateral sampling (x and y coordinates) and recorded surface heights (z coordinates), similarly to the erosion deconvolution method. However, instead of finding the surface of deepest penetration, geometric modelling of tip and simulation of tip translates is used to find tip-sample contact points. These tip-sample contact points contain information on the true surface of the sample, which is otherwise recorded in magnified, or dilated, form. Thus, the total number of data points remains the same but the pixel coordinates in both xy-plane and surface heights on the z-axis, are shifted, revealing the enhanced local sampling of the upward convex surface features encoded in the image data. This contact point deconvolution approach can be applied to any AFM topograph and is demonstrated on a sphere, a cylinder, and a randomly generated rough surface (**Fig. 3.2**). Contact points are found by iterative rounds of tip-sample simulations, in which the sample

surface is initially assumed to be circular, until convergence of the deconvoluted surface coordinates. The corrected images can then be interpolated onto a finely spaced even grid for visualisation of the deconvoluted image. In Fig. 3.2, lateral sampling of the tops of the example objects and peaks of the random rough surface can be seen to increase in density and shift significantly from the original position of xy-gridlines (**Fig. 3.2**, 3rd column), especially for features with size similar to the radius of the tip.

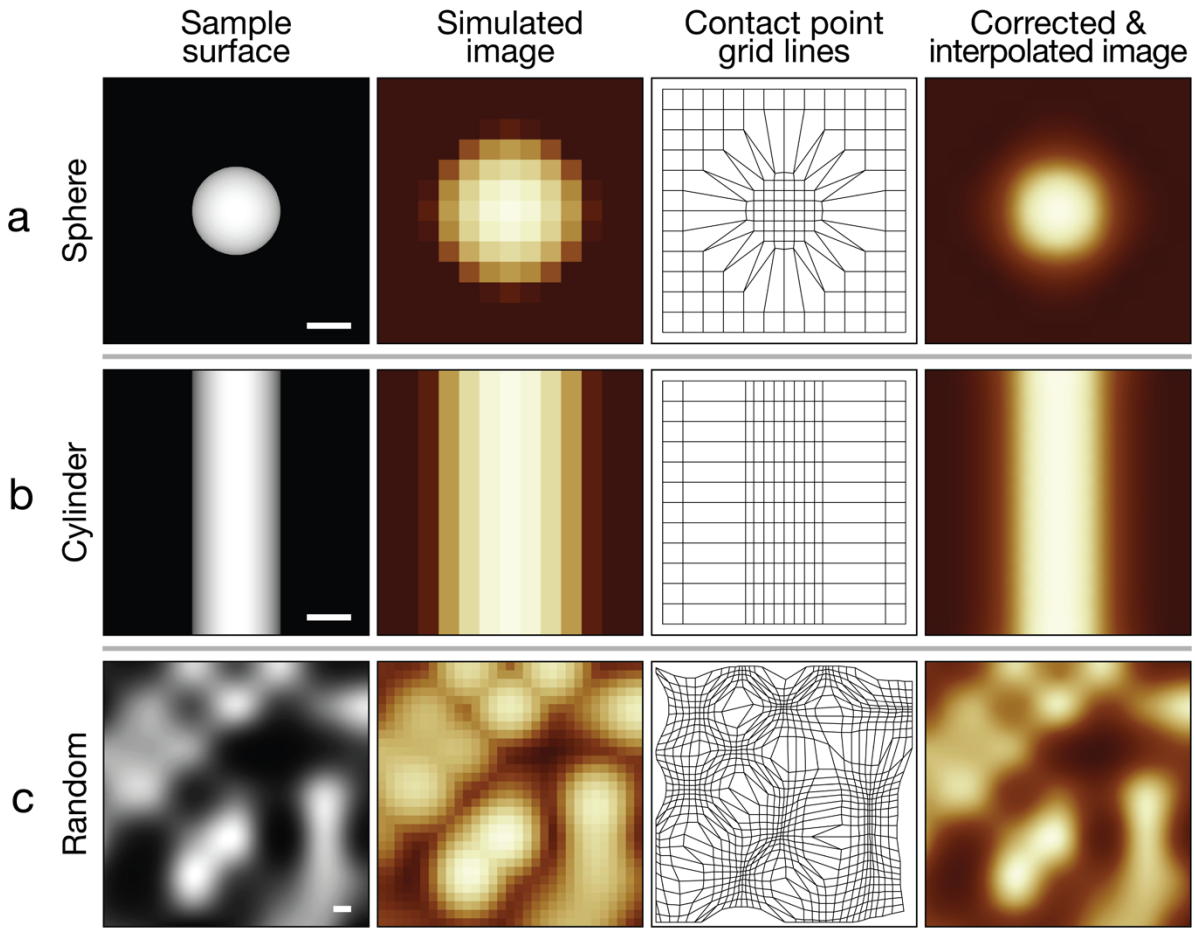

Figure 3.2 Contact-point deconvolution can be applied to any surface and results in increased local lateral sampling for upward convex sample features. Simulated AFM image (2nd column from left), shifted pixel grid lines after contact point deconvolution (3rd column from left), and a corrected image with contact points interpolated to a finer pixel grid (right most column) are shown for a sphere **(a)**, cylinder **(b)**, and a random surface **(c)** shown in the left-most column.

The sphere and the cylinder both have a radius of 2 nm. A symmetric conical tip with a radius of 2 nm and tip side angle of 18° was used for all simulations. The scale bars represent 2 nm.

The effect of locating the contact points off the pixel grid on the images of upward concave features is, however, less favourable as the depth of a trough can only be accessed if the sides of the tip do not come into contact with the sample. This can be seen in the Fig. 3.2 bottom row example as the decrease in contact point density in these areas. In the case of biological filaments such as DNA, cytoskeletal and amyloid filaments, major upward concave surface features include grooves, which can vary ~1-50 nm in width. They may be resolvable by AFM, depending on the geometric parameters of the tip, as well as depth of the features.

The deconvolution and lateral sampling enhancement of a convoluted surface depends on both the geometry of the sample, geometry of the tip, and the lateral pixel sampling frequency. The effect of these various factors on the sampling enhancement is here assessed with scan-line simulations using a circular cross-section as the sample and a symmetric tip model constructed from typical tip parameters (**Fig. 3.3**). The sampling enhancement factor is measured as a ratio of deconvoluted image signal density to original image signal density, where signal density is found as the number of moved pixel coordinates that result from tip-sample contact per surface area. The sampling enhancement factor describes the increase in lateral sampling frequency as a result of tip-sample contact point deconvolution. The effect of sample diameter as well as tip radius on the enhancement factor is illustrated in Fig. 3.3. As seen, the sampling enhancement factor of a sub-nm circular cross-section is more than three times with a 2 nm tip-radius, representing more than 3 times increase in lateral sampling compared to the convoluted image (**Fig. 3.3 left column**). The sampling enhancement then decreases as the circle diameter increases and plateaus at ~1.4 times enhancement compared to a convoluted surface. The sampling enhancement fluctuates for non-continuous sampling realistic to actual imaging

experiments and the stepwise large increases represent increases at which the tip and circle first come into contact at a sampled pixel as the radius of the circle increases, allowing a new contact point to be found. Enhancement then slightly decreases with the increase in circle radius as no new contact points are added and existing contact points become spaced further apart, therefore decreasing information density.

For a symmetric conical tip, the most important tip parameters for determining tip-sample interactions are the apical radius of the tip and the angle at which the sides of the tip widen. Although AFM tips with smaller tip radii and tip angles produce higher resolution images by minimising the tip-sample convolution effect, with the contact-point deconvolution method, larger tip radii and tip angles result in higher sampling enhancement as the tip interacts with the sample at more xy-coordinates, allowing proportionally more contact points to be recovered (**Fig. 3.3b**). Thus, with finite scanning precision, increasing resolution of images becomes an optimisation problem that involves finding optimum tip geometry with any given sampling frequency and specimen geometry. Importantly, simulations of tip-sample interactions with an estimate of sample geometry or an already corrected sample surface in which tip model and pixel size parameters are varied can guide the selection of an optimal tip geometry and sampling frequency to maximise resulting image resolution for a specific sample.

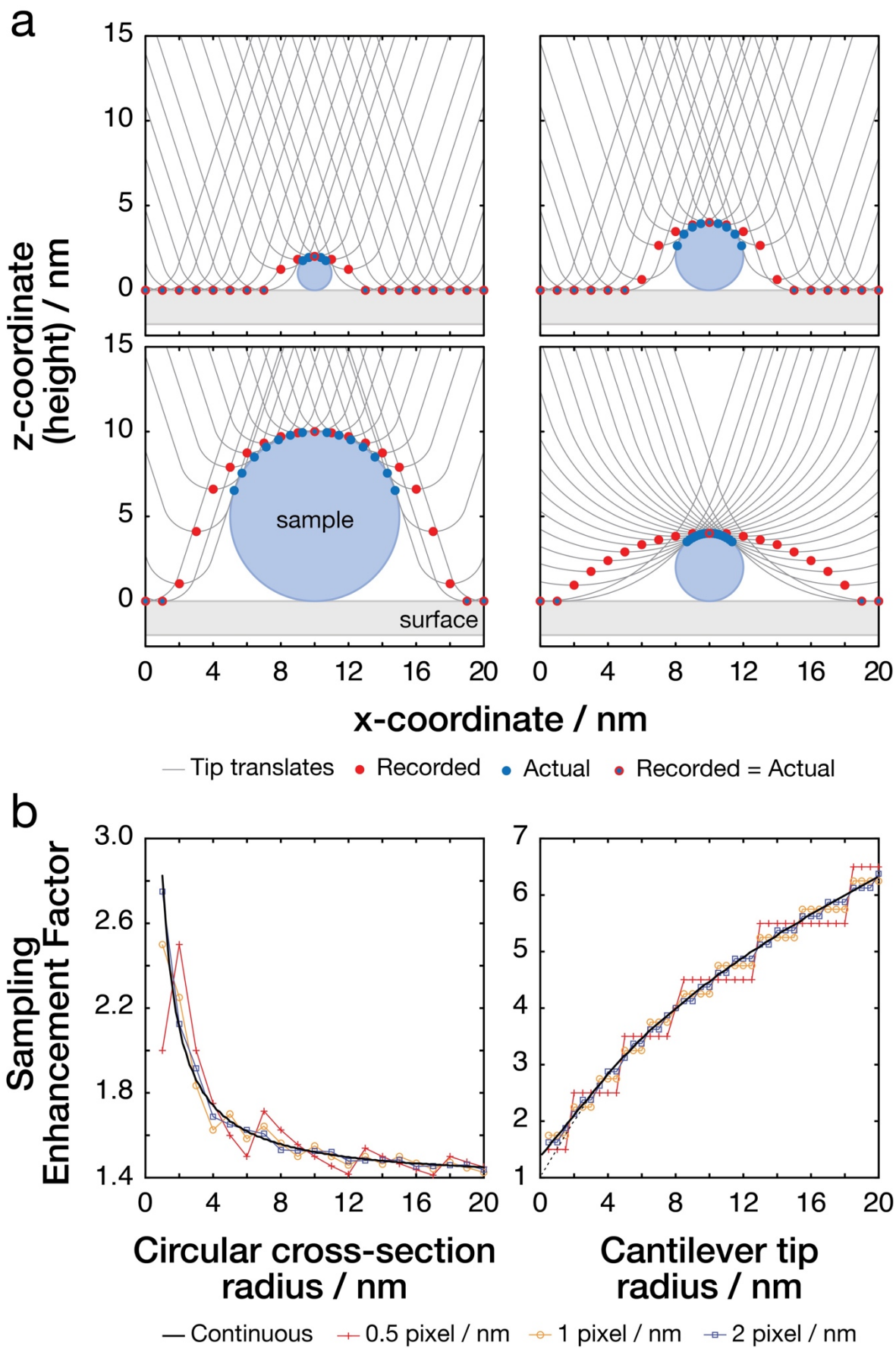
a
z-coordinate (height) / nm
15
10
5
0
sample
surface
0
4
8
12
16
20
x-coordinate / nm
Tip translates
Recorded
Actual
Recorded = Actual
b
Sampling Enhancement Factor
3.0
2.6
2.2
1.8
1.4
7
6
5
4
3
2
1
Circular cross-section radius / nm
Cantilever tip radius / nm
Continuous
0.5 pixel / nm
1 pixel / nm
2 pixel / nm

Figure 3.3 Image sampling enhancement effect after image correction by contact-point deconvolution shown with varying sample and sampling parameters. Schematic diagrams are shown in **(a)** and results from simulations in **(b)**. Red circles on schematics represent original convoluted coordinates at each sampled pixel and blue circles represent tip-sample contact points at each sampled pixel. The sampling enhancement factor is defined as the ratio of pixel density of these points within the circle envelope. Left column shows the enhancement effect seen with a circle with varying radius. A symmetric conical tip model with a radius of 2 nm and tip side-angle of 18° was used. Right column shows the enhancement effect observed with a circle with a constant radius of 2 nm with varying tip radius and a tip side-angle of 18°. The dashed line represents the same simulation but with a tip with side-angle of 0°.

3.4.3 Contact-point deconvolution of an AFM amyloid fibril topograph

The deconvolution algorithm and resulting lateral sampling enhancement are demonstrated on an AFM topograph of an amyloid fibril formed from a short amyloid forming peptide with the amino acid sequence HYFNIF (section 3.6 Materials and Methods and (Aubrey et al., 2020)). The fibril example is first traced from the AFM image across the fibril central line and subsequently straightened and interpolated to an evenly spaced pixel grid (Egelman, 1986), while maintaining pixel size identical to that in raw data. In order to apply the contact point deconvolution algorithm as shown on the examples above, the convoluted surface, as well as a model of the tip used to scan the specimen are needed. For experimental image data, the variation in the tip radius from their nominal value, which results from the tip manufacturing process, should be considered (Hill et al., 2009). It is also important to consider that the tip can become blunter with scanning and its tip radius can widen over time. Here, the tip radius can be estimated for each individual fibril on an image from the extent of convolution seen in data. An estimate of the tip radius Is found by assuming the twisted amyloid fibrils have ideal corkscrew symmetry, and the average cross-section of the fibril perpendicular to its axis of rotation is, therefore, circular with a radius defined by half of the maximal z-height value. Least-square regression analysis is then performed to fit a simulated convoluted scan-line

generated from modelling interactions of the tip with the circular cross-section model to the average convoluted cross-section observed in data, while letting the tip radius vary as a parameter. It is assumed that the overall tip geometry and side angles do not change. In the example shown in Fig. 3.4, while the nominal tip radius provided by the manufacturer was 2 nm, using the approach described here the tip radius estimate was 11.2 nm. The deconvolution algorithm is then applied to the 3D topograph to find corrected grid lines and surface heights (**Fig. 3.4c-d**). The deconvoluted contact points follow the twisting pattern of the fibril and increase lateral sampling of the fibril surface as predicted. The ungridded data points are then interpolated back onto a finer evenly spaced grid for visualisation of the de-convoluted contact-points (**Fig. 3.4c**).

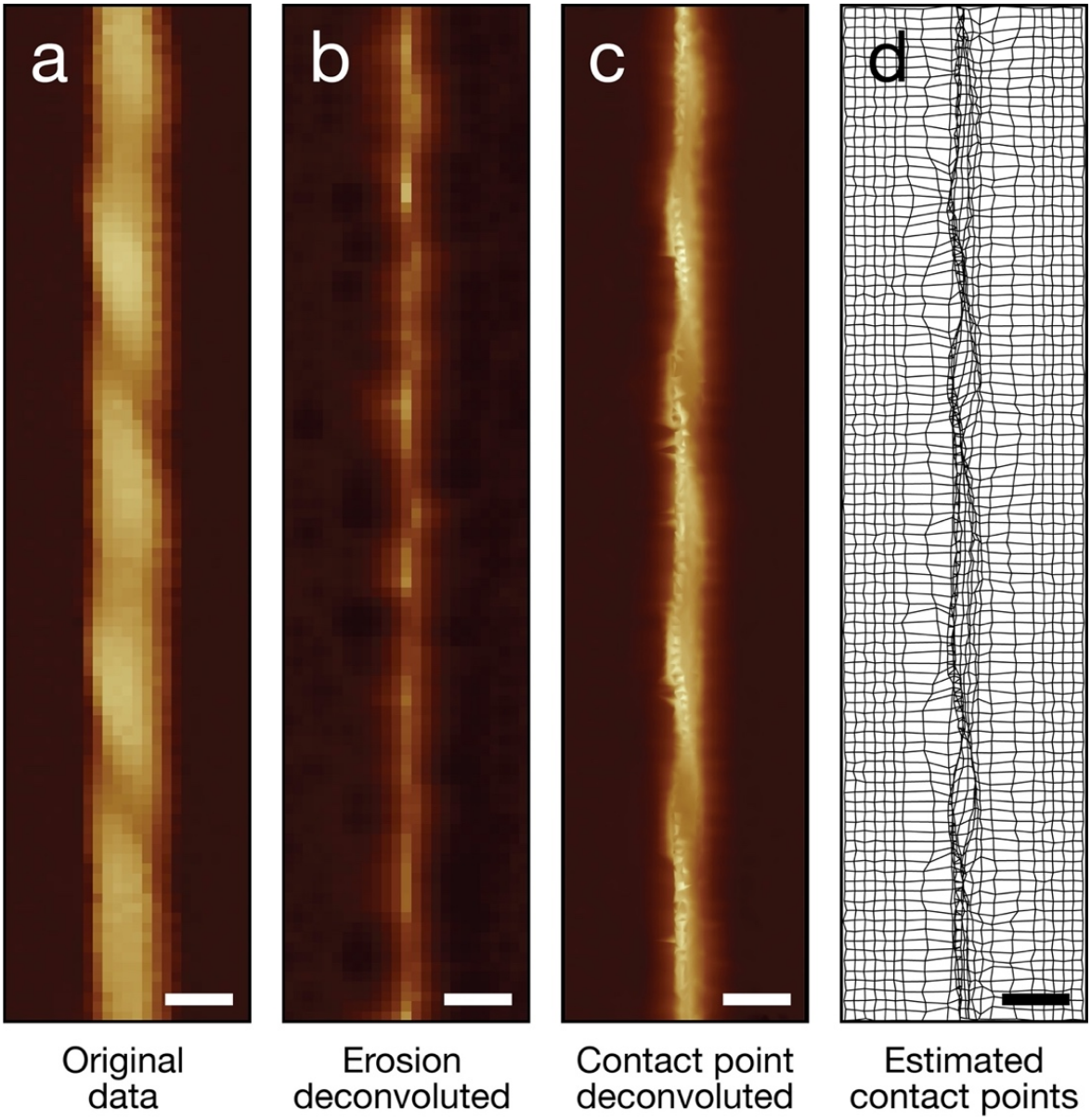

Figure 3.4 Typical example of contact-point deconvolution of an AFM topograph of a helically twisted amyloid fibril. **(a)** Digitally straightened AFM topography image of an amyloid fibril. **(b)** Image deconvoluted using the erosion algorithm. **(c)** Contact-point deconvoluted and interpolated image. **(d)** Corrected lateral (x/y) grid lines after tip-sample contact-point deconvolution. A symmetric conical tip model with a radius of 11.2 nm and side angle of 18° was used. A short section of the total fibril is shown for detail and the corresponding part of the same fibril is shown on each panel. The scale bars represent 20 nm.

3.4.4 Assessment of AFM topograph lateral resolution

Because AFM topographs are extraordinarily high signal-to-noise, the lateral resolution of a single uncorrected AFM topographs is typically determined by the spatial frequency of sampling in the xy-plane. According to the Nyquist sampling theorem, the minimal sampling rate that contains the information to reconstruct a signal is twice the maximum frequency component, thus the Nyquist resolution limit for images is twice the pixel size. For example, the image used in the example in Fig. 3.4 has a pixel size of 2.93 nm and the resolution is, therefore, limited to 5.86 nm. Deconvolution using our approach shifts pixel coordinates to subpixel positions off the pixel grid. Therefore, recovering structural information of the sample by shifting the sample surface coordinates present in magnified form results in recovering of the true higher lateral sampling frequencies present in the image data. Fig. 3.5 shows the lateral resolution of deconvoluted AFM images assessed using a feature-based lateral resolution assessment method (Fechner et al., 2009) and compared with the original convoluted image of the same fibril shown in Fig. 3.4. The feature-based method applies a low-pass filter to an image in spatial frequency domain from higher towards lower spatial frequencies and measures the correlation between the filtered and unfiltered images in real space. Increases in correlation, seen as peaks in a log-log plot of the first derivative of cross-correlation vs. spatial frequencies, indicate presence of structural information at the specific spatial frequency. Fig. 3.5b shows the correlation curves with peaks indicating the presence of structural information. Comparison of the normalised correlation between the convoluted and deconvoluted amyloid fibril images shows a shift of the correlation curve towards the right, indicating a shift of information content towards higher spatial resolutions due to correcting of sampling frequency during deconvolution. However, the contact point deconvolution has a much larger effect on the x-axis (across the width of the filament) than on the y-axis (along the length of the filament), which leads to broadening of the peaks on the 1st derivative of correlation graph. Analysis of lateral resolution suggests that the highest resolution at which structural information is found

on the convoluted example fibril image is ~60 Å (consistent with the Nyquist frequency of the original image data) and on the deconvoluted image the highest resolution is ~30 Å, indicating that deconvolution results in approximately doubling of the lateral resolution, for this amyloid fibril, due to the recovery of the enhanced sampling in the image data.

3.4.5 3D modelling of helical amyloid fibrils from corrected AFM topographs

While AFM provides 3-dimensional topographic data, only the top surface of the sample is accessible to the tip, preventing the visualisation of the full sample surface envelopes in 3D. However, for helically symmetric structures such as amyloid fibrils, we describe below an algorithm that can be used to reconstruct 3D surface envelopes by taking advantage of the screw-axis symmetry of the filaments. This approach is demonstrated on AFM topographs of deconvoluted amyloid fibrils. The workflow of AFM image processing for 3D surface envelope reconstructions is summarised below (**Table 3.1**).

Table 3.1 Flow chart of AFM topograph processing and 3D helical fibril surface envelope reconstruction.

Step	Description	Input(s)	Output(s)
1	Tracing of individual fibril from AFM topograph	– AFM topology image	– Fibril contour (x and y) coordinates
2	Fibril straightening	– AFM topology image – Fibril contour (x and y) coordinates	– Cropped topology image of the straightened fibril
3	Determining tip parameters used to record fibril image	– Cropped topology image of the straightened fibril	– Tip geometry model

4*	Contact-point deconvolution of straightened fibril with tip model	– Cropped topology image of the straightened fibril – Tip geometry model	– Contact point coordinates
5	Selecting number of coordinate-lines to use for 3D reconstruction based on deconvolution uncertainty	– Contact point coordinates	– Edited list of contact point coordinates
6	Determining fibril twist periodicity and handedness	– Cropped topology image of the straightened fibril	– Fibril twist periodicity – Fibril twist handedness
7	Reconstruction of models with various symmetry estimates	– Edited list of contact point coordinates	– 2D FFT spectra of fibril symmetry models
8	Comparison of symmetry model and original fibril image Fourier spectra	– Cropped topology image of the straightened fibril – 2D FFT spectra of fibril symmetry models	– Fibril helical symmetry
9	Real-space reconstruction of the final 3D surface envelope with selected symmetry	– Edited list of contact point coordinates – Fibril twist periodicity – Fibril twist handedness – Fibril helical symmetry	– 3D surface envelope model of the fibril
10	Simulation of a convoluted AFM image from 3D envelope	– Cropped topology image of the straightened fibril – 3D surface envelope model of the fibril	– Validated 3D surface envelope model of the fibril

* Contact-point deconvolution was performed on straightened and cropped fibril image rather than the full original image (as step 2) to reduce the amount of contact-point calculations needed but assumes long-straight fibril and symmetrical tip geometries.

Following contact-point deconvolution of traced and digitally straightened fibril image, the surface envelopes are reconstructed using a moving window approach in which rotation and translation is applied to each corrected contact point coordinates within the window, thus reconstructing fibril cross-sections as the window is slid along the length of the fibril. The width of the moving window is one complete rotation of the fibril cross-section along the fibril axis (i.e. one nominal helical pitch), determined by its periodicity and screw axis symmetry. The rotation of each data point within the window depends on the distance of the point from the central cross-section of the window. Rotation angle values are negative in one direction from the centre of the window and positive in the other direction, with the specific direction depending on the twist-handedness of the fibril. The rotation angles are kept constant along the length of the filament. After deconvolution of the amyloid fibril, the number of lines along the length of the filament that are to be used for the 3D reconstruction are determined. Data points further away from the centre of the filament can be more frequently affected by artefacts during scanning and the uncertainty of the deconvolution algorithm tends to be higher for surface heights that lie further away from the central line. However, data points further away from the centre of the filament also contain additional structural information and information on the fibril twist and width which is harder to determine from the lines closer to the centre alone. Therefore, the number of pixel-lines used is determined by visual inspection of the deconvolution result. The deconvoluted surface coordinates that correspond to the selected pixel-lines are then used for the 3D modelling approach. The deconvoluted contact points off the pixel-grid are interpolated onto an evenly spaced grid along the screw axis, creating ‘slices’ perpendicular to the fibril axis, while the data remains ungridded along the x-axis. In order to determine the length of the reconstruction window for the deconvoluted amyloid fibril image, the periodicity of the fibril is first determined by applying a 1D Fast Fourier Transform (FFT)

to the surface height profile of the fibril central line (**Fig. 3.6a-b**). This determines the spatial frequencies of repeating patterns in the signal. The spatial frequency with the highest amplitude represents the periodicity of the fibril. For an asymmetric fibril cross-sections, one period represents a complete turn (one helical pitch) whereas for a fibril with *n*-fold symmetry periodicity represents *1/n* of a complete turn. Fibril symmetry is then estimated by constructing 3D models with systematically varied symmetries and comparing these to the original straightened fibril image to find the best match (**Fig. 3.6c**). Symmetry determination is a critical step for reconstructing the surface of a helical specimen. Different screw axis symmetries result in differences in the twisting pattern observed on the fibril top surface. In order to make the comparison of a 2D convoluted image and 3D deconvoluted reconstructions, the tip model is used to simulate convoluted AFM images from the symmetry models. The straightened experimental fibril image and various symmetry simulations are zero-padded to square images and compared as 2D Fourier spectra to estimate fibril screw-axis symmetry that best describes the original image data. The 2D Fourier spectra contain information on repeating patterns of fibril top surface and are analogous to a diffraction pattern. Fourier-based analysis of helical biomolecule structures dates to first diffractions patterns that describe the structure of DNA and has been since used to reconstruct helical biomolecules from electron cryo-microscopy images by indexing the Bessel functions of the diffraction pattern layer lines (Diaz et al., 2010, p.). However, in many cases, resolving individual layer lines and indexing them is not possible, especially for amyloid fibrils with long helical repeat distances and small twist angles of individual subunits. Differences in rotational symmetry of a fibril cross-section causes the Bessel orders to change significantly while the layer lines on the spectrum remain identical (Sachse, 2015). Here, using this property and assuming that the screw-axis of the filament lies straight along the centre of the fibril, the differences in layer line Bessel orders observed for different symmetry models, which contain information on the handedness and screw axis

symmetry of the fibril and represent the twisting pattern on top of the fibril, were used to estimate the fibril screw-axis symmetry. For example, if the line between most intense off-centre spots in the 2D FFT (+ symbols in **Fig. 3.6c**) has a positive slope then the fibril is left-handed, and if the slope is negative the fibril is right-handed. The steepness of the slope contains information on the screw-axis symmetry of the fibril and the closest match of a symmetry model to the original fibril image is used to estimate the symmetry for an individual fibril. For the amyloid fibril example shown in this demonstration (**Fig. 3.6**), the 2-fold symmetry model gives the best fit to data **(Fig. 3.6c)**, suggesting that the fibril cross-section has a pseudo 2-fold screw axis symmetry. These 2D Fourier spectra from AFM images are less ambiguous compared to analogous 2D Fourier patterns of TEM images as only the top of the fibril surface contributes to the signal, facilitating the direct measurement of handedness and symmetry.

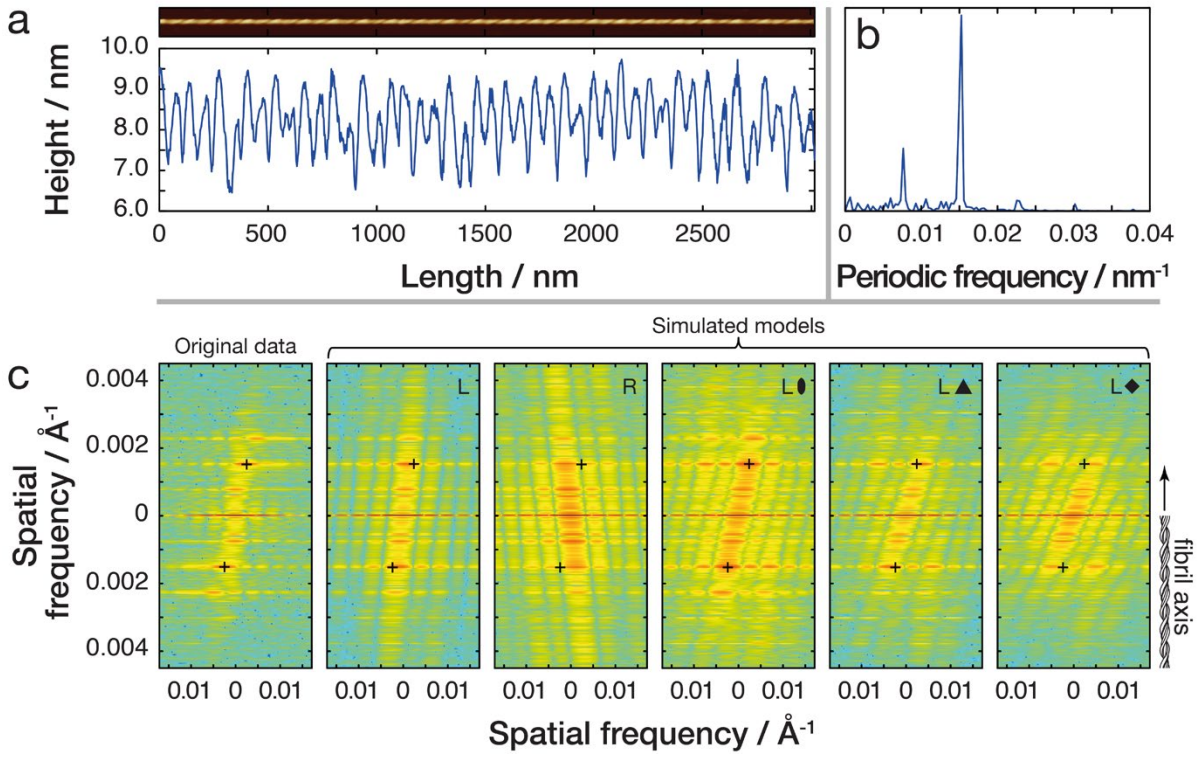

Figure 3.6 Estimation of the fibril twist periodicity and handedness. The same fibril image as Fig. 3.4 is used as example. **(a)** Fibril central line height profile. **(b)** One-dimensional FFT power spectrum of the central line is used to determine the periodicity of the fibril. **(c)** The screw axis symmetry and the twist handedness of the fibril is estimated by reconstructing 3D models of the fibril with varying symmetries, simulating convoluted AFM images from the models and comparing the 2D FFT spectra of the symmetry model images to that of the original straightened fibril image. The crosses are drawn on the most intense peaks on the original fibril 2D FFT image and their position is then applied onto each symmetry model 2D FFT spectra to guide finding the closest match. In this example, a left-hand twisted fibril with a pseudo two-fold screw-axis symmetry shows the best match to the data.

Having determined the periodicity, handedness and screw-axis symmetry of the fibril, the 3D surface envelope can be reconstructed using the moving window approach described above (**Fig. 3.7**). A cross-section of the fibril is obtained at each y-coordinate and a cubic spline is fitted to the cross-sections for smoothing. The number of spline pieces is determined by manual testing, taking into account the periodicity and symmetry of the fibril, which affects the number of times each cross-section is sampled. For validation of the image deconvolution and reconstructed 3D models, the final 3D surface envelope and tip model are used to simulate a convoluted AFM image that can then be compared with the uncorrected straightened fibril image (**Fig. 3.7b**). Although there are small differences, the simulated image twist, periodicity and local surface features generally correspond well to the original fibril image, validating the reconstruction approach here as a useful method for reconstruction of individual fibrils without cross-particle averaging.

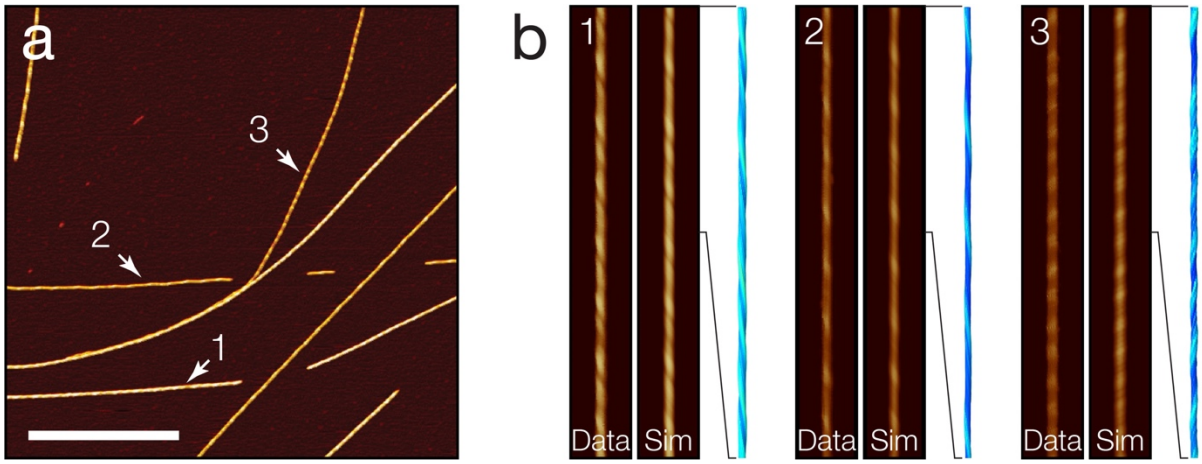

Figure 3.7 3D surface envelope reconstruction of amyloid fibrils from AFM topography. **(a)** AFM topology image of amyloid fibrils assembled from short peptide with the sequence HYFNIF (Aubrey et al., 2020; Morris et al., 2013). The scale bars represent 1 μm. **(b)** 3D surface envelope models for each fibril indicated in (a) are shown together with a comparison of the original straightened uncorrected fibril images and the simulated AFM images from the final 3D models. Segments of 500 nm are shown for each fibril model and 1 μm for the images for detail.

3.5 DISCUSSION

Tip-sample convolution leads to lateral dilation of upward convex surface features on AFM topographs, which has been seen as a significant limitation to the usefulness of AFM images for structural biology applications. Here we show that the convolution effect results in the magnification of the sample top surface and non-uniform distribution of structural information on the image. The structural information, present in an un-gridded form at sub-pixel tip-sample contact points, can be recovered at its true lateral resolutions without loss of information using a contact-point based deconvolution algorithm, which is demonstrated here on an amyloid fibril formed from a short peptide sequence. This approach improves on the previous erosion-based deconvolution algorithms and facilitates the use of AFM imaging of nanostructures in structural studies. Furthermore, we show how the 3-dimensional coordinates encoded in the

topographic data on AFM images and the helical symmetry of the twisted fibrils can be used to reconstruct 3D surface envelopes, allowing analysis of structural parameters, such as the fibril cross-sectional area, which are not otherwise present directly on AFM images of these samples. Thus, the reconstruction will facilitate the integration of 3D AFM envelope models with data from other structural biology tools for integrated global structural analysis. The moving window approach of 3D surface reconstruction conserves the high signal-to-noise feature of single-molecule imaging capability of the AFM, thus also allowing the intra-fibrillar and local structural variation to be preserved in the 3D model. Deconvolution and modelling facilitate the application of AFM to characterise and quantify amyloid fibril polymorphism at a true individual single molecule level.

Although there are many techniques available for studying the structures of biological macromolecules, each with their own advantages and disadvantages, AFM occupies a unique position among these tools due to its high signal-to-noise ratio capable of resolving morphological features of individual molecules. Ensemble averaging of structural information from many molecules is a key concept on which techniques like X-ray crystallography and cryo-EM rely and has led to the elucidation of numerous atomic and near-atomic resolution structural models of biological macromolecules. For example, recent advances in cryo-EM equipment and data processing have allowed the reconstruction of protein structures in various conformations from a set of micrographs and can even contain information on molecular dynamics (Dong et al., 2019). However, due to the low signal-to-noise ratio of individual particles on cryo-EM images, only ensemble-average structures can be reconstructed. Although the overall resolution of AFM images of macromolecular assemblies does not yet reach the order of Ångströms and only molecular surface features can be probed, it is able to resolve morphological features at the level of individual molecules. This allows AFM to tackle

biological problems in a unique way, especially in cases where polymorphism and structural variations of molecules is important for their biological effects. The lateral resolution, as defined by pixel size and tip radii, tends to be around 1-5 nm, although vertical resolution can reach the order of sub-Ångströms. Using the contact-point deconvolution approach demonstrated here on AFM images of biological nano-filaments, recovery of the true lateral sampling resolution at tip-sample contact points was estimated to typically result in doubling of lateral resolution for helical nano-filaments. Experimental improvements, such as using a tip with parameters that maximise sampling enhancement and better scanners could lead to a more pronounced improvement in lateral resolution. Further improvements to the deconvolution and envelope reconstruction algorithm approach will also likewise help to improve the overall resolution achievable with AFM.

The structural basis of why amyloid fibrils can have functional roles in a wide range of organisms, associated with pathological symptoms of neurodegeneration, or simply exist as inert aggregates is not clear (Lutter et al., 2019). Individual filament 3D reconstruction using the approach presented here on AFM topographs could help elucidate the link between morphological features of the fibrils to specific biological responses of amyloid populations. Reconstructed 3D surface envelopes of amyloid fibrils could also be used in an integrative way with other structural biology techniques. For example, in recent years numerous cryo-EM reconstructions of amyloid filaments from *ex vivo* patient tissue have been resolved. These are ensemble averages from thousands or more of individual fibrils from the total fibril population, which in some cases may appear homogenous, but in other cases may be made up of a varying amount of fibril polymorphs. The number of some of these polymorphs within the population may also be too low for reconstruction, although these species might have some specific biological effect. 3D envelope reconstruction from AFM images could be used as a

complementary technique as it allows the structural analysis and surface modelling of each individual fibril in the population, allowing rare members of the ensemble population as well as the population characteristics itself to be analysed. Classifying and quantifying the fibril structures could be used to determine the landscape of possible fibril structures within a specific population. Furthermore, this technique allows the intrafibrillar variation to be analysed, which may be indicative of fibril dynamics and stability. The 3D surface envelope could also be used in an integrative way with other techniques, contributing to the global information for modelling the atomic structure of a biomolecule.

The physics of AFM imaging is unique in producing its high signal-to-noise data at nano-scale and enables true single molecule approaches. Thus, the contact-point deconvolution and 3D envelope reconstruction approach presented here will facilitate the use of AFM for single-molecule structural studies. Imaging of any nano-structures with the AFM can benefit from the contact-point deconvolution approach to correct images while recovering structural information present at higher lateral resolutions. This includes high-speed AFM (Lyubchenko, 2018), which compromises spatial resolution for higher temporal resolution and allows imaging of biomolecule dynamics in the timescale down to milliseconds, and which could benefit from the computational deconvolution of image frames to recover the higher spatial resolution sampling of the sample surface. Furthermore, the 3D envelope reconstruction algorithm could also be applied to diverse biological samples with symmetries, including DNA, membrane proteins that form tubular arrays e.g. nicotinic acetylcholine receptor pore (Miyazawa et al., 2003) and the mitochondrial outer membrane protein TspO (Korkhov et al., 2010), as well as helical or spherical virus capsids and cytoskeletal filaments. AFM imaging of various small molecules and polymers assembled into helical supramolecular arrangements which are widely used in chemistry, materials science and nanotechnology could, likewise,

benefit from 3D surface reconstructions as AFM is widely used to characterise a wide range of such structures (Yashima et al., 2016), for example polymer wrapped functionalised carbon nanotubes (Bai et al., 2018; Zheng et al., 2003), Further developments could also lead to samples exhibiting different symmetries such as icosahedral viral capsids to be reconstructed.

In conclusion, the approach reported here will facilitate the use of AFM for structural studies of individual molecules in complex populations, and for integrative structural biology analysis of single molecular assemblies and their assembly mechanisms.

3.6 MATERIALS AND METHODS

3.6.1 Peptide amyloid fibril synthesis

The amyloidogenic peptide HYFNIF was synthesised by N-terminal acetylation and a C-terminal amidation. Multistage solid phase synthesis using Fmoc protection chemistry was used to generate a lyophilised powder with > 95 % purity measured by HPLC (JPT peptide technologies, or Biomolecular analysis facility, University of Kent). The lyophilised powder was suspended in 100 µl of filter sterilized milli-Q water to a final concentration of 10 mg/ml. The solution was incubated at room temperature for 1 week prior to imaging.

3.6.2 AFM sample preparation and image acquisition

The peptide samples were diluted to 0.05 mg/ml in a solution of HCl (pH2, using filter sterilised milli-Q water). 20 µL of sample was deposited onto freshly cleaved mica (Agar scientific, F7013) and incubated for 10 min. Following incubation, the sample was washed with 1 ml of filter sterilised milli-Q water and then dried using a stream of nitrogen gas. Fibrils were imaged using a Multimode AFM with a Nanoscope V (Bruker) controller operating under peak force tapping mode with ScanAsyst probes (silicon nitride triangular tip with tip height = 2.5-2.8

μm, nominal tip radius = 2 nm, nominal spring constant 0.4 N/m, Bruker). Images were collected with a scan size of 6 x 6 μm with 2048 x 2048 pixel resolution. A scan rate of 0.305 Hz was used with a noise threshold of 0.5 nm and the Z limit was reduced to 1.5 μm. The peak force set point was set automatically, typically to ~675 pN during image acquisition. Nanoscope analysis software (Version 1.5, Bruker) were used to process the image data by flattening the height topology data to remove tilt and scanner bow.

3.6.3 Image data analysis

Fibrils were traced and digitally straightened (Egelman, 1986; W.-F. Xue, 2014; W.-F. Xue, Homans, et al., 2009) using an in-house application and the height profile for each fibril was extracted from the centre contour line of the straightened fibrils. The periodicity of the fibrils was then determined using fast-Fourier transform of the height profile of each fibril. For 2D FFT analysis, the fibril images were rotated with the straightened fibril axis aligned vertically. The images were subsequently zero-padded to squares prior to 2D FFT. All data analyses were performed using Matlab (MathWorks, Natick, Massachusetts)

Chapter 4: Structural identification of individual helical amyloid filaments by integration of cryo-electron microscopy-derived maps in comparative morphometric atomic force microscopy image analysis

4.1 Summary

This chapter is based on paper IV in the List of Publications included in the thesis (Lutter, Al-Hilaly, et al., 2021). The atomic force microscopy image deconvolution and helical fibril 3D reconstruction algorithm developed in Chapter 3 facilitates the integration of the single-molecule information of amyloid fibrils with other structural biology techniques with different and complementary information content. Specifically, recent advances in the collection and processing of cryo-EM data have revealed amyloid fibril structures in high-resolution detail. Although this information is highly important for understanding amyloids in disease contexts, it relies on averaging more than tens of thousands of fibril segments in order to achieve this level of detail. This information is thus complementary to the single-molecule envelopes reconstructed from AFM images of amyloid fibril samples, which cannot provide information on the molecular arrangement of the fibril core but offer low-nanometre resolution single-molecule envelopes and mapping of the population polymorphism of a sample to the level of individual filaments.

Here, an approach to integrate structural information from AFM 3D reconstructed envelopes and cryo-EM density maps was developed and demonstrated on a fibril of dGAE tau, a tau fragment which forms fibrils *in vitro* without the addition of co-factors. Cryo-EM studies have revealed that fibrils from *ex vivo* extracted patient brain tissue from various tauopathies vary considerably in their molecular arrangements, all of which differ considerably from the structures of fibrils formed from heparin-induced *in vitro* self-assembled tau, which has been widely used to prepare tau filaments *in vitro* for further studies. Parametric comparison of both a 3D envelope of dGAE tau fibril reconstructed from an AFM image with cryo-EM density map-derived data, as well as direct comparison of simulated AFM images with the dGAE topograph, demonstrated that dGAE fibrils are unambiguously different from heparin-induced fibrils, and are most similar to paired helical filaments from Alzheimer's disease patient brain tissue. The results thus suggest that dGAE fibrils are a more physiological model system for *in vitro* formed tau amyloid compared to heparin-induced *in vitro* formed tau fibrils.

4.2 ABSTRACT

The presence of amyloid fibrils is a hallmark of more than 50 human disorders, including neurodegenerative diseases and systemic amyloidoses. A key unresolved challenge in understanding the involvement of amyloid in disease is to explain the relationship between individual structural polymorphs of amyloid fibrils, in potentially mixed populations, and the specific pathologies with which they are associated. Although cryo-electron microscopy and solid-state nuclear magnetic resonance spectroscopy methods have been successfully employed in recent years to determine the structures of amyloid fibrils with high resolution detail, they rely on ensemble averaging of fibril structures in the entire sample or significant subpopulations. Here, we report a method for structural identification of individual fibril structures imaged by atomic force microscopy by integration of high-resolution maps of amyloid fibrils determined by cryo-EM in comparative AFM image analysis. This approach was demonstrated using the hitherto structurally unresolved amyloid fibrils formed *in vitro* from a fragment of tau (297-391), termed 'dGAE'. Our approach established unequivocally that dGAE amyloid fibrils bear no structural relationship to heparin-induced tau fibrils formed *in vitro*. Furthermore, our comparative analysis resulted in the prediction that dGAE fibrils are closely related structurally to the paired helical filaments (PHFs) isolated from Alzheimer's disease (AD) brain tissue characterised by cryo-EM. These results show the utility of individual particle structural analysis using AFM, provide a workflow of how cryo-EM data can be incorporated into AFM image analysis and facilitate an integrated structural analysis of amyloid polymorphism.

4.3 INTRODUCTION

Amyloid fibril diversity has been elucidated recently by the development of high-resolution structural analysis of fibrillar amyloid by cryo-EM and ssNMR (Lutter, Aubrey, et al., 2021; Willbold et al., 2021), as well as X-ray and electron diffraction of small amyloid peptide crystals (Sawaya et al., 2007, 2016). Proteins with an identical sequence are able to form different core or filament arrangements (Gremer et al., 2017; Wälti et al., 2016). Differences have also been demonstrated for *ex vivo* extracted and *in vitro* assembled fibrils (Bansal et al., 2021), with further differences arising from varying *in vitro* sample preparation conditions and techniques (Colvin et al., 2016; M. Schmidt et al., 2015). In particular, recent advances in cryo-EM have led to the elucidation of an array of structures of amyloid filaments formed by the tau protein (Shi et al., 2021). Tau is well known for its involvement in Alzheimer's disease, but is also found in chronic traumatic encephalopathy, Pick's disease and numerous other neurodegenerative diseases (Spillantini & Goedert, 2013). Cryo-EM studies have revealed that structures of tau fibrils may be disease-specific, although different diseases can also share the same tau folds (Hallinan et al., 2021; Shi et al., 2021). Importantly, cryo-EM-based structural models of heparin-induced tau filaments revealed significant differences between fibrils extracted from patient tissues and those generated synthetically *in vitro* (Arakhamia et al., 2020; Falcon, Zhang, Schweighauser, et al., 2018; W. Zhang et al., 2019)

Although cryo-EM and ssNMR methods can provide detailed structural information of the amyloid fibril core, both require measurements of samples with homogenous populations, or significantly populated subpopulations. ssNMR requires a ^{15}N- and ^{13}C-labeled homogenous sample, often achieved through rounds of consecutive seeding of fibrils with fresh monomer (Paravastu et al., 2009). However, seeding *ex vivo* extracted fibrils with recombinant monomer

in vitro may not result in structures identical to those of the original *ex vivo* material (Koloteva-Levine et al., 2021; Lövestam et al., 2021). Non-seeded *in vitro* self-assembled fibril samples can also yield well-resolved spectra if the labelled starting material is mostly homogenous (Colvin et al., 2016), although *ex vivo* fibril structures cannot be studied without seeding with labelled monomer to produce fibrils amenable for ssNMR analysis. Cryo-EM can achieve high resolution structural models for significantly populated polymorphs of a heterogenous sample by classification of sub-populations. However, reconstruction requires averaging of tens to even hundreds of thousands of identical fibril segments. Therefore, it may not be possible to assess the polymorphic extent of the sample or to reconstruct polymorphs which are present in low numbers, but which may still be biologically relevant. Additionally, the analysis of intrafibrillar variation of structure and morphology of fibrils is limited due to the low signal-to-noise ratio from individual cryo-EM micrographs.

Atomic force microscopy has recently emerged as a method capable of addressing amyloid structural polymorphism on an individual fibril level (e.g. Adamcik and Mezzenga, 2018; Aubrey et al., 2020). It enables the surfaces of individual amyloid fibrils to be reconstructed and the polymorphism landscape of the sample to be analysed on a single-molecule basis (Aubrey et al., 2020; Lutter et al., 2020). Therefore, AFM is highly complementary to cryo-EM and ssNMR, which rely on particle or ensemble averaging to produce reconstructions of fibril core structures. The application of AFM to structural biology has been hampered by the imaging artefact that stems from the physical finite size of the AFM probe, resulting in dilation and distortion of surface features. However, we have recently shown that a computational deconvolution approach is able to correct for this artefact, and the recovered surface sampling can result in an increased local image resolution. Furthermore, samples exhibiting helical symmetry, including amyloid fibrils, can be reconstructed as 3D models, facilitating structural

analysis of the fibril surface envelopes (Lutter et al., 2020). AFM image deconvolution and 3D reconstruction of helical filaments can then be employed to carry out a quantitative mapping of amyloid fibril polymorphism at an individual fibril level (Aubrey et al., 2020). This deconvolution and reconstruction approach opens up the possibility of integrating high signal-to-noise individual filament 3D envelope structures from AFM data with high resolution ensemble-averaged core structural information available from cryo-EM and ssNMR methodologies. To date, AFM imaging of amyloid fibrils has been carried out alongside cryo-EM and ssNMR studies to determine fibril handedness or visualise the sample supra-structural morphology (U. Ghosh et al., 2021; Y. Li et al., 2018; Röder et al., 2019). However, a fully integrated approach that links AFM data with cryo-EM derived structural maps has the potential to enhance the structural analysis of amyloid fibril polymorphism as AFM provides structural data on an individual fibril level, which is highly complementary to the averaged structural models from cryo-EM and ssNMR data. Nevertheless, there is currently no unifying workflow which would enable comparison of 3D-information from AFM surface envelope reconstructions with the structural maps provided by cryo-EM and ssNMR.

Here, we report a new approach to quantitative structural comparison of individual amyloid fibrils imaged by AFM with ensemble-averaged structural data derived from cryo-EM. This approach integrates AFM 3D envelope models of individual fibrils with cryo-EM maps and has been applied to the structural characterisation and identification of individual filaments formed by tau (297-391) known as 'dGAE' (Al-Hilaly et al., 2020), which has not yet been structurally resolved to high resolution by cryo-EM or by ssNMR. dGAE tau self-assembles spontaneously *in vitro* without the presence of anionic cofactors, such as heparin, to form filaments that share the height and cross-over characteristics observed in paired helical filaments (PHFs) isolated from Alzheimer's disease tissue (Al-Hilaly et al., 2020). We

compared the 3D surface envelope models of synthetic, *in vitro* assembled dGAE tau filaments constructed from previously published AFM image data with existing cryo-EM density maps of both *ex vivo* extracted tau fibrils and those formed *in vitro* by the addition of heparin, found in the Electron Microscopy Data Bank (EMDB). This analysis showed that the surface of dGAE amyloid fibrils closely resembles that of the cryo-EM density maps arising from some of the tauopathy tissue-extracted tau filaments, notably those of PHFs isolated from *ex vivo* Alzheimer's disease tissue. Thus, our cryo-EM data-integrated AFM image analysis ruled out structural similarity of dGAE amyloid fibrils assembled *in vitro* to *in vitro* formed heparin-induced tau filaments, and has provided evidence that identified dGAE fibrils are structurally closely related to PHFs isolated from AD brain tissue. Individual fibril level structures in mixed polymorphic amyloid populations are likely to underpin properties such as overall fragmentation propensity, assembly kinetics and cytotoxic potential. Thus, by developing an integrative AFM image analysis, we reveal the potential for this form of AFM analysis to be used for identification of individual fibril structures in heterogeneous and polymorphic amyloid populations.

4.4 RESULTS

4.4.1 Three-dimensional reconstruction using AFM image data enabled structural analysis of individual dGAE tau amyloid filaments

AFM imaging of *in vitro* assembled dGAE filaments (Al-Hilaly et al., 2020) revealed a mixture of long individual fibrils and laterally associated, twisted bundles (**Fig. 4.1a**). All fibrils and bundles showed a left-handed twist, with variation in the cross-over distance (*cod*, defined

according to **Fig. 4.2a**). dGAE fibrils demonstrated a high propensity to bundle (**Fig. 4.1a-b**). This may be indicative of surface properties of the dGAE protofilaments or fibrils, which favour the formation of large, twisted bundles of various widths. To analyse the structure of individual dGAE fibrils, 3D envelopes of individually selected single, non-bundled dGAE fibrils can be reconstructed from the AFM topographs using previously developed methods (Lutter et al., 2020). Here, to demonstrate this approach, a 3D surface envelope model of a single selected well-separated canonical dGAE fibril was reconstructed (**Fig. 4.1c-d**). The central height profile of this dGAE filament showed peaks with the average height of 8.9 nm and grooves with the average height of 5.9 nm, with cross-over distances ranging from 43.1-58.6 nm, with an average of 47.7 nm (**Fig. 4.1d**). These morphometric parameters are in line with the ranges expected of a typical non-bundled dGAE fibril observed by AFM (Al-Hilaly et al., 2020). During the 3D reconstruction workflow (Lutter et al., 2020), the fibril was determined to have 2-fold helical symmetry, suggesting that it is composed of 2-protofilaments arranged symmetrically about the central helical axis. The reconstructed 3D envelope model also enabled the evaluation of the cross-sectional area and shape, perpendicular to the fibril axis (defined in **Fig. 4.2a**), which was subsequently used in comparison with cryo-EM density maps of a range of different tau fibril structures.

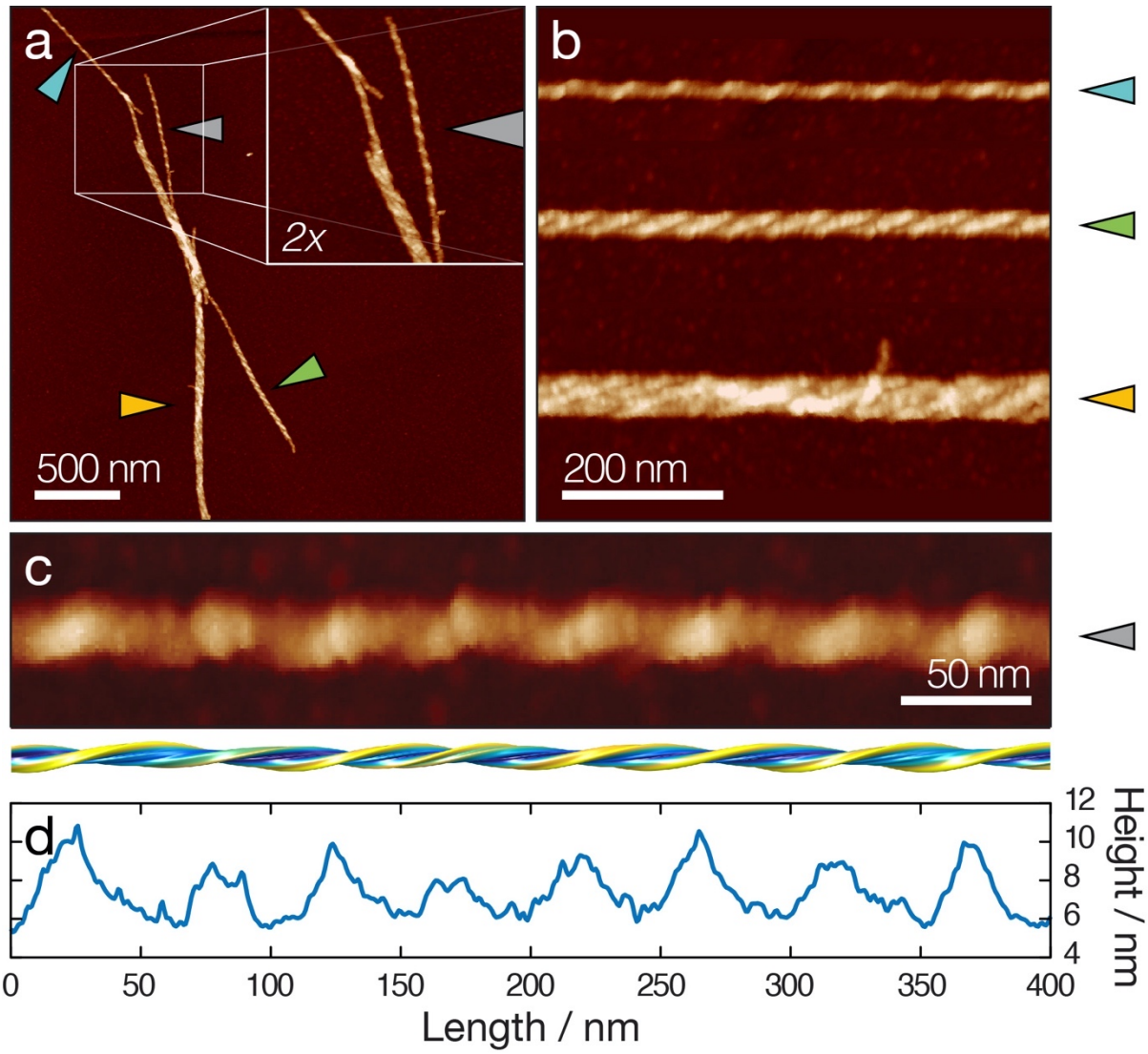

Figure 4.1. Analysis of individual dGAE filaments from a topographical AFM height image. **(a)** A typical AFM image of dGAE fibrils (Al-Hilaly et al., 2020) with an inset showing a 2x magnified view. Arrows point to the fibrils shown in (b) and (c). Scale bar represents 500 nm. **(b)** Digitally straightened images showing a typical dGAE fibril and typical fibril bundles. Scale bar represents 200 nm. **(c)** Digitally straightened AFM image of a canonical dGAE tau fibril together with a 3D reconstructed surface envelope model. Scale bar represents 50 nm. **(d)** The central line height profile of the fibril image shown in (c).

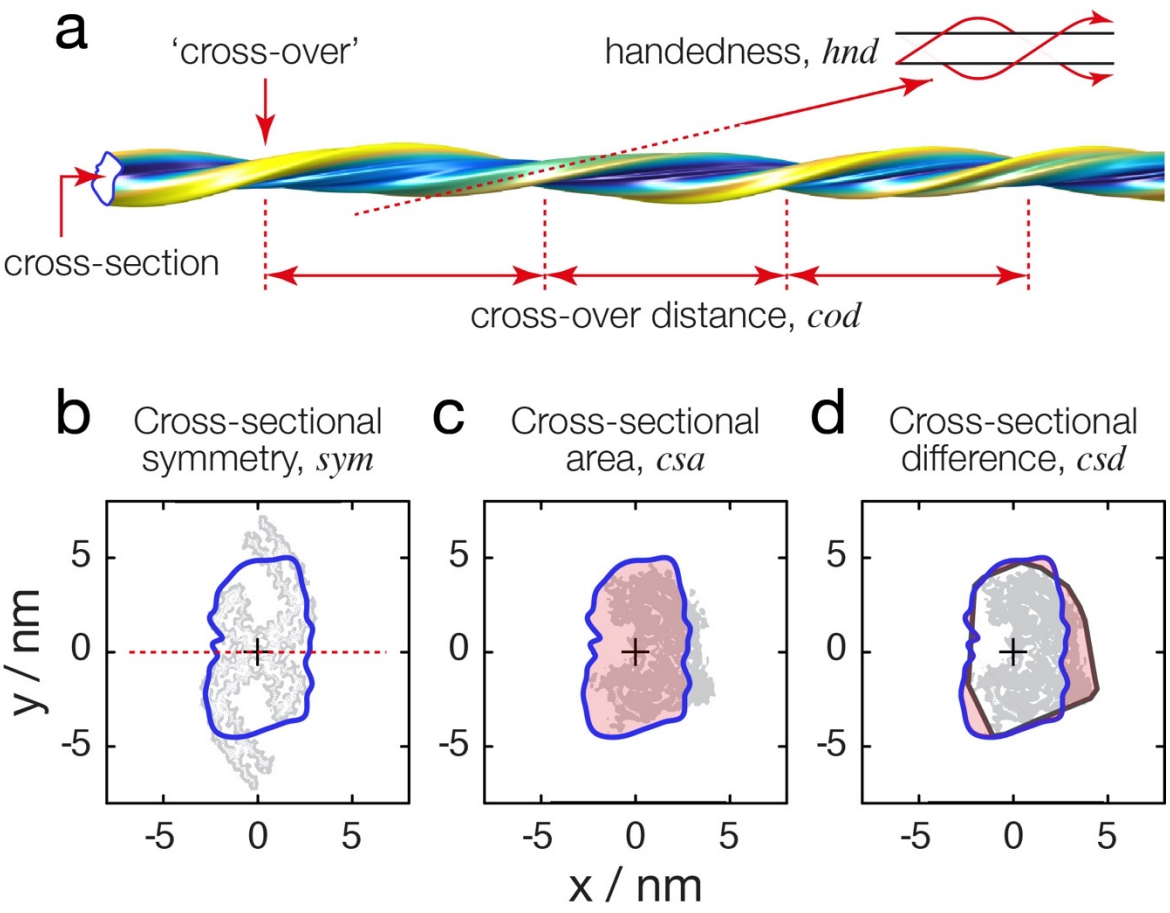

Figure 4.2. Schematic illustrations of the definitions of the morphometric parameters used for quantitative comparative structural analysis. **(a)** Schematic diagram illustrating the structural properties analysed, exemplified using a segment of the AFM derived dGAE fibril model shown in **Fig 4.1c**. The comparative morphometric parameters calculated by analysis of the cross-section are illustrated by the red line or areas in **(b)** for symmetry, **(c)** for cross-sectional area and **(d)** for cross-sectional difference area. Grey shapes show the cross-sections of cryo-EM density maps and the black line in (d) shows the tip-accessible cross-section, found by tracing a circle with the radius equivalent to that of the AFM tip radius around the cryo-EM density cross-section.

4.4.2 Simulation of topographic images from volumetric cryo-EM maps allowed integration of cryo-EM data in comparative AFM image analysis

AFM imaging is able to generate image data in the form of 3D topographic raster scans, which are typically displayed as coloured 2D images where the pixel value represents surface height. As the images have a high signal-to-noise ratio, topographs of individual filaments can be traced and extracted from the surface scan data (**Fig. 4.1**). In order to compare the 3D structural information from cryo-EM and AFM, simulated topographic AFM height images were generated from cryo-EM density maps (examples in **Fig. 4.3**). This enabled the comparative analysis of the dGAE fibril imaged by AFM (**Fig. 4.1c-d**) and cryo-EM data of patient derived *ex vivo* tau fibrils and *in vitro* self-assembled heparin-induced tau fibrils.

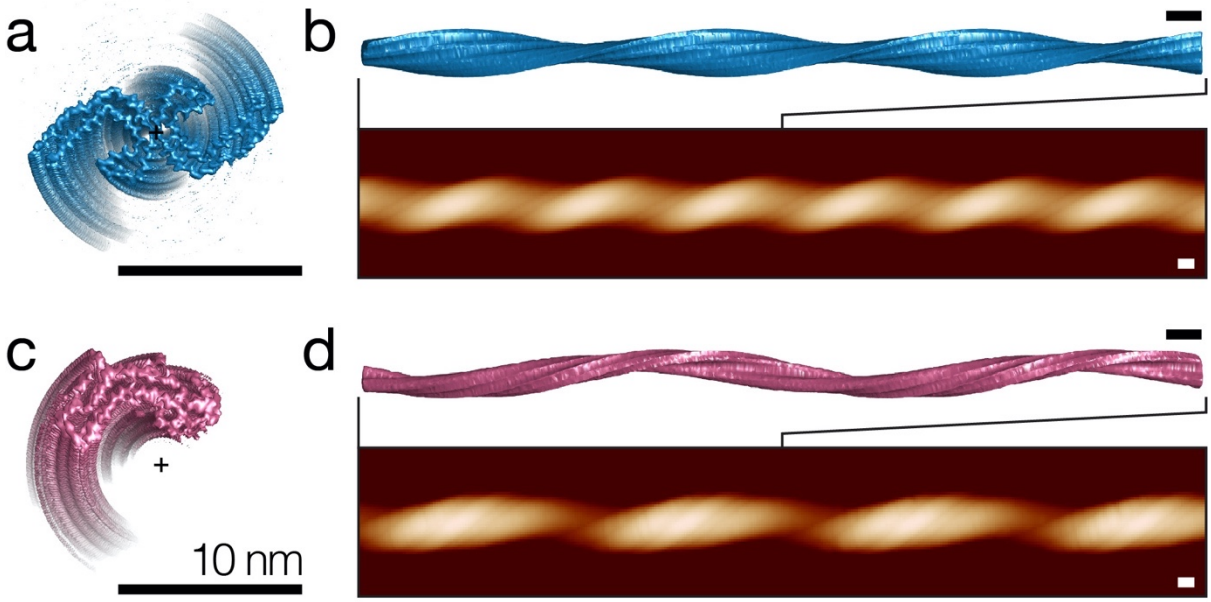

Figure 4.3 Simulation of topographic AFM height images from cryo-EM density maps. Cross-sectional views of axis-aligned cryo-EM density map iso-surfaces for **(a)** paired helical filaments (EMD-0259) and **(c)** 'heparin-snake' (EMD-4563) tau fibrils are shown with the position of the helical axis (+). Simulated topographic images of 500 nm fibril segments and the top view of extended 250 nm segments of iso-surfaces aligned to the simulated images are shown for PHF in **(b)** and 'heparin-snake' in **(d)**. All scale bars represent 10 nm.

Volumetric cryo-EM maps of tau amyloid fibrils were first downloaded from the Electron Microscopy Data Bank, followed by extraction of the map iso-surface 3D coordinates at the

iso-values specified by the authors of each cryo-EM entry. Where necessary, the individual maps were then denoised and the maps of the short fibril segments were extended by finding the helical axis of the map, followed by rotation and translation of multiple copies of the maps about their helical axes, using author reported twist and rise values, to a total map length equivalent to that of the AFM imaged dGAE fibril. Although helical twist and rise values are provided by the authors in experimental metadata, the position and angle of the fibril map screw-axis is unknown for all cryo-EM maps. Therefore, an iterative approach was used to find the rotation and translation parameters that provide the best alignment of the cryo-EM fibril maps to their respective helical axis positions (**Fig. 4.3a, c**). In some cases, for example heparin-induced recombinant tau 'snake' fibrils, the resulting screw-axis position lies off the fibril centre-of-mass, resulting in a hollow centre (**Fig. 4.3c)**, in line with previous analyses (W. Zhang et al., 2019). In order to simulate topographic AFM images of the extended iso-surfaces, a model of the AFM cantilever probe tip, which interacts with the filament surface, is then needed. The tip angle and geometry were estimated using the values provided by the manufacturer of the AFM probe used experimentally. The tip radius used in the simulations was matched to that used to image the dGAE fibril, which was estimated using AFM image data from the fibril (**Fig. 4.1c-d**) according to a previous published algorithm (Lutter et al., 2020). A simulated AFM tip constructed from these geometry, angle, and radius parameters was then used to find the tip-sample contact points with the extended fibril iso-surface, to account for, and to reproduce, the tip-sample convolution effect in the simulated images. The sampling rate was also set to be equivalent to that of the experimental AFM data (**Fig. 4.3b, d**). As both the tip radius and sampled pixel density of the simulated images match that of the individual fibril from the AFM image data, it was possible to make a direct comparison between the two.

4.4.3 Simulated topographic AFM images from cryo-EM maps of helical fibrils enabled validation of the AFM based 3D reconstruction methodology

Prior to a full comparative analysis of the AFM derived 3D model of the dGAE fibril with simulated AFM images from published cryo-EM structural data of tau fibrils, the simulated AFM images were first used to validate the AFM-based 3D reconstruction methodology used to construct the dGAE fibril model (**Fig. 4.1d**). In order to evaluate the 3D reconstruction method that we developed to reconstruct fibril 3D envelopes from AFM data and to determine their cross-sectional shapes and helical symmetries, reconstructions from simulated images of fibrils with known 3D structures were carried out, using cryo-EM maps of selected tau fibril structures (**Fig. 4.4** and **4.5**). In this validation process, AFM topographs were simulated as described above, using the same pixel size and AFM tip radius as seen in the experimental AFM image of the dGAE tau fibril. Reconstruction of 3D envelopes was then carried out from these simulated images in the same way as from experimental AFM images, with the aim of comparing the final 3D reconstructions to the known fibril structures from which the input images were simulated. This allowed the validation of the reconstruction method regarding the accuracy of the cross-sectional shape, symmetry assignment, and positioning of the screw-axis, which the comparative image and morphometric analyses of dGAE tau fibrils requires. During the reconstruction workflow (Lutter et al., 2020), fibril symmetry is initially unknown so envelopes of fibrils with various symmetries, as well as an asymmetrically cross-sectioned fibril, were reconstructed from the simulated image data. The correct symmetry can then be identified by the angle of the twisting pattern on the fibril surface by comparison of topographs re-simulated from various symmetry models with the input topograph of the experimental or simulated image, in direct, as well as in Fourier space (**Fig. 4.4f** and **4.5f**).

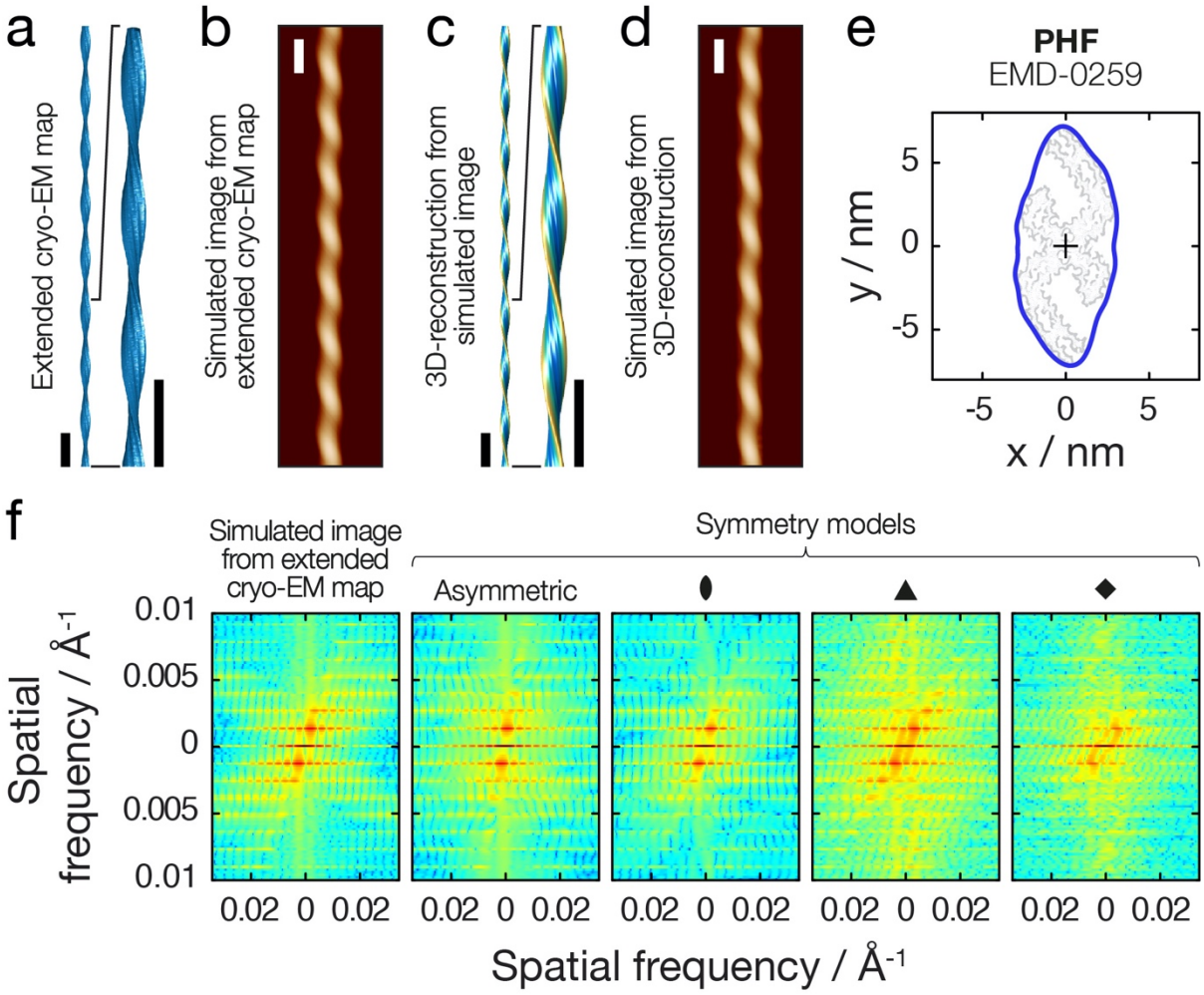

Figure 4.4. Validation of the 3D reconstruction and topograph simulation algorithms and workflow using a cryo-EM density map of PHF (EMD-0259). **(a)** Filament axis-aligned and lengthened cryo-EM density map of PHF. **(b)** Topographic AFM height image simulated from the density map in (a). **(c)** 3D surface envelope model reconstructed using the simulated image in (b). **(d)** Topographic AFM height image simulated from the 3D reconstructed model in (c). All scale bars represent 50 nm. (e) Comparison of the cross-sections of the EM density map (grey) and the AFM derived 3D model (blue). **(f)** Symmetry estimation during the 3D reconstruction process. As the symmetry is unknown, 3D reconstruction is performed with various symmetry estimates on the same AFM image data (here showing asymmetric, 2, 3, and 4-fold helical symmetries) and the 2D power spectra of the simulated topograph is compared to that of the original image (i.e. image shown in b). Here 2-fold symmetry gave the best match and was used for the final reconstruction.

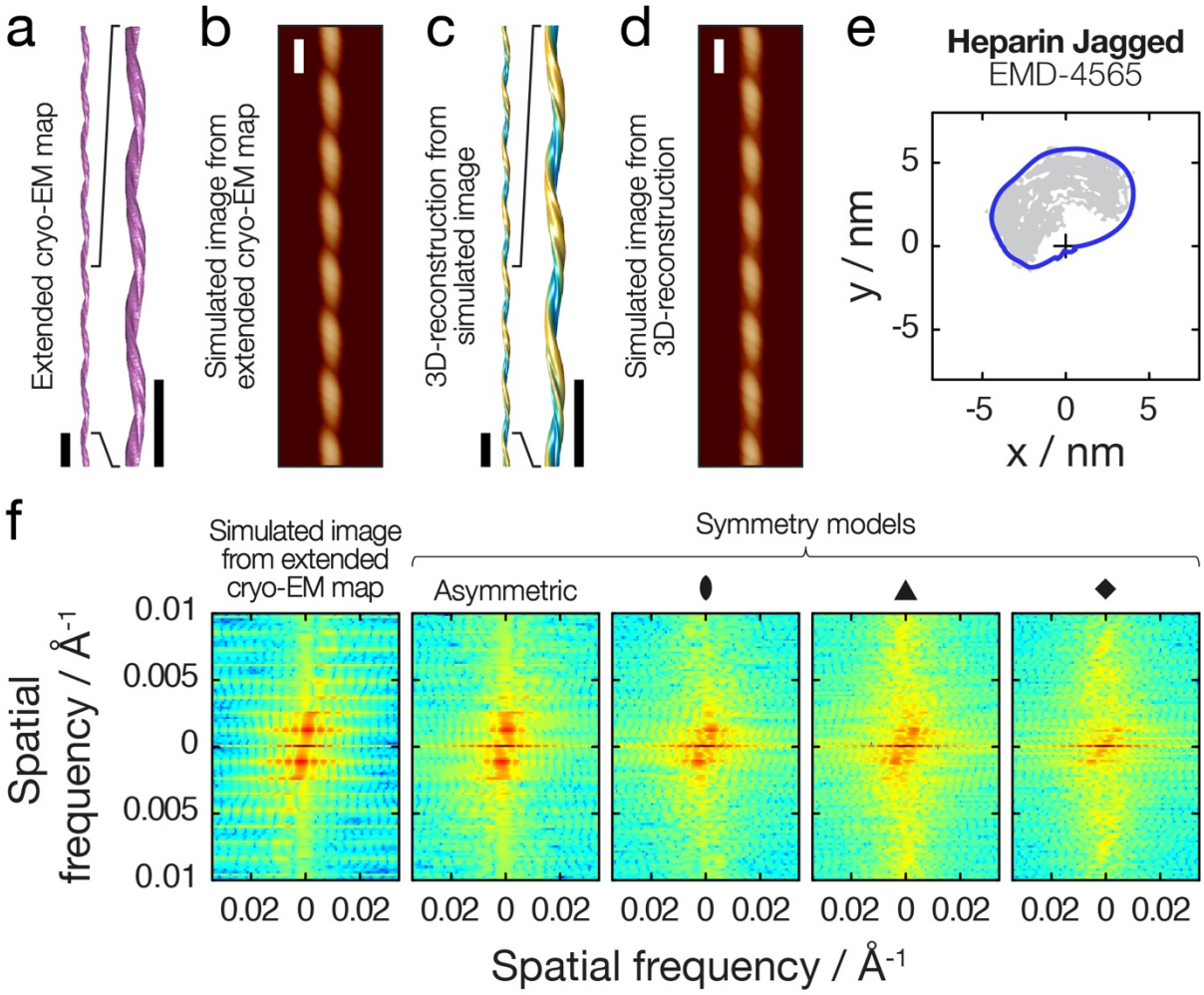

Figure 4.5. Validation of the 3D reconstruction and topograph simulation algorithms and workflow using a cryo-EM density map of a 'heparin-jagged' filament (EMD-4565). **(a)** Filament axis-aligned and lengthened cryo-EM density map of 'heparin-jagged'. **(b)** Topographic AFM height image simulated from the density map in (a). **(c)** 3D surface envelope model reconstructed using the simulated image in (b). **(d)** Topographic AFM height image simulated from the 3D reconstructed model in (c). All scale bars represent 50 nm. (e) Comparison of the cross-sections of the EM density map (grey) and the AFM derived 3D model (blue). (f) Symmetry estimation during the 3D reconstruction process. As the symmetry is unknown, 3D reconstruction is performed with various symmetry estimates on the same AFM image data (here showing asymmetric, 2, 3, and 4-fold helical symmetries) and the 2D power spectra of the simulated topograph is compared to that of the original image (i.e. image shown in b). Here the asymmetric model gave the best match and was used for the final reconstruction

The cryo-EM density iso-surfaces for PHF (EMD-0259) and heparin-jagged (EMD-4565) fibrils were used to validate the 3D reconstruction method by comparison of the final 3D model with the known input structures. PHF and heparin-jagged maps were chosen to evaluate the reconstruction method, as the structures have C2 and C1 rotational symmetry, respectively, allowing the reconstruction of different symmetry assignments to be assessed. In addition, heparin-jagged has a helical axis that lies off the centre-of-mass of the core density. Evaluation of the approach demonstrated that the 3D reconstruction method can accurately and unambiguously identify both the C2 and C1 helical symmetries from fibril topographs (**Fig. 4.4f** and **4.5f**). Furthermore, for PHF, the shape of the fibril cross-section closely matched that of the AFM tip-accessible cross-section from the original cryo-EM density map. The root-mean-square deviation (RMSD) between the tip-accessible PHF density map cross-section, which was obtained by tracing a circle with the radius equivalent to that of the AFM tip radius around the iso-surface cross-section to account for the topographic resolution imposed by the finite size of the AFM probe (**Fig. 4.2d**), and 3D reconstructed envelope (**Fig. 4.4e**) was 0.08 nm. For heparin-jagged fibril, with an off-centre screw-axis, cross-sectional RMSD was 0.23 nm (**Fig. 4.5e**), although the helical axis was correctly positioned to be lying off the fibril centre-of-mass (cross in **Fig. 4.5e**). These results validated the AFM based 3D reconstruction and simulation approach, although the RMSD values showed potential for improvement for the reconstruction workflow for asymmetric fibrils with off centre helical axes. More importantly, these results demonstrated that the approach correctly identified the symmetry and screw-axis position using known structural maps as input. This gave confidence that the 2-fold symmetry identified for the dGAE fibril from the experimental image data is accurate, indicating that it is composed of 2-protofilaments arranged symmetrically about a central helical axis, like the PHF from AD brain. Furthermore, as the RMSD between the known input and the 3D reconstruction was sub-Ångström for the 2-fold symmetric PHF example, the shape

of dGAE fibril is also not likely to be significantly misrepresented by the 3D reconstruction process from the AFM data, although limitations can still potentially arise from the sample structure's local mechanical stability and imaging conditions.

4.4.4 Comparison of cryo-EM derived topographs with dGAE tau AFM data ruled out structural similarity with heparin-induced tau fibrils

Simulated topographic images from helical axis-aligned and lengthened cryo-EM density maps of *ex vivo* tissue-extracted and *in vitro* assembled heparin-induced tau filaments were subsequently prepared for comparison with the topographic AFM image of the canonical dGAE tau filament (**Fig. 4.6**). This was achieved by carrying out topographic image simulations for all unique tau fibril cryo-EM maps available in the EMDB up to August 2021, which included structural maps of fibrils purified from tissues of patients with corticobasal degeneration (CBD), chronic traumatic encelopathy (CTE), Pick's disease (PiD), Alzheimer's disease (AD), as well as four fibril polymorphs formed *in vitro* by addition of heparin to recombinant tau monomers. In addition to the selected *ex vivo* fibril data, entries in the EMDB of near-identical structures to the selected PHFs and straight filaments (SFs) were also determined for filament structures from various other neurodegenerative diseases, including prion protein cerebral amyloid angiopathy (PrP-CAA) and primary age-related tauopathy (PART) (Hallinan et al., 2021; Shi et al., 2021). Where several near-identical structures have been reported for the same disease, the one with the highest map resolution was used. The helical twist of amyloid fibrils within a population of fibrils is variable even when the core structures are identical (W. Zhang et al., 2020), but the helical twist parameters presented in the population averaged cryo-EM maps represent only one of a continuum of possible values within a range, while AFM images report the full structural variation within an individual

filament. To account for this difference in the information content, the periodicities of the simulated fibril images were optimised to maximise the normalised cross-correlation of the simulated and experimental fibril images by allowing the long fibril axis of the simulated image to contract or dilate within a range (see section 4.6 Methods). This allowed for slight adjustments of the simulated fibril periodicity, which aids the assessment of image similarity between experimental AFM data and simulated images derived from cryo-EM maps.

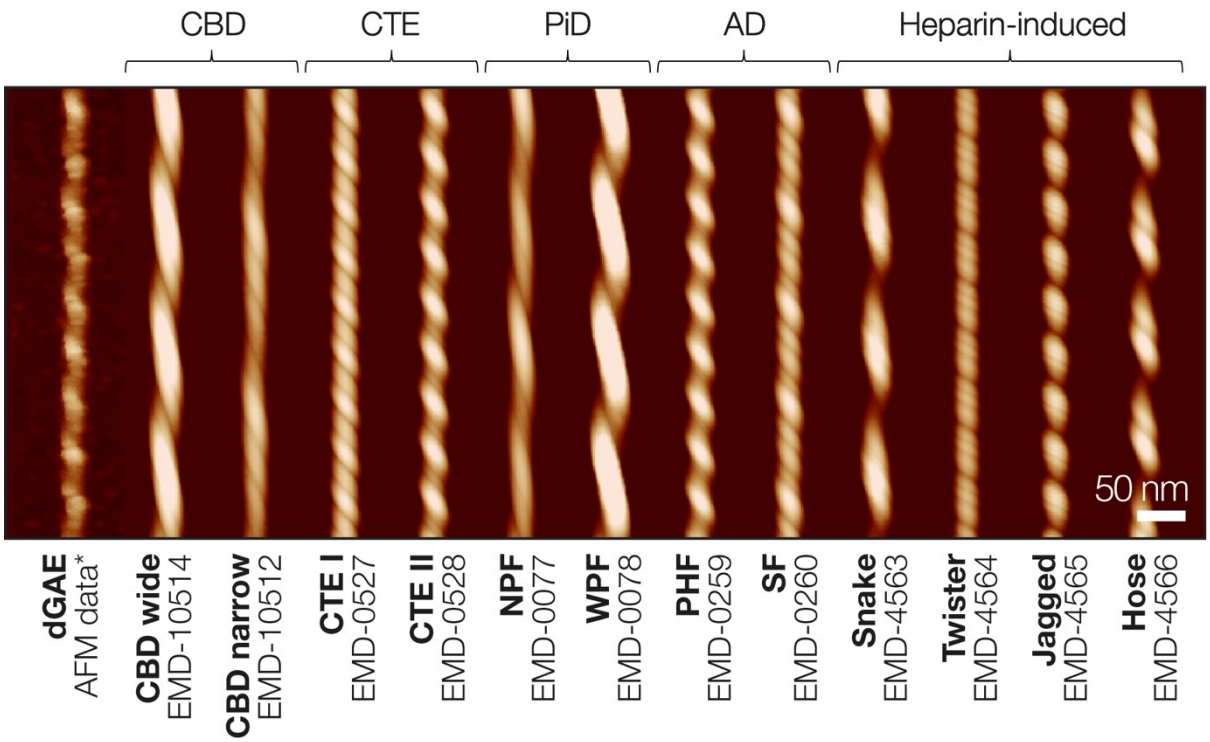

Figure 4.6. Comparison of the typical experimental AFM height image of dGAE tau fibril with topographical images of tau amyloid fibril polymorphs. The tau fibril polymorphs were simulated with identical tip (here estimated to be 11.7 nm) and sampling parameters using extended and axis-aligned cryo-EM map iso-surfaces. The '*' indicate image data shown in Fig. 1c. Length of the scale bar is 50 nm. The simulated images have been aligned to the same estimated helical axis height position as the experimental data image and, therefore, have comparable height colour coding. The EMDB accession codes of the cryo-EM density maps from which the topographs were simulated from are listed with the abbreviated names of the individual filaments. The sample origin is noted above the filaments' images. The following abbreviations were used for disease diagnoses and filament labels: CBD – corticobasal

degeneration, CTE – chronic traumatic encephalopathy, PiD – Pick's disease, AD – Alzheimer's disease, NPF – narrow Pick filament, WPF – wide Pick filament, PHF – paired helical filament, SF – straight filament.

The digitally straightened dGAE fibril (**Fig. 4.1c-d**) is shown in Fig. 3 together with all of the simulated images of tau fibrils from published cryo-EM maps. All simulated tau fibrils are left-handed, as is the dGAE filament. As with any topographic AFM height image, the intensity of the colour also represents the height value in the simulated topographs. The comparison of fibril heights (colour intensity in **Fig. 4.6)** immediately highlights the differences between the dGAE fibril and CBD wide filaments, as well as wide Pick filaments (WPF), both consisting of two intertwined protofilaments with larger cross-sectional areas compared to the dGAE fibril. However, CBD narrow filaments, narrow Pick filaments (NPF), and straight filaments (SF) from AD, which appear to be similar to dGAE in height, exhibit a difference in the repeating pattern compared to dGAE, due to their asymmetric cross-sections. These types of asymmetric cross-sections lead to a complex pattern of peaks and grooves along the length of the fibril, compared to the single visible peak and groove of the dGAE with 2-fold screw-symmetry, which in comparison is more similar to PHFs from AD. A similar pattern, although with a repeating unit consisting of a major and a minor peak, resulting from tip-sample contact with the rhombic cross-sections, are also seen on CTE type I and CTE type II filaments. Finally, the morphologies of all four heparin-induced tau fibrils differ from those of the other simulated images, and from the dGAE fibril image, due to their off-centre helical axis and asymmetric cross-sections. Although the dGAE fibril shown here matches the heparin-twister fibril well in height, the displayed repeating pattern differs substantially from the experimental dGAE fibril image due to differences in the cross-sectional shape and position of the screw-axis.

To quantify the similarity between the experimental dGAE fibril image and the simulated topographical AFM images derived from cryo-EM maps, a correlation distance based score (d_{img}, see section 4.6 Methods) was calculated between the dGAE fibril image and each of the simulated images (**Table 4.1**). Because the pixel sampling rate in the simulations was set to be identical to that of the experimental AFM image, each pixel value (height value) in the data image can be compared to the pixel value in a simulated image at the same coordinate location. The correlation distance score, d_{img}, is then one minus the correlation coefficient between the data pixel values and the simulated pixel values, with smaller distance scores signifying more similar images. The d_{img} score was calculated using the pixel value at the coordinates in the experimental AFM data image where the height values are above the estimated height of the fibril axis to minimise complex contributions from tip-sample convolution. The resulting d_{img} scores (**Table 4.1**) confirmed that the experimental dGAE fibril image showed closest similarity to the simulated AFM images derived from cryo-EM data of patient-tissue purified *ex vivo* PHF and CTE type II filaments.

Table 4.1 Quantitative comparison of image similarity and similarity in morphometric parameters between AFM image data of the dGAE fibril shown in Fig. 4.1c and cryo-EM derived tau fibril maps using the distance measure-based scoring system described in section 4.6 Methods. The similarity rank is based on the combined score $d_{\sum}$, from most similar with lowest $d_{\sum}$ value to least similar with highest $d_{\sum}$ value.

Filament type	*sym*	*hnd*[§]	*cod* / nm	*csa* / nm^2	*csd* / nm^2	d_{img}	d_{sym}	d_{hnd}	d_{cod}	d_{csa}	d_{csd}	$d_{\sum}$	Rank
dGAE, AFM data	2	-1	49.1[†]	44.1	0.0								
CBD wide, EMD-10514	2	-1	141.2	106.1	62.8	0.69	0	0	0.51	0.82	0.80	2.82	7
CBD narrow, EMD-10512	1	-1	203.9	54.8	24.3	0.70	1	0	0.86	0.14	0.31	3.01	10
CTE type I, EMD-0527	2	-1	71.1	83.5	40.2	0.41	0	0	0.12	0.52	0.51	1.57	3
CTE type II, EMD-0528	2	-1	71.1	64.4	21.3	0.25	0	0	0.12	0.27	0.27	0.91	2
Narrow Pick's filament (NPF) , EMD-0077	1	-1	229.4	39.6	11.5	0.62	1	0	1.00	0.06	0.15	2.83	8
Wide Pick's filament (WPF) , EMD-0078	2	-1	141.0	119.9	78.2	0.77	0	0	0.51	1.00	1.00	3.28	12
Paired helical filament (PHF) , EMD-0259	2	-1	77.6	61.3	18.4	0.26	0	0	0.16	0.23	0.23	0.88	1
Straight filament (SF) , EMD-0260	1	-1	164.8	70.5	27.9	0.37	1	0	0.64	0.35	0.36	2.71	6
Heparin snake, EMD-4563	1	-1	134.3	48.0	52.2	0.75	1	0	0.47	0.05	0.67	2.94	9
Heparin twister, EMD-4564	1	-1	50.1	37.3	12.9	0.46	1	0	0.01	0.09	0.16	1.72	4
Heparin jagged, EMD-4565	1	-1	83.3	45.2	38.8	0.29	1	0	0.19	0.01	0.50	1.99	5
Heparin hose, EMD-4566	1	-1	161.1	30.6	42.6	0.92	1	0	0.62	0.18	0.54	3.26	11

§. Left-hand twisted filaments are assigned a *hnd* value of -1 and right-hand twisted filaments are assigned a *hnd* value of 1

†. The mean cross-over distance of the selected dGAE fibril shown in **Fig 4.1c-d**. The overall comparative similarity rank is unchanged if the population mean *cod* value of dGAE fibrils of 72.7 nm (Al-Hilaly et al., 2020) is used instead.

4.4.5 Quantitative and comparative morphometric analysis of dGAE tau amyloid fibrils with cryo-EM derived structural maps confirms their structural similarity to patient-derived tau structures

To investigate further whether dGAE tau amyloid fibrils are structurally similar to the tau amyloid purified from patient tissues, a quantitative and comparative morphometric analysis was performed next. First, the rotational cross-section of the dGAE tau fibril from the 3D model constructed using AFM data (**Fig. 4.1c-d**), and those of the cryo-EM tau fibril density maps, were quantified in terms of their area and shape differences (cross-sectional area, *csa*, and cross-sectional difference, *csd*, respectively, defined according to **Fig. 4.2c-d)**. For cryo-EM density maps, the rotational cross-sections were calculated by de-rotating the cross-sections along their helical axes, followed by tracing of the boundaries of the resulting 2D-maps with a circle of a radius equivalent to that of the AFM tip of the experimental dGAE fibril image. This procedure made the cross-sections from cryo-EM and AFM data comparable by accounting for the finite size of the tip during AFM imaging and thus estimating 'tip-accessible' cross-sections from the cryo-EM maps. A visual comparison of the dGAE fibril cross-section with CTE type II, PHF, and heparin-twister filament cross-sections (**Fig. 4.7**) showed that although CTE II and PHF fibrils both display two-fold helical symmetry and show similarity in their simulated topographs to the dGAE fibril image data (**Fig. 4.6**), the dimensions of the dGAE fibril model cross-section are smaller. However, although the area of the heparin-twister fibril cross-section better matched that of the dGAE fibril, it has an asymmetric cross-sectional shape with the helical axis positioned off the centre-of-mass, like other heparin-induced fibrils, which are dissimilar to the dGAE fibril with two-fold helical symmetry. Therefore, the differences in the helical symmetry and average cross-over distance were also taken into account in the

comparative analysis, in addition to the cross-sectional difference and area parameters. The differences for all of these morphometric parameters between the dGAE tau fibril and patient tissue-extracted tau filament structures, or *in vitro* heparin-induced filaments, as determined by cryo-EM, were compiled and listed in Table 4.1. These morphometric distance-based similarity scores, together with the image similarity score, d_{img}, allowed the calculation of a combined score of similarity, $d_{\sum}$ (see section 4.6 Methods), between the dGAE fibril imaged by AFM and each of the unique previously determined cryo-EM tau fibril structural maps. This combined score enabled ranking of overall structural similarity (**Table 4.1**), showing that the canonical dGAE fibril (**Fig. 4.1c-d**) exhibits the highest overall structural similarity to PHF from Alzheimer's disease, followed closely by CTE type II filaments, while unequivocally ruling out any close structural similarity to *in vitro* heparin-induced tau fibrils, as well as other disease-associated tau fibrils (**Fig. 4.8**).

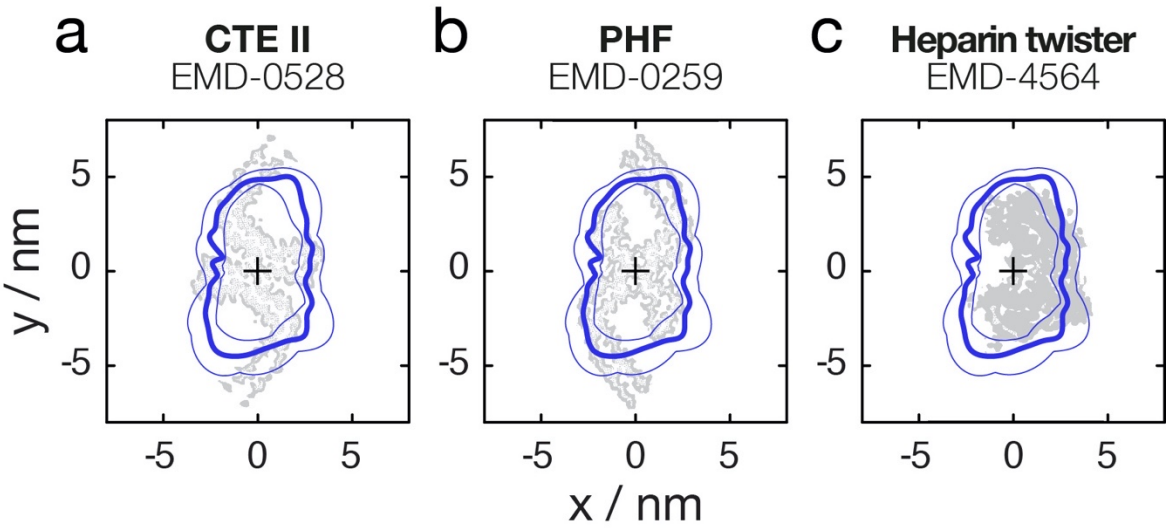

Figure 4.7 Comparison of the cross-section of the surface envelope model derived from the experimental AFM dGAE filament image and cryo-EM density maps cross-sections. The cross-sections for the CTE type II filaments **(a)** and PHF from AD patient tissue **(b)**, as well as *in vitro* assembled heparin-induced 'twister' filaments **(c)** are shown. The average cross-section of the AFM image derived 3D model is shown as thick blue lines, and the structural variation

observed along the fibril in the AFM image is indicated by the thin blue line denoting the 2.5 and 97.5 percentile bounds. The cryo-EM density cross-sections are shown in grey.

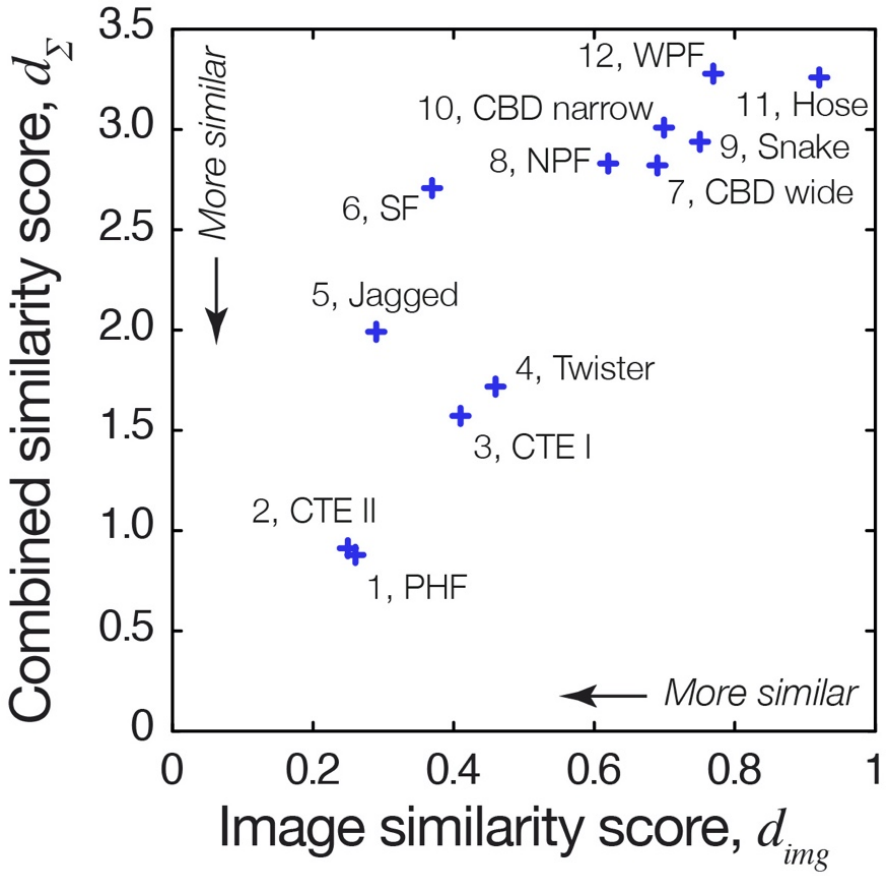

Figure 4.8 The image similarity score and the combined score of similarity between the dGAE fibril AFM image data and cryo-EM derived density maps of tau fibril polymorphs. Lower score denotes higher degree of similarity. The overall comparative rankings (from highest to lowest) based on the combined score of similarity (**Table 4.1**) are labelled for each entry.

4.5 DISCUSSION

Structural analysis of amyloid fibrils at the level of individual filaments is key to the understanding of the structural polymorphism displayed by amyloid assemblies, which in turn

may relate to the varying physiological effects of amyloid *in vivo*. AFM imaging is complementary to high-resolution, ensemble-averaging techniques like cryo-EM, due to its capability for the structural analyses of single, individual molecules, e.g. membrane proteins (Heath et al., 2021), DNA (A. L. B. Pyne et al., 2021) and amyloid filaments (Aubrey et al., 2020), as well as their chemical signatures, response to force, interactions and dynamics (Maity & Lyubchenko, 2019; Ruggeri et al., 2015; Watanabe-Nakayama et al., 2016) Here using dGAE tau amyloid fibrils, we show that the 3D information from AFM and cryo-EM can be integrated with each other by simulation of topographic images from cryo-EM density maps or by 3D reconstruction of fibril surface envelopes from AFM topographic data. As exemplified by the analysis of the dGAE tau amyloid structure, these workflows enable direct comparison between experimental AFM images and the increasing numbers of cryo-EM data deposited in the EMDB. We demonstrate this approach by comparing high-resolution structural maps of various tau amyloid fibril cores determined by cryo-EM with a single AFM topographic scan of a sample of dGAE tau fibrils formed *in vitro* without the addition of anionic cofactors. In this case, the quantitative comparison of simulated topographs derived from the cryo-EM density maps with an experimental AFM fibril image of a canonical dGAE tau fibril shows that the structure of dGAE fibrils differs unambiguously from the structures of *in vitro* assembled heparin-induced recombinant tau fibrils. The analysis also predicts a close structural match between dGAE tau fibrils and both PHFs and CTE type II fibrils extracted from patient brain tissues.

The biological implications of our findings are significant because It is necessary to establish conditions of tau self-assembly *in vitro* that could result in the formation of disease-relevant fibril structures, in order to enable studies of these structures along a disease-relevant aggregation pathway, as well as to facilitate accessibility to physiologically relevant fibril

structures for the development of aggregation modulators. Like dGAE fibrils, PHFs and CTE II fibrils also have 2-fold helical symmetry and have a similar cross-sectional shape. The cross-section of dGAE fibrils as estimated by the AFM derived 3D model is, however, smaller than those derived from CTE II fibrils and PHFs (**Fig. 4.7**). This may be due to the physical interactions of the AFM probe tip with the fibril surface despite the low force applied, the deposition of the fibrils for AFM scanning in air or underlying molecular differences. However, the similarity between dGAE fibrils and PHFs as well as CTE type II filaments is also supported by sequence comparison. The dGAE tau sequence contains residues that correspond to the repeat regions 3 (R3) and 4 (R4) of the 4-repeat tau isoform, as well as 9 residues from the C-terminus of the repeat region 2 (R2), and thus it is expected the morphology of the fibrils would more closely resemble that of the fibrils which also contain R3 and R4 residues in their cores but few or none R1 or R2 residues. Such fibrils include PHFs and SFs AD filaments, as well as the two CTE filaments (Falcon et al., 2019; Falcon, Zhang, Schweighauser, et al., 2018). In contrast, filaments from CBD, PiD, and heparin-induced recombinant tau also contain a larger numbers of residues from the R2 or R1 regions within their core structures (Falcon, Zhang, Murzin, et al., 2018; W. Zhang et al., 2019, 2020).

Although the sampling pixel density and tip-sample convolution effect are controlled for and matched to experimental values during the simulation of height images using cryo-EM maps, other factors arising from experimental imaging conditions such as the sample deposition process or residual monomeric or small aggregated species sticking onto the imaged fibril or the probe tip will affect the quality of experimental AFM data. Further improvements to the resolution and imaging parameters of the experimental dataset, either during data acquisition or by computational post-acquisition algorithms, could improve the accuracy of the quantitative comparison and the ranking of the similarity between experimental and simulated

fibril images. The method presented here can also be extended to include ssNMR derived structural models by using atomic coordinates deposited to the Protein Data Bank instead of cryo-EM density maps for comparison. Thus, the approach presented here demonstrates the vast potential of integrated structural analysis that utilises the complementary 3D information acquired by different physical principles.

4.6 METHODS

4.6.1 AFM image data

The AFM image data analysed here was collected on a Bruker MultiMode 8 scanning probe microscope with a Nanoscope III controller, and is part of a previously published data set (Al-Hilaly et al., 2020). The images were acquired using the ScanAsyst in Air mode using Bruker Scan Asyst Air probes with nominal spring constant of 0.04 N/m. The AFM image shown in Fig. 4.1 represents topographical height scans 3 μm × 3 μm in size at a resolution of 2048 × 2048 pixels. The height image was flattened using Bruker Nanoscope Analysis software to remove tilt and bow. All further image analysis was carried out in Matlab.

4.6.2 AFM image analysis

Fibrils were traced (W.-F. Xue, 2014; W.-F. Xue, Homans, et al., 2009) and digitally straightened (Egelman, 1986) using an in-house application. The radius of the AFM tip during scanning was estimated by a least-squares fit of tip-sample contact-point model on the mean cross-section of a straightened fibril across its length, with tip radius as fitted parameter (Lutter et al., 2020). A tip model was then constructed from the tip radius, and the tip angle and

geometry provided by the manufacturer. The same tip model was later used for simulating AFM topographs from cryo-EM data. The average fibril cross-over distance was found as the highest frequency peak from the Fourier transform of the fibril centre line height profile. The 3D reconstruction of the traced and straightened dGAE fibril was carried out as previously described (Lutter et al., 2020).

4.6.3 Cryo-EM volumetric data pre-processing

Cryo-EM density maps were downloaded from the Electron Microscopy Data Bank (EMDB). The voxel-based volumetric Coulomb density map data were imported into Matlab where all subsequent processing and analysis was carried out. The helical rise, twist and handedness values were obtained from the information provided in the EMDB metadata of each entry. The iso-surface of a density map was found by applying the isovalue provided by the authors of each of the EMDB data entries. The iso-surface vertices were rotated and translated, where necessary, so that the long fibril axis runs along the z-axis. Where necessary, the density maps were denoised by finding the nearest neighbours for all iso-surface vertices and subsequently applying a threshold value to remove vertices with a significantly larger mean distance from neighbours. The number of nearest neighbours and threshold were changed according to the noise level of each map by manual inspection. All maps were then further denoised by finding the alpha-shape of the iso-surface using an alpha radius of twice the voxel size of the EM density map, while suppressing holes and retaining only the vertices that belong to the largest single region of the isosurface.

4.6.4 Identifying and aligning the fibril screw-axis

The position of the fibril screw-axis was estimated by iterative optimisation of the rotation and translation parameters while maximising the overlap between a voxelised isosurface and the same isosurface rotated and translated about the z-axis by applying the helical rise and twist values from the EMDB entry of each density map. Depending on the map features, rotation and translation parameters of the map isosurface coordinates relative to the screw-axis were optimised jointly or either rotation or translation was initially optimised separately for an initial estimate, followed by joint optimisation of all parameters.

4.6.5 Simulation of AFM topographs from cryo-EM structural data

The axis-aligned iso-surface coordinates were extended to double the length of an experimental AFM image fibril to allow for periodic alignment. This was done by rotating and translating the iso-surface vertices along the long fibril axis (the z-axis in axis-aligned iso-surface) using the helical twist and rise values from the EMDB metadata, followed by a 90° rotation so that the filament axis aligned with the y-axis. The tip model with the radius specific to the experimentally imaged fibril was then used to find the contact points between the tip model and the fibril surface on an xy-grid constructed with the pixel size equivalent to that of the experimental AFM image. The periodicity pattern of the simulated fibril images was subsequently optimised to take into account possible structural variations in the twist of filaments by finding a possible best match to that of the experimental AFM fibril image within a plausible bounded range. This is achieved by an iterative optimisation of a parameter which dilates or contracts the simulated fibril image along the length of the fibril within a bounded interval of 0.5-2 times the nominal pixel size and maximises the cross-correlation between the transformed simulated image and the straightened experimental fibril image.

4.6.6 Calculation of cross-sectional area and shape differences

Filament cross-sections perpendicular to the fibril axis were found for both the AFM 3D envelope model of the dGAE tau amyloid fibril and tau amyloid fibril cryo-EM density maps by untwisting the coordinates to the same 2D plane along the length of the fibril, using the twist and rise values provided in the EMDB metadata for cryo-EM models, or the analysis of periodicity for AFM imaged fibrils. For EM density maps, the tip accessible cross-section was estimated as the alpha shape of the cross-section, which was then found with the alpha radius equivalent to the tip radius of the fibril on the experimental AFM image. The alpha shape was then rotated by 1° intervals for a total of 360° and for each interval, RMSD to the cross-section of the experimental AFM fibril envelope was calculated. The rotation angle that resulted in the lowest RMSD indicated the best rotational alignment of the two cross-sections. The cross-sectional area or difference area were then calculated as defined in Fig. 4.2 c-d.

4.6.7 Similarity scores and comparative structural ranking

A score to quantify the similarity between the digitally straightened experimental AFM image of the dGAE fibril and simulated AFM images using cryo-EM maps of different polymorph of tau filaments found in the EMDB was defined as the correlation distance, d_{img}, between the pixel height values, which is one minus the correlation coefficient, r, between the data pixel values and the simulated pixel values (**Eq. 4.1**)

$$d_{img} = 1 - r \qquad \textbf{Eq. 4. 1}$$

The d_{img} score was calculated using only the pixel value at the coordinates in the experimental AFM data image where the height values are above the estimated height of the fibril axis to

minimise complex contributions from tip-sample convolution. Scores to quantify the differences in the morphometric parameters (defined according to **Fig. 4.2**) helical symmetry, *sym*, twist handedness, *hnd*, average cross-over distance, *cod*, cross-sectional area, *csa* and cross-sectional difference area, *csd*, between each of the cryo-EM derived tau filament maps and the experimentally AFM-imaged dGAE fibril are defined as their individual Euclidian distances *d*, normalised to their observed maximum values, or the theoretical maximum value of 2 for *hnd*.

$$d_{par} = \frac{\left|par_{EM\ map} - par_{dGAE}\right|}{\left|par_{EM\ map} - par_{dGAE}\right|_{max}} \qquad \textbf{Eq. 4. 2}$$

In **Eq. 4.2**, '*par*' represents the parameters *sym, hnd, cod, csa* or *csd*. Defining of all the similarity scores using standardised distance measures means that lower numerical values indicate higher degree of similarity. The overall score of similarity, $d_{\sum}$, was then defined as the sum of the individual image and morphometric similarity scores (**Eq. 4.3**).

$$d_{\sum} \quad = d_{img} + d_{sym} + d_{hnd} + d_{cod} + d_{csa} + d_{csd} \qquad \textbf{Eq. 4. 3}$$

Chapter 5: Multivariate analysis of amyloid fibril structural polymorphism

5.1 Summary

In this unpublished manuscript a computational meta-analysis approach to amyloid fibril structural information is used to tackle the amyloid structure-function relationship. Amyloid fibrils elicit a variety of biological effects, from roles required for physiological functionality to cytotoxicity and disease-association. A similarly wide degree of variation is seen in the structures formed by amyloid fibrils, recently revealed by ssNMR and cryo-EM. Determining the nature of the relationship between structure, function, and dysfunction in biological contexts is a key unresolved challenge that will further our fundamental understanding of amyloid biology and facilitate identifying therapeutic strategies for the amyloid-associated neurodegenerative and systemic diseases.

This manuscript uses the structural information of amyloid fibril atomic coordinates and density maps deposited to the PDB and EMDB databases up to August 2021. A systematic meta-analysis is carried out to characterise the fibril models and determine differences in specific structural features between groups of amyloids, in order to generate hypotheses around features that may mediate biological effects. Amyloids are here broadly categorised as pathogenic, functional, and low complexity domain-containing (LCDs), which can be both functional or disease-associated. A statistical analysis of specific structural features revealed that LCDs have unique properties compared to pathogenic amyloids, including both more hydrophilic solvent-accessible surfaces and fibril core interiors. Furthermore, LCD folds are more compact compared to the folds of pathogenic amyloids and have, on average, more than three times as large protofilament interface areas. On the other hand, functional amyloids do not differ from pathogenic amyloids in these analysed features, but instead have, on average, smaller folds with less total solvent-accessible surface area and only half as extensive β-sheet interface areas in the fibril cores as compared to pathogenic amyloids. These features may mediate different biological properties and effects such as thermodynamic stability, reversibility of assemblies, as well as the rates of the nucleation, elongation, or fragmentation steps along the aggregation pathway. Future work on this manuscript will lead to more detailed analysis of structural features in order to advance our understanding of amyloid structure-function relationships.

5.2 ABSTRACT

Structural polymorphism is a key feature of amyloid assembly that results in fibrils of varied physicochemical properties, potentially leading to the diverse biological responses of amyloid observed in biological contexts, from functional roles to neurodegenerative disease-associated mechanisms of toxicity. To date, significant advances in structural analysis of amyloid fibrils have been made using cryo-electron microscopy and solid-state NMR, providing a wealth of high-resolution data on fibril structures, and revealing a high degree of structural variation. Although comparisons of a number of individual structures have thus far been used to identify structural characteristics which may mediate biological properties, a systematic quantitative analysis of variance in specific structural features across all amyloid structures is lacking. Here, we report a quantitative meta-analysis of amyloid core structural models in order to elucidate the amyloid structure-function relationship. The analysis reveals that structural models of low-complexity domain-containing amyloids (LCDs) have on average both more hydrophilic solvent-accessible surfaces and core packing arrangements compared to pathogenic amyloids. Furthermore, LCDs are more compact and have more than three times as large protofilament interface areas. Other functional amyloids do not significantly differ from pathogenic amyloids in these analysed structural features but are, on average, smaller and contain only half as much total β-sheet interface area relative to size. In summary, structural features including protofilament interface areas and packing of hydrophobic residues are potential mediators of biological properties for LCD-containing amyloids, whereas size and β-sheet interfaces may be key mediators of biological properties for other functional amyloids.

5.3 INTRODUCTION

The mechanisms of toxicity through which pathogenic amyloids exert their cytotoxic effects are varied, with the small oligomeric species emerging as the most cytotoxic via pathological processes including loss of membrane integrity (Tian et al., 2021), ionic homeostasis (Quist et al., 2005), and disruption of signalling pathways (Amar et al., 2017), whereas fibrillar species have been shown to exert toxicity via membrane disruption (Milanesi et al., 2012) and deleterious effects on the endo-lysosomal pathway (X. Zhang et al., 2020). In addition, loss-of-function toxicity can occur where the native function of the protein is disrupted due to misfolding and amyloid formation (S. Ghosh et al., 2017). However, the full extent of the mechanisms of toxicity employed by the various species along the aggregation pathway is yet to be elucidated. Furthermore, there is currently no consensus on which mechanisms might be most significant in *in vivo* disease contexts, why some amyloid plaques are seemingly inert and do not correlate with cognitive impairment, and how amyloid mechanisms of toxicity are affected by cellular changes during aging.

Similarly to the variations seen in amyloid mechanisms of toxicity, some amyloids have diverse mechanisms for carrying out biological functions, including structural support roles, storage of peptide hormones, and regulation of signalling pathways (Otzen & Riek, 2019). For example, the fibrillar state of the CPEB protein Orb2 leads to memory persistence through enhancing the translation of specific mRNAs (Hervas et al., 2020). In addition, some amyloidogenic proteins have functional roles in biomolecular condensates formed through liquid-liquid phase separation (LLPS) but undergo aberrant aggregation into pathological amyloid as a result of aging-related loss of homeostasis (Alberti & Hyman, 2021). How this diversity in biological effect, ranging from essential for physiological functions to an array of cytotoxic effects, arises

from fibrils sharing the amyloid state, is a key question to our understanding of fundamental amyloid biology in health and disease.

Studies of amyloid fibril structures have recently revealed that the large degree of variation in biological effects of amyloids is reflected in the diversity seen in their structures. Cryo-electron microscopy (cryo-EM) and solid-state NMR (ssNMR) methods have been instrumental in determining the structures of a wide variety of amyloid fibril cores, thus elucidating the polymorphic nature of amyloids in high-resolution detail (Iadanza, Jackson, et al., 2018). Although amyloid fibrils share the common cross-β core architecture comprised of β-strands that stack perpendicular to the fibril axis with a 4.7 Å inter-strand and 10 Å inter-sheet separation (Jahn et al., 2010), structural models now show a wide variety of differences in amyloid core features. Differences in the core architecture include the β-sheet forming regions, core arrangement, presence of co-factors, and packing of laterally associated protofilaments (Lutter, Aubrey, et al., 2021). Although most of the available structural data characterises *in vitro* formed fibrils, an increasing number of *ex vivo* fibril structural models are also available. Comparison of *in vitro* and *ex vivo* structures of the same protein monomers has revealed vastly different folds (Fitzpatrick et al., 2017; W. Zhang et al., 2019), highlighting the local *in vivo* microenvironment as an important factor in determining the polymorphism landscape of amyloid fibril populations. Furthermore, structural data from *ex vivo* extracted fibrils from neurodegenerative disease patients has shown that the fibril structures are near-identical for the same protein in patients with the same diagnosis (Falcon, Zhang, Schweighauser, et al., 2018), and holds the potential to determine whether fibril structures could also be tissue- or clinical subtype-specific for a disease. Finally, the structures of some reversible, functional amyloid fibrils have also recently been determined (Hervas et al., 2020; J. Lu et al., 2020; Seuring et al., 2020). Although considerably less functional amyloid structures are available due to the

critical need for a better understanding of pathological amyloid states to combat disease-associated aggregation, it provides an opportunity for a comparative approach towards elucidating the relationship between the variation of amyloid in biological contexts and their structural polymorphism.

The relationship between amyloid structure and function or dysfunction is often discussed by comparison of a number of structures with different biological effects, such as functional and pathogenic amyloids, or models of wild-type and familial mutation-carrying structures, in order to form hypotheses on the structural features which could mediate the differences in biological effects. For example, this has led to an observation that the Orb2 functional amyloid core has a much less hydrophobic interior compared to that of a model of a pathogenic $A\beta_{40}$ fibril (Ulamec & Radford, 2020). Although this approach offers detailed information on the specific structural folds, it is limited by the small number of analysed models, which does not facilitate drawing conclusions about general features of amyloids with different biological consequences. An alternative approach in which residue- and molecule-specific thermodynamic stability is calculated from the entropic and enthalpic contributions to the solvation free energies across all amyloid structural models has likewise provided valuable insights, demonstrating that pathogenic amyloids tend to be more stable (Sawaya et al., 2021). Although thermodynamic stability is likely to be a key element of determining the biological effects of amyloid fibrils, a parametrised approach would have the advantage of disentangling any specific structural features that lead to the observed differences in stability, which could further be useful for identification of therapeutic strategies.

A detailed understanding of key structural features is required to detangle the interplay between amyloid structural differences and biological consequences. Here, a parametric approach is

used in a systematic meta-analysis on 105 unique amyloid fibril structural models determined by cryo-EM and ssNMR up to August 2021. The models were computationally analysed by calculations of specific structural features in order to identify significant differences and relate these to biologically categories of pathogenic, functional, and low complexity domain-containing amyloids (LCDs). The general differences in characteristics including symmetry, number of protofilaments and fibril handedness are first analysed, along with the size and shape of the structural models. Further analysis then reveals significant differences in hydrophobic core arrangements, packing of the fibril core, as well as protofilament interface areas between LCDs and pathogenic amyloids. Contrastingly, functional amyloids did not on average differ from pathogenic amyloids in these features, but exhibited less exposed surface area per layer and a lower β-sheet interface area. Finally, differences between *ex vivo* and *in vitro* formed structures are highlighted and mechanisms through which the identified differences could lead to different biological effects are discussed.

5.4 RESULTS

5.4.1 Amyloid fibrils display a large degree of structural polymorphism

Amyloid structural models deposited to the EMDB and PDB databases up to August 2021 were selected, resulting in a total of 105 fibril models from which 92 had available atomic coordinates and secondary structure annotations (see section 5.6 Methods for further inclusion criteria). The general features of the 105 amyloid fibril core models were first assessed through characterisation of symmetry, handedness, and number of protofilaments (**Fig. 5.1a**). In analysis of fibril model symmetries, 2-fold helical symmetry was the most prevalent at 58 %, followed by 38 % of fibrils with asymmetrical cross-sections. Within the group of 2-fold

symmetries, pseudo-2_1 screw-symmetry was 20 % more prevalent than the C2 rotational symmetry, and for a small number of structures it was not possible to differentiate between these due to limited resolution. Finally, a small minority of 4 % of fibril models had C3 rotational symmetry. Variations in symmetry were reflected in similar variation in number of protofilaments, demonstrating that increased numbers of protofilaments often become symmetrically arranged about the helical axis. Nearly two thirds of the fibrils consisted of two protofilaments and a quarter consisted of a single protofilament. A small number of fibrils also had three protofilaments (8 %) or four protofilaments (3 %). The proportion of asymmetric fibrils is 13 % higher compared to models with single protofilament fibrils as protofilaments are not symmetrically arranged in all models and resulting in a relatively higher proportion of asymmetric fibril core structures. While the majority of the fibrils are left-handed, approximately one in six of the determined structural models exhibit right-handed twist instead. The major prevalence of left-hand twisted fibrils occurs as a result of the chirality of L-amino acids, which in β-sheet arrangements favour left-handed twist (Chothia, 1973). Thus it is possible that specific features of the folds of right-handed twisted fibrils act to compensate for this comparatively less favourable twist arrangement.

Amyloids were then grouped by biological effects into pathogenic, functional, and low complexity domain-containing proteins (LCDs). Pathogenic amyloid models (n = 76) included amyloid-β (Aβ), α-synuclein, tau, islet amyloid polypeptide (IAPP), immunoglobulin light-chain (IG LC), serum amyloid A (SAA), β_2-microglobulin (β2m), transthyretin (TTR), CA150, and the prion protein (PrP). The group of functional amyloid models (n = 7) included PI3K, RIPK1/3, glucagon, β-endorphin, and HET-s. Finally, the LCD models (n = 9), which contain both reversible and functional as well as pathogenic amyloid sharing the low complexity motif, included fused in sarcoma (FUS), TAR DNA-binding protein 43 (TDP-43), heterogeneous

nuclear ribonucleoprotein A1 and A2 (hnRNPA1/2), and Orb2. The biological groupings for each amyloid structural model, along with all the calculated parameters, can be seen in Supplementary Table 5.1.

The variations in sizes and shapes of the amyloid fibril structural models across the total 105 fibril data set were first assessed (**Fig. 5.1 b-c**). The mean cross-sectional area of the amyloid fibril models is 32.7 nm^2 with 88.6 % of the fibrils having cross-sectional areas less than 50 nm^2, and only a minority of the fibrils having larger cross-sections up to 106.9 nm^2. The shape of the fibril model cross-sections was assessed through measures of roundness, a function of perimeter and area, and eccentricity, a ratio of the minor and major axes. Shape analysis highlighted that the cross-sectional shapes formed by amyloid structures are both more elongated than circular, and have non-circular boundaries, suggesting that packing arrangements favour increased surface area rather than compactness.

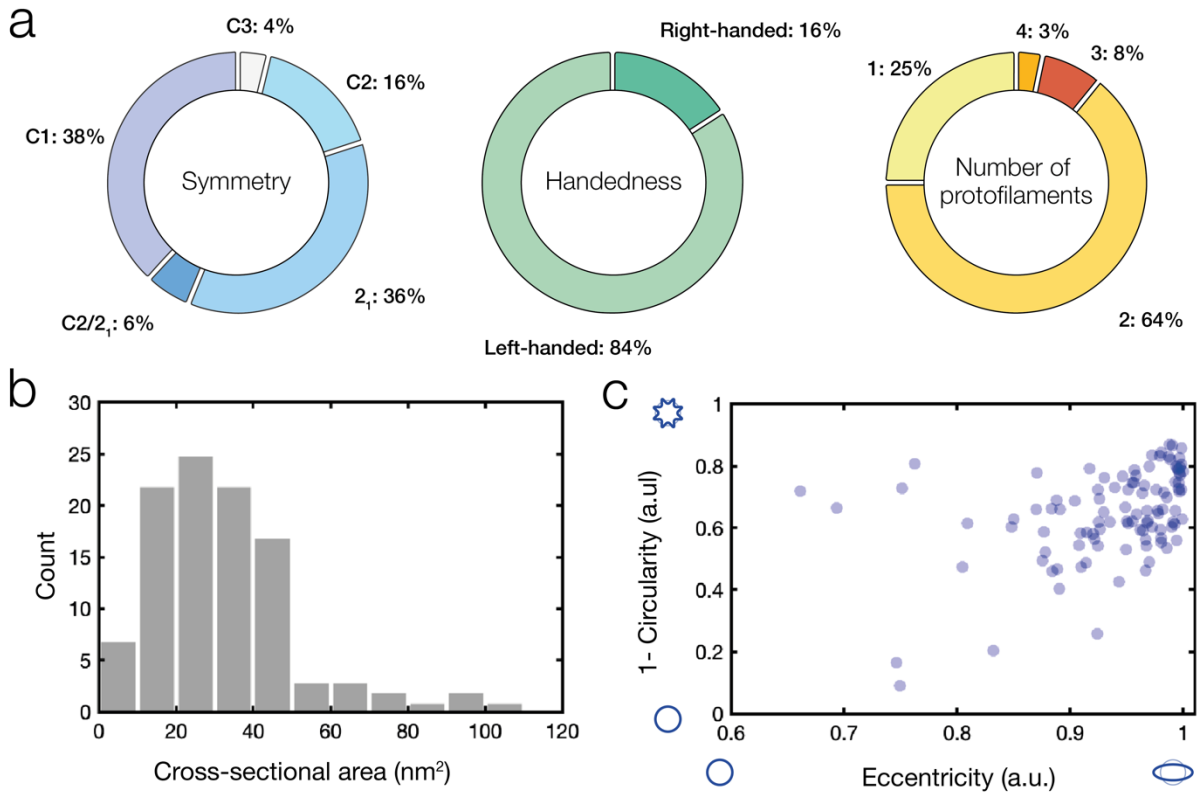

Figure 5.1 Statistical analysis of amyloid fibril model symmetry, handedness, number of protofilaments, size, and shape. **(a)** Symmetry, handedness, and number of protofilaments of amyloid fibril structural models. **(b)** Histogram of amyloid fibril model cross-sectional areas. **(c)** Shape analysis of amyloid fibril models by circularity and eccentricity measures.

5.4.2 Pathogenic, functional, and LCD-containing amyloid fibrils display on average no significant differences in β-sheet content

The general sequence composition of amyloid fibril structural models was characterised by the ratio of unique amino acids and the number of possible unique amino acids, as well as the β-sheet content, determined from the secondary structure assignments of each model. As expected, LCDs have on average less sequence complexity, with both pathogenic and functional amyloids having approximately 1.4 times as high unique amino acid ratios compared to LCDs (**Fig. 5.2a**; $p = 0.01$ and $p = 0.002$, respectively), whereas the β-sheet content per layer did not differ significantly between any of the amyloid groups (**Fig. 5.2b**).

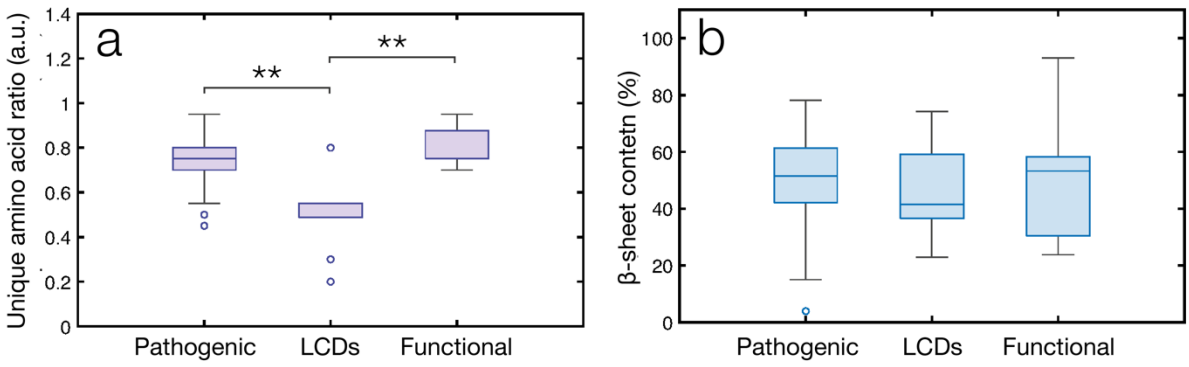

Figure 5.2 Comparison of general sequence features of amyloid fibril structural models shows that LCD-containing fibrils form structures with less unique amino acids compared to both pathogenic and functional amyloids, whereas β-sheet content does not significantly different between assigned biological categories. **(a)** Comparison of unique amino acid ratio. **(b)** Comparison of β-sheet content between different biological categories of amyloid. ** denotes significance at or below the 0.01 level. Statistical comparison of means was carried out between

all groups and was not significant if not otherwise indicated. Welch's ANOVA was used with Games-Howell post-hoc tests to correct for multiple comparisons while not assuming equal variance. On each box, the central mark indicates the median, and the bottom and top edges of the box indicate the 25th and 75th percentiles, respectively. The whiskers extend to the most extreme data points not considered outliers, and the outliers (defined here as values beyond ±2.7σ) are plotted individually using the symbol 'o'.

5.4.3 LCDs have more hydrophilic solvent-accessible surfaces, core packing arrangements, and are more compact than pathogenic amyloids

Amyloid fibril structural model core fold arrangements were analysed by measures assessing the relationship of residue-specific hydrophobicity with both solvent accessibility and distance from the fibril core interior. Although both measures use residue-specific hydrophobicity information, they differ in the second component, either solvent accessibility or distance from helical axis. These parameters are used as solvent-accessible hydrophobicity could potentially be linked to nonspecific sequestering of essential cellular components through hydrophobic interactions, whereas hydrophobicity of the core interior could instead be linked to higher thermodynamic stability. While the solvent-accessible hydrophobicity is an averaged measure and affected by the overall hydrophobicity of the amino acid sequence, the core hydrophobicity score does not depend on sequence hydrophobicity, as it is the relationship between distance from helical axis and residue-specific hydrophobicity that is measured, allowing the fold packing arrangement to be evaluated directly. In addition to the residue-specific hydrophobicity-based measures, fold arrangement is also evaluated as the total solvent-accessible surface area (SASA) per layer, which relates to the total size of the fibril core model. Finally, fold compactness is defined as an averaged measure of solvent accessibility in the folded state compared to the unfolded state of each amino acid. The differential contributions of hydrophobicity, solvent accessibility and distance on the measures are visualised in Fig.

5.3e, illustrating the principle behind each measure through examples of structural models with the highest and lowest scores.

Core arrangement and hydrophobicity analysis revealed that LCDs have on average more hydrophilic solvent-accessible surfaces, less hydrophobic core packing, and more compact folds (**Fig. 5.3b-d**). The solvent-accessible and core hydrophobicity measures were on average 32.8 % and 65.6 % lower for LCDs compared to pathogenic amyloids ($p = 0.015$ and $p = 0.009$, respectively). LCD fold arrangements were on average 5.6 % more compact, compared to pathogenic amyloids ($p = 0.001$), and 9.5 % more compact than those of functional amyloids ($p = 0.047$). In addition, the LCD core models were on average smaller than pathogenic amyloids, with 18.0 % less SASA per layer ($p = 0.041$).

Surprisingly, functional amyloids showed on average no differences to pathogenic amyloids in core and solvent-accessible hydrophobicity measures and did not have more compact fold arrangements (**Fig. 5.3b-d**). However, functional amyloids had overall smaller folds with 57.5 % less solvent-accessible surface area per layer compared to pathogenic amyloids ($p = 0.022$). Additionally, it was also noted that both anti-parallel $A\beta_{40}$ (**Fig. 5.3e**; PDB ID 2lnq), as well as the functional RIPK1/3 heteroamyloid (PDB ID 5v7z), had very low fold compactness and high solvent-exposed hydrophobicity scores (**Fig. 5.4**), highlighting the unique properties of these rare arrangements.

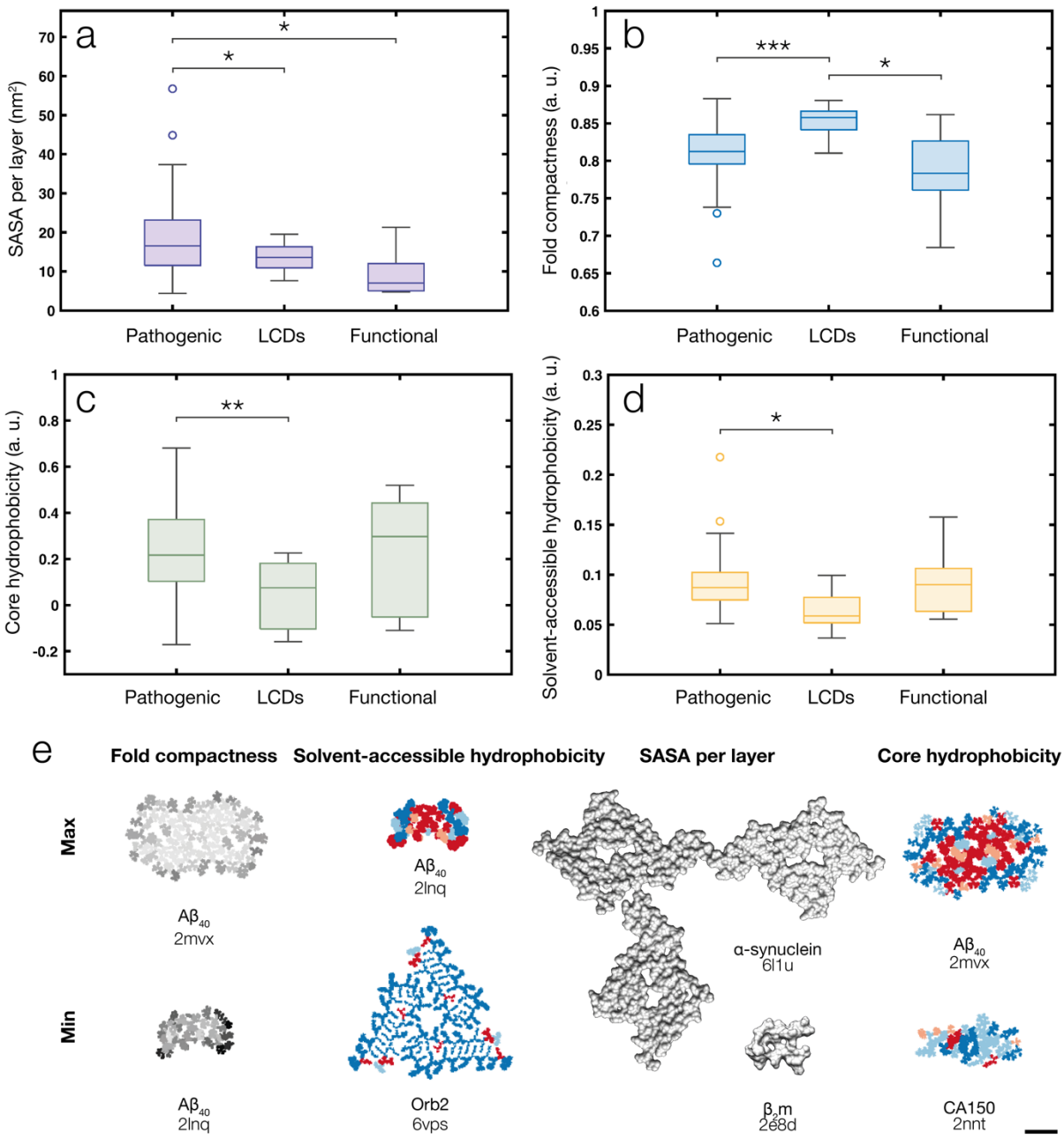

Figure 5.3 Statistical analysis of solvent-accessible surface area and hydrophobicity-based fibril structural features. **(a)** Total solvent-accessible surface area per layer. **(b)** Fold compactness. **(c)** Core hydrophobicity measure. **(d)** Solvent-exposed hydrophobicity measure. *, **, and *** denote significance at or below the 0.05, 0.01, and 0.001 levels, respectively. **(e)** Illustrative model representations of the calculated parameters on amyloid fibril structural models with the highest and lowest values for fold compactness, solvent-accessible hydrophobicity, SASA per layer, and core hydrophobicity. Fold compactness is illustrated by greyscale sphere models of the atomic coordinates, where the colour intensity corresponds to residue-specific solvent exposure in the fibrillar state, relative to the free state of the amino acid and main chain atoms of adjacent residues. For solvent-accessible and core

hydrophobicity, the red-blue colour scale indicates residue-specific hydrophobicity, with red representing more hydrophobic residues and blue more hydrophilic residues. For solvent-accessible hydrophobicity, the radii of the spheres representing atomic coordinates are scaled with solvent-exposure, so that more exposed residues appear larger and less exposed residues appear smaller. Similarly, for core hydrophobicity, sphere radii are scaled with distance of the residue from the helical axis to the solvent-accessible boundary, so that residues closer to the helical axis appear larger and residues further away appear smaller. SASA per layer is illustrated as surface representations of the atomic coordinates. All models are scaled equally and scale bar in bottom right corner represents 2 nm.

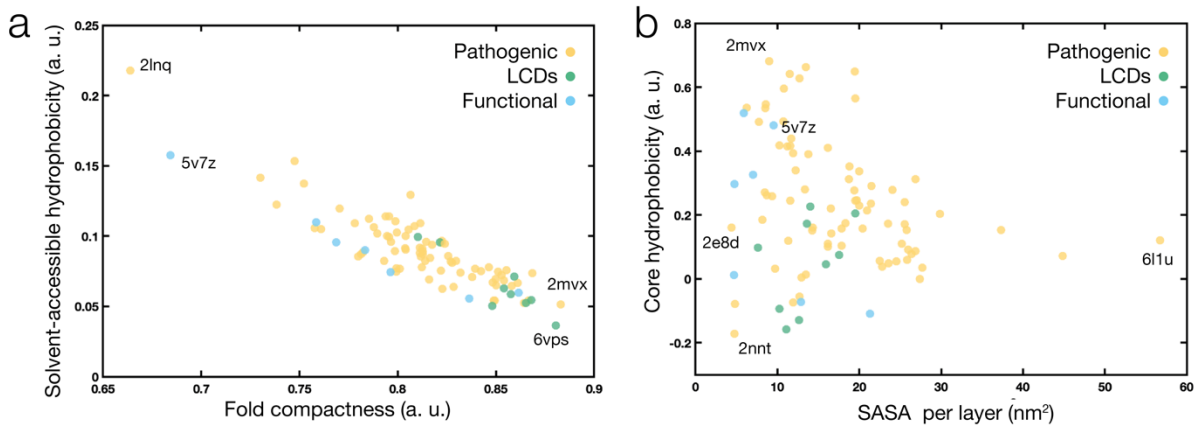

Figure 5.4 Visualisation of the variation in core and solvent-accessible hydrophobicity, fold compactness, and total solvent-accessible surface area per layer. **(a)** A scatter plot of fold compactness and solvent-accessible hydrophobicity shows a negative linear correlation the two variables ($r(93) = -0.88$, $p < 0.001$), which is expected as the calculations of the measures are related through the ratio of residue-specific solvent-accessible areas in folded and unfolded states. **(b)** A scatter plot of core solvent-accessible surface area per layer and core hydrophobicity does not show a significant correlation between these structural features. Structural models used to illustrate the plotted measures in Fig. 5.3e are also labelled in this figure, along with the RIPK1/3 heteroamyloid (PDB ID 5v7z). Pathogenic, functional and LCD amyloids are shown as yellow, blue, and green circles, respectively.

5.4.4 Low-complexity domain-containing amyloids have larger protofilament interface areas compared to pathogenic amyloids

The interface areas between protofilaments and between individual β-sheet forming β-strands were calculated for all structural models in order to detect differences between pathogenic, functional and LCD categorised amyloids, and determine whether these features may convey properties corresponding to the biological consequences of these amyloids. A relative interface area score was calculated for each amyloid structural model, taking into account differences in cross-sectional area, which affects the potential to form protofilament and β-sheet interfaces. The interface area measurements are illustrated in Fig. 5.5d on fibril structural models with the highest and lowest relative β-sheet and protofilament interface areas.

Analysis of the interface areas revealed that a LCDs are more prone to high interface areas relative to size compared to other amyloids (**Fig. 5.5c**) and where protofilament interfaces form, they are on average 230.7 % larger compared to the protofilament interfaces of pathogenic amyloids ($p < 0.001$), whereas no significant difference was observed for the relative β-sheet interface area between LCDs and pathogenic amyloids. On the other hand, functional amyloids were determined to have on average 47.4 % less relative β-sheet area compared to pathogenic amyloids ($p = 0.026$).

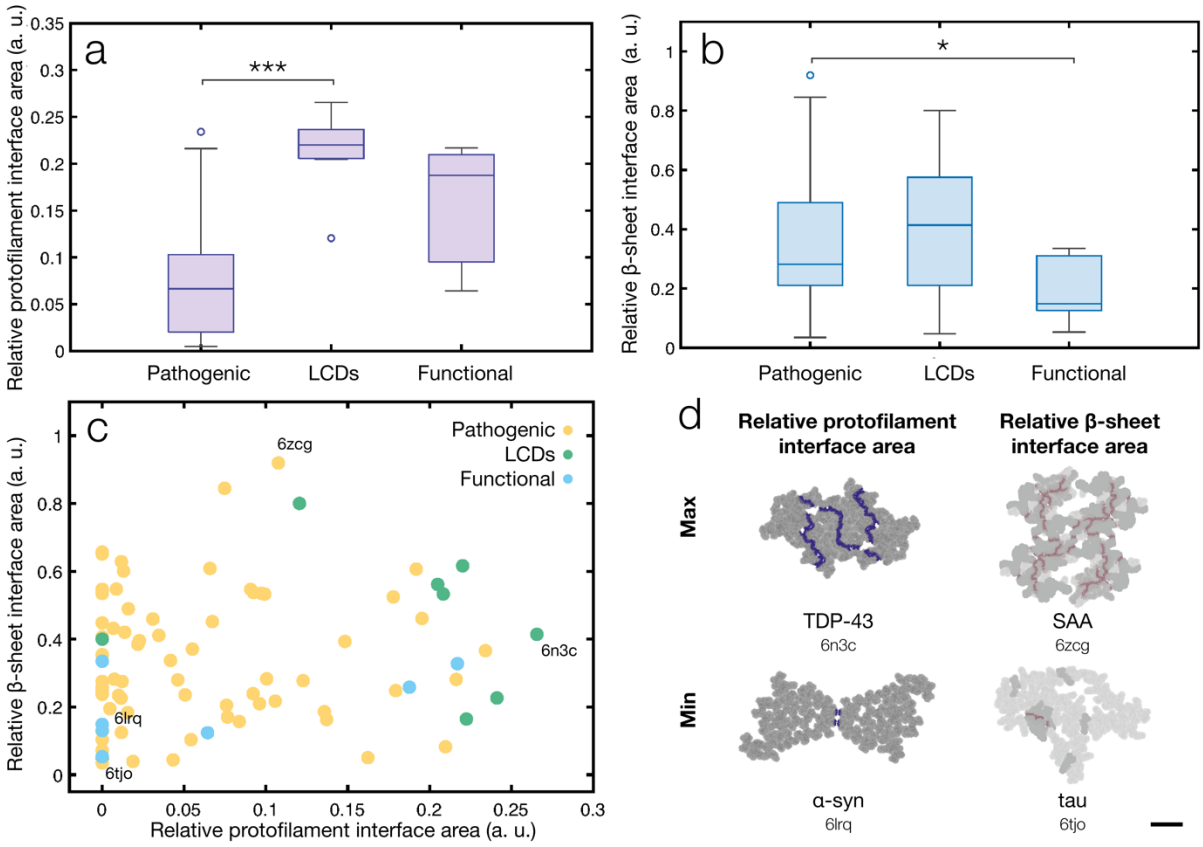

Figure 5.5 Protofilament and β-sheet interface area analysis between pathogenic, functional, and LCD amyloids. **(a)** Protofilament interface areas relative to the total cross-sectional areas of the fibrils. LCDs have significantly higher relative protofilament interface areas compared to pathogenic amyloids. **(b)** β-sheet interface areas relative to the total cross-sectional areas of the fibrils showing a significant difference between functional and pathogenic amyloid fibril structural models. * and *** denote significance at or below the 0.05 and 0.001 levels, respectively. **(c)** A scatter plot of relative protofilament and β-sheet interface areas further shows the differences in interface areas between groups but does not show a significant correlation between relative protofilament and β-sheet interface areas. Pathogenic, functional and LCD amyloids are shown as yellow, blue, and green circles, respectively. **(d)** Illustrations of the calculated parameters on amyloid fibril structural models with the highest and lowest relative protofilament and β-sheet interface areas. Protofilament and β-sheet interfaces are shown in purple and pink, respectively. For β-sheet interface illustrations, β-sheet regions are shown in darker grey and intervening residues are shown in lighter grey. For protofilament interface illustrations, all residues not at the interface are shown in dark grey. The four structural models used for illustrations are also labelled in (c). All models are scaled equally and scale bar in bottom right corner represents 2 nm.

5.4.5 Principal component analysis of structural features reveals differential extent of polymorphism between amyloid proteins

Structural features of amyloid models calculated in comparisons between pathogenic, functional, and LCD amyloids were then used in a principal component analysis (PCA), in order to determine whether visualisation by dimensionality-reduction will lead to grouping of structural models by either the assigned biological categories or by some other additional property. Parameters used for principal component analysis included the unique amino acid ratio, β-sheet content, total SASA per layer, fold compactness, core hydrophobicity, solvent-exposed hydrophobicity, as well as relative protofilament and β-sheet interface areas.

Principal component analysis of all amyloid models highlighted the large degree of variation resulting from the diversity of fibril structures and the polymorphism between amyloid forming even from the same or near-identical amino acid sequences. Visualisation of the multivariate data by dimensionality reduction and plotting of the first two principal components did not indicate clustering of the data based on the calculate parameters and the biological assigned groups of pathogenic, functional and LCD amyloids (**Fig. 5.6a**). However, PCA of the structural features of just tau amyloid fibril models and coloured grouping by sample origin did show large differences between the heparin-induced *in vitro* formed fibrils and fibrils extracted from *ex vivo* patient brain tissue (**Fig. 5.6b**). This was also accompanied by a relatively higher percentage of explained variance of the first two principal components for tau fibrils, as compared to all fibril models or α-synuclein models only. On the other hand, PCA of α-synuclein fibrils, coloured by sample origin as *ex vivo* extracted from multiple system atrophy (MSA) patient brain tissue or self-assembled *in vitro* from wild-type, N-terminally acetylated, or familial mutation-carrying sequences, did not show the same extent of

discrepancies between analysed structural features of *ex vivo* and *in vitro* formed fibrils as tau (**Fig. 5.6c**). This suggests that depending on the amyloid protein and assembly conditions, *in vitro* formed fibrils can differ in the extent of similarity compared to *ex vivo* extracted fibrils.

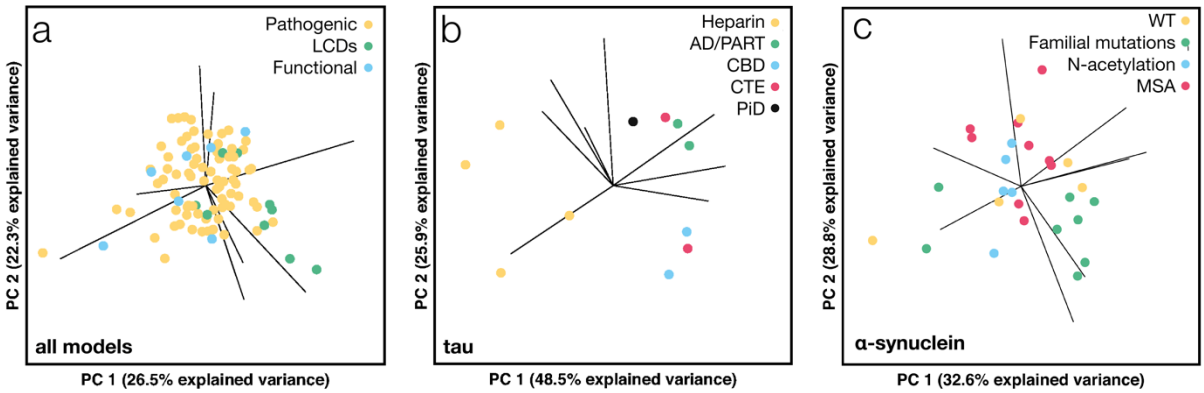

Figure 5.6 Principal component analysis of amyloid fibril model structural features shows the differential variation of structural features across amyloid proteins. **(a)** PCA of all analysed structural models, coloured by assigned biological categories, i.e. pathogenic, functional and LCD-containing amyloids. **(b)** PCA of tau fibril structures coloured by sample origin, which include *in vitro* assembled heparin-induced tau, as well as *ex vivo* fibrils extracted from tissue of patients with Alzheimer's disease (AD), primary age-related tauopathy (PART), corticobasal degeneration (CBD), chronic traumatic encephalopathy (CTE), Pick's disease (PiD). **(c)** PCA of α-synuclein fibril structural models, coloured by sample origin, including *ex vivo* extracted fibrils structures from multiple system atrophy (MSA) patient brain tissue, as well as *in vitro* formed wild-type (WT) fibrils, N-terminally acetylated fibrils, and fibrils with familial mutations. PC – principal component.

5.5 DISCUSSION

Amyloid fibrils exhibit extensive structural diversity and polymorphism despite sharing the same characteristic cross-β architecture, reflected by a wide range of biological activities from pathogenic effects to functional roles. Recent advances in structural biology techniques have led to the elucidation of amyloid core structures at sufficient resolutions to regularly allow

elucidation of amyloid fibril structures and atomic model building. The PDB and EMDB databases contain models of mostly pathogenic amyloid, but the addition of functional and reversible models facilitates development of hypotheses about the structural features that may convey different biological effects. In this study, a systematic meta-analysis of structural features across all deposited models revealed specific differences for low complexity domain-containing and functional amyloids as compared to pathogenic amyloids. It was found that LCDs have on average more hydrophilic solvent-accessible surfaces and interior core regions, as well as larger protofilament interfaces compared to pathogenic amyloids. In contrast, functional amyloids did not share these significant differences compared to pathogenic amyloids, but instead had less total solvent-accessible surface area per layer and only approximately half as extensive β-sheet areas.

Solvent-accessible hydrophobicity was on average significantly lower in LCDs compared to pathogenic amyloids. Hydrophobic surfaces could potentially lead to nonspecific interactions and sequestering of essential biomolecules in biological contexts or be more favourable for secondary nucleation by promoting unfolding or misfolding of monomer through hydrophobic interactions. However, residues which appear solvent-exposed in structural models may be shielded by flexible flanking regions which are absent from the models or may otherwise be inaccessible due to variations in the twist pattern or interactions with other macromolecules. Therefore, the calculated solvent-accessibility of the residues may reflect the solution conditions of the protein less well than the core hydrophobicity measure, which relies on distance from the helical axis and varies less as the structural biology tools used are better suited to resolve the rigid core about which the fibril twists than the dynamic regions that may surround it. The interior of the fibril core was also more hydrophilic for LCD amyloid models compared to those of pathogenic amyloids, which could result in lower thermodynamic

stability and facilitate reversible assemblies. Further techniques for distinguishing different types of stability will also be important for an improved understanding of amyloid structural characteristics. While thermodynamic stability could be a significant determinant for the reversibility, related features like mechanical stability or protease resistance could also be responsible for some of the observed differences in amyloid structure and function. For example, it is possible that lowered mechanical stability could lead to brittle fibrils with an increased fragmentation rate, which can result in increased cytotoxicity (W.-F. Xue, Hellewell, et al., 2009) and prion-like spread (Marchante et al., 2017). In cellular contexts, surface features which favour interactions with chaperones that lead to the formation of small seeds (Wentink et al., 2020) could likewise also have a similar effect.

Interestingly, an anti-parallel β-sheet structural model of Aβ (PDB ID 2lnq) had the highest solvent-exposed hydrophobicity score out of all analysed models, approximately 1.5 times higher than the median for pathogenic amyloids. Anti-parallel arrangements have previously been observed for Aβ oligomers, typically associated with higher cytotoxicity (Cerf et al., 2009). However, the functional RIPK1/3 heteroamyloid also had a high solvent-exposed hydrophobicity score at 0.8 times higher than the median score due to the alternating packing arrangement of monomer layers, and is not associated with toxic aggregation, indicating that the toxic effects of Aβ anti-parallel structures might not be mediated by this specific feature.

Surprisingly, LCDs also had on average 2.3 times larger protofilament interface areas relative to size compared to pathogenic amyloids, which would be expected to have a large stabilising effect on the structures. The lower intramolecular interactions in the low-complexity aromatic rich kinked segments (LARKS) motif of LCDs resulting from the kinking of the backbone (Hughes et al., 2021) thus here appears to be compensated by larger intermolecular interactions

between protofilament. It is possible that low number of unique residues allows the formation of tight complementary interfaces between protofilaments, thus speeding up aggregation kinetics and lowering the concentration of oligomeric species with potential cytotoxic effects. Furthermore, the median relative β-sheet interface area was the highest for LCDs. Although the difference was not statistically significant, it would instead be expected that these fibril models characterised as LARKS would have comparatively less β-sheet interface area due to a lack of dry steric zippers which is associated with pathogenic amyloids. Surprisingly, functional amyloids did not on average significantly differ in the solvent-exposed or core hydrophobicity measures. However, they did have nearly a fifth less total exposed surface area per layer, indicating that they are simply smaller than pathogenic amyloids and had nearly half as little β-sheet interface areas relative to size. A key feature of functional amyloids may be rapid aggregation kinetics which minimises the population of toxic oligomeric intermediates (Dear et al., 2020). Thus, smaller fibrils with less surface area could be favoured for functional amyloids compared to larger amyloids composed of several protofilaments, potentially changing the kinetic rates of aggregation towards favouring rapid elongation.

The meta-analysis is limited by the dataset available from the PDB and EMDB and the uneven sample sizes for the different categories. Although pathogenic amyloid structures are critical for the development of aggregation inhibiting therapeutics against amyloid-associated systemic neurodegenerative diseases, for the purposes of a comparative meta-analysis the reduced dataset available for reversible LCDs and functional amyloid limits the power of the study. The growing number of available amyloid fibril structural models with different biological effects in the PDB and EMDB databases will facilitate the use of these and other structural parameters in order to elucidate the relationship between amyloid structure and function.

5.6 METHODS

5.6.1 Atomic coordinate pre-processing

Atomic coordinates and accompanying metadata were obtained from the PDB for amyloid fibril structures with available atomic coordinates. Models formed from short peptide fragments of less than 12 amino acids were excluded as they do not represent the properties of the full-length proteins or larger protein fragments from which the fibrils form under physiological conditions. Models with added anti-amyloid compounds or dyes were also excluded. In cases where several models were deposited based on the analysis of the same NMR data, the most recent submission was chosen. Where alternative conformations were available for residues, the first conformation provided was used. Similarly, for depositions of an ensemble of models the first model was used as a representative. Where NMR models with both left- and right-handed twist were available from the same collected data, the left-handed twisted model was selected for calculation of structural parameters, and the twist information for that fibril was not included in the statistics on fibril handedness. Where only a cryo-EM density map was available, but no atomic model, volumetric density maps were downloaded from the EMDB and where several EM density maps of the same structure have been deposited, the one with the highest resolution was chosen. Where multiple PDB models were built into the same density, the first one was selected as a representative. The map recommended isovalue, helical rise, twist, and handedness were obtained from the information in the EMDB metadata. Data from both the PDB and the EMDB were imported into Matlab where all subsequent processing and analysis was carried out.

For cryo-EM density maps, the iso-surface of a density map was found by applying the isovalue provided by the authors. Where necessary, the density maps were denoised by finding the nearest neighbours of all iso-surface vertices and subsequently applying a threshold value to remove vertices with a significantly larger mean distance from neighbours. The number of nearest neighbours and the threshold were changed according to the noise level of each map by manual inspection. Maps were further denoised by finding the alpha shape of the iso-surface using an alpha radius of twice the voxel size of the EM density map, while suppressing holes and retaining only the vertices that belong to the largest single region of the isosurface. Finally, atomic model coordinates or iso-surface vertices were rotated and translated, where necessary, so that the long fibril axis runs along the z-axis, and then used in downstream analyses. Atomic model coordinates were analysed in sphere representation where the radius of atoms correspond to their Van der Waals radii, with surface sampling density of ~15 dots/Å^2.

5.6.2 Alignment of the fibril screw-axis

The position of the fibril screw-axis was estimated by iterative optimisation of rotation and translation parameters. For structures where cryo-EM density maps were available, the map iso-surfaces were used, as these are typically longer along the fibril axis compared to the corresponding PDB models, thus increasing the accuracy of the screw-axis parameter estimation. The objective function for finding the rotation and translation parameters consisted of maximising the overlap between the isosurface and the same isosurface translated and rotated about the z-axis by applying the helical rise and twist values from the EMDB entry of each density map. The rotational and translational parameters determined for screw-axis alignment from the density maps were then also used to align the corresponding PDB coordinates. In the case of ssNMR structures, helical twist values were not available and thus

the PDB coordinates were used to estimate both the screw-axis position, as well as the degree of helical twist, by iterative optimisation of rotation and translation parameters by minimising the standard deviation of twist angles and z-distances calculated between identical atoms in different layers of the fibril, relative to the screw-axis. Depending on the map features, rotation and translation were optimised jointly or either one was initially optimised separately for an initial estimate, followed by joint optimisation of all four parameters.

5.6.3 Determination of fibril symmetry and handedness

The symmetry along the fibril axis was found from accompanying publications or, if not discussed, assigned by visual inspection of the structures as asymmetric (C1), or having C2, 2_1, or C3 helical symmetries. In cases where resolution limitations did not enable distinguishing between C2 and 2_1 symmetry, general 2-fold rotational symmetry was marked as C2/2_1. Fibril handedness was determined from the sign of the twist values provided in the EMDB experimental metadata, or from the calculated mean twist values between identical atoms in different layers, for ssNMR structures. Where the sign of the twist value did not agree with visual inspection of map handedness, or maps of both left- and right-handed fibrils were deposited from analysis of the same data, no handedness value was assigned.

5.6.4 Calculation of fibril cross-sectional dimensions and area

The sizes and shapes of amyloid fibril structural models were analysed from a single repeating unit of the model. For most models the repeating unit is equivalent to a single layer of the fibril, whereas for hetero-amyloid (PDB IDs 6ti6, 6ti7, 5v7z), anti-parallel models (PDB IDs 2lnq, 6nzn), and a model where the monomer forms two consecutive layers of β-strands (PDB ID

2kj3), the repeating unit is composed of two layers. To calculate the cross-sectional area, A_{2D}, the solvent-exposed cross-sections of the atomic coordinates were found by tracing the coordinates with a sphere with the radius of 0.14 nm, an approximate radius of a water molecule, while suppressing holes and retaining only the coordinates that belong to the largest single region. Where only a density map was available, the iso-surfaces were first de-rotated about the helical axis by the corresponding twist and rise values, and a sphere with a radius of four times the voxel size was used for tracing, to account for differences in resolution between these density maps. The area and perimeter, P, of the cross-sections were then calculated. To measure cross-sectional dimensions, distances from the cross-sectional boundary to the helical axis were then found for a 360° rotation of the cross-section with 1° spacing, from which maximum and minimum distances, d_{max} and d_{min}, respectively, were found. Fibril cross-sectional shape was then analysed by measures of circularity (**Eq. 5.1**) and eccentricity (**Eq. 5.2**), which were calculated from the described cross-sectional parameters.

$$Circularity = \frac{4\pi A_{2D}}{P^2} \qquad \textbf{Eq. 5.1}$$

$$Eccentricity = \frac{\sqrt{d_{max}^2 - d_{min}^2}}{d_{max}} \qquad \textbf{Eq. 5.2}$$

5.6.5 Amino acid sequence analysis

Amino acid sequences of amyloid fibril core regions were analysed from single repeating units of atomic coordinates accessed from the PDB. The β-sheet content was found as a percentage of the number of residues annotated with a β-sheet secondary structure in the PDB metadata, n_β, compared to the total number of residues in the repeating units, n (**Eq. 5.3**).

$$\beta\text{-}sheet\ content\ (\%) = \frac{n_\beta}{n} \qquad \textbf{Eq. 5.3}$$

The unique amino acid ratio was then calculated from the total number of unique amino acid residues per repeating unit, n_{unique}, as shown in Eq. 5.4.

$$unique\ AA\ ratio = \frac{n_{unique}}{l} \qquad \textbf{Eq. 5.4}$$

Where $l = 20$ if $n \geq 20$, otherwise $l = n$, in order to account for differences in sequence length.

5.6.6 Calculation of solvent-accessible surface area

Solvent-accessible surface area was found for each individual residue of a repeating unit of the fibril atomic model in the folded and unfolded states, as well as for individual chains and β-sheets for the calculation of interface areas. The same process for calculating the SASA was carried out in all cases by first finding the solvent-excluded surface by tracing the input coordinates with a sphere with the radius of 0.14 nm, approximating a water molecule. The solvent-accessible surface was then found by translating the solvent-excluded surface coordinates 0.14 nm in the direction of their surface normals. Finally, SASA was calculated from the triangulation of the solvent-accessible surface coordinates.

5.6.7 Calculation of SASA and fold compactness

SASA per layer was calculated from the repeating units of PDB model atomic coordinates in sphere representation. Residue-specific solvent-accessible surface area was found by first extending the axis-aligned coordinates of a repeating unit by five additional units in both directions along the fibril axis by rotation and translation using the helical twist and rise values corresponding to each fibril, in order to simulate intermolecular contacts within a fibril. The

SASA of each residue i in the middle layer of the extended fibril, $SASA\ folded_i$, was then found as described above. SASA in the unfolded state was found by calculating the residue-specific SASA from the coordinates of each residue and the main chain atoms of adjacent residues, only. Total SASA per layer was then calculated as the sum of the residue-specific folded surface areas divided by the unfolded surface areas, in order to control for differences in the amino acid sequence (**Eq. 5.5**).

$$SASA = \sum_{i=1}^{n} \frac{SASA\ folded_i}{SASA\ unfolded_i} \qquad \textbf{Eq. 5.5}$$

Where the repeating unit consisted of two layers, the total SASA was divided by two. Fibril fold compactness was then found as a complement of the ratio of the summed SASAs in the folded and unfolded states across all residues of a repeating unit (**Eq. 5.6**).

$$fold\ compactness = 1 - \frac{\sum_{i=1}^{n} SASA\ folded_i}{\sum_{i=1}^{n} SASA\ unfolded_i} \qquad \textbf{Eq. 5.6}$$

5.6.8 Solvent-exposed and core hydrophobicity measures

The core hydrophobicity measure was calculated from the repeating units of PDB model atomic coordinates in sphere representation, which were first extended by five units in both directions along the fibril axis in order to simulate intermolecular contacts within the fibril. The residue-specific distances from the position of the helical axis to the solvent-excluded surface, d_i, were then found. In order to relate distance from screw-axis and hydrophobicity, the Kyte-Doolittle hydrophobicity scale of amino acids (Kyte & Doolittle, 1982) was scaled to a range of 0.1 to 1 and used to find the hydrophobicity corresponding to each residue in the repeating unit, h_i. The core hydrophobicity measure, CH, was finally calculated as the negative slope of the linear regression predictor that predicts hydrophobicity from distance to the helical axis (**Eq. 5.7**).

$$CH = -\frac{\sum_{i=1}^{n}(d_i - \bar{d})(h_i - \bar{h})}{\sum_{i=1}^{n}(d_i - \bar{d})^2} \quad \textbf{Eq. 5.7}$$

The solvent-exposed hydrophobicity, SEH, was then calculated as an averaged measure of residue-specific solvent-accessibility and hydrophobicity (**Eq. 5.8**).

$$SEH = \frac{\sum_{i=1}^{n}\left(h_i \frac{SASA\ folded_i}{SASA\ unfolded_i}\right)}{n} \quad \textbf{Eq. 5.8}$$

5.6.9 Surface area of protofilament interfaces

The total surface area of protofilament interfaces per layer, $A_{PF\ interface}$, was calculated from the repeating units of PDB model atomic coordinates in sphere representation, where each chain corresponds to a layer of an individual protofilament. Chain-specific solvent-accessible surface area was found by first extending the axis-aligned coordinates of a repeating unit by five additional units in both directions of the fibril axis by rotation and translation using the helical twist and rise values corresponding to each fibril, in order to simulate intermolecular contacts within a fibril. The surface area of the protofilament interface was calculated pairwise from the unique combinations of chains in the set of all chains, C. Each individual protofilament interface area was first calculated from the solvent-accessible surface areas of isolated and interfacing protofilament chains (**Eq. 5.9**).

$$A_{PF\ interface}(a, b) = \frac{SASA_a + SASA_b - SASA_{ab}}{2} \quad \textbf{Eq. 5.9}$$

The total interface surface area was then found as the sum of all interfaces between pairs of chains, further accounting for the total size of the model by dividing by the 2D cross-sectional area (**Eq. 5.10**).

$$A_{PF\ interface} = \frac{\sum_{\{j,k\}\in C}^{j<k} A_{interface}(C_j, C_k)}{A_{2D}} \quad \textbf{Eq. 5.10}$$

Where the repeating unit consisted of two layers, the protofilament interface area was calculated for each layer separately and averaged.

5.6.10 Surface area of β-sheet interfaces

The total surface area of β-sheet interfaces interface per layer, $A_{\beta\text{-sheet interface}}$, was calculated from the repeating units of PDB model atomic coordinates in sphere representation. Continuous regions of β-sheets, B, within the structure were identified from accompanying β-sheet annotations. Where models had different β-sheet assignments for different layers, the layer with the highest total β-sheet composition was used. The interface areas were calculated pairwise for all possible unique combinations of β-sheets and the total β-sheet interface area of a structure was found as the sum of all β-sheet interface areas relative to the 2D cross-sectional area (**Eq. 5.11**).

$$A_{\beta\text{-sheet interface}} = \frac{\sum_{\substack{j<k \\ \{j,k\}\in B}} A_{interface}(B_j, B_k)}{A_{2D}} \qquad \textbf{Eq. 5.11}$$

Where the repeating unit consisted of two layers, the protofilament interface area was calculated for each layer separately and averaged.

5.6.11 Statistical comparison of means

Statistical testing of calculated parameters between groups was carried out in SPSS. Welch's one-way ANOVA was used to test for multiple pair-wise comparisons without assuming equal variance, using the α level of 0.05. To correct for the effect of multiple comparisons, Games-Howell post-hoc testing was carried out, again allowing for unequal variances between groups.

SUPPLEMENTARY DATA

Table 5.1 Quantitative analysis of structural features from models of amyloid fibrils deposited to the PDB and EMDB up to August 2021. Entries are sorted alphabetically by name of the protein monomer and further by release date. Values are missing where atomic coordinate information was not available. Where not specified, units are arbitrary. The following abbreviations are used: *sym* – symmetry, *hnd* – handedness, #PF – number of protofilaments, A_{2D} – cross-sectional area, *circ* – circularity, *ecc* – eccentricity, *SAH* – solvent-accessible hydrophobicity, *CH* – core hydrophobicity, SASA – solvent-accessible surface area, PF – protofilament, *cat* – category, L – left-handed, R – right-handed, P – pathogenic, LCD – low-complexity domain-containing, F – functional.

	Protein	PDB/ EMDB ID	*sym*	*hnd*	#PF	A_{2D} (nm^2)	*circ*	*ecc*	β-sheet (%)	*SAH*	*CH*	SASA per layer (nm^2)	Fold compact-ness	Relative PF interface area	Relative β-sheet interface area	*cat*	Release date
1	$A\beta_{40}$	6w0o	2_1	L	2	19.6	0.28	0.98	61.3	0.09	0.42	10.27	0.83	0.23	0.37	P	13/01/2021
2	$A\beta_{40}$	6ti5	C2	L	2	19.2	0.40	0.85	66.7	0.09	0.49	10.70	0.82	0.12	0.28	P	22/07/2020
3	$A\beta_{40}$	4864	2_1	R	-	63.0	0.51	0.91	-	-	-	-	-	-	-	P	06/11/2019
4	$A\beta_{40}$	4866	2_1	R	-	106.9	0.47	0.95	-	-	-	-	-	-	-	P	06/11/2019
5	$A\beta_{40}$	6shs	2_1	R	2	27.0	0.38	0.97	43.8	0.11	0.22	16.51	0.80	0.08	0.17	P	06/11/2019
6	$A\beta_{40}$	6oc9	2_1	L	2	19.8	0.34	0.98	36.3	0.08	0.64	11.51	0.86	0.09	0.54	P	05/06/2019
7	$A\beta_{40}$	6328	$C2/2_1$	L	-	71.5	0.43	0.98	-	-	-	-	-	-	-	P	29/04/2015
8	$A\beta_{40}$	2mpz	C3	R	3	26.8	0.53	0.80	53.8	0.09	0.66	13.46	0.82	0.14	0.19	P	22/04/2015
9	$A\beta_{40}$	2mvx	C2	L	2	23.4	0.60	0.89	30.8	0.05	0.68	8.97	0.88	0.21	0.08	P	26/11/2014
10	$A\beta_{40}$	2m4j	C3	R	3	40.0	0.37	0.85	15.0	0.08	0.65	19.46	0.83	0.16	0.05	P	25/09/2013
11	$A\beta_{40}$	2lnq	C1	R	2	9.4	0.54	0.97	46.2	0.22	0.55	8.59	0.66	0.00	0.25	P	08/02/2012
12	$A\beta_{40}$	2lmn	C2	-	2	18.0	0.21	0.92	32.8	0.11	0.63	12.67	0.80	0.10	0.21	P	28/12/2011

Table 5.1 Continued.

13	$A\beta_{40}$	2lmq	C3	-	3	30.5	0.31	0.89	46.9	0.11	0.56	19.52	0.79	0.06	0.00	P	28/12/2011
14	$A\beta_{40}$	5008	$C2/2_1$	L	-	48.1	0.27	1.00	-	-	-	-	-	-	-	P	08/10/2009
15	$A\beta_{40}$	1650	$C2/2_1$	L	-	65.6	0.74	0.92	-	-	-	-	-	-	-	P	24/09/2009
16	$A\beta_{40/42}$	6ti6	C2	L	2	20.3	0.38	0.96	51.6	0.10	0.44	11.67	0.80	0.19	0.61	P	22/07/2020
17	$A\beta_{40/42}$	6ti7	C2	L	2	20.2	0.36	0.96	60.5	0.10	0.41	11.20	0.81	0.18	0.52	P	22/07/2020
18	$A\beta_{42}$	5oqv	2_1	L	2	27.2	0.45	0.91	71.4	0.05	0.60	10.81	0.87	0.08	0.20	P	13/09/2017
19	$A\beta_{42}$	2nao	C2	L	2	23.5	0.25	0.96	23.8	0.07	0.39	11.94	0.86	0.08	0.00	P	27/07/2016
20	$A\beta_{42}$	5kk3	2_1	L	2	17.5	0.48	0.88	40.6	0.07	0.53	8.52	0.87	0.15	0.39	P	13/07/2016
21	$A\beta_{42}$	5aef	$C2/2_1$	L	2	17.0	0.26	0.97	53.6	0.15	0.39	13.75	0.75	0.04	0.04	P	26/08/2015
22	$A\beta_{42}$	2mxu	C1	L	1	10.2	0.53	0.91	68.8	0.11	0.54	6.27	0.81	0.00	0.24	P	06/05/2015
23	$A\beta_{42}$	5052	$C2/2_1$	L	-	28.1	0.84	0.75	-	-	-	-	-	-	-	P	07/07/2010
24	$A\beta_{42}$	2beg	C1	L	1	8.3	0.57	0.94	76.9	0.13	-0.08	4.83	0.81	0.00	0.10	P	22/11/2005
25	α-syn	7c1d	2_1	R	2	27.6	0.24	0.93	3.9	0.10	0.24	19.50	0.79	0.06	0.00	P	05/05/2021
26	α-syn	7nca	C2	L	2	43.0	0.35	0.93	59.0	0.08	0.28	19.40	0.83	0.01	0.43	P	24/02/2021
27	α-syn	7ncg	C2	L	2	39.2	0.21	1.00	63.9	0.08	0.16	20.44	0.82	0.00	0.41	P	24/02/2021
28	α-syn	7nch	C2	L	2	42.0	0.42	0.92	37.5	0.07	0.31	18.71	0.85	0.01	0.23	P	24/02/2021
29	α-syn	7nci	C2	L	2	37.4	0.19	0.76	28.7	0.07	0.17	18.32	0.85	0.00	0.13	P	24/02/2021
30	α-syn	7ncj	C1	L	2	37.1	0.21	0.99	45.0	0.07	0.16	17.81	0.85	0.01	0.42	P	24/02/2021
31	α-syn	7nck	C1	L	1	19.1	0.44	0.99	64.1	0.07	0.27	8.47	0.86	0.00	0.65	P	24/02/2021
32	α-syn	6l1t	2_1	L	2	58.7	0.19	1.00	44.4	0.10	0.15	37.33	0.80	0.01	0.28	P	12/08/2020
33	α-syn	6l1u	C1	L	3	87.7	0.13	0.99	50.5	0.10	0.12	56.75	0.80	0.01	0.28	P	12/08/2020
34	α-syn	6l4s	2_1	R	2	31.3	0.28	0.95	29.1	0.08	0.35	18.80	0.81	0.08	0.16	P	29/04/2020
35	α-syn	6lrq	2_1	L	2	37.1	0.22	1.00	49.2	0.12	0.00	27.39	0.77	0.00	0.19	P	08/04/2020
36	α-syn	6ufr	C2	L	2	39.1	0.31	0.93	76.2	0.11	0.31	26.89	0.78	0.02	0.49	P	19/02/2020
37	α-syn	6xyo	C1	L	2	47.0	0.29	0.98	68.8	0.08	0.15	25.76	0.82	0.09	0.55	P	12/02/2020
38	α-syn	6xyp	C1	L	2	42.6	0.28	1.00	46.2	0.09	0.08	26.38	0.80	0.09	0.24	P	12/02/2020

Table 5.1 Continued.

39	α-syn	6xyq	C1	L	2	42.6	0.30	0.99	48.3	0.09	0.11	25.19	0.81	0.10	0.28	P	12/02/2020
40	α-syn	6sst	2_1	L	2	39.7	0.17	1.00	65.8	0.09	0.09	26.88	0.80	0.01	0.60	P	18/12/2019
41	α-syn	6ssx	C2	L	2	42.4	0.25	0.96	71.2	0.09	0.24	25.56	0.81	0.01	0.63	P	18/12/2019
42	α-syn	6peo	C1	L	1	18.1	0.38	0.93	78.1	0.11	0.28	13.36	0.79	0.00	0.55	P	27/11/2019
43	α-syn	6pes	C1	L	2	33.6	0.25	0.99	73.7	0.10	0.04	22.81	0.80	0.01	0.55	P	27/11/2019
44	α-syn	6osj	2_1	L	2	35.0	0.21	0.96	44.3	0.09	0.21	20.96	0.81	0.06	0.37	P	25/09/2019
45	α-syn	6osl	2_1	L	2	34.5	0.28	0.92	55.1	0.08	0.34	19.99	0.81	0.07	0.61	P	25/09/2019
46	α-syn	6osm	2_1	L	2	35.9	0.34	0.89	27.5	0.11	0.17	23.52	0.79	0.05	0.10	P	25/09/2019
47	α-syn	6cu7	2_1	L	2	35.8	0.23	0.96	48.3	0.09	0.29	21.47	0.80	0.05	0.24	P	12/09/2018
48	α-syn	6cu8	2_1	L	2	24.7	0.23	0.95	19.5	0.09	0.41	16.14	0.78	0.09	0.00	P	12/09/2018
49	α-syn	6h6b	2_1	L	2	34.7	0.31	0.90	44.8	0.08	0.11	16.14	0.85	0.07	0.45	P	08/08/2018
50	α-syn	6a6b	2_1	L	2	36.2	0.20	0.97	31.7	0.09	0.24	21.45	0.81	0.05	0.28	P	11/07/2018
51	α-syn	2n0a	C1	R	1	31.5	0.17	0.99	32.9	0.07	0.25	19.68	0.85	0.00	0.25	P	23/03/2016
52	α-syn	6482	C1	R	-	56.3	0.80	0.83	-	-	-	-	-	-	-	P	16/12/2015
53	β-endorphin	6tub	C1	L	1	9.1	0.51	0.97	25.8	0.06	0.30	4.72	0.84	0.00	0.13	F	28/10/2020
54	β2m	0019	C1	-	-	98.5	0.25	1.00	-	-	-	-	-	-	-	P	19/06/2019
55	β2m	0021	C1	-	-	25.2	0.22	0.87	-	-	-	-	-	-	-	P	29/05/2019
56	β2m	6gk3	C2	L	2	42.7	0.18	0.99	51.6	0.08	0.17	25.54	0.79	0.01	0.23	P	14/11/2018
57	β2m	2e8d	C1	R	1	6.1	0.41	0.96	54.5	0.11	0.16	4.37	0.81	0.00	0.35	P	13/02/2007
58	CA150	2nnt	C1	R	1	9.4	0.46	0.97	61.3	0.07	-0.17	4.78	0.84	0.00	0.66	P	14/11/2006
59	FUS	6xfm	2_1	L	2	23.7	0.53	0.89	61.5	0.05	-0.09	10.26	0.87	0.22	0.62	LCD	07/10/2020
60	glucagon	6nzn	C2	L	2	23.3	0.41	0.98	93.1	0.10	-0.07	12.85	0.77	0.22	0.33	F	05/06/2019
61	HET-s	2946	C1	L	-	21.6	0.91	0.75	-	-	-	-	-	-	-	F	15/04/2015
62	HET-s	2kj3	C1	L	1	13.8	0.40	0.93	44.3	0.07	0.33	7.04	0.80	0.00	0.15	F	02/06/2010
63	hnRNPA1	7bx7	2_1	L	2	22.9	0.41	0.88	37.8	0.06	-0.13	12.62	0.86	0.21	0.53	LCD	18/11/2020
64	hnRNPA2	6wqk	C1	L	1	14.9	0.38	0.97	22.8	0.05	0.10	7.62	0.85	0.00	0.05	LCD	26/08/2020

Table 5.1 Continued.

65	IAPP	6zrf	2_1	L	2	13.2	0.27	0.94	58.3	0.14	0.25	11.55	0.75	0.10	0.53	P	30/09/2020
66	IAPP	6zrq	2_1	L	2	12.8	0.45	0.98	59.1	0.10	0.49	7.72	0.82	0.03	0.46	P	30/09/2020
67	IAPP	6zrr	C1	L	3	20.0	0.46	0.99	56.1	0.10	0.12	11.33	0.82	0.10	0.53	P	30/09/2020
68	IAPP	6vw2	$C2/2_1$	L	2	14.0	0.39	0.95	45.8	0.09	0.19	8.15	0.81	0.18	0.25	P	10/06/2020
69	IAPP	10670	2_1	L	-	11.7	0.44	0.97	-	-	-	-	-	-	-	P	04/03/2020
70	IAPP	10671	2_1	L	-	40.5	0.28	1.00	-	-	-	-	-	-	-	P	04/03/2020
71	IAPP	6y1a	2_1	R	2	14.7	0.51	0.88	48.0	0.11	0.26	9.38	0.81	0.11	0.22	P	04/03/2020
72	IG LC	6z1i	C1	L	1	25.5	0.40	0.97	59.3	0.08	-0.07	11.93	0.85	0.00	0.53	P	24/02/2021
73	IG LC	6z1o	C1	L	1	27.8	0.39	0.99	59.6	0.07	-0.06	12.68	0.85	0.00	0.54	P	24/02/2021
74	IG LC	6ic3	C1	R	1	28.2	0.34	0.99	18.7	0.09	0.14	16.61	0.81	0.00	0.00	P	03/04/2019
75	IG LC	6hud	C1	L	1	24.3	0.40	0.99	67.5	0.10	0.10	16.17	0.79	0.00	0.27	P	27/03/2019
76	Orb2	6vps	C3	L	3	31.2	0.34	0.87	74.2	0.04	-0.16	11.08	0.88	0.12	0.80	LCD	18/03/2020
77	PI3K	6r4r	2_1	L	2	48.6	0.42	0.91	53.2	0.06	-0.11	21.32	0.86	0.06	0.12	F	28/08/2019
78	PrP	6lni	2_1	L	2	40.0	0.20	0.99	45.0	0.08	0.28	24.04	0.80	0.02	0.04	P	10/06/2020
79	PrP	6uur	2_1	L	2	22.8	0.44	0.92	57.5	0.07	0.42	11.57	0.83	0.20	0.46	P	15/04/2020
80	RIPK1/3	5v7z	C1	R	2	13.4	0.41	0.96	57.6	0.16	0.48	9.54	0.68	0.19	0.26	F	28/03/2018
81	RIPK3	7dac	C1	L	1	8.5	0.34	0.97	58.6	0.09	0.52	5.89	0.78	0.00	0.33	F	28/04/2021
82	RIPK3	6jpd	C1	L	1	6.4	0.37	1.00	23.8	0.11	0.01	4.71	0.76	0.00	0.05	F	28/10/2020
83	SAA	6zcf	2_1	L	2	23.9	0.38	0.95	73.0	0.08	0.00	12.95	0.83	0.07	0.84	P	17/02/2021
84	SAA	6zcg	C2	L	4	50.4	0.34	0.88	73.0	0.08	0.05	23.58	0.84	0.11	0.92	P	17/02/2021
85	SAA	6zch	C1	L	3	62.5	0.17	0.98	56.5	0.05	0.20	29.86	0.85	0.02	0.40	P	17/02/2021
86	SAA	6dso	2_1	L	2	41.5	0.48	6.4	43.5	0.05	0.23	20.0	0.85	0.72	0.80	P	13/03/2019
87	SAA	6mst	2_1	R	2	33.0	0.39	0.81	40.7	0.05	0.16	14.29	0.86	0.14	0.16	P	13/03/2019
88	tau	7nrq	2_1	L	2	47.1	0.16	0.98	46.8	0.06	0.06	24.54	0.83	0.04	0.34	P	24/03/2021
89	tau	7nrs	C1	L	2	46.6	0.14	1.00	58.4	0.06	0.09	25.95	0.82	0.02	0.38	P	24/03/2021
90	tau	6tjx	C2	L	2	74.2	0.20	1.00	40.2	0.09	0.07	44.86	0.78	0.01	0.12	P	05/02/2020

Table 5.1 Continued.

91	tau	6nwp	2_1	L	2	46.4	0.13	0.99	66.7	0.07	0.06	25.85	0.82	0.03	0.41	P	27/03/2019
92	tau	6nwq	2_1	L	2	47.8	0.16	0.97	28.0	0.08	0.03	27.69	0.80	0.05	0.00	P	27/03/2019
93	tau	6qjh	C1	L	1	18.0	0.27	0.75	54.2	0.11	0.01	13.50	0.76	0.00	0.26	P	20/02/2019
94	tau	6qjm	C1	L	1	12.0	0.33	0.95	59.5	0.14	0.03	9.71	0.73	0.00	0.07	P	20/02/2019
95	tau	6qjp	C1	L	1	11.3	0.33	0.69	71.4	0.12	0.26	8.70	0.74	0.00	0.35	P	20/02/2019
96	tau	6qjq	C1	L	2	17.9	0.28	0.66	57.4	0.11	0.34	12.21	0.76	0.22	0.28	P	20/02/2019
97	tau	0078	C2	L	-	97.4	0.38	0.99	-	-	-	-	-	-	-	P	12/09/2018
98	tau	6gx5	C1	L	1	29.1	0.22	1.00	64.9	0.08	0.10	17.86	0.80	0.00	0.45	P	12/09/2018
99	tau	6tjo	C1	L	1	36.4	0.35	0.98	15.9	0.09	0.06	22.49	0.78	0.00	0.03	P	05/02/2020
100	TDP-43	7kwz	C1	L	1	36.2	0.34	0.98	43.2	0.06	0.21	19.53	0.85	0.00	0.40	LCD	24/02/2021
101	TDP-43	6n37	2_1	L	2	21.0	0.42	0.91	33.3	0.10	0.17	13.58	0.81	0.22	0.16	LCD	26/06/2019
102	TDP-43	6n3a	2_1	L	4	33.4	0.29	0.96	58.3	0.07	0.07	17.53	0.86	0.20	0.56	LCD	26/06/2019
103	TDP-43	6n3b	C1	L	2	22.3	0.46	0.92	41.6	0.10	0.23	14.00	0.82	0.24	0.23	LCD	26/06/2019
104	TDP-43	6n3c	2_1	L	4	32.6	0.38	0.93	39.1	0.05	0.05	15.93	0.87	0.27	0.41	LCD	26/06/2019
105	TTR	6sdz	C1	L	1	29.3	0.54	0.88	51.1	0.08	0.15	14.25	0.84	0.00	0.24	P	13/11/2019

Chapter 6: Conclusions

Protein self-assembly into the amyloid state and the resulting structural polymorphism presents a considerable challenge to both our fundamental understanding of amyloid and their roles in physiological and pathogenic contexts, as well as the development of self-assembly modulators with potential therapeutic effects for the many amyloid-associated neurodegenerative diseases. In the work carried out as part of this thesis, chemical conjugation techniques, biophysical imaging methods, and computational analysis were used to investigate the polymorphic nature of amyloid fibrils.

In Chapter 2, two amyloid-DNA conjugation strategies were employed in order to modulate the self-assembly process, with the aim of reducing the prion-like spread of amyloid between cells, as well as directing the formation of amyloid-based nanomaterials. For both strategies the Sup35NM yeast prion protein fragment was used as a model system, with additional modifications to facilitate thiol-maleimide-based chemical conjugation to DNA with an attached maleimide linker. In the first strategy, reversible cross-linking of amyloid-conjugated complementary DNA strands was explored, and SDS-PAGE analysis of the reaction mixture indicated that the conjugation product had successfully formed. In the second strategy, a nucleobase analogue was conjugated to the modified Sup35NM protein in order to direct the amyloid self-assembly into modular building blocks with defined dimensions. Different reaction conditions were tested, and mass spectrometry results suggested that the amyloid-nucleobase analogue product had also formed. Further optimisation of the reaction conditions could improve conjugation efficiency, which would facilitate further characterisation of the amyloid-DNA conjugates and enable testing of the effects of their self-assembly when doped into unmodified Sup35NM protein monomer in *in vitro* and *in vivo* assays. In order to investigate whether the modified and unmodified monomer are capable of templated elongation, kinetic and morphological characterisation was carried out by a time course assay

with the fluorescent dye ThT and by imaging of the samples using atomic force microscopy. These analyses indicated that the modified and unmodified Sup35NM monomers interact, leading to changes in the kinetic profiles and fibril morphologies, although further characterisation is necessary to establish whether cross-elongation occurs.

In Chapter 3 it was shown that the convolution imaging artefact of atomic force microscopy topographs, which results from tip-sample interactions and has been a limiting factor for the use of AFM as a single molecule imaging technique, can be corrected via an iterative algorithm in which tip-sample contact points are recovered. This approach was demonstrated to be applicable to any surface and was further shown to result in approximate doubling of lateral local resolution on concave surface features, as well as correcting for the convolution effect. Furthermore, deconvolution of AFM images facilitates the 3D reconstruction of surface envelopes of samples with helical symmetry, which was demonstrated on polymorphic hexapeptide amyloid fibrils. These developed post-acquisition deconvolution and reconstruction algorithms facilitate the use of AFM as a single molecule technique and offer further potential for applications to investigate amyloid fibril polymorphism, as well as advance AFM data analysis methods. For example, the correction and 3D reconstruction approach allow more parameters to be determined from amyloid fibril samples, including cross-sectional shape, size, fibril symmetry and the position of screw axis. Due to the high signal-to-noise ratio of AFM topographs, this 3D information can be collected from hundreds of individual fibrils in a sample at low-nanometre resolution. This results in an enhanced, single molecule depiction of amyloid polymorphism. This approach was further applied to determine the effect on primary amino acid sequence on fibril polymorphism via analysis of three different hexapeptide fibril samples, showing a differential extent of polymorphism in samples formed from monomers of different sequences (Aubrey et al., 2020).

In Chapter 4 the deconvolution and 3D reconstruction approach developed to analyse amyloid fibril structural data from AFM images was extended to include integration of information from other structural biology techniques. Recently both cryo-EM and ssNMR methods have led to the elucidation of numerous amyloid fibril structures with resolutions which allow atomic models to be built through ensemble-averaging processes (Sawaya et al., 2021). The high-resolution molecular model data are complementary to the single molecule 3D envelope reconstructions developed here in Chapter 3. Thus, the workflow for analysing amyloid fibrils from AFM images was extended to include a comparative morphometrics approach with other available structural data. This integrated approach was demonstrated on AFM data of a dGAE tau amyloid fibril, a fragment of the tau protein containing the residues 297-391, which is capable of forming fibrils *in vitro* without the addition of anionic co-factors such as heparin (Al-Hilaly et al., 2020). Tau amyloid fibrils formed in the presence of heparin have been widely used to assemble tau *in vitro* for further biochemical and cellular studies (Goedert et al., 1996) but are structurally very different from fibrils from brain tissue of patients with various tauopathies (Shi et al., 2021; W. Zhang et al., 2019). 3D envelopes from AFM images of dGAE tau fibrils were compared by various parametrised features, including cross-sectional shape and size, periodicity, symmetry, and position of screw-axis, as well as a direct comparison of the dGAE image data and simulated AFM images from cryo-EM density-derived maps of tau fibrils. The comparative morphometrics approach demonstrated that dGAE fibrils are unambiguously different from fibrils formed *in vitro* in the presence of heparin and are instead most similar to paired helical filaments from Alzheimer's disease brain tissue, as well as type II filaments from chronic traumatic encephalopathy brain tissue. The integration of amyloid fibril data from AFM and cryo-EM methods thus reveals dGAE as a more physiological model system of *in vitro* formed tau fibrils, compared to heparin-induced tau amyloid, and highlights

the advantages of integrating methods based on different physical principles for the study of amyloid polymorphism.

In Chapter 5 of this thesis, a computational meta-analysis of amyloid fibril structural models determined by cryo-EM and ssNMR and deposited to the PDB or EMDB up to August 2021 was carried out in order to determine specific structural features that may mediate the different biological effects of amyloid, ranging from pathogenic to essential for physiological functioning. Specific structural features were calculated across all amyloids with available structural models, revealing significant differences between amyloids which were categorised as pathogenic, functional, and low-complexity domain-containing (LCDs). LCDs have on average significantly more hydrophilic solvent-accessible surfaces and core folds, as well as slightly smaller and more compact folds, compared to pathogenic amyloids. Furthermore, LCDs were found to have more than three times as large protofilament interfaces. Interestingly, similar differences were not seen for functional amyloids, which instead were on average smaller than pathogenic amyloids, and contained only nearly half as extensive β-sheet interface interfaces. These findings highlight that amyloids with different biological effects have different propensities towards forming structures with characteristics such as solvent-accessible or core hydrophobicity, as well as interface areas, which may modulate the different *in vivo* biological responses through affecting fibril stability or interactions with other biomolecules. In future revisions to this manuscript, additional parameters and further structural information on functional and LCD-containing amyloids could enhance the power of analysis.

6.1 SUMMARY OF MAJOR FINDINGS

- SDS-PAGE and mass spectrometry data suggest that the modified yeast prion Sup35NM was here successfully conjugated to complementary DNA strands, as well as a nucleobase analogue, via thiol-maleimide reactions. These amyloid-DNA conjugates can be further developed to test the *in vivo* effect of limiting the spread of the prion phenotype, as well as to design modular nanomaterials.

- The convolution imaging artefact on atomic force microscopy topographs can be corrected by identifying tip-sample contact points, thus facilitating the use of AFM as a single molecule imaging technique. Samples with helical symmetry can then be reconstructed as 3D envelopes from the AFM images, as demonstrated on scans of polymorphic hexapeptide amyloid fibrils. The deconvolution and reconstruction approach facilitate further single molecule studies of amyloid population diversity and polymorphism.

- The deconvoluted and 3D modelled fibril data from AFM topographs can be integrated with data collected with other structural biology techniques, including cryo-EM and ssNMR, which provide high resolution molecular models. An integrated approach to AFM and cryo-EM data using comparative morphometrics was demonstrated on a fibril sample of dGAE tau. A representative dGAE fibril was shown to be unambiguously different from heparin-induced *in vitro* assembled tau fibril structural models and most similar to PHFs from AD, highlighting dGAE as a physiological model system for *in vitro* self-assembled tau amyloid filaments.

- The structural data of amyloid fibrils deposited to the PDB and EMDB up to August 2021 determined by cryo-EM and ssNMR were used in a systematic computational meta-analysis of structural features between samples of different biological roles. Amyloid formed from proteins containing low-complexity domains have on average more hydrophilic surfaces and core interiors, as well as larger protofilament interfaces, compared to pathogenic amyloid proteins. On the other hand, functional amyloids are on average smaller and contain less β-sheet interfaces, compared to pathogenic amyloids.

6.2 FUTURE PERSPECTIVES

The chemical conjugation and biophysical data analysis algorithms developed here to investigate the polymorphic nature of amyloid fibrils offer various possibilities for future advances, including modulating the transmission of the amyloid state via amyloid-DNA conjugates, developing modular nanomaterials, investigating polymorphic amyloid populations on an individual fibril level, as well as further developments in computational methods towards advancing the use of AFM as a single molecule imaging technique. For example, the amyloid-DNA conjugated using the Sup35NM protein with attached complementary ssDNA strands could be tested for *in vivo* effects in yeast endogenously expressing the unmodified monomer to investigate whether this strategy could prevent the spread of the prion phenotype between cells and change the biological response. In addition, the nucleobase analogue strategy could be used to direct the self-assembly of amyloid into specific modular building blocks. Further DNA origami-based strategies could then be used to formed hybrid nanomaterials with a desired shape and size.

The developed deconvolution and 3D reconstruction workflow of AFM image analysis can be further applied to amyloid fibril datasets formed while systematically varying conditions during self-assembly, which would allow changes to the population polymorphism to be determined, thus providing an indirect measure of how the self-assembly energy landscape changes as a function of specific parameters. For example, fibrils can be formed in various buffer conditions to determine the effect of specific environmental parameters on the polymorphism of amyloid fibril populations. Similarly, time-course experiments could be carried out to investigate the polymorphic landscape of the fibril maturation process, which is broadly thought include increased lateral associations between protofilaments, but specific

changes are currently not well characterised. Furthermore, the effects of various other biomolecules with relevant roles in neurodegenerative diseases, such as chaperones, metal ions, and surfaces, on the fibril population polymorphism could also be determined on a single molecule level. The mapping of the polymorphic landscape could also be further combined with the comparative morphometrics approach, integrating AFM and cryo-EM or ssNMR data, and applied towards datasets from *ex vivo* patient brain tissue to investigate the fibril population on a single molecule level and determine which polymorphs are represented by the high resolution cryo-EM reconstructions. Thus, the deconvolution and 3D reconstruction workflow developed here offers a potential for a wide variety of experiments which allow the effects of many different variables on amyloid fibril self-assembly landscape to be assessed which will further our fundamental understanding of amyloid polymorphism.

The developed deconvolution and 3D reconstruction workflow of AFM image analysis could further be extended to incorporate 3D reconstruction of biomolecules with any symmetry as the 3D information the information content is present in the topographs, and the challenge lies in finding the rotational and translational alignments between particles. Although averaging would be required, similarly to cryo-EM and ssNMR techniques, the comparatively higher signal-to-noise ratio of AFM topographs would lead to a significantly smaller number of particles required for reconstruction thus bringing AFM 3D envelope reconstruction closer to a true single particle method, which could thus provide information complementary to other structural biology techniques. For example, as AFM allows the collection of biophysical parameters in addition to surface topographs properties such as stiffness of the sample or the strength of its chemical interactions with a functionalised probe, which could be additionally collected and mapped onto the 3D surface envelope reconstructions, thus potentially leading to multi-dimensional particle information on biomolecules with any symmetry.

Finally, the manuscript draft on meta-analysis of amyloid fibril structural features from atomic models deposited to the PDB and EMDB will be extended to further consider the different parameters of sample origins, for example whether the sample was formed *in vitro* or was extracted *ex vivo* from tissue, or whether the sample self-assembly was seeded, in order to yield further insights into the different biological properties. Additional structural features will also be explored, including extent of kinking of the protein backbone.

In conclusion, the developed chemical conjugation and biophysical analysis workflows offer potential for further advances towards modulating amyloid polymorphism, elucidating how polymorphism results from amyloid self-assembly, and what are its biological consequences.

BIBLIOGRAPHY

Abraham, R. S., Geyer, S. M., Price-Troska, T. L., Allmer, C., Kyle, R. A., Gertz, M. A., & Fonseca, R. (2003). Immunoglobulin light chain variable (V) region genes influence clinical presentation and outcome in light chain–associated amyloidosis (AL). *Blood*, *101*(10), 3801–3807. https://doi.org/10.1182/blood-2002-09-2707

Adamcik, J., Jung, J.-M., Flakowski, J., De Los Rios, P., Dietler, G., & Mezzenga, R. (2010). Understanding amyloid aggregation by statistical analysis of atomic force microscopy images. *Nature Nanotechnology*, *5*(6), 423–428. https://doi.org/10.1038/nnano.2010.59

Adamcik, J., & Mezzenga, R. (2012). Study of amyloid fibrils via atomic force microscopy. *Current Opinion in Colloid & Interface Science*, *17*(6), 369–376. https://doi.org/10.1016/j.cocis.2012.08.001

Adamcik, J., & Mezzenga, R. (2018). Amyloid polymorphism in the protein folding and aggregation energy landscape. *Angewandte Chemie International Edition*, *57*(28), 8370–8382. https://doi.org/10.1002/anie.201713416

Alberti, S., & Hyman, A. A. (2021). Biomolecular condensates at the nexus of cellular stress, protein aggregation disease and ageing. *Nature Reviews Molecular Cell Biology*, 1–18. https://doi.org/10.1038/s41580-020-00326-6

Al-Hilaly, Y. K., Foster, B. E., Biasetti, L., Lutter, L., Pollack, S. J., Rickard, J. E., Storey, J. M. D., Harrington, C. R., Xue, W.-F., Wischik, C. M., & Serpell, L. C. (2020). Tau (297-391) forms filaments that structurally mimic the core of paired helical filaments in Alzheimer's disease brain. *FEBS Letters*, *594*(5), 944–950. https://doi.org/10.1002/1873-3468.13675

Amar, F., Sherman, M. A., Rush, T., Larson, M., Boyle, G., Chang, L., Götz, J., Buisson, A., & Lesné, S. E. (2017). The amyloid-β oligomer Aβ*56 induces specific alterations in neuronal signaling that lead to tau phosphorylation and aggregation. *Science Signaling*, *10*(478), eaal2021. https://doi.org/10.1126/scisignal.aal2021

Ambadipudi, S., Biernat, J., Riedel, D., Mandelkow, E., & Zweckstetter, M. (2017). Liquid–liquid phase separation of the microtubule-binding repeats of the Alzheimer-related protein Tau. *Nature Communications*, *8*(1), 275. https://doi.org/10.1038/s41467-017-00480-0

Anfinsen, C. B. (1973). Principles that govern the folding of protein chains. *Science*, *181*(4096), 223–230. https://doi.org/10.1126/science.181.4096.223

Annamalai, K., Gührs, K.-H., Koehler, R., Schmidt, M., Michel, H., Loos, C., Gaffney, P. M., Sigurdson, C. J., Hegenbart, U., Schönland, S., & Fändrich, M. (2016). Polymorphism of amyloid fibrils *in vivo*. *Angewandte Chemie International Edition*, *55*(15), 4822–4825. https://doi.org/10.1002/anie.201511524

Aprile, F. A., Källstig, E., Limorenko, G., Vendruscolo, M., Ron, D., & Hansen, C. (2017). The molecular chaperones DNAJB6 and Hsp70 cooperate to suppress α-synuclein aggregation. *Scientific Reports*, *7*(1), 9039. https://doi.org/10.1038/s41598-017-08324-z

Arakhamia, T., Lee, C. E., Carlomagno, Y., Duong, D. M., Kundinger, S. R., Wang, K., Williams, D., DeTure, M., Dickson, D. W., Cook, C. N., Seyfried, N. T., Petrucelli, L., & Fitzpatrick, A. W. P. (2020). Posttranslational modifications mediate the structural diversity of tauopathy strains. *Cell*, *180*(4), 633-644.e12. https://doi.org/10.1016/j.cell.2020.01.027

Ares, P., Fuentes-Perez, M. E., Herrero-Galán, E., Valpuesta, J. M., Gil, A., Gomez-Herrero, J., & Moreno-Herrero, F. (2016). High resolution atomic force microscopy of double-stranded RNA. *Nanoscale*, *8*(23), 11818–11826. https://doi.org/10.1039/c5nr07445b

Armiento, V., Spanopoulou, A., & Kapurniotu, A. (2020). Peptide-based molecular strategies to interfere with protein misfolding, aggregation, and cell degeneration. *Angewandte Chemie International Edition*, *59*(9), 3372–3384. https://doi.org/10.1002/anie.201906908

Arosio, P., Knowles, T. P. J., & Linse, S. (2015). On the lag phase in amyloid fibril formation. *Physical Chemistry Chemical Physics*, *17*(12), 7606–7618. https://doi.org/10.1039/C4CP05563B

Arrasate, M., Mitra, S., Schweitzer, E. S., Segal, M. R., & Finkbeiner, S. (2004). Inclusion body formation reduces levels of mutant huntingtin and the risk of neuronal death. *Nature*, *431*(7010), 805–810. https://doi.org/10.1038/nature02998

Atarashi, R., Sim, V. L., Nishida, N., Caughey, B., & Katamine, S. (2006). Prion strain-dependent differences in conversion of mutant prion proteins in cell culture. *Journal of Virology*, *80*(16), 7854–7862. https://doi.org/10.1128/JVI.00424-06

Aubrey, L. D., Blakeman, B. J. F., Lutter, L., Serpell, C. J., Tuite, M. F., Serpell, L. C., & Xue, W.-F. (2020). Quantification of amyloid fibril polymorphism by nano-morphometry reveals the individuality of filament assembly. *Communications Chemistry*, *3*(1), 1–10. https://doi.org/10.1038/s42004-020-00372-3

Bai, Y., Olivier, J.-H., Bullard, G., Liu, C., & Therien, M. J. (2018). Dynamics of charged excitons in electronically and morphologically homogeneous single-walled carbon nanotubes. *Proceedings of the National Academy of Sciences*, *115*(4), 674–679. https://doi.org/10.1073/pnas.1712971115

Bansal, A., Schmidt, M., Rennegarbe, M., Haupt, C., Liberta, F., Stecher, S., Puscalau-Girtu, I., Biedermann, A., & Fändrich, M. (2021). AA amyloid fibrils from diseased tissue are structurally different from *in vitro* formed SAA fibrils. *Nature Communications*, *12*(1), 1013. https://doi.org/10.1038/s41467-021-21129-z

Bateman, D. A., & Wickner, R. B. (2013). The [*PSI*$^{+}$] prion exists as a dynamic cloud of variants. *PLOS Genetics*, *9*(1), e1003257. https://doi.org/10.1371/journal.pgen.1003257

Beal, D. M., Tournus, M., Marchante, R., Purton, T. J., Smith, D. P., Tuite, M. F., Doumic, M., & Xue, W.-F. (2020). The division of amyloid fibrils: Systematic comparison of fibril fragmentation stability by linking theory with experiments. *IScience*, *23*(9), 101512. https://doi.org/10.1016/j.isci.2020.101512

Bernstein, J. (2007). *Polymorphism in molecular crystals*. Oxford University Press. https://www.oxfordscholarship.com/view/10.1093/acprof:oso/9780199236565.001.0001/acprof-9780199236565

Berson, J. F., Theos, A. C., Harper, D. C., Tenza, D., Raposo, G., & Marks, M. S. (2003). Proprotein convertase cleavage liberates a fibrillogenic fragment of a resident glycoprotein to initiate melanosome biogenesis. *The Journal of Cell Biology*, *161*(3), 521–533. https://doi.org/10.1083/jcb.200302072

Biancardi, A., Biver, T., & Mennucci, B. (2017). Fluorescent dyes in the context of DNA-binding: The case of Thioflavin T. *International Journal of Quantum Chemistry*, *117*(8), e25349. https://doi.org/10.1002/qua.25349

Billings, L. M., Oddo, S., Green, K. N., McGaugh, J. L., & LaFerla, F. M. (2005). Intraneuronal Aβ causes the onset of early Alzheimer's disease-related cognitive deficits in transgenic mice. *Neuron*, *45*(5), 675–688. https://doi.org/10.1016/j.neuron.2005.01.040

Binnig, G., Quate, C. F., & Gerber, Ch. (1986). Atomic force microscope. *Physical Review Letters*, *56*(9), 930–933. https://doi.org/10.1103/PhysRevLett.56.930

Biogen. (2021). *A phase 3 multicenter, randomized, double-blind, placebo-controlled, parallel-group study to evaluate the efficacy and safety of aducanumab (BIIB037) in subjects with early Alzheimer's disease* (Clinical Trial Registration No. NCT02477800). clinicaltrials.gov. https://clinicaltrials.gov/ct2/show/NCT02477800

Biverstål, H., Kumar, R., Schellhaus, A. K., Sarr, M., Dantuma, N. P., Abelein, A., & Johansson, J. (2020). Functionalization of amyloid fibrils via the Bri2 BRICHOS domain. *Scientific Reports*, *10*(1), 21765. https://doi.org/10.1038/s41598-020-78732-1

Blancas-Mejia, L. M., Misra, P., Dick, C. J., Cooper, S. A., Redhage, K. R., Bergman, M. R., Jordan, T. L., Maar, K., & Ramirez-Alvarado, M. (2018). Immunoglobulin light chain amyloid aggregation. *Chemical Communications (Cambridge, England)*, *54*(76), 10664–10674. https://doi.org/10.1039/c8cc04396e

Blancas-Mejía, L. M., Misra, P., & Ramirez-Alvarado, M. (2017). Differences in protein concentration dependence for nucleation and elongation in light chain amyloid formation. *Biochemistry*, *56*(5), 757–766. https://doi.org/10.1021/acs.biochem.6b01043

Bode, D. C., Baker, M. D., & Viles, J. H. (2017). Ion channel formation by amyloid-β_{42} oligomers but not amyloid-β_{40} in cellular membranes. *Journal of Biological Chemistry*, *292*(4), 1404–1413. https://doi.org/10.1074/jbc.M116.762526

Bolisetty, S., & Mezzenga, R. (2016). Amyloid–carbon hybrid membranes for universal water purification. *Nature Nanotechnology*, *11*(4), 365–371. https://doi.org/10.1038/nnano.2015.310

Bose, K., Lech, C. J., Heddi, B., & Phan, A. T. (2018). High-resolution AFM structure of DNA G-wires in aqueous solution. *Nature Communications*, *9*. https://doi.org/10.1038/s41467-018-04016-y

Boyer, D. R., Li, B., Sun, C., Fan, W., Sawaya, M. R., Jiang, L., & Eisenberg, D. S. (2019). Structures of fibrils formed by α-synuclein hereditary disease mutant H50Q reveal new polymorphs. *Nature Structural & Molecular Biology*, *26*(11), 1044–1052. https://doi.org/10.1038/s41594-019-0322-y

Boyer, D. R., Li, B., Sun, C., Fan, W., Zhou, K., Hughes, M. P., Sawaya, M. R., Jiang, L., & Eisenberg, D. S. (2020). The α-synuclein hereditary mutation E46K unlocks a more stable, pathogenic fibril structure. *Proceedings of the National Academy of Sciences*, *117*(7), 3592–3602. https://doi.org/10.1073/pnas.1917914117

Brettschneider, J., Tredici, K. D., Lee, V. M.-Y., & Trojanowski, J. Q. (2015). Spreading of pathology in neurodegenerative diseases: A focus on human studies. *Nature Reviews Neuroscience*, *16*(2), 109–120. https://doi.org/10.1038/nrn3887

Breydo, L., Kurouski, D., Rasool, S., Milton, S., Wu, J. W., Uversky, V. N., Lednev, I. K., & Glabe, C. G. (2016). Structural differences between amyloid beta oligomers. *Biochemical and Biophysical Research Communications*, *477*(4), 700–705. https://doi.org/10.1016/j.bbrc.2016.06.122

Breydo, L., & Uversky, V. N. (2015). Structural, morphological, and functional diversity of amyloid oligomers. *FEBS Letters*, *589*(19, Part A), 2640–2648. https://doi.org/10.1016/j.febslet.2015.07.013

Bruce, M. E., McConnell, I., Fraser, H., & Dickinson, A. G. (1991). The disease characteristics of different strains of scrapie in *Sinc* congenic mouse lines: Implications for the nature of the agent and host control of pathogenesis. *The Journal of General Virology*, *72 (Pt 3)*, 595–603. https://doi.org/10.1099/0022-1317-72-3-595

Bucciantini, M., Giannoni, E., Chiti, F., Baroni, F., Formigli, L., Zurdo, J., Taddei, N., Ramponi, G., Dobson, C. M., & Stefani, M. (2002). Inherent toxicity of aggregates implies a common mechanism for protein misfolding diseases. *Nature*, *416*(6880), 507–511. https://doi.org/10.1038/416507a

Buell, A. K., Dhulesia, A., White, D. A., Knowles, T. P. J., Dobson, C. M., & Welland, M. E. (2012). Detailed analysis of the energy barriers for amyloid fibril growth. *Angewandte Chemie International Edition*, *51*(21), 5247–5251. https://doi.org/10.1002/anie.201108040

Buell, A. K., Galvagnion, C., Gaspar, R., Sparr, E., Vendruscolo, M., Knowles, T. P. J., Linse, S., & Dobson, C. M. (2014). Solution conditions determine the relative importance of nucleation and growth processes in α-synuclein aggregation. *Proceedings of the National Academy of Sciences of the United States of America*, *111*(21), 7671–7676. https://doi.org/10.1073/pnas.1315346111

Bulawa, C. E., Connelly, S., DeVit, M., Wang, L., Weigel, C., Fleming, J. A., Packman, J., Powers, E. T., Wiseman, R. L., Foss, T. R., Wilson, I. A., Kelly, J. W., & Labaudinière, R. (2012). Tafamidis, a potent and selective transthyretin kinetic stabilizer that inhibits the amyloid cascade. *Proceedings of the National Academy of Sciences*, *109*(24), 9629–9634. https://doi.org/10.1073/pnas.1121005109

Burdukiewicz, M., Sobczyk, P., Rödiger, S., Duda-Madej, A., Mackiewicz, P., & Kotulska, M. (2017). Amyloidogenic motifs revealed by n-gram analysis. *Scientific Reports*, *7*(1), 12961. https://doi.org/10.1038/s41598-017-13210-9

Burgold, S., Filser, S., Dorostkar, M. M., Schmidt, B., & Herms, J. (2014). *In vivo* imaging reveals sigmoidal growth kinetic of β-amyloid plaques. *Acta Neuropathologica Communications*, *2*, 30. https://doi.org/10.1186/2051-5960-2-30

Burré, J. (2015). The synaptic function of α-synuclein. *Journal of Parkinson's Disease*, *5*(4), 699–713. https://doi.org/10.3233/JPD-150642

Butt, H.-J., & Jaschke, M. (1995). Calculation of thermal noise in atomic force microscopy. *Nanotechnology*, *6*(1), 1–7. https://doi.org/10.1088/0957-4484/6/1/001

Butterfield, S. M., & Lashuel, H. A. (2010). Amyloidogenic protein–membrane interactions: Mechanistic insight from model systems. *Angewandte Chemie International Edition*, *49*(33), 5628–5654. https://doi.org/10.1002/anie.200906670

Campioni, S., Carret, G., Jordens, S., Nicoud, L., Mezzenga, R., & Riek, R. (2014). The presence of an air–water interface affects formation and elongation of α-synuclein fibrils. *Journal of the American Chemical Society*, *136*(7), 2866–2875. https://doi.org/10.1021/ja412105t

Campioni, S., Mannini, B., Zampagni, M., Pensalfini, A., Parrini, C., Evangelisti, E., Relini, A., Stefani, M., Dobson, C. M., Cecchi, C., & Chiti, F. (2010). A causative link between the structure of aberrant protein oligomers and their toxicity. *Nature Chemical Biology*, *6*(2), 140–147. https://doi.org/10.1038/nchembio.283

Canet-Ferrer, J., Coronado, E., Forment-Aliaga, A., & Pinilla-Cienfuegos, E. (2014). Correction of the tip convolution effects in the imaging of nanostructures studied through scanning force microscopy. *Nanotechnology*, *25*(39), 395703. https://doi.org/10.1088/0957-4484/25/39/395703

Cao, Q., Boyer, D. R., Sawaya, M. R., Ge, P., & Eisenberg, D. S. (2019). Cryo-EM structures of four polymorphic TDP-43 amyloid cores. *Nature Structural & Molecular Biology*, *26*(7), 619–627. https://doi.org/10.1038/s41594-019-0248-4

Cao, Q., Boyer, D. R., Sawaya, M. R., Ge, P., & Eisenberg, D. S. (2020). Cryo-EM structure and inhibitor design of human IAPP (amylin) fibrils. *Nature Structural & Molecular Biology*, *27*(7), 653–659. https://doi.org/10.1038/s41594-020-0435-3

Carulla, N., Caddy, G. L., Hall, D. R., Zurdo, J., Gairí, M., Feliz, M., Giralt, E., Robinson, C. V., & Dobson, C. M. (2005). Molecular recycling within amyloid fibrils. *Nature*, *436*(7050), 554–558. https://doi.org/10.1038/nature03986

Cerf, E., Sarroukh, R., Tamamizu-Kato, S., Breydo, L., Derclaye, S., Dufrêne, Y. F., Narayanaswami, V., Goormaghtigh, E., Ruysschaert, J.-M., & Raussens, V. (2009). Antiparallel β-sheet: A signature structure of the oligomeric amyloid β-peptide. *The Biochemical Journal*, *421*(3), 415–423. https://doi.org/10.1042/BJ20090379

Cerofolini, L., Ravera, E., Bologna, S., Wiglenda, T., Böddrich, A., Purfürst, B., Benilova, I., Korsak, M., Gallo, G., Rizzo, D., Gonnelli, L., Fragai, M., Strooper, B. D., Wanker, E. E., & Luchinat, C. (2020). Mixing Aβ(1–40) and Aβ(1–42) peptides generates unique amyloid fibrils. *Chemical Communications*, *56*(62), 8830–8833. https://doi.org/10.1039/D0CC02463E

Chen, G., Abelein, A., Nilsson, H. E., Leppert, A., Andrade-Talavera, Y., Tambaro, S., Hemmingsson, L., Roshan, F., Landreh, M., Biverstål, H., Koeck, P. J. B., Presto, J., Hebert, H., Fisahn, A., & Johansson, J. (2017). Bri2 BRICHOS client specificity and chaperone activity are governed by assembly state. *Nature Communications*, *8*(1), 2081. https://doi.org/10.1038/s41467-017-02056-4

Chen, J., & Seeman, N. C. (1991). Synthesis from DNA of a molecule with the connectivity of a cube. *Nature*, *350*(6319), 631–633. https://doi.org/10.1038/350631a0

Chen, S. W., Drakulic, S., Deas, E., Ouberai, M., Aprile, F. A., Arranz, R., Ness, S., Roodveldt, C., Guilliams, T., De-Genst, E. J., Klenerman, D., Wood, N. W., Knowles, T. P. J., Alfonso, C., Rivas, G., Abramov, A. Y., Valpuesta, J. M., Dobson, C. M., & Cremades, N. (2015). Structural characterization of toxic oligomers that are kinetically trapped during α-synuclein fibril formation. *Proceedings of the National*

Academy of Sciences, *112*(16), E1994–E2003. https://doi.org/10.1073/pnas.1421204112

Chen, Y., Radford, S. E., & Brockwell, D. J. (2015). Force-induced remodelling of proteins and their complexes. *Current Opinion in Structural Biology*, *30*, 89–99. https://doi.org/10.1016/j.sbi.2015.02.001

Chen, Y., Sun, W., Yang, C., & Zhu, Z. (2020). Scaling up DNA self-assembly. *ACS Applied Bio Materials*, *3*(5), 2805–2815. https://doi.org/10.1021/acsabm.0c00035

Cheng, Y., Zhu, B., Deng, Y., & Zhang, Z. (2015). *In vivo* detection of cerebral amyloid fibrils with smart dicynomethylene-4H-pyran-based fluorescence probe. *Analytical Chemistry*, *87*(9), 4781–4787. https://doi.org/10.1021/acs.analchem.5b00017

Chernoff, Y. O., Lindquist, S. L., Ono, B., Inge-Vechtomov, S. G., & Liebman, S. W. (1995). Role of the chaperone protein Hsp104 in propagation of the yeast prion-like factor [*psi*$^{+}$]. *Science (New York, N.Y.)*, *268*(5212), 880–884. https://doi.org/10.1126/science.7754373

Chi, E. Y., Frey, S. L., Winans, A., Lam, K. L. H., Kjaer, K., Majewski, J., & Lee, K. Y. C. (2010). Amyloid-β fibrillogenesis seeded by interface-induced peptide misfolding and self-assembly. *Biophysical Journal*, *98*(10), 2299. https://doi.org/10.1016/j.bpj.2010.01.056

Chidchob, P., & Sleiman, H. F. (2018). Recent advances in DNA nanotechnology. *Current Opinion in Chemical Biology*, *46*, 63–70. https://doi.org/10.1016/j.cbpa.2018.04.012

Chiti, F., & Dobson, C. M. (2006). Protein misfolding, functional amyloid, and human disease. *Annual Review of Biochemistry*, *75*, 333–366. https://doi.org/10.1146/annurev.biochem.75.101304.123901

Chiti, F., & Dobson, C. M. (2009). Amyloid formation by globular proteins under native conditions. *Nature Chemical Biology*, *5*(1), 15–22. https://doi.org/10.1038/nchembio.131

Chiti, F., & Dobson, C. M. (2017). Protein misfolding, amyloid formation, and human disease: A summary of progress over the last decade. *Annual Review of Biochemistry*, *86*(1), 27–68. https://doi.org/10.1146/annurev-biochem-061516-045115

Chiti, F., Webster, P., Taddei, N., Clark, A., Stefani, M., Ramponi, G., & Dobson, C. M. (1999). Designing conditions for *in vitro* formation of amyloid protofilaments and fibrils. *Proceedings of the National Academy of Sciences of the United States of America*, *96*(7), 3590–3594.

Chong, P. A., & Forman-Kay, J. D. (2016). Liquid–liquid phase separation in cellular signaling systems. *Current Opinion in Structural Biology*, *41*, 180–186. https://doi.org/10.1016/j.sbi.2016.08.001

Chothia, C. (1973). Conformation of twisted β-pleated sheets in proteins. *Journal of Molecular Biology*, *75*(2), 295–302. https://doi.org/10.1016/0022-2836(73)90022-3

Clavaguera, F., Akatsu, H., Fraser, G., Crowther, R. A., Frank, S., Hench, J., Probst, A., Winkler, D. T., Reichwald, J., Staufenbiel, M., Ghetti, B., Goedert, M., & Tolnay, M. (2013). Brain homogenates from human tauopathies induce tau inclusions in mouse brain. *Proceedings of the National Academy of Sciences of the United States of America*, *110*(23), 9535–9540. https://doi.org/10.1073/pnas.1301175110

Clavaguera, F., Tolnay, M., & Goedert, M. (2017). The prion-like behavior of assembled tau in transgenic mice. *Cold Spring Harbor Perspectives in Medicine*, *7*(10). https://doi.org/10.1101/cshperspect.a024372

Cline, E. N., Bicca, M. A., Viola, K. L., & Klein, W. L. (2018). The amyloid-β oligomer hypothesis: Beginning of the third decade. *Journal of Alzheimer's Disease: JAD*, *64*(s1), S567–S610. https://doi.org/10.3233/JAD-179941

Close, W., Neumann, M., Schmidt, A., Hora, M., Annamalai, K., Schmidt, M., Reif, B., Schmidt, V., Grigorieff, N., & Fändrich, M. (2018). Physical basis of amyloid fibril polymorphism. *Nature Communications*, *9*(1), 699. https://doi.org/10.1038/s41467-018-03164-5

Cohen, M. L., Kim, C., Haldiman, T., ElHag, M., Mehndiratta, P., Pichet, T., Lissemore, F., Shea, M., Cohen, Y., Chen, W., Blevins, J., Appleby, B. S., Surewicz, K., Surewicz, W. K., Sajatovic, M., Tatsuoka, C., Zhang, S., Mayo, P., Butkiewicz, M., Haines, J. L., Lerner, A. J., & Safar, J. G. (2015). Rapidly progressive Alzheimer's disease features distinct structures of amyloid-β. *Brain: A Journal of Neurology*, *138*(Pt 4), 1009–1022. https://doi.org/10.1093/brain/awv006

Cohen, S. I. A., Arosio, P., Presto, J., Kurudenkandy, F. R., Biverstål, H., Dolfe, L., Dunning, C., Yang, X., Frohm, B., Vendruscolo, M., Johansson, J., Dobson, C. M., Fisahn, A., Knowles, T. P. J., & Linse, S. (2015). A molecular chaperone breaks the catalytic cycle that generates toxic Aβ oligomers. *Nature Structural & Molecular Biology*, *22*(3), 207–213. https://doi.org/10.1038/nsmb.2971

Cohen, S. I. A., Linse, S., Luheshi, L. M., Hellstrand, E., White, D. A., Rajah, L., Otzen, D. E., Vendruscolo, M., Dobson, C. M., & Knowles, T. P. J. (2013). Proliferation of amyloid-β42 aggregates occurs through a secondary nucleation mechanism. *Proceedings of the National Academy of Sciences*, *110*(24), 9758–9763. https://doi.org/10.1073/pnas.1218402110

Colvin, M. T., Silvers, R., Ni, Q. Z., Can, T. V., Sergeyev, I., Rosay, M., Donovan, K. J., Michael, B., Wall, J., Linse, S., & Griffin, R. G. (2016). Atomic resolution structure

of monomorphic $A\beta_{42}$ amyloid fibrils. *Journal of the American Chemical Society*, *138*(30), 9663–9674. https://doi.org/10.1021/jacs.6b05129

Conway, K. A., Lee, S. J., Rochet, J. C., Ding, T. T., Williamson, R. E., & Lansbury, P. T. (2000). Acceleration of oligomerization, not fibrillization, is a shared property of both α-synuclein mutations linked to early-onset Parkinson's disease: Implications for pathogenesis and therapy. *Proceedings of the National Academy of Sciences of the United States of America*, *97*(2), 571–576.

Danzer, K. M., Kranich, L. R., Ruf, W. P., Cagsal-Getkin, O., Winslow, A. R., Zhu, L., Vanderburg, C. R., & McLean, P. J. (2012). Exosomal cell-to-cell transmission of α-synuclein oligomers. *Molecular Neurodegeneration*, *7*, 42. https://doi.org/10.1186/1750-1326-7-42

Das, S., Jacob, R. S., Patel, K., Singh, N., & Maji, S. K. (2018). Amyloid fibrils: Versatile biomaterials for cell adhesion and tissue engineering applications. *Biomacromolecules*, *19*(6), 1826–1839. https://doi.org/10.1021/acs.biomac.8b00279

Dear, A. J., Michaels, T. C. T., Meisl, G., Klenerman, D., Wu, S., Perrett, S., Linse, S., Dobson, C. M., & Knowles, T. P. J. (2020). Kinetic diversity of amyloid oligomers. *Proceedings of the National Academy of Sciences*, *117*(22), 12087–12094. https://doi.org/10.1073/pnas.1922267117

Dearborn, A. D., Wall, J. S., Cheng, N., Heymann, J. B., Kajava, A. V., Varkey, J., Langen, R., & Steven, A. C. (2016). α-synuclein amyloid fibrils with two entwined, asymmetrically associated protofibrils. *Journal of Biological Chemistry*, *291*(5), 2310–2318. https://doi.org/10.1074/jbc.M115.698787

Deshmukh, M., Evans, M. L., & Chapman, M. R. (2018). Amyloid by design: Intrinsic regulation of microbial amyloid assembly. *Journal of Molecular Biology*, *430*(20), 3631–3641. https://doi.org/10.1016/j.jmb.2018.07.007

Dey, S., Fan, C., Gothelf, K. V., Li, J., Lin, C., Liu, L., Liu, N., Nijenhuis, M. A. D., Saccà, B., Simmel, F. C., Yan, H., & Zhan, P. (2021). DNA origami. *Nature Reviews Methods Primers*, *1*(1), 1–24. https://doi.org/10.1038/s43586-020-00009-8

Di Scala, C., Yahi, N., Boutemeur, S., Flores, A., Rodriguez, L., Chahinian, H., & Fantini, J. (2016). Common molecular mechanism of amyloid pore formation by Alzheimer's β-amyloid peptide and α-synuclein. *Scientific Reports*, *6*, 28781. https://doi.org/10.1038/srep28781

Diaz, R., Rice, W. J., & Stokes, D. L. (2010). Fourier-Bessel reconstruction of helical assemblies. *Methods in Enzymology*, *482*, 131–165. https://doi.org/10.1016/S0076-6879(10)82005-1

Dobson, C. M. (1999). Protein misfolding, evolution and disease. *Trends in Biochemical Sciences*, *24*(9), 329–332.

Dobson, C. M. (2017). The amyloid phenomenon and its links with human disease. *Cold Spring Harbor Perspectives in Biology*, *9*(6). https://doi.org/10.1101/cshperspect.a023648

Dong, Y., Zhang, S., Wu, Z., Li, X., Wang, W. L., Zhu, Y., Stoilova-McPhie, S., Lu, Y., Finley, D., & Mao, Y. (2019). Cryo-EM structures and dynamics of substrate-engaged human 26S proteasome. *Nature*, *565*(7737), 49–55. https://doi.org/10.1038/s41586-018-0736-4

Drisaldi, B., Colnaghi, L., Fioriti, L., Rao, N., Myers, C., Snyder, A. M., Metzger, D. J., Tarasoff, J., Konstantinov, E., Fraser, P. E., Manley, J. L., & Kandel, E. R. (2015). SUMOylation is an inhibitory constraint that regulates the prion-like aggregation and activity of CPEB3. *Cell Reports*, *11*(11), 1694–1702. https://doi.org/10.1016/j.celrep.2015.04.061

Dugger, B. N., & Dickson, D. W. (2017). Pathology of neurodegenerative diseases. *Cold Spring Harbor Perspectives in Biology*, *9*(7), a028035. https://doi.org/10.1101/cshperspect.a028035

Egelman, E. H. (1986). An algorithm for straightening images of curved filamentous structures. *Ultramicroscopy*, *19*(4), 367–373. https://doi.org/10.1016/0304-3991(86)90096-3

Eichner, T., & Radford, S. E. (2011). Understanding the complex mechanisms of β2-microglobulin amyloid assembly. *The FEBS Journal*, *278*(20), 3868–3883. https://doi.org/10.1111/j.1742-4658.2011.08186.x

Eimer, W. A., Vijaya Kumar, D. K., Navalpur Shanmugam, N. K., Rodriguez, A. S., Mitchell, T., Washicosky, K. J., György, B., Breakefield, X. O., Tanzi, R. E., & Moir, R. D. (2018). Alzheimer's disease-associated β-amyloid is rapidly seeded by *Herpesviridae* to protect against brain infection. *Neuron*, *99*(1), 56-63.e3. https://doi.org/10.1016/j.neuron.2018.06.030

Eisenberg, D., & Jucker, M. (2012). The amyloid state of proteins in human diseases. *Cell*, *148*(6), 1188–1203. https://doi.org/10.1016/j.cell.2012.02.022

Engel, M. F. M., Khemtémourian, L., Kleijer, C. C., Meeldijk, H. J. D., Jacobs, J., Verkleij, A. J., Kruijff, B. de, Killian, J. A., & Höppener, J. W. M. (2008). Membrane damage by human islet amyloid polypeptide through fibril growth at the membrane. *Proceedings of the National Academy of Sciences*, *105*(16), 6033–6038. https://doi.org/10.1073/pnas.0708354105

Esbjörner, E. K., Chan, F., Rees, E., Erdelyi, M., Luheshi, L. M., Bertoncini, C. W., Kaminski, C. F., Dobson, C. M., & Kaminski Schierle, G. S. (2014). Direct observations of amyloid β self-assembly in live cells provide insights into differences

in the kinetics of Aβ(1–40) and Aβ(1–42) aggregation. *Chemistry & Biology*, *21*(6), 732–742. https://doi.org/10.1016/j.chembiol.2014.03.014

Falcon, B., Zhang, W., Murzin, A. G., Murshudov, G., Garringer, H. J., Vidal, R., Crowther, R. A., Ghetti, B., Scheres, S. H. W., & Goedert, M. (2018). Structures of filaments from Pick's disease reveal a novel tau protein fold. *Nature*, 1. https://doi.org/10.1038/s41586-018-0454-y

Falcon, B., Zhang, W., Schweighauser, M., Murzin, A. G., Vidal, R., Garringer, H. J., Ghetti, B., Scheres, S. H. W., & Goedert, M. (2018). Tau filaments from multiple cases of sporadic and inherited Alzheimer's disease adopt a common fold. *Acta Neuropathologica*, *136*(5), 699–708. https://doi.org/10.1007/s00401-018-1914-z

Falcon, B., Zivanov, J., Zhang, W., Murzin, A. G., Garringer, H. J., Vidal, R., Crowther, R. A., Newell, K. L., Ghetti, B., Goedert, M., & Scheres, S. H. W. (2019). Novel tau filament fold in chronic traumatic encephalopathy encloses hydrophobic molecules. *Nature*, *568*(7752), 420–423. https://doi.org/10.1038/s41586-019-1026-5

Faller, P., Hureau, C., & Berthoumieu, O. (2013). Role of metal ions in the self-assembly of the Alzheimer's amyloid-β peptide. *Inorganic Chemistry*, *52*(21), 12193–12206. https://doi.org/10.1021/ic4003059

Fändrich, M., Fletcher, M. A., & Dobson, C. M. (2001). Amyloid fibrils from muscle myoglobin. *Nature*, *410*(6825), 165–166. https://doi.org/10.1038/35065514

Fändrich, M., Meinhardt, J., & Grigorieff, N. (2009). Structural polymorphism of Alzheimer Aβ and other amyloid fibrils. *Prion*, *3*(2), 89–93. https://doi.org/10.4161/pri.3.2.8859

Fändrich, M., Nyström, S., Nilsson, K. P. R., Böckmann, A., LeVine, H., & Hammarström, P. (2018). Amyloid fibril polymorphism—A challenge for molecular imaging and therapy. *Journal of Internal Medicine*, *283*(3), 218–237. https://doi.org/10.1111/joim.12732

Fechner, P., Boudier, T., Mangenot, S., Jaroslawski, S., Sturgis, J. N., & Scheuring, S. (2009). Structural information, resolution, and noise in high-resolution atomic force microscopy topographs. *Biophysical Journal*, *96*(9), 3822–3831. https://doi.org/10.1016/j.bpj.2009.02.011

Ferguson, N., Becker, J., Tidow, H., Tremmel, S., Sharpe, T. D., Krause, G., Flinders, J., Petrovich, M., Berriman, J., Oschkinat, H., & Fersht, A. R. (2006). General structural motifs of amyloid protofilaments. *Proceedings of the National Academy of Sciences*, *103*(44), 16248–16253. https://doi.org/10.1073/pnas.0607815103

Fernandez-Escamilla, A.-M., Rousseau, F., Schymkowitz, J., & Serrano, L. (2004). Prediction of sequence-dependent and mutational effects on the aggregation of peptides and proteins. *Nature Biotechnology*, *22*(10), 1302–1306. https://doi.org/10.1038/nbt1012

Fitzpatrick, A. W. P., Debelouchina, G. T., Bayro, M. J., Clare, D. K., Caporini, M. A., Bajaj, V. S., Jaroniec, C. P., Wang, L., Ladizhansky, V., Müller, S. A., MacPhee, C. E., Waudby, C. A., Mott, H. R., Simone, A. D., Knowles, T. P. J., Saibil, H. R., Vendruscolo, M., Orlova, E. V., Griffin, R. G., & Dobson, C. M. (2013). Atomic structure and hierarchical assembly of a cross-β amyloid fibril. *Proceedings of the National Academy of Sciences*, *110*(14), 5468–5473. https://doi.org/10.1073/pnas.1219476110

Fitzpatrick, A. W. P., Falcon, B., He, S., Murzin, A. G., Murshudov, G., Garringer, H. J., Crowther, R. A., Ghetti, B., Goedert, M., & Scheres, S. H. W. (2017). Cryo-EM structures of tau filaments from Alzheimer's disease. *Nature*, *547*(7662), 185–190. https://doi.org/10.1038/nature23002

Fitzpatrick, A. W. P., & Saibil, H. R. (2019). Cryo-EM of amyloid fibrils and cellular aggregates. *Current Opinion in Structural Biology*, *58*, 34–42. https://doi.org/10.1016/j.sbi.2019.05.003

Flagmeier, P., De, S., Michaels, T. C. T., Yang, X., Dear, A. J., Emanuelsson, C., Vendruscolo, M., Linse, S., Klenerman, D., Knowles, T. P. J., & Dobson, C. M. (2020). Direct measurement of lipid membrane disruption connects kinetics and toxicity of Aβ42 aggregation. *Nature Structural & Molecular Biology*, *27*(10), 886–891. https://doi.org/10.1038/s41594-020-0471-z

Fowler, D. M., Koulov, A. V., Alory-Jost, C., Marks, M. S., Balch, W. E., & Kelly, J. W. (2005). Functional amyloid formation within mammalian tissue. *PLOS Biology*, *4*(1), e6. https://doi.org/10.1371/journal.pbio.0040006

Fowler, D. M., Koulov, A. V., Balch, W. E., & Kelly, J. W. (2007). Functional amyloid—From bacteria to humans. *Trends in Biochemical Sciences*, *32*(5), 217–224. https://doi.org/10.1016/j.tibs.2007.03.003

Gallardo, R., Iadanza, M. G., Xu, Y., Heath, G. R., Foster, R., Radford, S. E., & Ranson, N. A. (2020). Fibril structures of diabetes-related amylin variants reveal a basis for surface-templated assembly. *Nature Structural & Molecular Biology*, *27*(11), 1048–1056. https://doi.org/10.1038/s41594-020-0496-3

Gallardo, R., Ranson, N. A., & Radford, S. E. (2020). Amyloid structures: Much more than just a cross-β fold. *Current Opinion in Structural Biology*, *60*, 7–16. https://doi.org/10.1016/j.sbi.2019.09.001

Galvagnion, C., Buell, A. K., Meisl, G., Michaels, T. C. T., Vendruscolo, M., Knowles, T. P. J., & Dobson, C. M. (2015). Lipid vesicles trigger α-synuclein aggregation by stimulating primary nucleation. *Nature Chemical Biology*, *11*(3), 229–234. https://doi.org/10.1038/nchembio.1750

Gao, X., Carroni, M., Nussbaum-Krammer, C., Mogk, A., Nillegoda, N. B., Szlachcic, A., Guilbride, D. L., Saibil, H. R., Mayer, M. P., & Bukau, B. (2015). Human Hsp70 disaggregase reverses Parkinson's-linked α-synuclein amyloid fibrils. *Molecular Cell*, *59*(5), 781–793. https://doi.org/10.1016/j.molcel.2015.07.012

Garcia, D. M., & Jarosz, D. F. (2014). Rebels with a cause: Molecular features and physiological consequences of yeast prions. *FEMS Yeast Research*, *14*(1), 136–147. https://doi.org/10.1111/1567-1364.12116

Gelenter, M. D., Smith, K. J., Liao, S.-Y., Mandala, V. S., Dregni, A. J., Lamm, M. S., Tian, Y., Xu, W., Pochan, D. J., Tucker, T. J., Su, Y., & Hong, M. (2019). The peptide hormone glucagon forms amyloid fibrils with two coexisting β-strand conformations. *Nature Structural & Molecular Biology*, *26*(7), 592–598. https://doi.org/10.1038/s41594-019-0238-6

Gertz, M. A., Dispenzieri, A., & Sher, T. (2015). Pathophysiology and treatment of cardiac amyloidosis. *Nature Reviews Cardiology*, *12*(2), 91–102. https://doi.org/10.1038/nrcardio.2014.165

Ghosh, S., Salot, S., Sengupta, S., Navalkar, A., Ghosh, D., Jacob, R., Das, S., Kumar, R., Jha, N. N., Sahay, S., Mehra, S., Mohite, G. M., Ghosh, S. K., Kombrabail, M., Krishnamoorthy, G., Chaudhari, P., & Maji, S. K. (2017). p53 amyloid formation leading to its loss of function: Implications in cancer pathogenesis. *Cell Death & Differentiation*, *24*(10), 1784–1798. https://doi.org/10.1038/cdd.2017.105

Ghosh, U., Thurber, K. R., Yau, W.-M., & Tycko, R. (2021). Molecular structure of a prevalent amyloid-β fibril polymorph from Alzheimer's disease brain tissue. *Proceedings of the National Academy of Sciences*, *118*(4), e2023089118. https://doi.org/10.1073/pnas.2023089118

Glynn, C., Sawaya, M. R., Ge, P., Gallagher-Jones, M., Short, C. W., Bowman, R., Apostol, M., Zhou, Z. H., Eisenberg, D. S., & Rodriguez, J. A. (2020). Cryo-EM structure of a human prion fibril with a hydrophobic, protease-resistant core. *Nature Structural & Molecular Biology*, *27*(5), 417–423. https://doi.org/10.1038/s41594-020-0403-y

Goedert, M., Jakes, R., Spillantini, M. G., Hasegawa, M., Smith, M. J., & Crowther, R. A. (1996). Assembly of microtubule-associated protein tau into Alzheimer-like filaments induced by sulphated glycosaminoglycans. *Nature*, *383*(6600), 550–553. https://doi.org/10.1038/383550a0

Goldsbury, C., Frey, P., Olivieri, V., Aebi, U., & Müller, S. A. (2005). Multiple assembly pathways underlie amyloid-β fibril polymorphisms. *Journal of Molecular Biology*, *352*(2), 282–298. https://doi.org/10.1016/j.jmb.2005.07.029

Goldschmidt, L., Teng, P. K., Riek, R., & Eisenberg, D. (2010). Identifying the amylome, proteins capable of forming amyloid-like fibrils. *Proceedings of the National Academy of Sciences of the United States of America*, *107*(8), 3487–3492. https://doi.org/10.1073/pnas.0915166107

Gremer, L., Schölzel, D., Schenk, C., Reinartz, E., Labahn, J., Ravelli, R. B. G., Tusche, M., Lopez-Iglesias, C., Hoyer, W., Heise, H., Willbold, D., & Schröder, G. F. (2017). Fibril structure of amyloid-β(1–42) by cryo–electron microscopy. *Science*, *358*(6359), 116–119. https://doi.org/10.1126/science.aao2825

Grigolato, F., & Arosio, P. (2021). The role of surfaces on amyloid formation. *Biophysical Chemistry*, *270*, 106533. https://doi.org/10.1016/j.bpc.2020.106533

Griner, S. L., Seidler, P., Bowler, J., Murray, K. A., Yang, T. P., Sahay, S., Sawaya, M. R., Cascio, D., Rodriguez, J. A., Philipp, S., Sosna, J., Glabe, C. G., Gonen, T., & Eisenberg, D. S. (2019). Structure-based inhibitors of amyloid beta core suggest a common interface with tau. *ELife*, *8*, e46924. https://doi.org/10.7554/eLife.46924

Gross, L., Mohn, F., Moll, N., Liljeroth, P., & Meyer, G. (2009). The chemical structure of a molecule resolved by atomic force microscopy. *Science*, *325*(5944), 1110–1114. https://doi.org/10.1126/science.1176210

Guenther, E. L., Ge, P., Trinh, H., Sawaya, M. R., Cascio, D., Boyer, D. R., Gonen, T., Zhou, Z. H., & Eisenberg, D. S. (2018). Atomic-level evidence for packing and positional amyloid polymorphism by segment from TDP-43 RRM2. *Nature Structural & Molecular Biology*, *25*(4), 311–319. https://doi.org/10.1038/s41594-018-0045-5

Guerrero-Ferreira, R., Taylor, N. M., Arteni, A.-A., Kumari, P., Mona, D., Ringler, P., Britschgi, M., Lauer, M. E., Makky, A., Verasdonck, J., Riek, R., Melki, R., Meier, B. H., Böckmann, A., Bousset, L., & Stahlberg, H. (2019). Two new polymorphic structures of human full-length alpha-synuclein fibrils solved by cryo-electron microscopy. *ELife*, *8*, e48907. https://doi.org/10.7554/eLife.48907

Guerrero-Ferreira, R., Taylor, N. M., Mona, D., Ringler, P., Lauer, M. E., Riek, R., Britschgi, M., & Stahlberg, H. (2018). Cryo-EM structure of alpha-synuclein fibrils. *ELife*, *7*, e36402. https://doi.org/10.7554/eLife.36402

Guzenko, D., Lafita, A., Monastyrskyy, B., Kryshtafovych, A., & Duarte, J. M. (2019). Assessment of protein assembly prediction in CASP13. *Proteins: Structure, Function, and Bioinformatics*, *87*(12), 1190–1199. https://doi.org/10.1002/prot.25795

Habchi, J., Chia, S., Galvagnion, C., Michaels, T. C. T., Bellaiche, M. M. J., Ruggeri, F. S., Sanguanini, M., Idini, I., Kumita, J. R., Sparr, E., Linse, S., Dobson, C. M., Knowles, T. P. J., & Vendruscolo, M. (2018). Cholesterol catalyses Aβ42 aggregation through a heterogeneous nucleation pathway in the presence of lipid membranes. *Nature Chemistry*, *10*(6), 673–683. https://doi.org/10.1038/s41557-018-0031-x

Hallinan, G. I., Hoq, M. R., Ghosh, M., Vago, F. S., Fernandez, A., Garringer, H. J., Vidal, R., Jiang, W., & Ghetti, B. (2021). Structure of tau filaments in prion protein amyloidoses. *Acta Neuropathologica*. https://doi.org/10.1007/s00401-021-02336-w

Han, S., Kollmer, M., Markx, D., Claus, S., Walther, P., & Fändrich, M. (2017). Amyloid plaque structure and cell surface interactions of β-amyloid fibrils revealed by electron tomography. *Scientific Reports*, *7*. https://doi.org/10.1038/srep43577

Hannaoui, S., Maatouk, L., Privat, N., Levavasseur, E., Faucheux, B. A., & Haïk, S. (2013). Prion propagation and toxicity occur *in vitro* with two-phase kinetics specific to strain and neuronal type. *Journal of Virology*, *87*(5), 2535–2548. https://doi.org/10.1128/JVI.03082-12

Haruyama, T., Sugano, Y., Kodera, N., Uchihashi, T., Ando, T., Tanaka, Y., Konno, H., & Tsukazaki, T. (2019). Single-unit imaging of membrane protein-embedded nanodiscs from two oriented sides by high-speed atomic force microscopy. *Structure (London, England: 1993)*, *27*(1), 152-160.e3. https://doi.org/10.1016/j.str.2018.09.005

Hasecke, F., Miti, T., Perez, C., Barton, J., Schölzel, D., Gremer, L., Grüning, C. S. R., Matthews, G., Meisl, G., Knowles, T. P. J., Willbold, D., Neudecker, P., Heise, H., Ullah, G., Hoyer, W., & Muschol, M. (2018). Origin of metastable oligomers and their effects on amyloid fibril self-assembly. *Chemical Science*, *9*(27), 5937–5948. https://doi.org/10.1039/c8sc01479e

Hatters, D. M., MacRaild, C. A., Daniels, R., Gosal, W. S., Thomson, N. H., Jones, J. A., Davis, J. J., MacPhee, C. E., Dobson, C. M., & Howlett, G. J. (2003). The circularization of amyloid fibrils formed by apolipoprotein C-II. *Biophysical Journal*, *85*(6), 3979–3990.

Heath, G. R., Kots, E., Robertson, J. L., Lansky, S., Khelashvili, G., Weinstein, H., & Scheuring, S. (2021). Localization atomic force microscopy. *Nature*, *594*(7863), 385–390. https://doi.org/10.1038/s41586-021-03551-x

Hermanson, G. T. (2013). Chapter 6—Heterobifunctional crosslinkers. In G. T. Hermanson (Ed.), *Bioconjugate Techniques (Third Edition)* (pp. 299–339). Academic Press. https://doi.org/10.1016/B978-0-12-382239-0.00006-6

Herrmann, U. S., Schütz, A. K., Shirani, H., Huang, D., Saban, D., Nuvolone, M., Li, B., Ballmer, B., Åslund, A. K. O., Mason, J. J., Rushing, E., Budka, H., Nyström, S., Hammarström, P., Böckmann, A., Caflisch, A., Meier, B. H., Nilsson, K. P. R., Hornemann, S., & Aguzzi, A. (2015). Structure-based drug design identifies polythiophenes as antiprion compounds. *Science Translational Medicine*, *7*(299), 299ra123-299ra123. https://doi.org/10.1126/scitranslmed.aab1923

Hervas, R., Rau, M. J., Park, Y., Zhang, W., Murzin, A. G., Fitzpatrick, J. A. J., Scheres, S. H. W., & Si, K. (2020). Cryo-EM structure of a neuronal functional amyloid implicated in memory persistence in *Drosophila*. *Science (New York, N.Y.)*, *367*(6483), 1230–1234. https://doi.org/10.1126/science.aba3526

Hill, S. E., Robinson, J., Matthews, G., & Muschol, M. (2009). Amyloid protofibrils of lysozyme nucleate and grow via oligomer fusion. *Biophysical Journal*, *96*(9), 3781–3790. https://doi.org/10.1016/j.bpj.2009.01.044

Hu, Y., Wang, Y., Yan, J., Wen, N., Xiong, H., Cai, S., He, Q., Peng, D., Liu, Z., & Liu, Y. (2020). Dynamic DNA assemblies in biomedical applications. *Advanced Science*, *7*(14), 2000557. https://doi.org/10.1002/advs.202000557

Hu, Z.-W., Vugmeyster, L., Au, D. F., Ostrovsky, D., Sun, Y., & Qiang, W. (2019). Molecular structure of an N-terminal phosphorylated β-amyloid fibril. *Proceedings of*

the National Academy of Sciences, *116*(23), 11253–11258. https://doi.org/10.1073/pnas.1818530116

Hughes, M. P., Goldschmidt, L., & Eisenberg, D. S. (2021). Prevalence and species distribution of the low-complexity, amyloid-like, reversible, kinked segment (LARKS) structural motif in amyloid-like fibrils. *Journal of Biological Chemistry*, *0*(0). https://doi.org/10.1016/j.jbc.2021.101194

Iadanza, M. G., Jackson, M. P., Hewitt, E. W., Ranson, N. A., & Radford, S. E. (2018). A new era for understanding amyloid structures and disease. *Nature Reviews. Molecular Cell Biology*, *19*(12), 755–773. https://doi.org/10.1038/s41580-018-0060-8

Iadanza, M. G., Silvers, R., Boardman, J., Smith, H. I., Karamanos, T. K., Debelouchina, G. T., Su, Y., Griffin, R. G., Ranson, N. A., & Radford, S. E. (2018). The structure of a β2-microglobulin fibril suggests a molecular basis for its amyloid polymorphism. *Nature Communications*, *9*(1), 4517. https://doi.org/10.1038/s41467-018-06761-6

Iwata, K., Fujiwara, T., Matsuki, Y., Akutsu, H., Takahashi, S., Naiki, H., & Goto, Y. (2006). 3D structure of amyloid protofilaments of β2-microglobulin fragment probed by solid-state NMR. *Proceedings of the National Academy of Sciences*, *103*(48), 18119–18124. https://doi.org/10.1073/pnas.0607180103

Jack, C. R., Wiste, H. J., Lesnick, T. G., Weigand, S. D., Knopman, D. S., Vemuri, P., Pankratz, V. S., Senjem, M. L., Gunter, J. L., Mielke, M. M., Lowe, V. J., Boeve, B. F., & Petersen, R. C. (2013). Brain β-amyloid load approaches a plateau. *Neurology*, *80*(10), 890–896. https://doi.org/10.1212/WNL.0b013e3182840bbe

Jackrel, M. E., DeSantis, M. E., Martinez, B. A., Castellano, L. M., Stewart, R. M., Caldwell, K. A., Caldwell, G. A., & Shorter, J. (2014). Potentiated Hsp104 variants antagonize diverse proteotoxic misfolding events. *Cell*, *156*(1), 170–182. https://doi.org/10.1016/j.cell.2013.11.047

Jackson, M. P., & Hewitt, E. W. (2016). Cellular proteostasis: Degradation of misfolded proteins by lysosomes. *Essays in Biochemistry*, *60*(2), 173–180. https://doi.org/10.1042/EBC20160005

Jackson, M. P., & Hewitt, E. W. (2017). Why are functional amyloids non-toxic in humans? *Biomolecules*, *7*(4), 71. https://doi.org/10.3390/biom7040071

Jahn, T. R., Makin, O. S., Morris, K. L., Marshall, K. E., Tian, P., Sikorski, P., & Serpell, L. C. (2010). The common architecture of cross-β amyloid. *Journal of Molecular Biology*, *395*(4), 717–727. https://doi.org/10.1016/j.jmb.2009.09.039

Jakhria, T., Hellewell, A. L., Porter, M. Y., Jackson, M. P., Tipping, K. W., Xue, W.-F., Radford, S. E., & Hewitt, E. W. (2014). B2-microglobulin amyloid fibrils are nanoparticles that disrupt lysosomal membrane protein trafficking and inhibit protein degradation by lysosomes. *Journal of Biological Chemistry*, *289*(52), 35781–35794. https://doi.org/10.1074/jbc.M114.586222

Jameson, L. P., Smith, N. W., & Dzyuba, S. V. (2012). Dye-binding assays for evaluation of the effects of small molecule inhibitors on amyloid (Aβ) self-assembly. *ACS Chemical Neuroscience*, *3*(11), 807–819. https://doi.org/10.1021/cn300076x

Jaroniec, C. P., MacPhee, C. E., Bajaj, V. S., McMahon, M. T., Dobson, C. M., & Griffin, R. G. (2004). High-resolution molecular structure of a peptide in an amyloid fibril determined by magic angle spinning NMR spectroscopy. *Proceedings of the National Academy of Sciences*, *101*(3), 711–716. https://doi.org/10.1073/pnas.0304849101

Jean, L., Lee, C. F., & Vaux, D. J. (2012). Enrichment of amyloidogenesis at an air-water interface. *Biophysical Journal*, *102*(5), 1154–1162. https://doi.org/10.1016/j.bpj.2012.01.041

Jeon, I., Cicchetti, F., Cisbani, G., Lee, S., Li, E., Bae, J., Lee, N., Li, L., Im, W., Kim, M., Kim, H. S., Oh, S.-H., Kim, T.-A., Ko, J. J., Aubé, B., Oueslati, A., Kim, Y. J., &

Song, J. (2016). Human-to-mouse prion-like propagation of mutant huntingtin protein. *Acta Neuropathologica*, *132*(4), 577–592. https://doi.org/10.1007/s00401-016-1582-9

Jeong, J. S., Ansaloni, A., Mezzenga, R., Lashuel, H. A., & Dietler, G. (2013). Novel mechanistic insight into the molecular basis of amyloid polymorphism and secondary nucleation during amyloid formation. *Journal of Molecular Biology*, *425*(10), 1765–1781. https://doi.org/10.1016/j.jmb.2013.02.005

Jia, L., Liu, Y., Wang, W., Wang, Y., Liu, H., Liu, F., Chen, R., Dawson, V. L., Dawson, T. M., Lu, F., Liu, L., Wang, Y., & Mao, X. (2020). Molecular mediation of prion-like α-synuclein fibrillation from toxic PFFs to nontoxic species. *ACS Applied Bio Materials*. https://doi.org/10.1021/acsabm.0c00684

Jiménez, J. L., Nettleton, E. J., Bouchard, M., Robinson, C. V., Dobson, C. M., & Saibil, H. R. (2002). The protofilament structure of insulin amyloid fibrils. *Proceedings of the National Academy of Sciences of the United States of America*, *99*(14), 9196–9201. https://doi.org/10.1073/pnas.142459399

Jiménez, J. L., Tennent, G., Pepys, M., & Saibil, H. R. (2001). Structural diversity of *ex vivo* amyloid fibrils studied by cryo-electron microscopy. *Journal of Molecular Biology*, *311*(2), 241–247. https://doi.org/10.1006/jmbi.2001.4863

Jin, L.-W., Claborn, K. A., Kurimoto, M., Geday, M. A., Maezawa, I., Sohraby, F., Estrada, M., Kaminksy, W., & Kahr, B. (2003). Imaging linear birefringence and dichroism in cerebral amyloid pathologies. *Proceedings of the National Academy of Sciences*, *100*(26), 15294–15298. https://doi.org/10.1073/pnas.2534647100

Jordens, S., Isa, L., Usov, I., & Mezzenga, R. (2013). Non-equilibrium nature of two-dimensional isotropic and nematic coexistence in amyloid fibrils at liquid interfaces. *Nature Communications*, *4*, 1917. https://doi.org/10.1038/ncomms2911

Jumper, J., Evans, R., Pritzel, A., Green, T., Figurnov, M., Tunyasuvunakool, K., Ronneberger, O., Bates, R., Žídek, A., Bridgland, A., Meyer, C., Kohl, S., Potapenko, A., Ballard, A., Cowie, A., Romera-Paredes, B., Mikolov, S., Jain, R., Adler, J., Back, T., Petersen, S., Reiman, D., Steinegger, M., Pacholska, M., Silver, D., Vinyals, O., Senior, A., Kavukcuoglu, K., Kohli, P., & Hassabis, D. (2020). *High accuracy protein structure prediction using deep learning*. Fourteenth Critical Assessment of Techniques for Protein Structure Prediction (Abstract Book). https://predictioncenter.org/casp14/doc/CASP14_Abstracts.pdf

Kad, N. M., Myers, S. L., Smith, D. P., Alastair Smith, D., Radford, S. E., & Thomson, N. H. (2003). Hierarchical assembly of β2-microglobulin amyloid *in vitro* revealed by atomic force microscopy. *Journal of Molecular Biology*, *330*(4), 785–797. https://doi.org/10.1016/S0022-2836(03)00583-7

Kakio, A., Nishimoto, S., Yanagisawa, K., Kozutsumi, Y., & Matsuzaki, K. (2002). Interactions of amyloid β-protein with various gangliosides in raft-like membranes: Importance of GM1 ganglioside-bound form as an endogenous seed for Alzheimer amyloid. *Biochemistry*, *41*(23), 7385–7390. https://doi.org/10.1021/bi0255874

Kara, E., Marks, J. D., & Aguzzi, A. (2018). Toxic protein spread in neurodegeneration: Reality versus fantasy. *Trends in Molecular Medicine*, *24*(12), 1007–1020. https://doi.org/10.1016/j.molmed.2018.09.004

Kashchiev, D., & Auer, S. (2010). Nucleation of amyloid fibrils. *The Journal of Chemical Physics*, *132*(21), 215101. https://doi.org/10.1063/1.3447891

Kashchiev, D., Cabriolu, R., & Auer, S. (2013). Confounding the paradigm: Peculiarities of amyloid fibril nucleation. *Journal of the American Chemical Society*, *135*(4), 1531–1539. https://doi.org/10.1021/ja311228d

Katsumoto, A., Takeuchi, H., & Tanaka, F. (2019). Tau pathology in chronic traumatic encephalopathy and Alzheimer's disease: Similarities and differences. *Frontiers in Neurology*, *10*. https://doi.org/10.3389/fneur.2019.00980

Keller, D. (1991). Reconstruction of STM and AFM images distorted by finite-size tips. *Surface Science*, *253*(1), 353–364. https://doi.org/10.1016/0039-6028(91)90606-S

Keller, D. J., & Franke, F. S. (1993). Envelope reconstruction of probe microscope images. *Surface Science*, *294*(3), 409–419. https://doi.org/10.1016/0039-6028(93)90126-5

Khurana, R., Ionescu-Zanetti, C., Pope, M., Li, J., Nielson, L., Ramírez-Alvarado, M., Regan, L., Fink, A. L., & Carter, S. A. (2003). A general model for amyloid fibril assembly based on morphological studies using atomic force microscopy. *Biophysical Journal*, *85*(2), 1135–1144.

Knowles, T. P., Fitzpatrick, A. W., Meehan, S., Mott, H. R., Vendruscolo, M., Dobson, C. M., & Welland, M. E. (2007). Role of intermolecular forces in defining material properties of protein nanofibrils. *Science*, *318*(5858), 1900–1903. https://doi.org/10.1126/science.1150057

Knowles, T. P. J., & Buehler, M. J. (2011). Nanomechanics of functional and pathological amyloid materials. *Nature Nanotechnology*, *6*(8), 469–479. https://doi.org/10.1038/nnano.2011.102

Koffie, R. M., Meyer-Luehmann, M., Hashimoto, T., Adams, K. W., Mielke, M. L., Garcia-Alloza, M., Micheva, K. D., Smith, S. J., Kim, M. L., Lee, V. M., Hyman, B. T., & Spires-Jones, T. L. (2009). Oligomeric amyloid β associates with postsynaptic densities and correlates with excitatory synapse loss near senile plaques. *Proceedings of the National Academy of Sciences*, *106*(10), 4012–4017. https://doi.org/10.1073/pnas.0811698106

Koistinaho, M., Ort, M., Cimadevilla, J. M., Vondrous, R., Cordell, B., Koistinaho, J., Bures, J., & Higgins, L. S. (2001). Specific spatial learning deficits become severe with age in β-amyloid precursor protein transgenic mice that harbor diffuse β-amyloid deposits but do not form plaques. *Proceedings of the National Academy of Sciences of the United States of America*, *98*(25), 14675–14680. https://doi.org/10.1073/pnas.261562998

Kollmer, M., Close, W., Funk, L., Rasmussen, J., Bsoul, A., Schierhorn, A., Schmidt, M., Sigurdson, C. J., Jucker, M., & Fändrich, M. (2019). Cryo-EM structure and polymorphism of Aβ amyloid fibrils purified from Alzheimer's brain tissue. *Nature Communications*, *10*. https://doi.org/10.1038/s41467-019-12683-8

Kollmer, M., Meinhardt, K., Haupt, C., Liberta, F., Wulff, M., Linder, J., Handl, L., Heinrich, L., Loos, C., Schmidt, M., Syrovets, T., Simmet, T., Westermark, P., Westermark, G. T., Horn, U., Schmidt, V., Walther, P., & Fändrich, M. (2016). Electron tomography reveals the fibril structure and lipid interactions in amyloid deposits. *Proceedings of the National Academy of Sciences of the United States of America*, *113*(20), 5604–5609. https://doi.org/10.1073/pnas.1523496113

Koloteva-Levine, N., Aubrey, L. D., Marchante, R., Purton, T. J., Hiscock, J. R., Tuite, M. F., & Xue, W.-F. (2021). Amyloid particles facilitate surface-catalyzed cross-seeding by acting as promiscuous nanoparticles. *Proceedings of the National Academy of Sciences*, *118*(36). https://doi.org/10.1073/pnas.2104148118

Korkhov, V. M., Sachse, C., Short, J. M., & Tate, C. G. (2010). Three-dimensional structure of TspO by electron cryomicroscopy of helical crystals. *Structure*, *18*(6), 677–687. https://doi.org/10.1016/j.str.2010.03.001

Kotler, S. A., Brender, J. R., Vivekanandan, S., Suzuki, Y., Yamamoto, K., Monette, M., Krishnamoorthy, J., Walsh, P., Cauble, M., Holl, M. M. B., Marsh, E. N. G., &

Ramamoorthy, A. (2015). High-resolution NMR characterization of low abundance oligomers of amyloid-β without purification. *Scientific Reports*, *5*, 11811. https://doi.org/10.1038/srep11811

Krasnoslobodtsev, A. V., Deckert-Gaudig, T., Zhang, Y., Deckert, V., & Lyubchenko, Y. L. (2016). Polymorphism of amyloid fibrils formed by a peptide from the yeast prion protein Sup35: AFM and tip-enhanced Raman scattering studies. *Ultramicroscopy*, *165*, 26–33. https://doi.org/10.1016/j.ultramic.2016.03.011

Krebs, M. R. H., MacPhee, C. E., Miller, A. F., Dunlop, I. E., Dobson, C. M., & Donald, A. M. (2004). The formation of spherulites by amyloid fibrils of bovine insulin. *Proceedings of the National Academy of Sciences*, *101*(40), 14420–14424. https://doi.org/10.1073/pnas.0405933101

Kryshtafovych, A., Schwede, T., Topf, M., Fidelis, K., & Moult, J. (2019). Critical assessment of methods of protein structure prediction (CASP)—Round XIII. *Proteins: Structure, Function, and Bioinformatics*, *87*(12), 1011–1020. https://doi.org/10.1002/prot.25823

Kryshtafovych, A., Schwede, T., Topf, M., Fidelis, K., & Moult, J. (2021). Critical assessment of methods of protein structure prediction (CASP)—Round XIV. *Proteins*. https://doi.org/10.1002/prot.26237

Kuchibhotla, K. V., Goldman, S. T., Lattarulo, C. R., Wu, H.-Y., Hyman, B. T., & Bacskai, B. J. (2008). Aβ plaques lead to aberrant regulation of calcium homeostasis *in vivo* resulting in structural and functional disruption of neuronal networks. *Neuron*, *59*(2), 214–225. https://doi.org/10.1016/j.neuron.2008.06.008

Kumar, D. K. V., Choi, S. H., Washicosky, K. J., Eimer, W. A., Tucker, S., Ghofrani, J., Lefkowitz, A., McColl, G., Goldstein, L. E., Tanzi, R. E., & Moir, R. D. (2016). Amyloid-β peptide protects against microbial infection in mouse and worm models of

Alzheimer's disease. *Science Translational Medicine*, *8*(340), 340ra72. https://doi.org/10.1126/scitranslmed.aaf1059

Kushnirov, V. V., Vishnevskaya, A. B., Alexandrov, I. M., & Ter-Avanesyan, M. D. (2007). Prion and nonprion amyloids. *Prion*, *1*(3), 179–184.

Kyte, J., & Doolittle, R. F. (1982). A simple method for displaying the hydropathic character of a protein. *Journal of Molecular Biology*, *157*(1), 105–132. https://doi.org/10.1016/0022-2836(82)90515-0

Laron, Z. (2018). The era of cadaveric pituitary extracted human growth hormone (1958-1985): Biological and clinical aspects. *Pediatric Endocrinology Reviews: PER*, *16*(Suppl 1), 11–16. https://doi.org/10.17458/per.vol16.2018.la.hghcadavericpituitary

Lee, E. H. (2014). A practical guide to pharmaceutical polymorph screening & selection. *Asian Journal of Pharmaceutical Sciences*, *9*(4), 163–175. https://doi.org/10.1016/j.ajps.2014.05.002

Lee, M., Ghosh, U., Thurber, K. R., Kato, M., & Tycko, R. (2020). Molecular structure and interactions within amyloid-like fibrils formed by a low-complexity protein sequence from FUS. *Nature Communications*, *11*(1), 5735. https://doi.org/10.1038/s41467-020-19512-3

Lee, M.-C., Yu, W.-C., Shih, Y.-H., Chen, C.-Y., Guo, Z.-H., Huang, S.-J., Chan, J. C. C., & Chen, Y.-R. (2018). Zinc ion rapidly induces toxic, off-pathway amyloid-β oligomers distinct from amyloid-β derived diffusible ligands in Alzheimer's disease. *Scientific Reports*, *8*(1), 4772. https://doi.org/10.1038/s41598-018-23122-x

Lesné, S. E., Sherman, M. A., Grant, M., Kuskowski, M., Schneider, J. A., Bennett, D. A., & Ashe, K. H. (2013). Brain amyloid-β oligomers in ageing and Alzheimer's disease. *Brain*, *136*(5), 1383–1398. https://doi.org/10.1093/brain/awt062

Li, B., Ge, P., Murray, K. A., Sheth, P., Zhang, M., Nair, G., Sawaya, M. R., Shin, W. S., Boyer, D. R., Ye, S., Eisenberg, D. S., Zhou, Z. H., & Jiang, L. (2018). Cryo-EM of full-length α-synuclein reveals fibril polymorphs with a common structural kernel. *Nature Communications*, *9*(1), 3609. https://doi.org/10.1038/s41467-018-05971-2

Li, D., & Liu, C. (2021). Hierarchical chemical determination of amyloid polymorphs in neurodegenerative disease. *Nature Chemical Biology*, *17*(3), 237–245. https://doi.org/10.1038/s41589-020-00708-z

Li, J., Xun, K., Zheng, L., Peng, X., Qiu, L., & Tan, W. (2021). DNA-based dynamic mimicry of membrane proteins for programming adaptive cellular interactions. *Journal of the American Chemical Society*, *143*(12), 4585–4592. https://doi.org/10.1021/jacs.0c11245

Li, Q., Babinchak, W. M., & Surewicz, W. K. (2021). Cryo-EM structure of amyloid fibrils formed by the entire low complexity domain of TDP-43. *Nature Communications*, *12*(1), 1620. https://doi.org/10.1038/s41467-021-21912-y

Li, Y., Zhao, C., Luo, F., Liu, Z., Gui, X., Luo, Z., Zhang, X., Li, D., Liu, C., & Li, X. (2018). Amyloid fibril structure of α-synuclein determined by cryo-electron microscopy. *Cell Research*, 1. https://doi.org/10.1038/s41422-018-0075-x

Liao, C. R., Rak, M., Lund, J., Unger, M., Platt, E., Albensi, B. C., Hirschmugl, C. J., & Gough, K. M. (2013). Synchrotron FTIR reveals lipid around and within amyloid plaques in transgenic mice and Alzheimer's disease brain. *The Analyst*, *138*(14), 3991–3997. https://doi.org/10.1039/c3an00295k

Liberta, F., Loerch, S., Rennegarbe, M., Schierhorn, A., Westermark, P., Westermark, G. T., Hazenberg, B. P. C., Grigorieff, N., Fändrich, M., & Schmidt, M. (2019). Cryo-EM fibril structures from systemic AA amyloidosis reveal the species complementarity of

pathological amyloids. *Nature Communications*, *10*(1), 1104. https://doi.org/10.1038/s41467-019-09033-z

Liebman, S. W., & Derkatch, I. L. (1999). The yeast [PSI$^+$] prion: Making sense of nonsense. *Journal of Biological Chemistry*, *274*(3), 1181–1184. https://doi.org/10.1074/jbc.274.3.1181

Lindberg, D. J., Wesén, E., Björkeroth, J., Rocha, S., & Esbjörner, E. K. (2017). Lipid membranes catalyse the fibril formation of the amyloid-β (1-42) peptide through lipid-fibril interactions that reinforce secondary pathways. *Biochimica Et Biophysica Acta. Biomembranes*, *1859*(10), 1921–1929. https://doi.org/10.1016/j.bbamem.2017.05.012

Linse, S., Scheidt, T., Bernfur, K., Vendruscolo, M., Dobson, C. M., Cohen, S. I. A., Sileikis, E., Lundqvist, M., Qian, F., O'Malley, T., Bussiere, T., Weinreb, P. H., Xu, C. K., Meisl, G., Devenish, S. R. A., Knowles, T. P. J., & Hansson, O. (2020). Kinetic fingerprints differentiate the mechanisms of action of anti-Aβ antibodies. *Nature Structural & Molecular Biology*, *27*(12), 1125–1133. https://doi.org/10.1038/s41594-020-0505-6

Lövestam, S., Schweighauser, M., Matsubara, T., Murayama, S., Tomita, T., Ando, T., Hasegawa, K., Yoshida, M., Tarutani, A., Hasegawa, M., Goedert, M., & Scheres, S. H. W. (2021). Seeded assembly *in vitro* does not replicate the structures of α-synuclein filaments from multiple system atrophy. *FEBS Open Bio*, *11*(4), 999–1013. https://doi.org/10.1002/2211-5463.13110

Lu, J., Cao, Q., Hughes, M. P., Sawaya, M. R., Boyer, D. R., Cascio, D., & Eisenberg, D. S. (2020). CryoEM structure of the low-complexity domain of hnRNPA2 and its conversion to pathogenic amyloid. *Nature Communications*, *11*(1), 4090. https://doi.org/10.1038/s41467-020-17905-y

Lu, J.-X., Qiang, W., Yau, W.-M., Schwieters, C. D., Meredith, S. C., & Tycko, R. (2013). Molecular structure of β-amyloid fibrils in Alzheimer's disease brain tissue. *Cell*, *154*(6), 1257–1268. https://doi.org/10.1016/j.cell.2013.08.035

Lührs, T., Ritter, C., Adrian, M., Riek-Loher, D., Bohrmann, B., Döbeli, H., Schubert, D., & Riek, R. (2005). 3D structure of Alzheimer's amyloid-β(1–42) fibrils. *Proceedings of the National Academy of Sciences*, *102*(48), 17342–17347. https://doi.org/10.1073/pnas.0506723102

Lutter, L., Al-Hilaly, Y., Serpell, C. J., Tuite, M. F., Wischik, C. M., Serpell, L. C., & Xue, W.-F. (2021). Structural identification of individual helical amyloid filaments by integration of cryo-electron microscopy-derived maps in comparative morphometric atomic force microscopy image analysis. *BioRxiv*, 2021.10.19.464873. https://doi.org/10.1101/2021.10.19.464873

Lutter, L., Aubrey, L. D., & Xue, W.-F. (2021). On the structural diversity and individuality of polymorphic amyloid protein assemblies. *Journal of Molecular Biology*, 167124. https://doi.org/10.1016/j.jmb.2021.167124

Lutter, L., Serpell, C. J., Tuite, M. F., Serpell, L. C., & Xue, W.-F. (2020). Three-dimensional reconstruction of individual helical nano-filament structures from atomic force microscopy topographs. *Biomolecular Concepts*, *11*(1), 102–115. https://doi.org/10.1515/bmc-2020-0009

Lutter, L., Serpell, C. J., Tuite, M. F., & Xue, W.-F. (2019). The molecular lifecycle of amyloid – Mechanism of assembly, mesoscopic organisation, polymorphism, suprastructures, and biological consequences. *Biochimica et Biophysica Acta (BBA) - Proteins and Proteomics*, *1867*(11), 140257. https://doi.org/10.1016/j.bbapap.2019.07.010

Lyubchenko, Y. L. (2018). Direct AFM visualization of the nanoscale dynamics of biomolecular complexes. *Journal of Physics D: Applied Physics*, *51*(40). https://doi.org/10.1088/1361-6463/aad898

Maity, S., & Lyubchenko, Y. L. (2019). Force clamp approach for characterization of nano-assembly in amyloid beta 42 dimer. *Nanoscale*, *11*(25), 12259–12265. https://doi.org/10.1039/c9nr01670h

Maji, S. K., Perrin, M. H., Sawaya, M. R., Jessberger, S., Vadodaria, K., Rissman, R. A., Singru, P. S., Nilsson, K. P. R., Simon, R., Schubert, D., Eisenberg, D., Rivier, J., Sawchenko, P., Vale, W., & Riek, R. (2009). Functional amyloids as natural storage of peptide hormones in pituitary secretory granules. *Science*, *325*(5938), 328–332. https://doi.org/10.1126/science.1173155

Makarava, N., Ostapchenko, V. G., Savtchenko, R., & Baskakov, I. V. (2009). Conformational switching within individual amyloid fibrils. *Journal of Biological Chemistry*, *284*(21), 14386–14395. https://doi.org/10.1074/jbc.M900533200

Makin, S. (2018). The amyloid hypothesis on trial. *Nature*, *559*(7715), S4–S7. https://doi.org/10.1038/d41586-018-05719-4

Mankar, S., Anoop, A., Sen, S., & Maji, S. K. (2011). Nanomaterials: Amyloids reflect their brighter side. *Nano Reviews*, *2*, 10.3402/nano.v2i0.6032. https://doi.org/10.3402/nano.v2i0.6032

Mannini, B., Mulvihill, E., Sgromo, C., Cascella, R., Khodarahmi, R., Ramazzotti, M., Dobson, C. M., Cecchi, C., & Chiti, F. (2014). Toxicity of protein oligomers is rationalized by a function combining size and surface hydrophobicity. *ACS Chemical Biology*, *9*(10), 2309–2317. https://doi.org/10.1021/cb500505m

Manno, M., Giacomazza, D., Newman, J., Martorana, V., & San Biagio, P. L. (2010). Amyloid gels: Precocious appearance of elastic properties during the formation of an

insulin fibrillar network. *Langmuir*, *26*(3), 1424–1426. https://doi.org/10.1021/la903340v

Marchante, R., Beal, D. M., Koloteva-Levine, N., Purton, T. J., Tuite, M. F., & Xue, W.-F. (2017). The physical dimensions of amyloid aggregates control their infective potential as prion particles. *ELife*, *6*, e27109. https://doi.org/10.7554/eLife.27109

Marshall, K. E., Marchante, R., Xue, W.-F., & Serpell, L. C. (2014). The relationship between amyloid structure and cytotoxicity. *Prion*, *8*(2), 192–196. https://doi.org/10.4161/pri.28860

Martins, I. C., Kuperstein, I., Wilkinson, H., Maes, E., Vanbrabant, M., Jonckheere, W., Van Gelder, P., Hartmann, D., D'Hooge, R., De Strooper, B., Schymkowitz, J., & Rousseau, F. (2008). Lipids revert inert Aβ amyloid fibrils to neurotoxic protofibrils that affect learning in mice. *The EMBO Journal*, *27*(1), 224–233. https://doi.org/10.1038/sj.emboj.7601953

Masters, C. L., Bateman, R., Blennow, K., Rowe, C. C., Sperling, R. A., & Cummings, J. L. (2015). Alzheimer's disease. *Nature Reviews. Disease Primers*, *1*, 15056. https://doi.org/10.1038/nrdp.2015.56

Matheou, C. J., Younan, N. D., & Viles, J. H. (2015). Cu^{2+} accentuates distinct misfolding of $A\beta_{1–40}$ and $A\beta_{1–42}$ peptides, and potentiates membrane disruption. *The Biochemical Journal*, *466*(2), 233–242. https://doi.org/10.1042/BJ20141168

Maurer-Stroh, S., Debulpaep, M., Kuemmerer, N., de la Paz, M. L., Martins, I. C., Reumers, J., Morris, K. L., Copland, A., Serpell, L., Serrano, L., Schymkowitz, J. W. H., & Rousseau, F. (2010). Exploring the sequence determinants of amyloid structure using position-specific scoring matrices. *Nature Methods*, *7*(3), 237–242. https://doi.org/10.1038/nmeth.1432

Mayes, J., Tinker-Mill, C., Kolosov, O., Zhang, H., Tabner, B. J., & Allsop, D. (2014). β-amyloid fibrils in Alzheimer disease are not inert when bound to copper ions but can degrade hydrogen peroxide and generate reactive oxygen species. *Journal of Biological Chemistry*, *289*(17), 12052–12062. https://doi.org/10.1074/jbc.M113.525212

McGlinchey, R. P., Kryndushkin, D., & Wickner, R. B. (2011). Suicidal [PSI $^{+}$] is a lethal yeast prion. *Proceedings of the National Academy of Sciences*, *108*(13), 5337–5341. https://doi.org/10.1073/pnas.1102762108

Meersman, F., & Dobson, C. M. (2006). Probing the pressure–temperature stability of amyloid fibrils provides new insights into their molecular properties. *Biochimica et Biophysica Acta (BBA) - Proteins and Proteomics*, *1764*(3), 452–460. https://doi.org/10.1016/j.bbapap.2005.10.021

Mehta, D., Jackson, R., Paul, G., Shi, J., & Sabbagh, M. (2017). Why do trials for Alzheimer's disease drugs keep failing? A discontinued drug perspective for 2010–2015. *Expert Opinion on Investigational Drugs*, *26*(6), 735–739. https://doi.org/10.1080/13543784.2017.1323868

Meinhardt, J., Sachse, C., Hortschansky, P., Grigorieff, N., & Fändrich, M. (2009). Aβ(1-40) fibril polymorphism implies diverse interaction patterns in amyloid fibrils. *Journal of Molecular Biology*, *386*(3), 869–877. https://doi.org/10.1016/j.jmb.2008.11.005

Meisl, G., Yang, X., Hellstrand, E., Frohm, B., Kirkegaard, J. B., Cohen, S. I. A., Dobson, C. M., Linse, S., & Knowles, T. P. J. (2014). Differences in nucleation behavior underlie the contrasting aggregation kinetics of the Aβ40 and Aβ42 peptides. *Proceedings of the National Academy of Sciences*, *111*(26), 9384–9389. https://doi.org/10.1073/pnas.1401564111

Merlini, G., Dispenzieri, A., Sanchorawala, V., Schönland, S. O., Palladini, G., Hawkins, P. N., & Gertz, M. A. (2018). Systemic immunoglobulin light chain amyloidosis. *Nature Reviews. Disease Primers*, *4*(1), 38. https://doi.org/10.1038/s41572-018-0034-3

Meyer-Luehmann, M., Spires-Jones, T. L., Prada, C., Garcia-Alloza, M., Calignon, A. de, Rozkalne, A., Koenigsknecht-Talboo, J., Holtzman, D. M., Bacskai, B. J., & Hyman, B. T. (2008). Rapid appearance and local toxicity of amyloid-β plaques in a mouse model of Alzheimer's disease. *Nature*, *451*(7179), 720–724. https://doi.org/10.1038/nature06616

Michaels, T. C. T., Šarić, A., Habchi, J., Chia, S., Meisl, G., Vendruscolo, M., Dobson, C. M., & Knowles, T. P. J. (2018). Chemical kinetics for bridging molecular mechanisms and macroscopic measurements of amyloid fibril formation. *Annual Review of Physical Chemistry*, *69*, 273–298. https://doi.org/10.1146/annurev-physchem-050317-021322

Michaels, T. C. T., Šarić, A., Meisl, G., Heller, G. T., Curk, S., Arosio, P., Linse, S., Dobson, C. M., Vendruscolo, M., & Knowles, T. P. J. (2020). Thermodynamic and kinetic design principles for amyloid-aggregation inhibitors. *Proceedings of the National Academy of Sciences*, *117*(39), 24251–24257. https://doi.org/10.1073/pnas.2006684117

Milanesi, L., Sheynis, T., Xue, W.-F., Orlova, E. V., Hellewell, A. L., Jelinek, R., Hewitt, E. W., Radford, S. E., & Saibil, H. R. (2012). Direct three-dimensional visualization of membrane disruption by amyloid fibrils. *Proceedings of the National Academy of Sciences*, *109*(50), 20455–20460. https://doi.org/10.1073/pnas.1206325109

Miller, L. M., Wang, Q., Telivala, T. P., Smith, R. J., Lanzirotti, A., & Miklossy, J. (2006). Synchrotron-based infrared and X-ray imaging shows focalized accumulation of Cu

and Zn co-localized with β-amyloid deposits in Alzheimer's disease. *Journal of Structural Biology*, *155*(1), 30–37. https://doi.org/10.1016/j.jsb.2005.09.004

Miyazawa, A., Fujiyoshi, Y., & Unwin, N. (2003). Structure and gating mechanism of the acetylcholine receptor pore. *Nature*, *423*(6943), 949–955. https://doi.org/10.1038/nature01748

Mizuno, N., Baxa, U., & Steven, A. C. (2011). Structural dependence of HET-s amyloid fibril infectivity assessed by cryoelectron microscopy. *Proceedings of the National Academy of Sciences*, *108*(8), 3252–3257. https://doi.org/10.1073/pnas.1011342108

Mompeán, M., Li, W., Li, J., Laage, S., Siemer, A. B., Bozkurt, G., Wu, H., & McDermott, A. E. (2018). The structure of the necrosome RIPK1-RIPK3 core, a human hetero-amyloid signaling complex. *Cell*, *173*(5), 1244-1253.e10. https://doi.org/10.1016/j.cell.2018.03.032

Monsellier, E., Bousset, L., & Melki, R. (2016). α-synuclein and huntingtin exon 1 amyloid fibrils bind laterally to the cellular membrane. *Scientific Reports*, *6*(1), 19180. https://doi.org/10.1038/srep19180

Moores, B., Drolle, E., Attwood, S. J., Simons, J., & Leonenko, Z. (2011). Effect of surfaces on amyloid fibril formation. *PLoS ONE*, *6*(10). https://doi.org/10.1371/journal.pone.0025954

Morel, B., Varela, L., Azuaga, A. I., & Conejero-Lara, F. (2010). Environmental conditions affect the kinetics of nucleation of amyloid fibrils and determine their morphology. *Biophysical Journal*, *99*(11), 3801–3810. https://doi.org/10.1016/j.bpj.2010.10.039

Moreno-Herrero, F., Pérez, M., Baró, A. M., & Avila, J. (2004). Characterization by atomic force microscopy of Alzheimer paired helical filaments under physiological conditions. *Biophysical Journal*, *86*(1 Pt 1), 517–525. https://doi.org/10.1016/S0006-3495(04)74130-2

Morris, K. L., Rodger, A., Hicks, M. R., Debulpaep, M., Schymkowitz, J., Rousseau, F., & Serpell, L. C. (2013). Exploring the sequence–structure relationship for amyloid peptides. *Biochemical Journal*, *450*(Pt 2), 275–283. https://doi.org/10.1042/BJ20121773

Moult, J., Fidelis, K., Kryshtafovych, A., Schwede, T., & Tramontano, A. (2018). Critical assessment of methods of protein structure prediction (CASP)—Round XII. *Proteins*, *86 Suppl 1*, 7–15. https://doi.org/10.1002/prot.25415

Mukherjee, A., Morales-Scheihing, D., Butler, P. C., & Soto, C. (2015). Type 2 diabetes as a protein misfolding disease. *Trends in Molecular Medicine*, *21*(7), 439–449. https://doi.org/10.1016/j.molmed.2015.04.005

Mullard, A. (2021). Landmark Alzheimer's drug approval confounds research community. *Nature*, *594*(7863), 309–310. https://doi.org/10.1038/d41586-021-01546-2

Murray, D. T., Kato, M., Lin, Y., Thurber, K. R., Hung, I., McKnight, S. L., & Tycko, R. (2017). Structure of FUS protein fibrils and its relevance to self-assembly and phase separation of low-complexity domains. *Cell*, *171*(3), 615-627.e16. https://doi.org/10.1016/j.cell.2017.08.048

Narita, A., Usukura, E., Yagi, A., Tateyama, K., Akizuki, S., Kikumoto, M., Matsumoto, T., Maéda, Y., Ito, S., & Usukura, J. (2016). Direct observation of the actin filament by tip-scan atomic force microscopy. *Microscopy (Oxford, England)*, *65*(4), 370–377. https://doi.org/10.1093/jmicro/dfw017

Ni, X., McGlinchey, R. P., Jiang, J., & Lee, J. C. (2019). Structural insights into α-synuclein fibril polymorphism: Effects of Parkinson's disease-related C-terminal truncations. *Journal of Molecular Biology*, *431*(19), 3913–3919. https://doi.org/10.1016/j.jmb.2019.07.001

Nilsson, K. P. R., Aslund, A., Berg, I., Nyström, S., Konradsson, P., Herland, A., Inganäs, O., Stabo-Eeg, F., Lindgren, M., Westermark, G. T., Lannfelt, L., Nilsson, L. N. G., & Hammarström, P. (2007). Imaging distinct conformational states of amyloid-β fibrils in Alzheimer's disease using novel luminescent probes. *ACS Chemical Biology*, *2*(8), 553–560. https://doi.org/10.1021/cb700116u

Nokwe, C. N., Hora, M., Zacharias, M., Yagi, H., Peschek, J., Reif, B., Goto, Y., & Buchner, J. (2016). A stable mutant predisposes antibody domains to amyloid formation through specific non-native interactions. *Journal of Molecular Biology*, *428*(6), 1315–1332. https://doi.org/10.1016/j.jmb.2016.01.015

Novo, M., Freire, S., & Al-Soufi, W. (2018). Critical aggregation concentration for the formation of early Amyloid-β (1–42) oligomers. *Scientific Reports*, *8*(1). https://doi.org/10.1038/s41598-018-19961-3

Nowakowski, R., Luckham, P., & Winlove, P. (2001). Imaging erythrocytes under physiological conditions by atomic force microscopy. *Biochimica Et Biophysica Acta*, *1514*(2), 170–176.

Nussbaum, J. M., Schilling, S., Cynis, H., Silva, A., Swanson, E., Wangsanut, T., Tayler, K., Wiltgen, B., Hatami, A., Rönicke, R., Reymann, K., Hutter-Paier, B., Alexandru, A., Jagla, W., Graubner, S., Glabe, C. G., Demuth, H.-U., & Bloom, G. S. (2012). Prion-like behaviour and tau-dependent cytotoxicity of pyroglutamylated amyloid-β. *Nature*, *485*(7400), 651–655. https://doi.org/10.1038/nature11060

Nussbaum-Krammer, C. I., Park, K.-W., Li, L., Melki, R., & Morimoto, R. I. (2013). Spreading of a prion domain from cell-to-cell by vesicular transport in *Caenorhabditis elegans*. *PLoS Genetics*, *9*(3), e1003351. https://doi.org/10.1371/journal.pgen.1003351

O'Connor, S. D., Gamble, R. C., Eby, R. K., & Baldeschwieler, J. D. (1996). Noise reduction in atomic force microscopy: Resonance contact mode. *Review of Scientific Instruments*, *67*, 393–396.

Otzen, D., & Riek, R. (2019). Functional amyloids. *Cold Spring Harbor Perspectives in Biology*, *11*(12). https://doi.org/10.1101/cshperspect.a033860

Pansieri, J., Halim, M. A., Vendrely, C., Dumoulin, M., Legrand, F., Sallanon, M. M., Chierici, S., Denti, S., Dagany, X., Dugourd, P., Marquette, C., Antoine, R., & Forge, V. (2018). Mass and charge distributions of amyloid fibers involved in neurodegenerative diseases: Mapping heterogeneity and polymorphism. *Chemical Science*, *9*(10), 2791–2796. https://doi.org/10.1039/C7SC04542E

Paravastu, A. K., Leapman, R. D., Yau, W.-M., & Tycko, R. (2008). Molecular structural basis for polymorphism in Alzheimer's β-amyloid fibrils. *Proceedings of the National Academy of Sciences*, *105*(47), 18349–18354. https://doi.org/10.1073/pnas.0806270105

Paravastu, A. K., Qahwash, I., Leapman, R. D., Meredith, S. C., & Tycko, R. (2009). Seeded growth of β-amyloid fibrils from Alzheimer's brain-derived fibrils produces a distinct fibril structure. *Proceedings of the National Academy of Sciences*, *106*(18), 7443–7448. https://doi.org/10.1073/pnas.0812033106

Parsons, E. S., Stanley, G. J., Pyne, A. L. B., Hodel, A. W., Nievergelt, A. P., Menny, A., Yon, A. R., Rowley, A., Richter, R. P., Fantner, G. E., Bubeck, D., & Hoogenboom, B. W. (2019). Single-molecule kinetics of pore assembly by the membrane attack complex. *Nature Communications*, *10*(1), 1–10. https://doi.org/10.1038/s41467-019-10058-7

Parthasarathy, S., Inoue, M., Xiao, Y., Matsumura, Y., Nabeshima, Y., Hoshi, M., & Ishii, Y. (2015). Structural insight into an Alzheimer's brain-derived spherical assembly of

amyloid β by solid-state NMR. *Journal of the American Chemical Society*, *137*(20), 6480–6483. https://doi.org/10.1021/jacs.5b03373

Patel, N., Ramachandran, S., Azimov, R., Kagan, B. L., & Lal, R. (2015). Ion channel formation by tau protein: Implications for Alzheimer's disease and tauopathies. *Biochemistry*, *54*(50), 7320–7325. https://doi.org/10.1021/acs.biochem.5b00988

Pedersen, J. T., & Heegaard, N. H. H. (2013). Analysis of protein aggregation in neurodegenerative disease. *Analytical Chemistry*, *85*(9), 4215–4227. https://doi.org/10.1021/ac400023c

Peduzzo, A., Linse, S., & Buell, A. K. (2020). The properties of α-synuclein secondary nuclei are dominated by the solution conditions rather than the seed fibril strain. *ACS Chemical Neuroscience*, *11*(6), 909–918. https://doi.org/10.1021/acschemneuro.9b00594

Petkova, A. T., Leapman, R. D., Guo, Z., Yau, W.-M., Mattson, M. P., & Tycko, R. (2005). Self-propagating, molecular-level polymorphism in Alzheimer's β-amyloid fibrils. *Science (New York, N.Y.)*, *307*(5707), 262–265. https://doi.org/10.1126/science.1105850

Pettersen, E. F., Goddard, T. D., Huang, C. C., Couch, G. S., Greenblatt, D. M., Meng, E. C., & Ferrin, T. E. (2004). UCSF Chimera—A visualization system for exploratory research and analysis. *Journal of Computational Chemistry*, *25*(13), 1605–1612. https://doi.org/10.1002/jcc.20084

Peydayesh, M., & Mezzenga, R. (2021). Protein nanofibrils for next generation sustainable water purification. *Nature Communications*, *12*(1), 3248. https://doi.org/10.1038/s41467-021-23388-2

Pfreundschuh, M., Alsteens, D., Wieneke, R., Zhang, C., Coughlin, S. R., Tampé, R., Kobilka, B. K., & Müller, D. J. (2015). Identifying and quantifying two ligand-

binding sites while imaging native human membrane receptors by AFM. *Nature Communications*, *6*, 8857. https://doi.org/10.1038/ncomms9857

Plant, L. D., Boyle, J. P., Smith, I. F., Peers, C., & Pearson, H. A. (2003). The production of amyloid beta peptide is a critical requirement for the viability of central neurons. *The Journal of Neuroscience: The Official Journal of the Society for Neuroscience*, *23*(13), 5531–5535.

Prusiner, S. B. (1998). Prions. *Proceedings of the National Academy of Sciences of the United States of America*, *95*(23), 13363–13383.

Purro, S. A., Farrow, M. A., Linehan, J., Nazari, T., Thomas, D. X., Chen, Z., Mengel, D., Saito, T., Saido, T., Rudge, P., Brandner, S., Walsh, D. M., & Collinge, J. (2018). Transmission of amyloid-β protein pathology from cadaveric pituitary growth hormone. *Nature*, *564*(7736), 415–419. https://doi.org/10.1038/s41586-018-0790-y

Pyne, A. L. B., Noy, A., Main, K. H. S., Velasco-Berrelleza, V., Piperakis, M. M., Mitchenall, L. A., Cugliandolo, F. M., Beton, J. G., Stevenson, C. E. M., Hoogenboom, B. W., Bates, A. D., Maxwell, A., & Harris, S. A. (2021). Base-pair resolution analysis of the effect of supercoiling on DNA flexibility and major groove recognition by triplex-forming oligonucleotides. *Nature Communications*, *12*(1), 1053. https://doi.org/10.1038/s41467-021-21243-y

Pyne, A., Thompson, R., Leung, C., Roy, D., & Hoogenboom, B. W. (2014). Single-molecule reconstruction of oligonucleotide secondary structure by atomic force microscopy. *Small*, *10*(16), 3257–3261. https://doi.org/10.1002/smll.201400265

Qiang, W., Kelley, K., & Tycko, R. (2013). Polymorph-specific kinetics and thermodynamics of β-amyloid fibril growth. *Journal of the American Chemical Society*, *135*(18), 6860–6871. https://doi.org/10.1021/ja311963f

Qiang, W., Yau, W.-M., Lu, J.-X., Collinge, J., & Tycko, R. (2017). Structural variation in amyloid-β fibrils from Alzheimer's disease clinical subtypes. *Nature*, *541*(7636), 217–221. https://doi.org/10.1038/nature20814

Qiang, W., Yau, W.-M., Luo, Y., Mattson, M. P., & Tycko, R. (2012). Antiparallel β-sheet architecture in Iowa-mutant β-amyloid fibrils. *Proceedings of the National Academy of Sciences*, *109*(12), 4443–4448. https://doi.org/10.1073/pnas.1111305109

Quist, A., Doudevski, I., Lin, H., Azimova, R., Ng, D., Frangione, B., Kagan, B., Ghiso, J., & Lal, R. (2005). Amyloid ion channels: A common structural link for protein-misfolding disease. *Proceedings of the National Academy of Sciences of the United States of America*, *102*(30), 10427–10432. https://doi.org/10.1073/pnas.0502066102

Radamaker, L., Baur, J., Huhn, S., Haupt, C., Hegenbart, U., Schönland, S., Bansal, A., Schmidt, M., & Fändrich, M. (2021). Cryo-EM reveals structural breaks in a patient-derived amyloid fibril from systemic AL amyloidosis. *Nature Communications*, *12*(1), 875. https://doi.org/10.1038/s41467-021-21126-2

Radamaker, L., Lin, Y.-H., Annamalai, K., Huhn, S., Hegenbart, U., Schönland, S. O., Fritz, G., Schmidt, M., & Fändrich, M. (2019). Cryo-EM structure of a light chain-derived amyloid fibril from a patient with systemic AL amyloidosis. *Nature Communications*, *10*(1), 1103. https://doi.org/10.1038/s41467-019-09032-0

Ramalho, R., Rankovic, S., Zhou, J., Aiken, C., & Rousso, I. (2016). Analysis of the mechanical properties of wild type and hyperstable mutants of the HIV-1 capsid. *Retrovirology*, *13*, 17. https://doi.org/10.1186/s12977-016-0250-4

Reynolds, N. P., Soragni, A., Rabe, M., Verdes, D., Liverani, E., Handschin, S., Riek, R., & Seeger, S. (2011). Mechanism of membrane interaction and disruption by α-synuclein. *Journal of the American Chemical Society*, *133*(48), 19366–19375. https://doi.org/10.1021/ja2029848

Rezai-Zadeh, K., Arendash, G. W., Hou, H., Fernandez, F., Jensen, M., Runfeldt, M., Shytle, R. D., & Tan, J. (2008). Green tea epigallocatechin-3-gallate (EGCG) reduces β-amyloid mediated cognitive impairment and modulates tau pathology in Alzheimer transgenic mice. *Brain Research*, *1214*, 177–187. https://doi.org/10.1016/j.brainres.2008.02.107

Riek, R. (2017). The three-dimensional structures of amyloids. *Cold Spring Harbor Perspectives in Biology*, *9*(2), a023572. https://doi.org/10.1101/cshperspect.a023572

Röder, C., Kupreichyk, T., Gremer, L., Schäfer, L. U., Pothula, K. R., Ravelli, R. B. G., Willbold, D., Hoyer, W., & Schröder, G. F. (2020). Cryo-EM structure of islet amyloid polypeptide fibrils reveals similarities with amyloid-β fibrils. *Nature Structural & Molecular Biology*, *27*(7), 660–667. https://doi.org/10.1038/s41594-020-0442-4

Röder, C., Vettore, N., Mangels, L. N., Gremer, L., Ravelli, R. B. G., Willbold, D., Hoyer, W., Buell, A. K., & Schröder, G. F. (2019). Atomic structure of PI3-kinase SH3 amyloid fibrils by cryo-electron microscopy. *Nature Communications*, *10*(1), 3754. https://doi.org/10.1038/s41467-019-11320-8

Rodriguez, J. A., Ivanova, M. I., Sawaya, M. R., Cascio, D., Reyes, F. E., Shi, D., Sangwan, S., Guenther, E. L., Johnson, L. M., Zhang, M., Jiang, L., Arbing, M. A., Nannenga, B. L., Hattne, J., Whitelegge, J., Brewster, A. S., Messerschmidt, M., Boutet, S., Sauter, N. K., Gonen, T., & Eisenberg, D. S. (2015). Structure of the toxic core of α-synuclein from invisible crystals. *Nature*, *525*(7570), 486–490. https://doi.org/10.1038/nature15368

Rohou, A., & Grigorieff, N. (2014). Frealix: Model-based refinement of helical filament structures from electron micrographs. *Journal of Structural Biology*, *186*(2), 234–244. https://doi.org/10.1016/j.jsb.2014.03.012

Roland, B. P., Kodali, R., Mishra, R., & Wetzel, R. (2013). A serendipitous survey of prediction algorithms for amyloidogenicity. *Biopolymers*, *100*(6), 780–789. https://doi.org/10.1002/bip.22305

Rothemund, P. W. K. (2006). Folding DNA to create nanoscale shapes and patterns. *Nature*, *440*(7082), 297–302. https://doi.org/10.1038/nature04586

Rott, R., Szargel, R., Shani, V., Hamza, H., Savyon, M., Elghani, F. A., Bandopadhyay, R., & Engelender, S. (2017). SUMOylation and ubiquitination reciprocally regulate α-synuclein degradation and pathological aggregation. *Proceedings of the National Academy of Sciences*, *114*(50), 13176–13181. https://doi.org/10.1073/pnas.1704351114

Rouse, S. L., Stylianou, F., Wu, H. Y. G., Berry, J.-L., Sewell, L., Morgan, R. M. L., Sauerwein, A. C., & Matthews, S. (2018). The FapF amyloid secretion transporter possesses an atypical asymmetric coiled coil. *Journal of Molecular Biology*, *430*(20), 3863–3871. https://doi.org/10.1016/j.jmb.2018.06.007

Rovere, M., Sanderson, J. B., Fonseca-Ornelas, L., Patel, D. S., & Bartels, T. (2018). Refolding of helical soluble α-synuclein through transient interaction with lipid interfaces. *FEBS Letters*, *592*(9), 1464–1472. https://doi.org/10.1002/1873-3468.13047

Ruggeri, F. S., Flagmeier, P., Kumita, J. R., Meisl, G., Chirgadze, D. Y., Bongiovanni, M. N., Knowles, T. P. J., & Dobson, C. M. (2020). The influence of pathogenic mutations in α-synuclein on biophysical and structural characteristics of amyloid fibrils. *ACS Nano*, *14*(5), 5213–5222. https://doi.org/10.1021/acsnano.9b09676

Ruggeri, F. S., Longo, G., Faggiano, S., Lipiec, E., Pastore, A., & Dietler, G. (2015). Infrared nanospectroscopy characterization of oligomeric and fibrillar aggregates during

amyloid formation. *Nature Communications*, *6*(1), 7831. https://doi.org/10.1038/ncomms8831

Sachse, C. (2015). Single-particle based helical reconstruction—How to make the most of real and Fourier space. *AIMS Biophysics*, *2*(2), 219. https://doi.org/10.3934/biophy.2015.2.219

Sachse, C., Fändrich, M., & Grigorieff, N. (2008). Paired β-sheet structure of an Aβ(1-40) amyloid fibril revealed by electron microscopy. *Proceedings of the National Academy of Sciences of the United States of America*, *105*(21), 7462–7466. https://doi.org/10.1073/pnas.0712290105

Sachse, C., Grigorieff, N., & Fändrich, M. (2010). Nanoscale flexibility parameters of Alzheimer amyloid fibrils determined by electron cryo-microscopy. *Angewandte Chemie (International Ed. in English)*, *49*(7), 1321–1323. https://doi.org/10.1002/anie.200904781

SantaCruz, K. S., Sonnen, J. A., Pezhouh, M. K., Desrosiers, M. F., Nelson, P. T., & Tyas, S. L. (2011). Alzheimer disease pathology in subjects without dementia in two studies of aging: The Nun Study and the Adult Changes in Thought study. *Journal of Neuropathology and Experimental Neurology*, *70*(10), 832–840. https://doi.org/10.1097/NEN.0b013e31822e8ae9

Sant'Anna, R., Fernández, M. R., Batlle, C., Navarro, S., de Groot, N. S., Serpell, L., & Ventura, S. (2016). Characterization of amyloid cores in prion domains. *Scientific Reports*, *6*(1), 34274. https://doi.org/10.1038/srep34274

Santos, J., Pujols, J., Pallarès, I., Iglesias, V., & Ventura, S. (2020). Computational prediction of protein aggregation: Advances in proteomics, conformation-specific algorithms and biotechnological applications. *Computational and Structural Biotechnology Journal*, *18*, 1403–1413. https://doi.org/10.1016/j.csbj.2020.05.026

Sasahara, K., Morigaki, K., Okazaki, T., & Hamada, D. (2012). Binding of islet amyloid polypeptide to supported lipid bilayers and amyloid aggregation at the membranes. *Biochemistry*, *51*(35), 6908–6919. https://doi.org/10.1021/bi300542g

Sawaya, M. R., Hughes, M. P., Rodriguez, J. A., Riek, R., & Eisenberg, D. S. (2021). The expanding amyloid family: Structure, stability, function, and pathogenesis. *Cell*, *184*(19), 4857–4873. https://doi.org/10.1016/j.cell.2021.08.013

Sawaya, M. R., Rodriguez, J., Cascio, D., Collazo, M. J., Shi, D., Reyes, F. E., Hattne, J., Gonen, T., & Eisenberg, D. S. (2016). *Ab initio* structure determination from prion nanocrystals at atomic resolution by MicroED. *Proceedings of the National Academy of Sciences*, *113*(40), 11232–11236.

Sawaya, M. R., Sambashivan, S., Nelson, R., Ivanova, M. I., Sievers, S. A., Apostol, M. I., Thompson, M. J., Balbirnie, M., Wiltzius, J. J. W., McFarlane, H. T., Madsen, A. Ø., Riekel, C., & Eisenberg, D. (2007). Atomic structures of amyloid cross-β spines reveal varied steric zippers. *Nature*, *447*(7143), 453–457. https://doi.org/10.1038/nature05695

Scheckel, C., & Aguzzi, A. (2018). Prions, prionoids and protein misfolding disorders. *Nature Reviews Genetics*, *19*(7), 405–418. https://doi.org/10.1038/s41576-018-0011-4

Scheres, S. H. W. (2020). Amyloid structure determination in RELION-3.1. *Acta Crystallographica. Section D, Structural Biology*, *76*(Pt 2), 94–101. https://doi.org/10.1107/S2059798319016577

Schmidt, A., Annamalai, K., Schmidt, M., Grigorieff, N., & Fändrich, M. (2016). Cryo-EM reveals the steric zipper structure of a light chain-derived amyloid fibril. *Proceedings of the National Academy of Sciences*, *113*(22), 6200–6205. https://doi.org/10.1073/pnas.1522282113

Schmidt, M., Rohou, A., Lasker, K., Yadav, J. K., Schiene-Fischer, C., Fändrich, M., & Grigorieff, N. (2015). Peptide dimer structure in an Aβ(1–42) fibril visualized with cryo-EM. *Proceedings of the National Academy of Sciences*, *112*(38), 11858–11863. https://doi.org/10.1073/pnas.1503455112

Schmidt, M., Sachse, C., Richter, W., Xu, C., Fändrich, M., & Grigorieff, N. (2009). Comparison of Alzheimer Aβ(1–40) and Aβ(1–42) amyloid fibrils reveals similar protofilament structures. *Proceedings of the National Academy of Sciences*, *106*(47), 19813–19818. https://doi.org/10.1073/pnas.0905007106

Schmidt, M., Wiese, S., Adak, V., Engler, J., Agarwal, S., Fritz, G., Westermark, P., Zacharias, M., & Fändrich, M. (2019). Cryo-EM structure of a transthyretin-derived amyloid fibril from a patient with hereditary ATTR amyloidosis. *Nature Communications*, *10*(1), 5008. https://doi.org/10.1038/s41467-019-13038-z

Schütz, A. K., Soragni, A., Hornemann, S., Aguzzi, A., Ernst, M., Böckmann, A., & Meier, B. H. (2011). The amyloid–Congo red Interface at atomic resolution. *Angewandte Chemie International Edition*, *50*(26), 5956–5960. https://doi.org/10.1002/anie.201008276

Schütz, A. K., Vagt, T., Huber, M., Ovchinnikova, O. Y., Cadalbert, R., Wall, J., Güntert, P., Böckmann, A., Glockshuber, R., & Meier, B. H. (2015). Atomic-resolution three-dimensional structure of amyloid β fibrils bearing the Osaka mutation. *Angewandte Chemie International Edition*, *54*(1), 331–335. https://doi.org/10.1002/anie.201408598

Schweighauser, M., Shi, Y., Tarutani, A., Kametani, F., Murzin, A. G., Ghetti, B., Matsubara, T., Tomita, T., Ando, T., Hasegawa, K., Murayama, S., Yoshida, M., Hasegawa, M., Scheres, S. H. W., & Goedert, M. (2020). Structures of α-synuclein filaments from

multiple system atrophy. *Nature*, *585*(7825), 464–469. https://doi.org/10.1038/s41586-020-2317-6

Sciacca, M. F. M., Tempra, C., Scollo, F., Milardi, D., & La Rosa, C. (2018). Amyloid growth and membrane damage: Current themes and emerging perspectives from theory and experiments on Aβ and hIAPP. *Biochimica et Biophysica Acta (BBA) - Biomembranes*, *1860*(9), 1625–1638. https://doi.org/10.1016/j.bbamem.2018.02.022

Sebastiao, M., Quittot, N., Marcotte, I., & Bourgault, S. (2019). Glycosaminoglycans induce amyloid self-assembly of a peptide hormone by concerted secondary and quaternary conformational transitions. *Biochemistry*. https://doi.org/10.1021/acs.biochem.8b01206

Seidler, P. M., Boyer, D. R., Sawaya, M. R., Ge, P., Shin, W. S., DeTure, M. A., Dickson, D. W., Jiang, L., & Eisenberg, D. S. (2020). CryoEM reveals how the small molecule EGCG binds to Alzheimer's brain-derived tau fibrils and initiates fibril disaggregation. *BioRxiv*, 2020.05.29.124537. https://doi.org/10.1101/2020.05.29.124537

Serpell, L. C., Fraser, P. E., & Sunde, M. (1999). X-ray fiber diffraction of amyloid fibrils. In *Methods in Enzymology* (Vol. 309, pp. 526–536). Academic Press. https://doi.org/10.1016/S0076-6879(99)09036-9

Serra-Batiste, M., Ninot-Pedrosa, M., Bayoumi, M., Gairí, M., Maglia, G., & Carulla, N. (2016). Aβ42 assembles into specific β-barrel pore-forming oligomers in membrane-mimicking environments. *Proceedings of the National Academy of Sciences*, *113*(39), 10866–10871. https://doi.org/10.1073/pnas.1605104113

Serrano-Pozo, A., Betensky, R. A., Frosch, M. P., & Hyman, B. T. (2016). Plaque-associated local toxicity increases over the clinical course of Alzheimer disease. *The American Journal of Pathology*, *186*(2), 375–384. https://doi.org/10.1016/j.ajpath.2015.10.010

Seuring, C., Verasdonck, J., Gath, J., Ghosh, D., Nespovitaya, N., Wälti, M. A., Maji, S. K., Cadalbert, R., Güntert, P., Meier, B. H., & Riek, R. (2020). The three-dimensional structure of human β-endorphin amyloid fibrils. *Nature Structural & Molecular Biology*, *27*(12), 1178–1184. https://doi.org/10.1038/s41594-020-00515-z

Sgourakis, N. G., Yau, W.-M., & Qiang, W. (2015). Modeling an in-register, parallel "Iowa" Aβ fibril structure using solid-state NMR data from labeled samples with Rosetta. *Structure*, *23*(1), 216–227. https://doi.org/10.1016/j.str.2014.10.022

Shankar, G. M., Li, S., Mehta, T. H., Garcia-Munoz, A., Shepardson, N. E., Smith, I., Brett, F. M., Farrell, M. A., Rowan, M. J., Lemere, C. A., Regan, C. M., Walsh, D. M., Sabatini, B. L., & Selkoe, D. J. (2008). Amyloid-β protein dimers isolated directly from Alzheimer's brains impair synaptic plasticity and memory. *Nature Medicine*, *14*(8), 837–842. https://doi.org/10.1038/nm1782

Sheynis, T., Friediger, A., Xue, W.-F., Hellewell, A. L., Tipping, K. W., Hewitt, E. W., Radford, S. E., & Jelinek, R. (2013). Aggregation modulators interfere with membrane interactions of β2-microglobulin fibrils. *Biophysical Journal*, *105*(3), 745–755. https://doi.org/10.1016/j.bpj.2013.06.015

Shi, Y., Zhang, W., Yang, Y., Murzin, A. G., Falcon, B., Kotecha, A., van Beers, M., Tarutani, A., Kametani, F., Garringer, H. J., Vidal, R., Hallinan, G. I., Lashley, T., Saito, Y., Murayama, S., Yoshida, M., Tanaka, H., Kakita, A., Ikeuchi, T., Robinson, A. C., Mann, D. M. A., Kovacs, G. G., Revesz, T., Ghetti, B., Hasegawa, M., Goedert, M., & Scheres, S. H. W. (2021). Structure-based classification of tauopathies. *Nature*, 1–5. https://doi.org/10.1038/s41586-021-03911-7

Shorter, J., & Lindquist, S. (2005). Prions as adaptive conduits of memory and inheritance. *Nature Reviews Genetics*, *6*(6), 435–450. https://doi.org/10.1038/nrg1616

Sidhu, A., Vaneyck, J., Blum, C., Segers-Nolten, I., & Subramaniam, V. (2018). Polymorph-specific distribution of binding sites determines thioflavin-T fluorescence intensity in α-synuclein fibrils. *Amyloid: The International Journal of Experimental and Clinical Investigation: The Official Journal of the International Society of Amyloidosis*, *25*(3), 189–196. https://doi.org/10.1080/13506129.2018.1517736

Simonsen, A. H., Hansson, S. F., Ruetschi, U., McGuire, J., Podust, V. N., Davies, H. A., Mehta, P., Waldemar, G., Zetterberg, H., Andreasen, N., Wallin, A., & Blennow, K. (2007). Amyloid β1-40 quantification in CSF: comparison between chromatographic and immunochemical methods. *Dementia and Geriatric Cognitive Disorders*, *23*(4), 246–250. https://doi.org/10.1159/000100020

Smith, J. F., Knowles, T. P. J., Dobson, C. M., MacPhee, C. E., & Welland, M. E. (2006). Characterization of the nanoscale properties of individual amyloid fibrils. *Proceedings of the National Academy of Sciences of the United States of America*, *103*(43), 15806–15811. https://doi.org/10.1073/pnas.0604035103

Smith, J. F., Knowles, T. P. J., Dobson, C. M., Macphee, C. E., & Welland, M. E. (2006). Characterization of the nanoscale properties of individual amyloid fibrils. *Proceedings of the National Academy of Sciences of the United States of America*, *103*(43), 15806–15811. https://doi.org/10.1073/pnas.0604035103

Solomon, A., Weiss, D. T., Murphy, C. L., Hrncic, R., Wall, J. S., & Schell, M. (1998). Light chain-associated amyloid deposits comprised of a novel κ constant domain. *Proceedings of the National Academy of Sciences*, *95*(16), 9547–9551. https://doi.org/10.1073/pnas.95.16.9547

Soto, C. (2003). Unfolding the role of protein misfolding in neurodegenerative diseases. *Nature Reviews Neuroscience*, *4*(1), 49–60. https://doi.org/10.1038/nrn1007

Sparr, E., Engel, M. F. M., Sakharov, D. V., Sprong, M., Jacobs, J., Kruijff, B. de, Höppener, J. W. M., & Killian, J. A. (2004). Islet amyloid polypeptide-induced membrane leakage involves uptake of lipids by forming amyloid fibers. *FEBS Letters*, *577*(1–2), 117–120. https://doi.org/10.1016/j.febslet.2004.09.075

Spillantini, M. G., & Goedert, M. (2013). Tau pathology and neurodegeneration. *The Lancet Neurology*, *12*(6), 609–622. https://doi.org/10.1016/S1474-4422(13)70090-5

Stefani, M. (2007). Generic cell dysfunction in neurodegenerative disorders: Role of surfaces in early protein misfolding, aggregation, and aggregate cytotoxicity. *The Neuroscientist*, *13*(5), 519–531. https://doi.org/10.1177/1073858407303428

Stephan, J. S., Fioriti, L., Lamba, N., Colnaghi, L., Karl, K., Derkatch, I. L., & Kandel, E. R. (2015). The CPEB3 protein is a functional prion that interacts with the actin cytoskeleton. *Cell Reports*, *11*(11), 1772–1785. https://doi.org/10.1016/j.celrep.2015.04.060

Sternke-Hoffmann, R., Pauly, T., Norrild, R. K., Hansen, J., Dupré, M., Tucholski, F., Duchateau, M., Rey, M., Metzger, S., Boquoi, A., Platten, F., Egelhaaf, S. U., Chamot-Rooke, J., Fenk, R., Nagel-Steger, L., Haas, R., & Buell, A. K. (2021). Universal amyloidogenicity of patient-derived immunoglobulin light chains. *BioRxiv*, 2021.05.12.443858. https://doi.org/10.1101/2021.05.12.443858

Sulatskaya, A. I., Sulatsky, M. I., Antifeeva, I. A., Kuznetsova, I. M., & Turoverov, K. K. (2019). Structural analogue of Thioflavin T, DMASEBT, as a tool for amyloid fibrils study. *Analytical Chemistry*. https://doi.org/10.1021/acs.analchem.8b05737

Sun, Y., Hou, S., Zhao, K., Long, H., Liu, Z., Gao, J., Zhang, Y., Su, X.-D., Li, D., & Liu, C. (2020). Cryo-EM structure of full-length α-synuclein amyloid fibril with Parkinson's disease familial A53T mutation. *Cell Research*, *30*(4), 360–362. https://doi.org/10.1038/s41422-020-0299-4

Sun, Y., Zhao, K., Xia, W., Feng, G., Gu, J., Ma, Y., Gui, X., Zhang, X., Fang, Y., Sun, B., Wang, R., Liu, C., & Li, D. (2020). The nuclear localization sequence mediates hnRNPA1 amyloid fibril formation revealed by cryoEM structure. *Nature Communications*, *11*(1), 6349. https://doi.org/10.1038/s41467-020-20227-8

Sweeny, E. A., & Shorter, J. (2016). Mechanistic and structural insights into the prion-disaggregase activity of Hsp104. *Journal of Molecular Biology*, *428*(9, Part B), 1870–1885. https://doi.org/10.1016/j.jmb.2015.11.016

Swuec, P., Lavatelli, F., Tasaki, M., Paissoni, C., Rognoni, P., Maritan, M., Brambilla, F., Milani, P., Mauri, P., Camilloni, C., Palladini, G., Merlini, G., Ricagno, S., & Bolognesi, M. (2019). Cryo-EM structure of cardiac amyloid fibrils from an immunoglobulin light chain AL amyloidosis patient. *Nature Communications*, *10*(1), 1269. https://doi.org/10.1038/s41467-019-09133-w

Tagliavini, F., Tiraboschi, P., & Federico, A. (2021). Alzheimer's disease: The controversial approval of aducanumab. *Neurological Sciences*, *42*(8), 3069–3070. https://doi.org/10.1007/s10072-021-05497-4

Tanaka, M., Chien, P., Yonekura, K., & Weissman, J. S. (2005). Mechanism of cross-species prion transmission: An infectious conformation compatible with two highly divergent yeast prion proteins. *Cell*, *121*(1), 49–62. https://doi.org/10.1016/j.cell.2005.03.008

Tanaka, M., Collins, S. R., Toyama, B. H., & Weissman, J. S. (2006). The physical basis of how prion conformations determine strain phenotypes. *Nature*, *442*(7102), 585–589. https://doi.org/10.1038/nature04922

Tarutani, A., Arai, T., Murayama, S., Hisanaga, S., & Hasegawa, M. (2018). Potent prion-like behaviors of pathogenic α-synuclein and evaluation of inactivation methods. *Acta Neuropathologica Communications*, *6*(1), 29. https://doi.org/10.1186/s40478-018-0532-2

Taylor, J. D., & Matthews, S. J. (2015). New insight into the molecular control of bacterial functional amyloids. *Frontiers in Cellular and Infection Microbiology*, *5*, 33. https://doi.org/10.3389/fcimb.2015.00033

Tian, Y., Liang, R., Kumar, A., Szwedziak, P., & H. Viles, J. (2021). 3D-visualization of amyloid-β oligomer interactions with lipid membranes by cryo-electron tomography. *Chemical Science*, *12*(20), 6896–6907. https://doi.org/10.1039/D0SC06426B

Törnquist, M., Michaels, T. C. T., Sanagavarapu, K., Yang, X., Meisl, G., Cohen, S. I. A., Knowles, T. P. J., & Linse, S. (2018). Secondary nucleation in amyloid formation. *Chemical Communications*, *54*(63), 8667–8684. https://doi.org/10.1039/C8CC02204F

Torrente, M. P., & Shorter, J. (2013). The metazoan protein disaggregase and amyloid depolymerase system: Hsp110, Hsp70, Hsp40, and small heat shock proteins. *Prion*, *7*(6), 457–463.

Tuite, M. F. (2000). Yeast prions and their prion-forming domain. *Cell*, *100*(3), 289–292. https://doi.org/10.1016/S0092-8674(00)80663-7

Tuttle, M. D., Comellas, G., Nieuwkoop, A. J., Covell, D. J., Berthold, D. A., Kloepper, K. D., Courtney, J. M., Kim, J. K., Barclay, A. M., Kendall, A., Wan, W., Stubbs, G., Schwieters, C. D., Lee, V. M. Y., George, J. M., & Rienstra, C. M. (2016). Solid-state NMR structure of a pathogenic fibril of full-length human α-synuclein. *Nature Structural & Molecular Biology*, *23*(5), 409–415. https://doi.org/10.1038/nsmb.3194

Tycko, R. (2011). Solid state NMR studies of amyloid fibril structure. *Annual Review of Physical Chemistry*, *62*, 279–299. https://doi.org/10.1146/annurev-physchem-032210-103539

Tycko, R. (2015). Amyloid polymorphism: Structural basis and neurobiological relevance. *Neuron*, *86*(3), 632–645. https://doi.org/10.1016/j.neuron.2015.03.017

Udomprasert, A., Bongiovanni, M. N., Sha, R., Sherman, W. B., Wang, T., Arora, P. S., Canary, J. W., Gras, S. L., & Seeman, N. C. (2014). Amyloid fibrils nucleated and organized by DNA origami constructions. *Nature Nanotechnology*, *9*(7), 537–541. https://doi.org/10.1038/nnano.2014.102

Ulamec, S. M., & Radford, S. E. (2020). Spot the difference: Function versus toxicity in amyloid fibrils. *Trends in Biochemical Sciences*. https://doi.org/10.1016/j.tibs.2020.04.007

Vahdat Shariat Panahi, A., Hultman, P., Öllinger, K., Westermark, G. T., & Lundmark, K. (2019). Lipid membranes accelerate amyloid formation in the mouse model of AA amyloidosis. *Amyloid: The International Journal of Experimental and Clinical Investigation: The Official Journal of the International Society of Amyloidosis*, *26*(1), 34–44. https://doi.org/10.1080/13506129.2019.1576606

Van Melckebeke, H., Wasmer, C., Lange, A., AB, E., Loquet, A., Böckmann, A., & Meier, B. H. (2010). Atomic-resolution three-dimensional structure of HET-s(218−289) amyloid fibrils by solid-state NMR spectroscopy. *Journal of the American Chemical Society*, *132*(39), 13765–13775. https://doi.org/10.1021/ja104213j

Verma, M., Vats, A., & Taneja, V. (2015). Toxic species in amyloid disorders: Oligomers or mature fibrils. *Annals of Indian Academy of Neurology*, *18*(2), 138–145. https://doi.org/10.4103/0972-2327.144284

Vigolo, D., Zhao, J., Handschin, S., Cao, X., deMello, A. J., & Mezzenga, R. (2017). Continuous isotropic-nematic transition in amyloid fibril suspensions driven by thermophoresis. *Scientific Reports*, *7*(1), 1211. https://doi.org/10.1038/s41598-017-01287-1

Viles, J. H. (2012). Metal ions and amyloid fiber formation in neurodegenerative diseases. Copper, zinc and iron in Alzheimer's, Parkinson's and prion diseases. *Coordination Chemistry Reviews*, *256*(19), 2271–2284. https://doi.org/10.1016/j.ccr.2012.05.003

Villarrubia, J. S. (1997). Algorithms for scanned probe microscope image simulation, surface reconstruction, and tip estimation. *Journal of Research of the National Institute of Standards and Technology*, *102*(4), 425–454. https://doi.org/10.6028/jres.102.030

Walsh, I., Seno, F., Tosatto, S. C. E., & Trovato, A. (2014). PASTA 2.0: An improved server for protein aggregation prediction. *Nucleic Acids Research*, *42*(W1), W301–W307. https://doi.org/10.1093/nar/gku399

Wälti, M. A., Ravotti, F., Arai, H., Glabe, C. G., Wall, J. S., Böckmann, A., Güntert, P., Meier, B. H., & Riek, R. (2016). Atomic-resolution structure of a disease-relevant Aβ(1–42) amyloid fibril. *Proceedings of the National Academy of Sciences*, *113*(34), E4976–E4984. https://doi.org/10.1073/pnas.1600749113

Wang, L.-Q., Zhao, K., Yuan, H.-Y., Wang, Q., Guan, Z., Tao, J., Li, X.-N., Sun, Y., Yi, C.-W., Chen, J., Li, D., Zhang, D., Yin, P., Liu, C., & Liang, Y. (2020). Cryo-EM structure of an amyloid fibril formed by full-length human prion protein. *Nature Structural & Molecular Biology*, *27*(6), 598–602. https://doi.org/10.1038/s41594-020-0441-5

Wang, Y., Yan, T., Lu, H., Yin, W., Lin, B., Fan, W., Zhang, X., & Fernandez-Funez, P. (2017). Lessons from anti-amyloid-β immunotherapies in Alzheimer disease: Aiming at a moving target. *Neuro-Degenerative Diseases*, *17*(6), 242–250. https://doi.org/10.1159/000478741

Wasmer, C., Lange, A., Van Melckebeke, H., Siemer, A. B., Riek, R., & Meier, B. H. (2008). Amyloid fibrils of the HET-s(218-289) prion form a β solenoid with a triangular

hydrophobic core. *Science (New York, N.Y.)*, *319*(5869), 1523–1526. https://doi.org/10.1126/science.1151839

Watanabe-Nakayama, T., Ono, K., Itami, M., Takahashi, R., Teplow, D. B., & Yamada, M. (2016). High-speed atomic force microscopy reveals structural dynamics of amyloid β_{1-42} aggregates. *Proceedings of the National Academy of Sciences*, *113*(21), 5835–5840. https://doi.org/10.1073/pnas.1524807113

Waters, J. (2010). The concentration of soluble extracellular amyloid-β protein in acute brain slices from CRND8 mice. *PloS One*, *5*(12), e15709. https://doi.org/10.1371/journal.pone.0015709

Wegenast-Braun, B. M., Skodras, A., Bayraktar, G., Mahler, J., Fritschi, S. K., Klingstedt, T., Mason, J. J., Hammarström, P., Nilsson, K. P. R., Liebig, C., & Jucker, M. (2012). Spectral discrimination of cerebral amyloid lesions after peripheral application of luminescent conjugated oligothiophenes. *The American Journal of Pathology*, *181*(6), 1953–1960. https://doi.org/10.1016/j.ajpath.2012.08.031

Wentink, A. S., Nillegoda, N. B., Feufel, J., Ubartaitė, G., Schneider, C. P., De Los Rios, P., Hennig, J., Barducci, A., & Bukau, B. (2020). Molecular dissection of amyloid disaggregation by human HSP70. *Nature*, *587*(7834), 483–488. https://doi.org/10.1038/s41586-020-2904-6

Wickner, R. B. (1994). [URE3] as an altered URE2 protein: Evidence for a prion analog in *Saccharomyces cerevisiae*. *Science (New York, N.Y.)*, *264*(5158), 566–569.

Willander, H., Presto, J., Askarieh, G., Biverstål, H., Frohm, B., Knight, S. D., Johansson, J., & Linse, S. (2012). BRICHOS domains efficiently delay fibrillation of amyloid β-peptide. *The Journal of Biological Chemistry*, *287*(37), 31608–31617. https://doi.org/10.1074/jbc.M112.393157

Willbold, D., Strodel, B., Schröder, G. F., Hoyer, W., & Heise, H. (2021). Amyloid-type protein aggregation and prion-like properties of amyloids. *Chemical Reviews*. https://doi.org/10.1021/acs.chemrev.1c00196

Winkler, J., Tyedmers, J., Bukau, B., & Mogk, A. (2012). Hsp70 targets Hsp100 chaperones to substrates for protein disaggregation and prion fragmentation. *The Journal of Cell Biology*, *198*(3), 387–404. https://doi.org/10.1083/jcb.201201074

Wu, X.-L., Hu, H., Dong, X.-Q., Zhang, J., Wang, J., Schwieters, C. D., Liu, J., Wu, G.-X., Li, B., Lin, J.-Y., Wang, H.-Y., & Lu, J.-X. (2021). The amyloid structure of mouse RIPK3 (receptor interacting protein kinase 3) in cell necroptosis. *Nature Communications*, *12*(1), 1627. https://doi.org/10.1038/s41467-021-21881-2

Xiao, Y., Ma, B., McElheny, D., Parthasarathy, S., Long, F., Hoshi, M., Nussinov, R., & Ishii, Y. (2015). Aβ(1-42) fibril structure illuminates self-recognition and replication of amyloid in Alzheimer's disease. *Nature Structural & Molecular Biology*, *22*(6), 499–505. https://doi.org/10.1038/nsmb.2991

Xue, C., Lin, T. Y., Chang, D., & Guo, Z. (2017). Thioflavin T as an amyloid dye: Fibril quantification, optimal concentration and effect on aggregation. *Royal Society Open Science*, *4*(1). https://doi.org/10.1098/rsos.160696

Xue, W.-F. (2014). Chapter 2—Amyloid fibril length quantification by atomic force microscopy. In V. N. Uversky & Y. L. Lyubchenko (Eds.), *Bio-nanoimaging* (pp. 17–25). Academic Press. https://doi.org/10.1016/B978-0-12-394431-3.00002-X

Xue, W.-F., Hellewell, A. L., Gosal, W. S., Homans, S. W., Hewitt, E. W., & Radford, S. E. (2009). Fibril fragmentation enhances amyloid cytotoxicity. *The Journal of Biological Chemistry*, *284*(49), 34272–34282. https://doi.org/10.1074/jbc.M109.049809

Xue, W.-F., Hellewell, A. L., Hewitt, E. W., & Radford, S. E. (2010). Fibril fragmentation in amyloid assembly and cytotoxicity. *Prion*, *4*(1), 20–25.

Xue, W.-F., Homans, S. W., & Radford, S. E. (2008). Systematic analysis of nucleation-dependent polymerization reveals new insights into the mechanism of amyloid self-assembly. *Proceedings of the National Academy of Sciences*, *105*(26), 8926–8931. https://doi.org/10.1073/pnas.0711664105

Xue, W.-F., Homans, S. W., & Radford, S. E. (2009). Amyloid fibril length distribution quantified by atomic force microscopy single-particle image analysis. *Protein Engineering, Design and Selection*, *22*(8), 489–496. https://doi.org/10.1093/protein/gzp026

Yang, J., J. Dear, A., Yao, Q.-Q., Liu, Z., M. Dobson, C., J. Knowles, T. P., Wu, S., & Perrett, S. (2020). Amelioration of aggregate cytotoxicity by catalytic conversion of protein oligomers into amyloid fibrils. *Nanoscale*. https://doi.org/10.1039/D0NR01481H

Yashima, E., Ousaka, N., Taura, D., Shimomura, K., Ikai, T., & Maeda, K. (2016). Supramolecular helical systems: Helical assemblies of small molecules, foldamers, and polymers with chiral amplification and their functions. *Chemical Reviews*, *116*(22), 13752–13990. https://doi.org/10.1021/acs.chemrev.6b00354

Younan, N. D., & Viles, J. H. (2015). A comparison of three fluorophores for the detection of amyloid fibers and prefibrillar oligomeric assemblies. ThT (Thioflavin T); ANS (1-Anilinonaphthalene-8-sulfonic Acid); and bisANS (4,4′-Dianilino-1,1′-binaphthyl-5,5′-disulfonic Acid). *Biochemistry*, *54*(28), 4297–4306. https://doi.org/10.1021/acs.biochem.5b00309

Young, L. M., Ashcroft, A. E., & Radford, S. E. (2017). Small molecule probes of protein aggregation. *Current Opinion in Chemical Biology*, *39*, 90–99. https://doi.org/10.1016/j.cbpa.2017.06.008

Zapadka, K. L., Becher, F. J., Uddin, S., Varley, P. G., Bishop, S., Gomes Dos Santos, A. L., & Jackson, S. E. (2016). A pH-induced switch in human glucagon-like peptide-1 aggregation kinetics. *Journal of the American Chemical Society*, *138*(50), 16259–16265. https://doi.org/10.1021/jacs.6b05025

Zeng, G., Vad, B. S., Dueholm, M. S., Christiansen, G., Nilsson, M., Tolker-Nielsen, T., Nielsen, P. H., Meyer, R. L., & Otzen, D. E. (2015). Functional bacterial amyloid increases *Pseudomonas* biofilm hydrophobicity and stiffness. *Frontiers in Microbiology*, *6*, 1099. https://doi.org/10.3389/fmicb.2015.01099

Zhang, R., Hu, X., Khant, H., Ludtke, S. J., Chiu, W., Schmid, M. F., Frieden, C., & Lee, J.-M. (2009). Interprotofilament interactions between Alzheimer's $A\beta_{1–42}$ peptides in amyloid fibrils revealed by cryoEM. *Proceedings of the National Academy of Sciences*, *106*(12), 4653–4658. https://doi.org/10.1073/pnas.0901085106

Zhang, W., Falcon, B., Murzin, A. G., Fan, J., Crowther, R. A., Goedert, M., & Scheres, S. H. (2019). Heparin-induced tau filaments are polymorphic and differ from those in Alzheimer's and Pick's diseases. *ELife*, *8*, e43584. https://doi.org/10.7554/eLife.43584

Zhang, W., Tarutani, A., Newell, K. L., Murzin, A. G., Matsubara, T., Falcon, B., Vidal, R., Garringer, H. J., Shi, Y., Ikeuchi, T., Murayama, S., Ghetti, B., Hasegawa, M., Goedert, M., & Scheres, S. H. W. (2020). Novel tau filament fold in corticobasal degeneration. *Nature*, *580*(7802), 283–287. https://doi.org/10.1038/s41586-020-2043-0

Zhang, X., Wesén, E., Kumar, R., Bernson, D., Gallud, A., Paul, A., Wittung-Stafshede, P., & Esbjörner, E. K. (2020). Correlation between cellular uptake and cytotoxicity of fragmented α-synuclein amyloid fibrils suggests intracellular basis for toxicity. *ACS*

Chemical Neuroscience, *11*(3), 233–241. https://doi.org/10.1021/acschemneuro.9b00562

Zhao, H., Tuominen, E. K. J., & Kinnunen, P. K. J. (2004). Formation of amyloid fibers triggered by phosphatidylserine-containing membranes. *Biochemistry*, *43*(32), 10302–10307. https://doi.org/10.1021/bi049002c

Zhao, K., Li, Y., Liu, Z., Long, H., Zhao, C., Luo, F., Sun, Y., Tao, Y., Su, X., Li, D., Li, X., & Liu, C. (2020). Parkinson's disease associated mutation E46K of α-synuclein triggers the formation of a distinct fibril structure. *Nature Communications*, *11*. https://doi.org/10.1038/s41467-020-16386-3

Zhao, K., Lim, Y.-J., Liu, Z., Long, H., Sun, Y., Hu, J.-J., Zhao, C., Tao, Y., Zhang, X., Li, D., Li, Y.-M., & Liu, C. (2020). Parkinson's disease-related phosphorylation at Tyr39 rearranges α-synuclein amyloid fibril structure revealed by cryo-EM. *Proceedings of the National Academy of Sciences*, *117*(33), 20305–20315. https://doi.org/10.1073/pnas.1922741117

Zheng, M., Jagota, A., Semke, E. D., Diner, B. A., Mclean, R. S., Lustig, S. R., Richardson, R. E., & Tassi, N. G. (2003). DNA-assisted dispersion and separation of carbon nanotubes. *Nature Materials*, *2*(5), 338–342. https://doi.org/10.1038/nmat877

APPENDIX

Appendix I: The molecular lifecycle of amyloid – Mechanism of assembly, mesoscopic organisation, polymorphism, suprastructures, and biological consequences.

BBA - Proteins and Proteomics 1867 (2019) 140257

Contents lists available at ScienceDirect

BBA - Proteins and Proteomics

journal homepage: www.elsevier.com/locate/bbapap

Review Article

The molecular lifecycle of amyloid – Mechanism of assembly, mesoscopic organisation, polymorphism, suprastructures, and biological consequences

Liisa Lutter[a], Christopher J. Serpell[b], Mick F. Tuite[a], Wei-Feng Xue[a,*]

[a] Kent Fungal Group, School of Biosciences, University of Kent, CT2 7NJ Canterbury, UK
[b] School of Physical Sciences, University of Kent, CT2 7NH Canterbury, UK

ARTICLE INFO

Keywords:
Amyloid
Prions
Polymorphism
Suprastructure
Self-assembly

ABSTRACT

The formation of a diverse range of amyloid structures from normally soluble proteins and peptides is a hallmark of devastating human disorders as well as biological functions. The current molecular understanding of the amyloid lifecycle reveals four processes central to their growth and propagation: primary nucleation, elongation, secondary nucleation and division. However, these processes result in a wide range of cross-β packing and filament arrangements, including diverse assemblies formed from identical monomeric precursors with the same amino acid sequences. Here, we review current structural and mechanistic understanding of amyloid self-assembly, and discuss how mesoscopic, i.e. micrometre to nanometre, organisation of amyloid give rise to suprastructural features that may be the key link between the polymorphic amyloid structures and the biological response they elicit. A greater understanding of the mechanisms governing suprastructure formation will guide future strategies to combat amyloid associated disorders and to use and control the amyloid quaternary structure in synthetic biology and materials applications.

1. Introduction

Amyloid forming proteins are at the centre of various protein misfolding disorders as well as having normal physiological functions in a wide variety of organisms from bacteria to mammals. The main characteristic of amyloid forming proteins is their propensity to form ordered fibrils with a core made of tightly packed β-sheets perpendicular to the fibril axis. The organisation of soluble peptides or proteins into insoluble amyloid fibrils has been identified in many human pathologies [1], including amyloid β (Aβ) and tau involved in Alzheimer's disease (AD), α-synuclein (α-syn) in Parkinson's disease, and huntingtin in Huntington's disease. Other amyloid-associated disorders include type II diabetes and several types of systemic amyloidoses [2–4]. However, not all amyloid structures are disease associated. In fact, a range of non-disease associated amyloid structures participate in an array of normal physiological processes without any apparent harmful effects to their hosts [5,6]. Thus, it is difficult to establish direct causal relationships between amyloid protein precursors, the large range of structures they form, and the diseases they are associated with due to a lack of evidence linking structural and mechanistic understanding of neurodegenerative disease aetiology.

The building blocks of amyloid fibrils are soluble monomeric proteins or peptides. Their primary sequences typically include amyloidogenic motifs containing amino acids with high propensity to assembly into amyloid fibrils, influenced by both the physiochemical properties of these amino acids, as well as their order in the sequence. These motifs tend to be hydrophobic, more rigid and have a tendency to form β secondary structures [7]. Despite differences in the primary sequence between amyloid-forming proteins, the monomeric precursors form fibrils with a characteristic cross-β structure in all amyloid [8,9]. The cross-β architecture that defines the amyloid core is composed of β-strands packed perpendicularly to the fibril axis, and can be readily observed by X-ray fibre diffraction usually showing a characteristic 4.7 Å reflection on the meridian of the diffraction pattern that corresponds to the spacing between β-strands and indicates that they are stacked perpendicular to the fibril axis. The β-sheets can be arranged in parallel or antiparallel arrangements, forming a stable cross-β configuration that resists degradation by proteases, detergents and heat. Pairs of β-sheets usually intermesh with close side chain complementarity in a variety of possible steric zipper arrangements [10]. The ~10 Å equatorial reflection corresponds to the spacing between β-sheets and indicates that there are usually two or more sheets in amyloid filaments [9]. The supramolecular fibril structure is supported by intermolecular hydrogen bonds parallel to the fibril axis, making amyloid fibrils strong fibrous materials [11]. Amyloid fibrils typically have diameters of approximately 5-20 nm and can be up to several micrometres long

* Corresponding author.
E-mail address: W.F.Xue@kent.ac.uk (W.-F. Xue).

https://doi.org/10.1016/j.bbapap.2019.07.010
Received 25 March 2019; Received in revised form 12 July 2019; Accepted 23 July 2019
Available online 25 July 2019

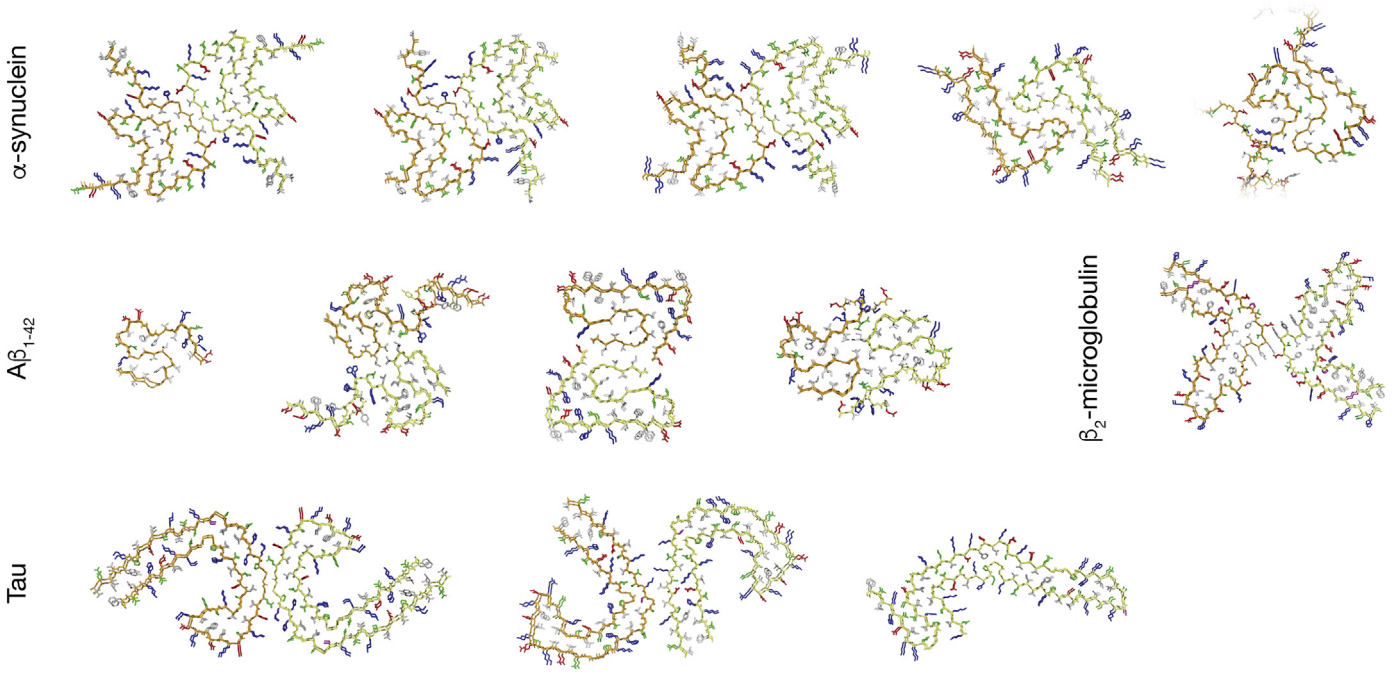

Fig. 1. Recent structural models of amyloid fibrils determined using ssNMR and cryo-EM. These structures illustrate the similarities in cross-β core structure despite distinct primary sequences, as well as the different polymorphic structures that identical monomeric precursors can assemble into. PDB structures are shown with a yellow or orange backbone, blue basic side chain residues, red acidic side chain residues, grey hydrophobic side chain residues and green polar side chain residues. The models are oriented so that the fibrils are viewed from their ends and two layers along the fibril axis are shown for each fibril model for clarity. From upper left to lower right, the structures are drawn in Pymol from PDB entries: 6A6B [169], 6H6B [170], 6CU7 [12], 6CU8 [12], 2N0A [171], 2MXU [172], 2NAO [173], 5OQV [174], 5KK3 [175], 6GK3 [74], 5O3L [73], 5O3T [73], and 6GX5 [72].

[12–14].

The structure of amyloid fibrils has been studied to high detail using atomic force microscopy (AFM), solid state NMR spectroscopy (ssNMR) and cryo-electron microscopy (cryo-EM), which provide information on β-strand content within a monomer, arrangements of β-sheets, specific interactions between residues and the conformation of non-β-strand segments. In particular, the advent of high resolution cryo-EM and ssNMR methods has led to the elucidation of a range of amyloid species at near-atomic resolution, including several formed from the same monomeric precursors (Fig. 1). In this case, differences in fibril forming conditions, such as pH, temperature and salt concentration affect the morphology of fibrils formed. In fact, identical monomers under the same conditions can often form a mix of highly polymorphic suprastructures, and the heterogeneity exhibited by amyloid samples complicates structural and functional studies while their mechanistic origins and biological consequences are not understood.

The aggregation pathway by which soluble monomers form oligomeric intermediates and eventually fibrils is thought to be similar for all amyloid, despite differences in primary sequences and pathological presentation. The aggregation process starts with protein misfolding events in which native state monomers adopt amyloidogenic states and aggregate into nuclei that grow into oligomeric intermediates of increasing size distributions. Monomers are then added to the oligomeric intermediates, forming larger, more flexible, often elongated oligomers, frequently called protofibrils. These intermediate species are then lengthened into ordered assemblies of cross-β filaments that can elongate further with the addition of monomers at their ends. At the same time, two or more filaments can associate to form fibrils. Amyloid fibrils

Table 1
Glossary of commonly used terms relevant to the amyloid lifecycle shown in Fig 2.

Term	Description
Elongation	Growth of fibrils in a direction parallel to the fibril axis by templated monomer addition at fibril ends.
Fibril ends	Active sites where elongation by templated monomer addition occur.
Fibril fragmentation	Breakage or division of fibrils, which can be mediated by mechanical agitation, thermal stress, chemical perturbation or chaperone catalysis.
Fibrils	Long filaments formed typically by two or more intertwined proto-filaments, sometimes loosely referred to as “mature” fibrils.
Nuclei	Smallest oligomeric aggregates on which further growth by attachment of new monomers result in aggregates with faster further monomer attachement than detachment of existing monomers in the aggregates.
Oligomers	There is no universal definition but commonly sub-100-mer aggregates featuring a heterogeneous and transient nature, and small enough to be disperse and not sedimented by centrifugation.
Primary nucleation	*De novo* formation of the amyloid state through nucleated assembly of soluble monomers either in solution (primary homogeneous nucleation), or at surfaces or interfaces (primary heterogeneous nucleation).
Proto-filaments	Single elongated amyloid filament with a cross-β core structure.
Proto-fibrils	Curve-linear or worm-like fibrils that are less ordered and elongated compared to fibrils, thought to be structurally comparable to some oligomers.
Secondary nucleation	Special case of heterogeneous nucleation in which nucleation events occur on the surface of already existing fibrils.
Secondary processes	Secondary nucleation and fibril fragmentation, which result in the acceleration and exponential growth of amyloid, as opposed to primary processes of primary nucleation and elongation.
Seeds	Aggregates that are capable of accelerating amyloid assembly reactions, for example post-nucleation amyloid species capable of growth by elongation, or species capable of promoting secondary nucleation.

can further cluster into a variety of suprastructures, which include extracellular plaques, as in the case of Aβ, or intracellular inclusions, as in the case of huntingtin and tau.

Despite the shared core cross-β architecture, the detailed structures and surface features of oligomeric intermediates, fibrils and suprastructures depend on the specific precursor protein, and they elicit varied biological effects [15]. For example, polymorphs of *in vitro* formed $A\beta_{40}$ can have different levels of toxicity on neuronal cell cultures [16]. Amyloid fibrils are then able to undergo division, for example by fragmentation through mechanical stress, catalysis by specific cellular components such as chaperones [17], or due to biochemical changes in the cellular environment, into shorter fibril particles that act as seeds. The seeds are further elongated by monomers, which are continuously produced by their host organism. Thus, rather than a linear process, amyloid assembly represents a molecular lifecycle in which a 'cloud' of species and suprastructures in a heterogeneous mixture are continuously being produced, and the species populations in this cycle will evolve as a function of time in response to changes in the conditions.

This review will discuss the molecular lifecycle of amyloid assembly in terms of the current understandings of the key molecular processes involved. It remains poorly understood how some amyloid aggregates are tolerated or even beneficial while others, despite having similar core structures are associated with debilitating neurodegenerative diseases. Moreover, identical monomer sequences can also form fibrils with different morphological and phenotypic consequences, adding complexity to finding the structural determinants behind amyloid aggregation, toxicity, and biological response. The wide degree of heterogeneity and structural polymorphism of amyloid fibrils will be discussed in this review to demonstrate that all species in the amyloid lifecycle are an integral part of the lifecycle and form a population that may contribute to the pathogenic potential of amyloid as a whole. Finally, this review will also address in what manner the suprastructural arrangement of amyloid assemblies may represent a fundamental link between amyloid structures and their functional variations in biological systems. This will be discussed in terms of how suprastructures may affect fibril division and propagation of the amyloid state in the amyloid lifecycle, as well as how they affect the infectious and cytotoxic potentials of amyloid.

2. The amyloid lifecycle and its defining molecular processes

The molecular details of amyloid fibril formation are debated, but the self-assembly reaction fundamentally consists of four key processes: nucleation, elongation, division [18] and secondary nucleation [19] (Fig. 2). However, the current description of amyloid aggregation and the resulting fibril assembly pathway is influenced by *in vitro* kinetic studies where the reactions are limited by the amount of monomers present. This process is better represented as a lifecycle, considering that *in vivo*, monomer production, misfolding, nucleation, elongation, division and secondary nucleation all occur continuously and simultaneously, and it is their relative rates that change over time as defined by the microscopic rate constants associated with each step. It should also be noted that all of the steps along the amyloid lifecycle are dynamic and reversible, although some reverse reactions are associated with high kinetic barriers.

In the initial stages of the amyloid lifecycle, partial unfolding and/or conformational changes are required to convert amyloidogenic proteins in their native states to misfolded states capable of further conversion into the amyloid state. The monomeric or small oligomeric amyloid precursors initially exist in a dynamic equilibrium of conformations with varying degrees of structural order and can aggregate to form small amyloid oligomers. These intermediate oligomers can be structurally similar to fibrils in their conformation and β-sheet content as shown by binding of conformation-specific antibodies and analysis of secondary structure content. They can also be highly disordered, or

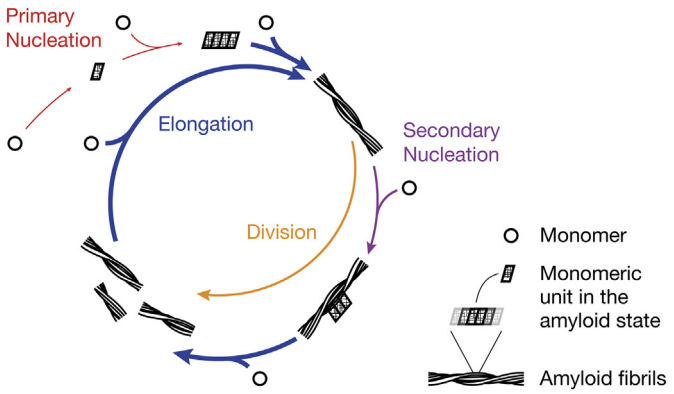

Fig. 2. Schematic illustration of the amyloid lifecycle. Soluble monomeric proteins (circles) are continuously generated and can adopt the amyloid state with a cross-β conformation (parallelograms). Coloured arrows represent the four main processes in amyloid assembly: primary nucleation (red), which may occur as homogeneous nucleation in solution or heterogeneous nucleation at interfaces; secondary nucleation (purple), which may occur as heterogeneous nucleation on fibril surfaces; elongation, which is growth at fibril ends (blue); and fibril division, for example through spontaneous or catalysed fibril fragmentation (yellow). See Table 1 for glossary of terms associated with the amyloid lifecycle. The arrows represent dynamic and reversible steps along the lifecycle.

indeed anywhere in-between [20]. Thus, at some point along these initial aggregation events, monomers or small oligomers adopt a conformation with a high β-content. This process can be accelerated by specific mutations and environmental factors. This initial aggregation process of primary nucleation can be seen as a phase transition of the amyloidogenic protein from an aqueous solution phase to the 'solid phase' represented by amyloid fibrils. Primary nucleation can proceed as homogenous nucleation occurring in solution, or heterogeneous nucleation occurring on surfaces or interfaces. As biological environments are rich in surfaces, it is possible that many spontaneous primary amyloid nucleation events occur as heterogeneous nucleation *in vivo*. Thus, surfaces may have profound effects on aggregation kinetics depending on their composition and properties [21]. Nucleation events generally occur after a "critical concentration" of monomers in solution has been reached and exceeded [22,23]; these solutions are called supersaturated solutions [24]. The smallest oligomeric aggregate on which further growth is more likely to occur than reduction in size is called the nucleus, although the generic nature of amyloid nuclei remains unresolved.

Once formed, amyloid nuclei can grow by templated elongation, in which free monomers are converted to the amyloid state and added to growing filament ends. Although elongation is a reversible reaction, dissociation of monomers is usually negligible due to the highly stable fibril structure contributing to a slower relative detachment rate compared to the attachment rate during elongation. Nucleation and elongation are concentration-dependent processes [25], and their relative contributions to amyloid formation varies between different amyloid proteins and solution conditions [23,26,27]. Post-nucleation species capable of templating elongation growth are called seeds. Seeds can grow into protofilaments, which are elongated structures with monomeric units in the amyloid state. Protofilaments can subsequently twist around each other forming fibrils. Thus, fibril ends act as the growth active sites of amyloid fibrils. A fibril typically may consist of 2-6 protofilaments, and can be further elongated and adopt a more ordered fibril arrangement. Some fibrils are quite flexible and can circularise and grow into loops [28]. Adding to the ambiguity of amyloid formation terminology, there is no objective definition for "mature" fibrils. This term is typically used to refer to long and straight fibrils observed in an end-stage *in vitro* assembly reaction, but there is no formal length, width or twist definition for these.

In the *in vivo* amyloid lifecycle, the large and possibly biologically inert fibrillary aggregates will be part of a heterogeneous population of aggregates of a range of sizes and states, including small intermediate oligomeric species, often referred to simply as 'oligomers'. There is currently no universal definition of what constitutes an amyloid oligomer, but common features include a 'soluble' (i.e. not true soluble in a physiochemical sense but small enough to be disperse and not sedimented by centrifugation), heterogeneous and transient nature. Such small oligomeric amyloid aggregates vary in subunit composition and morphology, for example, disordered, spherical and annular structures having been identified *in vitro* [29–31]. Major oligomer types include fibrillar oligomers, which structurally and immunochemically closely resemble short fibril particles, and prefibrillar oligomers, which are intermediate species having a distinct but not well characterised structure [32]. There is also a type of oligomer that is formed off-pathway from fibril formation that may be highly cytotoxic *in vitro* [33].

Additional complexity arises from the fact that oligomer populations are inherently highly polymorphic. Oligomeric structures have been determined under different conditions using diverse techniques, and it is not always clear whether, or in what form, they exist *in vivo*. This raises the question of what the toxic physiochemical or structural properties of amyloid species might be. In addition to the formation of amyloid species, which represents a phase transition of protein precursors in aqueous solution to an insoluble solid phase, amorphous aggregates with no ordered cross-β core may instead result from transition to a liquid phase, forming liquid droplets through liquid-liquid phase separation (LLPS). It has been hypothesized that the LLPS process is utilised by cells to compartmentalise proteins and biochemical reactions and consequently has physiological roles in cell signalling and regulation of gene expression [34]. Such liquid phase separated structures include P granules, nucleoli and stress granules, and are typically made up of aggregates of nucleic acids and protein. Intrinsically disordered proteins are also often found in cellular liquid droplets as their exposed hydrophobic areas and structural freedom may facilitate aggregation. Similarly, amyloid liquid-liquid demixing could be promoted by molecular chaperones [35]. Demixing allows high local concentrations of specific proteins, and as the droplets stabilise and mature over time, they may provide a driving force to further phase transition to a solid phase, characterised by amyloid fibril formation.

Lateral sides of protofilaments or fibrils are able to catalyse the formation of new amyloid nuclei and oligomeric species capable of growth by monomer addition in a process known as secondary nucleation [27,36]. Secondary nucleation is a special case of heterogeneous nucleation where the catalysing surface is specifically that of preformed amyloid instead of any surface. New nuclei formed through this secondary process then detach and can be further elongated. Indeed, it has been suggested that once a critical concentration of fibrils has been reached, fibril-catalysed secondary nucleation becomes the major source of toxic oligomeric species [27]. Despite secondary nucleation events occurring on pre-existing fibrils, amyloid fibrils are not considered to grow into branched suprastructures as each protofilament in a fibril remains unbranched.

Finally, amyloid fibrils are capable of dividing into smaller fibril particles. The division of amyloid fibrils propagates the amyloid state and the conformation associated with the parent fibril assemblies [18]. Amyloid division can occur due to fibril fragmentation caused by thermal energy or mechanical forces, or be catalysed enzymatically by chaperone proteins [37]. Division increases the number of fibrils particles and, therefore, reactive fibril ends that can lead to further growth by elongation. For prions, which are amyloid that are transmissible between hosts, division of amyloid fibrils is required for infectivity and propagation of the prion phenotype [38], which suggests a similar mechanism could occur in prion-like amyloid correlated with neurodegenerative disease. As a single prion or amyloid forming sequence can assemble into a wide range of fibril polymorphs, the differences in their ability to divide may result in the selection of specific prion strains under specific corresponding conditions. These properties will affect phenotype strength of the prions and will depend on the structural stability of the amyloid fibrils. Thus, fibril stability changes may alter its propensity for division which, in turn, affects amyloid toxicity and prion infectivity [39]. The biological implications of these structural differences could reveal a key element of the amyloid structure-function relationship.

3. Mapping the kinetics mechanisms of amyloid assembly

The complex nature of amyloid aggregation kinetics due to non-linear growth processes in the amyloid lifecycle, combined with their high sensitivity to environmental and experimental factors, has challenged the development of kinetic assays and derivation of rate laws. While the outline of the amyloid lifecycle as discussed above is generally well understood and documented based on *in vitro* assembly experiments, the specific structures of the species involved and the rates of their formation and exchange remain unclear.

3.1. Amyloid assembly in vitro

Currently, the kinetics of amyloid self-assembly is frequently assayed *in vitro* utilising the tinctorial property of amyloid following development of high-throughput microplate-based kinetic assays [25] using the dye thioflavin T (ThT). ThT shows enhanced fluorescence emission upon binding to in-register side-chains within the β-sheets of amyloid fibrils, and a kinetic assay with ThT as amyloid reporter is widely used as it is simple and relatively sensitive compared to turbidity and light scattering approaches [40]. ThT assays have allowed in-depth studies of amyloid formation kinetics and derivation of rate laws that have elucidated the molecular mechanisms of amyloid assembly and aid in determining the mode of action of fibril formation inhibitors [41]. Also, ThT fluorescence intensity may reflect fibril morphology, regardless of the β-sheet content due to different accessibility to binding sites [42].

Although ThT is a useful tool for quantifying the relative amounts of fibrillar cross-β content over time, it does have some limitations and shortcomings. For example, ThT cannot be used for specific identification of amyloid fibrils, as it is not sufficiently specific to amyloid aggregates and can for example, bind to DNA [43], nor can it be used to distinguish between amyloid fibrils and prefibrillar species [44]. Additionally, screening the effect of small molecule inhibitors on fibril formation using ThT is prone to false positives as the candidate inhibitors may interfere with the binding of the dye, rather than the fibrillation process [45]. The study of amyloid aggregation should always be complemented with various other biophysical techniques, including circular dichroism (CD) and Fourier transfer infrared spectroscopy (FTIR) for secondary structure characterisation, and AFM and EM for fibril imaging. Several derivatives of ThT have been developed for *in vivo* detection of amyloid fibrils in the organs and tissues of live patients [46,47]. Amyloid probes also include luminescent conjugated oligothiophenes, which are fluorescent amyloid ligands that can report on the fibrillar conformation, facilitating the *in vitro* and *ex vivo* analysis of polymorphism [48,49]. The continued development of novel reporters for use in animal models and in future clinical applications will contribute to a better understanding of the formation and spread of amyloid aggregates under *in vivo* conditions.

The main distinctive characteristic of amyloid aggregation, as measured *in vitro* using ThT, which gives a fluorescent signal increase upon binding amyloid fibrils, is a sigmoidal growth curve (Fig. 3). The lag phase represents early reaction times where primary nucleation events that lead to nuclei and small intermediate oligomer formation dominates. Nucleation is initially thermodynamically unfavourable and kinetically rate limiting as the nucleation process is associated with a free-energy barrier, with pre-nucleation species in the reaction

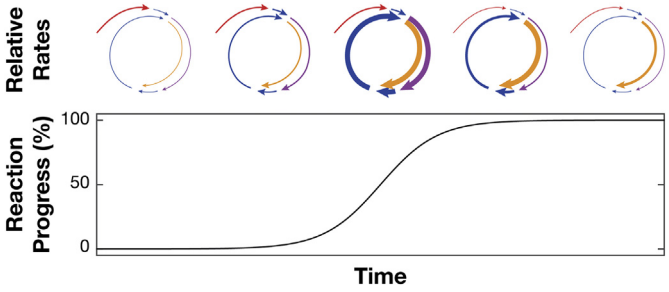

Fig. 3. Schematic illustration of the amyloid aggregation growth curve as measured *in vitro* with kinetic ThT assay. Coloured arrows represent the four main processes in amyloid assembly (Fig. 1). Primary nucleation (red) is the driver of de novo amyloid aggregation in the initial stages of the reaction, although primary nucleation will continue to take place, at much lower rates, in the later stages as free monomer concentration drop. The rate of elongation growth at fibril ends (blue) peaks during the exponential growth phase of the fibrils. Elongation continues to occur once a plateau has been reached as the fibrils are in dynamic exchange with residual monomers and/or small oligomers, as well as other species along the fibril formation pathway. Secondary nucleation (purple), which requires both the presence of monomers and fibrils, dominates nuclei formation as soon as first fibrils have formed in the lag phase. Fibril division through fragmentation (yellow) occurs continuously after the formation of first fibrils and continues to have a significant role in the capacity to increase fibril load. The relative magnitudes of the rates of these main processes (exemplified by the thickness of the arrows) also vary by the type of amyloid monomer, their concentration and environmental conditions.

coordinate favouring dissociation compared to further growth by monomer association [25,50,51]. The lag phase can be eliminated by introducing preformed fibrillar amyloid seeds, enabling the conversion and addition of monomers directly to fibril ends in the amyloid state, thereby bypassing the rate-limiting nucleation process. At the end of the lag phase, while most of the protein is still monomeric, there is a transient population of intermediate oligomeric species, some of which are referred to as protofibrils because they are sufficiently and observably elongated species [52]. Small transient oligomers grow and fully convert into protofilaments with amyloid cross-β core that are then elongated by further addition of monomers to fibril ends. As fibrils form during lag phase, secondary processes such as secondary nucleation and fibril fragmentation become the major mechanism of amyloid formation, peaking during the exponential growth phase [25,27]. Fibril mass increases as protofilaments are elongated and twist around each other. Finally, growth plateaus as most monomers in solution have been added to fibril ends. The population in such a sample remains in dynamic exchange (Fig. 2). For example, monomers and oligomers may continuously break off and reattach to fibril ends [53]. Importantly, these key steps are part of the lifecycle of all amyloid fibril formation, but their rate constants and thermodynamic driving forces vary for different monomers [50].

3.2. Amyloid assembly in vivo

While the fundamental kinetic principles governing the self-assembly of amyloid are the same *in vitro* as *in vivo*, the kinetics of the amyloid lifecycle under *in vivo* conditions would be expected to be significantly different from the well-characterised *in vitro* conditions. One of the main differences is the unlimited and continuous production of monomers *in vivo*. Other key differences include the added complexities associated with genetic variations of amyloid monomer or its precursor and other risk factors, components of the cellular and extracellular environment that affect amyloid aggregation kinetics, spatiotemporal variations in monomer production affecting local monomer concentrations, and amyloid clearance mechanisms. Using fluorescence lifetime imaging (FLIM), the kinetics of Aβ aggregation, as well as its cellular uptake and trafficking, have been studied in live neuronal cells [54]. The aggregation of Aβ in human APP-expressing mice was analysed using a fluorescent amyloid dye and a cranial window through which images were collected using two-photon imaging over a period of two years [55]. The plaque volume change was found to have a sigmoidal shape, with many small plaques forming initially, when the concentration of free Aβ is high, and growing in volume until they plateau when Aβ production becomes rate-limiting. However, while transgenic murine models of AD are useful research tools for familial AD, they fail to represent the most abundant type of AD in humans, which is sporadic. Amyloid positron emission tomography (PET), a method for visualizing amyloid deposition in the brain using radiopharmaceuticals that bind fibrillar amyloid, has also been used to collect and assemble Aβ load data from cognitively impaired patients to create a long-term disease model that showed a sigmoidal curve of increasing amyloid load in the brain over the course of more than 30 years [56]. Overall, few studies have been done on the *in vivo* aggregation kinetics of amyloid in animal models or humans in any molecular detail.

The rates governing the amyloid lifecycle and its kinetics are specific to protein sequence and environmental conditions. For example, aggregation propensity is affected by charge and exposed hydrophobic surfaces of the monomer. The lag phase can also be shortened by an increased fragmentation propensity. Although a key feature of many amyloid-forming proteins is being intrinsically disordered as monomers, or having significant stretch of unstructured regions due to extensive exposed hydrophobic areas, others can be folded, globular, and with low aggregation-propensity in their native states [57]. Such proteins, including β_2 microglobulin associated with systemic dialysis related amyloidosis, require local unfolding to initiate aggregation [58]. In these cases, physiological thermal fluctuations may be sufficient for native conformation destabilisation [59] and hence enough for initiating assembly. Conditions such as temperature, pH, protein-denaturing agents, presence of other proteins, metal ions, surfaces and their composition and properties can have an impact on the aggregation of amyloid proteins [21,60–63]. Even many physiologically non-amyloidogenic proteins can be made to adopt the characteristic cross-β structure under specific environmental conditions [64,65]. Deviations from the typical kinetic characteristics of amyloid aggregation have been identified under varying environmental conditions, which has implications for the biomedical use of amyloid-prone proteins, and for developing drugs targeting amyloid assembly. For example, the human glucagon-like peptide 1, analogues of which are used for treatment of type II diabetes, exhibits kinetics consistent with the standard nucleation-polymerisation mechanism at pH 8.2, but at pH 7.5 the kinetics showed a highly unusual profile, with the lag phase becoming longer with increasing monomer concentration [66]. This was attributed to the formation of off-pathway oligomers, with unknown physiological effects. One plausible explanation is that metastable oligomers and protofibrils could be off-pathway competitors and inhibitors of fibril formation, instead of on-pathway precursors [67].

4. Amyloid assembly polymorphism

Amyloid fibrils, by definition, share a cross-β core arrangement. Their assembly, either from precursors of different or identical sequences, nevertheless result in fibrils with a varying degree of structural differences (Figs. 1, 4). Polymorphism of molecular crystals has been characterised in the context of small molecules and pharmaceuticals, for which the varying physiochemical properties including the stability and bioavailability of a substance with an identical molecular structure and dissimilar suprastructure has been documented [68,69]. Analogously, the fibrillar amyloid state can be viewed as a pseudo one dimensional “crystal-like” form in which different polymorphs may also have varying biological properties. Variance in fibril structure, i.e. the polymorphic nature of amyloid fibrils, has been characterised for fibrils formed from synthetic or recombinant monomeric amyloid precursors,

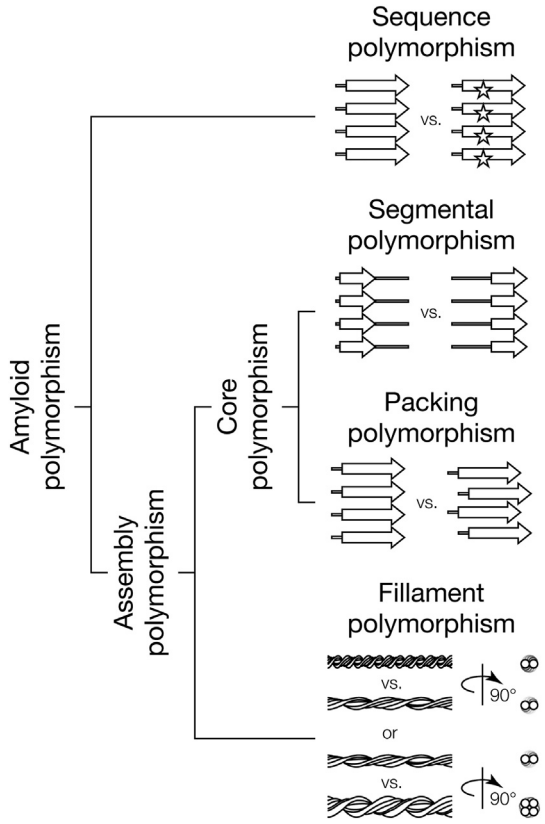

Fig. 4. Hierarchical classification of amyloid polymorphism types with schematic illustrations exemplifying each type. Amyloid polymorphs can be classified into sequence polymorphs and assembly polymorphs. Assembly polymorphs can be further divided into core polymorphs and filament polymorphs, and core polymorphs can be divided in turn into segmental polymorphs and packing polymorphs. The different types of polymorphism are organised from top to bottom to indicate the hierarchical effects of polymorphism types. For example, sequence polymorphs where one polymorph contains a single amino acid residue change (top schematic, stars depict an amino acid sequence variation) would also affect which segment of the chain forms the amyloid core (segmental polymorphism), how the amyloid core is packed (packing polymorphism) and how the protofilaments are arranged (filament polymorphism). On the other hand, polymorphism based on the varied number and arrangement of the protofilaments (bottom schematic depicting filament polymorphism) may occur without changes in the sequence, the core segment or the packing of the core (all placed above filament polymorphism in the schematic).

as well as those formed *in vivo* in tissue or by seeding with fibrils from brain tissue of patients with various neurodegenerative diseases [70–72]. Amyloid assembly polymorphism resulting from assembly of precursors of identical sequence can be broadly divided into two classes: core polymorphism with differences in the arrangement of monomeric units in the cross-β core, or filament polymorphism with differences in the lateral arrangement of protofilaments in a fibril and the specific contacts they form (Fig. 4). In core polymorphism, the core structure can vary in β-sheet content, conformation of non-β-strand segments, steric zipper packing and specific contacts between residues. Core polymorphism can be further categorised into segment polymorphism where different segments of a polypeptide may form different cross-β cores, and packing polymorphism where the same segment of a polypeptide chain is involved in the cross-β core. For example, inter-sheet contacts can be stabilised by steric zippers, as well as hydrophobic contacts and salt bridges. Eight potential classes of steric zipper packing arrangements were described by Eisenberg and colleagues [10] forming the basis for core and assembly polymorphisms. These steric zipper arrangements vary by whether β-strands that make up β-sheets are parallel or antiparallel, whether adjacent β-sheets that form the steric zipper pack same or different surfaces together, or whether the β-sheets themselves are oriented parallel or antiparallel relative to each other. In terms of filament polymorphism, the current confirmed examples include cryo-EM reconstructions of purified paired helical and straight tau filaments, which show indistinguishable cross-β and β-helical structures, surrounded by a fuzzy coat of disordered domains, but distinctive inter-protofilament arrangements [73] and β_2-microglobulin, for which several morphologies were identified using cryo-EM, although all shared the same core structure, as shown by NMR [74].

Amyloid populations regularly contain heterogeneous mixtures of fibril polymorphs. Often, several subpopulations of amyloid fibril polymorphs can form under identical conditions, for example paired helical and straight fibrils of tau or striated ribbon and twisted fibrils of Aβ [73,75]. In studies in which a single fibril structure is reconstructed, the sample may have contained a broad range of morphologies, as in the case of the recent β_2-microglobulin structure [74]. These individual fibril polymorphs can sometimes be distinguished by their width, as they may vary in the number of protofilaments (Fig. 4), or other morphological differences such as twist periodicity and persistence length in terms of curvature. Additionally, fibril polymorphs may vary in stability and dynamic behaviour which may, for example, affect their fragmentation rate and consequently cytotoxicity [76]. Fibrils differing in twist and length can also result in differences in their cytotoxic potential [16,39].

From fibril structures determined from patient brain tissue, it emerges that there may be disease-specific association with certain amyloid fibril polymorphs. For instance, tau fibrils from an Alzheimer's patient and a Pick's disease patient have remarkably different core arrangements [72,73]. Additionally, structural polymorphs of Aβ are thought to correlate with variations in AD pathological phenotypes [77]. For example, recent ssNMR analysis of Aβ fibrils seeded from AD patient brain tissue showed a link between clinical AD subtypes and specific features of fibril polymorphism. $A\beta_{40}$ aggregates were shown to have a single major morphology in patients with typical prolonged-duration AD and posterior cortical atrophy variant (PCA-AD) and a higher proportion of alternative structures in the rapidly progressive form of AD. By contrast, $A\beta_{42}$ aggregates were found as several polymorphs across both categories [77]. In another study, $A\beta_{40}$ fibrils seeded from brain tissue of two AD patients with different clinical histories were relatively homogenous for the individual patients, although analysis of the predominant fibril structures by ssNMR between the two patients indicated significant differences in their cores [78].

Due to amyloid and prions have structural and mechanistic similarities, and the morphological heterogeneity of amyloid populations potentially linked with disease progression, the idea of whether structural amyloid polymorphs propagate phenotypically as strains has been tested. For prions, the prion strains give rise to specific pathologies and disease phenotypes, which are maintained when the strains are introduced *de novo* into a genetically identical host where they continue to be stably propagated. Some studies have also suggested the spread of tau and α-synuclein as distinct strains [79]. Thus, identifying the structure of distinct fibril polymorphs, the suprastructures they form, and characterising the environmental factors that drive structural changes, as well as their biological effects, could be the key link to elucidating the dramatic variations in amyloid disease pathological presentation and provide a structural rationalisation of the strain phenomenon. The structural differences between amyloid polymorphs could also be mediated by changing the propensity to the various fibril associated pathology mechanisms, including interactions with membranes, ability to sequester proteins essential for the cell, differences in metal binding and creation of reactive oxygen species, or some as yet unknown mechanism of fibril toxicity. Thus, in terms of disease association, environmental changes may modulate amyloid structure and exert pressure to select for specific polymorphs, and the selected polymorphs in turn reinforce the disease-associated environmental

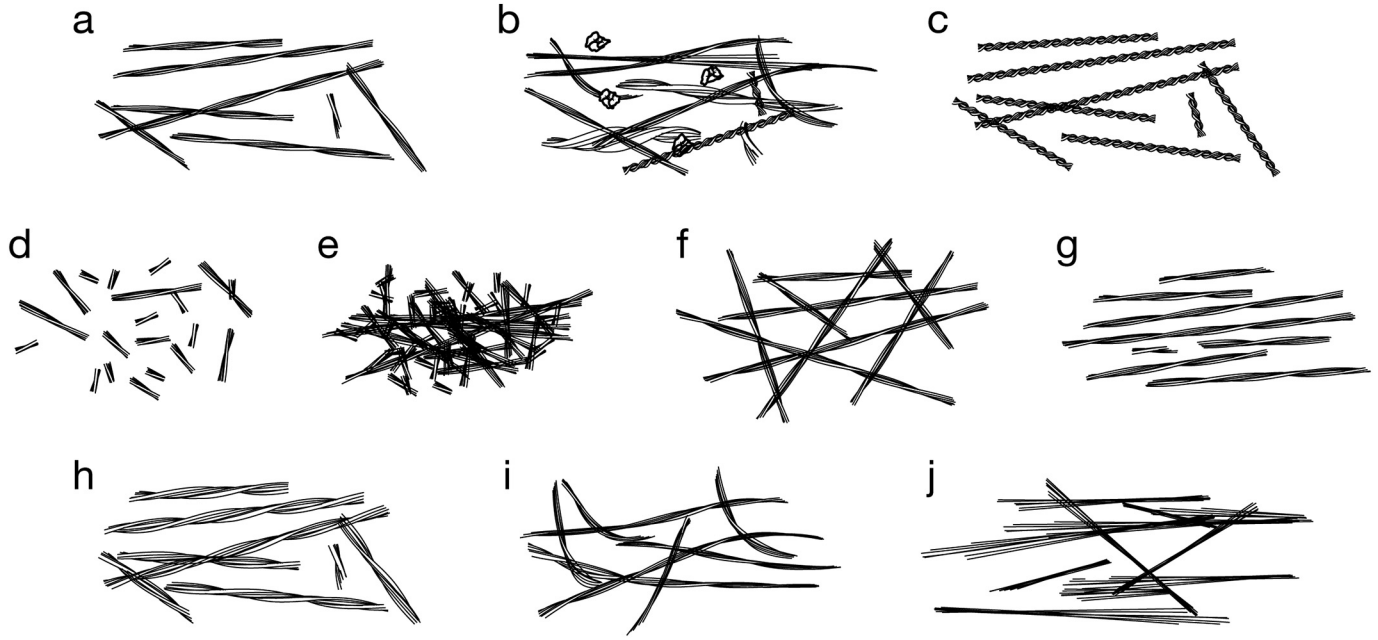

Fig. 5. Schematic illustration of possible variations in the suprastructural properties of amyloid at mesoscopic (micrometre to nanometre) length scales. a) Long-straight fibrils of varying length; b) highly heterogeneous population with filaments and bundles decorated with small oligomeric species. c) fibrils of tight twist properties d) highly fragmented fibril population with abundance of small particles; e) fibril cluster f) fibril network; g) aligned fibrils h) thick and bundled fibrils; i) flexible or curve-linear fibrils with low persistence length; j) crystalline-like fibril bundles.

changes.

5. Amyloid suprastructures

As amyloid fibrils are highly polymorphic, the heterogeneous populations of amyloid species that result from the amyloid lifecycle also show a variety of different mesoscopic arrangements on the micrometre to nanometre scale, forming a variety of possible suprastructures (Fig. 5). Amyloid fibrils vary in width, with some self-associating into thick bundles by protofilament interactions, whereas other fibrils may consist of a single protofilament only [80]. The length distribution of the fibrils in a population can similarly vary, depending on the mechanical properties of the fibrils, such as stiffness, and their fragmentation rate [18]. Each fibril population formed from the same amyloid sequence may contain varying proportions of fibril polymorphs, ranging from a uniform ensemble to almost continuous variation in twist [13,78]. While some fibrils self-associate into packed clusters or networks, others do not form such structures and remain separated, sometimes in a parallel alignment with directional order [81,82]. Although various suprastructures have been identified, little is known about their relative biological impact. At liquid interfaces amyloid fibrils can exist in a liquid crystalline nematic phase in which the fibrils are aligned parallel to each other [83]. *In vitro* studies of entangled amyloid networks have also identified gel-like behaviour at the mesoscopic scale. Interestingly, elastic properties appear as early as during nucleation events in the lag phase [84]. Electron tomography studies of Aβ suprastructures have revealed three main types of aggregates: amorphous meshwork, fibril bundle and amyloid star, all within the same overall deposit [85]. Interestingly in each case, the fibrils themselves were morphologically indistinguishable. Additionally amyloid fibrils have been observed to form spherulites which show a typical Maltese cross pattern when observed under polarised light in both *in vitro* and *ex vivo* [86,87]. Furthermore, between fibril networks, extracellular vesicles of various sizes are found [85] and lipid membrane components have been identified also within and around dense Aβ plaques in human brains of AD patients [88].

Morphological differences observed in plaque deposits reflect the suprastructural assembly preferences and features of amyloid aggregates, and seeded fibrils from AD patient brains have been correlated to differences in clinical subtypes [77]. Thus, it is possible that the different suprastructures that differ in their mesoscopic arrangements also have different toxic or infectivity profiles. The suprastructural arrangements of fibrils can also be affected by the dominance of individual fibril polymorphs as they can have different surface properties which affect their interactions. Thus, aggregates with different suprastructural features will also have different surface properties and propensities to sequester other metastable essential constituents of the cellular proteome. Characterising the various suprastructural parameters such as length and width distribution, twist, stiffness, clustering and heterogeneity of amyloid assemblies and correlating these with biological activity could lead to essential insights into the amyloid structure-function relationship.

6. Regulation of functional and pathological amyloid structure and assembly

Defining an amyloid suprastructure-toxicity relationship would help us elucidate why some amyloid formations are highly toxic whereas others are inert. Given the presence of amyloid aggregates in numerous neurodegenerative diseases, it is perhaps surprising that an increasing number of amyloid structures have been found to participate in an array of normal physiological processes without any observable harmful effects to their hosts [6]. In humans these include melanin biosynthesis, regulation of long-term potentiation (LTP) and peptide hormone storage [89–91]. Functional amyloid assemblies have also been discovered in numerous other organisms, including bacteria, fungi and metazoa. For instance, in some bacteria, fibrillar matrix of extracellular amyloid proteins such as curli and Fap are required for surface adhesion and colony formation [92–95]. In insects and fish, the eggshell is primarily made up of chorion proteins with a characteristic amyloid fibril structure [6]. The line between functional and pathogenic amyloid is also increasingly blurred, as subtle changes in processing or regulation may cause an amyloid with normal physiological roles to become pathogenic. For example, Aβ is produced from the

amyloid precursor protein (APP) in neural and other cells throughout the human lifetime [96]. The precursor can be cleaved by α- and γ-secretases leading to production of non-amyloidogenic fragments or by β- and γ-secretases, which produces several isoforms of Aβ correlated with AD. However, there is evidence that monomeric Aβ and other peptides resulting from precursor cleavage might have important roles in cellular signalling pathways, regulating synaptic activity and might even be essential for survival of neurons [97]. Moreover, fibrillar forms of Aβ have been suggested to have protective effects against fungal and bacterial infections in mouse, nematode and cell culture models of Alzheimer's disease, thus suggesting that they might have a role in innate immunity [98]. Recently, human neural cell culture models have also been used to investigate the role of a herpes simplex 1 virus infection on amyloid aggregation and it was reported that Aβ oligomers bind virus surface glycoproteins and mediate resistance to the virus [99]. This finding suggests that even small oligomeric amyloid species may have functional roles.

Amyloidogenic proteins lack sequence homology and can have diverse structural and catalytic functions in their normal non-amyloid states. The ability to self-assemble into an amyloid state could be a generic structural feature of polypeptide chains [100]. Therefore, understanding the mechanistic and structural differences between functional and pathogenically-associated amyloid, which share the same cross-β core structure by definition, is a key requirement for treating amyloid-associated diseases as any potential treatment must be able to recognise essential functional features of amyloid and differentiate these from the pathogenically-associated features. A key aspect of functional amyloid may lie in their controlled and localised assembly initiation and termination in response to environmental cues, which is sometimes achieved with post-translational modifications. For example, the CPEB3 protein activates the transcription of mRNAs that promote long-term potentiation (LTP), but only when ubiquitylated and deSUMOylated, which promotes its assembly into the functional fibrillar form [90,101]. SUMOylation of CPEB3 makes it soluble and inactive, although in other amyloid proteins it can promote aggregation and toxicity [102]. Additionally, many peptide hormones that are stored within endocrine granules require both the compartmentalised acidic pH environment and the presence of glycosaminoglycans (GAGs) for fibril formation. GAGs accelerate fibril formation by abolishing the lag-phase and some can interfere with potentially harmful fibril-membrane interactions [103,104].

Another regulatory mechanism of controlling amyloid assembly involves chaperones. Recently chaperones DNAJB6 and Hsp70 were identified as part of a natural control mechanism to prevent the aggregation of α-synuclein, found as toxic aggregates in Parkinson's Disease patients [105]. α-syn is expressed at high levels in healthy individuals in various tissues of the body and, in the monomeric state, has important synaptic functions related to neurotransmitter release and synaptic plasticity, although the exact mechanisms are not known [106]. Chaperone proteins such as Hsp70, Hsp40, and others are also involved degradation and refolding of amyloid aggregates. The chaperone Hsp104 is essential for propagation of [PSI^+] prion phenotype in yeast that is associated with the functional amyloid state of Sup35; Hsp104 promotes division and propagation of Sup35 amyloid by catalysing fibril fragmentation *in vivo* [107,108].

On the basis that amyloid associated with pathology may have roles in normal physiological processes, it has been suggested that it is a dysfunctional protein degradation machinery that leads to disruption in proteostasis and build-up of toxic amyloid aggregates [109]. Some functional amyloid systems, for example pre-melanosomal protein, aggregate into fibrils much more rapidly than non-functional amyloid, thus preventing accumulation of intermediate oligomeric species with potential for harmful effects [110].

All the above-mentioned mechanisms may have evolved to ensure the normal roles of functional and/or to prevent the pathogenic features of amyloid assemblies, which have important implications in numerous physiological processes involving amyloid or amyloid precursors with no deleterious effects. Safety mechanisms that control and regulate amyloid localisation, compartmentalisation, processing and degradation, as well as their assembly kinetics and interactions with other cellular structures, may present some of the differences between functional and disease associated amyloid.

7. Structural and molecular origins of amyloid toxicity

Although the hallmark of neurodegenerative disease is deposits of amyloid fibrils, the neuropathological and clinical symptoms vary significantly. Therefore, the identity of the toxic species, and the molecular origin of the cytotoxic potential associated with amyloid is widely debated. For example, AD is characterised by progressive loss of synapses, neuronal death and atrophy of the affected areas, resulting in decline of memory and cognitive functions, whereas the main pathophysiological characteristic of Parkinson's disease is degeneration of dopaminergic neurons in the substantia nigra resulting in loss of motor function leading to rigidity and tremors. Other neurodegenerative and prion diseases also involve progressive neuronal death in various areas of the brain and result in different symptoms. Severe cases of amyloid deposition has also been found in the brains of human subjects with no cognitive decline or symptoms of dementia upon post-mortem assessment of neuropathology [111]. Thus, several underlying toxicity mechanisms involving a range of amyloid species have been suggested for these symptoms, including disruption of cell membranes, dysregulation of calcium homeostasis, mitochondrial dysfunction and oxidative stress.

7.1. Toxicity potential of small oligomeric amyloid species

Amyloid toxicity is currently thought to result from pathological effects associated with small amyloid oligomers as they are ubiquitous in the brains of neurodegenerative amyloid disease patients and their cytotoxicity has been well characterised *in vitro*. According to this hypothesis, large deposits such as amyloid plaques and inclusion bodies are thought to be relatively inert. Indeed, small oligomeric species from post-mortem human brains can disrupt long-term potentiation, synaptic plasticity and memory when injected into a mouse hippocampus [112]. This view is supported by evidence of neurodegeneration and cognitive defects preceding plaque formation *in vivo* [113,114]. In the case of mutant huntingtin, the formation of inclusion bodies was also found to reduce the risk of cell death from toxic mutant huntingtin aggregates [115]. Furthermore, the formation of prefibrillar oligomers is accelerated by mutations in α-syn causing a familial, early-onset form of Parkinson's [116]. However, the precise molecular nature of the small oligomeric species that confers toxicity remains to be established and a large number of species of varied structures and suprastructures have been observed. For example, according to the 'ion channel hypothesis', oligomeric species with a ring-like structure insert into cell membranes and act as aberrant ion channels, disrupting the homeostasis of ions and leading to cell death [117]. Such oligomers have been suggested to form membrane-associated annular structures *in vitro* through interactions with specific lipids in the membrane, and possibly form a β-barrel pore [118–120]. However, specific structural features may be required for ion channel formation, as it has been suggested that oligomers of $A\beta_{42}$ but not $A\beta_{40}$ are capable of channel formation in membranes [121]. Disruption of calcium homeostasis has been observed in proximity of amyloid plaques, which may act as a reservoir of cytotoxic species [122]. Loss of calcium compartmentalisation leads to distortion of neuritic morphology and as calcium is essential for neural integration of signals, dysregulation of its homeostasis disrupts local neural networks [122]. Amyloid oligomer cytotoxicity has also been linked to the size and conformation of the oligomers, with smaller and more exposed hydrophobic surfaces with structural flexibility displaying the most toxic potential [123,124]. Thus, the dynamic and hydrophobic nature of prefibrillar oligomers may provide a rationale to their propensity to

aggregate and display cytotoxic properties though their interaction with membrane bilayers.

The elucidation of the role of small oligomeric species in amyloid diseases is complicated not only due to their varied structures and heterogeneity, but also due to their transient nature. Thus, in terms of species formed during the amyloid lifecycle *in vivo*, due to experimental limitations it is only possible to study stable species secreted by *in vitro* cell cultures or those extracted from post-mortem patients' brains. Furthermore, the population and the concentration of amyloid species in the brain is unknown. Attempts to quantify the concentration of Aβ in the brain has focused mostly on mouse models, with some studies on human brain tissue and cerebrospinal fluid [125–127]. However, results are inconclusive as there is currently no method for quantifying whole amyloid populations ranging from prefibrillar oligomeric species to fibrillar species *in vivo* without exposing them to non-native conditions that could affect their aggregation states, leading to unreliable estimates. Additionally, very little is known about how the local environment in the *in vivo* human brain affects amyloid structure and toxicity, especially as the amyloid population are likely to be highly heterogeneous and distinct oligomeric species can vary in toxicity.

7.2. Toxicity potential of fibrillar amyloid species

In addition to the cytotoxic effects displayed by prefibrillar oligomeric species, amyloid fibrils also have direct cytotoxic properties via disruptive effects on the phospholipid bilayer during fibril growth [128]. Localised neuronal damage, characterised by progressive neuronal dystrophy and microglial activation, has been correlated with plaque formation and shown to worsen over the clinical course of the disease [129,130]. Several indirect mechanisms of fibril toxicity have been proposed, including secondary nucleation events where fibrils catalyse the formation of small oligomeric species through surface interactions, thereby contributing to the neurotoxic effects of amyloid [27]. Additionally, fibrils may act as a reservoir for toxic species, which may be released to generate a local pool of toxic species as a halo around fibrillar deposits [131]. Besides these indirect mechanisms, fibrils can also contribute directly to cell damage under conditions in which non-fibrillar aggregates are not detectable by spectroscopy or antibody-binding, thus suggesting a role as a direct contributor of cytotoxicity.

Fibril fragmentation is key to amyloid cytotoxicity by increasing the number of termini through division of fibrils, which provides increased reactive growth competent surface, and also creates smaller fibrillar amyloid species that decrease cell viability and increase disruptive effects on membrane bilayers. The increase in the toxic potential cannot be solely attributed to the increased number of fibril ends, suggesting other yet unknown surface-dependent mechanisms [39]. Furthermore, short fibril particles are also readily internalised by endocytosis, causing disruption within the cell by inhibiting the degradation of proteins within lysosomes and altering trafficking of lysosomal membrane proteins [132]. Disruptive interactions of fibrils with membranes have been visualised in 3D using electron tomography, surrounded by lipid inclusions of varying sizes [133]. Extraction and clustering of lipids around amyloid aggregates and their potential links to toxicity have also been previously characterised [134]. Fibril-membrane interactions also promote the shedding of oligomers from fibril ends that then diffuse rapidly through the brain and impair cognitive function in mice [135]. These oligomers formed through reverse assembly reactions were found to have a highly heterogeneous size distribution, but similar biochemical and physical properties to those formed by nucleation and forward assembly reactions [135]. Another potentially physiologically harmful effect of amyloid could arise from fibril interactions with metal ions [136], as several co-localise with amyloid plaques in AD patient brains [137]. $A\beta_{42}$ fibril interactions with copper (Cu^{2+}) enable retention of redox activity and generation of reactive oxygen species *in vitro* [138]. The presence of metal ions also affects fibril aggregation morphology, which may have additional consequences on biological and pathogenic properties [136,138,139].

7.3. Modulating factors of amyloid cytotoxicity

In the complex, crowded environment of cells and nervous tissue, the cellular milieu plays an important role in affecting how the amyloid lifecycle progresses, and how amyloid species and populations form and interact with other cellular structures. Surfaces, such as those presented by membranes, can promote protein misfolding and aggregation, thus potentially speeding up nucleation events in the amyloid lifecycle, promoting the *de novo* formation of amyloid species [140]. This effect depends on the lipid composition of the membrane. Differing membrane composition could potentially explain the variable vulnerability of various cell types to toxic amyloid species. Phosphatidylserine and other acidic phospholipids could provide a local low-pH environment that promotes fibril formation [141]. Interestingly, functional amyloid assemblies are often compartmentalised into membrane-bound organelles without causing damage. A specific membrane composition could explain why this key toxicity target is not harmed by functional amyloid aggregates. Furthermore, hydrophobic surfaces and the air-water interface are also capable of inducing heterogeneous nucleation and formation of small amyloid oligomers, as well as leading to the formation of fibrils with a distinct morphology compared to fibrils formed by homologous nucleation away from surfaces [142,143].

The lack of clear correlation between amyloid fibril aggregates with clinical symptoms in neurodegenerative diseases promoted the view that small oligomeric pre-fibrillar species are the main toxic species. While some oligomeric species display significant cytotoxic potential, not all oligomeric species share this potential. In the same manner, some amyloid fibril structures possess cytotoxic potential while others appear to be inert. Difficulties in studying the mechanisms and structures associated with amyloid toxicity under physiologically relevant conditions also add to the fact that the composition of the amyloid populations that are associated with disease as a whole, and their combined modes of action, have not been resolved. It is possible that the incoherence between the amyloid species and the neurodegenerative disease symptoms and progression they are associated with could be better explained not by individual amyloid structures but the sum of their presence in a population as a whole. The variation in the composition of the heterogeneous amyloid population resulting from the amyloid lifecycle may drive different characteristics and clinical symptoms associated with amyloid.

8. The infectious potential of amyloid: prions and prion-like amyloid

Prions are infectious amyloid particles with the self-propagating amyloid cross-β state. Mammalian prions are correlated with a number of currently untreatable neurodegenerative diseases termed transmissible spongiform encephalopathies (TSEs) which include kuru, Creutzfeldt-Jakob disease, bovine spongiform encephalopathy, and scrapie in sheep. These diseases can arise spontaneously, be inherited, or acquired through an infection by prion particles. TSEs are associated with an amyloidogenic form of the mammalian prion protein (PrP) and can be transmitted between individuals and sometimes even across species [144,145]. However, not all prion replication is disease-associated and in fungi in particular they can have neutral or beneficial effects. For example in yeast, prions confer phenotypic plasticity through evolutionary selective advantages [146]. For example, the *Saccharomyces cerevisiae* protein Sup35 is a subunit of the eukaryotic translation release factor, required for termination of mRNA translation. The amyloid form of Sup35 is associated with the [PSI^+] prion phenotype [147]. Similarly, [*URE3*] is the prion phenotype associated with the *S. cerevisiae* Ure2 protein [147]. Both of these prion proteins can form several strain variants with different characteristics and have

been studied extensively to elucidate the molecular mechanisms and structural determinants of amyloid proteins [148].

Prions have been be considered a subclass of amyloid that can be transmitted between cells and organisms [149]. However, there is now increasing evidence to suggest that some pathogenic amyloid proteins can also be transmissible from cell-to-cell. For example, cross-cell transmission has been demonstrated for Aβ [150], α-syn [151], huntingtin [152] and tau [153], blurring the distinction between 'prions' and 'amyloid'. As the likelihood of transmissibility of these pathogenic amyloid proteins between individuals, an essential aspects of prion behaviour, is probably low, they are consequently typically classified as 'prion-like' amyloid. Nevertheless, these proteins may be infectious to an extent, as shown for tau where injection of tau-containing brain extract of human origin can induce tau inclusions in transgenic mice expressing wild type human tau [154]. Recently, further evidence was found to support iatrogenic transmission of Aβ by identifying $A\beta_{40}$ and $A\beta_{42}$, along with tau, in archived vials of human cadaveric pituitary-derived growth hormone [155], which was used to treat patients until 1985 when some were diagnosed with Creutzfeldt-Jacob-Disease (CJD) [156]. This raises concerns over accidental transmission of prion and prion-like amyloid during medical procedures and through potentially amyloid-contaminated surgical equipment.

How some amyloid can show a type of prion-like behaviour is not known, but fibril fragmentation seems to play a key role in facilitating infectivity [157], as in the case of prion particles, division and propagation through fibril fragmentation could also be a key determinant for infectivity and amyloid phenotype strength [38]. Fibril fragmentation could facilitate vesicular cell-to-cell transport, due to the smaller size of fragmented particles, as cell-to-cell spreading is thought to be mediated by intracellular amyloid particles weakening the lysosomal protein degradation pathway, leading to exocytosis of oligomeric species capable of propagating the amyloid state that are then taken up by recipient cells [158]. Thus, the stability of amyloid particles towards fibril fragmentation, which may be modulated by their suprastructure, could represent a link between amyloid structure and their infective potential as prions.

9. Challenges in establishing amyloid structure-function relationships

Many important aspects of amyloid toxicity, propagation, and their role in neurodegenerative diseases remain elusive. A significant gap in knowledge relates to the specific mechanisms of amyloid pathogenicity in terms of the structural properties associated with the toxic and infective potential displayed by amyloid structures. To effectively develop therapeutics that specifically target toxic or infective properties or species, it is first necessary to understand the mechanisms of toxicity, transmission and propagation in detail. However, for amyloid-associated diseases it is not yet clear whether amyloid aggregates are a cause or a consequence of the disease, and by which mechanisms they could exert toxic effects to the cells. Consequently, no safe and effective anti-amyloid treatments have yet been developed despite efforts by academia and pharmaceutical companies alike. Although aggregates of amyloid fibrils are an important hallmark for diagnosis of amyloid disease, their role in pathology is debated. It is thought that earlier species in the amyloid lifecycle, specifically the small intermediate, oligomeric, pre-fibrillary species, are responsible for some of the cytotoxic and neurodegenerative effects in amyloid associated pathologies [159]. However, there is also evidence of fibrils with a shorter length distribution having cytotoxic effects [160]. Additionally, they could have important roles in amyloid propagation and other indirect mechanisms of toxicity, as well as being involved in the infective activities associated with prions and prion-like amyloid. The problem is exacerbated by the lack of high-resolution structural information of intermediate species on or off the fibril formation pathway as they have remained largely elusive due to conformational heterogeneity and transient nature.

Often, populations containing a heterogeneous mixture of amyloid polymorphs or amyloid species from different precursor sequences can be present in the brain of an affected individual, which might be part of the complex and varied nature of neurodegenerative diseases [71,161]. As discussed above, a plethora of amyloid fibril polymorphs may form and grow under the same conditions, but each individual polymorph may have different effects on cells. However, it is often necessary to achieve a homogenous sample of fibrils of a single morphology by progressive seeding or stabilising fibrils of a specific polymorph for structural characterisation and when assaying biological effects of amyloid fibrils. A nearly homogenous population can be achieved by repeated seeding because fibrils with different morphologies have different rates of self-assembly [75]. However, the species distribution as a whole may have an impact on the pathological properties associated with amyloid. For example, in a population, some species may contribute directly to the accelerated propagation of the amyloid state in the amyloid lifecycle and only indirectly in the accumulation of toxic species, while other species may act as cytotoxic entities directly. Whole population effects could also rest in the varied concentrations of different species in the population as the toxic potential of the whole amyloid population will be a sum of the toxic potential displayed by individual species in the population, weighted by their concentrations. Just like for any toxic substances, the classic principle "*sola dosis facit venenum*" (the dose makes the poison) will also apply to amyloid species. Furthermore, the infectious and toxic potential of amyloid will be modulated by their suprastructural states, such as clustering and filament lateral assembly, at a mesoscopic scale. This information can be obtained using - for example - atomic force spectroscopy (AFM) and transmission electron microscopy (TEM) and will be highly complementary to higher resolution structural information on individual filament types obtainable by ssNMR and cryo-EM.

Various anti-amyloid therapeutics targeting different processes in the amyloid lifecycle have reached clinical trials although so far none have been successful. Part of the problem lies with the fact that the holistic role of amyloid lifecycle in disease mechanisms has not been fully elucidated. Potential mechanisms to target amyloid formation include kinetic stabilisation of native and inert states, inhibitors of enzymes that process amyloid precursors, sequestering small toxic oligomeric species with antibodies, inhibition of amyloid-membrane interactions, prevention of elongation through blocking fibril ends, and potentially increasing elongation rates to force smaller, more toxic, states to form part of longer fibrils with less cytotoxic potential. For example, a molecular chaperone BRICHOS can effectively bind to the surface of Aβ fibrils, thus preventing secondary nucleation [162,163]. Engineered and enhanced disaggregases, including Hsp104, are capable of clearing amyloid inclusions and could also potentially lead to development of therapeutics that upregulate amyloid aggregate clearance [164]. Immunotherapies targeting Aβ oligomers or fibrils have been thus far been unsuccessful, although results are yet to emerge for their ability to prevent disease in asymptomatic people with a genetic predisposition [165]. This highlights the fact that developing drugs for amyloid disease treatments is not as straightforward as designing an inhibitor for monomer production. A deeper holistic and systems understanding of the effects of pathogenic amyloid in the biological context is required for effective development of therapeutics.

The potential for exploiting functional amyloid as natural bio-nanomaterials has inspired the development and rational design of artificial nanomaterials which use their unique materials properties for a variety of prospective applications in biotechnology and biomedicine. The self-assembly mechanism produces highly stable fibrils with a tensile strength comparable to that of steel [166]. These properties make them highly lucrative for novel biomaterial development. Additionally, amyloidogenic proteins are amenable to significant sequence and chemical modifications to alter their physio-chemical properties as the fibrils are able to maintain their structure under a wide range of

conditions. Potential applications of synthetic amyloid include mechanisms of drug delivery as a reservoir for controlled release of drugs, and tissue repair as a molecular scaffold promoting cell adhesion, migration and differentiation. Another possible use of amyloid fibrils includes forming biosensors by entrapping proteins or other sensory molecules, depending on the desired application, or the formation of nanowires by forming long hollow tubes [167]. Amyloid-carbon hybrid membranes have also been developed for inexpensive water purification, efficiently removing heavy metal ions and radioactive waste [168]. Thus, if bespoke amyloid can be designed and negatively selected against molecular features that are associated with toxic properties, amyloid fibrils will make excellent nanomaterials for biotechnology and biomedical purposes.

10. Closing remarks

Despite increasing research efforts, the specific roles of amyloid structures in neurodegenerative disease remains elusive. There is still a lack of clear understanding of the identity of the toxic amyloid species, their mechanism of action and their infectious potential in relation to their structural properties. Indeed, high-resolution structural models of amyloid fibrils have now been resolved using emergent ssNMR and cryo-EM methodologies, and these advances confirm that despite sharing the same cross-β core characteristics, amyloidogenic proteins form fibrils with differences in the arrangements of the steric zipper core packing, β-sheet content, and the number and packing arrangement of protofilaments. The formation of different polymorphs and the heterogeneity of the amyloid populations can be affected by environmental conditions, and fibrils and small oligomeric species with different morphologies can form under the same conditions, including *in vivo* and in disease-affected patients. There is also now increasing evidence to show that fibrils are not inert end-stage structures, but are an integral member of the amyloid lifecycle. Through division, replication and propagation processes such as enzyme-catalysed fibril fragmentation, several potential pathways of toxicity can have key roles in the amyloid lifecycle and their pathological effects. Simultaneously, there is a large degree of variability in the biological roles of amyloid, ranging from those essential for physiological functions to those associated with debilitating neurodegenerative diseases.

Variability in fibril polymorphs and their suprastructures on the mesoscopic scale could rationalise the variations in functional and pathogenic consequences of amyloid. Thus, conflicting evidence regarding varied cytotoxicity of amyloid fibrils could be resolved by fibrils having different levels of stability, structural rigidity, surface properties, and suprastructural formations that affect cytotoxicity, aggregation, interactions with chaperones, propensity to shed oligomers or sequester essential cellular proteins. This could also rationalise why amyloid deposits in the brain do not always correlate well with clinical symptoms of neurodegenerative disease or how some amyloid can have important physiological roles without any harmful effects. Additionally, patients with the same neurodegenerative disease form different predominant types of polymorphs of the same amyloid protein that could influence disease progression and clinical symptoms. Thus, a key challenge is to establish a correlation between amyloid structure, specific mechanisms of toxicity, and variability in clinical symptoms. Fully understanding mechanisms of the amyloid lifecycle, and the behaviour of the heterogeneous and polymorphous amyloid populations and their suprastructural properties in the mesoscopic scale, is essential to ensure the efficacy of future therapeutics targeting amyloid as well as biotechnological applications of amyloid.

Acknowledgments

This work was supported by funding from the Biotechnology and Biological Sciences Research Council (BBSRC), UK grants BB/M02427X/1 and BB/S003312/1, as well as Engineering and Physical Sciences Research Council (EPSRC), UK DTP grant (EP/R513246/1 for L.L).

References

[1] C. Soto, Unfolding the role of protein misfolding in neurodegenerative diseases, Nat. Rev. Neurosci. 4 (2003) 49–60.
[2] M.A. Gertz, A. Dispenzieri, T. Sher, Pathophysiology and treatment of cardiac amyloidosis, Nat. Rev. Cardiol. 12 (2015) 91–102.
[3] G. Merlini, A. Dispenzieri, V. Sanchorawala, S.O. Schönland, G. Palladini, P.N. Hawkins, M.A. Gertz, Systemic immunoglobulin light chain amyloidosis, Nat. Rev. Dis. Primers 4 (2018) 38.
[4] A. Mukherjee, D. Morales-Scheihing, P.C. Butler, C. Soto, Type 2 diabetes as a protein misfolding disease, Trends Mol. Med. 21 (2015) 439–449.
[5] F. Chiti, C.M. Dobson, Protein misfolding, functional amyloid, and human disease, Annu. Rev. Biochem. 75 (2006) 333–366.
[6] D.M. Fowler, A.V. Koulov, W.E. Balch, J.W. Kelly, Functional amyloid—from bacteria to humans, Trends Biochem. Sci. 32 (2007) 217–224.
[7] M. Burdukiewicz, P. Sobczyk, S. Rödiger, A. Duda-Madej, P. Mackiewicz, M. Kotulska, Amyloidogenic motifs revealed by n-gram analysis, Sci. Rep. 7 (2017) 12961.
[8] T.R. Jahn, O.S. Makin, K.L. Morris, K.E. Marshall, P. Tian, P. Sikorski, L.C. Serpell, The common architecture of cross-β amyloid, J. Mol. Biol. 395 (2010) 717–727.
[9] L.C. Serpell, P.E. Fraser, M. Sunde, X-ray fiber diffraction of amyloid fibrils, Methods in Enzymology, Academic Press, 1999, pp. 526–536.
[10] M.R. Sawaya, S. Sambashivan, R. Nelson, M.I. Ivanova, S.A. Sievers, M.I. Apostol, M.J. Thompson, M. Balbirnie, J.J.W. Wiltzius, H.T. McFarlane, A.Ø. Madsen, C. Riekel, D. Eisenberg, Atomic structures of amyloid cross-β spines reveal varied steric zippers, Nature 447 (2007) 453–457.
[11] J.F. Smith, T.P.J. Knowles, C.M. Dobson, C.E. MacPhee, M.E. Welland, Characterization of the nanoscale properties of individual amyloid fibrils, Proc. Natl. Acad. Sci. U. S. A. 103 (2006) 15806–15811.
[12] B. Li, P. Ge, K.A. Murray, P. Sheth, M. Zhang, G. Nair, M.R. Sawaya, W.S. Shin, D.R. Boyer, S. Ye, D.S. Eisenberg, Z.H. Zhou, L. Jiang, Cryo-EM of full-length α-synuclein reveals fibril polymorphs with a common structural kernel, Nat. Commun. 9 (2018) 3609.
[13] J. Meinhardt, C. Sachse, P. Hortschansky, N. Grigorieff, M. Fändrich, Aβ(1-40) fibril polymorphism implies diverse interaction patterns in amyloid fibrils, J. Mol. Biol. 386 (2009) 869–877.
[14] P. Swuec, F. Lavatelli, M. Tasaki, C. Paissoni, P. Rognoni, M. Maritan, F. Brambilla, P. Milani, P. Mauri, C. Camilloni, G. Palladini, G. Merlini, S. Ricagno, M. Bolognesi, Cryo-EM structure of cardiac amyloid fibrils from an immunoglobulin light chain (AL) amyloidosis patient, BioRxiv 444901 (2018).
[15] M.P. Jackson, E.W. Hewitt, Why are functional amyloids non-toxic in humans? Biomolecules 7 (2017).
[16] A.T. Petkova, R.D. Leapman, Z. Guo, W.-M. Yau, M.P. Mattson, R. Tycko, Self-propagating, molecular-level polymorphism in Alzheimer's β-amyloid fibrils, Science 307 (2005) 262–265.
[17] J. Winkler, J. Tyedmers, B. Bukau, A. Mogk, Hsp70 targets Hsp100 chaperones to substrates for protein disaggregation and prion fragmentation, J. Cell Biol. 198 (2012) 387–404.
[18] D.M. Beal, M. Tournus, R. Marchante, T. Purton, D.P. Smith, M.F. Tuite, M. Doumic, W.-F. Xue, et al., BioRxiv (2018) 506386.
[19] M. Törnquist, T.C.T. Michaels, K. Sanagavarapu, X. Yang, G. Meisl, S.I.A. Cohen, T.P.J. Knowles, S. Linse, Secondary nucleation in amyloid formation, Chem. Commun. 54 (2018) 8667–8684.
[20] L. Breydo, V.N. Uversky, Structural, morphological, and functional diversity of amyloid oligomers, FEBS Lett. 589 (2015) 2640–2648.
[21] J. Habchi, S. Chia, C. Galvagnion, T.C.T. Michaels, M.M.J. Bellaiche, F.S. Ruggeri, M. Sanguanini, I. Idini, J.R. Kumita, E. Sparr, S. Linse, C.M. Dobson, T.P.J. Knowles, M. Vendruscolo, Cholesterol catalyses Aβ42 aggregation through a heterogeneous nucleation pathway in the presence of lipid membranes, Nat. Chem. 10 (2018) 673–683.
[22] M. Novo, S. Freire, W. Al-Soufi, et al., Sci. Rep. 8 (2018).
[23] L.M. Blancas-Mejía, P. Misra, M. Ramirez-Alvarado, Differences in protein concentration dependence for nucleation and elongation in light chain amyloid formation, Biochemistry 56 (2017) 757–766.
[24] D. Kashchiev, S. Auer, Nucleation of amyloid fibrils, J. Chem. Phys. 132 (2010) 215101.
[25] W.-F. Xue, S.W. Homans, S.E. Radford, Systematic analysis of nucleation-dependent polymerization reveals new insights into the mechanism of amyloid self-assembly, PNAS 105 (2008) 8926–8931.
[26] A.K. Buell, C. Galvagnion, R. Gaspar, E. Sparr, M. Vendruscolo, T.P.J. Knowles, S. Linse, C.M. Dobson, Solution conditions determine the relative importance of nucleation and growth processes in α-synuclein aggregation, Proc. Natl. Acad. Sci. U. S. A. 111 (2014) 7671–7676.
[27] S.I.A. Cohen, S. Linse, L.M. Luheshi, E. Hellstrand, D.A. White, L. Rajah, D.E. Otzen, M. Vendruscolo, C.M. Dobson, T.P.J. Knowles, Proliferation of amyloid-β42 aggregates occurs through a secondary nucleation mechanism, Proc. Natl. Acad. Sci. 110 (2013) 9758–9763.
[28] D.M. Hatters, C.A. MacRaild, R. Daniels, W.S. Gosal, N.H. Thomson, J.A. Jones, J.J. Davis, C.E. MacPhee, C.M. Dobson, G.J. Howlett, The circularization of amyloid fibrils formed by apolipoprotein C-II, Biophys. J. 85 (2003) 3979–3990.
[29] S.W. Chen, S. Drakulic, E. Deas, M. Ouberai, F.A. Aprile, R. Arranz, S. Ness,

C. Roodveldt, T. Guilliams, E.J. De-Genst, D. Klenerman, N.W. Wood, T.P.J. Knowles, C. Alfonso, G. Rivas, A.Y. Abramov, J.M. Valpuesta, C.M. Dobson, N. Cremades, Structural characterization of toxic oligomers that are kinetically trapped during α-synuclein fibril formation, Proc. Natl. Acad. Sci. 112 (2015) E1994–E2003.
[30] S.A. Kotler, J.R. Brender, S. Vivekanandan, Y. Suzuki, K. Yamamoto, M. Monette, J. Krishnamoorthy, P. Walsh, M. Cauble, M.M.B. Holl, E.N.G. Marsh, A. Ramamoorthy, High-resolution NMR characterization of low abundance oligomers of amyloid-β without purification, Sci. Rep. 5 (2015) 11811.
[31] S. Parthasarathy, M. Inoue, Y. Xiao, Y. Matsumura, Y. Nabeshima, M. Hoshi, Y. Ishii, Structural insight into an Alzheimer's brain-derived spherical assembly of amyloid β by solid-state NMR, J. Am. Chem. Soc. 137 (2015) 6480–6483.
[32] L. Breydo, D. Kurouski, S. Rasool, S. Milton, J.W. Wu, V.N. Uversky, I.K. Lednev, C.G. Glabe, Structural differences between amyloid beta oligomers, Biochem. Biophys. Res. Commun. 477 (2016) 700–705.
[33] M.-C. Lee, W.-C. Yu, Y.-H. Shih, C.-Y. Chen, Z.-H. Guo, S.-J. Huang, J.C.C. Chan, Y.-R. Chen, Zinc ion rapidly induces toxic, off-pathway amyloid-β oligomers distinct from amyloid-β derived diffusible ligands in Alzheimer's disease, Sci. Rep. 8 (2018) 4772.
[34] P.A. Chong, J.D. Forman-Kay, Liquid–liquid phase separation in cellular signaling systems, Curr. Opin. Struct. Biol. 41 (2016) 180–186.
[35] S. Ambadipudi, J. Biernat, D. Riedel, E. Mandelkow, M. Zweckstetter, Liquid–liquid phase separation of the microtubule-binding repeats of the Alzheimer-related protein Tau, Nat. Commun. 8 (2017) 275.
[36] J.S. Jeong, A. Ansaloni, R. Mezzenga, H.A. Lashuel, G. Dietler, Novel mechanistic insight into the molecular basis of amyloid polymorphism and secondary nucleation during amyloid formation, J. Mol. Biol. 425 (2013) 1765–1781.
[37] X. Gao, M. Carroni, C. Nussbaum-Krammer, A. Mogk, N.B. Nillegoda, A. Szlachcic, D.L. Guilbride, H.R. Saibil, M.P. Mayer, B. Bukau, Human Hsp70 disaggregase reverses Parkinson's-linked α-synuclein amyloid fibrils, Mol. Cell 59 (2015) 781–793.
[38] M. Tanaka, S.R. Collins, B.H. Toyama, J.S. Weissman, The physical basis of how prion conformations determine strain phenotypes, Nature 442 (2006) 585–589.
[39] W.-F. Xue, A.L. Hellewell, W.S. Gosal, S.W. Homans, E.W. Hewitt, S.E. Radford, Fibril fragmentation enhances amyloid cytotoxicity, J. Biol. Chem. 284 (2009) 34272–34282.
[40] C. Xue, T.Y. Lin, D. Chang, Z. Guo, et al., R. Soc. Open Sci. 4 (2017).
[41] T.C.T. Michaels, A. Šarić, J. Habchi, S. Chia, G. Meisl, M. Vendruscolo, C.M. Dobson, T.P.J. Knowles, Chemical kinetics for bridging molecular mechanisms and macroscopic measurements of amyloid fibril formation, Annu. Rev. Phys. Chem. 69 (2018) 273–298.
[42] A. Sidhu, J. Vaneyck, C. Blum, I. Segers-Nolten, V. Subramaniam, Polymorph-specific distribution of binding sites determines thioflavin-T fluorescence intensity in α-synuclein fibrils, Amyloid 25 (2018) 189–196.
[43] A. Biancardi, T. Biver, B. Mennucci, Fluorescent dyes in the context of DNA-binding: the case of Thioflavin T, Int. J. Quantum Chem. 117 (2017) e25349.
[44] N.D. Younan, J.H. Viles, A comparison of three fluorophores for the detection of amyloid fibers and prefibrillar oligomeric assemblies ThT (Thioflavin T); ANS (1-anilinonaphthalene-8-sulfonic Acid); and bisANS (4,4′-dianilino-1,1′-binaphthyl-5,5′-disulfonic acid), Biochemistry 54 (2015) 4297–4306.
[45] L.P. Jameson, N.W. Smith, S.V. Dzyuba, Dye-binding assays for evaluation of the effects of small molecule inhibitors on amyloid (Aβ) self-assembly, ACS Chem. Neurosci. 3 (2012) 807–819.
[46] Y. Cheng, B. Zhu, Y. Deng, Z. Zhang, In vivo detection of cerebral amyloid fibrils with smart dicynomethylene-4H-pyran-based fluorescence probe, Anal. Chem. 87 (2015) 4781–4787.
[47] A.I. Sulatskaya, M.I. Sulatsky, I.A. Antifeeva, I.M. Kuznetsova, K.K. Turoverov, Structural analogue of thioflavin T, DMASEBT, as a tool for amyloid fibrils study, Anal. Chem. 91 (2019) 3131–3140.
[48] K.P.R. Nilsson, A. Aslund, I. Berg, S. Nyström, P. Konradsson, A. Herland, O. Inganäs, F. Stabo-Eeg, M. Lindgren, G.T. Westermark, L. Lannfelt, L.N.G. Nilsson, P. Hammarström, Imaging distinct conformational states of amyloid-β fibrils in Alzheimer's disease using novel luminescent probes, ACS Chem. Biol. 2 (2007) 553–560.
[49] B.M. Wegenast-Braun, A. Skodras, G. Bayraktar, J. Mahler, S.K. Fritschi, T. Klingstedt, J.J. Mason, P. Hammarström, K.P.R. Nilsson, C. Liebig, M. Jucker, Spectral discrimination of cerebral amyloid lesions after peripheral application of luminescent conjugated oligothiophenes, Am. J. Pathol. 181 (2012) 1953–1960.
[50] A.K. Buell, A. Dhulesia, D.A. White, T.P.J. Knowles, C.M. Dobson, M.E. Welland, Detailed analysis of the energy barriers for amyloid fibril growth, Angew. Chem. Int. Ed. 51 (2012) 5247–5251.
[51] D. Kashchiev, R. Cabriolu, S. Auer, Confounding the paradigm: peculiarities of amyloid fibril nucleation, J. Am. Chem. Soc. 135 (2013) 1531–1539.
[52] P. Arosio, T.P.J. Knowles, S. Linse, On the lag phase in amyloid fibril formation, Phys. Chem. Chem. Phys. 17 (2015) 7606–7618.
[53] N. Carulla, G.L. Caddy, D.R. Hall, J. Zurdo, M. Gairí, M. Feliz, E. Giralt, C.V. Robinson, C.M. Dobson, Molecular recycling within amyloid fibrils, Nature 436 (2005) 554–558.
[54] E.K. Esbjörner, F. Chan, E. Rees, M. Erdelyi, L.M. Luheshi, C.W. Bertoncini, C.F. Kaminski, C.M. Dobson, G.S. Kaminski Schierle, Direct observations of amyloid β self-assembly in live cells provide insights into differences in the kinetics of Aβ(1–40) and Aβ(1–42) aggregation, Chem. Biol. 21 (2014) 732–742.
[55] S. Burgold, S. Filser, M.M. Dorostkar, B. Schmidt, J. Herms, In vivo imaging reveals sigmoidal growth kinetic of β-amyloid plaques, Acta Neuropathol. Commun. 2 (2014) 30.
[56] C.R. Jack, H.J. Wiste, T.G. Lesnick, S.D. Weigand, D.S. Knopman, P. Vemuri, V.S. Pankratz, M.L. Senjem, J.L. Gunter, M.M. Mielke, V.J. Lowe, B.F. Boeve, R.C. Petersen, Brain β-amyloid load approaches a plateau, Neurology 80 (2013) 890–896.
[57] M. Fändrich, M.A. Fletcher, C.M. Dobson, Amyloid fibrils from muscle myoglobin, Nature 410 (2001) 165–166.
[58] T. Eichner, S.E. Radford, Understanding the complex mechanisms of β2-microglobulin amyloid assembly, FEBS J. 278 (2011) 3868–3883.
[59] F. Chiti, C.M. Dobson, Amyloid formation by globular proteins under native conditions, Nat. Chem. Biol. 5 (2009) 15–22.
[60] C. Galvagnion, A.K. Buell, G. Meisl, T.C.T. Michaels, M. Vendruscolo, T.P.J. Knowles, C.M. Dobson, Lipid vesicles trigger α-synuclein aggregation by stimulating primary nucleation, Nat. Chem. Biol. 11 (2015) 229–234.
[61] B. Moores, E. Drolle, S.J. Attwood, J. Simons, Z. Leonenko, Effect of surfaces on amyloid fibril formation, PLoS One 6 (2011).
[62] B. Morel, L. Varela, A.I. Azuaga, F. Conejero-Lara, Environmental conditions affect the kinetics of nucleation of amyloid fibrils and determine their morphology, Biophys. J. 99 (2010) 3801–3810.
[63] P. Faller, C. Hureau, O. Berthoumieu, Role of metal ions in the self-assembly of the Alzheimer's amyloid-β peptide, Inorg. Chem. 52 (2013) 12193–12206.
[64] F. Chiti, P. Webster, N. Taddei, A. Clark, M. Stefani, G. Ramponi, C.M. Dobson, Designing conditions for in vitro formation of amyloid protofilaments and fibrils, Proc. Natl. Acad. Sci. U. S. A. 96 (1999) 3590–3594.
[65] L. Goldschmidt, P.K. Teng, R. Riek, D. Eisenberg, Identifying the amylome, proteins capable of forming amyloid-like fibrils, Proc. Natl. Acad. Sci. U. S. A. 107 (2010) 3487–3492.
[66] K.L. Zapadka, F.J. Becher, S. Uddin, P.G. Varley, S. Bishop, A.L. Gomes Dos Santos, S.E. Jackson, A pH-induced switch in human glucagon-like peptide-1 aggregation kinetics, J. Am. Chem. Soc. 138 (2016) 16259–16265.
[67] F. Hasecke, T. Miti, C. Perez, J. Barton, D. Schölzel, L. Gremer, C.S.R. Grüning, G. Matthews, G. Meisl, T.P.J. Knowles, D. Willbold, P. Neudecker, H. Heise, G. Ullah, W. Hoyer, M. Muschol, Origin of metastable oligomers and their effects on amyloid fibril self-assembly, Chem. Sci. 9 (2018) 5937–5948.
[68] E.H. Lee, A practical guide to pharmaceutical polymorph screening & selection, Asian J. Pharm. Sci. 9 (2014) 163–175.
[69] J. Bernstein, Polymorphism in Molecular Crystals, Oxford University Press, 2007.
[70] W. Close, M. Neumann, A. Schmidt, M. Hora, K. Annamalai, M. Schmidt, B. Reif, V. Schmidt, N. Grigorieff, M. Fändrich, Physical basis of amyloid fibril polymorphism, Nat. Commun. 9 (2018) 699.
[71] K. Annamalai, K.-H. Gührs, R. Koehler, M. Schmidt, H. Michel, C. Loos, P.M. Gaffney, C.J. Sigurdson, U. Hegenbart, S. Schönland, M. Fändrich, polymorphism of amyloid fibrils in vivo, Angew. Chem. Int. Ed. Eng. 55 (2016) 4822–4825.
[72] B. Falcon, W. Zhang, A.G. Murzin, G. Murshudov, H.J. Garringer, R. Vidal, R.A. Crowther, B. Ghetti, S.H.W. Scheres, M. Goedert, et al., Nature (2018) 1.
[73] A.W.P. Fitzpatrick, B. Falcon, S. He, A.G. Murzin, G. Murshudov, H.J. Garringer, R.A. Crowther, B. Ghetti, M. Goedert, S.H.W. Scheres, Cryo-EM structures of tau filaments from Alzheimer's disease, Nature 547 (2017) 185–190.
[74] M.G. Iadanza, R. Silvers, J. Boardman, H.I. Smith, T.K. Karamanos, G.T. Debelouchina, Y. Su, R.G. Griffin, N.A. Ranson, S.E. Radford, The structure of a β2-microglobulin fibril suggests a molecular basis for its amyloid polymorphism, Nat. Commun. 9 (2018) 4517.
[75] R. Tycko, Amyloid polymorphism: structural basis and neurobiological relevance, Neuron 86 (2015) 632–645.
[76] W.-F. Xue, A.L. Hellewell, E.W. Hewitt, S.E. Radford, Fibril fragmentation in amyloid assembly and cytotoxicity, Prion 4 (2010) 20–25.
[77] W. Qiang, W.-M. Yau, J.-X. Lu, J. Collinge, R. Tycko, Structural variation in amyloid-β fibrils from Alzheimer's disease clinical subtypes, Nature 541 (2017) 217–221.
[78] J.-X. Lu, W. Qiang, W.-M. Yau, C.D. Schwieters, S.C. Meredith, R. Tycko, Molecular structure of β-amyloid fibrils in Alzheimer's disease brain tissue, Cell 154 (2013) 1257–1268.
[79] E. Kara, J.D. Marks, A. Aguzzi, Toxic protein spread in neurodegeneration: reality versus fantasy, Trends Mol. Med. 24 (2018) 1007–1020.
[80] R. Khurana, C. Ionescu-Zanetti, M. Pope, J. Li, L. Nielson, M. Ramírez-Alvarado, L. Regan, A.L. Fink, S.A. Carter, A general model for amyloid fibril assembly based on morphological studies using atomic force microscopy, Biophys. J. 85 (2003) 1135–1144.
[81] M. Kollmer, K. Meinhardt, C. Haupt, F. Liberta, M. Wulff, J. Linder, L. Handl, L. Heinrich, C. Loos, M. Schmidt, T. Syrovets, T. Simmet, P. Westermark, G.T. Westermark, U. Horn, V. Schmidt, P. Walther, M. Fändrich, Electron tomography reveals the fibril structure and lipid interactions in amyloid deposits, Proc. Natl. Acad. Sci. U. S. A. 113 (2016) 5604–5609.
[82] D. Vigolo, J. Zhao, S. Handschin, X. Cao, A.J. de Mello, R. Mezzenga, et al., Sci. Rep. 7 (2017) 1211.
[83] S. Jordens, L. Isa, I. Usov, R. Mezzenga, Non-equilibrium nature of two-dimensional isotropic and nematic coexistence in amyloid fibrils at liquid interfaces, Nat. Commun. 4 (2013) 1917.
[84] M. Manno, D. Giacomazza, J. Newman, V. Martorana, P.L. San Biagio, Amyloid gels: precocious appearance of elastic properties during the formation of an insulin fibrillar network, Langmuir 26 (2010) 1424–1426.
[85] S. Han, M. Kollmer, D. Markx, S. Claus, P. Walther, M. Fändrich, Amyloid plaque structure and cell surface interactions of β-amyloid fibrils revealed by electron tomography, Sci. Rep. 7 (2017).
[86] L.-W. Jin, K.A. Claborn, M. Kurimoto, M.A. Geday, I. Maezawa, F. Sohraby, M. Estrada, W. Kaminksy, B. Kahr, Imaging linear birefringence and dichroism in cerebral amyloid pathologies, PNAS 100 (2003) 15294–15298.

[87] M.R.H. Krebs, C.E. MacPhee, A.F. Miller, I.E. Dunlop, C.M. Dobson, A.M. Donald, The formation of spherulites by amyloid fibrils of bovine insulin, PNAS 101 (2004) 14420–14424.

[88] C.R. Liao, M. Rak, J. Lund, M. Unger, E. Platt, B.C. Albensi, C.J. Hirschmugl, K.M. Gough, Synchrotron FTIR reveals lipid around and within amyloid plaques in transgenic mice and Alzheimer's disease brain, Analyst 138 (2013) 3991–3997.

[89] J.F. Berson, A.C. Theos, D.C. Harper, D. Tenza, G. Raposo, M.S. Marks, Proprotein convertase cleavage liberates a fibrillogenic fragment of a resident glycoprotein to initiate melanosome biogenesis, J. Cell Biol. 161 (2003) 521–533.

[90] B. Drisaldi, L. Colnaghi, L. Fioriti, N. Rao, C. Myers, A.M. Snyder, D.J. Metzger, J. Tarasoff, E. Konstantinov, P.E. Fraser, J.L. Manley, E.R. Kandel, SUMOylation is an inhibitory constraint that regulates the prion-like aggregation and activity of CPEB3, Cell Rep. 11 (2015) 1694–1702.

[91] S.K. Maji, M.H. Perrin, M.R. Sawaya, S. Jessberger, K. Vadodaria, R.A. Rissman, P.S. Singru, K.P.R. Nilsson, R. Simon, D. Schubert, D. Eisenberg, J. Rivier, P. Sawchenko, W. Vale, R. Riek, Functional amyloids as natural storage of peptide hormones in pituitary secretory granules, Science 325 (2009) 328–332.

[92] M. Deshmukh, M.L. Evans, M.R. Chapman, Amyloid by design: intrinsic regulation of microbial amyloid assembly, J. Mol. Biol. 430 (2018) 3631–3641.

[93] S.L. Rouse, F. Stylianou, H.Y.G. Wu, J.-L. Berry, L. Sewell, R.M.L. Morgan, A.C. Sauerwein, S. Matthews, The FapF amyloid secretion transporter possesses an atypical asymmetric coiled coil, J. Mol. Biol. 430 (2018) 3863–3871.

[94] J.D. Taylor, S.J. Matthews, New insight into the molecular control of bacterial functional amyloids, Front. Cell. Infect. Microbiol. 5 (2015) 33.

[95] G. Zeng, B.S. Vad, M.S. Dueholm, G. Christiansen, M. Nilsson, T. Tolker-Nielsen, P.H. Nielsen, R.L. Meyer, D.E. Otzen, Functional bacterial amyloid increases Pseudomonas biofilm hydrophobicity and stiffness, Front. Microbiol. 6 (2015) 1099.

[96] C.L. Masters, R. Bateman, K. Blennow, C.C. Rowe, R.A. Sperling, J.L. Cummings, Alzheimer's disease, Nat. Rev. Dis. Primers 1 (2015) 15056.

[97] L.D. Plant, J.P. Boyle, I.F. Smith, C. Peers, H.A. Pearson, The production of amyloid beta peptide is a critical requirement for the viability of central neurons, J. Neurosci. 23 (2003) 5531–5535.

[98] D.K.V. Kumar, S.H. Choi, K.J. Washicosky, W.A. Eimer, S. Tucker, J. Ghofrani, A. Lefkowitz, G. McColl, L.E. Goldstein, R.E. Tanzi, R.D. Moir, et al., Sci. Transl. Med. 8 (2016) 340ra72.

[99] W.A. Eimer, D.K. Vijaya Kumar, N.K. Navalpur Shanmugam, A.S. Rodriguez, T. Mitchell, K.J. Washicosky, B. György, X.O. Breakefield, R.E. Tanzi, R.D. Moir, et al., Neuron 99 (2018) 56–63 (e3).

[100] C.M. Dobson, Protein misfolding, evolution and disease, Trends Biochem. Sci. 24 (1999) 329–332.

[101] J.S. Stephan, L. Fioriti, N. Lamba, L. Colnaghi, K. Karl, I.L. Derkatch, E.R. Kandel, The CPEB3 protein is a functional prion that interacts with the actin cytoskeleton, Cell Rep. 11 (2015) 1772–1785.

[102] R. Rott, R. Szargel, V. Shani, H. Hamza, M. Savyon, F.A. Elghani, R. Bandopadhyay, S. Engelender, SUMOylation and ubiquitination reciprocally regulate α-synuclein degradation and pathological aggregation, PNAS 114 (2017) 13176–13181.

[103] T. Sheynis, A. Friediger, W.-F. Xue, A.L. Hellewell, K.W. Tipping, E.W. Hewitt, S.E. Radford, R. Jelinek, Aggregation modulators interfere with membrane interactions of β2-microglobulin fibrils, Biophys. J. 105 (2013) 745–755.

[104] M. Sebastiao, N. Quittot, I. Marcotte, S. Bourgault, Glycosaminoglycans induce amyloid self-assembly of a peptide hormone by concerted secondary and quaternary conformational transitions, Biochemistry 58 (2019) 1214–1225.

[105] F.A. Aprile, E. Källstig, G. Limorenko, M. Vendruscolo, D. Ron, C. Hansen, The molecular chaperones DNAJB6 and Hsp70 cooperate to suppress α-synuclein aggregation, Sci. Rep. 7 (2017) 9039.

[106] J. Burré, The synaptic function of α-synuclein, J. Park. Dis. 5 (2015) 699–713.

[107] E.A. Sweeny, J. Shorter, Mechanistic and structural insights into the prion-disaggregase activity of Hsp104, J. Mol. Biol. 428 (2016) 1870–1885.

[108] M.P. Torrente, J. Shorter, The metazoan protein disaggregase and amyloid depolymerase system: Hsp110, Hsp70, Hsp40, and small heat shock proteins, Prion 7 (2013) 457–463.

[109] M.P. Jackson, E.W. Hewitt, Cellular proteostasis: degradation of misfolded proteins by lysosomes, Essays Biochem. 60 (2016) 173–180.

[110] D.M. Fowler, A.V. Koulov, C. Alory-Jost, M.S. Marks, W.E. Balch, J.W. Kelly, Functional amyloid formation within mammalian tissue, PLoS Biol 4 (2006).

[111] K.S. SantaCruz, J.A. Sonnen, M.K. Pezhouh, M.F. Desrosiers, P.T. Nelson, S.L. Tyas, Alzheimer disease pathology in subjects without dementia in two studies of aging: the nun study and the adult changes in thought study, J. Neuropathol. Exp. Neurol. 70 (2011) 832–840.

[112] G.M. Shankar, S. Li, T.H. Mehta, A. Garcia-Munoz, N.E. Shepardson, I. Smith, F.M. Brett, M.A. Farrell, M.J. Rowan, C.A. Lemere, C.M. Regan, D.M. Walsh, B.L. Sabatini, D.J. Selkoe, Amyloid-β protein dimers isolated directly from Alzheimer's brains impair synaptic plasticity and memory, Nat. Med. 14 (2008) 837–842.

[113] M. Koistinaho, M. Ort, J.M. Cimadevilla, R. Vondrous, B. Cordell, J. Koistinaho, J. Bures, L.S. Higgins, Specific spatial learning deficits become severe with age in β-amyloid precursor protein transgenic mice that harbor diffuse β-amyloid deposits but do not form plaques, Proc. Natl. Acad. Sci. U. S. A. 98 (2001) 14675–14680.

[114] L.M. Billings, S. Oddo, K.N. Green, J.L. McGaugh, F.M. LaFerla, Intraneuronal Aβ causes the onset of early Alzheimer's disease-related cognitive deficits in transgenic mice, Neuron 45 (2005) 675–688.

[115] M. Arrasate, S. Mitra, E.S. Schweitzer, M.R. Segal, S. Finkbeiner, Inclusion body formation reduces levels of mutant huntingtin and the risk of neuronal death, Nature 431 (2004) 805–810.

[116] K.A. Conway, S.J. Lee, J.C. Rochet, T.T. Ding, R.E. Williamson, P.T. Lansbury, Acceleration of oligomerization, not fibrillization, is a shared property of both alpha-synuclein mutations linked to early-onset Parkinson's disease: implications for pathogenesis and therapy, Proc. Natl. Acad. Sci. U. S. A. 97 (2000) 571–576.

[117] A. Quist, I. Doudevski, H. Lin, R. Azimova, D. Ng, B. Frangione, B. Kagan, J. Ghiso, R. Lal, Amyloid ion channels: a common structural link for protein-misfolding disease, Proc. Natl. Acad. Sci. U. S. A. 102 (2005) 10427–10432.

[118] M. Serra-Batiste, M. Ninot-Pedrosa, M. Bayoumi, M. Gairí, G. Maglia, N. Carulla, Aβ42 assembles into specific β-barrel pore-forming oligomers in membrane-mimicking environments, Proc. Natl. Acad. Sci. 113 (2016) 10866–10871.

[119] C. Di Scala, N. Yahi, S. Boutemeur, A. Flores, L. Rodriguez, H. Chahinian, J. Fantini, Common molecular mechanism of amyloid pore formation by Alzheimer's β-amyloid peptide and α-synuclein, Sci. Rep. 6 (2016) 28781.

[120] N. Patel, S. Ramachandran, R. Azimov, B.L. Kagan, R. Lal, Ion Channel formation by tau protein: implications for Alzheimer's disease and tauopathies, Biochemistry 54 (2015) 7320–7325.

[121] D.C. Bode, M.D. Baker, J.H. Viles, Ion channel formation by amyloid-β42 oligomers but not amyloid-β40 in cellular membranes, J. Biol. Chem. 292 (2017) 1404–1413.

[122] K.V. Kuchibhotla, S.T. Goldman, C.R. Lattarulo, H.-Y. Wu, B.T. Hyman, B.J. Bacskai, Aβ plaques lead to aberrant regulation of calcium homeostasis in vivo resulting in structural and functional disruption of neuronal networks, Neuron 59 (2008) 214–225.

[123] B. Mannini, E. Mulvihill, C. Sgromo, R. Cascella, R. Khodarahmi, M. Ramazzotti, C.M. Dobson, C. Cecchi, F. Chiti, Toxicity of protein oligomers is rationalized by a function combining size and surface hydrophobicity, ACS Chem. Biol. 9 (2014) 2309–2317.

[124] S. Campioni, B. Mannini, M. Zampagni, A. Pensalfini, C. Parrini, E. Evangelisti, A. Relini, M. Stefani, C.M. Dobson, C. Cecchi, F. Chiti, A causative link between the structure of aberrant protein oligomers and their toxicity, Nat. Chem. Biol. 6 (2010) 140–147.

[125] S.E. Lesné, M.A. Sherman, M. Grant, M. Kuskowski, J.A. Schneider, D.A. Bennett, K.H. Ashe, Brain amyloid-β oligomers in ageing and Alzheimer's disease, Brain 136 (2013) 1383–1398.

[126] J. Waters, The concentration of soluble extracellular amyloid-β protein in acute brain slices from CRND8 mice, PLoS One 5 (2010) e15709.

[127] A.H. Simonsen, S.F. Hansson, U. Ruetschi, J. McGuire, V.N. Podust, H.A. Davies, P. Mehta, G. Waldemar, H. Zetterberg, N. Andreasen, A. Wallin, K. Blennow, Amyloid β1-40 quantification in CSF: comparison between chromatographic and immunochemical methods, Dement. Geriatr. Cogn. Disord. 23 (2007) 246–250.

[128] M.F.M. Engel, L. Khemtémourian, C.C. Kleijer, H.J.D. Meeldijk, J. Jacobs, A.J. Verkleij, B. de Kruijff, J.A. Killian, J.W.M. Höppener, Membrane damage by human islet amyloid polypeptide through fibril growth at the membrane, PNAS 105 (2008) 6033–6038.

[129] M. Meyer-Luehmann, T.L. Spires-Jones, C. Prada, M. Garcia-Alloza, A. de Calignon, A. Rozkalne, J. Koenigsknecht-Talboo, D.M. Holtzman, B.J. Bacskai, B.T. Hyman, Rapid appearance and local toxicity of amyloid-β plaques in a mouse model of Alzheimer's disease, Nature 451 (2008) 720–724.

[130] A. Serrano-Pozo, R.A. Betensky, M.P. Frosch, B.T. Hyman, Plaque-associated local toxicity increases over the clinical course of alzheimer disease, Am. J. Pathol. 186 (2016) 375–384.

[131] R.M. Koffie, M. Meyer-Luehmann, T. Hashimoto, K.W. Adams, M.L. Mielke, M. Garcia-Alloza, K.D. Micheva, S.J. Smith, M.L. Kim, V.M. Lee, B.T. Hyman, T.L. Spires-Jones, Oligomeric amyloid β associates with postsynaptic densities and correlates with excitatory synapse loss near senile plaques, PNAS 106 (2009) 4012–4017.

[132] T. Jakhria, A.L. Hellewell, M.Y. Porter, M.P. Jackson, K.W. Tipping, W.-F. Xue, S.E. Radford, E.W. Hewitt, β2-microglobulin amyloid fibrils are nanoparticles that disrupt lysosomal membrane protein trafficking and inhibit protein degradation by lysosomes, J. Biol. Chem. 289 (2014) 35781–35794.

[133] L. Milanesi, T. Sheynis, W.-F. Xue, E.V. Orlova, A.L. Hellewell, R. Jelinek, E.W. Hewitt, S.E. Radford, H.R. Saibil, Direct three-dimensional visualization of membrane disruption by amyloid fibrils, Proc. Natl. Acad. Sci. 109 (2012) 20455–20460.

[134] N.P. Reynolds, A. Soragni, M. Rabe, D. Verdes, E. Liverani, S. Handschin, R. Riek, S. Seeger, Mechanism of membrane interaction and disruption by α-synuclein, J. Am. Chem. Soc. 133 (2011) 19366–19375.

[135] I.C. Martins, I. Kuperstein, H. Wilkinson, E. Maes, M. Vanbrabant, W. Jonckheere, P. Van Gelder, D. Hartmann, R. D'Hooge, B. De Strooper, J. Schymkowitz, F. Rousseau, Lipids revert inert Aβ amyloid fibrils to neurotoxic protofibrils that affect learning in mice, EMBO J. 27 (2008) 224–233.

[136] J.H. Viles, Metal ions and amyloid fiber formation in neurodegenerative diseases Copper, zinc and iron in Alzheimer's, Parkinson's and prion diseases, Coord. Chem. Rev. 256 (2012) 2271–2284.

[137] L.M. Miller, Q. Wang, T.P. Telivala, R.J. Smith, A. Lanzirotti, J. Miklossy, Synchrotron-based infrared and X-ray imaging shows focalized accumulation of Cu and Zn co-localized with β-amyloid deposits in Alzheimer's disease, J. Struct. Biol. 155 (2006) 30–37.

[138] J. Mayes, C. Tinker-Mill, O. Kolosov, H. Zhang, B.J. Tabner, D. Allsop, β-Amyloid fibrils in alzheimer disease are not inert when bound to copper ions but can degrade hydrogen peroxide and generate reactive oxygen species, J. Biol. Chem. 289 (2014) 12052–12062.

[139] C.J. Matheou, N.D. Younan, J.H. Viles, Cu^{2+} accentuates distinct misfolding of $A\beta_{1\text{-}40}$ and $A\beta_{1\text{-}42}$ peptides, and potentiates membrane disruption, Biochem. J. 466 (2015) 233–242.

[140] M. Stefani, Generic cell dysfunction in neurodegenerative disorders: role of surfaces in early protein misfolding, aggregation, and aggregate cytotoxicity, Neuroscientist 13 (2007) 519–531.
[141] H. Zhao, E.K.J. Tuominen, P.K.J. Kinnunen, Formation of amyloid fibers triggered by phosphatidylserine-containing membranes, Biochemistry 43 (2004) 10302–10307.
[142] E.Y. Chi, S.L. Frey, A. Winans, K.L.H. Lam, K. Kjaer, J. Majewski, K.Y.C. Lee, Amyloid-β fibrillogenesis seeded by interface-induced peptide misfolding and self-assembly, Biophys. J. 98 (2010) 2299.
[143] L. Jean, C.F. Lee, D.J. Vaux, Enrichment of amyloidogenesis at an air-water interface, Biophys. J. 102 (2012) 1154–1162.
[144] S.B. Prusiner, Prions, Proc. Natl. Acad. Sci. U. S. A. 95 (1998) 13363–13383.
[145] M. Tanaka, P. Chien, K. Yonekura, J.S. Weissman, Mechanism of cross-species prion transmission: an infectious conformation compatible with two highly divergent yeast prion proteins, Cell 121 (2005) 49–62.
[146] J. Shorter, S. Lindquist, Prions as adaptive conduits of memory and inheritance, Nat. Rev. Genet. 6 (2005) 435–450.
[147] R.B. Wickner, [URE3] as an altered URE2 protein: evidence for a prion analog in Saccharomyces cerevisiae, Science 264 (1994) 566–569.
[148] M. Tanaka, S.R. Collins, B.H. Toyama, J.S. Weissman, The physical basis of how prion conformations determine strain phenotypes, Nature 442 (2006) 585–589.
[149] V.V. Kushnirov, A.B. Vishnevskaya, I.M. Alexandrov, M.D. Ter-Avanesyan, Prion and Nonprion Amyloids, Prion 1 (2007) 179–184.
[150] J.M. Nussbaum, S. Schilling, H. Cynis, A. Silva, E. Swanson, T. Wangsanut, K. Tayler, B. Wiltgen, A. Hatami, R. Rönicke, K. Reymann, B. Hutter-Paier, A. Alexandru, W. Jagla, S. Graubner, C.G. Glabe, H.-U. Demuth, G.S. Bloom, Prion-like behaviour and tau-dependent cytotoxicity of pyroglutamylated amyloid-β, Nature 485 (2012) 651–655.
[151] A. Tarutani, T. Arai, S. Murayama, S. Hisanaga, M. Hasegawa, Potent prion-like behaviors of pathogenic α-synuclein and evaluation of inactivation methods, Acta Neuropathol. Commun. 6 (2018) 29.
[152] I. Jeon, F. Cicchetti, G. Cisbani, S. Lee, E. Li, J. Bae, N. Lee, L. Li, W. Im, M. Kim, H.S. Kim, S.-H. Oh, T.-A. Kim, J.J. Ko, B. Aubé, A. Oueslati, Y.J. Kim, J. Song, Human-to-mouse prion-like propagation of mutant huntingtin protein, Acta Neuropathol. 132 (2016) 577–592.
[153] F. Clavaguera, M. Tolnay, M. Goedert, The prion-like behavior of assembled tau in transgenic mice, Cold Spring Harb. Perspect. Med. 7 (2017).
[154] F. Clavaguera, H. Akatsu, G. Fraser, R.A. Crowther, S. Frank, J. Hench, A. Probst, D.T. Winkler, J. Reichwald, M. Staufenbiel, B. Ghetti, M. Goedert, M. Tolnay, Brain homogenates from human tauopathies induce tau inclusions in mouse brain, Proc. Natl. Acad. Sci. U. S. A. 110 (2013) 9535–9540.
[155] S.A. Purro, M.A. Farrow, J. Linehan, T. Nazari, D.X. Thomas, Z. Chen, D. Mengel, T. Saito, T. Saido, P. Rudge, S. Brandner, D.M. Walsh, J. Collinge, Transmission of amyloid-β protein pathology from cadaveric pituitary growth hormone, Nature 564 (2018) 415–419.
[156] Z. Laron, The era of cadaveric pituitary extracted human growth hormone (1958-1985): biological and clinical aspects, Pediatr. Endocrinol. Rev. 16 (2018) 11–16.
[157] R. Marchante, D.M. Beal, N. Koloteva-Levine, T.J. Purton, M.F. Tuite, W.-F. Xue, et al., ELife 6 (2017).
[158] K.M. Danzer, L.R. Kranich, W.P. Ruf, O. Cagsal-Getkin, A.R. Winslow, L. Zhu, C.R. Vanderburg, P.J. McLean, Exosomal cell-to-cell transmission of alpha synuclein oligomers, Mol. Neurodegener. 7 (2012) 42.
[159] M. Bucciantini, E. Giannoni, F. Chiti, F. Baroni, L. Formigli, J. Zurdo, N. Taddei, G. Ramponi, C.M. Dobson, M. Stefani, Inherent toxicity of aggregates implies a common mechanism for protein misfolding diseases, Nature 416 (2002) 507–511.
[160] W.-F. Xue, A.L. Hellewell, W.S. Gosal, S.W. Homans, E.W. Hewitt, S.E. Radford, Fibril fragmentation enhances amyloid cytotoxicity, J. Biol. Chem. 284 (2009) 34272–34282.
[161] J.L. Jiménez, G. Tennent, M. Pepys, H.R. Saibil, Structural diversity of *ex vivo* amyloid fibrils studied by cryo-electron microscopy, J. Mol. Biol. 311 (2001) 241–247.
[162] G. Chen, A. Abelein, H.E. Nilsson, A. Leppert, Y. Andrade-Talavera, S. Tambaro, L. Hemmingsson, F. Roshan, M. Landreh, H. Biverstål, P.J.B. Koeck, J. Presto, H. Hebert, A. Fisahn, J. Johansson, Bri2 BRICHOS client specificity and chaperone activity are governed by assembly state, Nat. Commun. 8 (2017) 2081.
[163] H. Willander, J. Presto, G. Askarieh, H. Biverstål, B. Frohm, S.D. Knight, J. Johansson, S. Linse, BRICHOS domains efficiently delay fibrillation of amyloid β-peptide, J. Biol. Chem. 287 (2012) 31608–31617.
[164] M.E. Jackrel, M.E. DeSantis, B.A. Martinez, L.M. Castellano, R.M. Stewart, K.A. Caldwell, G.A. Caldwell, J. Shorter, Potentiated Hsp104 variants antagonize diverse proteotoxic misfolding events, Cell 156 (2014) 170–182.
[165] Y. Wang, T. Yan, H. Lu, W. Yin, B. Lin, W. Fan, X. Zhang, P. Fernandez-Funez, Lessons from anti-amyloid-β immunotherapies in alzheimer disease: aiming at a moving target, Neurodegener. Dis. 17 (2017) 242–250.
[166] J.F. Smith, T.P.J. Knowles, C.M. Dobson, C.E. Macphee, M.E. Welland, Characterization of the nanoscale properties of individual amyloid fibrils, Proc. Natl. Acad. Sci. U. S. A. 103 (2006) 15806–15811.
[167] S. Mankar, A. Anoop, S. Sen, S.K. Maji, Nanomaterials: amyloids reflect their brighter side, Nano Reviews 2 (2011).
[168] S. Bolisetty, R. Mezzenga, Amyloid–carbon hybrid membranes for universal water purification, Nat. Nanotechnol. 11 (2016) 365–371.
[169] Y. Li, C. Zhao, F. Luo, Z. Liu, X. Gui, Z. Luo, X. Zhang, D. Li, C. Liu, X. Li, Amyloid fibril structure of α-synuclein determined by cryo-electron microscopy, Cell Res. 1 (2018).
[170] R. Guerrero-Ferreira, N.M. Taylor, D. Mona, P. Ringler, M.E. Lauer, R. Riek, M. Britschgi, H. Stahlberg, Cryo-EM structure of alpha-synuclein fibrils, Elife 7 (2018).
[171] M.D. Tuttle, G. Comellas, A.J. Nieuwkoop, D.J. Covell, D.A. Berthold, K.D. Kloepper, J.M. Courtney, J.K. Kim, A.M. Barclay, A. Kendall, W. Wan, G. Stubbs, C.D. Schwieters, V.M.Y. Lee, J.M. George, C.M. Rienstra, Solid-state NMR structure of a pathogenic fibril of full-length human α-synuclein, Nat. Struct. Mol. Biol. 23 (2016) 409–415.
[172] Y. Xiao, B. Ma, D. McElheny, S. Parthasarathy, F. Long, M. Hoshi, R. Nussinov, Y. Ishii, Aβ(1-42) fibril structure illuminates self-recognition and replication of amyloid in Alzheimer's disease, Nat. Struct. Mol. Biol. 22 (2015) 499–505.
[173] M.A. Wälti, F. Ravotti, H. Arai, C.G. Glabe, J.S. Wall, A. Böckmann, P. Güntert, B.H. Meier, R. Riek, Atomic-resolution structure of a disease-relevant Aβ(1–42) amyloid fibril, Proc. Natl. Acad. Sci. 113 (2016) E4976–E4984.
[174] L. Gremer, D. Schölzel, C. Schenk, E. Reinartz, J. Labahn, R.B.G. Ravelli, M. Tusche, C. Lopez-Iglesias, W. Hoyer, H. Heise, D. Willbold, G.F. Schröder, Fibril Structure of Amyloid-β(1–42) by Cryo–electron Microscopy, (2017), p. 5.
[175] M.T. Colvin, R. Silvers, Q.Z. Ni, T.V. Can, I. Sergeyev, M. Rosay, K.J. Donovan, B. Michael, J. Wall, S. Linse, R.G. Griffin, Atomic resolution structure of monomorphic $A\beta_{42}$ amyloid fibrils, J. Am. Chem. Soc. 138 (2016) 9663–9674.

Appendix II: The molecular lifecycle of amyloid – Mechanism of assembly, mesoscopic organisation, polymorphism, suprastructures, and biological consequences.

Review Article

On the Structural Diversity and Individuality of Polymorphic Amyloid Protein Assemblies

Liisa Lutter, Liam D. Aubrey and Wei-Feng Xue *

School of Biosciences, *Division of Natural Sciences, University of Kent, CT2 7NJ Canterbury, UK*

Correspondence to Wei-Feng Xue: *W.F.Xue@kent.ac.uk (W.-F. Xue)*
https://doi.org/10.1016/j.jmb.2021.167124
Edited by Daniel Otzen

Abstract

The prediction of highly ordered three-dimensional structures of amyloid protein fibrils from the amino acid sequences of their monomeric self-assembly precursors constitutes a challenging and unresolved aspect of the classical protein folding problem. Because of the polymorphic nature of amyloid assembly whereby polypeptide chains of identical amino acid sequences under identical conditions are capable of self-assembly into a spectrum of different fibril structures, the prediction of amyloid structures from an amino acid sequence requires a detailed and holistic understanding of its assembly free energy landscape. The full extent of the structure space accessible to the cross-β molecular architecture of amyloid must also be resolved. Here, we review the current understanding of the diversity and the individuality of amyloid structures, and how the polymorphic landscape of amyloid links to biology and disease phenotypes. We present a comprehensive review of structural models of amyloid fibrils derived by cryo-EM, ssNMR and AFM to date, and discuss the challenges ahead for resolving the structural basis and the biological consequences of polymorphic amyloid assemblies.

Introduction

Amyloid structures represent a class of filamentous protein self-assemblies that are defined by their characteristic core structures containing β-strands arranged perpendicularly to the fibril axis.[1,2] This highly ordered three-dimensional (3D) structural arrangement, called the cross-β architecture, confers amyloid fibrils with high chemical, mechanical and biological stability, in part due to the network of hydrogen bonds running between the β-sheets present throughout the fibrils, parallel to the fibril axis. Deposits of amyloid are associated with pathology in more than 50 human disorders, including neurodegenerative diseases as well as type 2 diabetes, prion diseases and systemic amyloidosis.[3] Some amyloid proteins, however, form fibrils required for physiological functionalities.[4] In humans, more than 20 proteins have been shown to form amyloid, despite having vastly different amino acid sequences.[5] The assembly into the amyloid state proceeds through a nucleated polymerisation mechanism in which natively folded or intrinsically disordered protein monomers unfold or misfold, and aggregate into dynamic and transient oligomers.[6] Some of these species go through primary nucleation events to form nuclei, which are the smallest units from which growth of aggregates by energetically favourable elongation into fibrils can proceed by monomer addition to fibril ends.[7,8] The resulting amyloid state self-propagates by catalysis of new nucleation events by existing fibril surfaces, and through fibril fragmentation, which produces seeds by division of the fibrils without undergoing an additional nucleation phase.[9,10]

Compared to the folding reaction of globular proteins, amyloid formation stands out because it possesses unique properties. Firstly, the coupled

folding-assembly reaction of monomeric peptide chains into the amyloid state occurs as a result of intermolecular interactions between a large but variable number of monomers. Secondly, the resulting protein conformations of amyloid fibrils are capable of self-propagation. This property allows the information encoded in the individual 3D structures of amyloid and prions, which represent a class of infectious amyloid that can spread between individual organisms,[11] to be transmitted to monomers not yet in the amyloid state. Thirdly, although the end-products of a single type of amyloid assembly reaction are fibrils sharing the defining cross-β core architecture, there may be a wide degree of variation between their specific structures, even when the assembly reactions start with identical monomeric polypeptide chains under identical conditions. This property, called structural polymorphism, is biologically important because it affects the physicochemical properties of the fibrils, which subsequently may reflect the variation in the biological response to amyloid *in vivo*. For example, specific amyloid polymorphs formed from the same tau protein are found in different tauopathies,[12] and within each disease-specific amyloid population there can exist several types of polymorphic fibrils.[13–15] However, structural polymorphism complicates any attempt of predicting a protein's 3D shape from its amino acid sequence, because in the case of amyloid, one single amino acid sequence may fold/misfold and assemble into a spectrum of different 3D structures.

Experimental techniques that have been applied to study the polymorphous amyloid structures include cryo-electron microscopy (cryo-EM), solid-state nuclear magnetic resonance (ssNMR) spectroscopy, and atomic force microscopy (AFM) (Table 1). Methodological advances in Cryo-EM have, in recent years, led to the elucidation of numerous structural models of amyloid fibrils.[16] These cryo-EM based models are derived from 3D Coulomb potential maps, reconstructed nowadays routinely to sub-4 Å resolutions, using 2D projection images of fibrillar samples collected on modern cryo-EM microscopes. For ssNMR, spectroscopic data of nuclear resonance frequencies are collected on fibril samples formed from isotopically labelled protein monomers. The interpretation of the resulting chemical shifts and atomic distance constraints are used to reconstruct an ensemble of possible conformations of each single structural model.[17] AFM allows the morphologies of individual fibrils to be directly visualised on 2D topology images to a low-nanometre resolution, from which 3D envelope models of each individually observed fibril can then be reconstructed.[18] Combining AFM with infrared spectroscopy (AFM-IR)[19] or Raman spectroscopy (AFM-Raman),[20] allows the secondary structure content of individual fibrils or aggregates to also be assessed. The 3D structural models obtained by these techniques, and the subsequently observed structural polymorphism, are discussed in this review.

Recently, advances in the prediction of protein structures from their primary sequences by AlphaFold 2, a machine learning-based method developed by Google's DeepMind AI research group, showed that its structural predictions can now nearly match experimental results.[21] This was demonstrated by its participation in the 14th Community Wide Experiment on the Critical Assessment of Techniques for Protein Structure Prediction (CASP14), a biennial community experiment in which international research teams participate to evaluate the accuracy of their protein structure prediction methods (e.g. [22,23]). Despite this important advance, AlphaFold 2 has not yet been applied to multimeric protein structure prediction,[21] even though accurate prediction of multi-protein complex structures such as amyloid fibrils could revolutionise aspects of key applications, including drug design. This highlights the magnitude of unresolved challenges in structural prediction of large protein assemblies, and the need to establish a fundamental understanding between amino acid sequence, amyloid structure, function, and pathogenicity. Thus, predicting the 3D structures of polymorphic amyloid fibrils from primary amino acid sequences

Table 1 **Summary of experimental techniques for 3D structural characterisation of polymorphic amyloid fibrils**. Data type and structural information obtainable from the three methods highlighted in this review, i.e., cryo-electron microscopy (cryo-EM), solid-state nuclear magnetic resonance spectroscopy (ssNMR), and atomic force microscopy (AFM), are described.

	Cryo-EM	ssNMR	AFM
Data type	Projection images/transmission electron micrographs	Resonance frequencies/chemical shifts of atomic nuclei	Surface topography (height) images
Structural information	3D Coulomb potential maps	Atomic distances, bond angles, and local chemical environment information	3D molecular surface envelopes
Features	Can provide high-resolution (<4Å) averaged structural maps	Generates an ensemble of possible molecular models	Can provide individual particle information and allows collection of nano-mechanical or chemical information

is exceptionally challenging, but also offers important opportunities for contributing to our fundamental understanding of coupled protein folding and assembly free energy landscapes, as well as for potentially important applications in the development of anti-amyloid drugs for neurodegenerative diseases. This challenge can only begin to be addressed through the characterisation of the extent of amyloid polymorphism as well as the individual 3D structures of polymorphs formed. Here, we review recent advances in our understanding of amyloid polymorphism through recent structural data that reveal the diversity of amyloid fibril structures that can be formed, and the individuality of filament structures that exists within heterogeneous amyloid populations. We discuss the resulting physicochemical and biological consequences of amyloid polymorphism, the challenges of amyloid structure prediction, and opportunities where such contributions could provide new fundamental insights or applications.

The paradox of amyloid polymorphism: From one amino-acid sequence to many three-dimensional structures

Recent studies of the 3D structures of amyloid fibrils have revealed extensive presence of structural polymorphism in high-resolution detail. Different, but ordered and stable amyloid structures have been shown to assemble from polypeptide chains of the same primary amino acid sequence. This contradicts the uniqueness condition of Anfinsen's dogma stating that a uniquely dominating energy minimum in the free energy landscape of a polypeptide chain is required for it to fold into a unique native 3D structure.[24] Instead, it appears that the free energy landscape for amyloid protein folding/misfolding and assembly consists of many local minima of similar levels of free energy, and the extent of such local minima groups are affected by factors that include the primary amino acid sequence of the monomeric building blocks of the fibrils.[25] This structural polymorphism creates a considerable challenge for 3D structure prediction from primary sequence as one sequence can result in many different stably observable structures. Importantly, the structural polymorphs observed to date do not only result from different contacts between residues in the fibril cores that then lead to different overall folds, but instead involve a number of possible variations which interplay in a hierarchical manner[26,27] (Figure 1). Firstly, different amyloid structures may result from 'top-level' modifications in the primary amino acid sequence such as point-mutations, truncations/deletions and/or post-translational modifications (top row of Figure 1). However, these 'top-level' modifications involve changes in the covalent bonding pattern and can be classified as sequence polymorphism rather than structural polymorphism, and thus do not wholly reflect the complexities of amyloid sequence-structure relationships. Secondly, further complexities arise from the conformational arrangements of protofilaments, which are filamentous building blocks that make up the fibril structures. In the protofilament core, the extent and the packing of β-sheet- and random coil-forming regions, as well as disordered regions, often vary even for monomeric polypeptide chains of identical sequences. Co-factors in the fibril core may also be necessary for stabilising specific folds, further contributing to structural polymorphism. There are also known instances where protofilaments are formed by multiple different polypeptide sequences, thus resulting in heteroamyloid fibrils (second row of Figure 1). Thirdly, although conformational differences in the protofilament core formed from a single amyloid protein or peptide sequence can display remarkable structural diversity, it is also common for amyloid fibrils to assemble and form structures involving multiple protofilaments (third row of Figure 1). In this case, each monomeric layer of the fibril consists of multiple copies of the same peptide chain, which can be arranged in a number of different ways. Notably, the protofilament building blocks of amyloid fibrils can have identical or different folds, and their lateral arrangement can vary. Finally, structural polymorphism can also arise from variations in the fibrils' mesoscopic (nm to μm length-scale) arrangements like twist handedness, twist pitch, the position of the fibril screw-axis, and fibril length. These long-range properties contribute to the molecular individuality of amyloid fibrils, which may subsequently also impact the biological response the fibrils elicit.

Due to polymorphic folding and assembly landscapes, the prediction of amyloid structures from their constituent monomeric amino acid sequences is challenging. The hierarchical nature of structural polymorphism, which has been experimentally observed to give rise to many diverse structures from identical protein sequences, may lead to a continuous cloud of polymorphs within a population of amyloid fibrils, with individual fibrils populating the structure space defined by local energy minima with differing probabilities. Thus, the possibility of diverse and individualistic amyloid structures resulting from the folding/misfolding-assembly of identical polypeptide chains presents a conundrum in terms of whether the cloud of structures formed also translates into equally diverse biological or phenotypical responses, and whether it is possible to predict amyloid structures and subsequent function with some degree of certainty. It is currently not possible to assess how well structural prediction tools would predict amyloid structures as none have yet been included as CASP targets.

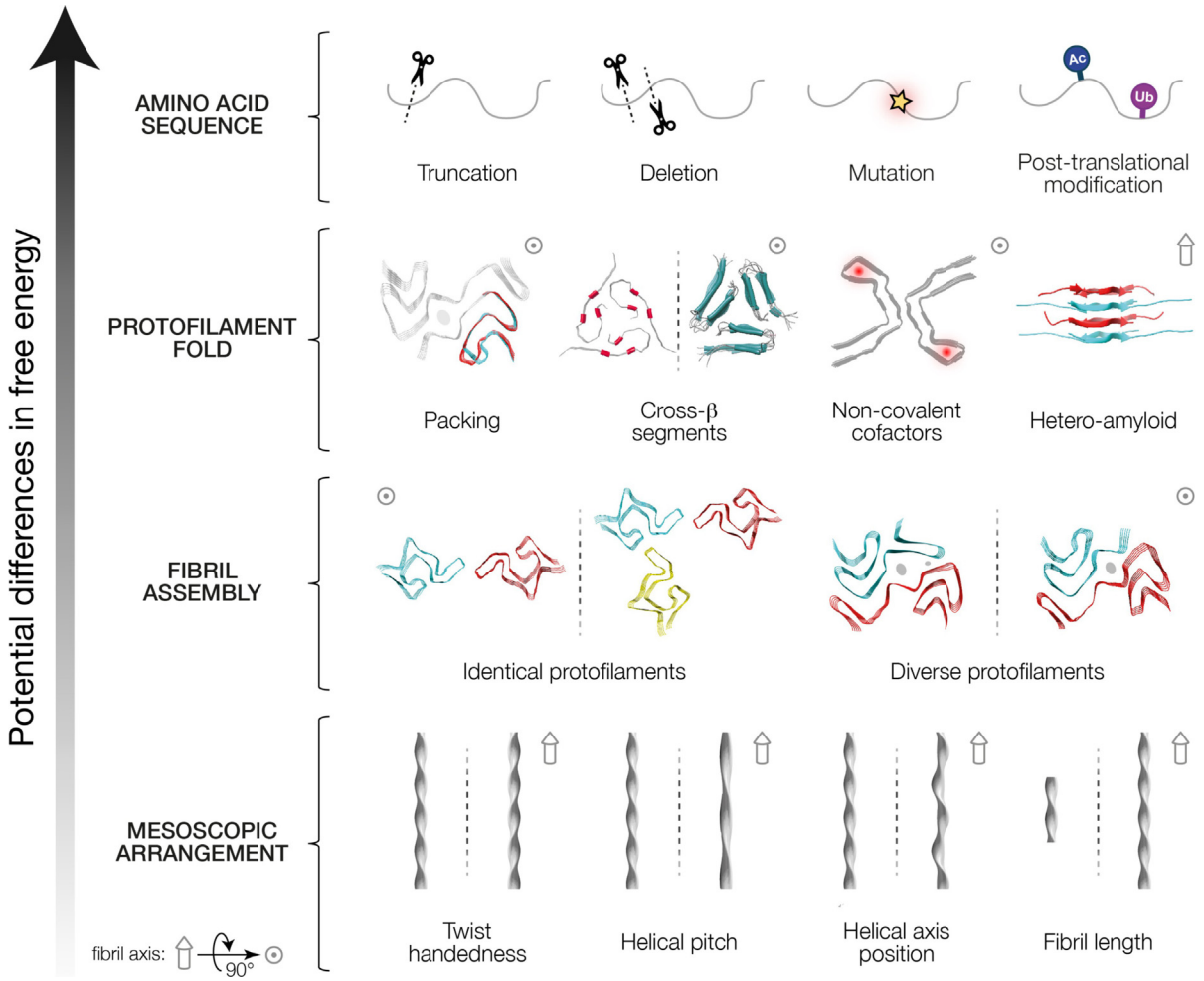

Figure 1. Hierarchical structural polymorphism of amyloid fibrils. Top row: Modifications of the primary amino acid sequence, including truncations, deletions, mutations, and post-translational modifications, represent the first layer of complexity that leads to the diversity of amyloid structures. Second row: Polypeptide chains with identical amino acid sequences may exhibit further differences in the adopted protofilament fold upon assembly, including differences in the β-sheet forming regions (segmental polymorphism; demonstrated by $A\beta_{40}$ PDB IDs 2M4J and 2LMQ on the left and right, respectively), the arrangement of the core fold (packing polymorphism; demonstrated by overlay of α-synuclein PDB IDs 6XYP and 6XYQ) and the presence of noncovalent co-factors (tau PDB ID 6NWP). Interestingly, heteroamyloid can result from alternate stacking of monomers with different sequences to form a fibril (RIPK1/3 PDB ID 5V7Z). Third row: Assembly of identical or different protofilaments by lateral associations can result in further diversity of amyloid structures. Assembly polymorphism with identical folds is illustrated by α-synuclein PDB IDs 6L1T (left) and 6L1U (right) and for fibrils with diverse folds the accession codes are 6XYO (left) and 6XYP (right), also showing α-synuclein fibrils. Bottom row: Polymorphism can also arise in the mesoscopic length scale from differences in twist handedness, helical pitch, the position of the helical axis and the number of monomers in the fibril, which determines the length. Molecular models were generated using UCSF Chimera.[104]

However, structural prediction of multimeric CASP targets is a greater challenge compared to monomeric targets due to the necessity of predicting how multiple monomeric subunits interface with each other.[28] Therefore, prediction of amyloid fibril structures, which have multiple interfacing monomeric subunits and, in addition, exhibit a wide degree of polymorphism (see Figure 1), will require significant additional advances to current methods. Current prediction tools specifically designed for amyloid sequences are focused on predicting the amyloid forming propensity of sequence regions, with some offering additional predictions of intrinsic disorder and secondary structure (e.g. [29–31]). Nevertheless, predicting the amyloidogenic regions and aggregation propensity has been challenging even for short peptides.[32,33]

The structural diversity of filamentous amyloid assemblies

Amyloid fibrils are defined by a characteristic cross-β structure formed by β-strands with 4.7 Å

spacing, stabilised by a hydrogen bonding network parallel to the fibril axis, and tight side-chain packing between two β-sheets with 10 Å spacing. This cross-β architecture can be experimentally readily observed in X-ray fibre diffraction patterns.[34] Importantly, the 3D structures of a growing number of amyloid fibrils have been experimentally resolved in the last five years, revealing extensive presence of structural polymorphism (see Table 2 and Figure 2 for a summary of structural data in the EMDB and the PDB released up until March 2021).

The elucidation of amyloid 3D structures in atomic detail was pioneered by X-ray diffraction experiments of amyloid peptide microcrystals, allowing the variation in the β-sheet arrangements to be experimentally characterised and the features that stabilise the cross-β fold to be studied.[35] This revealed, for example, the tight inter-digitating side chains that make up the dry interface between β-sheets, termed steric zippers, and the hydrogen-bonding ladders formed by stacking of specific side-chains along the length of the long fibril axis. Eight different possible classes of steric zippers have been described, with differences arising from the parallel or antiparallel direction of the β-sheets, and the relative orientations of the two connecting β-sheets.[35] More recently, microcrystal electron diffraction (microED) has been employed to elucidate the structures of amyloid peptide crystals, with the advantage that even nano-sized crystals too small for conventional X-ray crystallography experiments can be amenable for analysis.[36] Formation of crystals for structural studies is, however, limited by the length of the amyloid forming peptide. Therefore, amyloid structures formed from larger polypeptide fragments or full-length proteins have been mainly resolved using solid-state nuclear magnetic resonance spectroscopy and cryo-electron microscopy. Although ssNMR has been used to generate structural models of amyloid fibrils for nearly two decades, it was the 'resolution revolution' of cryo-EM that led to the increased rate in the number of data entries of amyloid fibrils deposited to the EMDB and PDB databases in recent years. The average resolution of cryo-EM maps has also markedly improved in the last five years (Figure 3). Advances in cryo-EM hardware and increased accessibility to equipment have driven the collection of evermore number of high-quality datasets of amyloid fibril samples, whereas improved software for helical reconstruction and refinement have facilitated 3D reconstruction with resolutions that regularly allow *de novo* building of molecular models.[37] These recent advances have made possible the wide-ranging characterisation of amyloid fibril structures and the types of polymorphic features they exhibit in detail, revealing the diversity in the conformation of the fibril cores, the possible presence of post-translational modifications (PTMs) and co-factors, the span of cross-β forming regions, and the extent of ordered and dynamic regions within amyloid fibrils. Here, structural models of amyloid fibrils determined by cryo-EM and ssNMR available in the EMDB and PDB databases up to March 2021 are listed in Table 2 and correspondingly visualised in Figure 2 to both illustrate the diversity of cross-β structures as well as provide an organised resource that facilitates comparison.

The evermore detailed information on amyloid fibril core structures has revealed a large degree of polymorphism, which can be classified in a hierarchical manner as illustrated in Figure 1. Especially interesting are polymorphic structures formed from protein chains with an identical sequence, which exhibit fibril polymorphism in protofilament folds, filament assemblies, and mesoscopic properties, as these features indicate sensitivity of the assembly process to environmental conditions in determining the extent of polymorphism and the individuality of the formed fibril structures. For example, amyloid fibrils formed from $A\beta_{40}$ and $A\beta_{42}$ result in considerably different structures with different protofilament folds and assemblies (see Figure 2, entries 1 to 24, and Table 2 for accession codes), likely due to the different conditions in which the fibrils were formed. Structures of otherwise identical proteins with different disease-associated mutations and post-translational modifications have also been shown to form structures with different morphologies. For example, structural data are available for α-synuclein with three different mutations related to early-onset Parkinson's disease, E46K, A53T, and H50Q (see Figure 2 and Table 2, entries 33, 34, 35, 41 and 42). Comparing the structures and their properties, such as stability and seeding propensity, to those of wild-type fibrils may indicate how polymorphism varies between familial and sporadic cases. Recently a combined cryo-EM and mass spectrometry approach has also revealed specific PTMs on tau fibrils from *ex vivo* patient brain tissue (see Figure 2 and Table 2, entries 97–99).[38] Identification of disease-relevant modifications is crucial for understanding how PTMs may modulate fibril polymorphism and its biological effects. Importantly, the current structural data have shown differences between fibril structures extracted from *ex vivo* tissues and those assembled *in vitro* from recombinant protein monomers (e.g. see Figure 2 and Table 2 entries 92–95).[39] This is indicative of the importance and the challenge of studying amyloid polymorphism in disease contexts in order to understand possible disease-relevant sequence modifications and local *in vivo* environmental factors. Additionally, it was recently shown that seeded formation of amyloid using fresh monomer incubated with *ex vivo* fibril seeds does not necessarily replicate the structure of the seed in the case of

Table 2 **Three-dimensional structural data entries of amyloid fibrils acquired by cryo-EM or ssNMR.** Entries that have been released in the EMDB and PDB databases running up to March 2021 are shown.

	Amyloid name *	Sample origin §	Experimental method	PDB ID ‡	EMDB ID †	Release date	Reference
1	$A\beta_{40}$	AD brain, seeded	ssNMR & cryo-EM	6w0o	21501	13/01/2021	105
2	$A\beta_{40}$		ssNMR	6ti5		22/07/2020	106
3	$A\beta_{40}$	AD brain	cryo-EM	6shs	10204	06/11/2019	56
4	$A\beta_{40}$	AD brain	cryo-EM		4864	06/11/2019	
5	$A\beta_{40}$	AD brain	cryo-EM		4866	06/11/2019	
6	$A\beta_{40}$		ssNMR	6oc9		05/06/2019	107
7	$A\beta_{40}$		cryo-EM		6326, 6327, 6328	29/04/2015	108
8	$A\beta_{40}$		ssNMR	2mpz		22/04/2015	109
9	$A\beta_{40}$		ssNMR	2mvx		26/11/2014	110
10	$A\beta_{40}$	AD brain, seeded	ssNMR	2m4j		25/09/2013	111
11	$A\beta_{40}$		ssNMR	2lnq		08/02/2012	112
12	$A\beta_{40}$		ssNMR	2lmq, 2lmp		28/12/2011	113
13	$A\beta_{40}$		ssNMR	2lmo, 2lmn		28/12/2011	
14	$A\beta_{40}$		cryo-EM		5008, 5132	08/10/2009	114,115
15	$A\beta_{40}$		cryo-EM		1650	24/09/2009	116
16	$A\beta_{40}/A\beta_{42}$		ssNMR	6ti6, 6ti7		22/07/2020	106
17	$A\beta_{42}$		cryo-EM	5oqv	3851	13/09/2017	117
18	$A\beta_{42}$		ssNMR	2nao		27/07/2016	118
19	$A\beta_{42}$		ssNMR	5kk3		13/07/2016	119
20	$A\beta_{42}$		cryo-EM	5aef	3132	26/08/2015	120
21	$A\beta_{42}$		ssNMR	2mxu		06/05/2015	121
22	$A\beta_{42}$		cryo-EM		5052	07/07/2010	122
23	$A\beta_{42}$		cryo-EM		1649	24/09/2009	116
24	$A\beta_{42}$		ssNMR	2beg		22/11/2005	123
25	α-syn	MSA brain, seeded	cryo-EM	7nck	12269	24/02/2021	40
26	α-syn	MSA brain, seeded	cryo-EM	7ncj	12268	24/02/2021	
27	α-syn	MSA brain, seeded	cryo-EM	7nci	12267	24/02/2021	
28	α-syn	MSA brain, seeded	cryo-EM	7nch	12266	24/02/2021	
29	α-syn	MSA brain, seeded	cryo-EM	7ncg	12265	24/02/2021	
30	α-syn	MSA brain, seeded	cryo-EM	7nca	12264	24/02/2021	
31	α-syn		cryo-EM	6l1t	0801	12/08/2020	124
32	α-syn		cryo-EM	6l1u	0803	12/08/2020	
33	α-syn		cryo-EM	6l4s	0833	29/04/2020	125
34	α-syn		cryo-EM	6lrq	0958	08/04/2020	126
35	α-syn		cryo-EM	6ufr	20759	19/02/2020	127
36	α-syn	MSA brain	cryo-EM	6xyo	10650	12/02/2020	128
37	α-syn	MSA brain	cryo-EM	6xyp	10651	12/02/2020	
38	α-syn	MSA brain	cryo-EM	6xyq	10652	12/02/2020	
39	α-syn		cryo-EM	6sst	10305	18/12/2019	129
40	α-syn		cryo-EM	6ssx	10307	18/12/2019	
41	α-syn		cryo-EM	6peo	20328	27/11/2019	130
42	α-syn		cryo-EM	6pes	20331	27/11/2019	
43	α-syn		cryo-EM	6osj	20183	25/09/2019	131
44	α-syn		cryo-EM	6osm	20186	25/09/2019	
45	α-syn		cryo-EM	6osl	20185	25/09/2019	
46	α-syn		cryo-EM	6cu7	7618	12/09/2018	132
47	α-syn		cryo-EM	6cu8	7619	12/09/2018	
48	α-syn		cryo-EM	6h6b	0148	08/08/2018	133
49	α-syn		cryo-EM	6a6b	0988	11/07/2018	134
50	α-syn		ssNMR	2n0a		23/03/2016	135
51	α-syn		cryo-EM		6482	16/12/2015	136
52	β-endorphin		ssNMR	6tub		28/10/2020	137
53	β2m		cryo-EM		0019	19/06/2019	138
54	β2m		cryo-EM		0021	29/05/2019	
55	β2m		cryo-EM	6gk3	0014	14/11/2018	
56	β2m		ssNMR	2e8d		13/02/2007	139
57	CA150		ssNMR	2nnt		14/11/2006	140
58	FUS		ssNMR & cryo-EM	6xfm	22169	07/10/2020	141
59	Glucagon		ssNMR	6nzn		05/06/2019	142
60	HET-s		ssNMR	2mus, 2lbu		01/02/2017	143,144
61	HET-s		cryo-EM		2946	15/04/2015	145

Table 2 (*continued*)

	Amyloid name *	Sample origin §	Experimental method	PDB ID ‡	EMDB ID †	Release date	Reference
62	HET-s		ssNMR	2kj3, 2rnm		02/06/2010	146,147
63	hnRNPA1		cryo-EM	7bx7	30235	18/11/2020	148
64	hnRNPA2		cryo-EM	6wqk	21871	26/08/2020	85
65	IAPP		cryo-EM	6zrf	11380	30/09/2020	53
66	IAPP		cryo-EM	6zrq	11382	30/09/2020	
67	IAPP		cryo-EM	6zrr	11383	30/09/2020	
68	IAPP		cryo-EM	6vw2	21410	10/06/2020	149
69	IAPP		cryo-EM	6y1a	10669	04/03/2020	150
70	IAPP		cryo-EM		10670	04/03/2020	
71	IAPP		cryo-EM		10671	04/03/2020	
72	IG LC	AL cardiac tissue	cryo-EM	6z1o	11031	24/02/2021	57
73	IG LC	AL cardiac tissue	cryo-EM	6z1i	11030	24/02/2021	
74	IG LC	AL cardiac tissue	cryo-EM	6ic3	4452	03/04/2019	98
75	IG LC	AL cardiac tissue	cryo-EM	6hud	0274	27/03/2019	99
76	IG LC		cryo-EM		3986	28/02/2018	151
77	IG LC		cryo-EM		3987	28/02/2018	
78	IG LC		cryo-EM		3988	28/02/2018	
79	IG LC		cryo-EM		3989	28/02/2018	
80	IG LC		cryo-EM		3990	28/02/2018	
81	IG LC		cryo-EM		3991	28/02/2018	
82	IG LC		cryo-EM		3992	28/02/2018	
83	IG LC		cryo-EM		3993	28/02/2018	
84	IG LC		cryo-EM		3994	28/02/2018	
85	IG LC		cryo-EM		3128	18/05/2016	152
86	Orb2	*D. melanogaster* brain	cryo-EM	6vps	21316	18/03/2020	87
87	PI3K		cryo-EM	6r4r	4727	28/08/2019	153
88	PrP		cryo-EM	6lni	0931	10/06/2020	154
89	PrP		cryo-EM	6uur	20900	15/04/2020	155
90	RIPK1/RIPK3		ssNMR	5v7z		28/03/2018	156
91	RIPK3		ssNMR	6jpd		28/10/2020	157
92	SAA	Murine liver	cryo-EM	6zch	11164	17/02/2021	39
93	SAA		cryo-EM	6zcg	11163	17/02/2021	
94	SAA		cryo-EM	6zcf	11162	17/02/2021	
95	SAA	Murine spleen	cryo-EM	6dso	8910	13/03/2019	158
96	SAA	Amyloidotic kidney	cryo-EM	6mst	9232	13/03/2019	
97	tau	CBD brain	cryo-EM	6vh7	21200	04/03/2020	38
98	tau	CBD brain	cryo-EM	6vha	21201	04/03/2020	
99	tau	AD brain	cryo-EM	6vhl	21207	04/03/2020	
100	tau	CBD brain	cryo-EM	6tjx	10514	05/02/2020	14
101	tau	CBD brain	cryo-EM	6tjo	10512	05/02/2020	
102	tau	CTE brain	cryo-EM	6nwp	0527	27/03/2019	15
103	tau	CTE brain	cryo-EM	6nwq	0528	27/03/2019	
104	tau		cryo-EM	6qjh	4563	20/02/2019	101
105	tau		cryo-EM	6qjm	4564	20/02/2019	
106	tau		cryo-EM	6qjp	4565	20/02/2019	
107	tau		cryo-EM	6qjq	4566	20/02/2019	
108	tau	AD brain	cryo-EM	6hre	0259	10/10/2018	92
109	tau	AD brain	cryo-EM	6hrf	0260	10/10/2018	
110	tau	Pick's disease brain	cryo-EM	6gx5	0077	12/09/2018	91
111	tau	Pick's disease brain	cryo-EM		0078	12/09/2018	
112	tau	AD brain	cryo-EM	5o3l	3741	26/07/2017	13
113	tau	AD brain	cryo-EM	5o3o	3742	26/07/2017	
114	tau	AD brain	cryo-EM	5o3t	3743	26/07/2017	
115	tau	AD brain	cryo-EM		3744	26/07/2017	
116	TDP-43		cryo-EM	7kwz	23059	24/02/2021	159
117	TDP-43		cryo-EM	6n3a	9349	26/06/2019	160
118	TDP-43		cryo-EM	6n3b	9350	26/06/2019	
119	TDP-43		cryo-EM	6n3c	0334	26/06/2019	
120	TDP-43		cryo-EM	6n37	9339	26/06/2019	
121	TDP-43		cryo-EM	5w7v	8781	14/03/2018	161
122	TTR	ATTR heart	cryo-EM	6sdz	10150	13/11/2019	162
123	TTR		ssNMR	2m5n		17/07/2013	54

(*continued on next page*)

Table 2 (*continued*)

	Amyloid name *	Sample origin §	Experimental method	PDB ID ‡	EMDB ID †	Release date	Reference
124	TTR		cryo-EM	2m5k	5590	03/04/2013	
125	TTR		cryo-EM	2m5m	2323	27/03/2013	
126	TTR		cryo-EM	3zpk	2324	27/03/2013	
127	TTR		ssNMR	1rvs		20/01/2004	[163]

*. Database entries are ordered alphabetically by their protein name. Entries of amyloid formed from the same protein are ordered by release date from the newest to the oldest. Where several models have been published based on reanalysis of the same original data, the entries are grouped and all accession codes are included in the same row.
§. The origin of the tissue from which *ex vivo* fibrils were extracted is noted. Where the species is not specified, the tissue is of human origin, with the following abbreviations for disease diagnoses: AD – Alzheimer's Disease, MSA – multiple system atrophy, CBD – corticobasal degeneration, CTE – chronic traumatic encephalopathy, ATTR – transthyretin amyloidosis.
†. The Protein Data Bank (PDB) ID code associated with the structural model.
‡. The Electron Microscopy Data Bank (EMDB) accession codes associated with the EM density map.

α-synuclein from multiple system atrophy patient brain tissue.[40] It is currently not known if seeding may not propagate fibril structures due to a non-matched PTM pattern of the monomer compared to that of the seeds, if co-factors that may be present in the fibril core are missing in the seeded reactions, or if the assembly conditions during seeding are too different to those during the formation of the seeds in general. It is also unclear how this may vary for different amyloid systems that exhibit different kinetic rates for templated elongation and secondary nucleation.[41] Nevertheless, these results demonstrate that structures of fibrils formed from seeded growth using *ex vivo* fibril seeds should not necessarily be assumed to be identical to those of the patient derived seeds without further evidence,[42,43] due to the complexities arising from the polymorphism-prone nature of amyloid. In summary, detailed structural characterisation of amyloid fibrils, enabled by methodological advances in cryo-EM and ssNMR, has demonstrated a remarkable tendency for many amyloid forming polypeptide sequences to each form a diverse range of polymorphic cross-β amyloid structures.

The individuality of amyloid structures

The potential of amyloid fibrils to display a diverse range of cross-β structures (Figure 2) due to polymorphism resulting from the vast number and combinations of possible arrangements of the polypeptide chains within each fibril (Figure 1) means that the structures of amyloid fibrils should also be considered with respect to individual fibrils. Each individual fibril in a heterogeneous amyloid population may be distinguishable from every other fibril in the same population in terms of its precise structure, stability, and biological properties, even when the primary sequence of the monomeric polypeptide chains making up the fibrils is the same. This is because many of the possible structural variations which underpin the observed amyloid polymorphism are based on differences in the pattern of the energetically weak non-covalent interactions (rows 2, 3 and 4 in Figure 1), especially those peripheral to the cross-β protofilament core (rows 3 and 4 in Figure 1). Experimental observations by negative-stain electron microscopy and atomic force microscopy (AFM) have shown that amyloid fibril populations can be highly heterogeneous.[44–48] Advances in AFM imaging over the last two decades have contributed to the discovery that the differences between structural polymorphs of amyloid, such as the number of protofilaments, twist patterns, and the thickness of fibrils, which are all influenced by the structure of the amyloid core, can indeed vary from fibril to fibril within a population.[25,46,48,49]

Modern AFM imaging methods can detect and characterise the structures of individual amyloid fibrils within complex and heterogeneous samples. While the imaging resolution achievable by AFM in one of the three spatial dimensions, i.e., the z- or height-axis, can now routinely reach sub-ångströms under ambient conditions, the overall 3D-resolution of AFM has not yet reached that currently achievable by cryo-EM. However, due to its underlying high signal-to-noise physics, the structures of individual particles of amyloid can be characterised to ~nm resolution without the extensive cross-particle averaging that cryo-EM methodologies rely on. Recently, we have developed a method to reconstruct the 3D surface envelopes of individual helical amyloid fibrils using the 3D information encoded in AFM height topology images[18] (Figure 4). This advance, combined with a systematic morphometric analysis and classification of individually reconstructed 3D fibril models, enables the detection and structural characterisation of individual, potentially rare, amyloid fibril species, and structural variations within individual fibrils. The heterogeneity of a polymorphic amyloid population can also be quantitatively assessed using AFM data by analysing the variations in fibril width, cross-sectional area and shape, twist periodicity and twist handedness of individual fibrils within the population. We demonstrated the potential of this approach to map the assembly

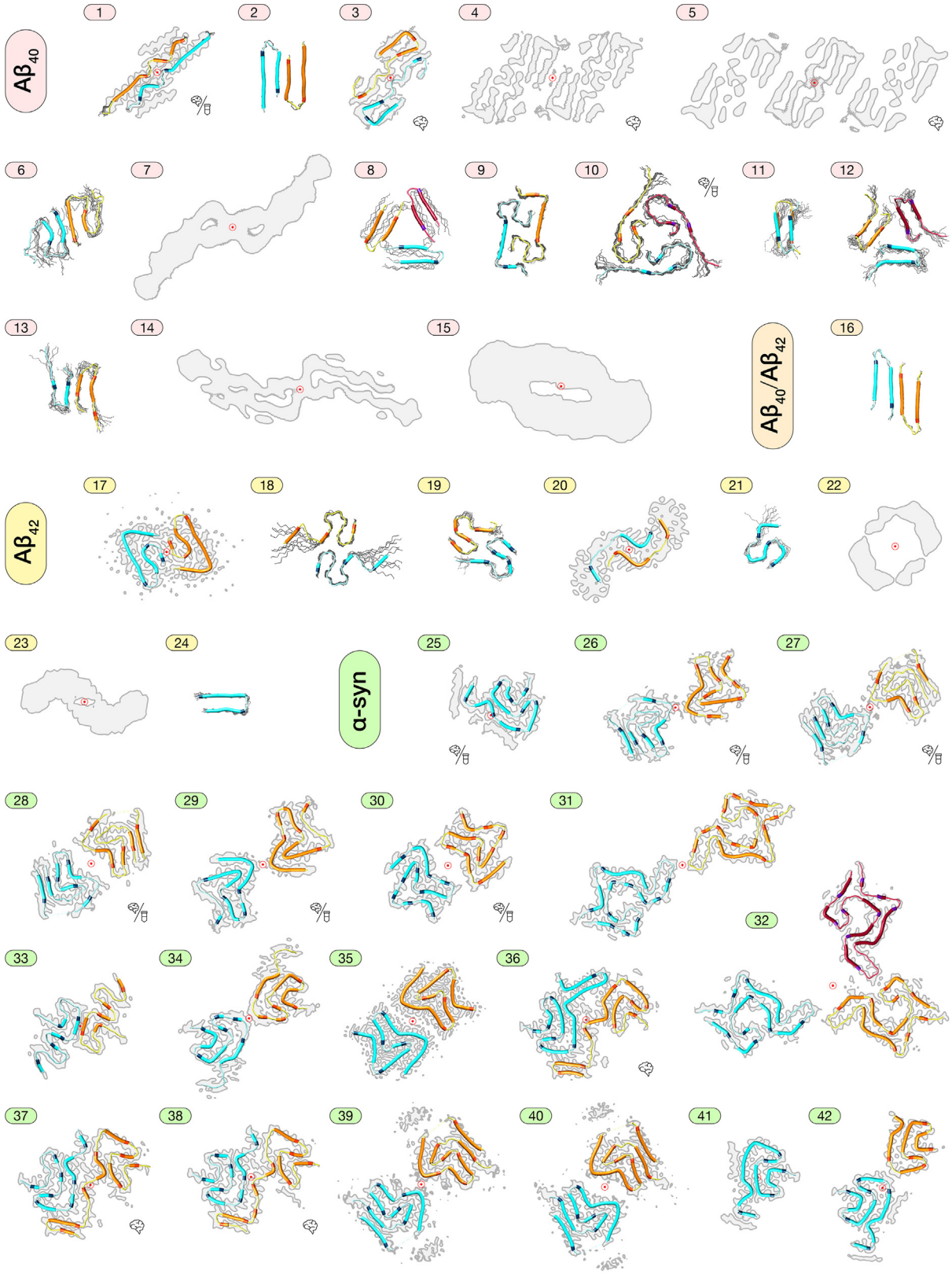

landscapes of amyloid by analysis of amyloid fibrils formed from three different peptide sequences (Figure 4 left column and Figure 5). The assembly landscape of these peptides show amino acid sequence-dependent continuums of structural polymorphs from each assembly population. This

discovery was revealed through the analysis of hundreds of individual fibrils in the population, with the fibril structures subsequently hierarchically classified into polymorphic classes.[25] In this study, each individual fibril observed on AFM images was used to generate a 3D model (e.g., left column in Figure 4 (**c**)), with no two fibril models being exactly the same. It is possible that the morphological differences observed between closely related but not identical fibrils are due to small variations in the helical twist and/or the packing of protofilaments with otherwise identical core conformations, but the differences can also reflect structural variations of the protofilament core, as illustrated in Figure 1. Thus, the data demonstrates the potential of amyloid fibrils to display strong structural individuality within the heterogeneous amyloid populations.

To date, AFM imaging has been used to characterise individual β-lactoglobulin amyloid fibrils by measuring their height profile and twist pattern,[49] as well as to analyse and compare the morphologies of fibrils formed from wild-type α-synuclein and its disease-relevant variants.[50] AFM has also been used to structurally characterise individual $A\beta_{40}$ filaments, revealing structurally polymorphic fibrils after long incubation times.[46] In addition, AFM methods have helped to reveal that when samples containing different structural polymorphs, identified by ssNMR, were used to seed new fibril samples, the elongation rate within the new samples was specific to the structural polymorph of the seed,[51] highlighting the relationship between fibril structures and physicochemical properties such as kinetics. Furthermore, developments in high-speed AFM have revealed the dynamics of individual $A\beta_{42}$ fibril structures, including that elongation occurs preferentially at one end of the fibrils.[52] This is a result that may contain clues to the organisation of protofilaments within individual fibrils. AFM can also provide complementary structural information in combination with other methods. An example of this includes the use of both AFM and cryo-EM to quantify the structural variation in samples of diabetes-related IAPP fibrils; from which structures of the fibril cores were also determined,[53] or the use of ssNMR, cryo-EM and AFM to determine the core structure of transthyretin fibrils.[54] Another example includes the use of AFM in combination with fluorescence microscopy in which evidence of structural variation within individual fibrils was observed by AFM when mouse and hamster variant prion protein fibrils were used to seed each other, resulting in individual fibrils with a conformational change.[55] Structural variations within individual fibrils have recently also been observed in *ex vivo* samples of immunoglobulin light chain fibrils from patients with systemic AL amyloidosis and in Aβ fibrils from patients with Alzheimer's disease (AD), both demonstrated using cryo-EM.[56,57] Using AFM, we have observed strong individuality and structural variations within $A\beta_{42}$ fibrils formed *in vitro* (Figure 4, middle column), demonstrating the extensive polymorphism exhibited by Aβ sequences. Interestingly, AFM images of amyloid fibrils formed from $tau_{297\text{-}391}$ (also termed dGAE), with a morphology that mimics the core of paired helical filaments extracted from Alzheimer's patient tissue,[58] show little structural variations between individual fibrils within its fibril population (Figure 4, right column), suggesting that the extent of structural polymorphism and fibril individuality is not the same for different amyloid forming sequences.

Figure 2. Diversity of cross-β structures demonstrated by a graphical summary of structural data of amyloid fibrils acquired by cryo-EM or ssNMR. Average cross-sections of cryo-EM density maps, ssNMR ensembles, and structural models of amyloid fibrils containing constituent polypeptide segments longer than 10 amino acids deposited in the EMDB and PDB databases up until March 2021 are shown in an orientation with the fibril axis perpendicular to the page plane. The entries are grouped by protein name and then by the release date of the data entry, with the newest data entry shown first. The numbers shown correspond to the entry numbers listed in Table 2. Structural models are displayed by a coloured ribbon representation in cases where PDB entries are available. Each polypeptide chain in the cross-section view is coloured differently, with the cross-β segments, where such segments are determined and labelled in the PDB entry, shown as a wider chains in a darker shade and their C-terminal residues shown in an even darker shade. A single layer of each fibril model along the helical axis is shown only, for clarity. For ssNMR ensembles, the first model is shown in the coloured ribbon representation and other models are shown in grey wire representation. Cryo-EM maps are shown as grey average cross-sections with a darker grey outline representing the iso-line that defines the density boundary. The cross-sections were drawn by first untwisting the map to a single slice along the length of the fibril using published twist and rise values, and isolines were subsequently generated using the recommended isovalue provided by the authors in the EMDB entry. A key is provided in the bottom right corner of the figure, showing the cartoon labels for entries of *ex vivo* samples or *ex vivo* seeded samples, used throughout. All models and representations are scaled equally, with the scale bar representing the length of 20 Å. Molecular models were generated using UCSF Chimera.[104]

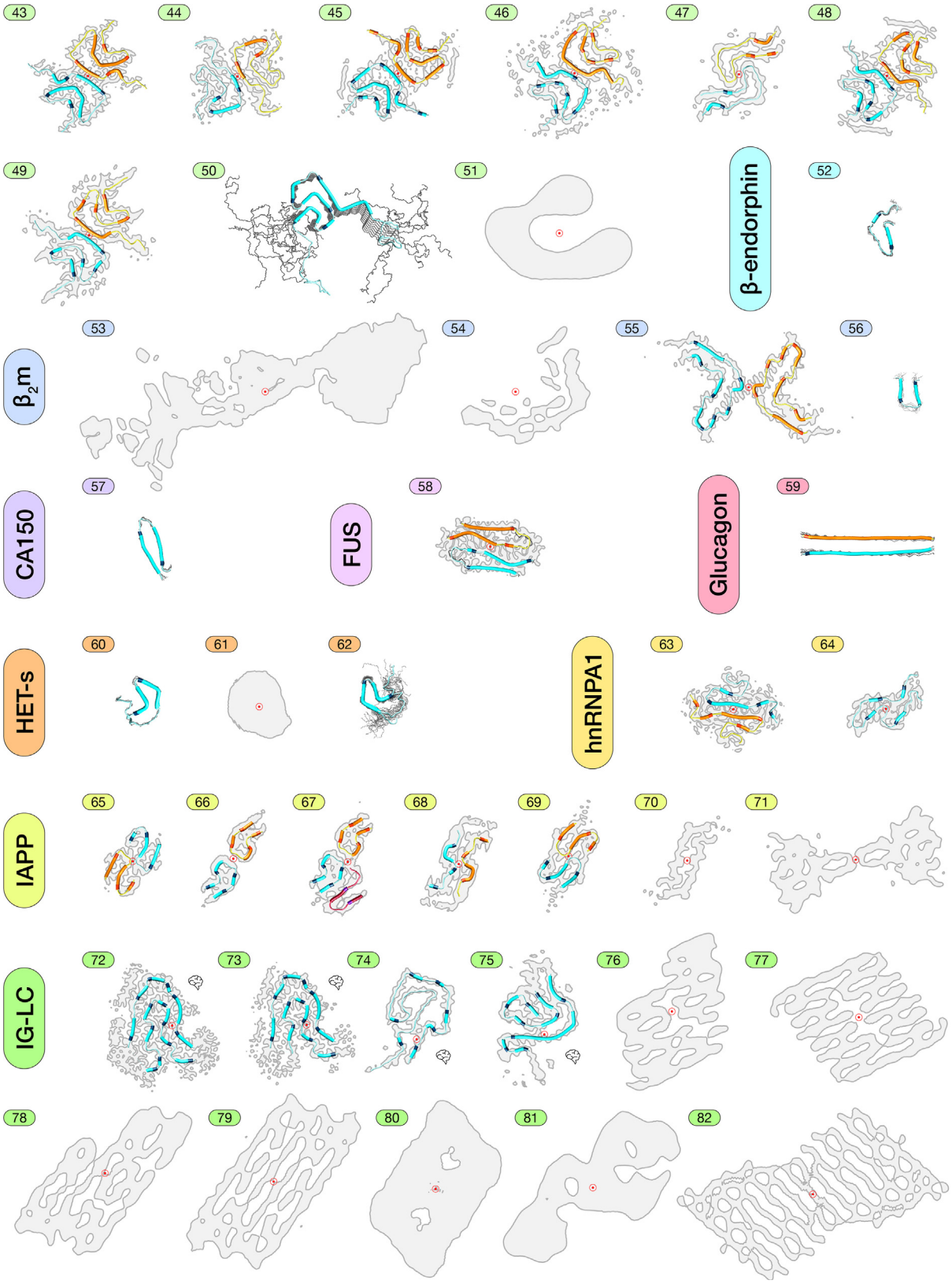

Fig 2. *(continued)*

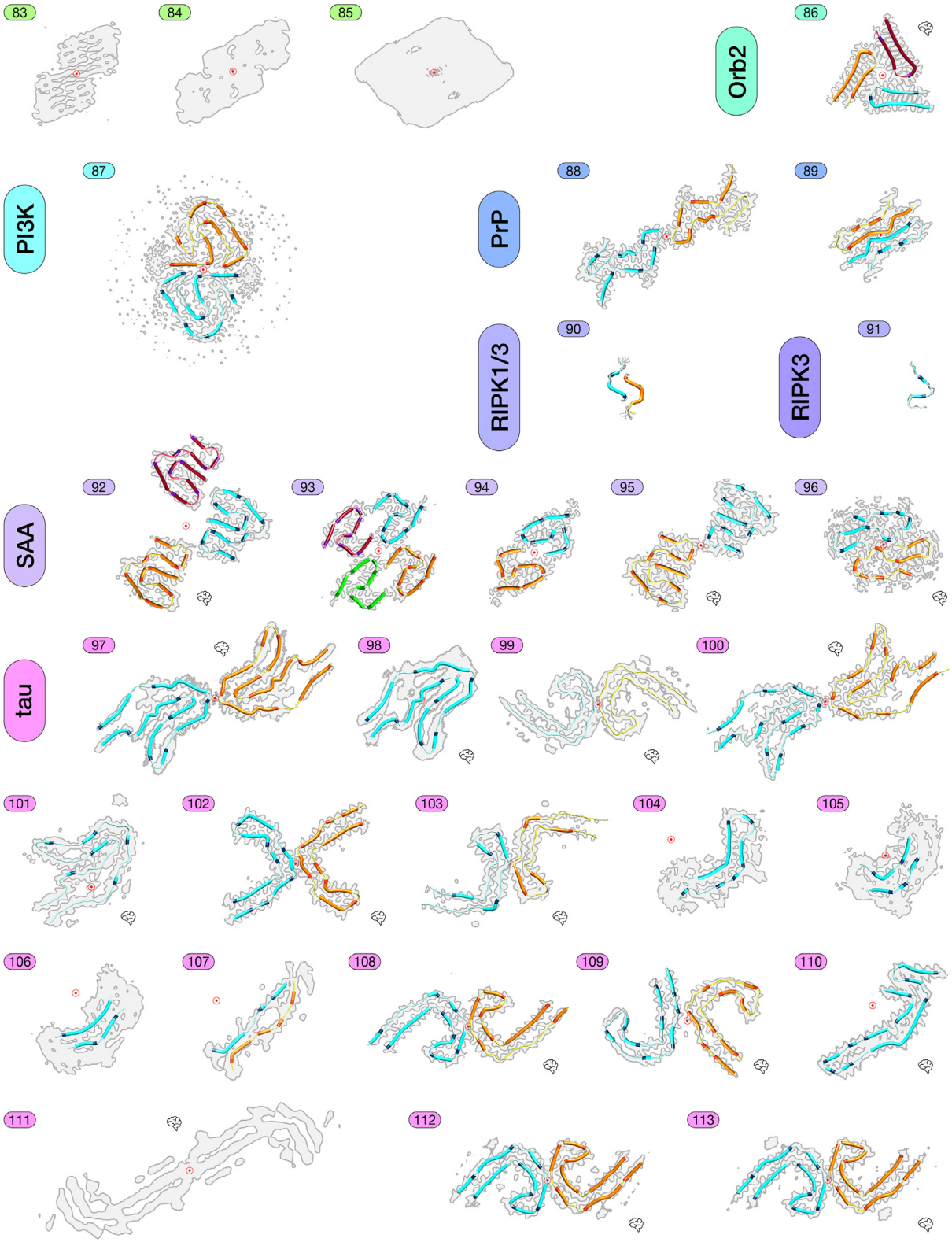

Fig 2. *(continued)*

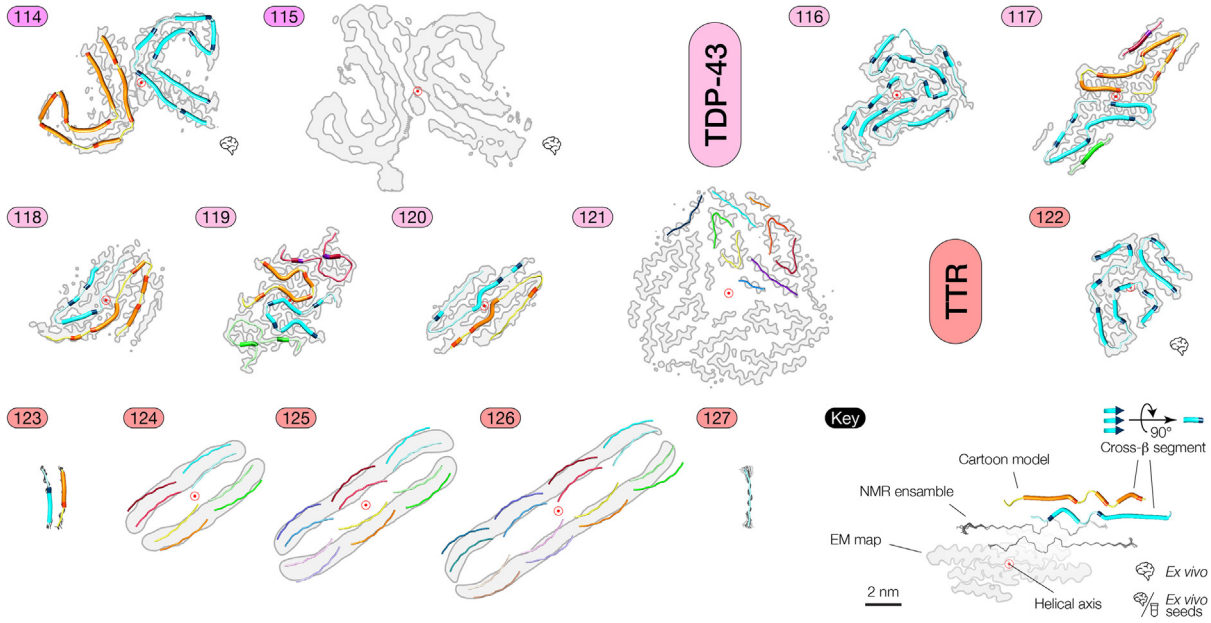

Fig 2. *(continued)*

Physicochemical consequences of amyloid polymorphism

Structural variations within and between individual fibrils in typically heterogeneous amyloid populations can exist on multiple length scales (Figure 1). These structural variations that define amyloid polymorphism can range from atomic scale differences in the order of ångströms, arising from packing variations of the polypeptide chains, to nanometre-scale variations in fibril width, or even reach the scale of hundreds of nanometres in variations of twist periodicity and handedness of amyloid fibrils.[25] At these different length scales, as a consequence of the diversity and individuality of polymorphic amyloid structures, the physicochemical properties of individual fibrils, such as the overall accessible surface area,[45] surface hydrophobicity and charge,[59] growth and disassembly kinetics and thermodynamics,[51] and mechanical properties that include persistence length and the second moment of inertia,[60] can also vary within a population. Therefore, in contrast to globular proteins which typically have a single native fold, the structural variation between individual fibrils within a population may impact the functional properties of the amyloid population *in vivo*, mediated by variation in their specific physicochemical properties. For example, different amyloid structures have different cross-sectional dimensions and shapes. Thicker fibrils with rounded cross-sections are likely to have a higher second moment of inertia than thin fibrils with elliptical cross-sections, making them more resistant to breakage. Fibrils with higher fragmentation rates are more likely to generate a larger number of small active amyloid particles and subsequently may be more effective in propagating their amyloid state,[61] compared to fibrils that are more stable and less susceptible to breakage. This is demonstrated through the size-dependent transfection efficiency relationship of Sup35NM amyloid particles that confer the [*PSI*$^{+}$] phenotype when transfected into yeast cells.[62] In studies of transmissible amyloid known as prions, specific strains are found to selectively propagate from cell to cell,[63–66] suggesting a possible relationship between the strain phenomenon, the structural polymorphism of amyloid fibrils, and the individual fibrils' stability towards fragmentation. Thus, the differences in the stability of individual fibrils, as a consequence of structural polymorphism, may lead to variations in the fitness of individual fibrils in an amyloid population, and subsequent 'selection' of specific amyloid conformation due to a polymorphic bias under certain conditions as well as adaptive 'evolution' processes of the dominant amyloid conformation due to changes in the environment. The structural constraints provided by the cross-β architecture coupled with a strong structural individuality in some amyloid populations, and the ability of some amyloid to efficiently propagate the information encoded in their conformational state, may suggest that some amyloid could behave in a manner similar to that of viral quasispecies. In addition to fibril fragmentation, secondary nucleation is another property that is affected by the fibril structural arrangement and could mediate the biological effects of amyloid. Fibrils with a higher surface-area-to-volume ratio might provide better access to active fibril surfaces that can catalyse secondary nucleation, compared to larger amyloid structures with proportionally less

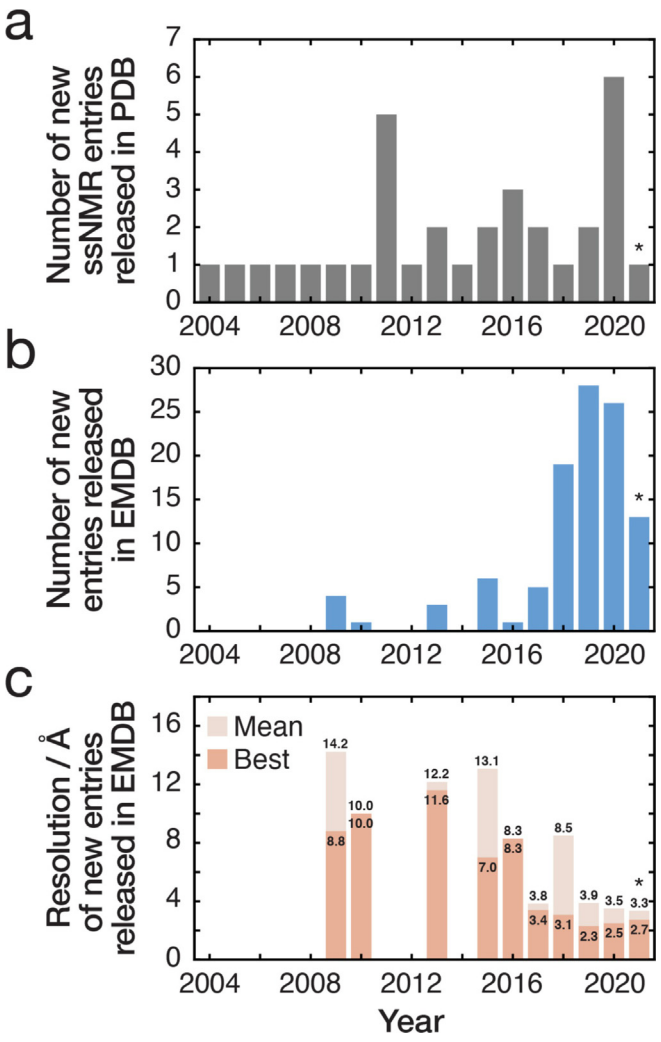

Figure 3. The number of structural data entries of amyloid fibrils deposited to the EMDB and PDB databases is rapidly growing, and the resolution of cryo-EM data is improving. (a) Number of new amyloid structural models determined by ssNMR deposited to the PDB released each year since 2004. (b) Number of new amyloid cryo-EM data deposited to the EMDB released each year since 2009. (c) Mean and best resolutions of cryo-EM data of amyloid fibrils each year. The star symbols (*) indicate that only entries released up until March are included for 2021.

available surface area. Secondary nucleation is a process in which new amyloid are formed through catalysis by existing amyloid fibril surfaces. The importance of secondary nucleation, in particular with respect to the biological impact of $A\beta_{42}$ amyloid fibrils, has become increasingly evident. For example, by combining kinetic analysis of $A\beta_{42}$ aggregation with impaired secondary nucleation using the molecular chaperone Brichos[67] and antibodies that bind to the fibril surface,[68] it has been shown that secondary nucleation events may be the source of cytotoxic oligomeric species during $A\beta_{42}$ aggregation. It is further possible, that secondary nucleation on the surface of amyloid fibrils is site-specific, potentially occurring at sites of defects or at locations where structural breaks occur. Individual fibril polymorphs with higher propensity to contain defects, have structural breaks, or those that simply have a larger accessible surface area might then provide more efficient surfaces for secondary nucleation, and, therefore, be responsible for a greater cytotoxic potential within the amyloid population.

The polymorphic features of individual amyloid fibrils can both influence and be influenced by interactions with other biological structures. For example, the formation of α-synuclein amyloid fibrils *in vitro* is modulated by the air water interface.[69] Since α-synuclein fibrils are found *in vivo* in patients with various diseases, where the air–water interface is likely to be absent, it suggests that other biological interfaces may provide sites for the heterogeneous nucleation of α-synuclein assembly. This type of surface-catalysed aggregation of amyloidogenic proteins

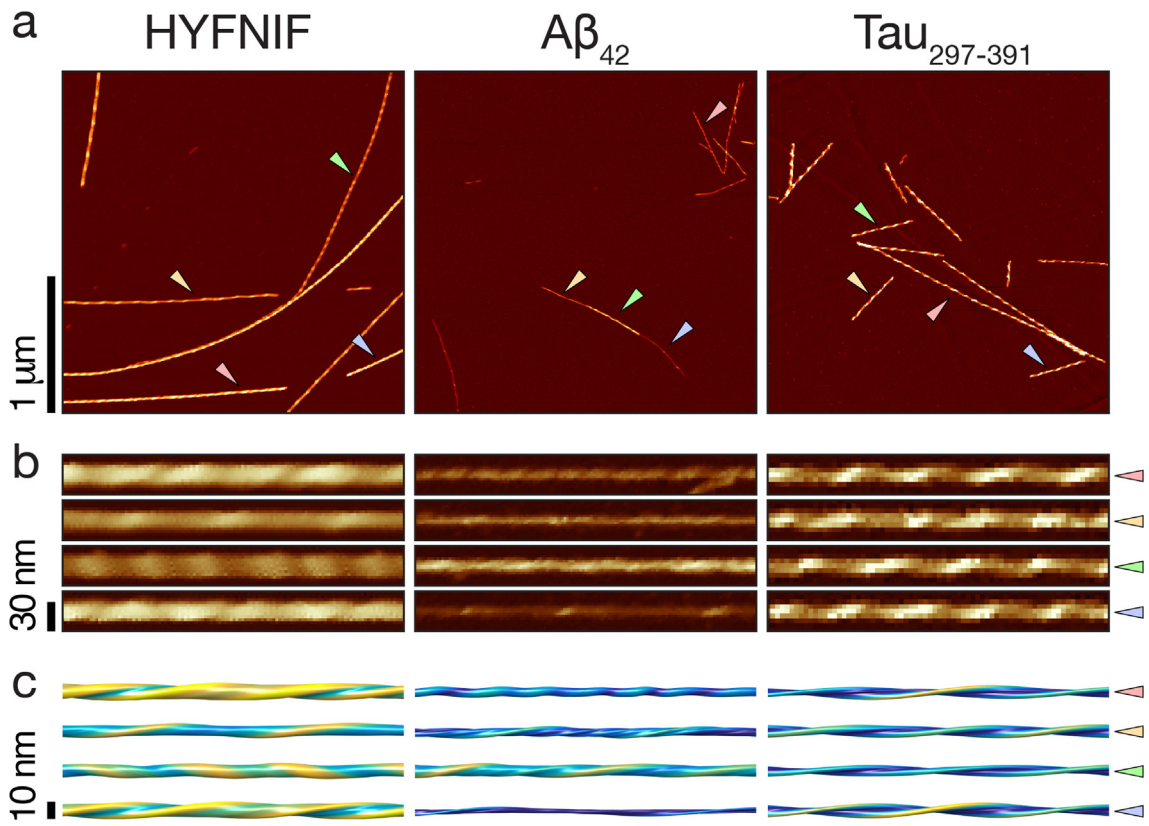

Figure 4. Structural details individual to each amyloid fibril are revealed by AFM. Gentle force-distance curve-based AFM imaging and 3D-reconstruction of fibril surface envelopes revealed the individuality of amyloid fibrils in amyloid populations, with no two fibrils being exactly the same. (a) AFM height topology images of amyloid fibrils formed from a hexapeptide of the primary sequence HYFNIF,[25] $A\beta_{42}$, and a $tau_{297\text{-}391}$ fragment (also called dGAE).[58] The images are shown with the same length and colour scale, with the scale bar to the left indicating the length of 1 μm in all three images. (b) Images of digitally straightened fibrils seen in the images in a), with the coloured triangle markers indicating their position in a). A 350 nm segment of each fibril is shown. (c) The 3D surface envelope models individually reconstructed for each fibril in (b) are shown with surface colours ranging from blue to yellow to indicate the distance to the fibril axis from thin to wide. A 200 nm segment of each 3D model is shown. These AFM images and individual fibril models suggest that the extent of structural polymorphism is not the same for different amyloid forming sequences, with fibrils formed from $tau_{297\text{-}391}$ showing the least extent of polymorphism amongst the three examples. Polymorphic structural variation within a fibril is also seen on the image of $A\beta_{42}$ fibrils.

involves adsorption of amyloid forming proteins onto surfaces, followed by a step that includes a conformational change, whether that be from a random coil to the core fold of the resultant amyloid fibril or to an oligomeric intermediate state.[70] Importantly, the precise amyloid structures that form, amongst the diverse possible structures that can be formed, may be dependent on the physicochemical characteristics of the catalysing surface. High local concentrations of self-assembling proteins adsorbed onto a surface can increase the rate of heterogeneous primary nucleation in a manner which is dependent on the mobility of the proteins once adsorbed onto the surface. Cell membranes and, in particular, their lipid bilayer components are amongst the most well-studied biological structures known to interact with amyloidogenic proteins in such a manner.[71–75] Fibril formation reactions can be catalysed by lipid bilayers,[76,77] but can also be damaging to lipid bilayers.[71,78,79] In fact, it may be possible to connect the aggregation kinetics to the toxicity of the aggregation reaction through their interaction with membranes.[80] In order for lipid bilayers to catalyse primary nucleation, the monomeric subunits must first adsorb to the bilayer surface. In some cases, lipid bilayers induce a conformational change in the monomeric subunits of an amyloidogenic protein. For example, α-synuclein undergoes a change in conformation, dependent on the fluidity of the lipid bilayer.[81] Additionally IAPP undergoes conformational changes upon insertion into a lipid bilayer, eventually forming amyloid fibrils in a lipid-mediated manner,[82] and when mixed with large unilamellar vesicles it has been observed that the secondary nucleation of $A\beta_{42}$ can be accelerated through lipid bilayer interactions.[76] Conformational changes upon binding to a surface imply that structural features of a

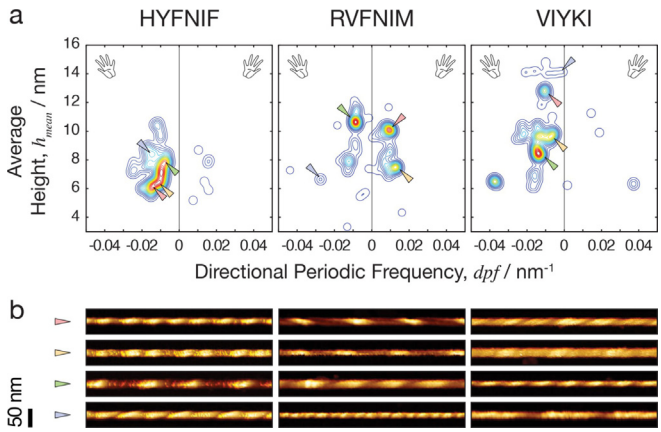

Figure 5. Structural analysis of individual fibrils using AFM allows mapping of the polymorphic amyloid assembly landscape. (a) The polymorphic amyloid assembly landscapes of three short amyloid forming peptide sequences are represented as smoothed 2D histograms and visualised as contour maps.[25] The colouring represents the density of the morphometric parameters; which include the average height and the number of repeating units per nm (directional periodic frequency, dpf) of the individual fibrils observed on AFM height images. Negative and positive dpf values correspond to fibrils with left-handed twist and right-handed twist, respectively. (b) Example images of digitally straightened fibrils formed from the three peptide sequences in (a), with the coloured triangle markers indicating their position in the maps in (a). A 500 nm segment of each fibril is shown.

resultant amyloid fibril can be dependent on the local physicochemical environment, and the precise structures of the fibrils, therefore, will vary and contribute to the individuality of each fibril in the population. Further biological structures which can impact fibril formation include additional cell membrane constituents such as gangliosides,[83] extracellular structures such as heparin,[84] as well as other heterologous amyloid fibrils through cross-seeding events. If cross-seeding events proceed through surface-catalysed reactions,[42] the resulting new amyloid structures could result in considerable fibril diversity and individuality, as heterogeneous nucleation events may also introduce heterogeneity in the resulting amyloid population, depending on the physicochemical conditions of local interfaces. Thus, surface interactions may enhance the potential for amyloid forming polypeptide sequences to display structural polymorphism.

Biological and pathological consequences of amyloid polymorphism

Amyloid fibrils display remarkable diversity in both the structures they form, as well as the biological contexts they are found in. Some amyloid structures are found to be disease-associated, while others may be essential for physiological functions. The wide range of *in vivo* biological functions or pathological consequences of amyloid may reflect the polymorphic diversity of amyloid fibril structures, mediated by the differing physicochemical properties of individual amyloid fibrils, as discussed above. However, specific molecular links between structural features, particular cellular pathways or processes, and biological consequences are not currently well-understood. One of such possible mediating properties could be the thermodynamic stability of the fibril core, determined by structural features like core hydrophobicity and steric zipper interactions, with lower stability leading to reversible assemblies.[85,86] Furthermore, amyloid with assembly-dependent functional roles may show less polymorphism compared to disease-associated amyloid,[85,87,88] which could indicate that the specific core fold of amyloid fibrils may convey corresponding specific biological properties that facilitate functional roles. In contrast, a wide range of polymorphs of disease-associated amyloid structures have been observed, with diverse patterns of polymorphic extent that include patient-specific polymorphism, clinical-subtype specific polymorphism for the same disease, and disease-specific polymorphism (Figure 6). Structural data obtained to date suggest that different amyloid systems behave differently in this respect, although more structural data of *ex vivo* amyloid assemblies is needed to resolve how the polymorphic landscape varies in different disease-states, spatial localisations within organs, or individual patients. Further structural characterisation of physiologically functional amyloid structures and comparison of these structures with those of disease-associated amyloid is also necessary to fundamentally understand the amyloid structure–function links.

Different neurodegenerative diseases show distinct patterns of spatial origins of amyloid aggregation as well as progression by prion-like spreading, which is mediated by neuronal

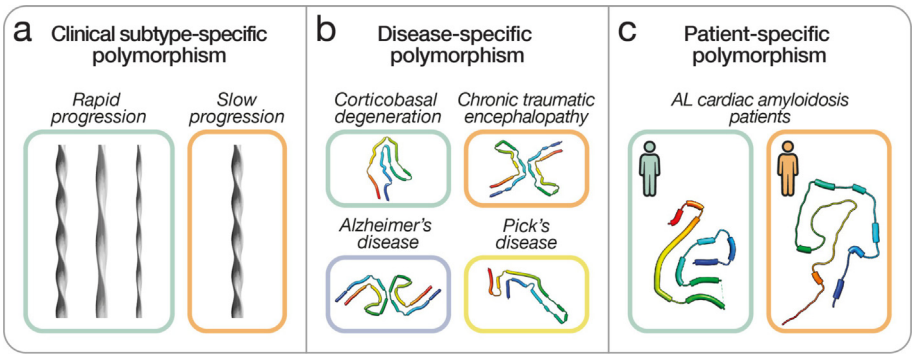

Figure 6. Amyloid polymorphism shows diverse patterns in disease-states. (a) Illustrations of the varying extent of structural polymorphism and the diverse types of polymorphic structures that may be present in clinical disease subtypes, for example shown for rapid and slow progressive Alzheimer's disease.[93,94] (b) Disease-specific polymorphism has been demonstrated for amyloid structures formed from tau protein in various tauopathies. A single representative cartoon model is shown of amyloid fibril cross-sections from samples originating from the brain tissue of patients with four different neurodegenerative diseases, with the thicker sections denoting the cross-β segments, where such segments are determined and labelled in the PDB entry. PDB accession codes for the models shown are 6VHA, 6NWP, 5O3L and 6GX5,[13,15,38,91] for chronic corticobasal degeneration, traumatic encephalopathy, Alzheimer's disease, and Pick's disease, respectively. c) Individual patients with the same diagnosis may have distinct structures of the same protein, for example in the case of AL amyloidosis. Cartoon models of the cross-sections of *ex vivo* amyloid fibrils extracted from the cardiac tissue of two patients with AL amyloidosis are shown, with PDB accession codes 6HUD and 6IC3,[98,99] respectively. Molecular models were generated using UCSF Chimera.[104]

connectivity and individual cell-type vulnerability.[89] For example, tau lesions originate in different regions of the brain in patients with Alzheimer's disease and chronic traumatic encephalopathy (CTE), despite being composed of the same protein isoforms.[90] The structural diversity of the amyloid aggregates involved can be affected by the local *in vivo* environment which could, in turn, elicit different biological effects based on the precise physicochemical properties of the individual fibrils formed. These complex relationships may result in biological feedback loops that subsequently contribute to the molecular and phenotypical differences between amyloid-associated diseases, even when the primary sequence of the original protein involved is identical. For example, in recent years, *ex vivo* amyloid fibrils of the tau protein have been well-characterised, and their structures have been resolved to high-resolution detail from the brain tissue of patients with various different diseases, including Alzheimer's disease, Pick's disease, corticobasal degeneration (CBD) and chronic traumatic encephalopathy.[13–15,91] Although tau isoforms forming the amyloid fibrils differ between some diseases, and thus have slightly different primary sequences, the structures of fibrils from Alzheimer's and CTE disease tissues, which both contain the 3R and 4R isoforms, are nevertheless different (Figure 6 panel **b**). Notably there is also polymorphism present within the fibril population of each disease-specific sample, e.g., paired helical filaments (see Figure 2 and Table 2 entries 99, 108, 112 and 113) and straight filaments (see Figure 2 and Table 2 entries 109, 114 and 115) in Alzheimer's disease brain tissue.[13,92] Other rare but potentially also biologically important polymorphs of amyloid in the same disease-associated amyloid populations may also be present,[56] but their 3D structures are currently inaccessible to characterisation by cryo-EM because they are present in low numbers; and therefore cannot satisfy the extensive particle-averaging required by cryo-EM methodologies.

In addition to disease-specific amyloid polymorphism, considerable structural variation may exist for Aβ amyloid from patients with different Alzheimer's disease clinical subtypes. Fibril samples formed through seeding with *ex vivo* fibrils extracted from the brain cortex of patients with Alzheimer's disease have been investigated by ssNMR.[93] While the structures of fibrils formed from seeding do not necessarily reflect that of the seeds,[40] it has been found that seed samples originating from patients with prolonged-duration AD resulted in fibrils of a single predominant $A\beta_{40}$ polymorph, whereas samples originating from patients with rapidly progressive AD resulted in a wider degree of structural diversity, suggesting that the seeds' structures were different. Aβ amyloid fibrils from patient brain tissue with slowly and rapidly progressing AD have also been shown to have different biochemical characteristics, including different stability upon chemical and thermal denaturation, and higher levels of oligomeric $A\beta_{42}$ in the rapidly progressive form,[94] further evidencing the possible presence of complex, clinical subtype-dependent amyloid polymorphism.

Cryo-EM structures from four patients with Alzheimer's disease have demonstrated common paired helical and straight filament structures of tau amyloid,[92] demonstrating that for some amyloid assemblies, the structures are specific to the disease, and not to the individual patients or disease subtypes. In addition, images of immunogold labelled tau amyloid fibril samples from 19 AD patients, as well as from different brain regions of the same patients, also show similar patterns. Subsequently, disease-specific fibril structures have been reported for various tauopathies, giving rise to a structure-based classification approach for these neurodegenerative diseases.[12] However, it is not yet known whether structures prevalent during earlier stages, which may drive disease progression, are also identical to those extracted from the tissues of individuals with end-stage disease and determined by cryo-EM.

Light chain (AL) amyloidosis is an example of patient-specific amyloid polymorphism. In AL amyloidosis, expansion of a B cell clone leads to overproduction of a free monoclonal immunoglobulin light chain protein, aggregation of which results in amyloid fibrils that accumulate in organs, such as the heart or the kidneys, leading to tissue damage. The specific sequence of the accumulating immunoglobulin light chain protein in each patient can affect the propensity of amyloid formation and thus, potentially also the disease aetiology through impact on the thermodynamic stability of the specific polypeptide sequence,[95] the tissues where amyloid deposits, and the clinical outcome.[96] However; it has been recently shown that extrinsic factors, especially susceptibility to proteolytic cleavage and presence of proteases that fragment the immunoglobulin light chain proteins under physiological conditions, could instead be a strong determinant of amyloid formation *in vivo*.[97] Amyloid structures have been resolved from the explanted cardiac tissue of three patients; demonstrating patient-specific structural differences in detail.[57,98,99] Contrary to the previous examples of tau and Aβ amyloid, the primary sequence of the monoclonal immunoglobulin light chain protein varies between patients as it depends on the selection of the germline gene and somatic mutations.[100] Thus, patient-specific amyloid polymorphism stems from the 'top-level' patient-specific variations in the primary polypeptide sequence (Figure 1 top row). It is, however, not yet known whether patient-specific amyloid polymorphism can arise for amyloid structures formed from the same monomeric polypeptide sequence. There remain currently many unanswered questions on the *in vivo* role of amyloid in disease-states, both related to how the environmental factors affect fibril growth and their structures, as well as how amyloid formation and structures affect the surrounding cells and tissue environments, including any cell-type specific vulnerabilities. Further insights into the relationship between fibril polymorphism and their biological consequences can be achieved from continued efforts in resolving *ex vivo* fibril structures from tissues of patients with different diagnoses or disease progression, from different regions of the brain or diseased tissues, and from multiple individual patients with the same diagnosis. Likewise, *in vitro* approaches in which the polymorphic landscape is modified in a controlled manner by systematically varying sequence or environmental factors to form specific structures will provide molecular and mechanistic evidence of pathological pathways. Both approaches will equally require the structural characterisation of amyloid fibrils to molecular and individual detail.

Challenges in predicting the polymorphic landscape of amyloid assembly

For globular proteins, AlphaFold 2 did exceptionally well in predicting 3D structures from primary amino-acid sequences.[21] The achievements of 3D structure prediction through deep learning methods, e.g., the trained neural network architecture of AlphaFold 2, to date on monomeric proteins in CASP14, is a result of both extensive computational resources for model training and inference of new structures, as well as the availability of approximately 170,000 publicly available protein structure entries in the RCSB Protein Data Bank, and many more protein sequences used for multiple sequence alignments, which inform structure prediction. Future developments to AlphaFold 2 will potentially include prediction of protein complexes. Although amyloid structures were not included as targets in CASP14, further developments in structure prediction of large protein complexes, including amyloid, could lead to fundamental understandings of how some of the biggest biological protein structures form. Considerable developments to the current prediction methods will, however, need to be incorporated to allow the prediction of many structures from a single primary sequence due to the extensive polymorphism displayed by amyloid fibrils, which form diverse structures even under identical environmental conditions and from identical amino acid sequences. This type of challenge can only be met if a sufficiently holistic understanding of the assembly landscape, in terms of both structures and energetics, is reached. However, with only around a hundred amyloid fibril structures currently available in the PDB for full-length or fragments of amyloidogenic proteins (Table 2, Figure 2, not including cases where the same data has been reanalysed), the limited training data available for structural prediction tool development, especially ones that rely on 'big-data' approaches, pose a severe limitation to such a holistic undertaking. A

further 108 PDB structures are available for amyloid fibrils formed from microcrystals of amyloid forming peptide sequences ranging from 4 to 11 amino acids in length, determined by X-ray and electron diffraction techniques, which could be useful for the prediction of local structural arrangements of the various steric-zipper motifs. Nevertheless, to predict the structures of large, multi-polypeptide chain, and highly polymorphic protein assemblies like amyloid, significant effort must first be spent on matching the quantity of high-quality structural data, such as currently seen for globular proteins.

Another key challenge for amyloid structure prediction is the high potential sensitivity of the amyloid conformation to a multitude of environmental factors, such as pH, ionic strength and interactions with other biomolecules and surfaces. As the precise local *in vivo* environments experienced by the various amyloid forming systems are unknown for disease-associated and functional amyloid, the characterisation of *ex vivo* amyloid fibrils needs to be carried out as indirect reporters on the relevant *in vivo* environments. These *in vivo* conditions are likely to differ from conditions used *in vitro,* since *ex vivo* amyloid structures have been found to differ compared to *in vitro* formed amyloid originating from monomers of the same amino acid sequence.[13,39,101] Direct structural characterisation for *ex vivo* amyloid without the need for further seeded amplification is currently only possible using cryo-EM. There are further challenges for resolving *ex vivo* amyloid structures, including limited access to patient-derived tissues, experimental challenges with extracting fibrils from these tissues, and the ability to only study the most prevalent fibril species despite the diversity of species present. As a result, currently, structural data of only fewer than thirty of such unseeded *ex vivo* amyloid have been deposited to the EMDB and the PDB. Although an increasing number of *ex vivo* amyloid fibrils are being studied every year, it remains a labour-intensive and costly endeavour. Thus, for predicting the 3D structures of amyloid under physiologically relevant environmental conditions, it may be necessary to first resolve how the assembly landscape is precisely modulated by environmental conditions through combined *ex vivo* and *in vitro* approaches, and then train a neural network using 3D structures formed under widely varying conditions.

The prediction of 3D protein structures gives rise to applications such as the ability to infer function associated with the predicted structure, as well as structure-based drug design. These applications rely on specific folds and motifs being predicted from amino acid sequences. For amyloid, there are likely to be unique challenges compared to other, well-studied classes of proteins such as enzymes, where a specific catalytic pocket could, for example, indicate a specific functional role. As more structural data of amyloid from different biological contexts, both disease-associated and functional, become available, it may be possible to predict whether an amyloid forming sequence may be associated with the formation of assemblies with toxic or infective potential. More structural data will facilitate this type of analysis and may potentially reveal the mediating physicochemical factors involved in the link between amyloid structure, function, and pathogenicity. Only once this relationship has been firmly established based on both structural data and biological context, could a predicted 3D structure be used to explore the potential biological consequences and aid structure-based therapeutic interventions. A significant amyloid-specific opportunity for structure prediction lies in cases where structures are disease subtype- or patient-specific. For example, in AL amyloidosis, each patient has a slightly different immunoglobulin light chain amino acid sequence that can be noninvasively determined from urine.[102] If the fibril structures could then be predicted from the primary amino-acid sequence, it could be helpful in determining a specific clinical subtype or indicate specific pathways of pathology. Furthermore, structure-based inhibitors of amyloid aggregation have been demonstrated for some proteins such as Aβ in cell-culture models.[103] If a structure-based approach would be demonstrated to be clinically effective, for example, for AL amyloidosis patients, prediction of structure from sequence could determine patient-specific epitopes that could be targeted in a personalised medicine approach.

Conclusions

Amyloid assembly presents unique challenges to protein 3D structure elucidation, prediction, and understanding of the relationship between structure and biological consequences. Unresolved challenges arise from the highly polymorphic nature of amyloid assembly, the subsequent individuality of each fibril formed within the heterogeneous amyloid populations, and the resulting differences in the fibrils' physicochemical properties arising even from monomers with identical amino acid sequences. This structural diversity is reflected in amyloid-associated biological roles which range from functionality to pathogenic effects in neurodegenerative diseases and systemic amyloidoses, with a potentially wide variation in disease subtypes and clinical outcomes. Successful amyloid structure prediction from the primary amino acid sequence of its monomeric polypeptide components will need to contain robust predictions of whether an amino acid sequence is likely to form the cross-β amyloid fold in the first place, followed by precise structural predictions that holistically takes into account the

assembly landscape and its sensitivity to the environmental conditions it experiences. Finally, the path towards solving the 'one sequence to many structures' problem amyloid assemblies represent, and the successful prediction of the full range of diverse amyloid structures, will inevitably push our fundamental understanding of the coupled protein folding-assembly processes commonly found in biology.

CRediT authorship contribution statement

Liisa Lutter: Software, Formal analysis, Visualization, Writing - original draft, Writing - review & editing. **Liam D. Aubrey:** Visualization, Writing - original draft, Writing - review & editing. **Wei-Feng Xue:** Conceptualization, Software, Formal analysis, Visualization, Supervision, Project administration, Funding acquisition, Writing - review & editing.

Acknowledgements

We thank Louise Serpell for all the discussions that inspired this review, as well as the members of the Xue research group and the Kent Fungal Group for helpful comments throughout the preparation of this manuscript. This work was supported by funding from the Biotechnology and Biological Sciences Research Council (BBSRC), UK grant BB/S003312/1 (LDA and WFX), as well as Engineering and Physical Sciences Research Council (EPSRC), UK DTP grant EP/R513246/1 (LL).

Declaration of Competing Interest

The authors declare that they have no known competing financial interests or personal relationships that could have appeared to influence the work reported in this paper.

Received 3 May 2021;
Accepted 26 June 2021;
Available online 2 July 2021

Keywords:
amyloid;
fibril structure;
polymorphism;
folding/misfolding;
protein aggregation

Abbreviations:
3D, three-dimensional; Å, ångström; AD, Alzheimer's disease; AFM, atomic force microscopy; AI, artificial intelligence; AL, amyloid light chain; $A\beta_{40}$, amyloid β peptide fragment, amino acid residues 1-40; $A\beta_{42}$, amyloid β protein fragment, amino acid residues 1-42; CASP, Critical Assessment of protein Structure Prediction; CASP14, 14th Community Wide Experiment on the Critical Assessment of Techniques for Protein Structure Prediction; CBD, corticobasal degeneration; Cryo-EM, cryogenic electron microscopy; dGAE, tau protein fragment, amino acid residues 297-391; EM, electron microscopy; EMDB, The Electron Microscopy Data Bank; IAPP, islet amyloid polypeptide; microED, microcrystal electron diffraction; PDB, The Protein Data Bank; PTMs, post-translational modifications; RCSB, Research Collaboratory for Structural Bioinformatics; ssNMR, solid-state nuclear magnetic resonance

References

1. Eisenberg, D., Jucker, M., (2012). The amyloid state of proteins in human diseases. *Cell*, **148**, 1188–1203. https://doi.org/10.1016/j.cell.2012.02.022.
2. Riek, R., (2017). The three-dimensional structures of amyloids. *Cold Spring Harb. Perspect. Biol.*, **9**, https://doi.org/10.1101/cshperspect.a023572 a023572.
3. Dobson, C.M., Knowles, T.P.J., Vendruscolo, M., (2020). The amyloid phenomenon and its significance in biology and medicine. *Cold Spring Harb. Perspect. Biol.*, **12** https://doi.org/10.1101/cshperspect.a033878.
4. Chiti, F., Dobson, C.M., (2017). Protein misfolding, amyloid formation, and human disease: A summary of progress over the last decade. *Annu. Rev. Biochem.*, **86**, 27–68. https://doi.org/10.1146/annurev-biochem-061516-045115.
5. M.D. Benson, J.N. Buxbaum, D.S. Eisenberg, G. Merlini, M.J.M. Saraiva, Y. Sekijima, J.D. Sipe, P. Westermark, Amyloid nomenclature 2020: update and recommendations by the International Society of Amyloidosis (ISA) nomenclature committee, Amyloid Int. J. Exp. Clin. Investig. Off. J. Int. Soc. Amyloidosis. 27 (2020) 217–222. https://doi.org/10.1080/13506129.2020.1835263.
6. Buell, A.K., Dobson, C.M., Knowles, T.P.J., (2014). The physical chemistry of the amyloid phenomenon: thermodynamics and kinetics of filamentous protein aggregation. *Essays Biochem.*, **56**, 11–39. https://doi.org/10.1042/bse0560011.
7. Michaels, T.C.T., Šarić, A., Habchi, J., Chia, S., Meisl, G., Vendruscolo, M., Dobson, C.M., Knowles, T.P.J., (2018). Chemical kinetics for bridging molecular mechanisms and macroscopic measurements of amyloid fibril formation. *Annu. Rev. Phys. Chem.*, **69**, 273–298. https://doi.org/10.1146/annurev-physchem-050317-021322.
8. Xue, W.-F., Homans, S.W., Radford, S.E., (2008). Systematic analysis of nucleation-dependent polymerization reveals new insights into the mechanism of amyloid self-assembly. *Proc. Natl. Acad. Sci.*, **105**, 8926–8931. https://doi.org/10.1073/pnas.0711664105.
9. Cohen, S.I.A., Linse, S., Luheshi, L.M., Hellstrand, E., White, D.A., Rajah, L., Otzen, D.E., Vendruscolo, M., Dobson, C.M., Knowles, T.P.J., (2013). Proliferation of amyloid-β42 aggregates occurs through a secondary nucleation mechanism. *Proc. Natl. Acad. Sci.*, **110**, 9758–9763. https://doi.org/10.1073/pnas.1218402110.

10. Xue, W.-F., Hellewell, A.L., Gosal, W.S., Homans, S.W., Hewitt, E.W., Radford, S.E., (2009). Fibril fragmentation enhances amyloid cytotoxicity. *J. Biol. Chem.*, **284**, 34272–34282. https://doi.org/10.1074/jbc.M109.049809.
11. Scheckel, C., Aguzzi, A., (2018). Prions, prionoids and protein misfolding disorders. *Nat. Rev. Genet.*, **19**, 405–418. https://doi.org/10.1038/s41576-018-0011-4.
12. Y. Shi, W. Zhang, Y. Yang, A. Murzin, B. Falcon, A. Kotecha, M. van Beers, A. Tarutani, F. Kametani, H.J. Garringer, R. Vidal, G.I. Hallinan, T. Lashley, Y. Saito, S. Murayama, M. Yoshida, H. Tanaka, A. Kakita, T. Ikeuchi, A.C. Robinson, D.M.A. Mann, G.G. Kovacs, T. Revesz, B. Ghetti, M. Hasegawa, M. Goedert, S.H.W. Scheres, Structure-based classification of tauopathies, BioRxiv. (2021) 2021.05.28.446130. https://doi.org/10.1101/2021.05.28.446130.
13. Fitzpatrick, A.W.P., Falcon, B., He, S., Murzin, A.G., Murshudov, G., Garringer, H.J., Crowther, R.A., Ghetti, B., Goedert, M., Scheres, S.H.W., (2017). Cryo-EM structures of tau filaments from Alzheimer's disease. *Nature*, **547**, 185–190. https://doi.org/10.1038/nature23002.
14. Zhang, W., Tarutani, A., Newell, K.L., Murzin, A.G., Matsubara, T., Falcon, B., Vidal, R., Garringer, H.J., Shi, Y., Ikeuchi, T., Murayama, S., Ghetti, B., Hasegawa, M., Goedert, M., Scheres, S.H.W., (2020). Novel tau filament fold in corticobasal degeneration. *Nature*, **580**, 283–287. https://doi.org/10.1038/s41586-020-2043-0.
15. Falcon, B., Zivanov, J., Zhang, W., Murzin, A.G., Garringer, H.J., Vidal, R., Crowther, R.A., Newell, K.L., Ghetti, B., Goedert, M., Scheres, S.H.W., (2019). Novel tau filament fold in chronic traumatic encephalopathy encloses hydrophobic molecules. *Nature*, **568**, 420–423. https://doi.org/10.1038/s41586-019-1026-5.
16. Fitzpatrick, A.W., Saibil, H.R., (2019). Cryo-EM of amyloid fibrils and cellular aggregates. *Curr. Opin. Struct. Biol.*, **58**, 34–42. https://doi.org/10.1016/j.sbi.2019.05.003.
17. Tycko, R., (2011). Solid state NMR studies of amyloid fibril structure. *Annu. Rev. Phys. Chem.*, **62**, 279–299. https://doi.org/10.1146/annurev-physchem-032210-103539.
18. Lutter, L., Serpell, C.J., Tuite, M.F., Serpell, L.C., Xue, W.-F., (2020). Three-dimensional reconstruction of individual helical nano-filament structures from atomic force microscopy topographs. *Biomol. Concepts.*, **11**, 102–115. https://doi.org/10.1515/bmc-2020-0009.
19. Ruggeri, F.S., Longo, G., Faggiano, S., Lipiec, E., Pastore, A., Dietler, G., (2015). Infrared nanospectroscopy characterization of oligomeric and fibrillar aggregates during amyloid formation. *Nat. Commun.*, **6**, 7831. https://doi.org/10.1038/ncomms8831.
20. Krasnoslobodtsev, A.V., Deckert-Gaudig, T., Zhang, Y., Deckert, V., Lyubchenko, Y.L., (2016). Polymorphism of amyloid fibrils formed by a peptide from the yeast prion protein Sup35: AFM and Tip-Enhanced Raman Scattering studies. *Ultramicroscopy*, **165**, 26–33. https://doi.org/10.1016/j.ultramic.2016.03.011.
21. J. Jumper, R. Evans, A. Pritzel, T. Green, M. Figurnov, K. Tunyasuvunakool, O. Ronneberger, R. Bates, A. Žídek, A. Bridgland, C. Meyer, S. Kohl, A. Potapenko, A. Ballard, A. Cowie, B. Romera-Paredes, S. Mikolov, R. Jain, J. Adler, T. Back, S. Petersen, D. Reiman, M. Steinegger, M. Pacholska, D. Silver, O. Vinyals, A. Senior, K. Kavukcuoglu, P. Kohli, D. Hassabis, High accuracy protein structure prediction using deep learning, (2020). https://predictioncenter.org/casp14/doc/CASP14_Abstracts.pdf.
22. Kryshtafovych, A., Schwede, T., Topf, M., Fidelis, K., Moult, J., (2019). Critical assessment of methods of protein structure prediction (CASP)—Round XIII. *Proteins Struct. Funct. Bioinforma.*, **87**, 1011–1020. https://doi.org/10.1002/prot.25823.
23. Moult, J., Fidelis, K., Kryshtafovych, A., Schwede, T., Tramontano, A., (2018). Critical assessment of methods of protein structure prediction (CASP)-Round XII. *Proteins.*, **86** (Suppl 1), 7–15. https://doi.org/10.1002/prot.25415.
24. Anfinsen, C.B., (1973). Principles that govern the folding of protein chains. *Science*, **181**, 223–230. https://doi.org/10.1126/science.181.4096.223.
25. Aubrey, L.D., Blakeman, B.J.F., Lutter, L., Serpell, C.J., Tuite, M.F., Serpell, L.C., Xue, W.-F., (2020). Quantification of amyloid fibril polymorphism by nano-morphometry reveals the individuality of filament assembly. *Commun. Chem.*, **3**, 1–10. https://doi.org/10.1038/s42004-020-00372-3.
26. Li, D., Liu, C., (2021). Hierarchical chemical determination of amyloid polymorphs in neurodegenerative disease. *Nat. Chem. Biol.*, **17**, 237–245. https://doi.org/10.1038/s41589-020-00708-z.
27. Lutter, L., Serpell, C.J., Tuite, M.F., Xue, W.-F., (2019). The molecular lifecycle of amyloid – Mechanism of assembly, mesoscopic organisation, polymorphism, suprastructures, and biological consequences. *Biochim. Biophys. Acta BBA - Proteins Proteomics.*, **1867**, https://doi.org/10.1016/j.bbapap.2019.07.010 140257.
28. Guzenko, D., Lafita, A., Monastyrskyy, B., Kryshtafovych, A., Duarte, J.M., (2019). Assessment of protein assembly prediction in CASP13. *Proteins Struct. Funct. Bioinforma.*, **87**, 1190–1199. https://doi.org/10.1002/prot.25795.
29. Fernandez-Escamilla, A.-M., Rousseau, F., Schymkowitz, J., Serrano, L., (2004). Prediction of sequence-dependent and mutational effects on the aggregation of peptides and proteins. *Nat. Biotechnol.*, **22**, 1302–1306. https://doi.org/10.1038/nbt1012.
30. Maurer-Stroh, S., Debulpaep, M., Kuemmerer, N., de la Paz, M.L., Martins, I.C., Reumers, J., Morris, K.L., Copland, A., Serpell, L., Serrano, L., Schymkowitz, J.W.H., Rousseau, F., (2010). Exploring the sequence determinants of amyloid structure using position-specific scoring matrices. *Nat. Methods.*, **7**, 237–242. https://doi.org/10.1038/nmeth.1432.
31. Walsh, I., Seno, F., Tosatto, S.C.E., Trovato, A., (2014). PASTA 2.0: an improved server for protein aggregation prediction. *Nucleic Acids Res.*, **42**, W301–W307. https://doi.org/10.1093/nar/gku399.
32. Roland, B.P., Kodali, R., Mishra, R., Wetzel, R., (2013). A serendipitous survey of prediction algorithms for amyloidogenicity. *Biopolymers*, **100**, 780–789. https://doi.org/10.1002/bip.22305.
33. Santos, J., Pujols, J., Pallarès, I., Iglesias, V., Ventura, S., (2020). Computational prediction of protein aggregation: Advances in proteomics, conformation-specific algorithms and biotechnological applications. *Comput. Struct. Biotechnol. J.*, **18**, 1403–1413. https://doi.org/10.1016/j.csbj.2020.05.026.
34. Jahn, T.R., Makin, O.S., Morris, K.L., Marshall, K.E., Tian, P., Sikorski, P., Serpell, L.C., (2010). The common

architecture of cross-β amyloid. *J. Mol. Biol.*, **395**, 717–727. https://doi.org/10.1016/j.jmb.2009.09.039.
35. Sawaya, M.R., Sambashivan, S., Nelson, R., Ivanova, M. I., Sievers, S.A., Apostol, M.I., Thompson, M.J., Balbirnie, M., Wiltzius, J.J.W., McFarlane, H.T., Madsen, A.Ø., Riekel, C., Eisenberg, D., (2007). Atomic structures of amyloid cross-β spines reveal varied steric zippers. *Nature*, **447**, 453–457. https://doi.org/10.1038/nature05695.
36. Rodriguez, J.A., Ivanova, M.I., Sawaya, M.R., Cascio, D., Reyes, F.E., Shi, D., Sangwan, S., Guenther, E.L., Johnson, L.M., Zhang, M., Jiang, L., Arbing, M.A., Nannenga, B.L., Hattne, J., Whitelegge, J., Brewster, A. S., Messerschmidt, M., Boutet, S., Sauter, N.K., Gonen, T., Eisenberg, D.S., (2015). Structure of the toxic core of α-synuclein from invisible crystals. *Nature*, **525**, 486–490. https://doi.org/10.1038/nature15368.
37. Scheres, S.H.W., (2020). Amyloid structure determination in RELION-3.1, Acta Crystallogr. *Sect. Struct. Biol.*, **76**, 94–101. https://doi.org/10.1107/S2059798319016577.
38. Arakhamia, T., Lee, C.E., Carlomagno, Y., Duong, D.M., Kundinger, S.R., Wang, K., Williams, D., DeTure, M., Dickson, D.W., Cook, C.N., Seyfried, N.T., Petrucelli, L., Fitzpatrick, A.W.P., (2020). Posttranslational modifications mediate the structural diversity of tauopathy strains. *Cell*, **180**, 633–644.e12. https://doi.org/10.1016/j.cell.2020.01.027.
39. Bansal, A., Schmidt, M., Rennegarbe, M., Haupt, C., Liberta, F., Stecher, S., Puscalau-Girtu, I., Biedermann, A., Fändrich, M., (2021). AA amyloid fibrils from diseased tissue are structurally different from in vitro formed SAA fibrils. *Nat. Commun.*, **12**, 1013. https://doi.org/10.1038/s41467-021-21129-z.
40. Lövestam, S., Schweighauser, M., Matsubara, T., Murayama, S., Tomita, T., Ando, T., Hasegawa, K., Yoshida, M., Tarutani, A., Hasegawa, M., Goedert, M., Scheres, S.H.W., (2021). Seeded assembly *in vitro* does not replicate the structures of α-synuclein filaments from multiple system atrophy. *FEBS Open Bio*,. https://doi.org/10.1002/2211-5463.13110.
41. Meisl, G., Yang, X., Hellstrand, E., Frohm, B., Kirkegaard, J.B., Cohen, S.I.A., Dobson, C.M., Linse, S., Knowles, T. P.J., (2014). Differences in nucleation behavior underlie the contrasting aggregation kinetics of the Aβ40 and Aβ42 peptides. *Proc. Natl. Acad. Sci.*, **111**, 9384–9389. https://doi.org/10.1073/pnas.1401564111.
42. N. Koloteva-Levine, R. Marchante, T.J. Purton, J.R. Hiscock, M.F. Tuite, W.-F. Xue, Amyloid particles facilitate surface-catalyzed cross-seeding by acting as promiscuous nanoparticles, BioRxiv. (2020) 2020.09.01.278481. https://doi.org/10.1101/2020.09.01.278481.
43. Peduzzo, A., Linse, S., Buell, A.K., (2020). The properties of α-synuclein secondary nuclei are dominated by the solution conditions rather than the seed fibril strain. *ACS Chem. Neurosci.*, **11**, 909–918. https://doi.org/10.1021/acschemneuro.9b00594.
44. Adamcik, J., Mezzenga, R., (2012). Study of amyloid fibrils via atomic force microscopy. *Curr. Opin. Colloid Interface Sci.*, **17**, 369–376. https://doi.org/10.1016/j.cocis.2012.08.001.
45. Fändrich, M., Meinhardt, J., Grigorieff, N., (2009). Structural polymorphism of Alzheimer Aβ and other amyloid fibrils. *Prion.*, **3**, 89–93. https://doi.org/10.4161/pri.3.2.8859.
46. Goldsbury, C., Frey, P., Olivieri, V., Aebi, U., Müller, S.A., (2005). Multiple assembly pathways underlie amyloid-β fibril polymorphisms. *J. Mol. Biol.*, **352**, 282–298. https://doi.org/10.1016/j.jmb.2005.07.029.
47. Jiménez, J.L., Nettleton, E.J., Bouchard, M., Robinson, C. V., Dobson, C.M., Saibil, H.R., (2002). The protofilament structure of insulin amyloid fibrils. *Proc. Natl. Acad. Sci. U. S. A.*, **99**, 9196–9201. https://doi.org/10.1073/pnas.142459399.
48. Kad, N.M., Myers, S.L., Smith, D.P., Alastair Smith, D., Radford, S.E., Thomson, N.H., (2003). Hierarchical assembly of β2-microglobulin amyloid *in vitro* revealed by atomic force microscopy. *J. Mol. Biol.*, **330**, 785–797. https://doi.org/10.1016/S0022-2836(03)00583-7.
49. Adamcik, J., Jung, J.-M., Flakowski, J., De Los Rios, P., Dietler, G., Mezzenga, R., (2010). Understanding amyloid aggregation by statistical analysis of atomic force microscopy images. *Nat. Nanotechnol.*, **5**, 423–428. https://doi.org/10.1038/nnano.2010.59.
50. Ruggeri, F.S., Flagmeier, P., Kumita, J.R., Meisl, G., Chirgadze, D.Y., Bongiovanni, M.N., Knowles, T.P.J., Dobson, C.M., (2020). The influence of pathogenic mutations in α-synuclein on biophysical and structural characteristics of amyloid fibrils. *ACS Nano*, **14**, 5213–5222. https://doi.org/10.1021/acsnano.9b09676.
51. Qiang, W., Kelley, K., Tycko, R., (2013). Polymorph-specific kinetics and thermodynamics of β-amyloid fibril growth. *J. Am. Chem. Soc.*, **135**, 6860–6871. https://doi.org/10.1021/ja311963f.
52. Watanabe-Nakayama, T., Ono, K., Itami, M., Takahashi, R., Teplow, D.B., Yamada, M., (2016). High-speed atomic force microscopy reveals structural dynamics of amyloid β_{1-42} aggregates. *Proc. Natl. Acad. Sci.*, **113**, 5835–5840. https://doi.org/10.1073/pnas.1524807113.
53. Gallardo, R., Iadanza, M.G., Xu, Y., Heath, G.R., Foster, R., Radford, S.E., Ranson, N.A., (2020). Fibril structures of diabetes-related amylin variants reveal a basis for surface-templated assembly. *Nat. Struct. Mol. Biol.*, **27**, 1048–1056. https://doi.org/10.1038/s41594-020-0496-3.
54. Fitzpatrick, A.W.P., Debelouchina, G.T., Bayro, M.J., Clare, D.K., Caporini, M.A., Bajaj, V.S., Jaroniec, C.P., Wang, L., Ladizhansky, V., Müller, S.A., MacPhee, C.E., Waudby, C.A., Mott, H.R., Simone, A.D., Knowles, T.P.J., Saibil, H.R., Vendruscolo, M., Orlova, E.V., Griffin, R.G., Dobson, C.M., (2013). Atomic structure and hierarchical assembly of a cross-β amyloid fibril. *Proc. Natl. Acad. Sci.*, **110**, 5468–5473. https://doi.org/10.1073/pnas.1219476110.
55. Makarava, N., Ostapchenko, V.G., Savtchenko, R., Baskakov, I.V., (2009). Conformational switching within individual amyloid fibrils. *J. Biol. Chem.*, **284**, 14386–14395. https://doi.org/10.1074/jbc.M900533200.
56. Kollmer, M., Close, W., Funk, L., Rasmussen, J., Bsoul, A., Schierhorn, A., Schmidt, M., Sigurdson, C.J., Jucker, M., Fändrich, M., (2019). Cryo-EM structure and polymorphism of Aβ amyloid fibrils purified from Alzheimer's brain tissue. *Nat. Commun.*, **10** https://doi.org/10.1038/s41467-019-12683-8.
57. Radamaker, L., Baur, J., Huhn, S., Haupt, C., Hegenbart, U., Schönland, S., Bansal, A., Schmidt, M., Fändrich, M., (2021). Cryo-EM reveals structural breaks in a patient-derived amyloid fibril from systemic AL amyloidosis. *Nat.*

Commun., **12**, 875. https://doi.org/10.1038/s41467-021-21126-2.
58. Al-Hilaly, Y.K., Foster, B.E., Biasetti, L., Lutter, L., Pollack, S.J., Rickard, J.E., Storey, J.M.D., Harrington, C.R., Xue, W.-F., Wischik, C.M., Serpell, L.C., (2020). Tau (297–391) forms filaments that structurally mimic the core of paired helical filaments in Alzheimer's disease brain. *FEBS Lett.*, **594**, 944–950. https://doi.org/10.1002/1873-3468.13675.
59. Pansieri, J., Halim, M.A., Vendrely, C., Dumoulin, M., Legrand, F., Sallanon, M.M., Chierici, S., Denti, S., Dagany, X., Dugourd, P., Marquette, C., Antoine, R., Forge, V., (2018). Mass and charge distributions of amyloid fibers involved in neurodegenerative diseases: mapping heterogeneity and polymorphism. *Chem. Sci.*, **9**, 2791–2796. https://doi.org/10.1039/C7SC04542E.
60. Knowles, T.P., Fitzpatrick, A.W., Meehan, S., Mott, H.R., Vendruscolo, M., Dobson, C.M., Welland, M.E., (2007). Role of intermolecular forces in defining material properties of protein nanofibrils. *Science*, **318**, 1900–1903. https://doi.org/10.1126/science.1150057.
61. Beal, D.M., Tournus, M., Marchante, R., Purton, T.J., Smith, D.P., Tuite, M.F., Doumic, M., Xue, W.-F., (2020). The division of amyloid fibrils: Systematic comparison of fibril fragmentation stability by linking theory with experiments. *IScience.*, **23**, https://doi.org/10.1016/j.isci.2020.101512 101512.
62. Marchante, R., Beal, D.M., Koloteva-Levine, N., Purton, T. J., Tuite, M.F., Xue, W.-F., (2017). The physical dimensions of amyloid aggregates control their infective potential as prion particles. *ELife.*, **6**, https://doi.org/10.7554/eLife.27109 e27109.
63. Atarashi, R., Sim, V.L., Nishida, N., Caughey, B., Katamine, S., (2006). Prion strain-dependent differences in conversion of mutant prion proteins in cell culture. *J. Virol.*, **80**, 7854–7862. https://doi.org/10.1128/JVI.00424-06.
64. Bateman, D.A., Wickner, R.B., (2013). The *PSI*$^{+}$ prion exists as a dynamic cloud of variants. *PLOS Genet.*, **9**, https://doi.org/10.1371/journal.pgen.1003257 e1003257.
65. Bruce, M.E., McConnell, I., Fraser, H., Dickinson, A.G., (1991). The disease characteristics of different strains of scrapie in *Sinc* congenic mouse lines: implications for the nature of the agent and host control of pathogenesis. *J. Gen. Virol.*, **72** (Pt 3), 595–603. https://doi.org/10.1099/0022-1317-72-3-595.
66. Hannaoui, S., Maatouk, L., Privat, N., Levavasseur, E., Faucheux, B.A., Haïk, S., (2013). Prion propagation and toxicity occur *in vitro* with two-phase kinetics specific to strain and neuronal type. *J. Virol.*, **87**, 2535–2548. https://doi.org/10.1128/JVI.03082-12.
67. Cohen, S.I.A., Arosio, P., Presto, J., Kurudenkandy, F.R., Biverstål, H., Dolfe, L., Dunning, C., Yang, X., Frohm, B., Vendruscolo, M., Johansson, J., Dobson, C.M., Fisahn, A., Knowles, T.P.J., Linse, S., (2015). A molecular chaperone breaks the catalytic cycle that generates toxic Aβ oligomers. *Nat. Struct. Mol. Biol.*, **22**, 207–213. https://doi.org/10.1038/nsmb.2971.
68. Michaels, T.C.T., Šarić, A., Meisl, G., Heller, G.T., Curk, S., Arosio, P., Linse, S., Dobson, C.M., Vendruscolo, M., Knowles, T.P.J., (2020). Thermodynamic and kinetic design principles for amyloid-aggregation inhibitors. *Proc. Natl. Acad. Sci.*, **117**, 24251–24257. https://doi.org/10.1073/pnas.2006684117.
69. Campioni, S., Carret, G., Jordens, S., Nicoud, L., Mezzenga, R., Riek, R., (2014). The presence of an air–water interface affects formation and elongation of α-synuclein fibrils. *J. Am. Chem. Soc.*, **136**, 2866–2875. https://doi.org/10.1021/ja412105t.
70. Grigolato, F., Arosio, P., (2021). The role of surfaces on amyloid formation. *Biophys. Chem.*, **270**, https://doi.org/10.1016/j.bpc.2020.106533 106533.
71. Bode, D.C., Baker, M.D., Viles, J.H., (2017). Ion channel formation by amyloid-β_{42} oligomers but not amyloid-β_{40} in cellular membranes. *J. Biol. Chem.*, **292**, 1404–1413. https://doi.org/10.1074/jbc.M116.762526.
72. Butterfield, S.M., Lashuel, H.A., (2010). Amyloidogenic protein–membrane interactions: Mechanistic insight from model systems. *Angew. Chem. Int. Ed.*, **49**, 5628–5654. https://doi.org/10.1002/anie.200906670.
73. Milanesi, L., Sheynis, T., Xue, W.-F., Orlova, E.V., Hellewell, A.L., Jelinek, R., Hewitt, E.W., Radford, S.E., Saibil, H.R., (2012). Direct three-dimensional visualization of membrane disruption by amyloid fibrils. *Proc. Natl. Acad. Sci.*, **109**, 20455–20460. https://doi.org/10.1073/pnas.1206325109.
74. Monsellier, E., Bousset, L., Melki, R., (2016). α-Synuclein and huntingtin exon 1 amyloid fibrils bind laterally to the cellular membrane. *Sci. Rep.*, **6**, 19180. https://doi.org/10.1038/srep19180.
75. Sciacca, M.F.M., Tempra, C., Scollo, F., Milardi, D., La Rosa, C., (1860). Amyloid growth and membrane damage: Current themes and emerging perspectives from theory and experiments on Aβ and hIAPP. *Biochim. Biophys. Acta BBA - Biomembr.*, **2018**, 1625–1638. https://doi.org/10.1016/j.bbamem.2018.02.022.
76. Lindberg, D.J., Wesén, E., Björkeroth, J., Rocha, S., Esbjörner, E.K., (1859). Lipid membranes catalyse the fibril formation of the amyloid-β (1–42) peptide through lipid-fibril interactions that reinforce secondary pathways. *Biochim. Biophys. Acta Biomembr.*, **2017**, 1921–1929. https://doi.org/10.1016/j.bbamem.2017.05.012.
77. A. Vahdat Shariat Panahi, P. Hultman, K. Öllinger, G.T. Westermark, K. Lundmark, Lipid membranes accelerate amyloid formation in the mouse model of AA amyloidosis, Amyloid Int. J. Exp. Clin. Investig. Off. J. Int. Soc. Amyloidosis. 26 (2019) 34–44. https://doi.org/10.1080/13506129.2019.1576606.
78. Sparr, E., Engel, M.F.M., Sakharov, D.V., Sprong, M., Jacobs, J., de Kruijff, B., Höppener, J.W.M., Killian, J.A., (2004). Islet amyloid polypeptide-induced membrane leakage involves uptake of lipids by forming amyloid fibers. *FEBS Lett.*, **577**, 117–120. https://doi.org/10.1016/j.febslet.2004.09.075.
79. Engel, M.F.M., Khemtémourian, L., Kleijer, C.C., Meeldijk, H.J.D., Jacobs, J., Verkleij, A.J., de Kruijff, B., Killian, J.A., Höppener, J.W.M., (2008). Membrane damage by human islet amyloid polypeptide through fibril growth at the membrane. *Proc. Natl. Acad. Sci.*, **105**, 6033–6038. https://doi.org/10.1073/pnas.0708354105.
80. Flagmeier, P., De, S., Michaels, T.C.T., Yang, X., Dear, A. J., Emanuelsson, C., Vendruscolo, M., Linse, S., Klenerman, D., Knowles, T.P.J., Dobson, C.M., (2020). Direct measurement of lipid membrane disruption connects kinetics and toxicity of Aβ42 aggregation. *Nat. Struct. Mol. Biol.*, **27**, 886–891. https://doi.org/10.1038/s41594-020-0471-z.

81. Rovere, M., Sanderson, J.B., Fonseca-Ornelas, L., Patel, D.S., Bartels, T., (2018). Refolding of helical soluble α-synuclein through transient interaction with lipid interfaces. *FEBS Lett.*, **592**, 1464–1472. https://doi.org/10.1002/1873-3468.13047.
82. Sasahara, K., Morigaki, K., Okazaki, T., Hamada, D., (2012). Binding of islet amyloid polypeptide to supported lipid bilayers and amyloid aggregation at the membranes. *Biochemistry*, **51**, 6908–6919. https://doi.org/10.1021/bi300542g.
83. Kakio, A., Nishimoto, S., Yanagisawa, K., Kozutsumi, Y., Matsuzaki, K., (2002). Interactions of amyloid β-protein with various gangliosides in raft-like membranes: Importance of GM1 ganglioside-bound form as an endogenous seed for Alzheimer amyloid. *Biochemistry*, **41**, 7385–7390. https://doi.org/10.1021/bi0255874.
84. Goedert, M., Jakes, R., Spillantini, M.G., Hasegawa, M., Smith, M.J., Crowther, R.A., (1996). Assembly of microtubule-associated protein tau into Alzheimer-like filaments induced by sulphated glycosaminoglycans. *Nature*, **383**, 550–553. https://doi.org/10.1038/383550a0.
85. Lu, J., Cao, Q., Hughes, M.P., Sawaya, M.R., Boyer, D. R., Cascio, D., Eisenberg, D.S., (2020). CryoEM structure of the low-complexity domain of hnRNPA2 and its conversion to pathogenic amyloid. *Nat. Commun.*, **11**, 4090. https://doi.org/10.1038/s41467-020-17905-y.
86. Ulamec, S.M., Radford, S.E., (2020). Spot the difference: Function versus toxicity in amyloid fibrils. *Trends Biochem. Sci.*,. https://doi.org/10.1016/j.tibs.2020.04.007.
87. Hervas, R., Rau, M.J., Park, Y., Zhang, W., Murzin, A.G., Fitzpatrick, J.A.J., Scheres, S.H.W., Si, K., (2020). Cryo-EM structure of a neuronal functional amyloid implicated in memory persistence in *Drosophila*. *Science*, **367**, 1230–1234. https://doi.org/10.1126/science.aba3526.
88. Murray, D.T., Kato, M., Lin, Y., Thurber, K.R., Hung, I., McKnight, S.L., Tycko, R., (2017). Structure of FUS protein fibrils and its relevance to self-assembly and phase separation of low-complexity domains. *Cell*, **171**, 615–627.e16. https://doi.org/10.1016/j.cell.2017.08.048.
89. Brettschneider, J., Tredici, K.D., Lee, V.M.-Y., Trojanowski, J.Q., (2015). Spreading of pathology in neurodegenerative diseases: a focus on human studies. *Nat. Rev. Neurosci.*, **16**, 109–120. https://doi.org/10.1038/nrn3887.
90. Katsumoto, A., Takeuchi, H., Tanaka, F., (2019). Tau pathology in chronic traumatic encephalopathy and Alzheimer's disease: Similarities and differences. *Front. Neurol.*, **10** https://doi.org/10.3389/fneur.2019.00980.
91. Falcon, B., Zhang, W., Murzin, A.G., Murshudov, G., Garringer, H.J., Vidal, R., Crowther, R.A., Ghetti, B., Scheres, S.H.W., Goedert, M., (2018). Structures of filaments from Pick's disease reveal a novel tau protein fold. *Nature*,, 1. https://doi.org/10.1038/s41586-018-0454-y.
92. Falcon, B., Zhang, W., Schweighauser, M., Murzin, A.G., Vidal, R., Garringer, H.J., Ghetti, B., Scheres, S.H.W., Goedert, M., (2018). Tau filaments from multiple cases of sporadic and inherited Alzheimer's disease adopt a common fold. *Acta Neuropathol. (Berl.)*, **136**, 699–708. https://doi.org/10.1007/s00401-018-1914-z.
93. Qiang, W., Yau, W.-M., Lu, J.-X., Collinge, J., Tycko, R., (2017). Structural variation in amyloid-β fibrils from Alzheimer's disease clinical subtypes. *Nature*, **541**, 217–221. https://doi.org/10.1038/nature20814.
94. Cohen, M.L., Kim, C., Haldiman, T., ElHag, M., Mehndiratta, P., Pichet, T., Lissemore, F., Shea, M., Cohen, Y., Chen, W., Blevins, J., Appleby, B.S., Surewicz, K., Surewicz, W.K., Sajatovic, M., Tatsuoka, C., Zhang, S., Mayo, P., Butkiewicz, M., Haines, J.L., Lerner, A.J., Safar, J.G., (2015). Rapidly progressive Alzheimer's disease features distinct structures of amyloid-β. *Brain J. Neurol.*, **138**, 1009–1022. https://doi.org/10.1093/brain/awv006.
95. Nokwe, C.N., Hora, M., Zacharias, M., Yagi, H., Peschek, J., Reif, B., Goto, Y., Buchner, J., (2016). A stable mutant predisposes antibody domains to amyloid formation through specific non-native interactions. *J. Mol. Biol.*, **428**, 1315–1332. https://doi.org/10.1016/j.jmb.2016.01.015.
96. Abraham, R.S., Geyer, S.M., Price-Troska, T.L., Allmer, C., Kyle, R.A., Gertz, M.A., Fonseca, R., (2003). Immunoglobulin light chain variable (V) region genes influence clinical presentation and outcome in light chain–associated amyloidosis (AL). *Blood*, **101**, 3801–3807. https://doi.org/10.1182/blood-2002-09-2707.
97. R. Sternke-Hoffmann, T. Pauly, R.K. Norrild, J. Hansen, M. Dupré, F. Tucholski, M. Duchateau, M. Rey, S. Metzger, A. Boquoi, F. Platten, S.U. Egelhaaf, J. Chamot-Rooke, R. Fenk, L. Nagel-Steger, R. Haas, A.K. Buell, Universal amyloidogenicity of patient-derived immunoglobulin light chains, BioRxiv. (2021) 2021.05.12.443858. https://doi.org/10.1101/2021.05.12.443858.
98. Radamaker, L., Lin, Y.-H., Annamalai, K., Huhn, S., Hegenbart, U., Schönland, S.O., Fritz, G., Schmidt, M., Fändrich, M., (2019). Cryo-EM structure of a light chain-derived amyloid fibril from a patient with systemic AL amyloidosis. *Nat. Commun.*, **10**, 1103. https://doi.org/10.1038/s41467-019-09032-0.
99. Swuec, P., Lavatelli, F., Tasaki, M., Paissoni, C., Rognoni, P., Maritan, M., Brambilla, F., Milani, P., Mauri, P., Camilloni, C., Palladini, G., Merlini, G., Ricagno, S., Bolognesi, M., (2019). Cryo-EM structure of cardiac amyloid fibrils from an immunoglobulin light chain AL amyloidosis patient. *Nat. Commun.*, **10**, 1269. https://doi.org/10.1038/s41467-019-09133-w.
100. Blancas-Mejia, L.M., Misra, P., Dick, C.J., Cooper, S.A., Redhage, K.R., Bergman, M.R., Jordan, T.L., Maar, K., Ramirez-Alvarado, M., (2018). Immunoglobulin light chain amyloid aggregation. *Chem. Commun. Camb. Engl.*, **54**, 10664–10674. https://doi.org/10.1039/c8cc04396e.
101. Zhang, W., Falcon, B., Murzin, A.G., Fan, J., Crowther, R. A., Goedert, M., Scheres, S.H., (2019). Heparin-induced tau filaments are polymorphic and differ from those in Alzheimer's and Pick's diseases. *ELife.*, **8**, https://doi.org/10.7554/eLife.43584 e43584.
102. Solomon, A., Weiss, D.T., Murphy, C.L., Hrncic, R., Wall, J.S., Schell, M., (1998). Light chain-associated amyloid deposits comprised of a novel κ constant domain. *Proc. Natl. Acad. Sci.*, **95**, 9547–9551. https://doi.org/10.1073/pnas.95.16.9547.
103. Griner, S.L., Seidler, P., Bowler, J., Murray, K.A., Yang, T. P., Sahay, S., Sawaya, M.R., Cascio, D., Rodriguez, J.A., Philipp, S., Sosna, J., Glabe, C.G., Gonen, T., Eisenberg, D.S., (2019). Structure-based inhibitors of amyloid beta core suggest a common interface with tau. *ELife.*, **8**, https://doi.org/10.7554/eLife.46924 e46924.

104. Pettersen, E.F., Goddard, T.D., Huang, C.C., Couch, G. S., Greenblatt, D.M., Meng, E.C., Ferrin, T.E., (2004). UCSF Chimera–a visualization system for exploratory research and analysis. *J. Comput. Chem.*, **25**, 1605–1612. https://doi.org/10.1002/jcc.20084.
105. Ghosh, U., Thurber, K.R., Yau, W.-M., Tycko, R., (2021). Molecular structure of a prevalent amyloid-β fibril polymorph from Alzheimer's disease brain tissue. *Proc. Natl. Acad. Sci.*, **118**, https://doi.org/10.1073/pnas.2023089118 e2023089118.
106. Cerofolini, L., Ravera, E., Bologna, S., Wiglenda, T., Böddrich, A., Purfürst, B., Benilova, I., Korsak, M., Gallo, G., Rizzo, D., Gonnelli, L., Fragai, M., Strooper, B.D., Wanker, E.E., Luchinat, C., (2020). Mixing Aβ(1–40) and Aβ(1–42) peptides generates unique amyloid fibrils. *Chem. Commun.*, **56**, 8830–8833. https://doi.org/10.1039/D0CC02463E.
107. Hu, Z.-W., Vugmeyster, L., Au, D.F., Ostrovsky, D., Sun, Y., Qiang, W., (2019). Molecular structure of an N-terminal phosphorylated β-amyloid fibril. *Proc. Natl. Acad. Sci.*, **116**, 11253–11258. https://doi.org/10.1073/pnas.1818530116.
108. Rohou, A., Grigorieff, N., (2014). Frealix: Model-based refinement of helical filament structures from electron micrographs. *J. Struct. Biol.*, **186**, 234–244. https://doi.org/10.1016/j.jsb.2014.03.012.
109. Sgourakis, N.G., Yau, W.-M., Qiang, W., (2015). Modeling an in-register, parallel "Iowa" Aβ fibril structure using solid-state NMR data from labeled samples with Rosetta. *Structure.*, **23**, 216–227. https://doi.org/10.1016/j.str.2014.10.022.
110. Schütz, A.K., Vagt, T., Huber, M., Ovchinnikova, O.Y., Cadalbert, R., Wall, J., Güntert, P., Böckmann, A., Glockshuber, R., Meier, B.H., (2015). Atomic-resolution three-dimensional structure of amyloid β fibrils bearing the Osaka mutation. *Angew. Chem. Int. Ed.*, **54**, 331–335. https://doi.org/10.1002/anie.201408598.
111. Lu, J.-X., Qiang, W., Yau, W.-M., Schwieters, C.D., Meredith, S.C., Tycko, R., (2013). Molecular structure of β-amyloid fibrils in Alzheimer's disease brain tissue. *Cell*, **154**, 1257–1268. https://doi.org/10.1016/j.cell.2013.08.035.
112. Qiang, W., Yau, W.-M., Luo, Y., Mattson, M.P., Tycko, R., (2012). Antiparallel β-sheet architecture in Iowa-mutant β-amyloid fibrils. *Proc. Natl. Acad. Sci.*, **109**, 4443–4448. https://doi.org/10.1073/pnas.1111305109.
113. Paravastu, A.K., Leapman, R.D., Yau, W.-M., Tycko, R., (2008). Molecular structural basis for polymorphism in Alzheimer's β-amyloid fibrils. *Proc. Natl. Acad. Sci.*, **105**, 18349–18354. https://doi.org/10.1073/pnas.0806270105.
114. Sachse, C., Fändrich, M., Grigorieff, N., (2008). Paired β-sheet structure of an Aβ(1–40) amyloid fibril revealed by electron microscopy. *Proc. Natl. Acad. Sci. U. S. A.*, **105**, 7462–7466. https://doi.org/10.1073/pnas.0712290105.
115. Sachse, C., Grigorieff, N., Fändrich, M., (2010). Nanoscale flexibility parameters of Alzheimer amyloid fibrils determined by electron cryo-microscopy. *Angew. Chem. Int. Ed Engl.*, **49**, 1321–1323. https://doi.org/10.1002/anie.200904781.
116. Schmidt, M., Sachse, C., Richter, W., Xu, C., Fändrich, M., Grigorieff, N., (2009). Comparison of Alzheimer Aβ(1–40) and Aβ(1–42) amyloid fibrils reveals similar protofilament structures. *Proc. Natl. Acad. Sci.*, **106**, 19813–19818. https://doi.org/10.1073/pnas.0905007106.
117. Gremer, L., Schölzel, D., Schenk, C., Reinartz, E., Labahn, J., Ravelli, R.B.G., Tusche, M., Lopez-Iglesias, C., Hoyer, W., Heise, H., Willbold, D., Schröder, G.F., (2017). Fibril structure of amyloid-β(1–42) by cryo–electron microscopy. *Science*, **358**, 116–119. https://doi.org/10.1126/science.aao2825.
118. Wälti, M.A., Ravotti, F., Arai, H., Glabe, C.G., Wall, J.S., Böckmann, A., Güntert, P., Meier, B.H., Riek, R., (2016). Atomic-resolution structure of a disease-relevant Aβ(1–42) amyloid fibril. *Proc. Natl. Acad. Sci.*, **113**, E4976–E4984. https://doi.org/10.1073/pnas.1600749113.
119. Colvin, M.T., Silvers, R., Ni, Q.Z., Can, T.V., Sergeyev, I., Rosay, M., Donovan, K.J., Michael, B., Wall, J., Linse, S., Griffin, R.G., (2016). Atomic resolution structure of monomorphic $A\beta_{42}$ amyloid fibrils. *J. Am. Chem. Soc.*, **138**, 9663–9674. https://doi.org/10.1021/jacs.6b05129.
120. Schmidt, M., Rohou, A., Lasker, K., Yadav, J.K., Schiene-Fischer, C., Fändrich, M., Grigorieff, N., (2015). Peptide dimer structure in an Aβ(1–42) fibril visualized with cryo-EM. *Proc. Natl. Acad. Sci.*, **112**, 11858–11863. https://doi.org/10.1073/pnas.1503455112.
121. Xiao, Y., Ma, B., McElheny, D., Parthasarathy, S., Long, F., Hoshi, M., Nussinov, R., Ishii, Y., (2015). Aβ(1–42) fibril structure illuminates self-recognition and replication of amyloid in Alzheimer's disease. *Nat. Struct. Mol. Biol.*, **22**, 499–505. https://doi.org/10.1038/nsmb.2991.
122. Zhang, R., Hu, X., Khant, H., Ludtke, S.J., Chiu, W., Schmid, M.F., Frieden, C., Lee, J.-M., (2009). Interprotofilament interactions between Alzheimer's $A\beta_{1-42}$ peptides in amyloid fibrils revealed by cryoEM. *Proc. Natl. Acad. Sci.*, **106**, 4653–4658. https://doi.org/10.1073/pnas.0901085106.
123. Lührs, T., Ritter, C., Adrian, M., Riek-Loher, D., Bohrmann, B., Döbeli, H., Schubert, D., Riek, R., (2005). 3D structure of Alzheimer's amyloid-β(1–42) fibrils. *Proc. Natl. Acad. Sci.*, **102**, 17342–17347. https://doi.org/10.1073/pnas.0506723102.
124. Zhao, K., Lim, Y.-J., Liu, Z., Long, H., Sun, Y., Hu, J.-J., Zhao, C., Tao, Y., Zhang, X., Li, D., Li, Y.-M., Liu, C., (2020). Parkinson's disease-related phosphorylation at Tyr39 rearranges α-synuclein amyloid fibril structure revealed by cryo-EM. *Proc. Natl. Acad. Sci.*, **117**, 20305–20315. https://doi.org/10.1073/pnas.1922741117.
125. Zhao, K., Li, Y., Liu, Z., Long, H., Zhao, C., Luo, F., Sun, Y., Tao, Y., Su, X., Li, D., Li, X., Liu, C., (2020). Parkinson's disease associated mutation E46K of α-synuclein triggers the formation of a distinct fibril structure. *Nat. Commun.*, **11** https://doi.org/10.1038/s41467-020-16386-3.
126. Sun, Y., Hou, S., Zhao, K., Long, H., Liu, Z., Gao, J., Zhang, Y., Su, X.-D., Li, D., Liu, C., (2020). Cryo-EM structure of full-length α-synuclein amyloid fibril with Parkinson's disease familial A53T mutation. *Cell Res.*, **30**, 360–362. https://doi.org/10.1038/s41422-020-0299-4.
127. Boyer, D.R., Li, B., Sun, C., Fan, W., Zhou, K., Hughes, M.P., Sawaya, M.R., Jiang, L., Eisenberg, D.S., (2020). The α-synuclein hereditary mutation E46K unlocks a more stable, pathogenic fibril structure. *Proc. Natl. Acad. Sci.*, **117**, 3592–3602. https://doi.org/10.1073/pnas.1917914117.
128. Schweighauser, M., Shi, Y., Tarutani, A., Kametani, F., Murzin, A.G., Ghetti, B., Matsubara, T., Tomita, T., Ando, T., Hasegawa, K., Murayama, S., Yoshida, M., Hasegawa, M., Scheres, S.H.W., Goedert, M., (2020).

Structures of α-synuclein filaments from multiple system atrophy. *Nature*, **585**, 464–469. https://doi.org/10.1038/s41586-020-2317-6.
129. Guerrero-Ferreira, R., Taylor, N.M., Arteni, A.-A., Kumari, P., Mona, D., Ringler, P., Britschgi, M., Lauer, M.E., Makky, A., Verasdonck, J., Riek, R., Melki, R., Meier, B. H., Böckmann, A., Bousset, L., Stahlberg, H., (2019). Two new polymorphic structures of human full-length alpha-synuclein fibrils solved by cryo-electron microscopy. *ELife.*, **8**, https://doi.org/10.7554/eLife.48907 e48907.
130. Boyer, D.R., Li, B., Sun, C., Fan, W., Sawaya, M.R., Jiang, L., Eisenberg, D.S., (2019). Structures of fibrils formed by α-synuclein hereditary disease mutant H50Q reveal new polymorphs. *Nat. Struct. Mol. Biol.*, **26**, 1044–1052. https://doi.org/10.1038/s41594-019-0322-y.
131. Ni, X., McGlinchey, R.P., Jiang, J., Lee, J.C., (2019). Structural insights into α-synuclein fibril polymorphism: Effects of Parkinson's disease-related C-terminal truncations. *J. Mol. Biol.*, **431**, 3913–3919. https://doi.org/10.1016/j.jmb.2019.07.001.
132. Li, B., Ge, P., Murray, K.A., Sheth, P., Zhang, M., Nair, G., Sawaya, M.R., Shin, W.S., Boyer, D.R., Ye, S., Eisenberg, D.S., Zhou, Z.H., Jiang, L., (2018). Cryo-EM of full-length α-synuclein reveals fibril polymorphs with a common structural kernel. *Nat. Commun.*, **9**, 3609. https://doi.org/10.1038/s41467-018-05971-2.
133. Guerrero-Ferreira, R., Taylor, N.M., Mona, D., Ringler, P., Lauer, M.E., Riek, R., Britschgi, M., Stahlberg, H., (2018). Cryo-EM structure of alpha-synuclein fibrils. *ELife.*, **7**, https://doi.org/10.7554/eLife.36402 e36402.
134. Li, Y., Zhao, C., Luo, F., Liu, Z., Gui, X., Luo, Z., Zhang, X., Li, D., Liu, C., Li, X., (2018). Amyloid fibril structure of α-synuclein determined by cryo-electron microscopy. *Cell Res.*,, 1. https://doi.org/10.1038/s41422-018-0075-x.
135. Tuttle, M.D., Comellas, G., Nieuwkoop, A.J., Covell, D.J., Berthold, D.A., Kloepper, K.D., Courtney, J.M., Kim, J.K., Barclay, A.M., Kendall, A., Wan, W., Stubbs, G., Schwieters, C.D., Lee, V.M.Y., George, J.M., Rienstra, C.M., (2016). Solid-state NMR structure of a pathogenic fibril of full-length human α-synuclein. *Nat. Struct. Mol. Biol.*, **23**, 409–415. https://doi.org/10.1038/nsmb.3194.
136. Dearborn, A.D., Wall, J.S., Cheng, N., Heymann, J.B., Kajava, A.V., Varkey, J., Langen, R., Steven, A.C., (2016). α-synuclein amyloid fibrils with two entwined, asymmetrically associated protofibrils. *J. Biol. Chem.*, **291**, 2310–2318. https://doi.org/10.1074/jbc.M115.698787.
137. Seuring, C., Verasdonck, J., Gath, J., Ghosh, D., Nespovitaya, N., Wälti, M.A., Maji, S.K., Cadalbert, R., Güntert, P., Meier, B.H., Riek, R., (2020). The three-dimensional structure of human β-endorphin amyloid fibrils. *Nat. Struct. Mol. Biol.*, **27**, 1178–1184. https://doi.org/10.1038/s41594-020-00515-z.
138. Iadanza, M.G., Silvers, R., Boardman, J., Smith, H.I., Karamanos, T.K., Debelouchina, G.T., Su, Y., Griffin, R. G., Ranson, N.A., Radford, S.E., (2018). The structure of a β2-microglobulin fibril suggests a molecular basis for its amyloid polymorphism. *Nat. Commun.*, **9**, 4517. https://doi.org/10.1038/s41467-018-06761-6.
139. Iwata, K., Fujiwara, T., Matsuki, Y., Akutsu, H., Takahashi, S., Naiki, H., Goto, Y., (2006). 3D structure of amyloid protofilaments of β2-microglobulin fragment probed by solid-state NMR. *Proc. Natl. Acad. Sci.*, **103**, 18119–18124. https://doi.org/10.1073/pnas.0607180103.
140. Ferguson, N., Becker, J., Tidow, H., Tremmel, S., Sharpe, T.D., Krause, G., Flinders, J., Petrovich, M., Berriman, J., Oschkinat, H., Fersht, A.R., (2006). General structural motifs of amyloid protofilaments. *Proc. Natl. Acad. Sci.*, **103**, 16248–16253. https://doi.org/10.1073/pnas.0607815103.
141. Lee, M., Ghosh, U., Thurber, K.R., Kato, M., Tycko, R., (2020). Molecular structure and interactions within amyloid-like fibrils formed by a low-complexity protein sequence from FUS. *Nat. Commun.*, **11**, 5735. https://doi.org/10.1038/s41467-020-19512-3.
142. Gelenter, M.D., Smith, K.J., Liao, S.-Y., Mandala, V.S., Dregni, A.J., Lamm, M.S., Tian, Y., Xu, W., Pochan, D.J., Tucker, T.J., Su, Y., Hong, M., (2019). The peptide hormone glucagon forms amyloid fibrils with two coexisting β-strand conformations. *Nat. Struct. Mol. Biol.*, **26**, 592–598. https://doi.org/10.1038/s41594-019-0238-6.
143. U.S. Herrmann, A.K. Schütz, H. Shirani, D. Huang, D. Saban, M. Nuvolone, B. Li, B. Ballmer, A.K.O. Åslund, J.J. Mason, E. Rushing, H. Budka, S. Nyström, P. Hammarström, A. Böckmann, A. Caflisch, B.H. Meier, K. P.R. Nilsson, S. Hornemann, A. Aguzzi, Structure-based drug design identifies polythiophenes as antiprion compounds, Sci. Transl. Med. 7 (2015) 299ra123-299ra123. https://doi.org/10.1126/scitranslmed.aab1923.
144. Schütz, A.K., Soragni, A., Hornemann, S., Aguzzi, A., Ernst, M., Böckmann, A., Meier, B.H., (2011). The amyloid–Congo red Interface at atomic resolution. *Angew. Chem. Int. Ed.*, **50**, 5956–5960. https://doi.org/10.1002/anie.201008276.
145. Mizuno, N., Baxa, U., Steven, A.C., (2011). Structural dependence of HET-s amyloid fibril infectivity assessed by cryoelectron microscopy. *Proc. Natl. Acad. Sci.*, **108**, 3252–3257. https://doi.org/10.1073/pnas.1011342108.
146. H. Van Melckebeke, C. Wasmer, A. Lange, E. AB, A. Loquet, A. Böckmann, B.H. Meier, Atomic-resolution three-dimensional structure of HET-s(218−289) amyloid fibrils by solid-state NMR spectroscopy, J. Am. Chem. Soc. 132 (2010) 13765–13775. https://doi.org/10.1021/ja104213j.
147. Wasmer, C., Lange, A., Van Melckebeke, H., Siemer, A. B., Riek, R., Meier, B.H., (2008). Amyloid fibrils of the HET-s(218–289) prion form a β solenoid with a triangular hydrophobic core. *Science*, **319**, 1523–1526. https://doi.org/10.1126/science.1151839.
148. Sun, Y., Zhao, K., Xia, W., Feng, G., Gu, J., Ma, Y., Gui, X., Zhang, X., Fang, Y., Sun, B., Wang, R., Liu, C., Li, D., (2020). The nuclear localization sequence mediates hnRNPA1 amyloid fibril formation revealed by cryoEM structure. *Nat. Commun.*, **11**, 6349. https://doi.org/10.1038/s41467-020-20227-8.
149. Cao, Q., Boyer, D.R., Sawaya, M.R., Ge, P., Eisenberg, D.S., (2020). Cryo-EM structure and inhibitor design of human IAPP (amylin) fibrils. *Nat. Struct. Mol. Biol.*, **27**, 653–659. https://doi.org/10.1038/s41594-020-0435-3.
150. Röder, C., Kupreichyk, T., Gremer, L., Schäfer, L.U., Pothula, K.R., Ravelli, R.B.G., Willbold, D., Hoyer, W., Schröder, G.F., (2020). Cryo-EM structure of islet amyloid polypeptide fibrils reveals similarities with amyloid-β fibrils. *Nat. Struct. Mol. Biol.*, **27**, 660–667. https://doi.org/10.1038/s41594-020-0442-4.
151. Close, W., Neumann, M., Schmidt, A., Hora, M., Annamalai, K., Schmidt, M., Reif, B., Schmidt, V.,

Grigorieff, Fändrich, M., (2018). Physical basis of amyloid fibril polymorphism. *Nat. Commun.*, **9**, 699. https://doi.org/10.1038/s41467-018-03164-5.

152. Schmidt, A., Annamalai, K., Schmidt, M., Grigorieff, N., Fändrich, M., (2016). Cryo-EM reveals the steric zipper structure of a light chain-derived amyloid fibril. *Proc. Natl. Acad. Sci.*, **113**, 6200–6205. https://doi.org/10.1073/pnas.1522282113.
153. Röder, C., Vettore, N., Mangels, L.N., Gremer, L., Ravelli, R.B.G., Willbold, D., Hoyer, W., Buell, A.K., Schröder, G.F., (2019). Atomic structure of PI3-kinase SH3 amyloid fibrils by cryo-electron microscopy. *Nat. Commun.*, **10**, 3754. https://doi.org/10.1038/s41467-019-11320-8.
154. Wang, L.-Q., Zhao, K., Yuan, H.-Y., Wang, Q., Guan, Z., Tao, J., Li, X.-N., Sun, Y., Yi, C.-W., Chen, J., Li, D., Zhang, D., Yin, P., Liu, C., Liang, Y., (2020). Cryo-EM structure of an amyloid fibril formed by full-length human prion protein. *Nat. Struct. Mol. Biol.*, **27**, 598–602. https://doi.org/10.1038/s41594-020-0441-5.
155. Glynn, C., Sawaya, M.R., Ge, P., Gallagher-Jones, M., Short, C.W., Bowman, R., Apostol, M., Zhou, Z.H., Eisenberg, D.S., Rodriguez, J.A., (2020). Cryo-EM structure of a human prion fibril with a hydrophobic, protease-resistant core. *Nat. Struct. Mol. Biol.*, **27**, 417–423. https://doi.org/10.1038/s41594-020-0403-y.
156. Mompeán, M., Li, W., Li, J., Laage, S., Siemer, A.B., Bozkurt, G., Wu, H., McDermott, A.E., (2018). The structure of the necrosome RIPK1-RIPK3 core, a human hetero-amyloid signaling complex. *Cell*, **173**, 1244–1253. e10. https://doi.org/10.1016/j.cell.2018.03.032.
157. Wu, X.-L., Hu, H., Dong, X.-Q., Zhang, J., Wang, J., Schwieters, C.D., Liu, J., Wu, G.-X., Li, B., Lin, J.-Y., Wang, H.-Y., Lu, J.-X., (2021). The amyloid structure of mouse RIPK3 (receptor interacting protein kinase 3) in cell necroptosis. *Nat. Commun.*, **12**, 1627. https://doi.org/10.1038/s41467-021-21881-2.
158. Liberta, F., Loerch, S., Rennegarbe, M., Schierhorn, A., Westermark, P., Westermark, G.T., Hazenberg, B.P.C., Grigorieff, N., Fändrich, M., Schmidt, M., (2019). Cryo-EM fibril structures from systemic AA amyloidosis reveal the species complementarity of pathological amyloids. *Nat. Commun.*, **10**, 1104. https://doi.org/10.1038/s41467-019-09033-z.
159. Li, Q., Babinchak, W.M., Surewicz, W.K., (2021). Cryo-EM structure of amyloid fibrils formed by the entire low complexity domain of TDP-43. *Nat. Commun.*, **12**, 1620. https://doi.org/10.1038/s41467-021-21912-y.
160. Cao, Q., Boyer, D.R., Sawaya, M.R., Ge, P., Eisenberg, D.S., (2019). Cryo-EM structures of four polymorphic TDP-43 amyloid cores. *Nat. Struct. Mol. Biol.*, **26**, 619–627. https://doi.org/10.1038/s41594-019-0248-4.
161. Guenther, E.L., Ge, P., Trinh, H., Sawaya, M.R., Cascio, D., Boyer, D.R., Gonen, T., Zhou, Z.H., Eisenberg, D.S., (2018). Atomic-level evidence for packing and positional amyloid polymorphism by segment from TDP-43 RRM2. *Nat. Struct. Mol. Biol.*, **25**, 311–319. https://doi.org/10.1038/s41594-018-0045-5.
162. Schmidt, M., Wiese, S., Adak, V., Engler, J., Agarwal, S., Fritz, G., Westermark, P., Zacharias, M., Fändrich, M., (2019). Cryo-EM structure of a transthyretin-derived amyloid fibril from a patient with hereditary ATTR amyloidosis. *Nat. Commun.*, **10**, 5008. https://doi.org/10.1038/s41467-019-13038-z.
163. Jaroniec, C.P., MacPhee, C.E., Bajaj, V.S., McMahon, M. T., Dobson, C.M., Griffin, R.G., (2004). High-resolution molecular structure of a peptide in an amyloid fibril determined by magic angle spinning NMR spectroscopy. *Proc. Natl. Acad. Sci.*, **101**, 711–716. https://doi.org/10.1073/pnas.0304849101.

Appendix III: Three-dimensional reconstruction of individual helical nano-filament structures from atomic force microscopy topographs.

Research Article **Open Access**

Liisa Lutter, Christopher J. Serpell, Mick F. Tuite, Louise C. Serpell, Wei-Feng Xue*

Three-dimensional reconstruction of individual helical nano-filament structures from atomic force microscopy topographs

https://doi.org/10.1515/bmc-2020-0009
received March 3, 2020; accepted March 30, 2020.

Abstract: Atomic force microscopy, AFM, is a powerful tool that can produce detailed topographical images of individual nano-structures with a high signal-to-noise ratio without the need for ensemble averaging. However, the application of AFM in structural biology has been hampered by the tip-sample convolution effect, which distorts images of nano-structures, particularly those that are of similar dimensions to the cantilever probe tips used in AFM. Here we show that the tip-sample convolution results in a feature-dependent and non-uniform distribution of image resolution on AFM topographs. We show how this effect can be utilised in structural studies of nano-sized upward convex objects such as spherical or filamentous molecular assemblies deposited on a flat surface, because it causes 'magnification' of such objects in AFM topographs. Subsequently, this enhancement effect is harnessed through contact-point based deconvolution of AFM topographs. Here, the application of this approach is demonstrated through the 3D reconstruction of the surface envelope of individual helical amyloid filaments without the need of cross-particle averaging using the contact-deconvoluted AFM topographs. Resolving the structural variations of individual macromolecular assemblies within inherently heterogeneous populations is paramount for mechanistic understanding of many biological phenomena such as amyloid toxicity and prion strains. The approach presented here will also facilitate the use of AFM for high-resolution structural studies and integrative structural biology analysis of single molecular assemblies.

Keywords: atomic force microscopy; tip-sample convolution; amyloid fibril structure; image analysis.

Introduction

Atomic force microscopy (AFM) is a scanning probe microscopy method that enables the collection of three-dimensional topographic image data, and has been widely applied to characterisation of biological and non-biological macromolecules. AFM encompasses a range of techniques for structural studies of biological molecules, including the study of inter- and intramolecular interactions [1], molecular dynamics [2], molecular remodelling under force [3] and imaging of molecules in air [4] or in liquid [5,6]. AFM operating in non-contact mode is capable of reaching atomic resolution on samples of small molecules [7], whereas AFM imaging of biomolecules routinely reaches nanometre resolutions in single high signal-to-noise images, and is able to characterise biological populations at a true single molecule level. This technique has been applied to a range of different bio-molecules, including membrane proteins [8], viral capsids [9] and filamentous biomolecules, such as amyloid fibrils [10], nucleic acids [11,12], and various filaments involved in the cytoskeleton [13].

Amyloid fibrils represent a class of filamentous supramolecular assemblies frequently studied using AFM imaging. They can be self-assembled from a wide range of different proteins and peptides. Fibrils formed from some amyloidogenic sequences, including amyloid-β, and tau, have been identified to be involved in human neurodegenerative pathologies, such as Alzheimer's disease, whereas other amyloid forming sequences are known to be non-toxic and even required for normal physiological processes [14]. Although the amino acid sequences of the

***Corresponding author: Wei-Feng Xue,** Kent Fungal Group, School of Biosciences, University of Kent, CT2 7NJ, Canterbury, UK, E-mail: W.F.Xue@kent.ac.uk
Liisa Lutter, Mick F. Tuite, Kent Fungal Group, School of Biosciences, University of Kent, CT2 7NJ, Canterbury, UK
Christopher J. Serpell, School of Physical Sciences, University of Kent, CT2 7NH, Canterbury, UK
Louise C. Serpell, Sussex Neuroscience, School of Life Sciences, University of Sussex, BN1 9QG, Falmer, Brighton, UK

many amyloid forming proteins are typically unrelated, the fibrils they form share a well-defined common core structural architecture, namely the cross-β arrangement made up of β-strands that stack perpendicular to the fibril axis stabilised by intermolecular hydrogen bonds between β-strands that run parallel to the fibril axis [15,16]. Despite the fact that all amyloid fibrils share these core structural features, variations in filament packing arrangements, including fibrils assembled from the same precursors, result in a multitude of different fibril structures called polymorphs, which may be related to the varying types of biological response they elicit. Furthermore, specific structural polymorphs assembled from the same amyloid forming protein could be patient- or disease-specific and may correlate with neurodegenerative disease aetiology [14]. Due to the unresolved nature of the amyloid assembly structure-function relationship, fibrillar amyloid specimens are widely studied using AFM imaging to resolve the mechanistic roles of amyloid assembly and polymorphism [17].

AFM imaging of a sample, e.g. amyloid fibrils deposited on a flat surface, with typical intermittent contact imaging mode such as the tapping mode is achieved by scanning a sample on a flat surface using a sharp tip attached to a cantilever. As the cantilever oscillates up and down, the tip and sample are moved relative to each other along the horizontal x and y axes in a raster pattern. When the tip interacts with the sample, vertical displacement of the cantilever relative to sample determines the surface height on the z-axis, measured at discrete pixel locations in the xy-plane. The lateral (x- and y-dimension) sampling is determined by the user in terms of the number of pixels collected per image and the pixel size, which tends to have edge length in the order of Ångströms to nanometres. The output of AFM scans is a 3-dimensional topography map, usually represented by a 2-dimensional coloured image where pixel values contain information on sample surface height, typically represented by the intensity of colour. Resolution in the vertical and lateral dimensions of AFM topographs are distinct. Topographs have a high vertical signal-to-noise ratio, limited by noise in the order of sub-Ångströms, due to electrical noise in the detector and thermal noise causing fluctuations in the cantilever [18,19], whereas lateral resolution is defined by the pixel size and the tip dimensions. Both vertical and lateral resolution can be affected by distortions or artefacts caused by drift, ambient noise or deformation of the sample or tip through their interactions. However, a significant limitation to the application of AFM to structural characterisation of biomolecules has been the tip-sample convolution effect, which causes lateral broadening, or dilation, of upwards convex structural features on AFM topographs. Convolution arises from the finite size and geometry of the AFM probe tip and is especially pronounced when sample features are of similar size to the tip radius, usually between 1-10 nm, as is the case for many biological macromolecules. The tip convolution effect has been studied in detail since the development of the AFM technique in the 1980s [20]. In order to minimise the convolution effect, both experimental and computational approaches have been developed. For example, various tip modifications have been used in order to minimise the effect of tip-sample convolution some of which have led to atomic resolution topographs [7]. However, this application is limited to small flat molecules and is not currently suitable for imaging biological macromolecules. The advantage of a computational approach to deconvolution is that an algorithm can be applied to a topograph of any specimen, after data collection. Many deconvolution methods have been reported to date. However common to these methods, they rely on the same concept based on the 'erosion' algorithm with various mathematical approaches [21–23]. Although erosion corrects for the dilation of the sample width, it leads to a significant loss of lateral structural information present in the AFM topology images because it does not recognise or recover the structural information that is present at subpixel locations, as we will show below.

In this report, we show that the AFM tip-sample convolution effect results in a feature-dependent and non-uniform distribution of image resolution on AFM topographs, and is in fact an advantage in terms of image resolution, as it causes the 'magnification' of the sample surface. Upon correction, we reveal that subpixel resolution information of the sample surface can be recovered using a contact-point based deconvolution algorithm, thus revealing the enhanced lateral resolution encoded in the AFM topographs while minimising the dilation image distortion. Furthermore, while AFM imaging provides only information on the top of 3-dimensional molecular surfaces of the sample structures, we show that helically symmetrical structures can be reconstructed as 3D surface envelopes from AFM topographs. This approach is demonstrated on imaging analysis of twisted amyloid fibrils formed from short peptide sequences which have been previously characterised using X-ray fibre diffraction [24]. The deconvolution and 3D modelling approach facilitates the structural analysis of individual twisted filamentous assemblies at an individual particle level. It is therefore capable of resolving the structural variations of individual macromolecular assemblies within inherently heterogeneous populations such as amyloid fibrils, which is key for mechanistic understanding of many biological phenomenon such as amyloid toxicity and prion strains.

Results

Structural information is lost through erosion deconvolution of AFM topographs

The tip-sample convolution artefact arises from the finite shape and geometry of the cantilever tip. When the tip interacts with the sample, the surface height at the bottom of the tip is recorded, whereas the true surface of the sample may lie at a different location, probed at the tip-sample contact points (Figure 1a). This leads to convolution, or dilation in the case of upward convex surface features on AFM topographs. Image deconvolution by the erosion method corrects for the dilation of the sample by translating a model of the tip to the coordinates at which surface heights were recorded on the image and finding the tip's deepest penetration of the convoluted surface to reconstruct a deconvoluted image while conserving pixel coordinates and sampling in the xy-plane (Figure 1b and 1c) [23,25]. Thus, erosion resolves apparent clashes between the tip and convoluted sample surface image by lowering sample surface heights according to the known surface values of the tip translates. AFM tip geometry can be typically approximated as conical with varying apical radii, and side angles that can be modelled from the values provided by the manufacturer. Erosion deconvolution is efficient in minimising the dilating effect of convolution. However, it causes a significant loss of structural information (demonstrated on a twisted amyloid fibril in Figure 1c), because it replaces the existing vertical surface height values with the surface of deepest tip penetration without finer resampling of surface heights at tip-sample contact points, which contain structural information in the images. These contact points lie off the pixel grid at subpixel locations and contain structural information on the true sample surface. As shown on the twisted amyloid fibril example (Figure 1), deconvolution by erosion causes loss of information on the fibril helical periodicity and molecular surface features.

Tip-sample convolution results in enhanced lateral sampling

Although the tip-sample convolution effect causes upward convex surface features to appear dilated on topographs, this effect can in fact be used to advantage as it causes the 'magnification' of structural features present at tip-sample contact points located at subpixel coordinates, and results in higher lateral resolution topographic information being captured than what is recorded at pixel grid coordinates.

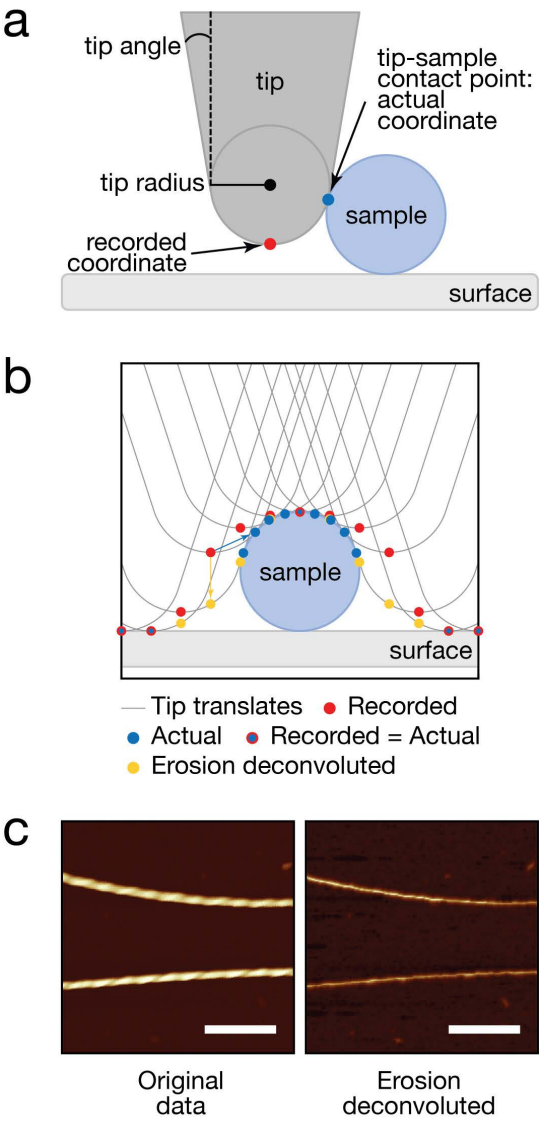

Figure 1: AFM image deconvolution by the erosion algorithm corrects for dilation but causes significant loss of structural information of the sample surface. **(a)** Schematic cross-sectional illustration of AFM tip-sample interactions that lead to lateral convolution and dilation of sample features. This imaging artefact is especially pronounced for sample objects on the same size range as the tip radius. **(b)** Schematic cross-sectional diagram of tip-sample deconvolution by erosion. The sample cross-section is illustrated as a blue circle. Red dots show original coordinates of the data, orange dots show erosion deconvoluted height coordinates at each pixel location and blue dots show the coordinates at tip-sample contact points for each pixel location. **(c)** Example of deconvolution by the erosion algorithm demonstrated on an example image of a twisted amyloid fibril. Left is an AFM topology image showing twisted amyloid fibrils. Right image shows the erosion-deconvoluted image of the same data, demonstrating substantial loss of structural information due to the erosion algorithm. A symmetric conical tip with a side angle of 18° (estimated from the tip geometry information provided by the manufacturer) and tip radius of 11.2 nm (estimated using the image features as described in the Results) was used as a model of the tip. The scale bars represent 200 nm.

This information can be recovered by a deconvolution method in which the tip, with a known geometry, radius and angle, is modelled on the recorded surface scan at translations that correspond to original lateral sampling (x and y coordinates) and recorded surface heights (z coordinates), similarly to the erosion deconvolution method. However, instead of finding the surface of deepest penetration, geometric modelling of tip and simulation of tip translates is used to find tip-sample contact points. These tip-sample contact points contain information on the true surface of the sample, which is otherwise recorded in magnified, or dilated, form. Thus, the total number of data points remains the same but the pixel coordinates in both xy-plane and surface heights on the z-axis, are shifted, revealing the enhanced local sampling of the upward convex surface features encoded in the image data. This contact point deconvolution approach can be applied to any AFM topograph and is demonstrated on a sphere, a cylinder, and a randomly generated rough surface (Figure 2). Contact points are found by iterative rounds of tip-sample simulations, in which the sample surface is initially assumed to be circular, until convergence of the deconvoluted surface coordinates. The corrected images can then be interpolated onto a finely spaced even grid for visualisation of the deconvoluted image. In figure 2, lateral sampling of the tops of the example objects and peaks of the randomly generated rough surface can be seen to increase in density and shift significantly from the original position of xy-gridlines (Figure 2, 3rd column), especially for features with size similar to the radius of the tip.

The effect of locating the contact points off the pixel grid on the images of upward concave features is, however, less favourable as the depth of a trough can only be accessed if the sides of the tip do not come into contact with the sample. This can be seen in the Fig 2 bottom row example as a decrease in contact point density at this type of areas. In the case of biological filaments such as DNA, cytoskeletal and amyloid filaments, major upward concave surface features include grooves, which can vary ~1-50 nm in width. They may be resolvable by AFM, depending on the geometric parameters of the tip, as well as depth of the features.

The deconvolution and lateral sampling enhancement of a convoluted surface depends on both the geometry of the sample, geometry of the tip, and the lateral pixel sampling frequency. The effect of these various factors on the sampling enhancement is here assessed with scan-line simulations using a circular cross-section as the sample and a symmetric tip model constructed from typical tip parameters (Figure 3). The sampling enhancement factor is measured as a ratio of deconvoluted image signal density to original image signal density, where signal density is found as the number of moved pixel coordinates that result from tip-sample contact per surface area. The sampling enhancement factor describes the increase in lateral sampling frequency as a result of tip-sample contact point deconvolution. The effect of sample diameter as well as tip radius on the enhancement factor is illustrated in Figure 3. As seen, the sampling enhancement factor of a sub-nm circular cross-section is more than 3 with a 2 nm tip-radius, representing more than 3 times increase in lateral sampling compared to the convoluted image (Figure 3 left column). The sampling enhancement then decreases as the circle diameter increases and apparently plateaus at ~1.4 times enhancement compared to a convoluted surface. The sampling enhancement fluctuates for non-continuous sampling realistic to actual imaging experiments and the stepwise large increases represent increases at which the tip and circle first come into contact at a sampled pixel as the radius of the circle increases, allowing a new contact point to be found. Enhancement then slightly decreases with the increase in circle radius as no new contact points are added and existing contact points become spaced further apart, therefore decreasing information density.

For a symmetric conical tip, the most important tip parameters for determining tip-sample interactions are the apical radius of the tip and the angle at which the sides of the tip widen. Although AFM tips with smaller tip radii and tip angles produce higher resolution images by minimising the tip-sample convolution effect, with the contact-point deconvolution method, larger tip radii and tip angles result in higher sampling enhancement as the tip interacts with the sample at more xy-coordinates, allowing proportionally more contact points to be recovered (Figure 3b). Thus, with finite scanning precision, increasing resolution of images becomes an optimisation problem that involves finding optimum tip geometry with any given sampling frequency and specimen geometry. Importantly, simulations of tip-sample interactions with an estimate of sample geometry or an already corrected sample surface in which tip model and pixel size parameters are varied can guide the selection of an optimal tip geometry and sampling frequency to maximise resulting image resolution for a specific sample.

Contact-point deconvolution of an AFM amyloid fibril topograph

The deconvolution algorithm and resulting lateral sampling enhancement are demonstrated on an AFM topograph of amyloid fibrils formed from a short amyloid

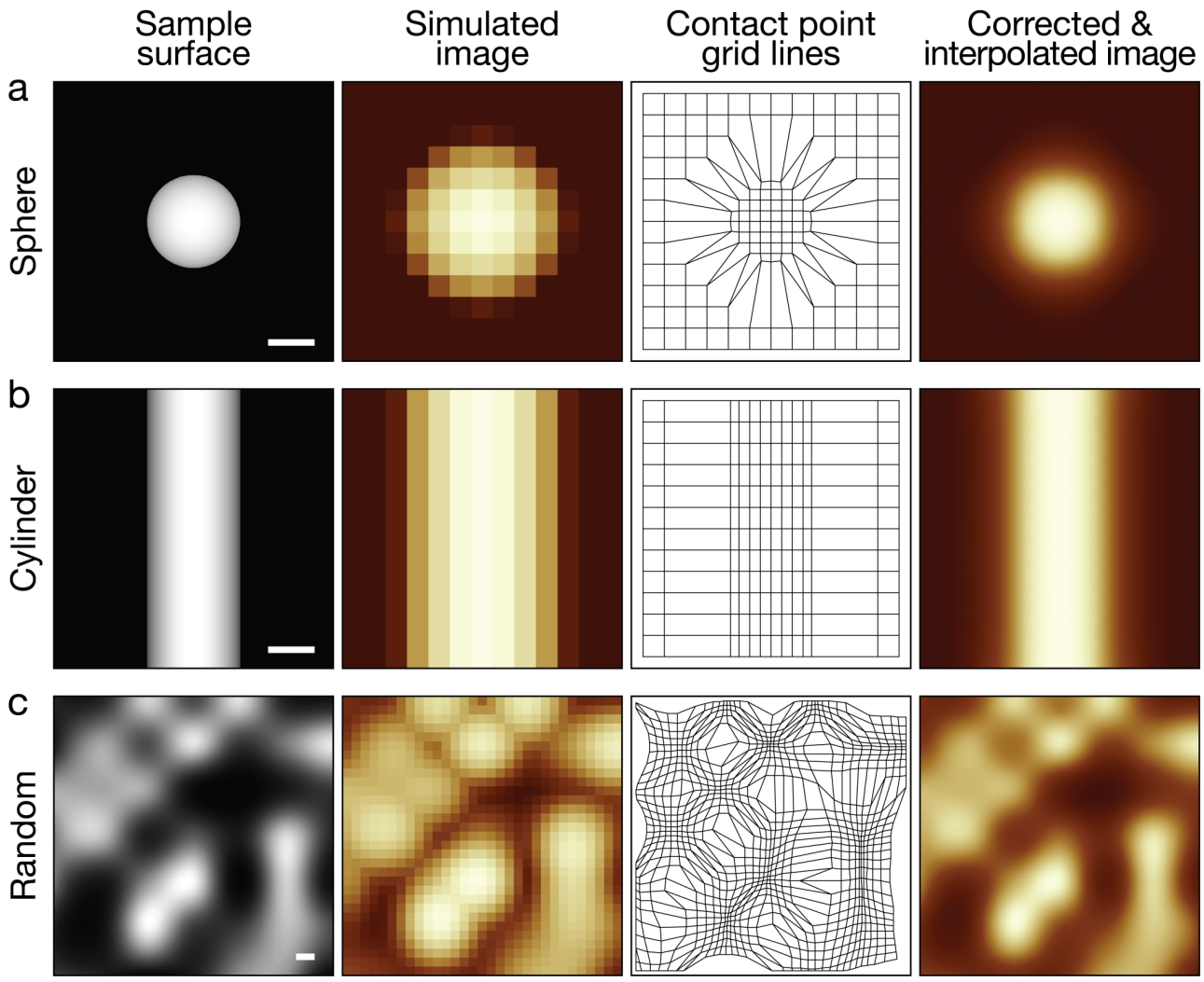

Figure 2: Contact-point deconvolution can be applied to any surface and results in increased local lateral sampling for upward convex sample features. Simulated AFM image (2nd column from left), shifted pixel grid lines after contact point deconvolution (3rd column from left) and a corrected image with contact points interpolated to a finer pixel grid (right most column) are shown for a sphere **(a)**, cylinder **(b)**, and a randomly generated surface **(c)** shown in the left-most column. The sphere and the cylinder both have a radius of 2 nm. A symmetric conical tip with a radius of 2 nm and tip side angle of 18° was used for all simulations. The scale bars represent 2 nm.

forming peptide with the amino acid sequence HYFNIF (Materials and Methods and [17]). The fibril example is first traced from the AFM image across the fibril central line and subsequently straightened and interpolated to an evenly spaced pixel grid [26], while maintaining pixel size identical to that in raw data. In order to apply the contact point deconvolution algorithm as shown on the examples above, the convoluted surface, as well as a model of the tip used to scan the specimen are needed. For experimental image data, the variation in the tip radius from their nominal value, which results from the tip manufacturing process, should be considered [27]. It is also important to consider that the tip can become blunter with scanning and its tip radius can widen over time. Here, the tip radius can be estimated for each individual fibril on an image from the extent of convolution seen in data. An estimate of the tip radius is found by assuming the twisted amyloid fibrils have ideal corkscrew symmetry, and the average cross-section of the fibril perpendicular to its axis of rotation is, therefore, circular with a radius defined by half of the maximal z-height value. Least-square regression analysis is then performed to fit a simulated convoluted scan-line generated from modelling interactions of the tip with the circular cross-section model to the average convoluted cross-section observed in data, while letting the tip radius vary as a parameter. It is assumed that the overall tip geometry and side angles do not change. In the example shown in Fig 4, while the nominal tip

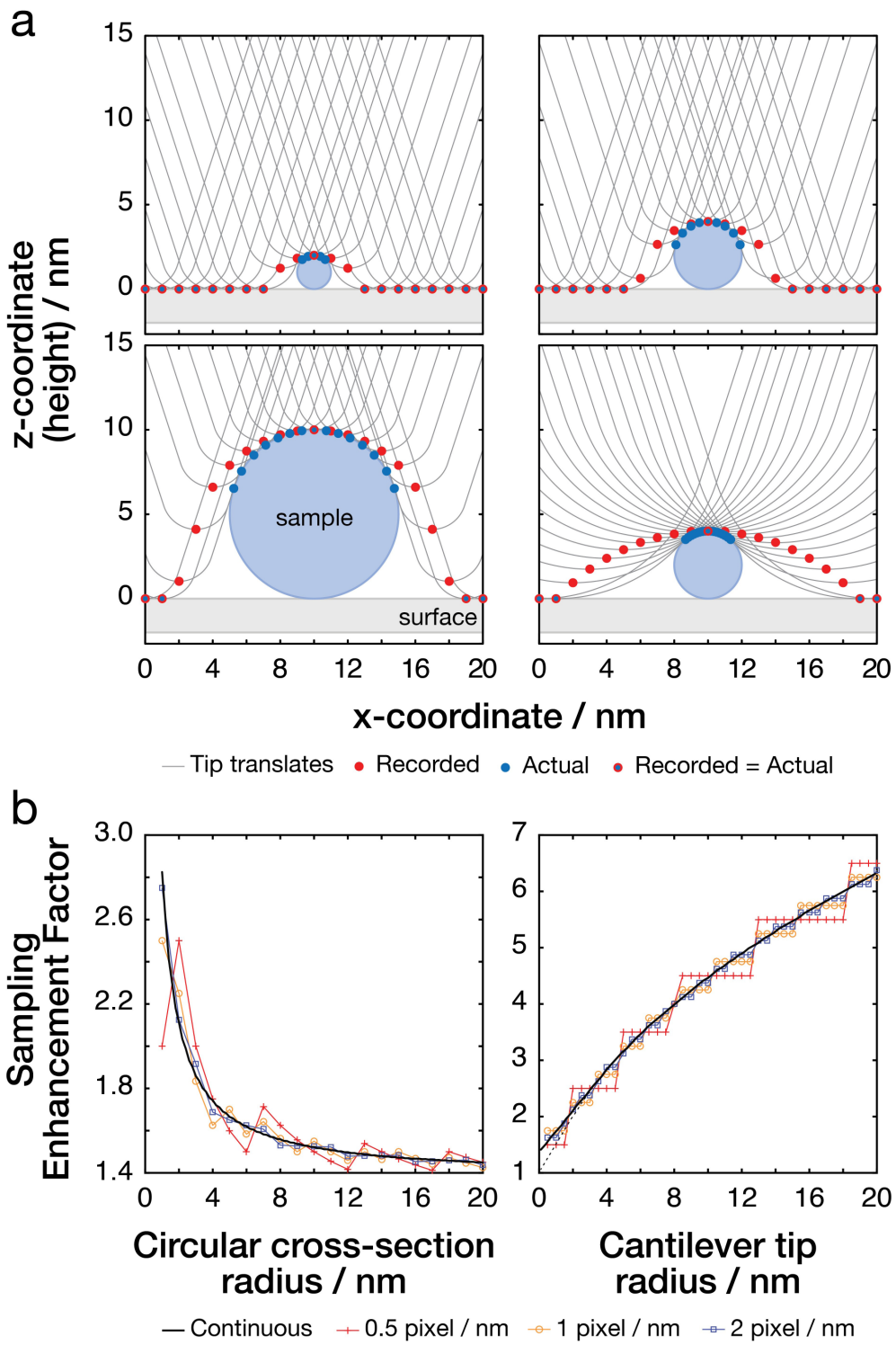

Figure 3: Image sampling enhancement effect after image correction by contact-point deconvolution shown with varying sample and sampling parameters. Schematic diagrams are shown in (a) and results from simulations in (b). Red circles on schematics represent original convoluted coordinates at each sampled pixel and blue circles represent tip-sample contact points at each sampled pixel. The sampling enhancement factor is defined as the ratio of pixel density of these points within the circle envelope. Left column shows the enhancement effect seen with a circle with varying radius. A symmetric conical tip model with a radius of 2 nm and tip side-angle of 18° was used. Right column shows the enhancement effect observed with a circle with a constant radius of 2 nm with varying tip radius and a tip side-angle of 18°. The dashed line represents the same simulation but with a tip with side-angle of 0°.

radius provided by the manufacturer was 2 nm, using the approach described here the tip radius estimate was 11.2 nm. The deconvolution algorithm is then applied to the 3D topograph to find corrected grid lines and surface heights (Figure 4c,d). The deconvoluted contact points follow the twisting pattern of the fibril and increase lateral sampling of the fibril surface as predicted. The ungridded data points are then interpolated back onto a finer evenly spaced grid for visualisation of the de-convoluted contact-points (Figure 4c).

Assessment of AFM topograph lateral resolution

Because AFM topographs are extraordinarily high signal-to-noise, the lateral resolution of a single uncorrected AFM topographs is typically determined by the spatial frequency of sampling in the xy-plane. According to the Nyquist sampling theorem, the minimal sampling rate that contains the information to reconstruct a signal is twice the maximum frequency component, thus the Nyquist resolution limit for images is twice the pixel size. For example, the image used in the example in Figure 4 has a pixel size of 2.93 nm and the resolution is, therefore, limited to 5.86 nm. Deconvolution using our approach shifts pixel coordinates to subpixel positions off the pixel grid. Therefore, recovering structural information of the sample by shifting the sample surface coordinates present in magnified form results in recovering of the true higher lateral sampling frequencies present in the image data. Figure 5 shows the lateral resolution of deconvoluted AFM images assessed using a feature-based lateral resolution assessment method [28] and compared with the original convoluted image of the same fibril shown in Figure 4. The feature-based method applies a low-pass filter to an image in spatial frequency domain from higher towards lower spatial frequencies and measures the correlation between the filtered and unfiltered images in real space. Increases in correlation, seen as peaks in a log-log plot of the first derivative of cross-correlation vs. spatial frequencies, indicate presence of structural information at the specific spatial frequency. Figure 5b shows the correlation curves with peaks indicating the presence of structural information. Comparison of the normalised correlation between the convoluted and deconvoluted amyloid fibril images shows a shift of the correlation curve towards the right, indicating a shift of information content towards higher spatial resolutions due to correcting of sampling frequency during deconvolution. However, the contact point deconvolution has a much larger effect on the x-axis

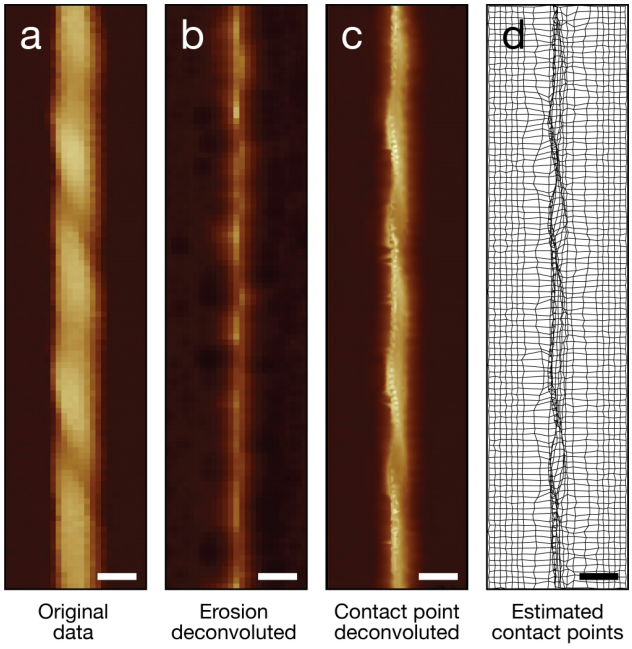

Figure 4: Typical example of contact-point deconvolution of an AFM topograph of a helically twisted amyloid fibril. **(a)** Digitally straightened AFM topography image of an amyloid fibril. **(b)** Image deconvoluted using the erosion algorithm. **(c)** Contact-point deconvoluted and interpolated image. (d) Corrected lateral (x/y) grid lines after tip-sample contact-point deconvolution. A symmetric conical tip model with a radius of 11.2 nm and side angle of 18° was used. A short section of the total fibril is shown for detail and the corresponding part of the same fibril is shown on each panel. The scale bars represent 20 nm.

(across the width of the filament) than on the y-axis (along the length of the filament), which leads to broadening of the peaks on the 1st derivative of correlation graph. Analysis of lateral resolution suggests that the highest resolution at which structural information is found on the convoluted example fibril image is ~60 Å (consistent with the Nyquist frequency of the original image data) and on the deconvoluted image the highest resolution is ~30 Å, indicating that deconvolution results in approximately doubling of the lateral resolution, for this amyloid fibril, due to the recovery of the enhanced sampling in the image data.

3D modelling of helical amyloid fibrils from corrected AFM topographs

While AFM provides 3-dimensional topographic data, only the top surface of the sample is accessible to the tip, preventing the visualisation of the full sample surface envelopes in 3D. However, for helically symmetric

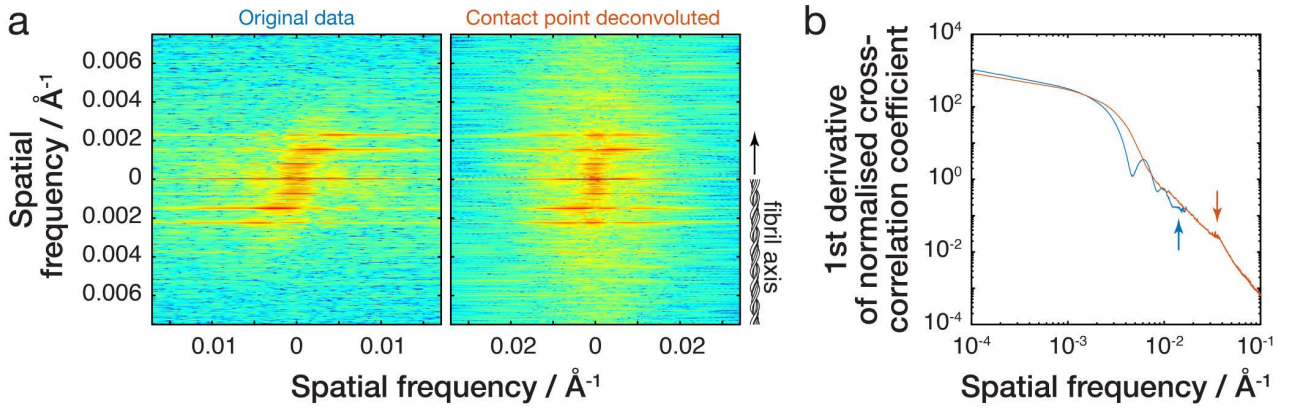

Figure 5: Resolution of original recorded and corrected AFM topographs are evaluated by the feature-based lateral resolution assessment method [28]. The same fibril image as Figure 4 is used as example. **(a)** 2D Fourier spectra of the original convoluted (left) and contact-point deconvoluted (right) images. The x-scale is expanded to accommodate peaks in the spectra for contact-point deconvoluted image as they are shifted to higher spatial frequencies. **(b)** Log-log plot of the first derivative of the normalised cross-correlation curve. Arrows indicate right-most peaks indicating the highest spatial frequency information present at 64Å resolution for the original convoluted fibril image and 28Å for the contact-point deconvoluted image.

structures such as amyloid fibrils, we describe below an algorithm that can be used to reconstruct 3D surface envelopes by taking advantage of the screw-axis symmetry of the filaments. This approach is demonstrated on AFM topographs of deconvoluted amyloid fibrils. The workflow of AFM image processing for 3D surface envelope reconstructions is summarised below (Table 1).

Following contact-point deconvolution of traced and digitally straightened fibril image, the surface envelopes are reconstructed using a moving window approach in which rotation and translation is applied to each corrected contact point coordinates within the window, thus reconstructing fibril cross-sections as the window is slid along the length of the fibril. The width of the moving window is one complete rotation of the fibril cross-section along the fibril axis (i.e. one nominal helical pitch), determined by its periodicity and screw axis symmetry. The rotation of each data point within the window depends on the distance of the point from the central cross-section of the window. Rotation angle values are negative in one direction from the centre of the window and positive in the other direction, with the specific direction depending on the twist-handedness of the fibril. The rotation angles are kept constant along the length of the filament. After deconvolution of the amyloid fibril, the number of lines along the length of the filament that are to be used for the 3D reconstruction are determined. Data points further away from the centre of the filament can be more frequently affected by artefacts during scanning and the uncertainty of the deconvolution algorithm tends to be higher for surface heights that lie further away from the central line. However, data points further away from the centre of the filament also contain additional structural information and information on the fibril twist and width which is harder to determine from the lines closer to the centre alone. Therefore, the number of pixel-lines used is determined by visual inspection of the deconvolution result. The deconvoluted surface coordinates that correspond to the selected pixel-lines are then used for the 3D modelling approach. The deconvoluted contact points off the pixel-grid are interpolated onto an evenly spaced grid along the screw axis, creating 'slices' perpendicular to the fibril axis, while the data remains ungridded along the x-axis. In order to determine the length of the reconstruction window for the deconvoluted amyloid fibril image, the periodicity of the fibril is first determined by applying a 1D Fast Fourier Transform (FFT) to the surface height profile of the fibril central line (Figure 6a-b). This determines the spatial frequencies of repeating patterns in the signal. The spatial frequency with the highest amplitude represents the periodicity of the fibril. For an asymmetric fibril cross-sections, one period represents a complete turn (one helical pitch) whereas for a fibril with n-fold symmetry periodicity represents $1/n$ of a complete turn. Fibril symmetry is then estimated by constructing 3D models with systematically varied symmetries and comparing these to the original straightened fibril image to find the best match (Figure 6c). Symmetry determination is a critical step for reconstructing the surface of a helical specimen. Different screw axis symmetries result in differences in the twisting pattern observed on the fibril top surface. In order to

Table 1: Workflow flow chart of AFM topograph processing and 3D helical fibril surface envelope reconstruction.

Step	Description	Input(s)	Output(s)
1	Tracing of individual fibril from AFM topograph	– AFM topology image	– Fibril contour (x and y) coordinates
2	Fibril straightening	– AFM topology image – Fibril contour (x and y) coordinates	– Cropped topology image of the straightened fibril
3	Determining tip parameters used to record fibril image	– Cropped topology image of the straightened fibril	– Tip geometry model
4*	Contact-point deconvolution of straightened fibril with tip model	– Cropped topology image of the straightened fibril – Tip geometry model	– Contact point coordinates
5	Selecting number of coordinate-lines to use for 3D reconstruction based on deconvolution uncertainty	– Contact point coordinates	– Edited list of contact point coordinates
6	Determining fibril twist periodicity and handedness	– Cropped topology image of the straightened fibril	– Fibril twist periodicity – Fibril twist handedness
7	Reconstruction of models with various symmetry estimates	– Edited list of contact point coordinates	– 2D FFT spectra of fibril symmetry models
8	Comparison of symmetry model and original fibril image Fourier spectra	– Cropped topology image of the straightened fibril – 2D FFT spectra of fibril symmetry models	– Fibril helical symmetry
9	Real-space reconstruction of the final 3D surface envelope with selected symmetry	– Edited list of contact point coordinates – Fibril twist periodicity – Fibril twist handedness – Fibril helical symmetry	– 3D surface envelope model of the fibril
10	Simulation of a convoluted AFM image from 3D envelope	– Cropped topology image of the straightened fibril – 3D surface envelope model of the fibril	– Validated 3D surface envelope model of the fibril

* Contact-point deconvolution was performed on straightened and cropped fibril image rather than the full original image (as step 2) to reduce the amount of contact-point calculations needed but assumes long-straight fibril and symmetrical tip geometries.

make the comparison of a 2D convoluted image and 3D deconvoluted reconstructions, the tip model is used to simulate convoluted AFM images from the symmetry models. The straightened experimental fibril image and various symmetry simulations are zero-padded to square images and compared as 2D Fourier spectra to estimate fibril screw-axis symmetry that best describes the original image data. The 2D Fourier spectra contain information on repeating patterns of fibril top surface and are analogous to a diffraction pattern. Fourier-based analysis of helical biomolecule structures dates to first diffractions patterns that describe the structure of DNA and has been since used to reconstruct helical biomolecules from electron cryo-microscopy images by indexing the Bessel functions of the diffraction pattern layer lines [29]. However, in many cases, resolving individual layer lines and indexing them is not possible, especially for amyloid fibrils with long helical repeat distances and small twist angles of individual subunits. Differences in rotational symmetry of a fibril cross-section causes the Bessel orders to change significantly while the layer lines on the spectrum remain identical [30]. Here, using this property and assuming that the screw-axis of the filament lies straight along the centre of the fibril, the differences in layer line Bessel orders observed for different symmetry models, which contain information on the handedness and screw axis symmetry of the fibril and represent the twisting pattern on top of the fibril, were used to estimate the fibril screw-axis

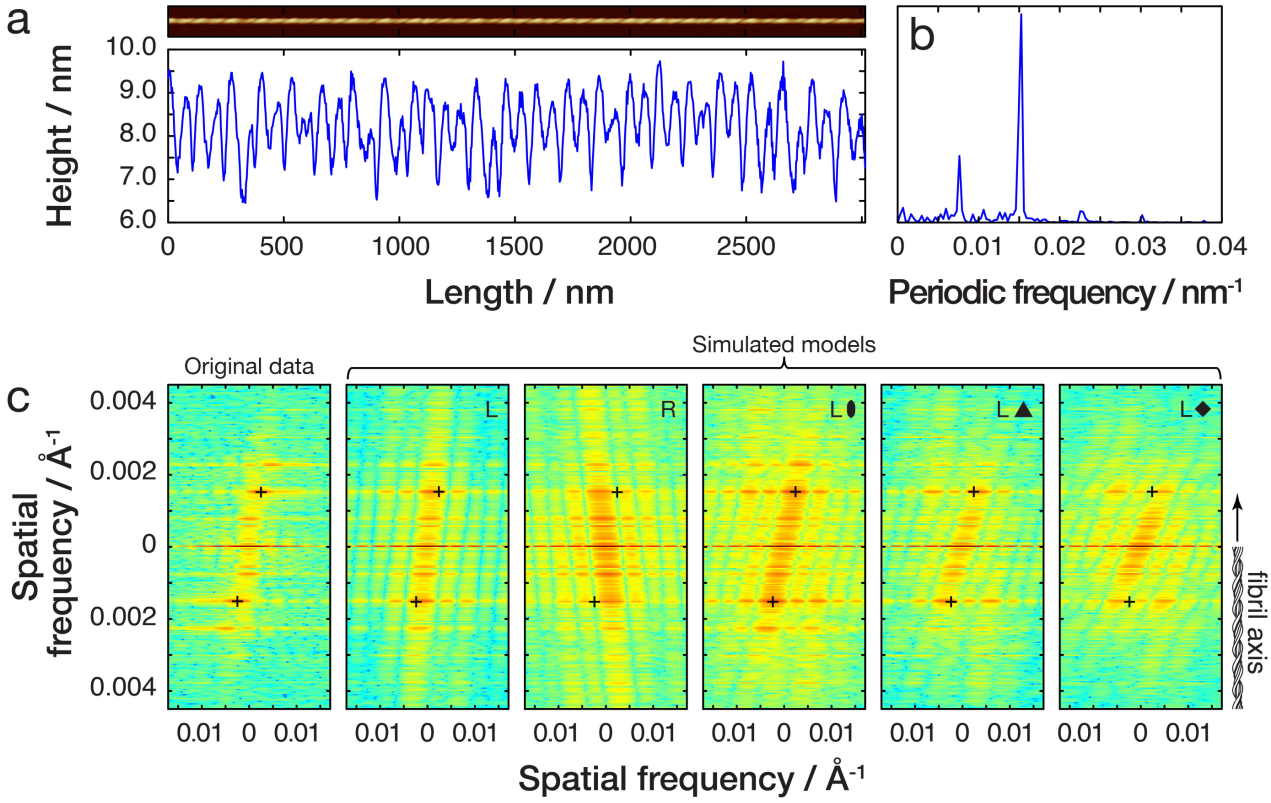

Figure 6: Estimation of the fibril twist periodicity and handedness. The same fibril image as Figure 4 is used as example. **(a)** Fibril central line height profile. **(b)** One-dimensional FFT power spectrum of the central line is used to determine the periodicity of the fibril. **(c)** The screw axis symmetry and the twist handedness of the fibril is estimated by reconstructing 3D models of the fibril with varying symmetries, simulating convoluted AFM images from the models and comparing the 2D FFT spectra of the symmetry model images to that of the original straightened fibril image. The crosses are drawn on the most intense peaks on the original fibril 2D FFT image and their position is then applied onto each symmetry model 2D FFT spectra to guide finding the closest match. In this example, a left-hand twisted fibril with a pseudo two-fold screw-axis symmetry shows the best match to the data.

symmetry. For example, if the line between most intense off-centre spots in the 2D FFT (+ symbols in Figure 6c) has a positive slope then the fibril is left-handed, and if the slope is negative the fibril is right-handed. The steepness of the slope contains information on the screw-axis symmetry of the fibril and the closest match of a symmetry model to the original fibril image is used to estimate the symmetry for an individual fibril. For the amyloid fibril example shown in this demonstration (Figure 6), the 2-fold symmetry model gives the best fit to data (Figure 6c), suggesting that the fibril cross-section has a pseudo 2-fold screw axis symmetry. These 2D Fourier spectra from AFM images are less ambiguous compared to analogous 2D Fourier patterns of TEM images as only the top of the fibril surface contributes to the signal, facilitating the direct measurement of handedness and symmetry.

Having determined the periodicity, handedness and screw-axis symmetry of the fibril, the 3D surface envelope can be reconstructed using the moving window approach described above (Figure 7). A cross-section of the fibril is obtained at each y-coordinate and a cubic spline is fitted to the cross-sections for smoothing. The number of spline pieces is determined by manual testing, taking into account the periodicity and symmetry of the fibril, which affects the number of times each cross-section is sampled. For validation of the image deconvolution and reconstructed 3D models, the final 3D surface envelope and tip model are used to simulate a convoluted AFM image that can then be compared with the uncorrected straightened fibril image (Figure 7b). Although there are small differences, the simulated image twist, periodicity and local surface features generally correspond well to the original fibril image, validating the reconstruction approach here as a useful method for reconstruction of individual fibrils without cross-particle averaging.

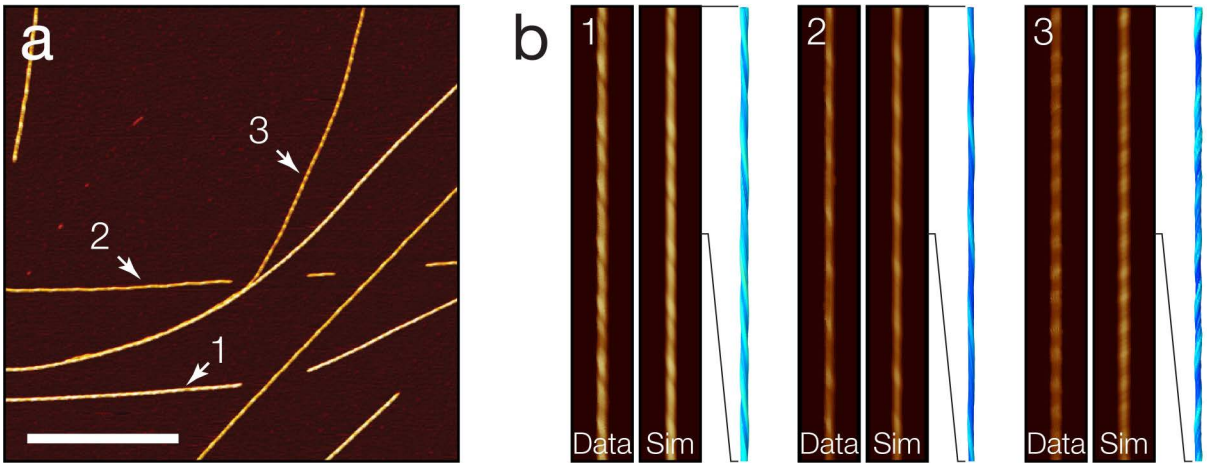

Figure 7: 3D surface envelope reconstruction of amyloid fibrils from AFM topography. **(a)** AFM topology image of amyloid fibrils assembled from short peptide with the sequence HYFNIF [17,24]. The scale bars represent 1 mm. (b) 3D surface envelope models for each fibril indicated in (a) are shown together with a comparison of the original straightened uncorrected fibril images and the simulated AFM images from the final 3D models. Segments of 500 nm are shown for each fibril model and 1 mm for the images for detail.

Discussion

Tip-sample convolution leads to lateral dilation of upward convex surface features on AFM topographs, which has been seen as a significant limitation to the usefulness of AFM images for structural biology applications. Here we show that the convolution effect results in the magnification of the sample top surface and non-uniform distribution of structural information on the image. The structural information, present in an un-gridded form at sub-pixel tip-sample contact points, can be recovered at its true lateral resolutions without loss of information using a contact-point based deconvolution algorithm, which is demonstrated here on an amyloid fibril formed from a short peptide sequence. This approach improves on the previous erosion-based deconvolution algorithms and facilitates the use of AFM imaging of nanostructures in structural studies. Furthermore, we show how the 3-dimensional coordinates encoded in the topographic data on AFM images and the helical symmetry of the twisted fibrils can be used to reconstruct 3D surface envelopes, allowing analysis of structural parameters, such as the fibril cross-sectional area, which are not otherwise present directly on AFM images of these samples. Thus, the reconstruction will facilitate the integration of 3D AFM envelope models with data from other structural biology tools for integrated global structural analysis. The moving window approach of 3D surface reconstruction conserves the high signal-to-noise feature of single-molecule imaging capability of the AFM, thus also allowing the intra-fibrillar and local structural variation to be preserved in the 3D model. Deconvolution and modelling facilitate the application of AFM to characterise and quantify amyloid fibril polymorphism at a true individual single molecule level.

Although there are many techniques available for studying the structures of biological macromolecules, each with their own advantages and disadvantages, AFM occupies a unique position among these tools due to its high signal-to-noise ratio capable of resolving morphological features of individual molecules. Ensemble averaging of structural information from many molecules is a key concept on which techniques like X-ray crystallography and cryo-EM rely and has led to the elucidation of numerous atomic and near-atomic resolution structural models of biological macromolecules. For example, recent advances in cryo-EM equipment and data processing have allowed the reconstruction of protein structures in various conformations from a set of micrographs and can even contain information on molecular dynamics [31]. However, due to the low signal-to-noise ratio of individual particles on cryo-EM images, only ensemble-average structures can be reconstructed. Although the overall resolution of AFM images of macromolecular assemblies does not yet reach the order of Ångströms and only molecular surface features can be probed, it is able to resolve morphological features at the level of individual molecules. This allows AFM to tackle biological problems in a unique way, especially in cases where polymorphism and structural variations of molecules is important for their biological effects. The lateral resolution, as defined by pixel size and tip radii, tends to be around 1-5 nm, although vertical resolution

can reach the order of sub-Ångströms. Using the contact-point deconvolution approach demonstrated here on AFM images of biological nano-filaments, recovery of the true lateral sampling resolution at tip-sample contact points was estimated to typically result in doubling of lateral resolution for helical nano-filaments. Experimental improvements, such as using a tip with parameters that maximise sampling enhancement and better scanners could lead to a more pronounced improvement in lateral resolution. Further improvements to the deconvolution and envelope reconstruction algorithm approach will also likewise help to improve the overall resolution achievable with AFM.

The structural basis of why amyloid fibrils can have functional roles in a wide range of organisms, associated with pathological symptoms of neurodegeneration, or simply exist as inert aggregates is not clear [14]. Individual filament 3D reconstruction using the approach presented here on AFM topographs could help elucidate the link between morphological features of the fibrils to specific biological responses of amyloid populations. Reconstructed 3D surface envelopes of amyloid fibrils could also be used in an integrative way with other structural biology techniques. For example, in recent years numerous cryo-EM reconstructions of amyloid filaments from *ex vivo* patient tissue have been resolved. These are ensemble averages from thousands or more of individual fibrils from the total fibril population, which in some cases may appear homogenous, but in other cases may be made up of a varying amount of fibril polymorphs. The number of some of these polymorphs within the population may also be too low for reconstruction, although these species might have some specific biological effect. 3D envelope reconstruction from AFM images could be used as a complementary technique as it allows the structural analysis and surface modelling of each individual fibril in the population, allowing rare members of the ensemble population as well as the population characteristics itself to be analysed. Classifying and quantifying the fibril structures could be used to determine the landscape of possible fibril structures within a specific population. Furthermore, this technique allows the intrafibrillar variation to be analysed, which may be indicative of fibril dynamics and stability. The 3D surface envelope could also be used in an integrative way with other techniques, contributing to the global information for modelling the atomic structure of a biomolecule.

The physics of AFM imaging is unique in producing its high signal-to-noise data at nano-scale and enables true single molecule approaches. Thus, the contact-point deconvolution and 3D envelope reconstruction approach presented here will facilitate the use of AFM for single-molecule structural studies. Imaging of any nano-structures with the AFM can benefit from the contact-point deconvolution approach to correct images while recovering structural information present at higher lateral resolutions. This includes high-speed AFM [32], which compromises spatial resolution for higher temporal resolution and allows imaging of biomolecule dynamics in the timescale down to milliseconds, and which could benefit from the computational deconvolution of image frames to recover the higher spatial resolution sampling of the sample surface. Furthermore, the 3D envelope reconstruction algorithm could also be applied to diverse biological samples with symmetries, including DNA, membrane proteins that form tubular arrays e.g. nicotinic acetylcholine receptor pore [33] and the mitochondrial outer membrane protein TspO [34], as well as helical or spherical virus capsids and cytoskeletal filaments. AFM imaging of various small molecules and polymers assembled into helical supramolecular arrangements which are widely used in chemistry, materials science and nanotechnology could, likewise, benefit from 3D surface reconstructions as AFM is widely used to characterise a wide range of such structures [35], for example polymer wrapped functionalised carbon nanotubes [36,37], Further developments could also lead to samples exhibiting different symmetries such as icosahedral viral capsids to be reconstructed. In conclusion, the approach reported here will facilitate the use of AFM for structural studies of individual molecules in complex populations, and for integrative structural biology analysis of single molecular assemblies and their assembly mechanisms.

Materials and Methods

Peptide amyloid fibril synthesis

The amyloidogenic peptide HYFNIF was synthesised by N-terminal acetylation and a C-terminal amidation. Multistage solid phase synthesis using Fmoc protection chemistry was used to generate a lyophilised powder with > 95% purity measured by HPLC (JPT peptide technologies, or Biomolecular analysis facility, University of Kent). The lyophilised powder was suspended in 100 µl of filter sterilized milli-Q water to a final concentration of 10 mg/ml. The solution was incubated at room temperature for 1 week prior to imaging.

AFM sample preparation and image acquisition

The peptide samples were diluted to 0.05 mg/ml in a solution of HCl (pH2, using filter sterilised milli-Q water). 20 µl of sample was deposited onto freshly cleaved mica (Agar scientific, F7013) and incubated for 10 minutes. Following incubation, the sample was washed with 1 ml of filter sterilised milli-Q water and then dried using a stream of nitrogen gas. Fibrils were imaged using a Multimode AFM with a Nanoscope V (Bruker) controller operating under peak force tapping mode with ScanAsyst probes (silicon nitride triangular tip with tip height = 2.5-2.8 µm, nominal tip radius = 2 nm, nominal spring constant 0.4 N/m, Bruker). Images were collected with a scan size of 6 x 6 µm with 2048 x 2048 pixel resolution. A scan rate of 0.305 Hz was used with a noise threshold of 0.5 nm and the Z limit was reduced to 1.5 µm. The peak force set point was set automatically, typically to ~675 pN during image acquisition. Nanoscope analysis software (Version 1.5, Bruker) were used to process the image data by flattening the height topology data to remove tilt and scanner bow.

Image data analysis

Fibrils were traced and digitally straightened [26,38,39] using an in-house application and the height profile for each fibril was extracted from the centre contour line of the straightened fibrils. The periodicity of the fibrils was then determined using fast-Fourier transform of the height profile of each fibril. For 2D FFT analysis, the fibril images were rotated with the straightened fibril axis aligned vertically. The images were subsequently zero-padded to squares prior to 2D FFT. All data analyses were performed using Matlab (MathWorks, Natick, Massachusetts)

Authors Contrubutions: L.L. designed the research, developed the analytical software tools, analysed the data and drafted the manuscript. C.J.S. and M.F.T. designed the research and analysed the data. L.C.S. designed the research, provided assembly reagents and methods, and analysed the data. W.F.X. designed the research, developed the analytical software tools, analysed the data, managed the research, and drafted the manuscript. The manuscript was edited through contributions of all authors.

Acknowledgements: We thank the members of the Xue, the CJ Serpell, and the LC Serpell groups, as well as the Kent Fungal Group for helpful comments throughout the preparation of this manuscript. We thank Ben Blakeman for acquiring and sharing the image data used in this report. This work was supported by funding from Biotechnology and Biological Sciences Research Council (BBSRC), UK grant BB/S003312/1, as well as Engineering and Physical Sciences Research Council (EPSRC), UK DTP grant (EP/R513246/1 for L.L).

References

1. Pfreundschuh M, Alsteens D, Wieneke R, Zhang C, Coughlin SR, Tampé R, Kobilka BK, Müller DJ. Identifying and quantifying two ligand-binding sites while imaging native human membrane receptors by AFM. Nat Commun. 2015 Nov 12;6:8857.
2. Parsons ES, Stanley GJ, Pyne ALB, Hodel AW, Nievergelt AP, Menny A, Yon AR, Rowley A, Richter RP, Fantner GE, Bubeck D, Hoogenboom BW. Single-molecule kinetics of pore assembly by the membrane attack complex. Nat Commun. 2019 May 6;10(1):1–10.
3. Chen Y, Radford SE, Brockwell DJ. Force-induced remodelling of proteins and their complexes. Curr Opin Struct Biol. 2015 Feb 1;30:89–99.
4. Ares P, Fuentes-Perez ME, Herrero-Galán E, Valpuesta JM, Gil A, Gomez-Herrero J, Moreno-Herrero F. High resolution atomic force microscopy of double-stranded RNA. Nanoscale. 2016 Jun 9;8(23):11818–26.
5. Moreno-Herrero F, Pérez M, Baró AM, Avila J. Characterization by atomic force microscopy of Alzheimer paired helical filaments under physiological conditions. Biophys J. 2004 Jan;86(1 Pt 1):517–25.
6. Nowakowski R, Luckham P, Winlove P. Imaging erythrocytes under physiological conditions by atomic force microscopy. Biochim Biophys Acta. 2001 Oct 1;1514(2):170–6.
7. Gross L, Mohn F, Moll N, Liljeroth P, Meyer G. The chemical structure of a molecule resolved by atomic force microscopy. Science. 2009 Aug 28;325(5944):1110–4.
8. Haruyama T, Sugano Y, Kodera N, Uchihashi T, Ando T, Tanaka Y, Konno H, Tsukazaki T. Single-unit imaging of membrane protein-embedded nanodiscs from two oriented sides by high-speed atomic force microscopy. Struct Lond Engl 1993. 2019 Jan 2;27(1):152-160.e3.
9. Ramalho R, Rankovic S, Zhou J, Aiken C, Rousso I. Analysis of the mechanical properties of wild type and hyperstable mutants of the HIV-1 capsid. Retrovirology. 2016 Mar 15;13:17.
10. Adamcik J, Jung J-M, Flakowski J, De Los Rios P, Dietler G, Mezzenga R. Understanding amyloid aggregation by statistical analysis of atomic force microscopy images. Nat Nanotechnol. 2010 Jun;5(6):423–8.
11. Bose K, Lech CJ, Heddi B, Phan AT. High-resolution AFM structure of DNA G-wires in aqueous solution. Nat Commun. 2018 May 17;9.
12. Pyne A, Thompson R, Leung C, Roy D, Hoogenboom BW. Single-molecule reconstruction of oligonucleotide secondary structure by atomic force microscopy. Small. 2014;10(16):3257–61.
13. Narita A, Usukura E, Yagi A, Tateyama K, Akizuki S, Kikumoto M, Matsumoto T, Maéda Y, Ito S, Usukura J. Direct observation of

the actin filament by tip-scan atomic force microscopy. Microsc Oxf Engl. 2016;65(4):370–7.
14. Lutter L, Serpell CJ, Tuite MF, Xue W-F. The molecular lifecycle of amyloid – Mechanism of assembly, mesoscopic organisation, polymorphism, suprastructures, and biological consequences. Biochim Biophys Acta BBA - Proteins Proteomics. 2019 Nov 1;1867(11):140257.
15. Jahn TR, Makin OS, Morris KL, Marshall KE, Tian P, Sikorski P, Serpell LC. The common architecture of cross-β amyloid. J Mol Biol. 2010 Jan 29;395(4):717–27.
16. Serpell LC, Fraser PE, Sunde M. [34] X-Ray fiber diffraction of amyloid fibrils. In: Methods in Enzymology. Academic Press; 1999. p. 526–36. (Amyloid, Prions, and Other Protein Aggregates; vol. 309).
17. Aubrey LD, Blakeman BJF, Lutter L, Serpell CJ, Tuite MF, Serpell LC, Xue W-F. Quantification of amyloid fibril polymorphism by nano-morphometry reveals the individuality of filament assembly. bioRxiv. 2020 Jan 15;2020.01.14.905877.
18. Butt H-J, Jaschke M. Calculation of thermal noise in atomic force microscopy. Nanotechnology. 1995 Jan;6(1):1–7.
19. O'Connor SD, Gamble RC, Eby RK, Baldeschwieler JD. Noise reduction in atomic force microscopy: Resonance contact mode. Rev Sci Instrum. 1996 Feb;67:393–6.
20. Binnig G, Quate CF, Gerber Ch. Atomic Force Microscope. Phys Rev Lett. 1986 Mar 3;56(9):930–3.
21. Canet-Ferrer J, Coronado E, Forment-Aliaga A, Pinilla-Cienfuegos E. Correction of the tip convolution effects in the imaging of nanostructures studied through scanning force microscopy. Nanotechnology. 2014 Oct 3;25(39):395703.
22. Keller DJ, Franke FS. Envelope reconstruction of probe microscope images. Surf Sci. 1993 Sep 10;294(3):409–19.
23. Villarrubia JS. Algorithms for scanned probe microscope image simulation, surface reconstruction, and tip estimation. J Res Natl Inst Stand Technol. 1997 Aug;102(4):425–54.
24. Morris KL, Rodger A, Hicks MR, Debulpaep M, Schymkowitz J, Rousseau F, Serpell LC. Exploring the sequence–structure relationship for amyloid peptides. Biochem J. 2013 Mar 1;450(Pt 2):275–83.
25. Keller D. Reconstruction of STM and AFM images distorted by finite-size tips. Surf Sci. 1991 Aug 1;253(1):353–64.
26. Egelman EH. An algorithm for straightening images of curved filamentous structures. Ultramicroscopy. 1986 Jan 1;19(4):367–73.
27. Hill SE, Robinson J, Matthews G, Muschol M. Amyloid protofibrils of lysozyme nucleate and grow via oligomer fusion. Biophys J. 2009 May 6;96(9):3781–90.
28. Fechner P, Boudier T, Mangenot S, Jaroslawski S, Sturgis JN, Scheuring S. Structural information, resolution, and noise in high-resolution atomic force microscopy topographs. Biophys J. 2009 May 6;96(9):3822–31.
29. Diaz R, Rice WJ, Stokes DL. Fourier-Bessel reconstruction of helical assemblies. Methods Enzymol. 2010;482:131–65.
30. Sachse C. Single-particle based helical reconstruction—how to make the most of real and Fourier space. AIMS Biophys. 2015 Jun 22;2(2):219.
31. Dong Y, Zhang S, Wu Z, Li X, Wang WL, Zhu Y, Stoilova-McPhie S, Lu Y, Finley D, Mao Y. Cryo-EM structures and dynamics of substrate-engaged human 26S proteasome. Nature. 2019 Jan;565(7737):49–55.
32. Lyubchenko YL. Direct AFM visualization of the nanoscale dynamics of biomolecular complexes. J Phys Appl Phys. 2018;51(40).
33. Miyazawa A, Fujiyoshi Y, Unwin N. Structure and gating mechanism of the acetylcholine receptor pore. Nature. 2003 Jun;423(6943):949–55.
34. Korkhov VM, Sachse C, Short JM, Tate CG. Three-dimensional structure of TspO by electron cryomicroscopy of helical crystals. Structure. 2010 Jun 9;18(6):677–87.
35. Yashima E, Ousaka N, Taura D, Shimomura K, Ikai T, Maeda K. Supramolecular helical systems: helical assemblies of small molecules, foldamers, and polymers with chiral amplification and their functions. Chem Rev. 2016 Nov 23;116(22):13752–990.
36. Bai Y, Olivier J-H, Bullard G, Liu C, Therien MJ. Dynamics of charged excitons in electronically and morphologically homogeneous single-walled carbon nanotubes. Proc Natl Acad Sci. 2018 Jan 23;115(4):674–9.
37. Zheng M, Jagota A, Semke ED, Diner BA, Mclean RS, Lustig SR, Richardson RE, Tassi NG. DNA-assisted dispersion and separation of carbon nanotubes. Nat Mater. 2003 May;2(5):338–42.
38. Xue W-F. Chapter 2 - Amyloid fibril length quantification by atomic force microscopy. In: Uversky VN, Lyubchenko YL, editors. Bio-nanoimaging. Boston: Academic Press; 2014. p. 17–25.
39. Xue W-F, Homans SW, Radford SE. Amyloid fibril length distribution quantified by atomic force microscopy single-particle image analysis. Protein Eng Des Sel. 2009 Aug;22(8):489–96.